Imperial College London

ENGINEERING CARDIAC MODELS THROUGH ADVANCED PATTERNING TECHNOLOGIES

Ekaterina Pchelintseva

Submitted in accordance with the requirements for the degree of Doctor of Philosophy

and Diploma of Imperial College London

Imperial College London
Department of Materials

DECEMBER 16, 2022

DECLARATION OF ORIGINALITY

I, Pchelintseva Ekaterina, hereby declare that:

1). All the work presented in this thesis was performed by me, unless stated otherwise.

2). Any contributions from collaborators are acknowledged and clearly stated either in the corresponding Materials section of each chapter, in the context of a particular experiment, or in the appropriate figure legends.

3). All the information and resources from previously published works that have been used to develop this thesis have been appropriately recognised and listed in the references section.

4). All the work for this thesis was performed at Imperial College London (UK) and Karolinska Institute (Sweden).

COPYRIGHT DECLARATION

'The copyright of this thesis rests with the author. Unless otherwise indicated, its contents are licensed under a Creative Commons Attribution-NonCommercial 4.0 International Licence (CC BY-NC).

Under this licence, you may copy and redistribute the material in any medium or format. You may also create and distribute modified versions of the work. This is on the condition that: you credit the author and do not use it, or any derivative works, for a commercial purpose.

When reusing or sharing this work, ensure you make the licence terms clear to others by naming the licence and linking to the licence text. Where a work has been adapted, you should indicate that the work has been changed and describe those changes.

Please seek permission from the copyright holder for uses of this work that are not included in this licence or permitted under UK Copyright Law.'

ABSTRACT

Recapitulating microscopic cellular organisation is key to the successful engineering of functional bioinspired tissues. In cardiac muscle, the alignment of cardiomyocytes plays a major role in the synchronization of conduction and contraction, necessary for efficient heart function. *In vitro* engineered cardiac models seek to replicate this structural and functional anisotropy; however, they require laborious fabrication methods, or have limited spatial resolution.

Here, two different advanced patterning approaches are combined with human induced pluripotent stem cell (hiPSC) differentiation protocols to produce three independent micropatterned cardiac models. Acoustic cell patterning is a non-invasive, label-free, cytocompatible technique, able to rapidly arrange cells within a fluid medium into uniform structures. First, the development process of a novel acoustic device is outlined, ultimately combining ultrasound fields with commercial multielectrode arrays to generate two-dimensional anisotropic arrays of hiPSC-derived cardiomyocytes (hiPSC-CMs) with the potential for quantifiable output. The resultant model adds a degree of structural complexity to standard monolayer cultures used for high-throughput drug screening. Second, 2½-dimensional anisotropic cardiac fibres with physiologically-relevant dimensions, improved electrophysiological properties and directional signal propagation are engineered by immobilising acoustically-patterned hiPSC arrays in hydrogels and subjecting them to cardiac differentiation *in situ.* Notably, this is the first demonstration of acoustic patterning of hiPSCs with subsequent directed differentiation, which is anticipated to be a valuable platform for engineering other spatially organised tissues. Third, an *in situ* cardiac differentiation protocol was applied to hiPSC clusters encapsulating a highly ordered fibrous scaffold, creating synchronous interconnected cardiac meshes suitable for the injured myocardium remuscularisation. The preliminary results of mesh-mediated cardiomyocyte transfer to an *ex vivo* cardiac tissue highlight the importance of interface stability and duration for efficient cell therapy.

Overall, the work of this thesis emphasises how implementing acoustic or material-guided cell patterning in cardiac engineering can improve the functional performance and biological relevance of next generation *in vitro* models.

SCOPE OF THE THESIS

The work in this thesis showcases how acoustic cell patterning or ordered fibrous scaffolds can be used to produce three distinct patterned cardiac models. Two of these models aim to replicate the aligned organisation of cardiomyocytes in heart tissue through acoustic patterning, with one model using pre-differentiated hiPSC-CMs, while the other uses hiPSCs and later directs their differentiation to cardiomyocytes *in situ*. The third model makes use of fibrous scaffolds for structural support of differentiating hiPSCs, making an interconnected cardiac patch for cardiac repair.

Chapter 1 introduces the general concepts of cardiac tissue engineering, including the native organisation of cardiomyocytes in the myocardium, stem cell cardiac differentiation protocols, types of existing engineered cardiac platforms, ways of assessing the properties of engineered tissues, and available technologies for cell patterning.

Chapter 2 focusses specifically on acoustic cell patterning as a method for the spatial organisation of cardiomyocytes in 2D combined with a quantifiable readout for drug screening applications. The results show a detailed design process and optimisation of a novel device that integrates solution-based acoustic patterning of hiPSC-CMs with multielectrode arrays.

Chapter 3 describes how anisotropic cardiac fibres can be engineered by applying acoustic cell patterning at the stem cell stage. The patterned structures are immobilised within a hydrogel and the construct is directed to cardiac fate using *in situ* differentiation. The cardiac fibres are then characterised using gene expression analysis, immunostaining and electrical field stimulation.

Chapter 4 demonstrates how an ordered fibrous scaffold can be used a substrate for hiPSC attachment and expansion prior to cardiac differentiation. The resultant interconnected cardiac meshes are then characterised using immunostaining and electrical field stimulation, and their potential for tissue remuscularisation is explored using *ex vivo* rat myocardial slices.

Chapter 5 provides a summary of the key results from the previous chapters and compares the features of each new engineered cardiac models with other systems in their respective fields.

ACKNOWLEDGEMENTS

I am extremely fortunate to stand tall on the shoulders of so many giants, that it would take another thesis just to acknowledge all the people without whom this work, this writing and this scientist would not have been possible. At various times you all believed in me, motivated me, supported me, and you were all right – turns out, I can do it, but I would not have done it without you. No words can truly grasp the influence of these people on me through the years, but I will try my best to capture a fraction of it.

First, I would like to thank my supervisor Prof. Molly Stevens, for believing in me even when I tried my hardest to convince her she shouldn't and for supporting me through the years. Molly, thank you for giving me this opportunity of a lifetime and for masterfully building such an incredibly curious, intelligent, supportive, kind and extremely fun scientific family that is the Stevens Group. I don't think there is any other workplace that could match the environment of your group, and it has been an honour and a privilege to be contribute to it through the years. The members of the Stevens Group have made me who I am today, and on many occasions I looked around me and couldn't believe that these extraordinary people are my colleagues and friends.

I would like thank Dr Alice Agliano, who has been my postdoctoral supervisor, my mentor inside the lab and out, my role model, my friend and my closest confidante. Alice, this win is as much yours as it is mine. For all your scientific knowledge, for your kind words, for cheering me on when it felt like I couldn't do it, for always making me feel heard and valid – thank you, truly, from the bottom of my heart, I would not have done it without you. Thank you for always teaching me how to extract the key goals from the endless parameter space of multidisciplinary research, and for giving me all the necessary tools to achieve them.

I would also like to thank my second postdoctoral supervisor, Dr James Armstrong, for patiently showing this lost biologist the ropes of acoustic cell patterning through the years. James, your infectious enthusiasm for science has always been a source of inspiration. Thank you for being excited about my work even when I struggled to, and, importantly, for moulding my scientific

approach to what it has become today. Thank you for teaching me the art of clear and intricate writing (still learning!) and for showing me, by example, that a crazy messy desk space doesn't mean you can't be a good scientist.

To the both of you I am eternally grateful. These skills and memories will stay with me for the rest of my life and I will never take them for granted.

I would also like to thank Dr Richard Wang, for his wizardly MATLAB skills that created codes for analysis of calcium imaging (often after 5 hour-long discussions over each line of code!). Rich, thank you also for always discussing all things cardiac with me, and for always making me feel like your equal even though you are so much more knowledgeable about science than me. Thank you for feeding my cells on hundreds of occasions whenever I needed a break and for being the greatest friend. I hope even years after I finish, you will still complain about the Red Bull F1 team.

Huge thank you to the two pillars of my PhD life and beyond: Dr Leah Frenette and Ms Brittany Rae, who made this time full of colour, music and laughter. I have experienced life in my 20s together with you, we almost moulded into one person, making so many memories along the way. Thank you for the daily coffees, for Bake-Off sweepstakes (I owe you bakes, I know, I know), for wine Fridays, for stitching club, for dancing in the garden, for the best lockdown birthday I could ever imagine, for conspiring mischievous pranks together, for indulgent chakshucherias, for the warmest hugs, for your unconditional love. Additional thank you for proofreading this thesis with me the night of submission and keeping me calm!

Leah, thank you for teaching me that being fun and a life of the party makes a person an even better scientist. You really made me who I am today and it is such an honour to see the resemblance with you. Thank you for the ducks, for my music taste, for Ha-Lu-Mi, for always being up for an adventure, for never missing important life events (like me getting my passport!!), for countless leaving do collaborations (these PowerPoint editing skills really helped with figure making!), for your wittiest sense of humour that never fails to make me laugh, for often being my voice of reason, for taking time to brainstorm my project with me and always having the greatest insights, for the advent

calendar that made me feel so loved. For your endless thoughtfulness and kindness, that got me through the dark days, for your wisdom in giving me perspective. You mean the world to me.

Brittles, thank you for your kindness, your constant encouragement, for singing Crazy Ex-Girlfriend songs in the cell lab like nobody is listening, for always being a friend I could rely on, for taking care of my cells so expertly, for organising the logistics and paperwork for me (which is really not my strongest suit), for being the greatest lab manager the Stevens group has seen, for taking me on walks in COVID when I was going seriously stir-crazy, for teaching the art of flowy skirts and mom jeans, for trying to get me to do tag, for the countless cobs and your most delicious bakes, especially the citrus ones for my birthdays. Your smile brightened up my every day and it has been an absolute honour to be your friend.

I would also like to thank my PhD cohort for sharing these years with me and for always lending me a hand. Dr Charlotte Lee-Reeves, for the sass, for gossiping in the microscopy room and for being the most loyal and protective friend. Dr Maxine Chan, for her strong will, for always giving honest feedback and for encouraging me to live life to the fullest. Dr Raya El Laham, for her infinite kindness and care, for spreading positivity through the office and for the warmest hugs. Dr Daniel Boland, for his calm reassurance and for the pugs. Going through the PhD with you guys was so fun and full of so much laughter, and I already miss the days when we saw each other daily. Dr Kaja Ritzau-Reid, for her invaluable contribution on the cardiac meshes project, both intellectually and experimentally, for (trying to) teach me discipline and for being a very wise friend.

I am also very grateful to Dr Alessondra Speidel, for taking me under her wing at the group weekend in 2017 and never leaving me since, for her scientific rigour, for encouraging me and checking in on me every two days while I was writing, for her positive attitude to science and life. Dr Jonathan Wojciechowski, for his help with 3D printing, GelMA and rheology, for his unlimited curiosity, and for teaching me that in the world where anyone can be clever, you need to distinguish yourself by being kind. Dr Adam Creamer, for conversations about everything in the world, for always hearing me out and checking in on me, and for the incredibly fun times we spent as colleagues (and definitely not

friends). Dr Christopher Larry Grigsby, for melt electrospinning writing of the PCL scaffolds in short notices and in large abundances, but also for the escapades of Christmas parties and Group Weekends, and for embracing the tea cake crew. To the Burgers and Doughnuts aka Taco party club (Dr Stacey Skaalure and Sabrina Skeete) – thank you for welcoming me and showing me the way in Stevens Group when I was only little, for accepting me as your own and for supporting me throughout, with good food, great music and even better conversations. To Dr Sebastien Callens,, my FFF, for his warmest smile and motivational chats. To my original crew: Dr Axel Moore, Dr Eoghan Cunnane, Dr Hakon Hogset (my BFF), Dr Isaac Pence, Dr Ioanna Mylonaki, Dr Daniel Richards – thank you for looking out for me, I miss you and I can't wait to reunite at the alumni party someday. Thank you to the students and postdocs that have been cheering me on through the stresses of the final year, always making me laugh: James Foote, Thomas Benge, Tristan Dell, Ijeoma Patrick, Sara Carvalho, Lino Prados Martin. A special thank you to Thomas Fernandez-Debets, whose thoughtfulness has no boundaries, for always lending me an ear, for TFD café and for tolerating my sass. Huge thanks also to Meg McCandless, who kept me in check with daily morning coffees and pre-lab pep talks.

I would also like to thank my collaborator and second supervisor, Professor Cesare Terracciano, for so warmly welcoming me into his group and for always respecting my work. Thank you for your guidance through cardiac electrophysiology, for your patience with the challenges of multidisciplinary science, for all your advice through the years and for your passion for science. I would also like to thank his team, who have prepared myocardial slices for the cardiac mesh experiments: Dr Worrapong Kit-Anan, Dr Raquel Nunez-Toldra and Laura Nicastro. Thank you for your time and your knowledge, I really appreciate it.

I also would like to thank several people for their expertise that was instrumental to the data collection and analysis for this thesis. First, I would like to recognize the Imperial College Facility for Imaging by Light Microscopy, in particular, Dr Stephen Rothery and Dr David Gaboriau for their expertise in image analysis and microscopy. I would also like to acknowledge Mr Steven Nelson from Imperial Mechanical Instrumentation Workshop for laser-cutting of the acoustic patterning devices.

Thank you to Dr Hyemin Kim for her help with calcium handling frequency analysis. I would also like to thank the Stevens Group support staff for making the work in the group so smooth, and in particular Dr Akemi Nogiwa-Valdez, for her impressive attention to detail and all the help with submission. I also gratefully acknowledge the funding sources that made the work of this thesis possible: the British Heart Foundation and the Rosetrees Trust.

I would like to also thank my old mentor, Professor Mustafa Djamgoz, who has seen the potential in me as a wide-eyed 19 year-old undergraduate and took a chance on me. Thank you for always thinking so highly of me despite all odds, for treating me like a serious scientist from day 1, for our priceless writing sessions together, where we debated the meaning of every word. For guiding me through my first ever academic writing, for trusting me with peer review, for always pushing me to be better, for our eureka moments and telepathy. Your opinion has and always mean a lot to me.

There are also many people from outside of my academic work that have helped make this PhD thesis happen. Firstly, thank you to Dr Caoimhe Canavan, who has been my biggest cheerleader from the very first day (she celebrated me getting my funding like it was her own), and I would not have completed this PhD without her. Caoimhe, thank you for being there literally through thick and thin, for lifting me every single time I refused to get up. Thank you for teaching me compassion and for defending me to me, which is not an easy job. Thank you also for all the cycling, for watching every single crime drama with me, for loving me truly unfiltered, with all the good and the bad. You are the best friend I could have ever dreamed of.

Thank you to my university friends, who have always reminded me of my roots and that I am bigger than my experiments. To Mollie Gupta, for always giving me the peace of mind and for teaching me how to put myself first. To Will Downham, for subtly taking care of me, often through the means of golf, baking and Taylor Swift. To Giacomo Boscaini-Gilroy, for reminding me that life shouldn't be taken too seriously. To Nick Dunn, for being the stable source of calm energy. To Rachel Renken, for all the walking Wednesdays, for taking interest in every detail of my hour-long stories and for being

such an inspirational successful and caring person. You guys have treated me with such kindness, and I am forever grateful.

Thank you to my housemates, old and new. To Dr Maruša Levstek, for making our house a home, for literally feeding me the most part of the last year, for all the teas, for all the times she had to reassure me. You have been a blessing and I am so grateful for all you do for me. To David Lamb, for doing the same back when we lived together. For always listening to me, for curing any sadness away with some takeaway and a good vinyl, for the countless belly laughs we shared, for all the silliness and the singing. Big thanks go out also to the London Humanist Choir, for accompanying my early PhD days with wonderful music and companionship.

Finally, I would like to thank my family, for the fundamental values that they taught me and for always being by my side. To my brother, Ivan Pchelintsev, for having to be the older one this year and looking out for me, thank you for stepping in. I can't wait to spend the rest of my life hanging out with you. To my dad, Sergey Pchelintsev, for his inherent curiosity for science and for teaching me by example how to think outside the box. Dad, you used to say that for me to make you proud it wouldn't take much – I would just need to create a crystal that can store your consciousness. Sorry, I didn't go for the minds, but I now can grow hearts through three different mediums – I hope that's a worthy compromise and you still will be proud. To my mum, Olga Pchelintseva, who has been my rock every single day of my life. Mum, you are the best person I know, and I love you more than anything. You have shown me what it takes to be a strong woman, you have been the wind under my wings, you made me learn English, you sacrificed so much to give me the life in Europe I couldn't have ever dreamed of, you kept me safe, you always accepted me for who I am and didn't expect anything in return. You have always said that you and I together can achieve anything. Well, we did it, Mum, we finished the PhD.

TABLE OF CONTENTS

Abstract 2

Scope of the Thesis 3

Acknowledgements 4

Table of contents 10

List of figures 18

List of tables 24

List of abbreviations 25

Chapter 1. Introduction 30

1.1 Cardiac muscle biology and disease 30

1.1.1 Structure and function of heart muscle 30

1.1.2 Cardiovascular disease burden 34

1.1.3 Models of cardiac tissue 35

1.2 Cell sources for cardiac tissue engineering 38

1.2.1 Isolated cardiomyocytes 38

1.2.2 Immortalised cell lines 39

1.2.3 Pluripotent stem cells 40

1.3 Stem cell technologies for cardiac engineering 42

1.3.1 Evolution of cardiac differentiation protocols 42

1.3.2 Differences between stem cell-derived and adult cardiomyocytes 45

1.4 Assessment of cardiac tissue platforms 49

1.4.1 Structural evaluation 51
1.4.2 Gene expression analysis 52
1.4.3 Metabolic activity 52
1.4.4 Contractility 52
1.4.5 Electrophysiology 54
1.5 Applications of cardiac tissue models 57
1.5.1 Cardiogenesis modelling 57
1.5.2 Disease modelling 58
1.5.3 Drug screening 59
1.5.4 Regenerative medicine 60
1.6 Approaches to generating patterned cardiac models 61
1.6.1 Lithography-based topographical cues 62
1.6.2 Cell-laden fibrous biomaterial scaffolds 63
1.6.3 3D bioprinting 64
1.6.4 Remote field engineering 65
Chapter 2. Solution-based acoustic patterning for 2d cellularised cardiac drug screening models .....
..... 68
2.1 Introduction 68
2.1.1 Acoustic cell patterning 68
2.1.1.1 Acoustic patterning technique overview and principles 68
2.1.1.2 Types of acoustic patterning 70
2.1.1.3 Solution-based acoustic cell patterning 73

2.1.2 Multielectrode Arrays 74
2.1.2.1 Electrophysiology measurements 74
2.1.2.2 MEA structure and function 75
2.1.2.3 Cardiomyocyte patterning on MEA 77
2.2 Aims and objectives 77
2.3 Materials and methods 79
2.3.1 Device fabrication 79
2.3.2 Huygens pressure modelling 81
2.3.3 MDA-MB-231 culture and fixation 81
2.3.4 hiPSC culture and differentiation 82
2.3.5 Solution-based acoustic cell patterning protocol 84
2.3.6 Image analysis 85
2.3.7 Imaging 85
2.4 Results 86
2.4.1 Typical acoustic patterning device components and functionality 86
2.4.2 Solution-based acoustic cell patterning on MEA 89
2.4.3 Effects of central cavity geometry on patterning quality 93
2.4.3.1 Huygens pressure modelling 94
2.4.3.2 The modular acoustic patterning device 97
2.4.4 Optimisation of live hiPSC-CM patterning on MEA 101
2.4.4.1 Patterning parameter optimisation 101
2.4.4.2 Acoustic patterning of hiPSC-CMs on MEA 106

2.5 Conclusions and future work 109

Chapter 3. *In situ* cardiac DIfferentiation of acoustically-patterned stem cell constructs. 113

3.1 Introduction 113

3.1.1 Hydrogel properties, applications and fabrication methods 113

3.1.2 GelMA-based hydrogels in tissue engineering 116

3.1.3 Hydrogel bioprinting 118

3.1.4 Acoustic patterning in hydrogel systems 120

3.1.5 hiPSC *in situ* differentiation 123

3.2 Aims and objectives 125

3.3 Materials and methods 127

3.3.1 GelMA synthesis 127

3.3.2 Fluoraldehyde assay 128

3.3.3 Rheology measurements 129

3.3.4 Acoustic cell patterning in hydrogels 130

3.3.4.1 Device fabrication 130

3.3.4.2 Cell culture 131

3.3.4.3 Patterning setup and preparation 132

3.3.4.4 Tissue engineering 133

3.3.5 Gel immunostaining 134

3.3.5.1 Single-layer gels 134

3.3.5.2 Double-layer gels 135

3.3.5.3 Imaging 135

3.3.6 RNA extraction, cDNA synthesis and RT-qPCR 136
3.3.7 Ultrasound exposure studies 138
3.3.7.1 AlamarBlue™ metabolic activity assay 138
3.3.7.2 PicoGreen DNA quantification assay 140
3.3.7.3 Viability staining 141
3.3.8 Calcium imaging and electrical stimulation 142
3.3.9 Analysis 143
3.3.9.1 Frequency analysis 143
3.3.9.2 Activation maps and directionality analysis 144
3.3.9.3 Statistical analysis 145
3.4 Results and discussion 146
3.4.1 Optimisation of hiPSC patterning in hydrogels 146
3.4.1.1 Device design and patterning conditions optimisation 146
3.4.1.2 GelMA degree of functionalisation quantification 149
3.4.1.3 Light source optimisation 152
3.4.1.4 Hydrogel rheology for assessment of viscoelastic properties 156
3.4.1.5 GelMA batch variation assessment 158
3.4.1.6 Cell density optimisation 163
3.4.1.7 CHIR induction timing optimisation 163
3.4.2 Effects of ultrasound and light exposure on hiPSC physiology 171
3.4.2.1 Viability assessment in acoustically-patterned cardiac constructs 172
3.4.2.2 Pluripotency assessment in acoustically-patterned cardiac constructs 173

3.4.2.3 Metabolic activity and proliferation assessment upon ultrasound and light exposure 174

3.4.3 Differentiation of patterned cardiac constructs *in situ* 179

3.4.4 Characterisation of acoustically-patterned cardiac constructs 187

3.4.4.1 Gene expression during in situ differentiation 187

3.4.4.2 Immunofluorescent staining 195

3.4.5 Functional electrophysiological assessment of differentiated cardiac hydrogels 203

3.4.5.1 Spontaneous calcium activity 203

3.4.5.2 Directional propagation of calcium signal in patterned hydrogels 204

3.4.5.3 Electrical field stimulation of acoustically-patterned hydrogels 215

3.5 Conclusions and future work 219

Chapter 4. Interconnected fibre-reinforced cardiac scaffolds for tissue remuscularisation 224

4.1 Introduction and motivation 224

4.1.1 Approaches and challenges of cardiomyocyte cell therapies 224

4.1.1.1 Intramyocardial injection for cardiomyocyte delivery 224

4.1.1.2 Injectable hydrogel-based systems for increased cardiomyocyte retention 226

4.1.1.3 Cardiac patches as an alternative mode of cell therapy 228

4.1.2 Electrospinning methods for cardiac tissue engineering 230

4.1.2.1 Principles of electrospinning 230

4.1.2.2 Melt electrospinning writing 231

4.1.2.3 Melt electrospun fibrous scaffolds in tissue engineering 233

4.1.3 Living myocardial slices for *ex vivo* cardiac tissue modelling 234

4.2 Aims and objectives 237

4.3 Methods 239

4.3.1 Melt electrospinning writing 239

4.3.2 Scanning electron microscopy (SEM) 239

4.3.3 Cell culture 240

4.3.3.1 Scaffold preparation for cell culture experiments 240

4.3.3.2 In situ hiPSC differentiation on the scaffold 240

4.3.3.3 hiPSC-CM seeding on the scaffold for slice interface optimisation 241

4.3.4 Optical mapping 242

4.3.4.1 Calcium imaging 242

4.3.4.2 Generation of activation maps 242

4.3.4.3 Calcium image analysis 243

4.3.5 Cardiac slice preparation and co-culture with cardiac meshes 244

4.3.6 Viability assessment of Histoacryl tissue adhesive 246

4.3.7 Force transducer measurements and analysis 246

4.3.8 Fluorescence immunostaining 247

4.3.8.1 Wholemount immunostaining of cardiac meshes 247

4.3.8.2 Optical tissue clearing protocol 248

4.3.8.3 Wholemount immunostaining of cardiac mesh – cardiac slice co-cultures 249

4.3.9 Image acquisition 249

4.4 Results and discussion 250

4.4.1 Optimisation of PCL scaffolds for stem cell culture and cardiac differentiation 250

4.4.2 Cell seeding density optimisation for cardiac differentiation 253
4.4.3 Generation of two distinct cardiac construct types through geometry modulation .. 256
4.4.4 Morphological and electrophysiological changes in cardiac meshes 258
4.4.5 Immunofluorescent cell phenotype profiling of cardiac meshes 263
4.4.6 *Ex vivo* myocardiac slice as a model for cardiomyocyte delivery 267
4.4.7 Optimisation of cardiac mesh and slice interface 271
4.4.7.1 Pilot interface study 271
4.4.7.2 Histoacryl tissue adhesive-based interface strategy 275
4.4.7.3 Refining the histoacryl tissue adhesive-based strategy for mesh-slice interface ... 281
4.4.7.4 Troubleshooting the slice-mesh interface 284
4.4.7.5 Investigation of the required timescale for hiPSC-CM transfer from the cardiac mesh 286
4.5 Conclusions and future work 289
5 Conclusions 294
6 References 302

LIST OF FIGURES

Figure 1-1 **The structure of a mammalian heart, showing the tissue layers of the cardiac wall.**.....30

Figure 1-2 **Hierarchical organisation of cardiac tissue.** 33

Figure 1-3 **Classes of cardiac tissue engineered models arranged by descending throughput and ascending biological representativeness**.....38

Figure 1-4 **Signalling pathways in cardiac development.**.....44

Figure 1-5 **Categories and methods of assessing the structural and functional properties of engineered cardiac models.** 51

Figure 1-6 **Overview of cell patterning methods.**.....62

Figure 2-1 **Acoustic cell patterning.** 69

Figure 2-2 **Acoustic patterning setup examples.** 73

Figure 2-3 **Schematic representation of a typical acoustic patterning device.** 79

Figure 2-4. **Acoustic patterning setup.**.....86

Figure 2-5 **A typical acoustic patterning device.**.....88

Figure 2-6 **MEA-housing acoustic patterning device fabrication and testing.**. 90

Figure 2-7. **MEA cell culture cavity optimisation.**.....92

Figure 2-8 **Consistency of patterning on an MEA chip across four independent experiments**. 93

Figure 2-9 **Huygens pressure field modelling of the acoustic devices with varying central cavity and transducer dimensions**.....97

Figure 2-10 **Modular acoustic patterning device design and assembly.** 99

Figure 2-11 **Design iterations of the acoustic component of the modular device.** 100

Figure 2-12 **KP3 device characterisation.**.....102

Figure 2-13 **Optimisation of cellular array alignment with the MEA electrode grid.**.....105

Figure 2-14 **Optimisation of sterile conditions for the culture of acoustically patterned live hiPSC-CMs on MEA chips**.....107

Figure 2-15 **Live cell patterning in sterilised KP3 device.** 108

Figure 3-1 **Schematic of the reaction schemes for gelatin methacryloyl (GelMA) synthesis using (A) the protocol by Meinert et al., 2016, (B) the protocol by Hoon Lee et al., 2015**. 127

Figure 3-2 **Acoustic patterning device design optimisation** 148

Figure 3-3 **Effect of temperature on acoustic patterning in thermosetting GelMA hydrogels.** 149

Figure 3-4 **Fluoraldehyde assay results of home-made GelMA characterisation.**. 151

Figure 3-5 **Survival of hiPSCs in home-made GelMA hydrogels.** 151

Figure 3-6 **Effect of 365 nm UV light exposure on hiPSC cell growth.**. 153

Figure 3-7 **Optimisation of gelation timing for porcine (A) and fish (B) GelMA hydrogels cross-linked by LAP photoinitiator with 405 nm blue light source.** 154

Figure 3-8 **Effect of light source on hiPSC survival and differentiation**. 155

Figure 3-9 **Viscoelastic properties of commercial porcine and fish GelMA, purchased from Gelomics.** 157

Figure 3-10 **Visual comparison between 7 samples of porcine GelMA from batch 2.** 159

Figure 3-11 **Variability in mechanical properties of 7 different bottles of commercial GelMA samples of batch 2**. 160

Figure 3-12 **Comparison of storage and loss moduli between the two batches of porcine GelMA and one batch of fish GelMA.** 161

Figure 3-13 **Cell density optimisation of hiPSC acoustic patterning in GelMA.** 163

Figure 3-14 **Pattern preservation in acoustically-assembled hiPSC arrays over the course of cardiac differentiation**. 165

Figure 3-15 **Optimisation of differentiation induction timing**. 167

Figure 3-16 **Effect of differentiation induction timing on pattern preservation in acoustically-patterned fish GelMA hydrogels** 167

Figure 3-17 **Effect of differentiation induction timing on pattern preservation in acoustically-patterned porcine GelMA hydrogels**. 168

Figure 3-18 **Calcium activation maps of functional cardiomyocytes in differentiated acoustically-assembled fish and porcine GelMA hydrogels, with differentiation initiated 1 day, 2 days or 3 days after patterning**. 171

Figure 3-19 **Widefield fluorescent microscopy of a LIVE/DEAD® viability assay of acoustically-patterned and unpatterned porcine GelMA hydrogel constructs on day 0 (A-C) and day 1 (D-F) after exposure to ultrasound**. 173

Figure 3-20 **Pluripotency marker fluorescence immunostaining of acoustically-patterned hiPSC clusters in porcine GelMA hydrogels 1 day after ultrasound exposure.**. 174

Figure 3-21 **AlamarBlue™ assay 48 hours after hiPSC ultrasound (2.0 MHz) and blue light (405 nm, 1 minute) exposure on hiPSC metabolic activity**. 176

Figure 3-22 **PicoGreen quantification of DNA content 1 day (A), 3 days (B) and fold change (C) indicating proliferation rate after hiPSC ultrasound (2.0 MHz) and blue light (405 nm, 1 minute) exposure.** 178

Figure 3-23 **Fabrication of supporting GelMA layer for prevention of interconnectivity between adjacent patterned cellular arrays.** 181

Figure 3-24 **Changes in the morphology of acoustically-patterned hiPSCs during differentiation in single layer and double layer GelMA hydrogels.** 183

Figure 3-25 **Distribution and activation sequence of functional cardiomyocytes within acoustically-patterned single layer (A) and double layer (B) GelMA hydrogels.** 184

Figure 3-26 **Immunofluorescent staining of cTnT showing the distribution of cardiomyocytes in single layer (A) and double layer (B) acoustically-patterned GelMA hydrogels.** 185

Figure 3-28 **Ct values of three candidate housekeeping genes: GAPDH, RPL13 and HRPT1 measured in four acoustically-patterned samples collected from two different timepoints..** 188

Figure 3-27 **Schematic of the timeline for RT-qPCR sample collection.** 188

Figure 3-29 **Changes in relative expression of pluripotency (POU5F1, NANOG), intermediate differentiation (MESP1, ISL1) and cardiac (TNNT2 and MYH6) genes in acoustically-patterned and unpatterned samples over time**. 190

Figure 3-30 **Post-hoc analysis of Ct values of two housekeeping genes (GAPDH and RPL13) in patterned (A,C) and unpatterned (B,D) samples separated by time of sample collection**. 194

Figure 3-31 **Comparison of relative gene expression of pluripotent (POU5F1 and NANOG) and cardiac (TNNT2 and MYH6) target genes between patterned and unpatterned samples collected at day 20+**..... 195

Figure 3-32 **Fluorescence immunostaining protocol optimisation of double layer acoustically-patterned cardiac gels**. 197

Figure 3-33 **Immunofluorescent staining for pluripotency marker (SOX2) of two differentiated acoustically-patterned hydrogels (replicate 1 and replicate 2) 20 days after ultrasound exposure and one control undifferentiated patterned gel 1 day after ultrasound exposure**. 198

Figure 3-34 **Overview confocal images of immunostaining of cardiomyocyte markers' cTnT (red) and α-Actinin (yellow) distribution in three double layer acoustically-patterned hydrogels differentiated up to day 20**. 199

Figure 3-35 **10x magnification confocal imaging of immunostaining for cardiomyocyte marker cTnT (red) and endothelial cell marker-CD31 (yellow) distribution in three double layer hydrogels differentiated up to day 20**. 201

Figure 3-36 **Medium magnification confocal imaging (10x) of immunostaining for cardiomyocyte marker α-actinin (red) and smooth muscle/myofibroblast cell marker α-SMA (green) distribution in three double layer hydrogels differentiated up to day 20**. 202

Figure 3-37 **Spontaneous calcium activity in acoustically-patterned double layer cardiac hydrogels on day 20 after ultrasound exposure**. 204

Figure 3-38 **Frame-by-frame analysis of calcium signal propagation in three independent unpatterned samples**. 205

Figure 3-39 **Frame-by-frame analysis of calcium signal propagation in three independent patterned samples.**. 207

Figure 3-40 **Sequential calcium activation along the longitudinal axis of acoustically-patterned cardiac fibres**. 208

Figure 3-41 **Progression of a frame obtained from calcium imaging through pre-processing steps**. 210

Figure 3-42 **Image pre-processing artefacts after applying binary functions 'Close gaps' and 'Fill holes'** 211

Figure 3-43 **Processed frames of the calcium videos using the original pre-processing protocol (left) or the updated protocol with a rolling projection preceding the binary function step**. 212

Figure 3-44 **The effect of 'Close gaps' and 'Fill holes' binary functions on the vector angle distribution of calcium propagation signal in the sample from Figure 3-42A.**. 213

Figure 3-45 **A typical stimulation profile and a representative output trace from a single regin of interest (ROI) during the electrical field stimulation experiments.** 215

Figure 3-46 **Calculated output frequency distribution in patterned (A) and unpatterned (B) samples during spontaneous calcium activity and during 1 Hz, 2 Hz and 3 Hz pacing.** 216

Figure 3-47 **Recorded output frequency of calcium signal in acoustically-patterned cardiac fibres and unpatterned controls under 1 Hz, 2 Hz, 3 Hz electrical field stimulation.**. 217

Figure 4-1 **Electrospinning methods.**. 232

Figure 4-2 **SEM imaging of structural organisation of uncoated (A,C,E) and coated (B,D,F) 1000 µm melt electrospun PCL scaffolds.** 251

Figure 4-3 **Optimisation of hiPSC seeding on the fibrous PCL scaffolds**. 252

Figure 4-4 **Brightfield images of the uniform distribution of hiPSC constructs on PCL scaffolds with varying geometries**. 253

Figure 4-5 **Effect of cell density on construct morphology over the course of cardiac differentiation.**. 255

Figure 4-6 **Geometry-dependent differences in characteristics between the cardiac nodes grown on 800 µm (A,C,E) and cardiac meshes grown on 500 µm (B,D,F) scaffolds at day 30.** 257

Figure 4-7 **Morphological and electrophysiological transformation of cardiac meshes over time.** 260

Figure 4-8 **Electrical field stimulation of cardiac meshes at day 30 and day 40.** 262

Figure 4-9 **Immunofluorescent staining of cardiomyocyte distribution in cardiac meshes at day 30 (A) and day 40 (B).** 263

Figure 4-10 **Immunofluorescent staining of cardiac, endothelial and mesenchymal marker expression on cardiac meshes at day 30 and day 40.** 265

Figure 4-11 **Full-volume immunofluorescent staining at the junction areas of optically-cleared cardiac meshes.** 267

Figure 4-12 **Schematic of the preparation and setup of cardiac mesh interface experiments with myocardial slices.**. 269

Figure 4-13 **Exogenous cardiomyocyte delivery to a myocardial slice during the pilot study.** 274

Figure 4-14 **Alternative mesh-slice interface protocol using Histoacryl tissue adhesive.** 278

Figure 4-15 **Immunofluorescent staining of hiPSC-CMs delivered to the myocardial slice using the Histoacryl interface method.** 280

Figure 4-16 **Adapted protocol for interfacing cardiac meshes with myocardial slices and its delivery efficiency.** 282

Figure 4-17 **The effect of cardiac mesh orientation on hiPSC-CM delivery to the slice.** 284

Figure 4-18 **Confocal imaging of the cardiac mesh-slice interface in situ using an upright microscope.**. 286

Figure 4-19 **hiPSC-CM transfer onto a basement membrane-functionalised tissue culture surface.**. 286

LIST OF TABLES

Table 1-1 Comparison of some of the structural, metabolic and functional characteristics of ventricular-like hiPSC-CMs and adult cardiomyocytes. 48

Table 2-1 Dimensions of the four device designs used for acoustic cell patterning. 80

Table 3-1 Overview of hydrogel systems commonly used for myocardial infarction repair in animal models..... 116

Table 3-2 Quantification of GelMA degree of functionalisation (DoF) from the results of fluoraldehyde assay.. 151

Table 3-3 Fluoraldehyde assay results of three porcine GelMA samples from two different batches.. 162

Table 3-4 A summary of p-values and significance levels of the effect of time on a given gene expression. 193

Table 3-5 A summary of adjusted p-values of Sidak multiple comparisons test between patterned and unpatterned samples at each differentiation stage for 6 genes of interest performed on repeated measures mixed model of RT-qPCR results. 193

Table 3-6 Significance testing of effects of electrical stimulation on output frequency using repeated measures mixed effects model with Tukey's multiple comparisons correction and Geisser-Greenhouse correction.. 217

Table 3-7 Significance testing of differences in output frequency response to electrical field stimulation between patterned and unpatterned in situ differentiated cardiac hydrogels.. 218

Table 4-1 Chemical composition of the Tyrode's solution for slice preparation (slicing) and electrophysiological measurements (recording). 245

LIST OF ABBREVIATIONS

1D	1-dimensional
2D	2-dimensional
3D	3-dimensional
AA	Antibiotic-antimycotic
ALP	Alkaline phosphatase
AP	Action potential
ASC	Adipose stem cell
BAL	Bioacoustic levitation
BAW	Bulk acoustic waves
BDM	2,3-butanedione 2-monoxime
BMP-4	Bone morphogenic protein 4
BSA	Bovine serum albumin
c	Speed of sound
CHIR	CHIR99021
CICR	Calcium-induced calcium release
CiPA	Comprehensive *in vitro* Proarrhythmia Assay
ColMA	Collagen methacryloyl
cTnT	Cardiac troponin T
CVD	Cardiovascular disease
DAPI	Diamidino-2-phenylindole
DDR2	Discoidin domain receptor 2
Dkk-1	Dickkopf-related protein-1
DMEM	Dulbecco's Modified Eagle Medium
DMSO	Dimethyl sulfoxide

DoF	Degree of functionalisation
E8	Essential 8 medium
EB	Embryoid body
ECAR	Extracellular acidification rate
ECC	Excitation-contraction coupling
ECM	Extracellular matrix
EHT	Engineered heart tissue
ESC	Embryonic stem cells
f	Frequency
FBS	Foetal bovine serum
FGF-2	Fibroblast growth factor 2
FHF	First heart field
FoV	Field of view
FP	Field potential
Fps	Frames per second
F_{rad}	Primary radiation force
FSP1	Fibroblast specific protein 1
G'	Storage modulus
G''	Loss modulus
GCaMP	Green fluorescent protein-modified calmodulin M13 peptide complex
GECI	Genetically encoded calcium indicator
GelMA	Gelatin methacryloyl
GEVI	Genetically encoded voltage indicator
HDF	Human dermal fibroblast
hESC	Human embryonic stem cells

hESC-CM	Human embryonic stem cell-derived cardiomyocytes
hiPSC	Human induced pluripotent stem cell
hiPSC-CM	Human induced pluripotent stem cell-derived cardiomyocytes
hMSC	Human mesenchymal stem cells
HMVEC	Human lung microvascular endothelial cell
HPA	Hydroxyphenylpropionic acid
hPSC	Human pluripotent stem cell
IDT	Interdigitated transducers
IHD	Ischemic heart disease
LAP	Lithium phenyl(2,4,6-trimethylbenzoyl)phosphinate
LVR	Linear viscoelastic region
MAA	Methacrylic anhydride
MEA	Multielectrode array
MEF	Mouse embryonic fibroblast
MEW	Melt electrospinning writing
MI	Myocardial infarction
MMP	Matrix metalloproteinase
MNP	Magnetic nanoparticle
MTF	Muscular thin films
NIR	Near-infrared
NMR	Nuclear magnetic resonance
OCR	Oxygen consumption rate
P	Peak pressure amplitude
PAA	Poly(acrylic acid)
PBS	Phosphate-buffered saline

PCL	Polycaprolactone
PDMS	Polydimethylsiloxane
PEG	Poly(ethylene glycol)
PFA	Paraformaldehyde
pHMGCL	Poly(hydroxymethylglycolide-co-ε-caprolactone
PLA	Poly(lactic acid)
PMGI	Polydimethylglutarimide
pNIPAAMm	Poly(N-isopropylacrylamide)
PSC	Pluripotent stem cell
PVA	Polyvinyl alcohol
ROI	Region of interest
ROCK	Rho-associated Protein Kinase
RPMI	Roswell Park Memorial Institute
RT-qPCR	Reverse Transcription – quantitative Polymerase Chain Reaction
SEM	Scanning electron microscopy
SERCA	Sarco/endoplasmic reticulum calcium-ATPase
SHF	Second heart field
SSAW	Surface acoustic waves
UV	Ultraviolet
V	Sphericall volume of the cell/particle
V_{p-p}	Peak-to-peak voltage
WHO	World Health Organisation
α-SMA	Smooth muscle actin
Φ	Acoustic contrast factor
β	Cell/particle compressibility

ζ	Distance from nodal planes
λ	Wavelength

CHAPTER 1. INTRODUCTION

1.1 Cardiac muscle biology and disease

1.1.1 Structure and function of heart muscle

The heart is a central pump of the body that regulates the efficient cycling of blood. In mammals and birds the heart has developed into a four-chambered organ, consisting of two atria, the chambers through which the blood enters the heart, and two ventricles, the chambers that eject the blood to the rest of the body during contraction (Figure 1-1, Flanigan & Gaskell, 2004). A central septum separates the left and right sides of the heart to segregate pulmonary circulation of deoxygenated blood to the lungs and systemic circulation of oxygenated blood to the rest of the body.

In extremely simple terms, the heart can be divided into three main constituent parts: i) the conduction system of the heart, which coordinates the contractile function on the whole-heart level, ii) the valves that spatially segregate the blood during different stages of the heart contraction, and iii) the muscular wall of the heart, which exerts the contractile force upon stimulation. The endocardium is the thin inner lining of the heart consisting primarily of endothelial cells. The epicardium is the outer layer of the wall formed by connective tissue, which serves as an anchoring site for nerves, coronary arteries, and lymph vessels, supplying nutrients, paracrine and electrical signals to the myocardium.

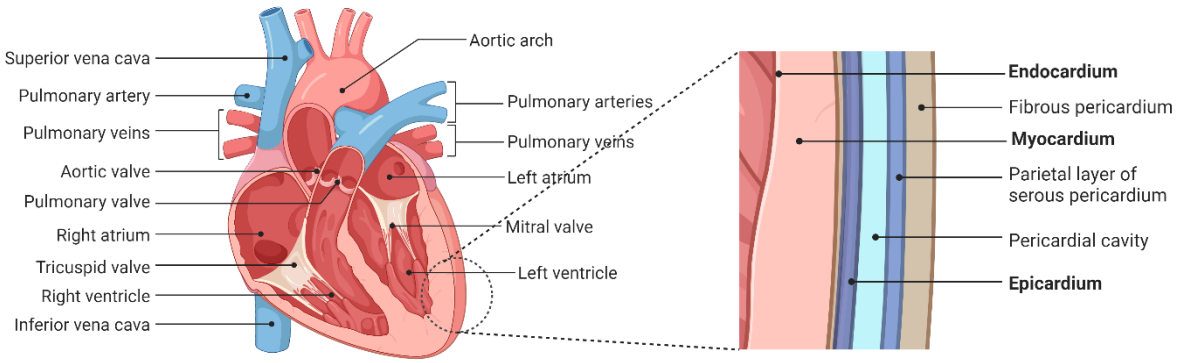


Figure 1-1 ***The structure of a mammalian heart, showing the tissue layers of the cardiac wall.*** *Adapted from "The Heart: From the Organ to the Cell", by BioRender.com (2022). Retrieved from https://app.biorender.com/biorender-templates.*

The myocardium is the thickest layer of the heart wall, comprising several cell types, including endothelial cells, fibroblasts, smooth muscle cell and peri-vascular cells (Vliegen et al., 1991). The contractile forces of the myocardium, central to the function of the heart, are generated by specialised cells occupying ≈75% of total myocardial volume, called cardiomyocytes: rod-like striated cells consisting of aligned bundles of myofibrils (Zhou & Pu, 2016). Each myofibril, in turn, is composed of repeating ultrastructural units called sarcomeres. A sarcomere is a single contractile element of the cardiomyocyte, which consists of thick microfilaments (myosin) and thin microfilaments (a complex of actin, tropomyosin and troponin) (Peng et al., 2014). Upon binding of calcium ions, the troponin proteins of the thin filament undergo conformational changes and, through complex biomolecular processes interact with myosin, resulting in a sliding motion. The motion causes temporary shortening of sarcomere length (≈15% reduction), generating a mechanical force leading to cardiomyocyte contraction, ultimately building the pressure within the cardiac wall and leading to the ejection of blood (systole) (Terracciano & Guymer, 2019). The relaxation of the muscle (diastole) through the restoration of the sarcomere length is achieved by ion channel and pump-driven depletion of cytosolic calcium. The repeated contraction-relaxation cycle forms the basis of the rhythmic contraction of the heart muscle.

Although adult atrial and ventricular cardiomyocytes can exert contractile forces, these subtypes do not possess intrinsic automaticity, meaning they do not contract spontaneously (Satin et al., 2004). The beating of the heart is instead driven by the clusters of pacemaker cells: cardiomyocyte subtypes that spontaneously depolarise and generate action potentials propagating through the muscle wall. When transmitted to ventricular or atrial cardiomyocytes, action potentials are converted into mechanical contraction by calcium fluxes in a well-known process called excitation-contraction coupling (ECC) (Bers, 2002). The detailed mechanism, involvement of ionic currents and sequential activation of ion channels, ion transporters and cascades of protein-protein interactions involved in ECC are extensively described elsewhere, and are summarised below (Terracciano & Guymer, 2019). Briefly, membrane depolarisation causes the opening of sarcolemmal voltage-

sensitive calcium ion channels (e.g. L-type calcium channels and sodium-calcium exchanger), leading to a flux of extracellular calcium into the cytoplasm. This stimulates ryanodine receptors and calcium channels in the sarcoplasmic reticulum to release more calcium, leading to an amplified sharp rise in cytosolic calcium concentration, known as calcium-induced calcium release (CICR), which facilitates microfilament sliding described above. The calcium is subsequently extruded from the cytoplasm via calcium ATPases (e.g. Sarco/Endoplasmic Reticulum Calcium-ATPase (SERCA) and sarcolemmal calcium ATPases), sodium-calcium exchanger and mitochondrial transporters, with the decline in cytosolic calcium leading to its dissociation from the microfilaments. During ECC of a single heartbeat, the concentration of intracellular calcium in a healthy adult cardiomyocyte oscillates from 100 nM to 1 μM (Marks, 2003). The magnitude and kinetics of calcium fluxes, known as calcium transients, tightly regulate the amplitude and dynamics of the contraction, that are necessary for efficient cardiac function.

Cardiac tissue is hierarchically structured, enabling its coordinated function and maximising its pumping efficiency (Figure 1-2). A series of sarcomeres form a subcellular structure called myofibril, while several parallel bundles of myofibrils in turn form a cardiomyocyte (England & Loughna, 2013). Cardiomyocytes are rod-shaped cells with a high aspect ratio, which are aligned longitudinally, and both mechanically and electrically coupled by intercalated discs to adjacent cells (Sheikh, Ross & Chen, 2009). The coupling occurs through desmosomes, fascia adherens junctions and unidirectional gap junctions, leading to efficient directional conduction parallel to the long axis of the cell. Some lateral branching occurs between adjacent rows of cardiomyocytes, forming secondary sheetlet structures of approximately 8-12 cardiomyocytes in width, behaving synchronously (Terracciano & Guymer, 2019). Individual sheetlets have a dominant direction and form the building units of the cardiac muscle wall with the global helical organisation of the sheetlets within the muscle. During systole, the sheetlet shortening within the helix causes their rotation and multidirectional deformation of the myocardium, leading to torsion movement building up the pressure within a chamber required for ejection (Nielles-Vallespin et al., 2017; Terracciano & Guymer, 2019).

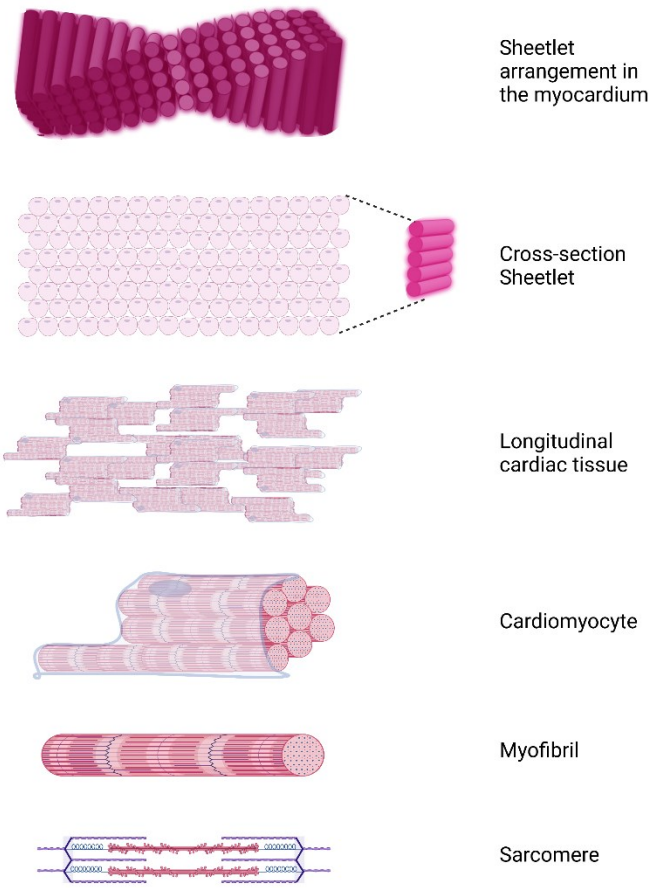


Figure 1-2 ***Hierarchical organisation of cardiac tissue.*** *The series of sarcomeres arrange into a myofibril, a bundle of myofibrils form a cardiomyocyte. Cardiomyocytes are mechanically and electrically coupled on the longitudinal plane, and are arranged in 3D in sheetlets (shown in cross-section), that in turn form a helical structure. Figure created with BioRender.com.*

From early development, cardiac tissue experiences several mechanical forces that provide cues for structural organisation. Those include shear stress from blood circulation, active cyclic strain generated from repeated contractions and stretch generated during chamber filling, which are generated from the first heartbeat and sustained throughout an organism's life (Carlos-Oliveira et al., 2021). The physical forces can trigger the opening of mechanosensitive ion channels of the Piezo family expressed in cardiomyocytes, leading to a non-selective cation influx (e.g. Ca^{2+} and Na^{+}) into the cytoplasm of the cell (Shah, Patel & Shah, 2022). Piezo1 channels have been shown to facilitate homeostatic Ca^{2+} signalling and the downstream reactive oxygen species-related pathways in mouse cardiomyocytes, with their knockout leading to cardiomyopathy development and impairment of cardiac function (Jiang et al., 2021).

Overall, the heart is an extremely intricate organ with complex, well-preserved hierarchical organisation, with each component playing a vital role in cardiac performance. The contractile function of the heart is achieved through a complex interplay within its structure, precisely organised from the subcellular level of sarcomeres to the intricate helical arrangement of sheetlets and anatomical features, and unique electrophysiology, arising from the coordinated regulation of ionic currents and protein interactions. Any inherited or acquired perturbations to the structural or functional features of the heart lead to cardiac dysfunction and the development of cardiovascular disease (CVDs), reducing the quality of life and shortening life expectancy.

1.1.2 Cardiovascular disease burden

CVDs are a broad term encompassing disorders affecting the heart and blood vessels, and are the leading cause of mortality worldwide, with 17.9 million deaths recorded globally in 2019 (32% of all deaths) (World Health Organisation, 2021). Although generally CVD-related deaths have been gradually decreasing over the years due to advances in CVD detection and treatment, the rate of decline has been stalling since 2011 (Collins et al., 2022). The prevalence has also been growing with the ageing population and increase in risk factors (e.g. lack of exercise and tobacco use), with approximately 1 in 14 people currently living with CVDs posing a significant concern for the public health sector (British Heart Foundation, 2022). The nature and mechanisms of CVDs are often extremely complex: cardiac dysfunction can be driven or exacerbated by various genetic mutations, lifestyle choices, infections, or combinations of the three (Abbate, Sticchi & Fatini, 2008; Sato et al., 2021; Pothineni et al., 2017; Abdullah Said, Verweij & van der Harst, 2018). Some examples of CVDs include ischaemic heart disease (IHD), myocardial infarction (MI), stroke, various types of arrythmias and cardiomyopathies. The available treatments are mostly palliative and aim to slow down the disease progression and alleviate the symptoms. Over time, several CVDs, for example IHD, MI and arrythmia, can deteriorate and lead to heart failure, a pathological condition whereby the efficiency of cardiac function is drastically reduced and is not able to meet the demands of the body (Velagaleti & Vasan, 2007). Unfortunately, heart failure prognosis is extremely poor, with only a 50% predicted

survival rate across 5 years and donor heart transplantation available as the only cure (Savarese & Lund, 2017). The necessary health and social care for CVD patients also comes at a huge economic cost, with the UK alone projected to spend ≈ £54 billion between 2019 and 2029 (Collins et al., 2022). Crucially, the same study estimated a loss of ≈540,000 quality-adjusted life years over a decade, which represents a devastating decline in quality of life, disability and mortality linked to CVDs.

1.1.3 Models of cardiac tissue

Given the vital function of the heart combined with the complexity of its structure and the severity of the burden of its disease, cardiac tissue engineering has been a major target of medical research. Reproducibly modelling the physiology and disease pathology of cardiac tissues has not only been informing the field on underlying mechanisms of disease, but also has been serving as a platform for preclinical drug screening and assessment of novel biological therapeutics. There are four levels of platform complexity that have been used for these purposes: i*n vivo, ex vivo, in vitro* and *in silico*. *In vivo* models are performed in well-defined small (e.g. mice, rats), medium (e.g. rabbits, dogs) or large (e.g. pigs, non-human primates) animal models, and provide invaluable information on disease progression and treatment efficacy systemically. However, interspecies variability poorly represents human physiology, for example, the resting heart rate of a rodent is approximately 5-6 times faster than that of a human (Passier, van Laake & Mummery, 2008). Such electrophysiological differences lead to significant disparities in immune responses, metabolic processes, and disease features, lowering the predictive value of animal *in vivo* experiments for human trials (Honek, 2017). Additionally, although in late-stage investigations the systemic evaluation provides important information on inter-organ effects of a drug/treatment, at the early research stages it is difficult to uncouple the individual contribution of drug of interest on different aspects of heart physiology and it is challenging to perform detailed functional measurements of cardiac output. *Ex vivo* systems,

such as the Langendorff heart model (perfused intact heart) or myocardial slices (thin tissue sections of the heart), can be used to isolate the tissue and interrogate its behaviour on a single-organ scale in real-time (Knight et al., 2020; Watson, Terracciano & Perbellini, 2019). Langendorff measurements can also be performed at the end-point of *in vivo* experiments to record the cardiac output following a treatment (Jain et al., 2001; Zhang et al., 2005). However, the species variability remains of concern, and isolated tissue can only remain viable short-term, with Langendorff heart experiments lasting 6-8 hours on average, while myocardial slices are usually cultured up to 5 days (Wiechert et al., 2003; Watson, Terracciano & Perbellini, 2019). Finally, both *in vivo* and *ex vivo* models rely on highly-skilled surgical procedures, require extensive ethical considerations and are, consequently, low throughput. *In silico* computational models have advanced significantly in the last decade, capable of simulating the cardiac tissue from molecular interactions on a subcellular level to whole-heart modelling of mechanical and electrical features of arrhythmia (Bartolucci et al., 2022; Winslow & Trayanova, 2011). While these are increasingly powerful tools for high-throughput drug screening, *in silico* models are based on a reductionist approach, and lack genetic and biological variation, limiting their predictive power.

There is a large demand, therefore, for *in vitro* human cardiac tissue models, that would possess an intermediate biological complexity between *in silico* and *in vivo* and allow for long-term functional assessments. The main challenge in *in vitro* cardiac tissue modelling is in how accurately it can represent native tissue: an ideal model would recapitulate the architecture of the human heart, contain all relevant cell phenotypes, exert equivalent contractile properties, and possess similar electrophysiology of electrical and calcium signalling (Kałużna et al., 2022). Cardiac tissue engineering seeks to achieve that by combining novel biomaterials, human-derived cells, biomolecular cues and advanced fabrication methods (Vunjak-Novakovic, 2017). If successful, such *in vitro* systems would serve as useful models in elucidating the mechanisms of heart development and disease, as physiological platforms for drug screening, and even as sources of functional artificial cardiac tissue for regenerative medicine.

To date, cardiac tissue engineering has developed an impressive range of heart mimics through both bottom-up and top-down approaches. Their biological relevance and fabrication throughput are often a trade-off, and the specific models must be chosen depending on the desired application (Figure 1-3). By far the simplest and highest throughput models are two-dimensional (2D) monolayer cultures, containing cardiomyocytes grown on a flat substrate, sometimes geometrically arranged using adhesion protein surface micropatterning (Badie & Bursac, 2009). Muscular thin films (MTF) build upon these simplistic models, utilising the properties of thermosensitive polymers to detach cardiac cells from the culture surface as a whole 2D construct without disrupting the cell-cell contacts (Alford et al., 2010). A higher level of tissue complexity can be achieved with cardiac spheroids or microtissues, which are usually produced through the aggregation of cardiomyocytes alone or with other relevant cell types into clusters respectively, providing control over phenotype ratios while modelling the 3D environment of the tissue (Polonchuk et al., 2017; Giacomelli et al., 2020). Cardiac organoids further increase the multicellular complexity by stochastically differentiating clusters of stem cells into spherical structures with diverse lineages present during heart development (Richards et al., 2020; Hoang et al., 2018). Precisely controlled modular heart-on-a-chip devices introduce microfluidics to mimic blood flow and shear forces in circulation as well as allow integration with other organ compartments (Takebe, Zhang & Radisic, 2017). Finally, engineered heart tissues (EHTs) make use of biomaterial scaffolds that act as extracellular matrix (ECM) mimics and incorporate mechanical and/or electrical stimulation to replicate the dynamic electrophysiological environment of the heart (Lemoine et al., 2017; Mannhardt et al., 2017; Hirt et al., 2014; Weinberger et al., 2016). Although the cardiac tissue models listed above have some general defining characteristics, it should be noted that each of them represents a huge subfield of cardiac tissue engineering, encompassing a plethora of sophisticated fabrication methods, functional biomaterials, culture systems and cellular compositions.

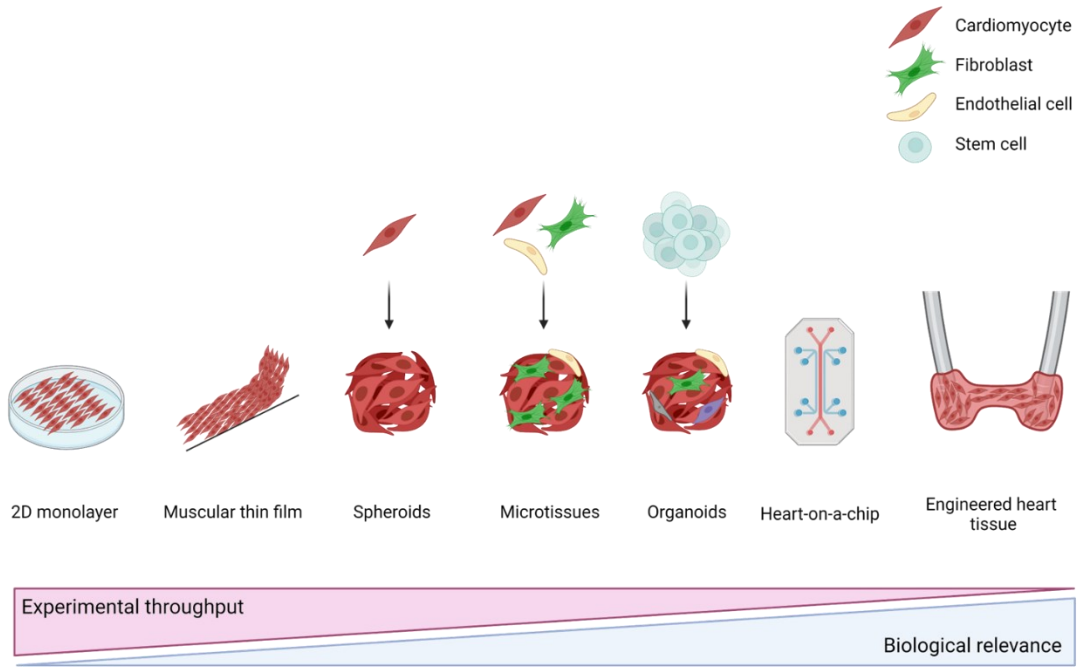


Figure 1-3 ***Classes of cardiac tissue engineered models arranged by descending throughput and ascending biological representativeness****. Figure created using Biorender.com.*

1.2 Cell sources for cardiac tissue engineering

1.2.1 Isolated cardiomyocytes

Although several cells, such as human mesenchymal stem cells (hMSCs), skeletal myoblasts or cardiac fibroblasts have been used previously for engineering cardiac tissues, the primary role of cardiomyocytes in contraction makes them the most desired cell type for cardiac tissue engineering.

Isolated cardiomyocytes from a small animal model can also be used for tissue engineering as they preserve the rod-like cell morphology, electrophysiological characteristics and contractile forces of the native tissue (Roth et al., 2014). However, after isolation these primary cells undergo phenotypic transformation in 2D culture conditions, losing their elongated morphology, distinct striations and experiencing changes in functional characteristics (e.g. membrane potential, action potential duration, membrane capacitance) (Mitcheson, Hancox & Levi, 1996; Louch et al., 2004). Isolated primary cardiomyocytes are therefore suitable as acute culture models (up to 2 weeks) and are limited by species variability and lack of proliferation, leading to poor representability and scalability

of such systems (Louch, Sheehan & Wolska, 2011; Mohamed et al., 2018). Furthermore, mature adult cardiomyocytes rapidly exit the cell cycle and reduce their annual turnover rate to ≈1%, making it challenging to expand isolated cells in culture for large-scale experiments (Bergmann et al., 2009).

1.2.2 Immortalised cell lines

Isolated human and rodent primary cardiomyocytes (e.g. H9C2, HL-1, AC16, i-AM1) have been previously immortalised to provide an alternative source of functional cardiac cells (Onódi et al., 2022; Liu et al., 2018a). Characterised by their unlimited proliferation potential and maintenance of the cardiac phenotype and function in culture, immortalised cardiomyocytes have been a valuable tool in cardiovascular research, used to study cellular signalling pathways and electrophysiology (Liu et al., 2018a; White, Constantin & Claycomb, 2004). However, when compared to their primary cell sources, three different immortalised cell lines have shown a markedly lower expression of cardiac markers *TNNT2* and *RYR2* and a less pronounced cardiac transcriptome (Onódi et al., 2022). Prolonged subculturing of immortalised cell lines has been shown to cause unnatural genetic and epigenetic drift, as shown by a substantial loss of 5-hydroxymethylcytosine in human embryonic fibroblasts after three days in culture (Horvath et al., 2016; Nestor et al., 2015). These findings demonstrate that adaptations of immortalised cells in culture lead to their divergence from the primary cell genetic and epigenetic profiles.

Epigenetic modifications, such as DNA methylation or histone modifications, are responsible for the changes in chromatin structure, which ultimately control gene expression. On a cellular level, a cardiomyocyte's epigenome changes throughout development. For example, a chromatin remodeler Brahma-related gene 1 (Brg1) complex was found to control the switch from beta myosin heavy chain expression in foetal cardiomyocytes to alpha myosin heavy chain expression in adult cardiomyocytes (Hang et al., 2010). Dynamic *de novo* DNA methylation patterns were also observed during the transition from perinatal to adult mouse cardiomyocytes, which mediated the switch of

sarcomeric protein isoforms, known as one of the hallmarks of maturation (Gilsbach et al., 2014). Similarly, CpG methylation of both enhancers and genic regions, as well as histone marks were detected throughout progression from foetal to infant to adult cardiomyocytes, mediating gene expression progression from immature markers (*MYL4, NPPA, TNNI1)* towards a mature phenotype (*MYH6*, *RYR2*, *TNNI3*) (Gilsbach et al., 2018).

Changes in the epigenetic patterns, known as epigenetic drift, have been discovered to be tightly associated with ageing. To that effect, the level and rate of methylation of CpG dinucleotides has been used to train predictive models of 'biological clocks' – an epigenetic estimate of lifespan and functional decline independent of chronological age (Li, Koch & Ideker, 2022). In the context of cardiovascular disease (CVD), the epigenetic clock GrimAge was proved to be a useful marker of transition from a disease-free to a subclinical CVD state from young to middle-age patient groups (Joyce et al., 2021). Taken together, these studies highlight the importance of controlled epigenetic modification throughout healthy and diseased cardiac development and maturation. Prolongued subculturing-induced epigenetic drift of immortalised cell lines could therefore introduce unknown variability to the epigenome of the tissue engineered constructs.

Foetal serum-based media used for the fast expansion of immortalised cells in culture could also introduce another source of variation by recreating a neonatal-like microenvironment (Horvath et al., 2016). Overall, immortalised cell lines can only serve as a rough approximation to the native cardiomyocytes, and their use in long-term culture for cardiac tissue engineering is limited.

1.2.3 Pluripotent stem cells

Human pluripotent stem cells are undifferentiated cells that are capable of extended self-renewal while maintaining stable genetic and epigenetic profiles and have the potential to give rise to specialised cells of any lineage (Garitaonandia et al., 2015). They include embryonic stem cells (ESCs), which are totipotent cells that are either isolated from inner cell mass of surplus blastocysts

from fertilisation treatments, or, less commonly, generated through somatic cell nuclear transfer (Amit & Itskovitz-Eldor, 2006; Tachibana et al., 2013; Hackett & Fortier, 2011). ESCs can be successfully cultured and differentiated to produce large quantities of cardiomyocytes and have been used to engineer a variety of cardiac models, for example microtissues, mechanically-loaded engineered heart tissues and ring-like chamber-mimicking tissues (Stevens et al., 2009; Goldfracht et al., 2020; Schaaf et al., 2011). However, their use in cardiac models is limited by embryo availability and association with extensive ethical considerations.

The discovery of induced pluripotent stem cells (iPSC) has revolutionised the field of bioengineering. iPSCs are pluripotent stem cells derived from somatic cells (commonly, fibroblasts) through overexpression of the key pluripotency genes: *POU5F1 (*OCT3/4*), SOX2, KLF4* and *c-Myc*, identified in Nobel prize-winning work by Takahashi and Yamanaka (Takahashi & Yamanaka, 2006). Originally derived from mouse fibroblasts using retroviral reprograming, iPSCs have also been generated from other animal origins, including humans (hiPSCs). There is some evidence of iPSCs maintaining parts of the epigenetic landscape of their original cell type and some studies have shown higher sensitivity to pharmacological agents of hiPSC-derived cells than hESC-derived cells (Kim et al., 2010; Hwang et al., 2015; Sheng et al., 2012). However, in comparison to ESCs, iPSCs possess several advantages. They have fewer ethical considerations, are often obtained non-invasively or low-invasively (e.g. skin biopsies), and in theory can be generated from any cell types, addressing the epigenetic memory concerns. Crucially, iPSCs can be derived from patient- and disease-specific cells, making them an invaluable tool for disease modelling and drug screening. Indeed, hiPSC-derived cardiomyocytes (hiPSC-CMs) have been successfully used to model the structural and electrophysiological disease profiles of genetically-linked arrhythmias (long QT syndromes, Brugada syndrome) cardiomyopathies (dilated and hypertrophic) and cardiometabolic disorders (Barth syndrome lysosomal storage disorders) (Liang et al., 2016; Moretti et al., 2010; Sun et al., 2012; Han et al., 2014; Wang et al., 2014; Borger et al., 2017). Finally, the ability of hiPSCs to retain the patient's genetic information holds the promise of their use for personalised therapies in the future.

1.3 Stem cell technologies for cardiac engineering

1.3.1 Evolution of cardiac differentiation protocols

Since their discovery, numerous protocols have been developed to differentiate human pluripotent stem cells (hPSCs) into adult cell types descending from all three germ layers (endoderm, mesoderm and ectoderm). Existing directed differentiation protocols to form human pluripotent stem cell-derived cardiomyocytes (hPSC-CMs) can be divided into two categories: embryoid body (EB)-based and two-dimensional (2D) monolayer-based. EB formation, whereby 3D stem-cell aggregates are cultured on a layer of mouse embryonic fibroblast (MEF) feeder layer, was the first method to stochastically produce spontaneously contracting beating cardiomyocytes, however it was limited by 10% efficiency and cell line-specificity (Kehat et al., 2001; Zhang et al., 2009). Several modifications, such as EB size homogenisation, the addition of demethylating agents, low oxygen conditions and addition of endoderm-like cell lines were implemented in an attempt to increase the differentiation yield (Rajala, Pekkanen-Mattila & Aalto-Setälä, 2011; Mummery et al., 2003). While the reported cardiomyocyte efficiency varied from 2% to 70% contracting cells of the total EB area, these methods remained unreliable, with their dependency on the mouse feeder layer leading to zoonotic concerns and challenges in cardiomyocyte isolation.

Cardiogenesis stems from the mesodermal cells of the primitive streak, established after gastrulation. This process is tightly regulated through an interplay of key signalling pathways, including Wnt signalling, Activin/Nodal/TGF-β and BMP4 signalling. While cardiogenesis is an intricate and complex process, some roles of these pathways in cardiac development have previously been elucidated through extensive knockout and overexpression studies in mouse, chick and zebrafish embryos. For example, the Activin/Nodal/TGF signalling pathway was found to be crucial for gastrulation, primitive streak formation and mesoderm induction, with loss-of-function mutations of *Nodal*, activin receptors or their downstream targets resulting in impaired anterior-posterior axis and a lack of mesoderm phenotypes in mouse and frog embryos (Barnes & Black,

2016; Conlon et al., 1994). The canonical Wnt/β-catenin pathway was also established as a key regulator of embryonic axis formation in vertebrates, with targeted *Wnt3*$^{-/-}$ mutation in mouse resulting in undifferentiated epiblasts lacking anterior-posterior orientations and failing to form a primitive streak (Liu et al., 1999; Fu et al., 2009). The latter result was also further substantiated through a mutation of a *PORCN,* a gene encoding a membrane-bound regulator of Wnt ligand secretion and activity, which also led to disruption of gastrulation entirely, with the embryos lacking markers of mesoderm and endoderm (Biechele, Cox & Rossant, 2011). Some role of BMP signalling in mesoderm formation was also observed, with knockout BMP receptor *Bmpr1a* knockout mice lacking mesoderm (Wang, Greene & Martin, 2011; Mishina et al., 1995). Overall, these studies confirmed that Wnt, Nodal and BMP signalling pathways are vital for axis and mesoderm development.

Upon gastrulation completion, cardiac precursors are formed in the primitive streak. These precursors first form a cardiac crescent consisting of the first and second heart fields (SHF and FHF), which then fuse to form a linear cardiac tube, followed by cardiac looping and chamber formation (Buckingham, Meilhac & Zaffran, 2005). BMP signalling pathway was found to be instrumental in driving the specification of cardiac mesoderm, with *Bmp2* mutations disrupting the ectopic expression of early cardiac markers *Nkx2.5* and *GATA4* and *Bmp4* mutations affecting cardiac looping (Brand, 2003; Breckenridge, Mohun & Amaya, 2001; Wang, Greene & Martin, 2011). BMP-2 treatment of mesoderm explants from chick embryos resulted in an upregulation of cardiac transcription factors *Nkx-2.5, GATA-4, GATA-5, GATA-6, MEF2, eHAND,* and *dHAND* as well as the gene encoding structural sarcomeric protein ventricular myosin heavy chain (vMHC), confirming the key role of BMP-2 in cardiac development (Schlange et al., 2000; Schultheiss, Burch & Lassar, 1997). However, when the explants were cocultured with cells expressing Wnt ligands, the cardiogenesis was significantly subdued, suggesting Wnt signalling playing an antagonising role to BMP pathway at the later stages of cardiac development (Fu et al., 2018; Tzahor & Lassar, 2001). Indeed, inhibition of Wnt post-gastrulation through overexpression of a known Wnt inhibitor Dkk-1 led to an

upregulation of sarcomeric myosin light chain protein Cmlc2 (Ueno et al., 2007). Concurrently, overexpression of Wnt activator *Wnt8* led to a decrease in Cmlc2, confirming the importance of Wnt signalling inhibition post-gastrulation for efficient cardiac differentiation (Ueno et al., 2007). Interestingly, sustained Wnt signalling after gastrulation completion resulted in an increase of hematopoietic and vascular cell types (Naito et al., 2006). Overall, these developmental studies served as the basis for establishing efficient cardiac differentiation protocols *in vitro.*

High-density monolayer stem cells, plated on a Matrigel-functionalised surface and cultured using MEF-conditioned media, were successfully differentiated into cardiomyocytes with a 30% efficiency, demonstrating the first instance of feeder-free cardiac differentiation (Laflamme et al., 2007). Further improvement could be achieved by building upon the biphasic role of canonical Wnt/β-catenin pathway in the differentiation process, whereby its activation was found to be required for mesoderm induction, while subsequent inhibition led to cardiac specification (Naito et al., 2006). Indeed, applying growth factor-induced Wnt activation followed by Dickkopf-related protein-1 (Dkk-

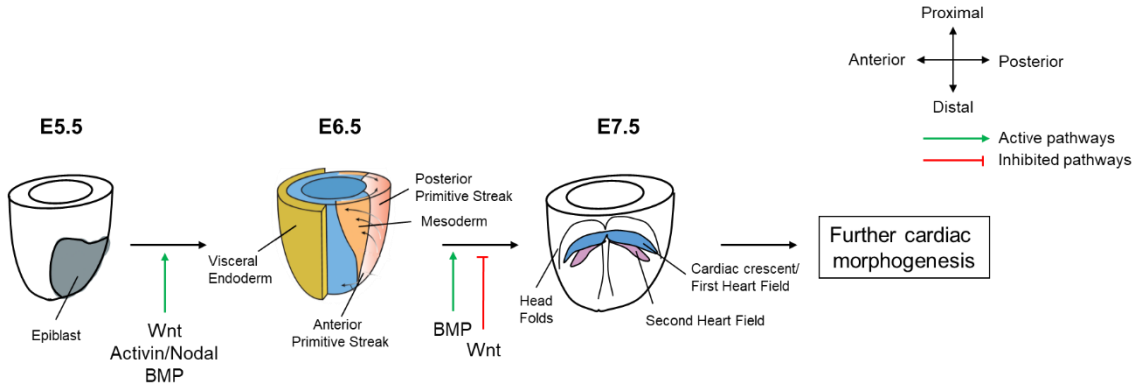


Figure 1-4 ***Signalling pathways in cardiac development.*** *A schematic representation of Wnt, Activin/Nodal and BMP signalling pathways involvement in progression through mouse cardiac development, from gastrulation (E5.5 to E6.5) to early cardiogenesis (E6.5 to E7.5). Adapted with permission from* (*Duelen & Sampaolesi, 2017; Freire et al., 2014*) *under the Creative Commons CC BY License.*

1) inhibition to both EB and monolayer-based protocols increased the cardiomyocyte yield to 50% (Paige et al., 2010; Yang et al., 2008). The method has been further refined through the years, leading to a switch to chemically-defined media and optimisation of timing and concentrations of small molecule-based Wnt pathway modulation, which remains the most common approach to hiPSC-CM production (Lyra-Leite et al., 2022).

Several variations of the small molecule-based monolayer hiPSC-CM differentiation protocols exist. Generally, the serum-free differentiation medium consists of an RPMI medium and a B-27 supplement or some of its components (Burridge et al., 2014; Lian et al., 2012). Insulin-free media is used in the first 5 days of differentiation due to its inhibitory role in mesoderm formation (Lian et al., 2013; Xu et al., 2008). Small molecule activators (CHIR99021) and inhibitors (IWP-2, Wnt-C59, IWR-1) are added sequentially to first direct the cells to a mesoderm phenotype and then stimulate cardiac lineage specification, followed by metabolic selection-based purification methods (Zhang et al., 2015). As a result, a mixture of mostly ventricular, but also containing atrial and nodal spontaneously beating cardiomyocytes is produced with 80-90% cardiac differentiation efficiency (Zhang et al., 2015; Burridge et al., 2014; Minami et al., 2012; Lian et al., 2012). Although stem cell differentiation technologies have shown significant improvement in the reliability of differentiation protocols over the last 20 years, current work is focussed on targeting the differentiation precision to individual subtypes and advancing the maturation of hiPSC-CMs (Lyra-Leite et al., 2022).

1.3.2 Differences between stem cell-derived and adult cardiomyocytes

Although hiPSC-CMs have a huge potential in biomedical research and engineering, they exhibit an immature structural and functional phenotype reminiscent of neonatal-like cardiomyocytes present in the early stages of embryogenesis, rather than adult cells (Table 1-1). Structurally, adult ventricular cardiomyocytes are large, elongated (≈100-150 µm by 20-35 µm dimensions), often multi-nucleated cells with distinct organisation containing transverse tubules (T-tubules) and aligned sarcomere bands with optimal 2.2 µm spacing (Hanft & McDonald, 2010; Robertson, Tran & George,

2013; Lieu et al., 2009; Wu et al., 2021). In contrast, ventricular-like hiPSC-CMs (the most abundant products of differentiation protocols) are small, rounded and mononucleated, with irregular and short sarcomeres (1.6 μm) and lacking T-tubules (Ivashchenko et al., 2013; Lieu et al., 2009; Wu et al., 2021). Adult cardiomyocytes contain large mitochondria, which occupy 20-40% of the cell volume, are spatially organised in intermyofibrillar, subsarcolemmal and perinuclear spaces, and predominantly utilise the products of fatty acid β-oxidation to produce sufficient energy required to generate large contractile forces (≈40-80 mN/mm^2) (Correia et al., 2022; Ahmed et al., 2020). In contrast, hiPSC-CMs contain substantially fewer mitochondria (2% total cell volume), mostly present in the perinuclear space, and their energy production heavily relies on glycolysis, reminiscent of foetal heart metabolism (Dai et al., 2017; Wu et al., 2021).

The immature phenotype of hiPSC-CMs is also reflected in their epigenome, consistent with the role of epigenetic regulators in cardiac development and maturation, previously discussed in section 1.2.2. For example, approximately a 2-fold upregulation of genes encoding histone methyltransferases, demethylases and deacetylases was observed in hiPSC-CMs when compared with adult cardiomyocytes across two independent studies (Pozo, Meredith & Entcheva, 2022; Gupta et al., 2010; Babiarz et al., 2012). Suppression of epigenetic modifications, through administering pharmacological inhibitors of histone deacetylases to differentiating hiPSCs, resulted in improved differentiation efficiency, higher beating rate and upregulation of cardiac marker gene expression (Otsuji et al., 2012; Lim et al., 2013). Additional evidence for the importance of epigenome for cardiac maturity comes from hiPSCs generated from somatic cells of cardiac origin. hiPSCs have been shown to maintain the 'epigenetic memory', with cardiac-derived hiPSCs containing notably less methylation of the promoter of *Nkx2.5* gene than the hiPSCs of non-cardiac origin (Pianezzi et al., 2020). Consistently, iPSCs derived from either isolated murine ventricular cardiomyocytes or isolated human cardiac progenitor cells demonstrated an improved cardiac differentiation efficiency, with an increase in expression of sarcomeric proteins and a more physiologically-relevant response to ion channel blockers (Pianezzi et al., 2020; Xu et al., 2011).

Taken together, these studies suggest that modulation of the hiPSC epigenome can be used to achieve a more advanced maturation status of hiPSC-CMs.

Excitation-contraction coupling (ECC) is the property of cardiomyocytes whereby an electrophysiological signal, which broadly consists of ionic currents and, in particular, changes in cytoplasmic calcium concentration, is converted into mechanical force (Bers, 2002). There are major differences in electrophysiological profiles of hiPSC-CMs and adult cardiomyocytes. For example, the resting membrane potential in adult myocytes is ≈-80 mV, significantly lower than that of hiPSC-CMs (≈-60 mV) (Denning et al., 2016). hiPSC-CMs also have significantly reduced ionic currents that govern the progression of phases in action potentials, leading to differences in the action potential morphology and overall slower dynamics (e.g. ≈ 20-150 V/s reduction in maximum upstroke velocity relative to adult ventricular cardiomyocyte) (Wang, Kit-Anan & Terracciano, 2018). Notably, the presence of a pacemaker current (I_{Kf}) in all subtypes of hiPSC-CMs leads to their characteristic spontaneous beating, which *in vivo* is restricted to only nodal-like adult cardiomyocytes (Verkerk & Wilders, 2015; Saito et al., 2015; Wu et al., 2021). Slower kinetics are also observed in the calcium transients, attributed to the complex interplay of lower expression of ion channels (e.g. L-type and T-type calcium channels, SERCAs, ryanodine receptors) and lack of ultrastructural organisation of T-tubules (Gherghiceanu et al., 2011; Hwang et al., 2015; Itzhaki et al., 2011). Taken together, the immature electrophysiological and structural phenotypes of hiPSC-CMs lead to a slower conduction velocity (10-20 cm/s vs 60 cm/s in adult cells) and smaller contractile forces (0.08-4 mN/mm^2) (Ahmed et al., 2020; Denning et al., 2016).

Table 1-1 ***Comparison of some of the structural, metabolic and functional characteristics of ventricular-like hiPSC-CMs and adult cardiomyocytes.***

	Parameter	Ventricular-like hiPSC-CMS	Ventricular adult cardiomyocytes
Structural	Shape	Rounded	Rod-like
	Size	5-10 μm diameter	100 μm × 20 μm
	Sarcomeres	Irregular, 1.6 μm	Ordered, 1.8-2.2 μm
	Nucleation	Mono	Mono, bi, multi
	T-tubules	Absent	Present
Metabolic	Mitochondria structure and location	Small, perinuclear	Large, intermyofibrillar, subsarcolemmal, perinuclear
	Mitochondria abundance	2% of total cell volume	20-40% of total cell volume
	Predominant metabolism	Glycolysis	Fatty acid β oxidation
Functional	Resting membrane potential	-60 mV	-80 mV
	Spontaneous contraction	Present	Absent
	Conduction velocity	10-20 cm/s	60 cm/s
	Maximum upstroke velocity	44-187 V/s	200 V/s
	Contractile force	0.08-4 mN/mm^2	40-80 mN/mm^2

Given that *in vivo* the mature adult phenotype can develop over the course of 10 years, the proximity of structural, metabolic, electrophysiological and contractile properties of hiPSC-CMs to that of neonatal-like cardiomyocytes is understandable (Vreeker et al., 2014; Ahmed et al., 2020). The progression of hiPSC-CMs further down the maturation spectrum is therefore an ongoing priority of cardiac stem cell technologies. The existing strategies utilise the knowledge of cardiogenesis from developmental biology, trying to replicate the complex environment *in vivo*. To that effect, long-term culture (up to 1 year) showed an improvement in cell size, myofibril density, calcium handling dynamics and cardiac gene expression (Lewandowski et al., 2018; Kamakura et al., 2013; Lundy et al., 2013). Biochemical cues present in cardiac development, such as thyroid hormone and glucocorticoidal treatment, or fatty acid-enriched media also have been shown to improve myofibril organisation, mitochondrial activity and calcium handling (Horikoshi et al., 2019; Parikh et al., 2017; Yang et al., 2014; Ahmed et al., 2020). In recent years, several studies have implemented three-dimensional (3D) culture systems, as either acellular microtissues or cell-laden

biomaterial scaffolds, which showed improved maturation status of the structural and functional hiPSC-CM parameters (Giacomelli et al., 2020; Huebsch et al., 2022; Shadrin et al., 2017; Lemoine et al., 2017). Furthermore, the inclusion of non-cardiomyocyte cell types in 3D cultures has improved sarcomeric organisation and electrophysiology (Iseoka et al., 2018; Giacomelli et al., 2020; King et al., 2022). Since cardiomyocytes are subjected to a variety of mechanical stimuli during development, as mentioned in section 1.1.1, a vast array of mechanical (static or dynamic loading) and electrical stimulation modalities of both 2D and 3D cultures have been used to generate a more advanced cardiac phenotype of hiPSC-CMs in culture (Hirt et al., 2014; Chan et al., 2013b; Ruan et al., 2016; Tulloch et al., 2011; Mummery et al., 2021). Several permutations of all maturation strategies have also been explored, demonstrating synergistic effects of biochemical cues, biophysical stimulation, dimensionality and culture length on hiPSC-CM maturation. For example, 3D hydrogel-encapsulated hiPSC-CMs were conditioned with static mechanical loading and electrical field stimulation training gradually increasing in frequency in three different studies (Nunes et al., 2013; Zhao et al., 2019; Ronaldson-Bouchard et al., 2018). The authors reported adult-like gene expression, increased ultrastructural organisation, the presence of T-tubules and enhanced calcium handling in hiPSC-CMs derived from three different hiPSC cell lines after 40-50 days in culture.

Indeed, the ongoing work on cardiac maturation will pave the way for future hiPSC-CM culture protocols, the mechanisms behind the individual contributions of maturation components are still not fully understood, leading to heterogeneity in stimulation and culture parameters, and overall lack of consensus on good manufacturing practice for hiPSC-CM generation. The existing protocols, although an improvement from the current gold-standard monolayer differentiations, yield cells that possess structure and function still far from those of the desired adult cardiomyocyte. The reproducibility, robustness and predictability of novel maturation protocols also remain undefined.

1.4 Assessment of cardiac tissue platforms

Cardiac tissue engineering is a field that aims to replicate the cellular composition, architecture and function of the native heart muscle *in vitro*. The development of hiPSC-CM protocols has significantly advanced the field, allowing the creation of models of human heart tissue using either scaffold-free methods (e.g. cardiac spheroids, organoids, microtissues or sheets) or cell-laden 3D biomaterial scaffolds (e.g. engineered heart tissues).

After fabrication and culture, engineered constructs are often characterised in order to determine how the structural and functional properties of the hiPSC-CMs in the novel *in vitro* models compare to those of the native tissue and other existing systems. There are five main parameters that are commonly assessed in cardiac tissues: ultrastructure, gene expression, contractility, metabolic activity, and electrophysiology (Figure 1-5).

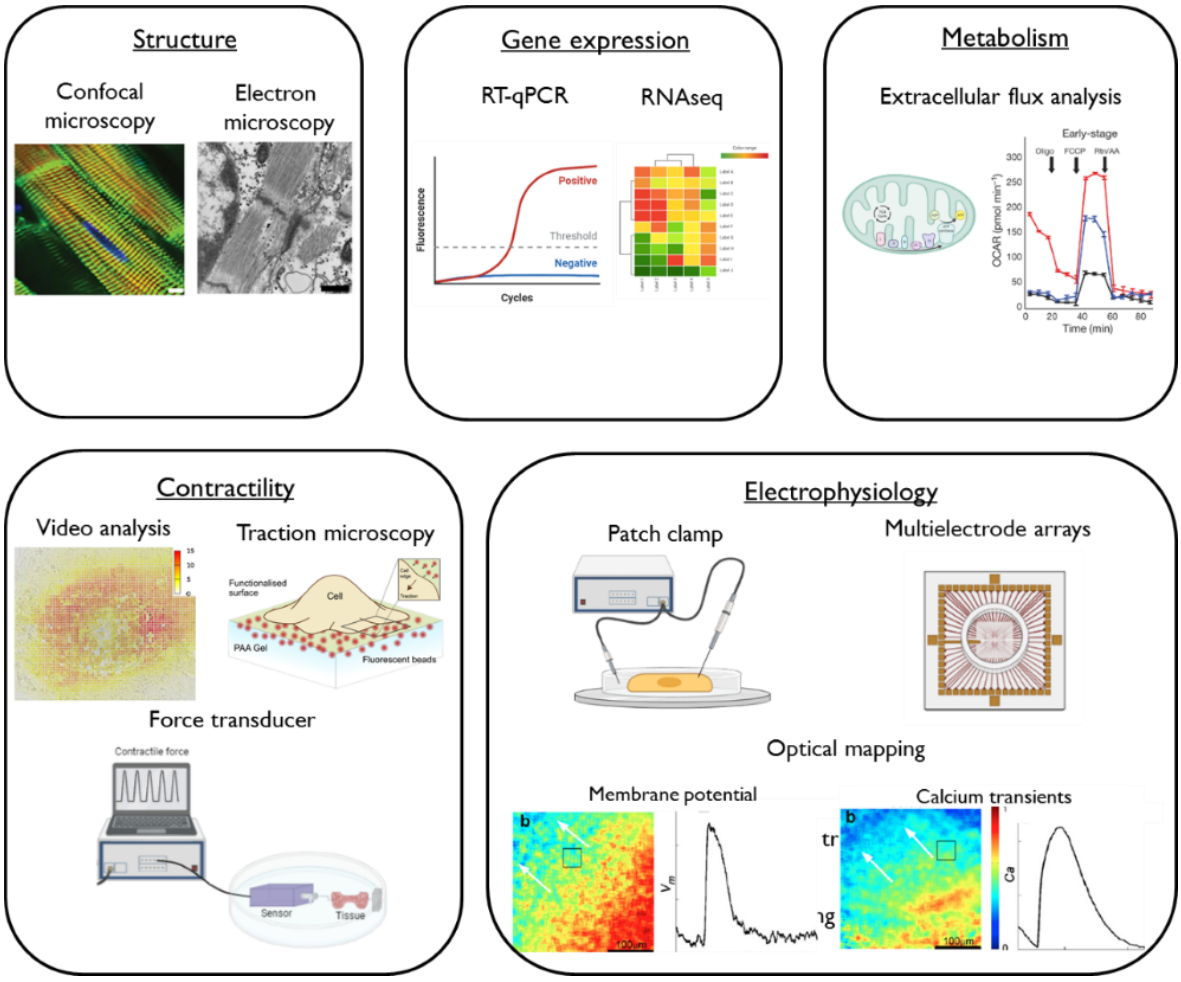


Figure 1-5 ***Categories and methods of assessing the structural and functional properties of engineered cardiac models.*** *Figure created using BioRender and PowerPoint. Examples images for confocal and electron microscopy, video analysis, traction microscopy and optical mapping reprinted with permissions from (Colin-York & Fritzsche, 2018; Blazeski et al., 2012; Czirok et al., 2017; Ronaldson-Bouchard et al., 2018)*

1.4.1 Structural evaluation

Immunofluorescent imaging and electron microscopy can be used to analyse changes in the cellular ultrastructure of hiPSC-CMs. Using fluorescent imaging, the distribution of sarcomeric proteins can be finely resolved and sarcomere length can be quantified through image analysis. Electron microscopy is used to detect the presence, abundance and localisation of the nascent T-tubules and mitochondria, which often serve as hallmarks of advanced maturation (Brandão et al., 2017). These imaging techniques can be performed at a relatively medium throughput and provide useful insights into how the ultrastructure of hiPSC-CMs is affected by the tissue engineering method. However, their sample preparation protocols are extensive and destructive, while the often-manual image analysis required for quantification further limits the throughput. Furthermore, the high

magnification is only possible at a small field of view (FoV), often leading to only partial imaging of the engineered construct.

1.4.2 Gene expression analysis

Complementary gene expression analysis methods can be used to globally assess the cell phenotypes of the engineered construct. Routinely for hiPSC-CM, there will be an assessment of the expression of genes encoding the structural proteins (e.g. cardiac troponins I and T, myosin heavy chain isoforms 6 and 7, cardiac titin, sarcomeric α-actinin), key ion channels (e.g. ryanodine receptors, SERCAs) or gap junction proteins (e.g. Connexin 43). The expression of genes of interest is usually obtained through reverse transcription-quantitative polymerase chain reaction (RT-qPCR) assays, although some studies also use single-cell or bulk RNA sequencing to compare the full transcriptome of complex engineered constructs with isolated cardiac tissues (Lewis-Israeli et al., 2021; Drakhlis et al., 2021; Goldfracht et al., 2020; Nakazato et al., 2022).

1.4.3 Metabolic activity

To assess the active metabolism of the cells, extracellular flux analysis can also be performed to determine the oxygen consumption rate (OCR) or the extracellular acidification rate (ECAR) of the cells within engineered constructs. Importantly, their ratio can be used to measure the relative reliance of hiPSC-CM metabolism on oxidative phosphorylation over glycolysis, useful for tissue engineered approaches to enhance hiPSC-CM maturation (McNally et al., 2021). However, as these measurements rely on the diffusion of the active component, they are most accurately performed on a 2D monolayer, with complex 3D engineered constructs being limited due to inhomogenous penetration of the reagents. Therefore, the metabolic profile of the hiPSC-CMs *in situ* cannot be measured or tracked over time.

1.4.4 Contractility

Functionally, the engineered tissue can be assessed through its contractility or electrophysiology. The contractile output of the tissue is defined by both the amplitude of generated forces and the kinetics of the contraction (Janssen, 2010). Contractility measurements on single-cell and tissue-level are possible, with varying degrees of hardware and analysis complexity, and can be classified as indirect and direct methods (Zimmermann et al., 2006; van der Velden et al., 2001). For example, indirect brightfield microscopy can be used to non-invasively estimate the exerted forces *via* motion detection of individual cells, whole tissues or solid structures affixed to them (Hayakawa et al., 2012; Ma et al., 2014; Nunes et al., 2013). Advances in image analysis software allow rapid quantification of the recorded videos at high throughput (Sala et al., 2018). It should be noted, however, that optical assessments of contractility often only measure contraction in 2D, and estimate the whole tissue contraction through several assumptions (e.g. uniform cell density, predictable 3D shape of the tissue). The low temporal resolution of brightfield force measurements also limits their use for contractile kinetics assessment, however, these methods are still widely used as they are performed at medium-throughput, are non-invasive and compatible with other imaging techniques. Alternatively, advanced traction force microscopy methods can be used for higher resolution 3D measurements, but they require an encapsulation of the contractile cells in a specialist fluorescent bead-embedding matrix, as well as long imaging times to capture the cells from several angles (Lekka et al., 2021).

Directly, contractile forces and dynamics can be measured more accurately using force transducer setups, whereby the engineered tissue is immobilised on one end and attached to either a movable or a piezoelectric sensor on the other (Liau, Zhang & Bursac, 2012). The displacement or deformation of the sensor caused by tissue shortening is converted into a highly resolved contractility trace, which can be analysed to extract the bulk forces and kinetic parameters of an engineered cardiac construct. Although they require specialist equipment and are low-throughput, force transducers offer a non-destructive and precise characterisation of contractile function on a whole-tissue construct level.

1.4.5 Electrophysiology

Quantification of electrophysiological parameters that regulate cardiac contraction is another way to assess the functionality of cardiac tissue. To that effect, calcium handling properties and/or dynamic changes in membrane voltage can be recorded and analysed. Resting membrane, conduction velocity, action potentials and calcium flux kinetics can be used to approximate maturity levels of hiPSC-CMs, while long-distance recordings of both voltage and calcium transients can be used to evaluate the synchronicity and functional anisotropy of the engineered construct (Brandão et al., 2017).

Patch clamping is the gold standard of membrane potential recordings, whereby a glass micropipette electrode is used to form a tight seal with an ion channel of the cell, allowing measurement of the activity of individual channels or the whole action potential (Brandão et al., 2017; Liau, Zhang & Bursac, 2012). These measurements characterise the action potential dynamics of the cell and can be used to estimate the subtypes of individual hiPSC-CMs, since they are thought to differ by their action potential profile. However, traditional patch clamp is performed manually on single cells, requiring dissociation of 3D constructs, and is associated with extremely low throughput. Some automated patch clamp platforms exist, increasing throughput to 700 cells per measurement, however during the recordings the cell must be in suspension, restricting their use for intact whole-tissue constructs (Obergrussberger et al., 2018, Rajamohan et al., 2016). Furthermore, patch clamp measurements lack information on the synchronicity of the tissue, and therefore dynamics of signal propagation through the construct cannot be assessed.

Multielectrode arrays (MEAs) offer a compromise between throughput and sensitivity, as well as the ability to quantify propagation. These devices will be described in detail in section 2.1.2. Briefly, each micropatterned electrode of the array records changes in local extracellular current, generated by a group of cells (Reppel et al., 2005). Although they cannot be used to measure the action potentials of individual cells, MEAs are valuable tools for non-invasive, multi-site repeated measurements of

electrical activity, capable of tracking propagation dynamics in cardiac constructs. Although some nanoneedle fabrication methods have been developed to probe 3D tissues, the majority of traditional commercially available MEA electrodes are planar, and therefore assessment of 3D electrophysiology remains challenging.

Another method for large-scale non-invasive assessment of transmembrane potential changes is fluorescent optical mapping. A typical setup for optical mapping involves cells loaded with a voltage-sensitive fluorescent dye (e.g. di-4-ANEPPS) and a fluorescence microscope with a high-speed camera (80-1000 frames per second) (O'Shea et al., 2020). Generally, changes in transmembrane voltage lead to a proportional shift in the excitation/emission spectra of such dyes, which subsequently alters the emitted fluorescence intensity detected through a given filter (Yu et al., 2017). The dynamic changes in fluorescence are recorded and image processing can be used to reconstruct the action potential at several sites as well as track its propagation across the engineered tissue. Optical mapping can be performed on the scale of hundreds of micrometers to several millimetres by switching the recording optics, given the sufficient acquisition rate of the camera (Liau, Zhang & Bursac, 2012). However, optical mapping only provides relative changes in voltage and cannot be used to measure exact values. The major limitations of such a method is that dye labelling efficiency can be variable, especially in thick tissue constructs, excessive dye loading can alter cell physiology and repeated labelling is required for long-term optical mapping measurements (Brandão et al., 2017). hiPSCs with genetically encoded voltage indicators (GEVI) can be differentiated to produce hiPSC-CMs with inherent electrophysiological output as a cytocompatible alternative with more stable fluorescence intensity than the potentiometric dyes (Lin & Schnitzer, 2016). Such hiPSC-CMs are increasingly used in cardiac tissue engineered models as it provides a non-invasive quantifiable output of tissue functionality.

Optical mapping is also used to identify and measure the dynamic changes in cytosolic calcium concentrations that translate an electrical impulse into a physical contraction of cardiomyocytes.

This can be achieved through calcium-sensitive dyes, such as Fluo-4, which increase in fluorescence intensity upon binding to calcium ions (Liau, Zhang & Bursac, 2012). The change in fluorescence intensity is then used to reconstruct traces of calcium transients, from which calcium kinetics can be extracted, providing physiological insights into the durations of activity for different calcium ion channels during contraction (Jaimes et al., 2016b). Calcium dyes suffer from the same drawbacks as potentiometric dyes, with several hiPSC cell lines containing genetically encoded calcium indicators (GECI) that address the issues associated with dye loading (Jiang et al., 2018).

Overall, voltage and calcium optical mapping provide information on electrophysiological signalling underlying contraction and are often used individually or in synergy to characterise the functional performance of engineered cardiac tissues. The spatial propagation of voltage and calcium transients can be used to calculate conduction velocities and produce isochronal activation maps demonstrating sequential activation of the functional syncytium (Jaimes et al., 2016b). Notably, while such measurements can be performed on a single cell level in 2D monolayers, in complex 3D tissues the recorded signal is a sum of the fluorescence obtained from all planes of the construct. Therefore, the more complex propagation paths in 3D of whole-tissue measurements are often unaccounted for and absolute quantification of voltage or calcium amplitudes cannot be performed (Jaimes et al., 2016b).

Taken together, the ultrastructure, gene expression, metabolism, contractility and electrophysiology assessment form a valuable toolkit of engineered tissue characterisation methods. Subcellular imaging assesses individual hiPSC-CM maturity on a structural level, gene expression analysis provides information on changes in global cell phenotypes, metabolism assays inform on bioenergetic resources of the tissue, while contractility and electrophysiology amplitudes and kinetics determine the functional output of the tissue engineered constructs. A combination of several assessments is usually performed depending on the target application of a given tissue engineered model.

1.5 Applications of cardiac tissue models

There are four main applications for cardiac models: developmental biology, disease modelling, drug screening platforms and regenerative medicine, although often engineered constructs can be valuable for more than one application. Importantly, depending on the application, the design requirements and priorities for cardiac tissue engineering vary.

1.5.1 Cardiogenesis modelling

Translating our knowledge of natural heart organogenesis into complex multi-step cell culture protocols allows generation of hiPSC cultures that self-organise into cardiac organoids. Organoids are self-organised 3D cellular aggregates that replicate the complex multi-cellularity of the native tissue as well as aspects of its architecture and function, making them an attractive platform for *in vitro* modelling of cardiac morphogenesis. Mouse ESCs aggregates have been used to demonstrate first and second heart field (FHF and SFH) generation and cardiac crescent-like structure formation, characteristic of the tissues formed during early heart tube development (Rossi et al., 2021). Additionally, distinct myocardial and endothelial layers were observed in both mouse and human hiPSC spheroid cultures, along with other cell types of the germ layers (Rossi et al., 2021; Drakhlis et al., 2021). The later stages of development, post heart tube formation, were also reproduced, forming primitive hiPSC-derived cardiac tissues with defined cardiomyocyte, epicardial-like and epithelial-like structures alongside the nascent gut-like tube (Silva et al., 2021). The functional features of such systems remain limited by the lack of chamber development. A recent study used repeated Wnt activation to trigger epicardial layer induction in self-assembled cardioids that contained endothelial cell-lined chamber-like cavities, significantly advancing the structural organisation of cardiac developmental models (Lewis-Israeli et al., 2021). However, the chambers were generated stochastically and were not interconnected, and the epicardial layer was not continuous. Another approach of co-culturing partially committed *ISL1*$^{+}$ cardiac progenitors with cardiomyocytes in spheroids led to the formation of a single core chamber fully enclosed in spontaneously contracting cardiac cells (Ho et al., 2021).

Overall, the existing models of cardiac development promisingly replicate the multicellularity, early developmental stages and a degree of chamber development, however, the intricate architecture of the interconnected chambered heart or its characteristic pumping feature have not been captured yet. While the question of whether such systems are true organoids or simply cardiac spheroids remains, future advances in cardiac organoids would provide not only an insight into healthy heart development, but also the complex mechanisms of hereditary cardiomyopathies and channelopathies.

1.5.2 Disease modelling

Disease modelling in engineered cardiac tissues can be achieved by using disease-associated biophysical cues or disease-specific hiPSC-derived cells to illuminate the mechanisms and environments of chronic and acute cardiac diseases, as well as to investigate the efficiency of novel treatment strategies. For example, tissue engineered constructs of hiPSC-CMs grown in a collagen I/fibrin hydrogel was subjected to hypoxic conditions and ischemia-mimicking buffer to replicate the pathophysiology of ischemia-reperfusion injury (Chen & Vunjak-Novakovic, 2019). Alternatively, pathological hypertrophy has been observed in hiPSC-CMs-laden fibrin tissues when they were supplied with increased afterload (Leonard et al., 2018). Modelling of inherited diseases has also been possible by generating cardiac organoid-like structures from CRISPR/Cas9 edited hiPSCs with loss-of-function *Nkx2.5* mutation, representative of Ebstein's anomaly – a heart condition with a malformed tricuspid valve (Feng et al., 2022). Alternatively, hiPSCs from patients can be used. For example, hiPSC-CMs containing a rare mutation of myosin isoform have been used to produce engineered cardiac constructs and study how the mutation impairs cardiomyocyte alignment and contractile function (Yang et al., 2018). Building on this knowledge, hiPSC-CM disease models can also be used to investigate the effects of gene editing for hereditary diseases associated with cardiomyopathies. In one study, engineered heart tissue, produced with PSCs-CMs from patients with three different Duchenne muscular dystrophy mutations, showed significant restoration of

contractile function upon CRISPR/Cas9 mutation editing (Long et al., 2018). Overall, there are many avenues for disease modelling with the continuously growing library of patient-specific and disease-specific hiPSCs. Combining those with biophysical cues associated with disease, such models would present an invaluable tool for *in vitro* drug screening.

1.5.3 Drug screening

Engineered i*n vitro* drug screening models can bridge the gap between the over-simplified 2D monolayer cultures and complex, expensive, and labour-intensive animal models. Utilising hiPSC-CMs also allows the study of compounds in the context of human physiology/pathology, improving the predictability of the assays prior to translation towards *in vivo* animal work and clinical trials. Most modern published cardiac models, from 2D monolayers of hiPSC-CMs to cardiac organoids and heart-on-a-chip, include a proof-of-concept drug screening study. 3D models have previously shown a 93% accuracy in their contractile and calcium transient response to 28 drugs with known inotropic effects, significantly outperforming 2D monolayers with 85% accuracy (Saleem et al., 2020). To that effect, 3D cardiac tissue models of varying complexities have been validated for drug screening applications. For example, high-throughput multi-cellular cardiac spheroids have been successfully used to screen 29 FDA-approved compounds, however, the readout only provided information on cell viability and structural perturbations (Archer et al., 2018). Some functional information of spheroids has been obtained either through indirect contraction amplitude estimation from brightfield video analysis, or by using voltage-sensitive dyes for optical mapping (Richards et al., 2020; Kofron et al., 2021). Increasing the complexity to microtissue strips by immobilising the engineered constructs between flexible posts has achieved direct measurements of contractility kinetics and forces in several systems, and this approach was successfully used to evaluate the functional effects of 105 compounds in one study (Mannhardt et al., 2017; Goldfracht et al., 2020; Lu et al., 2017; Saleem et al., 2020; Mills et al., 2019; Nunes et al., 2013). A key advancement in readouts for drug screening platforms has been achieved by ventricle-like cardiac chambers, the only

engineered cardiac system capable of recreating the pressure-volume loops and measurements of ejection fraction (proportion of ejected blood over total volume of the heart) (Keung et al., 2019; Li et al., 2018a). Such chambers have been shown to enable a more physiological response to 25 cardioactive compounds than the simpler strip-like cardiac microtissues, however, their intricate fabrication protocol makes the upscaling process challenging (Keung et al., 2019). Overall, there is a lot of potential and demand for cardiac tissue engineered models in drug screening applications. However, the trade-off between high throughput, reproducibility, tissue complexity and functional readout is a limiting factor in the translation of such models to a pharmacological setting (Bremner et al., 2022).

1.5.4 Regenerative medicine

Cardiac tissue engineered constructs can also be used in regenerative medicine to remuscularise the injured cardiac muscle with exogenous hiPSC-CMs, with the promise of autologous cell therapy in the future. Scaffold-free hiPSC-CM cardiac sheets were among the earlier demonstrations of the therapeutic potential of cardiac patches, leading to improved ejection fraction and decreased fibrosis in the myocardial infarction model (Kawamura et al., 2012, 2013). Later, 3D biomaterial scaffolds were found to improve the maturation status of hiPSC-CMs, increase exogenous cell retention and provide mechanical support to the damaged tissue, making cell-laden biomaterial scaffold increasingly popular. For example, human engineered heart tissues (hEHTs), commonly produced by maturing hiPSC-CMs encapsulated in fibrin or collagen hydrogels through electrical and mechanical stimulation, have been shown to reduce the infarcted area and partially restore the cardiac function in guinea pig and rabbit MI models (Weinberger et al., 2016; Jabbour et al., 2021). The mechanical stretch during EHT culture increases the alignment of cardiomyocytes within the scaffold, in parts replicating the cytoarchitecture of the native tissue. To further improve on that organisation, advanced fabrication strategies have also been used to replicate the anisotropic structure of ECM and stimulate alignment of the exogenous cells. For example, nanofiber-aligned

cardiomyocytes and endothelial cells showed higher therapeutic efficacy than equivalent patches with random fibre and cell orientation (Lin et al., 2014). Similarly, cardiomyocytes cultured on ECM-mimicking nano-grooves improved wall thickness and collagen organisation of the infarcted tissue upon transplantation (Kim et al., 2012). However, since these two studies were performed with isolated cardiomyocytes or pre-committed cardiac progenitors, it would be interesting to see such approaches applied to hiPSC-CM culture in combination with EHT maturation protocols. More recently, hiPSC-CMs have been 3D printed to produce anisotropic patches matured through mechanical loading prior to transplantation *in vivo* (Cui et al., 2020).

To conclude, in the last 20 years the breakthrough in stem cell technologies has led to the development of hiPSC-CM methods, allowing robust production of functional cardiac cells of human origin. Combined with materials, biophysical cues and advanced fabrication methods, these cells can be used to create cardiac tissue models of varying complexities that serve as powerful tools for cardiogenesis studies, disease modelling, drug screening or tissue remuscularisation. However, there are two general limitations of the engineered models that still restrict their biological relevance. On a cell level, hiPSC-CMs remain immature and foetal-like and do not resemble the adult cardiomyocyte phenotype, while on a tissue level most models lack physiologically-relevant structural organisation. The work of this thesis focusses on the latter, and in the next section the fabrication methods that seek to address the structural limitation through cell patterning are described.

1.6 Approaches to generating patterned cardiac models

As often seen in biological systems, the intricately organised architecture of heart muscle facilitates its coordinated contractile function and directional signal propagation. Aligned cardiomyocytes surrounded by ECM that forms electrically- and mechanically- coupled parallel bundles, which in turn are spatially arranged to form a functional anisotropic syncytium. Such complex multi-scale hierarchical arrangement is rarely replicated *in vitro*, with many cardiac tissue models formed by

encapsulation of disorganised hiPSC-CMs in the bulk material. However, directional biomaterial features have been shown to improve hiPSC-CM functionality, demonstrated by more efficient calcium handling and anisotropic contractility in comparison to their disordered controls (Rao et al., 2013; Allen et al., 2019; Khan et al., 2015). The vast diversity of material-based cell organisation methods therefore aim to add structural sophistication to produce next-generation tissue engineering constructs (Figure 1-5).

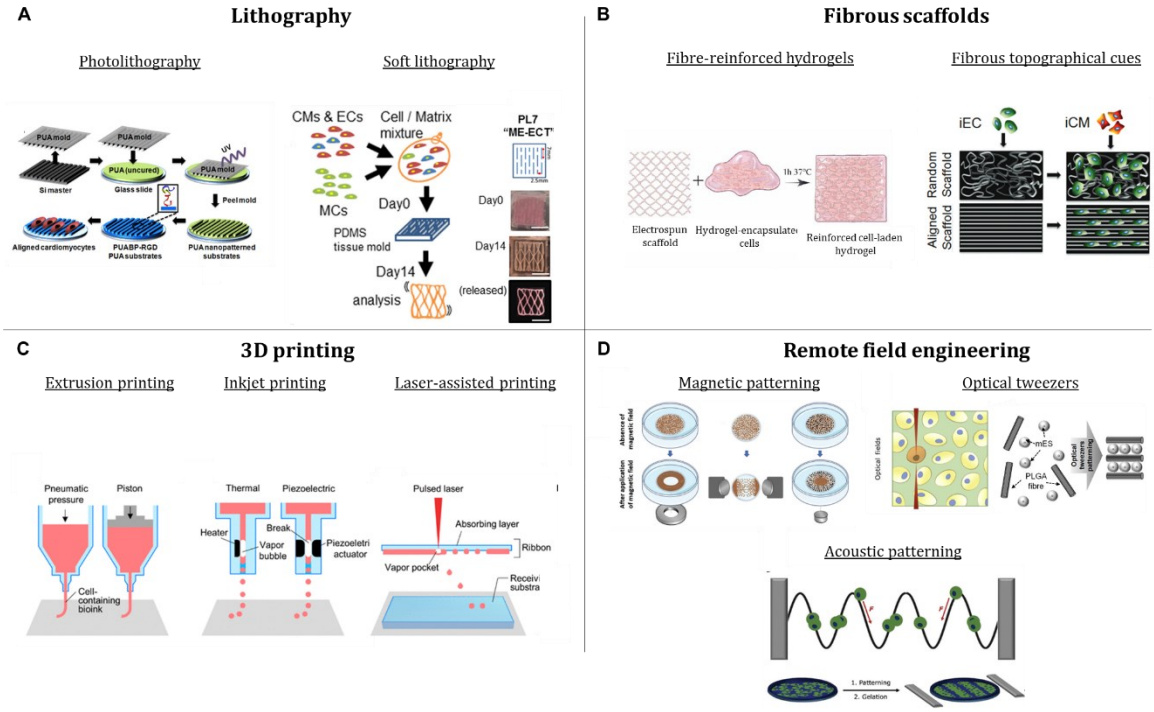


Figure 1-6 ***Overview of cell patterning methods.*** *Four classes of techniques often used for controlling the spatial organisation of the cells. (A). Some of the lithography methods include photolithography and soft lithography (Left) Adapted with permission from* (Carson et al., 2016)*. © 2016 American Chemical Society. (Right) . In soft lithography, the cells (e.g. cardiomyocytes, CMs, endothelial cells, ECs and mural cells, MCs), are mixed with the matrix, added to a PDMS mould at day 0 and are grown until the experimental endpoint (e.g. day 14). An example of the construct progression from the mould design to the fully grown engineered tissue is shown on the right. Adapted from* (Nakane et al., 2017) *with permission under the Creative Commons CC BY License. (B). Fibrous scaffolds can be used either to add the structure to hydrogel systems or as substrates for cell growth. (Left) Adapted from* (Montero-Calle et al., 2022) *with permission under the Creative Commons CC-BY license. (Right) Adapted with permission from* (Wanjare et al., 2017)*. (C). 3D-printing methods, such as extrusion, inkjet and laser-assisted printing can be used to print acellular or cellular bioinks. Adapted with permission from (Jang, Yi & Cho, 2016). © 2016 American Chemical Society. (D). Remote field engineering methods that utilise magnetic and acoustic fields or optical traps to manipulate cell positioning within a medium. Images reproduced from (Zwi-Dantsis et al., 2020; Armstrong et al., 2018; Armstrong & Stevens, 2020; Kirkham et al., 2015).*

1.6.1 Lithography-based topographical cues

Lithography-based patterning introduces topographical features to material substrates, replicating the nano- and/or micro-scale topography of the native ECM, with which cells can interact (Teo et al., 2010). In photolithography, a photomask is introduced between a light source and a photosensitive material, leading to selective curing at the exposure sites and producing a construct with geometry predefined by the photomask pattern (Ermis, Antmen & Hasirci, 2018). The patterned construct can then be: i) replicated onto biocompatible elastomeric materials, such as polydimethylsiloxane (PDMS), and coated with biomolecules to facilitate cell adhesion (traditional photolithography); ii) used for replica moulding of cell-laden hydrogels (soft lithography); or iii) coated in bioactive molecules and used for surface stamping (microcontact printing). All three approaches have been applied to generate patterned structures of hiPSC-CMs. For example, adhesion peptide-functionalised polyurethane acrylate nanogrooves have been used as substrates to induce cardiomyocyte alignment on the tissue-level and increase sarcomere length on the single-cell level, while net-like PDMS moulds have been used to introduce a mesh macropattern to EHTs (Carson et al., 2016; Nakane et al., 2017; Jabbour et al., 2021; Zhang et al., 2013). Although photolithography can be used to introduce high-resolution topographical features in 2D, its design complexity and precision is a lot lower in 3D. Furthermore, there are limited materials that can be topographically patterned, and their stiffness and chemistry can impact cell physiology.

1.6.2 Cell-laden fibrous biomaterial scaffolds

Aligned fibrous biomaterial scaffolds are another way of introducing anisotropic features to cardiac models. Such scaffolds are often fabricated using electrospinning techniques, covered in detail in section 4.1.2. Briefly, a polymer solution or melt is jetted onto a collector across a high-voltage electric field. Varying collector geometry and motion, pre-defined orientations of individual fibres or the whole construct can be achieved. Through pre-fabrication material or post-fabrication surface functionalisation, bioactive molecules can be introduced onto the scaffold to provide adhesion and matrix remodelling sites for cellular interactions. The scaffolds are then used either as structural

support for hydrogel-encapsulated cell constructs or as substrates for cell seeding and growth directly. For example, nanofibre-guided hiPSC-CM alignment has previously been achieved, leading to improved contractile function (Wanjare et al., 2017; Liu et al., 2016). Varying the spacing and aspect ratio of the fibre grid has also been used to mimic the dimensions of cardiac ECM, which led to increased conduction velocity in fibre-reinforced hiPSC-CM-collagen models (Montero-Calle et al., 2022). Impressive control of fibre diameter can be achieved, ranging from 3 to 5000 nm (Meireles et al., 2018). The micron-sized diameter fibres can be used to create a range of predictable geometries, from simple rectangular to complex auxetic patterns (Jin et al., 2021; Liashenko et al., 2020). However, the design flexibility of fibrous scaffolds is mostly limited to 2D, with the z-plane dimensions of the scaffold achieved through stacking and lacking complexity. Furthermore, the patterning is performed acellularly due to the use of high voltages, incompatible with cell viability.

1.6.3 3D bioprinting

Additive manufacturing, or 3D bioprinting, can be used to achieve finer architecture control. Broadly, bioprinting approaches can be classified into three methods based on their material deposition technique. In ink-jet printing individual droplets of ink are dispensed onto a substrate. Extrusion-based bioprinting relies on mechanical forces to guide viscous ink deposition. Finally, laser-assisted bioprinting utilises a UV light source to selectively cross-link photopolymerisable bioinks into 3D structures. The inks used for bioprinting can be acellular and used for fabrication of 3D structures that are later seeded with cells, or cellular, whereby a cell suspension is mixed with a printable biomaterial. The theoretical resolution of 3D-printing differs depending on the method and ink properties. The droplet size determines the resolution of ink-jet printing, capable of producing features of sub-20 µm, while the nozzle size and ink viscosity of extrusion-based printing limit it to ≈200 µm (Miri et al., 2019). Some light-assisted bioprinting methods can achieve as high as ≈5 µm resolution (Ovsianikov et al., 2014). However, in practice, the shear forces, UV exposure and

photoinitiator toxicity severely affect the viability of cellular bioinks, reducing the resolution limit of most bioprinting methods to ≈100 µm (Miri et al., 2019).

Acellular 3D-printed ECM scaffolds has been used for structural support of hiPSC-CMs, endothelial and smooth muscle cells, to engineer an aligned functional tissue (Gao et al., 2017). Cellular 3D bioprinting can generate complex bioinspired structures, with the promise of high-throughput organotypic models. Impressively, a complex perfusable 3D cardiac structure with two functional chambers has been created by extrusion-printing hiPSCs with subsequent differentiation (Kupfer et al., 2020). hiPSC-CMs have also been recently incorporated into bioinks (Esser & Engel, 2021; Maiullari et al., 2018). However, the low proliferation rate of hiPSC-CMs combined with high shear forces and prolonged UV exposures often required for 3D printing methods can limit their compatibility for cellularised bioprinting.

Overall, 3D printing methods increase the complexity and design flexibility of cell patterning. However, the resolution of the printing is limited and the cytocompatibility of these biofabrication methods is variable. Although intricate structures can be generated using bioprinting, the patterning occurs on the macroscale, with both the matrix and the incorporated cells assuming the same shape. Therefore, the cells are distributed homogenously within the bulk material of the patterned structures.

1.6.4 Remote field engineering

Less invasive remote field engineering is an emerging research area, whereby the positioning of cells (or particles) within a medium is manipulated through gradients of externally applied optical, magnetic, or acoustic forces (Armstrong & Stevens, 2020). The pre-defined shape of the remote field determines the geometry of the pattern, which can be subsequently immobilised either on a substrate or within a bulk material to create 2D and 3D models respectively. Since the forces generated by remote fields are relatively small and can be counteracted by viscous forces, the latter requires the use of a medium that undergoes a triggered transition from a liquid to a solid hydrogel.

All three remote fields methods have been used for cell patterning applications, with magnetic and acoustic patterning implementing hiPSC-CMs to create cardiac tissues (Zwi-Dantsis et al., 2020; Serpooshan et al., 2017).

In magnetic patterning, either the media or the cells must be magnetised in order to respond to the applied field. Cell labelling can be achieved by either tagging cell surface receptors with antibody-functionalised magnetic nanoparticles (MNPs), or through the passive uptake of unfunctionalized MNPs (Lee et al., 2014). The shape of the magnetic field is defined by a single magnet geometry and/or the interference of magnetic fields from several magnets, allowing the orientation of magnetised cells in a range of patterns. For example, applying a circular, ring, or a pair of square magnets to MNP-labelled hiPSC-CMs suspended in collagen produced three beating cardiac constructs with distinct cellular gradients (Zwi-Dantsis et al., 2020). However, the labelling of cells prior to the patterning can have variable efficiency, lead to reduced viability, or affect cellular processes (Chen et al., 2017; Liße et al., 2017). Furthermore, the poor flexibility of magnetic field design leads to the generation of relatively simplistic patterns with low resolution.

Significantly higher precision patterning can instead be achieved using optical tweezers, whereby a focussed laser beams traps a cell or a particle in place and can be directed to control its position (Guo & Li, 2013). In contrast to the magnetic field, this approach does not require any prior labelling or treatment of the target cells. Optical tweezer cell manipulation occurs at a single cell level, which has been useful to study early developmental stages or cell-cell interactions (Kirkham et al., 2015; Linnenberger et al., 2013). The high resolution of optical trapping, however, comes in exchange for extremely low throughput, restricting the use of such tweezers in large scale tissue engineering. In the cardiac field, optical tweezers have only been applied as a characterisation tool for hESC-CM biomechanical properties, and currently no literature on optical cardiomyocyte manipulation or patterning has been reported (Tan et al., 2012, 2011).

Acoustic patterning supersedes the other remote field tissue engineering approaches due to high versatility and throughput as well as minimal requirements of cell and media properties (Armstrong & Stevens, 2020). The principles and uses of acoustic patterning in tissue engineering and, in particular, its benefits for engineering cardiac models will be discussed in detail below in Chapters 2 and 3 of this thesis.

CHAPTER 2. SOLUTION-BASED ACOUSTIC PATTERNING FOR 2D CELLULARISED CARDIAC DRUG SCREENING MODELS

2.1 Introduction

2.1.1 Acoustic cell patterning

2.1.1.1 Acoustic patterning technique overview and principles

Acoustic patterning is a remote manipulation tool that uses the interference of ultrasonic waves to aggregate particles or cells in geometries pre-defined by the shape of the resultant acoustic field (Armstrong & Stevens, 2020; Cox, Croxford & Drinkwater, 2022). Ultrasound is a longitudinal pressure wave oscillating at frequencies above 20 kHz that causes vibration of the particles in the medium parallel to the direction of the wave. One way of creating sound waves is by using piezoelectric transducers driven with alternating current. The piezo material converts electrical energy into mechanical, leading to transducer expansion and contraction and producing vibrations. 1-dimensional standing waves are established through the interaction of two waves travelling in the same medium in opposite directions (Figure 2-1). This can be achieved using either a pair of opposing transducers or a single transducer and a reflecting surface. The two waves interact through constructive (the sum of amplitudes of sound waves that are in phase) and destructive (the subtraction of amplitudes of sound waves that are out of phase) interference, producing a well-defined pressure field. When the whole number of half wavelengths fits between the opposing wave sources, a standing wave confined to the boundaries of the patterning cavity is formed.

A standing wave consists of a series of stationary alternating pressure difference minima (nodes) and maxima (anti-nodes), with fixed pressure gradients generated between those regions. These pressure gradients become steeper when the transducers are operated at resonant frequencies. Importantly, the pressure gradients produce an acoustic radiation force, that directs the suspended cells or particles along the pressure gradient towards nodes or anti-nodes, depending on their elastic properties (Ding et al., 2012). The acoustic radiation force can be given by:

$$F_{rad} = \left(\frac{-\pi P^2 V \beta}{2\lambda}\right) \times \phi \times \sin\left(\frac{4\pi\zeta}{\lambda}\right),$$

with primary radiation force (F_{rad}), peak pressure amplitude (P), wavelength (λ), the spherical volume of the cell/particle (V), cell/particle compressibility (β), acoustic contrast factor (Φ) and distance from nodal planes (ζ). Generally, the positive or negative sign of the acoustic contrast factor determines whether the acoustic radiation force acts towards the nodes or anti-nodes respectively (Laurell, Petersson & Nilsson, 2007). To that effect, since the cells have positive Φ, they are patterned down the pressure gradient towards the region of low acoustic potential energy, accumulating at the nodes (Figure 2-1) (Augustsson & Laurell, 2012; Yan et al., 2017).

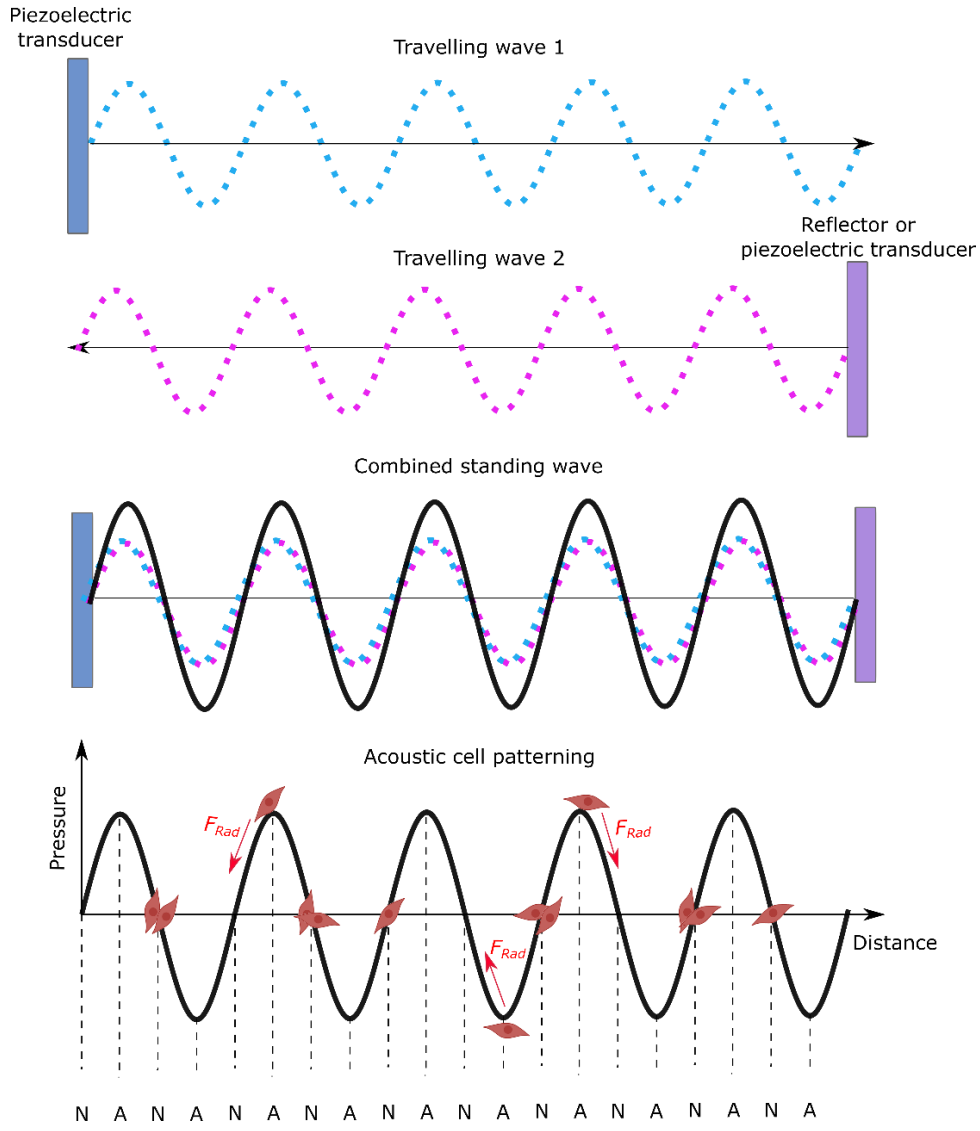


Figure 2-1 ***Acoustic cell patterning.*** *Two travelling ultrasound pressure waves acting across the same distance interfere to produce a standing wave consisting of a series of pressure minima (nodes, N) and maxima (anti-nodes, A). Acoustic radiation force (F_{rad}) acts on the cells to direct them to regions of zero pressure difference.*

For successful patterning, the acoustic radiation force experienced by cells needs to outpower the forces acting to oppose it, such as gravity, viscosity, mechanical agitation and cell-material interactions. Furthermore, exposure of a liquid to high-amplitude acoustic waves results in a steady fluid motion, known as acoustic streaming, which can disrupt the movement of cells towards the nodes if the acoustic radiation force is low (Frampton, Martin & Minor, 2003). The quality of cell patterning therefore depends on the magnitude of F_{rad}. The parameters that have the largest effect on F_{rad} are media viscosity, cell size and whether the driving frequency is at resonance.

While patterning using a single standing wave can be thought of as 1D-patterning, the introduction of more transducers or whole transducer arrays can generate multiple acoustic standing waves simultaneously, leading to multi-dimensional patterning. Furthermore, acoustic waves can either be acting in a single plane or in full volume. Commonly in literature, the waves propagate through the full volume, however the cells are accumulated in a single plane due to gravity, thus resulting in horizontal single plane patterning. Indeed, linear arrays generated by a single transducer pair led to horizontal 1D trapping, while clusters produced by two orthogonal transducer pairs is horizontal 2D trapping (Bernassau et al., 2012; Cai et al., 2020). Further degree of complexity can be introduced through sequential patterning in the multi-transducer pair device and phase shift, showing promise for multi-layered cell systems in 3D (Gesellchen et al., 2014). Different transducer orientations, number of standing waves and media chemistries allow to pattern cells in a variety of biologically relevant geometries.

2.1.1.2 Types of acoustic patterning

Several acoustic methods have been developed to apply sound to cell suspensions in solution, generating uniform ordered patterns. Below, four different approaches to acoustic cell manipulation and their applications and limitations are outlined: surface acoustic waves, bulk acoustic waves, Faraday waves and holographic patterning (Figure 2-2).

Surface acoustic waves

Standing surface acoustic waves (SSAWs) are produced when the interdigitated transducers (IDTs) are coupled with the piezoelectric substrate, allowing a sound wave to propagate across the surface of an elastic material (Campbell & Burgess, 1999). They can be integrated with microfluidic systems, giving rise to acoustofluidic droplet-based or continuous flow-based lab-on-a-chip devices. For example, altering the frequency and input power of SSAW can induce acoustic streaming within the boundaries of a single droplet, leading to its micromixing, motion, jetting or atomization (Dung Luong & Trung Nguyen, 2012). Some of the applications of those droplet operations include small-scale reactions, low-cost ink-jet printing, or low-volume polymerase chain reactions (Reboud et al., 2012; Xu et al., 2018; Castro et al., 2018). In continuous flow devices, changing parameters of the SSAW acoustic field (e.g. phase and amplitude) can be used for focussing and streaming the suspended particles or cells, with applications in circulation mimics or flow cytometry (Wang & Zhe, 2011; Chen et al., 2014).

SSAW-based devices are capable of precision single-cell trapping, operate across a large frequency range and require a lower power supply, making them attractive for device miniaturisation and cell manipulation on the microscale (Collins et al., 2015). However, SSAWs depend on the integration of a piezoelectric substrate within the patterning chamber, which causes solution overheating and in turn limits their compatibility with already existing culture systems. Furthermore, such devices are difficult to upscale, particularly in 3D, limiting their use for macroscale tissue engineering.

Bulk acoustic waves

In contrast with SSAWs transmitted on a confined surface, bulk acoustic waves (BAWs) are propagating through the bulk of a liquid or a material (Zhang et al., 2020). BAWs are generated using electrically-driven piezoelectric transducers (commonly, lead zirconate titanate), acting across a cavity at its resonance (Uchino, 2012; Guex et al., 2021). BAW systems are easy to integrate with the standard cell culture systems: the piezo-transducers can be isolated from the culture chamber to

minimise heating, with the standing wave established through the bulk of the media. BAW-based devices are more robust, have higher throughput, are easier to fabricate and can generate macro-scale patterns in 3D volume, making them preferable to SSAWs in tissue engineering and drug screening applications. The acoustically trapped cells are either allowed to settle and adhere to the patterning surface by gravity or are immobilised using hydrogel polymerisation. The latter approach is discussed in detail in Chapter 3.

Faraday waves

Faraday waves can be produced using a single low-frequency (< 200 Hz) generator acting vertically across an open fluid-filled chamber (Guex et al., 2021; di Marzio et al., 2022). The vibrations form a standing wave that destabilises the air-liquid interface, generating non-linear patterns of hydrodynamic drag force that leads to cell or particle assembly. Some of the periodic structures produced by Faraday waves include stripes, rings, hexagons, squares and their combinations. While Faraday waves have the advantage of no overheating and increased pattern complexity, there is a mismatch between the location of nodes at the air-liquid interface and the final arrangement of cells, making it hard to tailor to specific geometries (Guex et al., 2021)

Acoustic holography

Acoustic holography is a growing field whereby a custom 3D-printed hologram is introduced in the path of ultrasound emitted from a transducer (Melde et al., 2016). The holograph encodes a sequence of phase shifts that distorts the planar incident wave, generating the desired interference pattern. A proof-of-concept study demonstrated that holographs can be applied to engineer cell systems, with the complex pattern of HCT-116 colon cancer cells immobilised in collagen type I hydrogel (Ma et al., 2020a) Dynamic particle manipulation can be achieved by combining 3D-printed holograms with phased arrays or by utilising the impedance mismatch in programmable microbubbles (Ma et al., 2020b; Cox et al., 2019). Acoustic holograms are also capable of an impressive pattern control in 3D by superimposing multiple pressure fields from several holograms,

producing complex C2C12 myoblast cell structures immobilised in a slow-curing hydrogel (Melde et al., 2022). Acoustic holography is indeed an exciting approach that offers complete freedom in pattern design; however it is often limited by the resolution of the 3D printer used to fabricate the hologram.

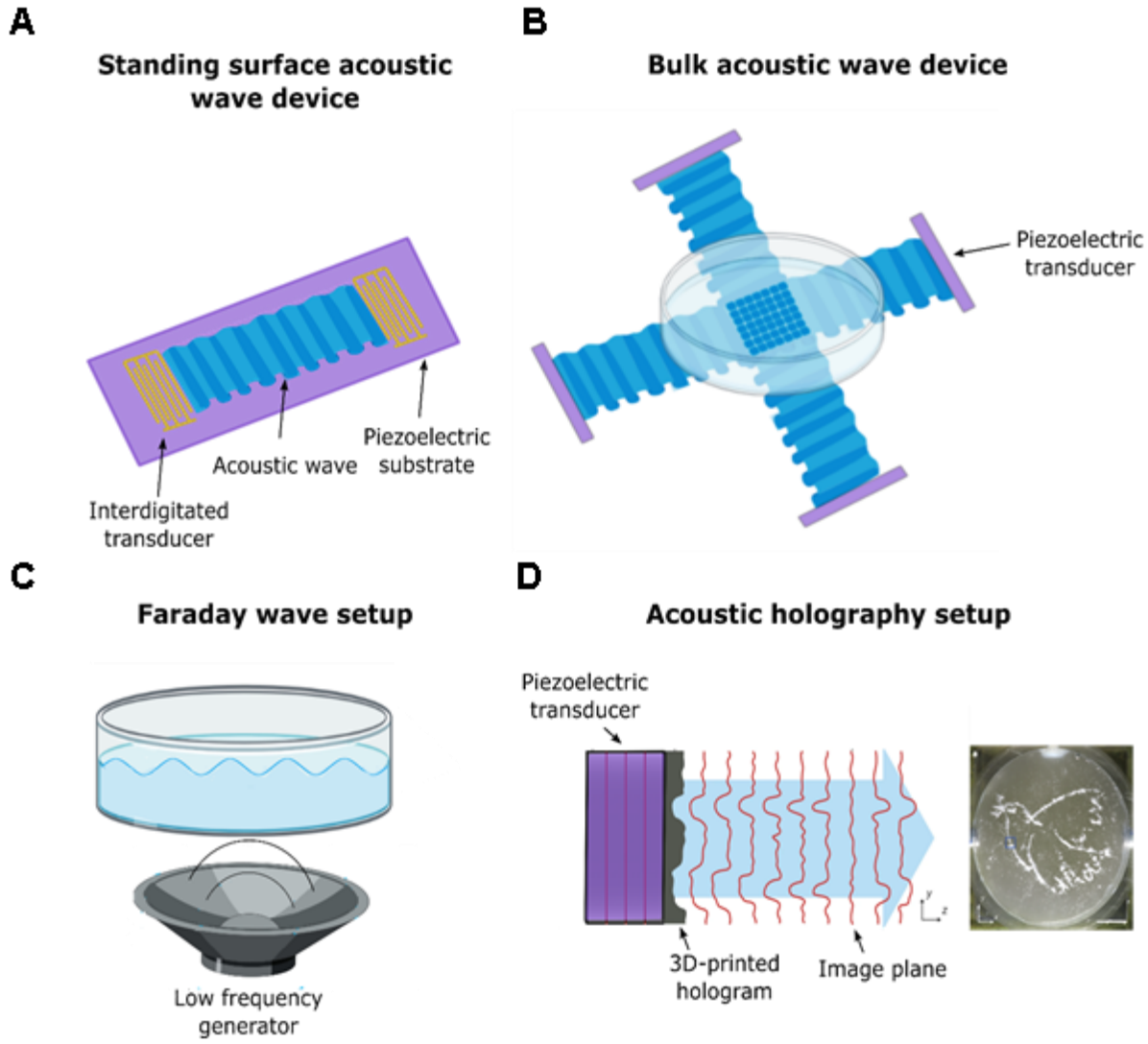


Figure 2-2 ***Acoustic patterning setup examples.*** *Standing surface acoustic wave device, with a single pair of interdigitated transducers (IDTs) on a piezoelectric substrate. (A). Bulk acoustic wave device setup with two pairs of opposing piezoelectric transducers acting across a single culture dish (B). Faraday wave setup with a low frequency generator acting vertically across a culture dish. Generator image reproduced from brgfx on Freepik. (C). Acoustic holography setup with a piezoelectric transducer emitting sound through a 3D-printed hologram (D). Reprinted with permission from* (Melde et al., 2016).

2.1.1.3 Solution-based acoustic cell patterning

Importantly, acoustic assembly methods can be applied to pattern cells in solution for biological studies. For example, linear arrays of HeLa and human lung microvascular endothelial cell (HMVEC)

cocultures were created using SSAWs to investigate migratory properties of cancer cells (Li et al., 2014). The effect of neurone patterning on neurite outgrowth has also been studied on a piezoelectric chip using SSAWs and on a collagen scaffold using BAWs (Brugger et al., 2018; Cohen et al., 2020). Cell spheroids can be aggregated at high throughput using BAWs or at high precision using SSAWs, demonstrated previously with homogenous carcinoma cell lines or heterogenous neurospheres (Olofsson et al., 2018; Cai et al., 2020; Sriphutkiat, Kasetsirikul & Zhou, 2018). The dynamics of biofilm production has been previously studied using *E.Coli* patterned with Faraday waves (Hong et al., 2020). Faraday waves can also be used for large-scale assembly of multicellular structures, for example to arrange ring-shaped fibroblast structures in a 96-well plate (Ren et al., 2020).

Solution-based patterning allows to introduce a degree of architectural complexity to otherwise unpatterned monolayer cell cultures. In the context of cardiac culture models, solution-based patterning could be used to produce linear arrays of cardiomyocytes, resembling a 2D projection of cardiac fibres of the native tissue. Although such models do not recapitulate all aspects of the complex microenvironment of the heart, their structural anisotropy could provide insights to the dynamics of electrical signal propagation, useful for drug screening applications.

2.1.2 Multielectrode Arrays

2.1.2.1 Electrophysiology measurements

Electrophysiology measurements are the key quantitative outputs of the cardiac tissue, which can be performed either as single cell patch-clamp or multielectrode array (MEA) recordings. Patch clamp measurements utilise a micropipette filled with an ionic solution, which is brought into contact to form a tight seal with the lipid bilayer of the cell membrane, forming an electrical circuit. There are many variations of this technique, with the majority being able to record kinetics and gating properties of individual ion channels with high resolution and accuracy, making it the gold standard

for electrophysiology measurements (Brandão et al., 2017). In cardiac drug screening, patch clamp measurements are used to evaluate the changes in contributions of different ionic currents to the overall action potential (AP) of a single cell. However, patch clamp is a laborious technique operating at a very low throughput, with no possibility of repeated measurements of the same cell (Kussauer, David & Lemcke, 2019). Automated patch-clamp measurements can address the former limitation, as mentioned in section 1.4.5, however the increase in throughput is achieved at the expense of accuracy (Obergrussberger et al., 2018).

MEAs were developed to achieve a compromise between sensitivity and high-throughput, while also allowing to conduct long-term non-invasive measurements of electrical activity of the cells (Desbiolles et al., 2019). In contrast to intracellular patch-clamp AP measurements, MEAs are used to record the field potential (FP) – an electrical signal profile generated by the superimposition of extracellular ionic currents of a group of cells (Kussauer, David & Lemcke, 2019). Several FP parameters have been shown to successfully correlate with AP characteristics using comparative patch-clamp and voltage-dye imaging experiments (Halbach et al., 2003; Asakura et al., 2015). For example, FP duration corresponds to the QT interval of the echocardiogram, which in turn correlates with the duration between ventricle depolarisation to full repolarisation (Ambhore et al., 2014). Also, the number of FPs over time represents the beating frequency and sequential FP detection across the electrode array can be used to calculate conduction directionality and velocity (Kussauer, David & Lemcke, 2019).

2.1.2.2 MEA structure and function

Traditionally, MEAs are composed of glass substrates suitable for cell culture and a grid of 10-30 µm diameter electrodes, arranged in square geometry in the centre of the device. Each electrode is connected via an electrically-isolated track to its individual contact pad, located on the periphery of the device. The contact pads are used to interface the MEA chip with the controller headstage for

signal recording. Any of the electrodes can be used for both electrical point stimulation, and subsequent recording of cellular response, providing information on conduction velocity and local FPs. With many available designs, commercially-available MEAs offer a range of spatial resolutions (30-700 µm interelectrode distances) and allow performing measurements on tens to thousands of microns scale.

Most commercial MEAs are limited to maximum 256 × 256 electrodes per MEA. The PHARMEA project was launched in 2009 to improve MEA throughput to 1024 × 1024 electrodes for more efficient drug screening (Ryan et al., 2013). One of the limitations of MEAs in comparison to patch clamp is that MEA measurements most often are recorded from the changes in extracellular environment of the cells surrounding each electrode. Some groups addressed this issue by using complementary metal oxide semiconductor-based customised MEA chips to locally electroporate the cells and record intracellularly (Jans et al., 2017). Localised electroporation was also recently integrated with 16384-electrode MEA, making it capable of both extra- and intracellular measurements (Lopez et al., 2018).

MEA is a particularly promising high-throughput tool for the assessment of drug-induced perturbations to ionic currents, as shown by testing the effect of 27 known drugs on an human induced pluripotent stem cell-derived cardiomyocyte (hiPSC-CM) monolayer cultured on MEA (Liang et al., 2013). In another pharmacological study, MEAs were used to evaluate the personalised cardiotoxic effects of sotalol (a beta-blocker used in atrial fibrillation treatment) on hiPSC-CMs derived from 92 patients (Stillitano et al., 2017). hiPSC-CM-MEA platforms were also validated across 10 separate studies of 8 drugs of known cardiotoxicity as part of the comprehensive *in vitro* Proarrhythmia Assay (CiPA) initiative (Millard et al., 2018). Overall, the non-invasive, multi-site long-term recordings of electrical activity using MEAs are of high value to pharmacology, and interfacing MEAs with smart culture systems will significantly advance the monitoring of drug effects on engineered cardiac models.

2.1.2.3 Cardiomyocyte patterning on MEA

Surface modification is the most common method of aligning cardiomyocytes on the MEA chip. For example, microcontact printing of fibronectin on MEA using PDMS stamps has been previously used to record signal propagation through arrays of isolated rat cardiomyocytes (Wang et al., 2013). Electrospun polydimethylglutarimide (PMGI) fibres have also been printed onto the MEA surface to provide a direction for hiPSC-CMs alignment (Li et al., 2016a). Another approach used PEG self-assembled monolayer patterned with photolithography as a cell/protein repellent to align rat cardiomyocytes on MEA (Natarajan et al., 2011). Though the results were successful in recording excitation propagation through cardiomyocyte arrays, these methods require laborious material fabrication and extensive MEA surface treatment. Thus, there remains the need for higher resolution, higher throughput and less invasive patterning approach, which can be addressed by techniques such as acoustic cell patterning.

2.2 Aims and objectives

In this chapter, the aim was to develop a novel platform for hiPSC-CM alignment on commercially-available MEA chips by using acoustic patterning. To achieve that, solution-based BAW cell manipulation was chosen, as its rapid high throughput patterning and minimal substrate modification requirements make BAWs compatible with MEA chips. It was envisaged that the structural organisation produced by the patterning would mimic the anisotropy observed *in vivo*, while the MEA recordings would provide an instant electrophysiological readout. As a result, the aim was to produce linear cardiac microstructures aligned with the electrodes of the MEA, laying the groundwork for a new *in vitro* model that would bridge the gap between monolayer cardiomyocyte cultures and *in vivo* animal models, ultimately improving the predictability value of the current drug screening platforms. Notably, the term ‘alignment’ here and in the rest of the thesis refers to the global alignment of the cells within the engineered models and does not include the sub-cellular

arrangement of the sarcomeres, which would be interesting to investigate as part of the future work. To achieve these goals, the following objectives were identified:

i) To design, fabricate and assemble a BAW acoustic patterning device, compatible with MEA,

ii) To test and optimise the patterning and culture parameters, achieving alignment of cells with MEA electrodes,

iii) To pattern and culture live hiPSC-CMs on the MEA chips.

2.3 Materials and methods

2.3.1 Device fabrication

All acoustic patterning devices were designed using Inkscape open-source software (v.0.92). 10 mm-thick acrylic frame was laser cut by Mr Steven Nelson at Imperial Mechanical Instrumentation Workshop. Briefly, four or two outer cavities were cut to allow for transducer fitting on the outside of the central patterning cavity (Figure 2-3). The dimensions of the outer frame and all cavities were specified by the device design (Table 2-1). The spacing between the transducer cavities and the central cavity was kept at 2 mm. NCE51 (Noliac, Denmark), customised piezoelectric transducers with wrap-around silver electrodes, were mounted onto the inner wall of transducer cavities using GP medium-viscosity superglue (Everbuild, UK) and soldered using 0.5 mm diameter low temperature $Sn_{62}Pb_{36}Ag_2$ solder alloy (RS Components, UK) with Kylar insulated 0.05 mm^2 electrical wire (RS components, UK). KP1 device was sealed with 120 mm × 95 mm acetate sheet using Fixo Gum Rubber Cement (Marabu, UK). Transducer cavities of KP2, KP3 and KP4 devices were individually sealed with 15.0 mm × 12.0 mm acetate sheets using GP medium viscosity superglue.

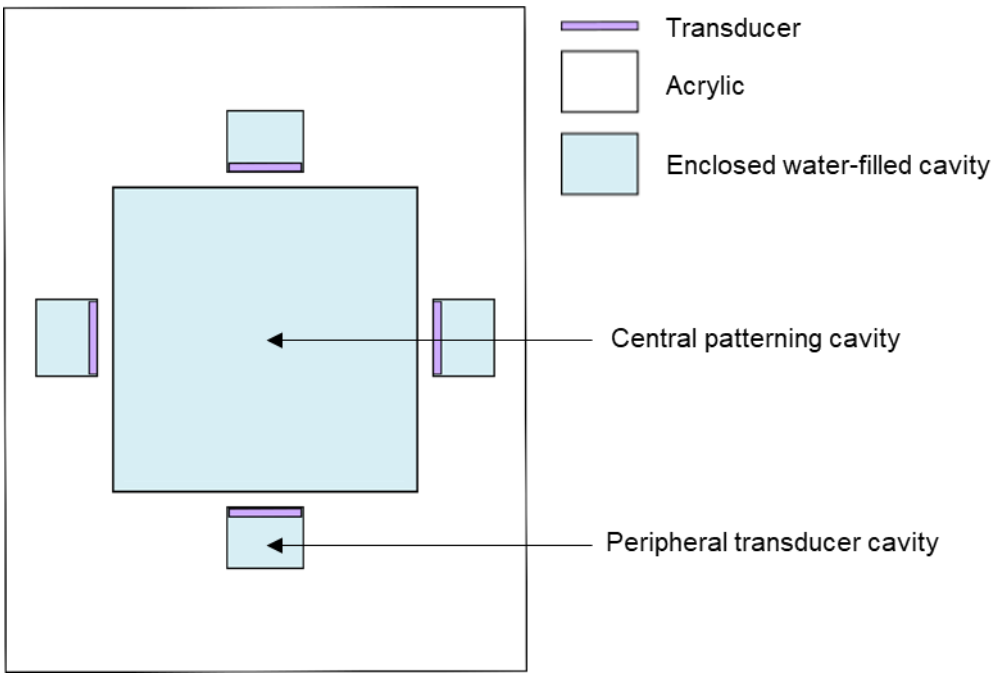


Figure 2-3 ***Schematic representation of a typical acoustic patterning device.***

Table 2-1 ***Dimensions of the four device designs used for acoustic cell patterning.***

Device name	Outer frame (mm × mm)	Transducer cavity (mm × mm)	Central cavity (mm × mm)	Transducers (mm × mm × mm)
KP1	127.0 × 95.0	12.5 × 10.0	51.4 × 51.4	12.0 × 4.0 × 1.0
KP2	71.7 × 71.7	12.5 × 10.0	30.0 × 30.0	12.0 × 4.0 × 1.0
KP3	71.7 × 71.7	35.5 × 10.0	20.0 × 20.0	12.0 × 4.0 × 1.0
KP4	71.7 × 71.7	12.5 × 10.0	20.0 × 20.0	35.0 × 4.0 × 1.0

The base holder and a lid of a modular acoustic patterning device were designed as follows. The outer dimensions of the holder were 78.19 mm by 77.97 mm by 9 mm, while the inner dimensions were 70.19 mm × 69.97 mm × 6 mm with 1 mm radius circular features in all four corners. The thickness of the wall was 3 mm. The dimensions of the MEA groove were 49.3 mm × 49.3mm × 1.0 mm, with a 3.33 mm radius circular feature in one corner. The imaging window dimensions were 20 mm by 20 mm by 2 mm. The outer dimensions of the lid were 70.19 mm × 69.97 mm × 4 mm, and the inner were 70.19 mm × 69.97 mm × 3 mm with 1 mm radius circular features in all four corners. A 5 mm × 1.5 mm × 1 mm slit was positioned in the centre of the lid.

The designs were created in SolidWorks and printed by Dr Jonathan Wojciechowski using a stereolithography-based Formlabs Form 2 3D-printer and White V4 resin (Formlabs, USA). Upon printing completion, the excess material was washed in 100% (v/v) isopropyl alcohol (VWR International, USA), followed by resin curing in at 60°C for 30 minutes in the Form Cure UV box (Formlabs, USA). The supports were removed using flush cutters.

For contact pad isolation, the following methods were used to create a square central cavity:

1) manual cutting of 0.25 mm Ultra Thin Silicone Sheet (Silax Silicones Ltd, UK).
2) the casting of polydimethylsiloxane (PDMS) SYLGARD® 184 (VWR, UK) into a 50.0 mm × 50.0 mm square mould with 8.5 mm wall thickness by mixing the elastomer and the crosslinker components at 10:1 (w/w) ratio followed by overnight curing in 60°C oven. The cavity was also manually cut to reduce the wall thickness to 4 mm during the experiment.

The silicone gaskets for KP2-4 devices sealing were manually cut from a 4 mm Silicone Solid Rubber Sheet (Silax Silicones Ltd, UK).

2.3.2 Huygens pressure modelling

The Huygens pressure field modelling was adapted from a MATLAB script provided by Prof Bruce Drinkwater and previously published in the literature (Nichols et al., 2018). The pressure field was calculated for KP1-KP4 devices using the cavity and transducer length dimensions outlined in Table 2-1. The radial position of the transducers was defined as the distance from the centre of the device, and set at 27.7, 17 or 12 mm for the 51.4 × 51.4, 30 × 30 and 20 × 20 mm central cavities respectively. A two-transducer configuration (1D wave) was chosen for all models, with a single pair of opposing transducers driven at 2.10 MHz. The acoustic properties of the cell culture medium were approximated to water, with 1000 kg/m^3 density and 1500 m/s speed of sound (Yang et al., 2021).

2.3.3 MDA-MB-231 culture and fixation

The breast cancer cell line MDA-MB-231 was used for the optimisation of patterning conditions using fixed cells. Briefly, 0.75 × 10^6 cells were seeded in tissue culture-treated T225 flasks, cultured in Dulbecco's Modified Eagle Medium (DMEM, Gibco, UK) supplemented with 10% (w/v) Foetal Bovine Serum (FBS, Gibco, UK) and 1% (v/v) antibiotic-antimycotic (AA, Gibco, UK) until they reached confluency. The cells were washed once with phosphate-buffered saline (PBS, Gibco, UK) and harvested using a 5-minute incubation with 0.05% (v/v) Trypsin-EDTA (Gibco, UK), followed by centrifugation at 300 g for 5 minutes and removal of the supernatant. The cells were washed with 2 mL PBS and centrifuged at 300 g for 5 minutes. The supernatant was removed, and the cells were incubated in 2 mL of 4% (v/v) paraformaldehyde (PFA, Fisher Scientific, UK) for 15 minutes minimum. The solution was then centrifuged at 300 g for 5 minutes, the cells were washed with 2 mL of PBS twice and stored in PBS at 4°C. Prior to use, the fixed cell suspension was vortexed and added to the central cavity of the acoustic patterning, as described below.

2.3.4 hiPSC culture and differentiation

Cultrex Reduced Growth Factor Basement Membrane Extract (R&D Systems, USA) solution was diluted 1:1 (v/v) with RPMI 1640 medium (Gibco, UK) and aliquoted for storage. The aliquots were further diluted at a 1:80 (v/v) ratio with DMEM/F12 medium for coating (Gibco, UK). 6-well tissue culture plates (Corning, UK) were treated with 1 mL of basement membrane solution and incubated either for 1 hour at 37°C or overnight at 4°C. These plates were used for all expansion and differentiation of hiPSCs and hiPSC-CMs.

For thawing, a vial of WTC-11-GCaMP hiPSC cell line (courtesy of Prof Bruce Conklin, Gladstone Institute, USA) was briefly submerged in 37°C water bath, diluted in 10 mL of Essential 8 (E8) medium (Gibco, UK) and centrifuged at 400 g for 5 minutes. After removing the supernatant, the cells were resuspended in 6 mL of E8 supplemented with 2 µM of Rho kinase (ROCK) inhibitor thiazovivin (Stratech Scientific, UK). 1.5 mL of this media was added to three wells of the tissue culture plate. 500 µL of cell suspension was pipetted into each well in a circular motion, followed by gentle orthogonal shaking. The cells were cultured at 37°C for 24 hours, after which the media was changed to basal E8, replaced daily until the cells reached 80-90% confluency.

To passage hiPSCs, the cells were briefly washed with 1 mL of PBS (Gibco, UK) and incubated with 1 mL of 0.5 mM EDTA (Life Technologies, UK) for 7 minutes at room temperature. The EDTA solution was then aspirated and the cells were triturated using 1 mL of E8 supplemented with 2 µM thiazovivin in P1000 Gibson pipette. The cells were diluted to make up 6 mL of total cell suspension and cultured as described above.

To freeze hiPSCs, the cells were dissociated as described above and resuspended in E8, supplemented with 5% (v/v) foetal bovine serum (FBS, Gibco, UK) and 10% (v/v) dimethyl sulfoxide (DMSO, Sigma-Aldrich, USA). The resulting cell suspension was transferred into a cryopreservation vial and gradually frozen to -80°C in CoolCell™ LX cryopreservation box (Corning, UK) prior to transfer in a - 140°C freezer for long-term storage.

Cardiac differentiation was initiated when the cells reached 80-90% confluency, approximately 3-4 days after hiPSC passaging. First, 6 µM small-molecule Wnt activator CHIR99021 (tebu-bio, France) solution was prepared in RB- media, consisting of RPMI 1640 (Gibco, UK) supplemented with B27 without insulin (Gibco, UK), and added to each well for 48 hours. The media was then changed for RB- media only for 24 hours, after which RB- media with 2.5 µM small-molecule Wnt inhibitor Wnt-C59 (Stratech Scientific, UK) was added for 24 hours. The solution was then replaced with RB- media daily until spontaneous beating was observed, after which RPMI 1640 (Gibco, UK) supplemented with B27 (Gibco, UK) was added (RB+ media) and exchanged for fresh media every 2 days. On day 13, the cells were metabolically selected to purify the cardiomyocyte population. Metabolic selection media, consisting of RPMI-1640 without glucose (Gibco, UK) and B27 supplement, was added for 2 days and then replenished for another 2 days. The final purified cardiomyocytes were cultured in RB+ media for 7 days prior to replating.

To replate hiPSC-CMs, collagenase type II (Gibco, UK) was dissolved at 200 U/mL concentration in 1 mM HEPES (Gibco, UK) buffer prepared in PBS, supplemented with 2 µM of thiazovivin and filter-sterilised through 0.22 µm syringe filter (Sartorius, Germany). The cells were washed twice with 2 mL of PBS and incubated with 1.5 mL of collagenase solution at 37°C for 3 hours. DNAse I (Roche, Switzerland) was diluted in RPMI 1640 at 24 µg/mL concentration, warmed up to 37°C in the water bath and added in equal volume to the wells containing collagenase. The cells were gently triturated with 10 mL stripette, collected into a Falcon tube (Corning, UK) and centrifuged at 100 g for 15 minutes at room temperature. Meanwhile, the replating media was prepared by adding 20% (v/v) FBS and 2 µM thiazovivin to RB+ media. The supernatant was removed, and the cells were gently resuspended in replating media at 1.5×10^6 cells/mL. hiPSC-CMs were then seeded in basement membrane-coated 6 well plates (Corning, UK) at 3×10^6 cells per well and cultured for 24 hours, after which the media was exchanged for RB+. The replated cardiomyocytes were fed fresh media every 2 days and cultured until their use for experiments.

2.3.5 Solution-based acoustic cell patterning protocol

Acoustic patterning with live cells was performed in sterile conditions under a cell culture safety hood. Prior to use, all device components and tools were sterilised. The acrylic acoustic patterning device was either i) wiped with 70% (v/v) ethanol (Sigma-Aldrich, UK) and UV-irradiated for 30 minutes, ii) submerged in 70% (v/v) ethanol and air-dried overnight prior to 30 minute UV exposure, iii) submerged in 100% (v/v) ethanol either for 30 minutes or overnight prior to either 30 or 60 minute UV irradiation, or iv) submerged in ethanol for 10 minutes, washed overnight in 1% (v/v) AA solution prepared in sterile distilled H_2O (dH_2O, Gibco, UK) and air-dried for 48 hours. The silicone gasket, 3D-printed holder and lid were submerged in 70% ethanol and air-dried overnight. Four 12 mm × 50 mm foldback clips (Ryman, UK) were autoclaved. MEA was soaked in 1% (w/v) Tergazyme® (Alconox, USA) in deionised water for 1 hour, rinsed thoroughly, submerged in 70% (v/v) ethanol and air-dried overnight prior to functionalisation of the recording area with 50 µL of basement membrane solution for 1 hour at 37 °C.

The device was then assembled by either i) positioning the MEA in the central cavity of the KP1 device, or ii) positioning the MEA in the groove of the acoustic holder, overlaying it with a silicone gasket and placing the acoustic patterning device on the top for modular KP2-KP4 devices. The device was then covered with a 3D-printed lid and the whole system was secured with four foldback clips. Opposing transducer pairs were connected to TG120 20 MHz Function Generator (Aim TTi, UK), supplying 20 $V_{p\text{-}p}$, while Digital Storage Oscilloscope RS PRO IDS6052U (RS Components, UK) was used to read the load voltage. The transducer cavities were filled with sterile dH_2O. Optimisations using fixed MDA-MB-231 cells were performed in non-sterile conditions using the same setup and workflow, with driving frequencies ranging from 1.87 to 2.14 MHz. The concentration of MDA-MB-231 in suspension varied from 0.5 to 2 × 10^6 cells/mL.

For live patterning in the KP2-KP4 modular devices, the cells (either hiPSC or hiPSC-CMs) were dissociated as described above, diluted to 0.5 × 10^6 cells/mL in replating media and added a total of

1.5×10^6 cells to the central cavity. For the KP1 device a total of 5.0×10^6 cells was added, and the MEA was stabilised within the device using two rectangular acrylic posts (50 mm × 10 mm × 10 mm). The transducers were supplied with a 1.87 MHz sinusoidal wave, and the cells were patterned and allowed to settle for 15 minutes, after which the ultrasound was turned off and the cells were left to adhere for 45 minutes. The device was then disassembled, and the MEA was extracted using autoclave-sterilised tweezers, placed in a 100 mm-diameter Petri dish (Fischer Scientific, UK) filled with replating media containing 1% (v/v) AA and cultured overnight.

For repeated experiments, the MEA chips were cleaned with Tergazyme® (Alconox, USA) as described above and reused, as per manufacturer's instructions (MultiChannel Systems, Germany). It should be noted, however, that long-term the repeated use of the same chips and incomplete cleaning of the MEA could lead to the build-up of ECM matrix over the electrodes and/or electrode surface erosion, affecting cell behaviour and the electrophysiological measurements, therefore the chips need to be regularly changed.

2.3.6 Image analysis

Open-source Fiji image analysis software (v. 1.53f51) was used to measure the line-to-line separation distance at different frequencies. The interval between two adjacent arrays was measured three times, and the average distance was calculated. For each frequency, four intervals were measured in total.

2.3.7 Imaging

Brightfield images of patterning optimisations with fixed cells were collected using Olympus BX51 widefield microscope (Olympus, Japan) with a 4x magnification objective. Brightfield images of hiPSCs for partial functionalisation experiment and hiPSC-CMs for live cell patterning experiment were acquired using EVOS XL Core imaging system (Invitrogen, UK).

2.4 Results

2.4.1 Typical acoustic patterning device components and functionality

The setup for BAW acoustic patterning, compatible with cell culture, was replicated based on the previously published protocol (Armstrong et al., 2018). A standing wave was generated across an acoustic patterning device using a 20 V function generator that supplied a continuous sinusoidal signal to a single opposing pair of piezoelectric transducers, connected through wires and crocodile clips (Figure 2-4). The generator was also connected to an oscilloscope, allowing to monitor the changes in the waveform, in particular, the load voltages of the setup referred to thereafter as peak-to-peak voltage (V_{p-p}). All the components were connected in parallel, with the final circuit setup shown in Figure 2-4B.

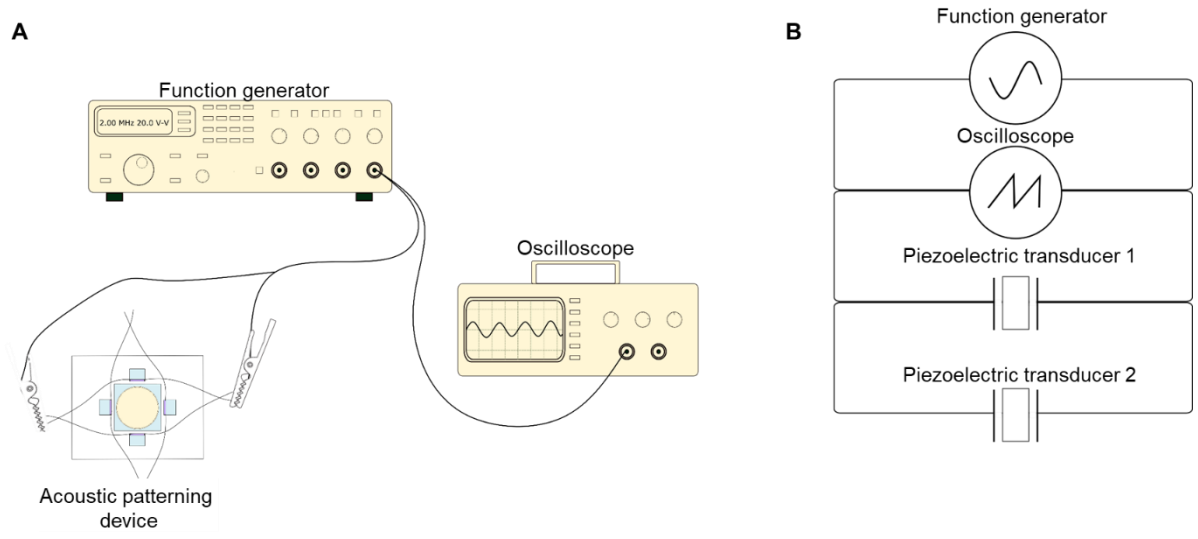


Figure 2-4. ***Acoustic patterning setup.*** *(A). Schematic of the acoustic patterning setup with function generator supplying a waveform to the patterning device and oscilloscope (B). Electrical circuit of the patterning setup, with a function generator, oscilloscope and two transducers connected in parallel.*

The typical acoustic patterning device was also fabricated and assembled according to the previously published protocol (Armstrong et al., 2018). The device frame was manufactured by laser cutting a 1 cm-thick transparent acrylic. Acoustic impedance is a material property that describes the resistance that ultrasound flow experiences when travelling through a given material. When the ultrasound passes through a series of media with different impedances, the efficiency of signal transmission

from one layer to the other is dependent on the difference in impedances of adjacent materials. Impedance matching is therefore required to maximise signal transmission. Acrylic is a material with an acoustic impedance of ≈ 3.2 × 10^6 kg m^{-2} s^{-1}, similar to that of water (1.5 × 10^6 kg m^{-2} s^{-1}), which has previously been used as a matching layer in acoustic devices, making it a suitable material for acoustic patterning device fabrication (Rathod, 2020; Bakhtiari-Nejad, Hajj & Shahab, 2020; Bakhtiari-Nejad et al., 2018; Takeda, 2012).

The device design included one central cavity, designed to fit a standard 35-mm Petri dish, in which the patterning occurred and four peripheral cavities containing piezoelectric transducers with wrap-around electrodes (Figure 2-5A,B). The positive and negative surfaces of the opposing transducers were aligned to maximise constructive interference and the successful generation of a standing wave. Electrical wires were soldered to the electrodes and the device was sealed with an acetate sheet, allowing to fill all the cavities with water to enable ultrasound transmission and to dissipate the heat generated by the transducers.

The regions of resonant frequencies for the piezoelectric transducers in the above setup were previously identified to be within the 2.1 - 2.3 MHz, 6.7 - 6.9 MHz and 11.3 - 11.5 MHz through impedance spectroscopy (Armstrong et al., 2018). While the standing wave would successfully be generated at any frequencies within this range, the exact resonant frequencies that would achieve the best quality patterning slightly varied based on the specific device dimensions as well as variations in manufacturing and device assembly. Therefore, after fabrication, the impedance of each device was estimated indirectly through the drop in load voltage (V_{p-p}) during a frequency sweep. In simple terms, the resonant frequency of a piezotransducer can be thought of as the frequency at which the element vibrates most readily, efficiently converting electrical energy into a mechanical wave (APC International, 2002). During this process, the impedance of the transducer is at a minimum, leading to a decrease in voltage, assuming that the supplied current is constant. The frequencies with the largest voltage drop can therefore be estimated to be at resonance and used

for acoustic patterning experiments. For a standard device fitting a 35 mm Petri dish, the representative sweep of two transducer pairs allowed to determine the optimal patterning frequency of transducer pairs 1 and 2 to be 2.04 MHz and 2.10 MHz respectively (Figure 2-5C).

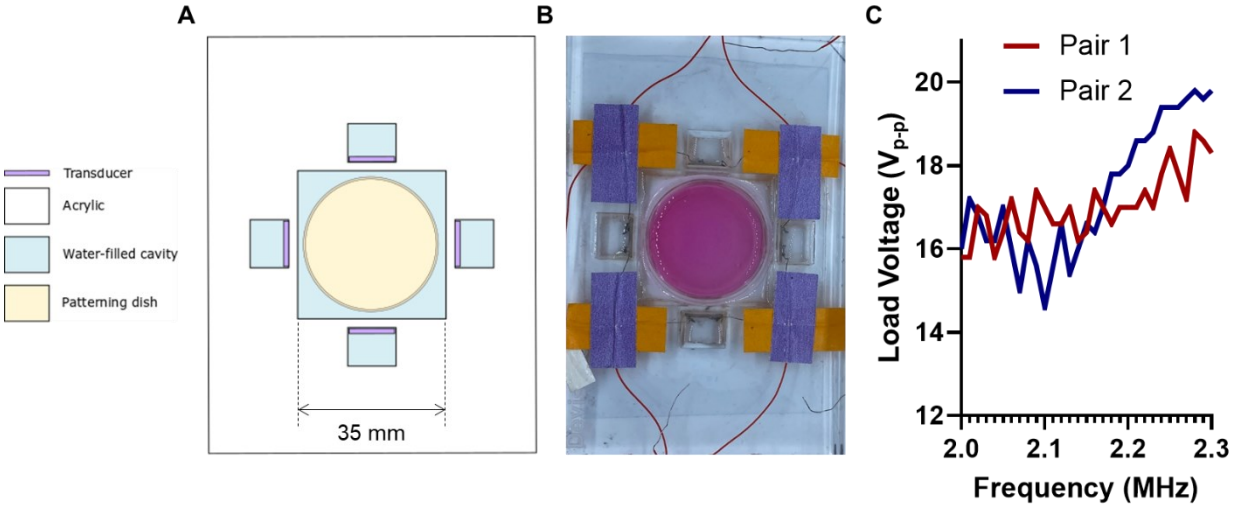


Figure 2-5 ***A typical acoustic patterning device.*** *(A). Design of acoustic patterning device housing a 35 mm dish. (B). A photograph of the assembled standard acoustic patterning device. (C). Load voltage measurements across a frequency sweep of the device, showing the change in V_{p-p} for the two transducer pairs.*

2.4.2 Solution-based acoustic cell patterning on MEA

MEAs used were commercially-available devices with standard dimensions of 50 mm × 50 mm. The device design was therefore modified to increase the central cavity dimensions to 51.4 mm × 51.4 mm and ensure fit (Figure 2-6A). The resonant frequency of the device was determined to be at 2.14 MHz (Figure 2-6B) and used to pattern fixed MDA-MD-231 cells on a glass MEA with an affixed ring for cell culture (Figure 2-6C). Although the presence of cell patterning was apparent, validating the functionality of the device, the geometry of the cell pattern was distorted, leading to a non-uniform distribution (Figure 2-6D). The culture ring on the MEA had a diameter of 26 mm, therefore exhibiting a higher curvature than that of a previously used 35-mm dish. Since this curvature was in the middle of the propagation path of the ultrasound wave, it could cause wave deflection and alter the geometry of the acoustic field. Indeed, when patterning fixed cells on a surface of a flat MEA without a culture chamber, more uniform linear arrays of cells were generated (Figure 2-6E,F).

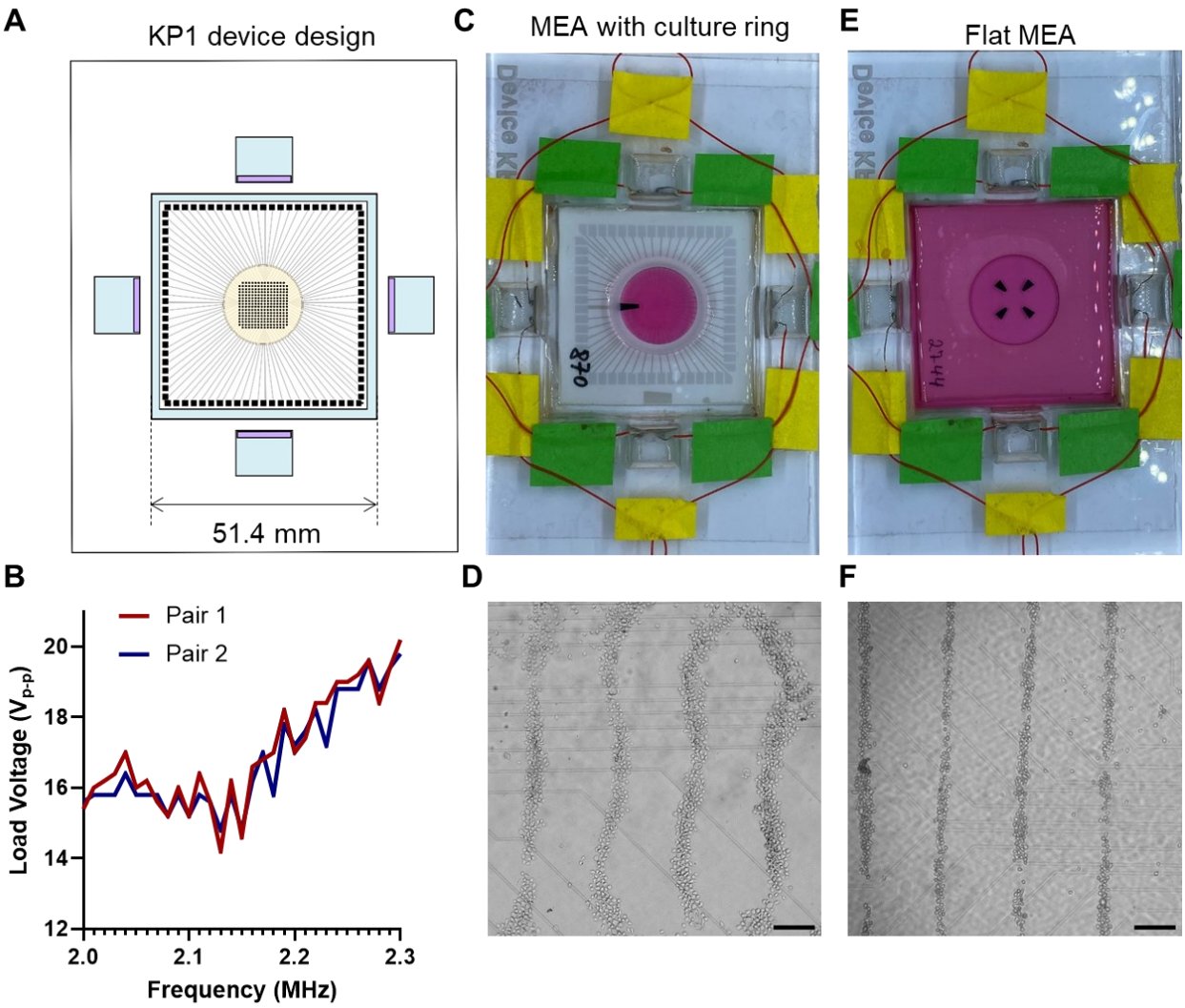


Figure 2-6 ***MEA-housing acoustic patterning device fabrication and testing.*** *(A). Design of acoustic patterning device with central cavity made to fit a standard MEA chip. (B). Load voltage measurements during a frequency sweep of the MEA-housing device, showing the change in V_{p-p} for the two transducer pairs. (C). Assembled MEA-housing device with an MEA chip containing a culture ring. (D). Brightfield image of fixed MDA-MB-231 cells, patterned in the MEA culture ring at 2.14 MHz. (E). Assembled MEA-housing device with a flat MEA chip. (F). Brightfield image of fixed MDA-MB-231 cells, patterned on flat MEA at 2.14 MHz. Scale bars = 200 µm.*

A square-shaped cell culture chamber would therefore be preferable, with the straight edges of the wall allowing the ultrasound to pass through without affecting the direction of propagation. First, a PDMS mould was used to generate an 8-mm wide square culture chamber, with the wall of the chamber directly interfacing with the acrylic frame (Figure 2-7A). However, even after 15 minutes of ultrasound exposure, the patterning quality was low, with a majority of the cells scattered randomly across the patterning surface. As the PDMS was simply cast in a square mould, it likely produced imperfect edges. Using a laser mill to cut precisely vertical walls could improve patterning quality,

with some successful patterning through a PDMS layer previously observed elsewhere (Leibacher et al., 2013). The large thickness of PDMS could also dampen the ultrasound further.

An alternative chamber was fabricated from a 250 µm tall silicone sheet, with wall thickness reduced to a 2-mm wide square chamber. The chamber was positioned in the centre of the MEA, and the outer cavity between the chamber and the acrylic wall was filled with water, to allow for a smoother transition between high and low impedance regions. Although the patterning quality was visibly improved with cell patterning occurring after 4 minutes of ultrasound exposure (Figure 2-7B), the interface between the chamber boundaries and the MEA was unstable, leading to the mixing of water with cell suspension. Furthermore, the geometry of the pattern was still slightly distorted when compared to patterning directly on a flat MEA (Figure 2-7C). It was decided that to avoid compromising the quality of the patterning, no additional culture chamber should be used, with the patterning occurring directly on the MEA surface (Figure 2-7C).

As previously described, the MEA chip contains contact pads on the periphery, that are used to interface the MEA chip with the headstage and therefore should be isolated from cell growth. In a traditional setup, the culture chamber acts as a physical barrier between the cell suspension and the contact pads. Partial functionalisation of the MEA chip was tested as an alternative method for contact pad isolation. Briefly, 40 µL of basement membrane solution was dropcasted on the glass surface, seeded with hiPSCs and cultured for 48 hours (Figure 2-7D). After 24 hours, the cells attached to the surface and formed characteristic compacted cell structures on the functionalised region. Outside of this region, the cells were not able to attach and remained floating in suspension. After 48 hours, some cell growth was observed in the functionalised region, but not beyond the functionalisation boundary. Therefore, partial functionalisation could be used for preferential cell adhesion on the MEA chip.

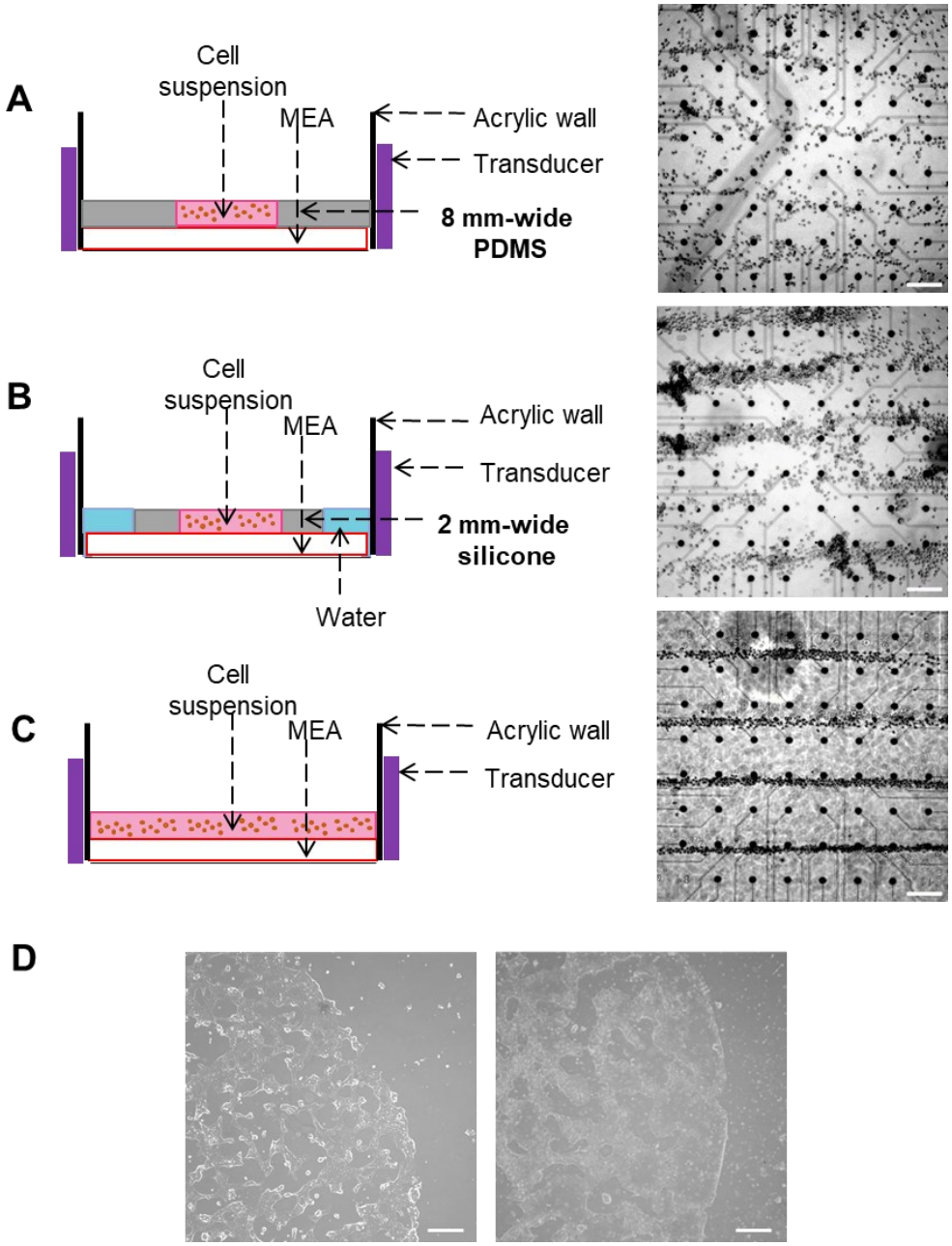


Figure 2-7. ***MEA cell culture cavity optimisation.*** *(A). Cross-section of the acoustic patterning device with flat MEA, fit with 8-mm square PDMS culture chamber (left) and distribution of fixed MDA-MB-231 cells when patterned in PDMS chamber at 2.14 MHz for 15 minutes (right). (B). Cross-section of the acoustic patterning device with flat MEA, fit with 2 mm square silicone culture chamber (left) and distribution of fixed MDA-MB-231 cells when patterned in silicone chamber at 2.14 MHz for 4 minutes (right). (C). Cross section of the acoustic patterning device with flat MEA only (left), and distribution of fixed MDA-MB-231 cells when patterned on top of the MEA at 2.14 MHz for 5 minutes (right). (D). Brightfield images of hiPSC growth on a glass surface functionalised with 40 µL of basement membrane solution 24h (left) and 48h (right) post cell seeding. Scale bar = 200 µm.*

2.4.3 Effects of central cavity geometry on patterning quality

The patterning quality on the MEA chip was variable across four independent experiments performed using the same device (Figure 2-8). In the centre of the MEA, where the recording electrodes were located, the packing of fixed MDA-MB-231 cells into lines was tight and linear during the first experiment (Figure 2-8A). However, when the setup was repeated, no patterning at all was observed (Figure 2-8B). During the third experimental replicate, although some patterning was visible over 50% of the recording area, the pattern degenerated over the second half of the space, appearing completely unpatterned (Figure 2-8C). Finally, during the fourth experiment, the patterning was tight, but the distribution of the lines was non-uniform and distorted (Figure 2-8D). In the regions outside the recording area, however, the patterning quality was a lot more reproducible, with clear, uniform patterned lines generated in all four experiments (Figure 2-8E,F,G,H). Since the setup and the device used were kept consistent, it was hypothesised that the larger central cavity of the device could be affecting the wave interference in the centre. The cells would need to be in direct contact with recording electrodes for successful electrical signal measurements, therefore high-quality patterning in the centre of the device was a priority and required troubleshooting.

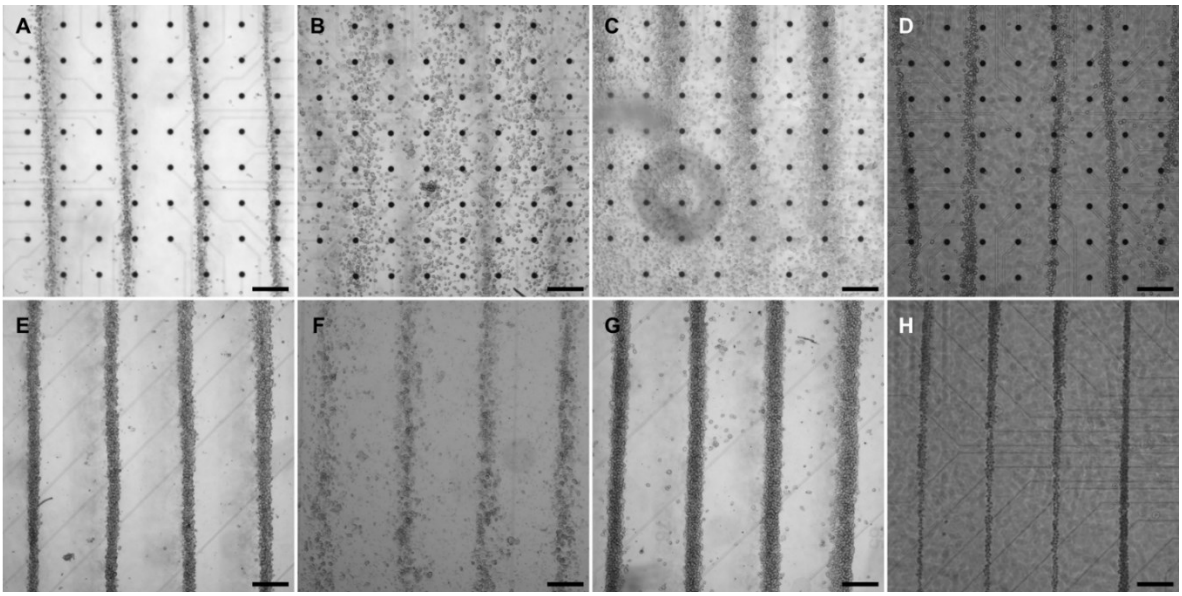


Figure 2-8 ***Consistency of patterning on an MEA chip across four independent experiments.*** *Acoustically-patterned MDA-MB-231 cells at the recording area in the centre of the MEA (A-D) and outside of the recording area (E-F). Scale bar = 200 µm.*

2.4.3.1 Huygens pressure modelling

Computational modelling was performed using a MATLAB code developed by Prof Bruce Drinkwater and previously described in the literature (Drinkwater & Wilcox, 2006). The relative pressures within the acoustic patterning device were modelled based on the Huygens principle. The Huygens principle assumes that the transducer is emitting a primary wavefront which in turn consists of a continuous series of secondary point emitters, or wavelets (Kapralos, Jenkin & Milios, 2005). The interference of the signal, generated by those wavelets, produces a secondary wavefront, propagating in the same direction as the primary wave. This principle is often used for the prediction of acoustic pressure distribution in acoustofluidic systems (Tiwari et al., 2018; Buiochi et al., 2006; Poon, Drinkwater & Wilcox, 2004; Bernassau et al., 2011).

Using Huygens wave modelling allowed us to simulate how changing the transducer and device dimensions would affect the pressure field distribution in the device. The acoustic properties of the cell culture media were approximated to those of water, with the speed of sound and density set at 1500 m s^{-1} and 1000 kg m^{-3} respectively (Yang et al., 2021). The transducer arrangement was chosen as an opposing pair of in-phase transducers driven simultaneously at 2.1 MHz. Each transducer was modelled as a 1-D linear emitter, with variable user-defined parameters of length and radial position from the centre. The resulting acoustic field was plotted as a colour-coded distribution of relative pressure amplitudes, with the highest pressure denoted as yellow and the lowest as blue. The plots were generated across the whole width of the central cavity of interest and of the centre of the device, where the recording area of the MEA would be located.

First, the 51.4 mm × 51.4 mm central cavity of the MEA-fitting acoustic device was modelled, with 12 mm-long transducers positioned 27.7 mm away from the device centre (Figure 2-9A). The model prediction demonstrated an acoustic field with alternating regions of high and low pressure across the width of a central cavity, signifying local pressure gradients. However, in the device centre, where the MEA recording area was, the relative pressure at the anti-nodes was half of the maximum

pressure amplitude achieved in the device. The highest pressures were located just outside the device centre. Therefore, since the sharper pressure gradients would generate the best quality acoustic trapping, in the device with these dimensions best trapping would be observed outside of the recording area, consistent with the experimental observations (Figure 2-8). Indeed, acoustic field modelling confirmed that the devices with central cavity dimensions made to fit the MEA chip are not suitable for high-quality cell patterning.

Reducing the central cavity to 30 mm × 30 mm, with the transducer radial position set to 17 mm maximised the pressure at anti-nodes in the device centre, however the high-pressure regions did not span the width of the whole recording area (Figure 2-9B). Decreasing the dimensions even further to 20 mm × 20 mm with a 12 mm radial position slightly improved the uniformity of acoustic pressure distribution in the centre, with the sharpest pressure gradients predicted at the edges of the recording area. However, although the computed pressure gradients were sharper than in the 51.4 mm × 51.4 mm cavity, they were lower than those of the 30 mm × 30 mm cavity (Figure 2-9C). Increasing the length of the transducers slightly increased the pressure amplitude across the centre of the 20 mm × 20 mm central cavity, with a higher density of yellow regions visible in the middle of the recording area; however, the interference pattern appeared less uniform than the previous design iterations (Figure 2-9D).

Huygens pressure modelling is a powerful tool, providing information on pressure distribution of an acoustic field. Specifically, varying the dimensions of the device and transducers as well as patterning frequency can be used to inform effective device design prior to fabrication. Indeed, here the computational modelling was successfully applied to determine how decreasing the central cavity generated significantly higher pressure gradients in the centre of the device, which would improve the precision of the acoustic trapping. These results also confirmed the experimental observations, whereby the large MEA-fitting central cavity exhibited consistent high quality acoustic patterning on the edges of the device but was less accurate at the recording area of the MEA.

Notably, there were a few considerations of the modelling. First, the amplitude at which the transducers were driven was not included in the model, and the generated pressure fields were treated as relative. While that is sufficient for device design predictions, for in-depth device characterisation hydrophone measurements can be performed to calibrate the model. Secondly, the model did not account for the presence of an acrylic wall between the transducer and the central cavity, effectively reducing the system to transducers acting freely in the water-like medium. The acrylic width throughout the device design was kept fixed at 2 mm, and since this parameter was kept constant, it was assumed the effects of the ultrasound transmission through acrylic would be the same irrespective of device geometry. Some scattering effects could occur at the material boundary, leading to a change in the shape of the acoustic field in the central cavity. Overall, since Huygens pressure modelling was consistent at predicting the pressure gradient distribution in a 51.4 mm × 51.4 mm acoustic patterning device, the next step was to validate its prediction of other device designs experimentally.

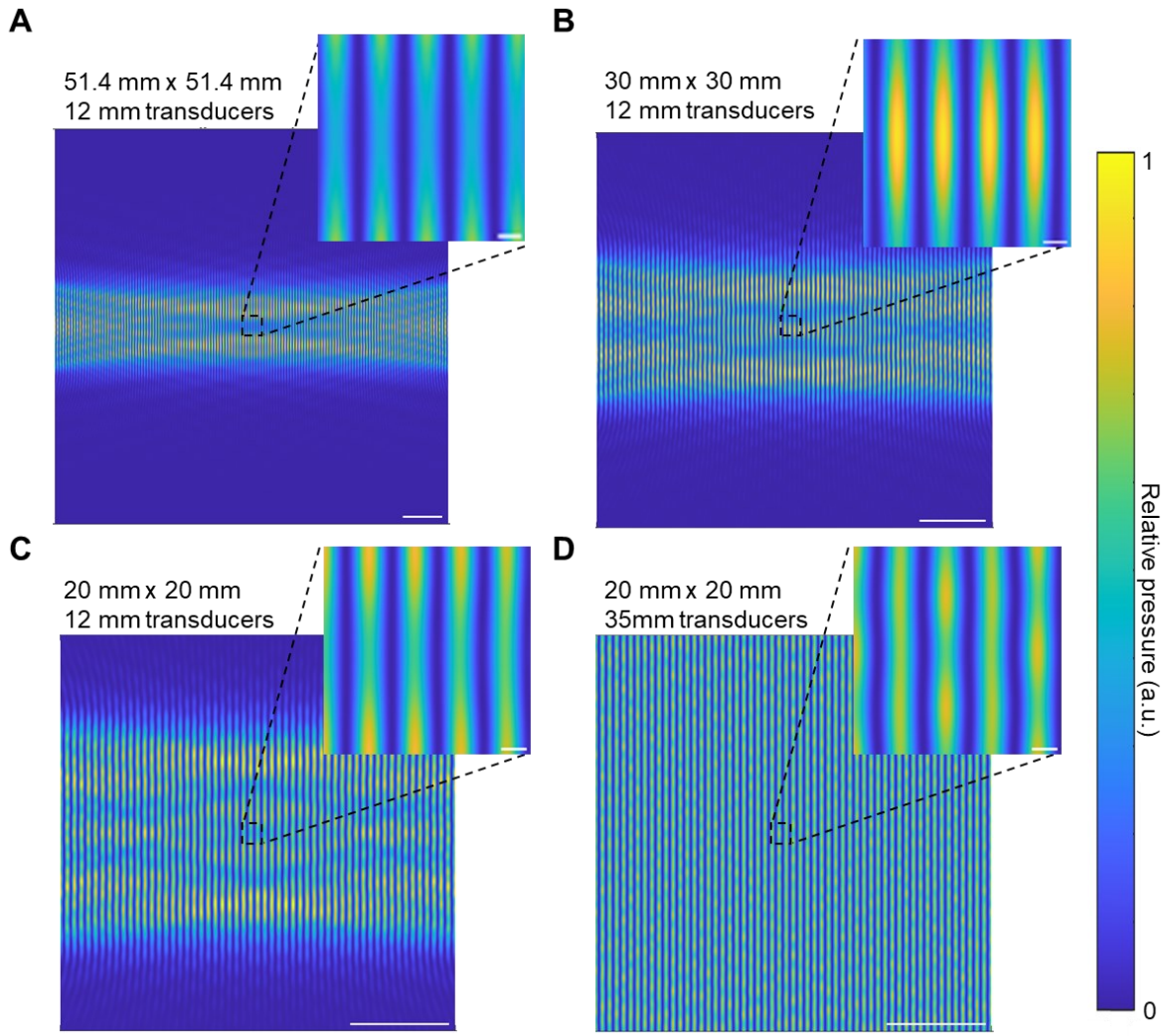


Figure 2-9 ***Huygens pressure field modelling of the acoustic devices with varying central cavity and transducer dimensions.*** *(A). Model prediction of pressure in a device with a 51.4 mm × 51.4 mm central cavity and a pair of opposing 12 mm transducers. (B). Model prediction of pressure in a device with a 30 mm × 30 mm central cavity and a pair of opposing 12 mm transducers. (C). Model prediction of pressure in a device with a 20 mm × 20 mm central cavity and a pair of opposing 12 mm transducers. (D). Model prediction of pressure in a device with a 20 mm × 20 mm central cavity and a pair of opposing 35 mm transducers. Scale bars = 5 mm overview, 200 µm insert.*

2.4.3.2 The modular acoustic patterning device

Since the smaller cavity dimensions generally improved the theoretical pressure field, it was no longer possible to use the central cavity for the placement of the whole MEA chip. An alternative approach to acoustic patterning on MEA systems was therefore developed by designing a modular device that isolated the surface of the MEA chip from the central cavity of the acoustic component (Figure 2-10A). 3D printing was used to fabricate a base holder, containing a groove precisely matching the dimensions of an MEA chip with a circular feature to facilitate MEA handling and an

imaging window in the centre. The incorporation of the holder separated the MEA chip from the acoustic device, making the central cavity dimensions independent of the MEA size, thus introducing freedom of design to acoustic device dimensions, and allowing the central cavity size to be reduced.

The acoustic component, housing piezoelectric transducers, was kept the same: an acrylic frame laser cut with four transducer cavities and a single central cavity. This allowed ensuring that the materials and fabrication methods used are consistent with those previously published, known to achieve good quality patterning (Armstrong et al., 2022, 2018). The transducer cavities were sealed with acetate sheets to allow them to be filled with water, while the central cavity was left open to interface with the MEA. A silicone gasket, fabricated as a negative of the acoustic device, was positioned between the MEA and the acoustic component, to minimise leakage of the cell suspension from the central cavity out onto the base holder. On top of the acoustic component, a 3D-printed lid was positioned, with a small opening in the centre for cell suspension pipetting. All device components were assembled and fixed in place using clamping with foldback clips to ensure sealing (Figure 2-10B,C,D).

Modular acoustic patterning devices held several advantages over the original device design. In the MEA chip, the recording area was the only region of interest, and any cell patterning or adhesion that occurred outside of this region would not be recorded. Reducing the central cavity dimensions therefore allowed to minimise cell loss outside of the recording area. This was particularly important for the precious hiPSC-CM cells, which are non-proliferative and require a minimum of 3 weeks in culture prior to use. Secondly, the separation of the MEA chip from the central cavity of the device ensured that the contact pads were not only isolated from the cell adhesion, but also from any liquid, keeping them dry and accessible for interface with the MEA headstage.

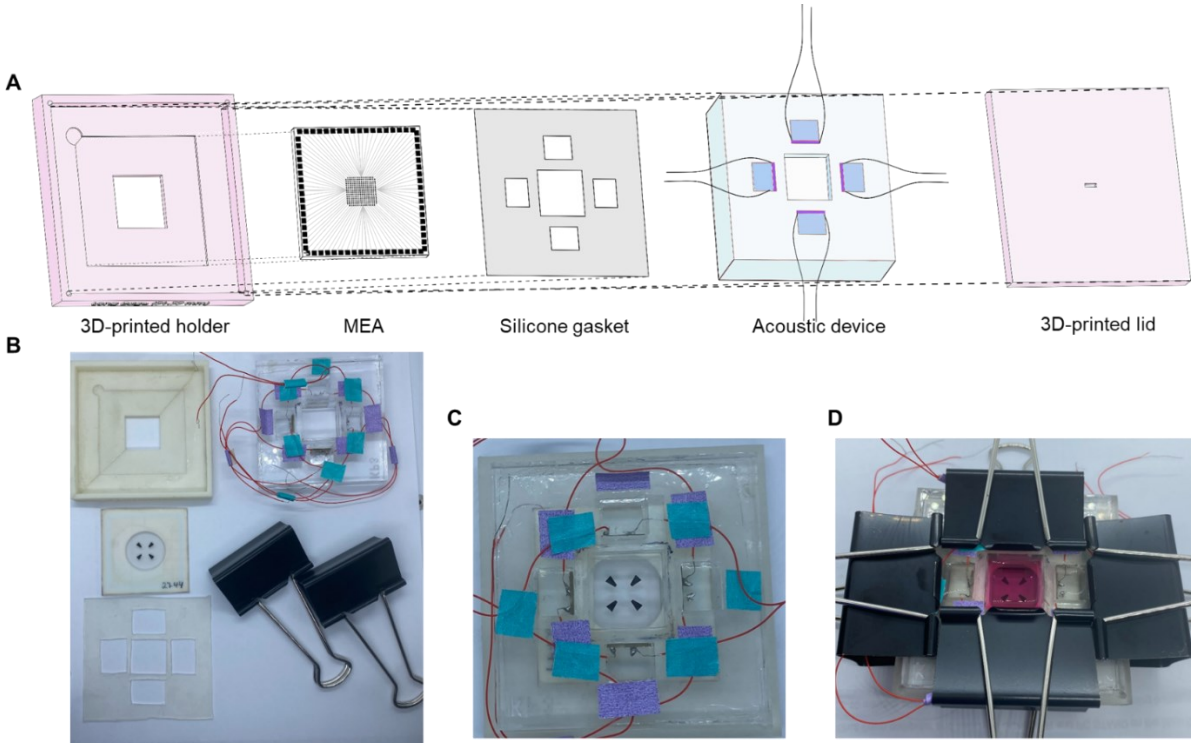


Figure 2-10 ***Modular acoustic patterning device design and assembly.*** *(A). Schematic of the components and assembly order of the modular acoustic patterning device. (B). A photograph of a 3D printed base holder, flat MEA, silicone gasket, acoustic component and foldback clips. (C). Partially assembled modular device, prior to clamping. (D). Fully assembled modular device, containing a cell suspension in the patterning cavity.*

Three acoustic components were then fabricated using the geometries that were modelled above: KP2 with 12 mm transducers and 30 mm × 30 mm central cavity, KP3 with 12 mm transducers and 20 mm × 20 mm central cavity and KP4 with 35 mm transducers and 20 mm × 20 mm central cavity (Figure 2-11A,C,E). Each component was assembled within the modular patterning device and driven at 2.1 MHz to pattern fixed MDA-MB-231 cells prepared at 1.5×10^6 cells/mL (Figure 2-11B,D,F). The lowest patterning quality was observed in the KP4 device, with only two distinct lines visible in the field of view (FoV, Figure 2-11E,F). The inconsistency of the KP4 device with the model prediction was likely due to the diffraction occurring at the acrylic boundary, which was not accounted for by the model. Unpredictable diffraction angles could occur since the transducer length was larger than the central cavity, generating complex wave deflection patterns emanating from the corners of the device. The patterning quality in KP2 and KP3 devices was comparable, with continuous linear arrays of cells generated in both devices (Figure 2-11A,B and C,D). Since the central cavity dimensions in

the KP3 device were smaller, this design was chosen for subsequent experiments to minimise cell loss.

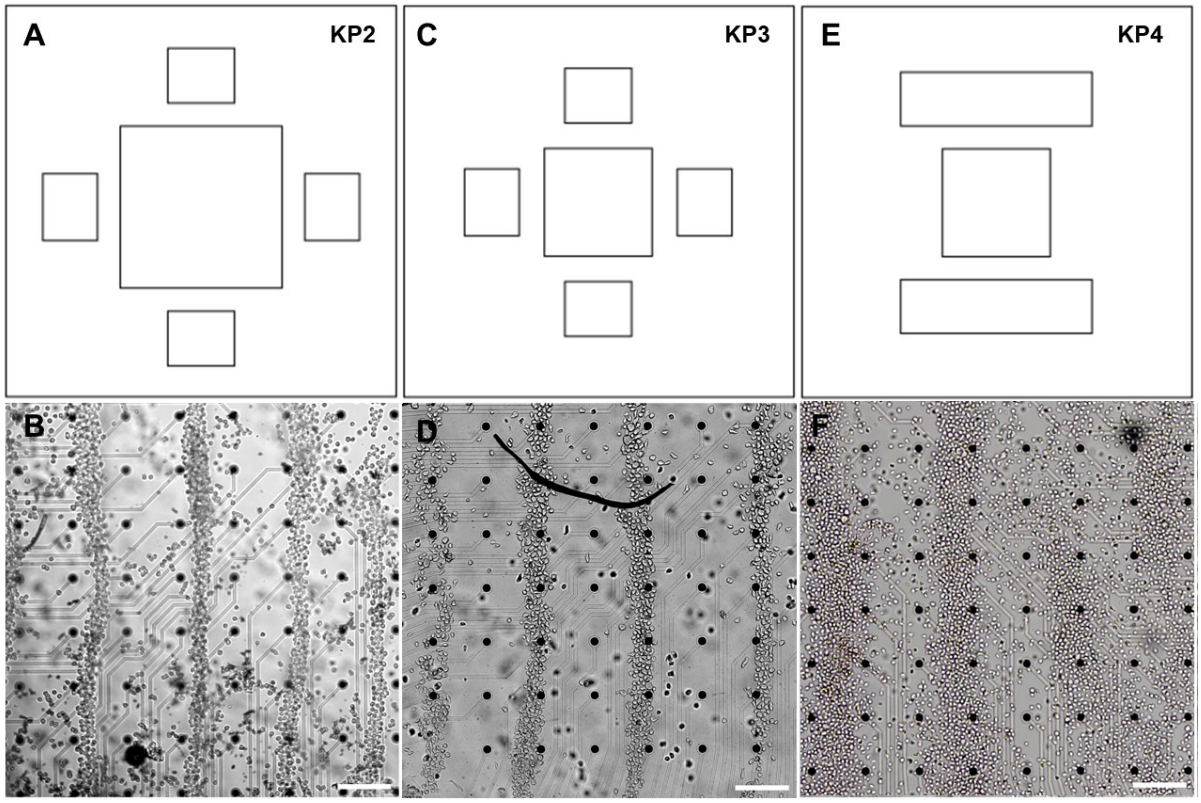


Figure 2-11 ***Design iterations of the acoustic component of the modular device.*** *(A). KP2 device design with 30 mm × 30 mm central cavity and four 12 mm-wide transducer cavities. (B). Brightfield image of fixed MDA-MB-231 cells patterned using KP2 device. (C). KP3 device design with 20 mm × 20 mm central cavity and four 12 mm-wide transducer cavities. (D). Brightfield image of fixed MDA-MB-231 cells patterned using KP3 device. (E). KP4 device design with 20 mm × 20 mm central cavity and two 35 mm-wide transducer cavities. (F). Brightfield image of fixed MDA-MB-231 cells patterned using KP4 device. Scale bars = 200 µm.*

2.4.4 Optimisation of live hiPSC-CM patterning on MEA

2.4.4.1 Patterning parameter optimisation

KP3 device was then characterised using the V_{p-p} measurements across a frequency sweep, identifying resonant frequencies for the two transducer pairs (Figure 2-12A). 2.01 MHz frequency was chosen as it produced the largest drop in V_{p-p}. 1.5×10^6 MDA-MB-231 cells were then added to the central cavity and their behaviour was recorded over time, either under exposure to ultrasound at 2.01 MHz (P) or without ultrasound (UP). Linear arrays of cells were visible immediately after the addition of the ultrasound field, visible from 15 s onwards (Figure 2-12B). The arrays were out-of-focus of the imaging plane, demonstrating the patterning occurring through the bulk of the cell suspension. As the cells sedimented down on the MEA surface, the patterned arrays aggregated on the imaging plane, with the suspension fully settled after 7 minutes of ultrasound exposure (Figure 2-12B). No patterned structures were visible in the unpatterned control.

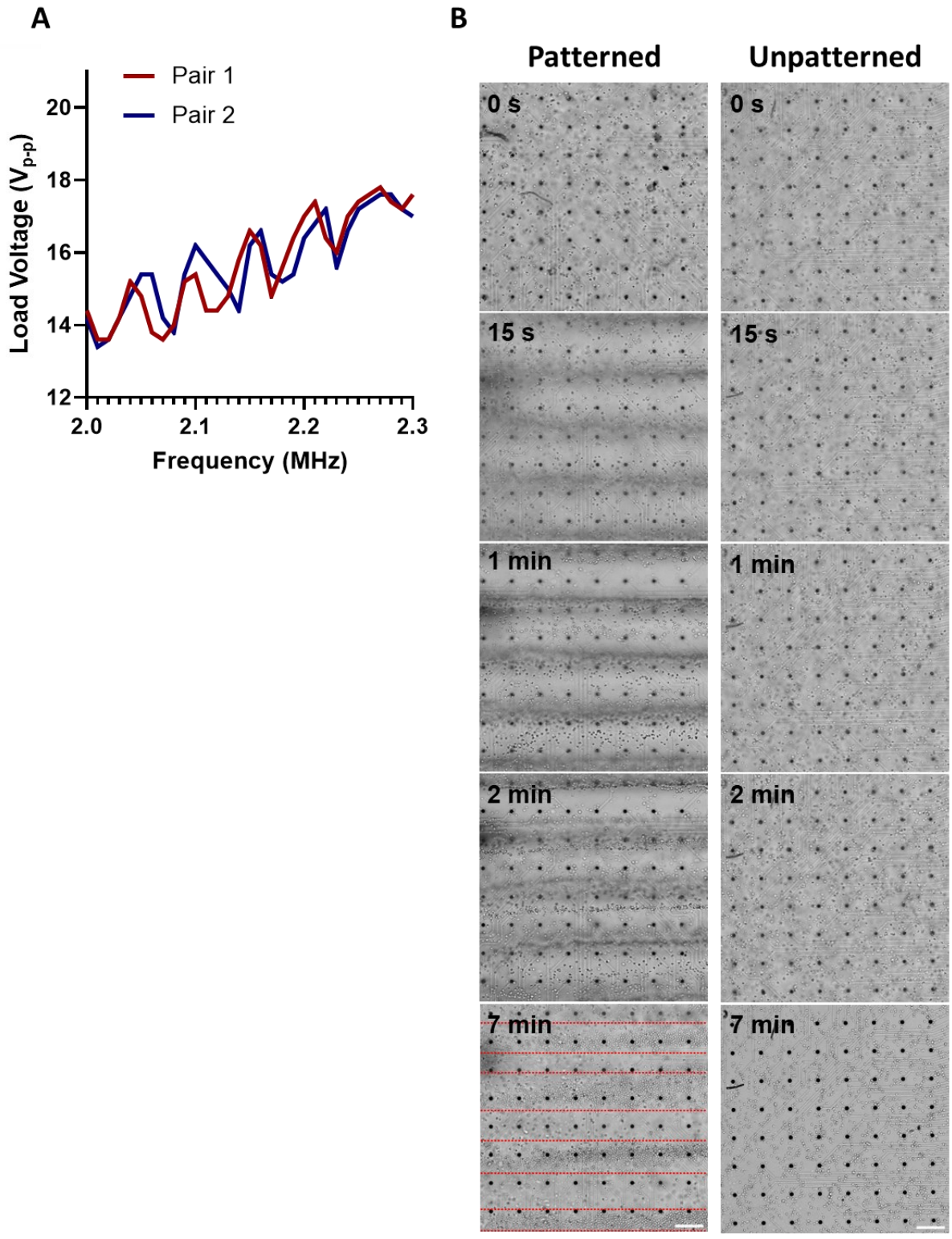


Figure 2-12 ***KP3 device characterisation.*** *(A). Oscilloscope measurements during a frequency sweep of KP3 modular device, showing the change in V_{p-p} for the two transducer pairs. (B). Brightfield timelapse of fixed MDA-MB-231 in KP3 device when patterned at 2.01 MHz (P) or settled in the absence of an acoustic field (UP) for 7 minutes. Dash lines indicating the position of cellular arrays upon settling. Scale bar = 200 µm.*

The ultimate goal of the integration of acoustic patterning with the MEA was to improve the isotropic cell distribution observed in traditional single monolayer cultures by advancing the geometry towards linear arrays of cardiomyocytes, allowing recording signal propagation through individual cardiac fibres. Precisely positioning the cellular arrays on top of the electrode grid, rather than in the inter-electrode space. is therefore required to ensure contact between the cells and the recording electrodes. The distance between the electrodes of commercially available MEAs is fixed, with the most common interelectrode spacing of 30, 60, 100, 200, or 700 µm. The distance between the cell arrays is defined by the number of pressure nodes, which occur at every half wavelength (λ/2) of the ultrasound wave. The number of nodes can be tailored by adjusting the frequency.

To align cells with every array of the electrode grid, $\lambda/2$ would need to be at 200 µm, therefore the frequency (*f)* can be calculated as:

$$f = \frac{c}{\lambda} = \frac{1500\ m/s}{400\ \times 10^{-6}} = 3.75\ MHz$$

However, the transducers need to be driven at resonant frequencies that produce steep enough pressure gradients to achieve high-quality patterning. The range of suitable frequencies is therefore limited by the resonance of the device, making a trade-off between patterning quality and inter-array spacing. From published impedance measurements, the second harmonic of the system would lie in around 6.7 MHz, therefore 3.7 MHz would be completely out of range of resonant frequencies (Armstrong et al., 2018).

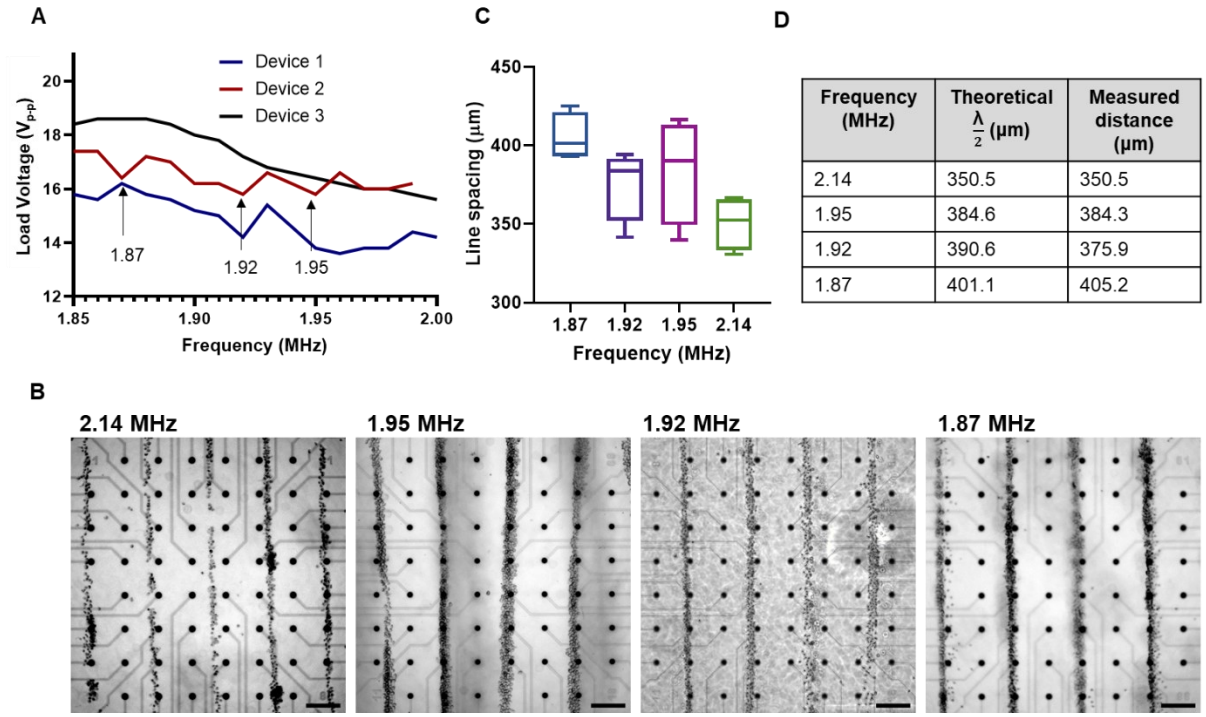
Previously, device characterisation was performed for frequencies over 2 MHz. The maximum inter-line distance for those frequencies was then calculated from the speed of sound (*c*) in water as follows:

$$\lambda = \frac{c}{f} = \frac{1500\ m/s}{2.00\ x\ 10^{6}\ Hz} = 750\ \mu m$$

$$\frac{\lambda}{2} = 375\ \mu m$$

This theoretical value was close to the alignment with every *other* array of 200 µm electrode grid. Ideally, λ/2 would need to be at 400 µm, therefore the transducers needed to be driven at a slightly lower frequency than previously used.

The frequency sweep below 2 MHz was performed on three KP3 devices to identify any local resonant frequencies available for patterning (Figure 2-13A). As discussed previously, the local resonant frequencies largely depend on the device fabrication and assembly precision, leading to device-to-device variability. Device 2 exhibited three local minima at frequencies below 2 MHz: 1.87, 1.92 and 1.95 MHz. Those frequencies, along with 2.14 MHz that was previously identified as resonant for the same device, were then used to pattern fixed MDA-MB-231 cells (Figure 2-13B). The cells patterned with 2.14 and 1.95 MHz did not align with the electrodes of the MEA, while 1.92 and 1.87 MHz showed considerable alignment. The distance between the centres of adjacent cellular arrays was then quantified, demonstrating that 1.87 MHz patterning successfully produced an average 400 µm inter-line distance (Figure 2-13C,D). The experimental distances for 1.87, 1.95 and 2.14 MHz were consistent with the theoretically predicted λ/2 (Figure 2-13D). Since the experimental result and theoretical prediction converged for 1.87 MHz, this frequency was used for all future experiments with this device. The compatibility of this frequency with other devices would need to be tested experimentally since it would not be resonant for every device iteration, and therefore could result in lower quality patterning.



Frequency (MHz)	Theoretical $\frac{\lambda}{2}$ (µm)	Measured distance (µm)
2.14	350.5	350.5
1.95	384.6	384.3
1.92	390.6	375.9
1.87	401.1	405.2

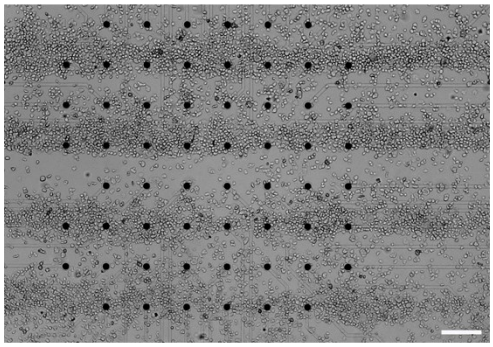
Figure 2-13 ***Optimisation of cellular array alignment with the MEA electrode grid.*** *(A). Oscilloscope measurements during a frequency sweep below 2 MHz of three different KP3 devices, showing the change in V_{p-p} for the one transducer pair. (B). Brightfield images of fixed MDA-MB-231 cells patterned using 2.14, 1.95, 1.92 or 1.87 MHz frequencies. Scale bars = 200 µm. (C). Median and interquartile range of inter-line spacing measurements of cells patterned using 2.14, 1.95, 1.92 or 1.87 MHz frequencies. N = 1, n = 4, where N is the number of analysed images and n is the number of inter-line distances measured. Error bars show minimum and maximum values of the dataset. (D). A table summary of theoretically predicted and experimentally measured inter-line spacing between cell arrays patterned using 2.14, 1.95, 1.92 or 1.87 MHz frequencies.*

2.4.4.2 Acoustic patterning of hiPSC-CMs on MEA

After optimising the device design, patterning times and parameters, acoustic patterning on MEA was performed using live hiPSC-CMs. The sterilisation protocol from the previous work with live cells in a 35 mm culture dish the acoustic patterning device was wiped with ethanol and UV sterilised for 30 minutes. The cells were exposed to a 1.87 MHz ultrasound standing wave field for 15 minutes and left to adhere for 45 minutes. The cells were clearly arranged in continuous linear arrays and aligned with every other electrode array (Figure 2-14A). Although these results demonstrated the compatibility of the optimised setup with live cell patterning, severe bacterial contamination was observed when the MEA with patterned hiPSC-CMs was cultured overnight in a Petri dish, likely due to the direct interface between MEA and acoustic device components.

To improve the sterilisation protocol, the device was then soaked in ethanol for 2 minutes and allowed to air-dry prior to UV sterilisation, however, this method also led to contamination (Figure 2-14B). It was hypothesised that the acoustic component was the source of infection since silicone gasket and 3D printed resin materials are commonly sterilised using ethanol and UV. Increasing ethanol concentration and soaking time as well as UV exposure time failed to fully sterilise the setup. Submerging the acoustic component in 70% (v/v) ethanol for 10 minutes, followed by 48 hours of washes with 1% (v/v) antibiotic-antimycotic solution, combined with 30-minute UV irradiation was the only sterilisation protocol that did not result in contamination (Figure 2-14B).

A



B

Ethanol concentration	Ethanol soaking time	Washing step	Drying method	UV exposure time	UV and EtOH simultaneous?	Infected?
70%	N/A	N/A	Wiping	30 min	No	Yes
70%	2 minutes	N/A	Air-dry	30 min	No	Yes
100%	Overnight	N/A	Air-dry	60 min	No	Yes
100%	30 min	N/A	Air-dry	30 min	Yes	Yes
70%	10 + 10 min partial submerging	N/A	Air-dry	10 +10 min either side	Yes	Yes
70%	10 min	Sterile dH_2O + 1% AA, 48 h	Air-dry	30 min	No	No

Figure 2-14 ***Optimisation of sterile conditions for the culture of acoustically patterned live hiPSC-CMs on MEA chips.*** *(A). Brightfield image of live hiPSC-CMs attached to the MEA chip after 15-minute acoustic patterning at 1.87 MHz frequency and 45-minute incubation for cell attachment. Scale bar = 200 µm. (B). Summary of sterilisation strategies of the acoustic component with varying ethanol concentrations, soaking time, washing, drying and UV exposure times.*

Using the optimised sterilisation protocol, live hiPSC-CMs were successfully patterned and cultured for 24 hours (Figure 2-15). The cellular arrays were visible immediately after patterning on day 0, however, the patterning quality was low, with many cells occupying the inter-line space (Figure 2-15A). Nevertheless, on day 1, hiPSC-CMs were attached, spread over the MEA surface and spontaneously beating (data not shown). The patterning was still visible on day 1, although the linear arrays were less apparent (Figure 2-15B). However, the pattern quality was not sufficient for long-term experiments.

Soaking the acoustic component in ethanol led to the fracturing of the acrylic frame and frosting of the transducer-affixed surfaces (Figure 2-15C,D). While frame fracturing could be tolerated, the frosting indicated the presence of microfractures in the acrylic wall. The smooth and transparent acrylic surface is key for uniform ultrasound transmission from the transducer to the central cavity, therefore any damage to the wall would lead to lower-quality patterning. Although such extreme

fracturing was not observed in shorter ethanol treatments (10-30 minutes), some defects in the acrylic wall were likely to occur. Overall, ethanol-based sterilisation affected the patterning quality in comparison to unsterilised devices, however, to our knowledge, using KP3 modular device successfully achieved patterned live hiPSC-CM patterning on MEA surface for the first time.

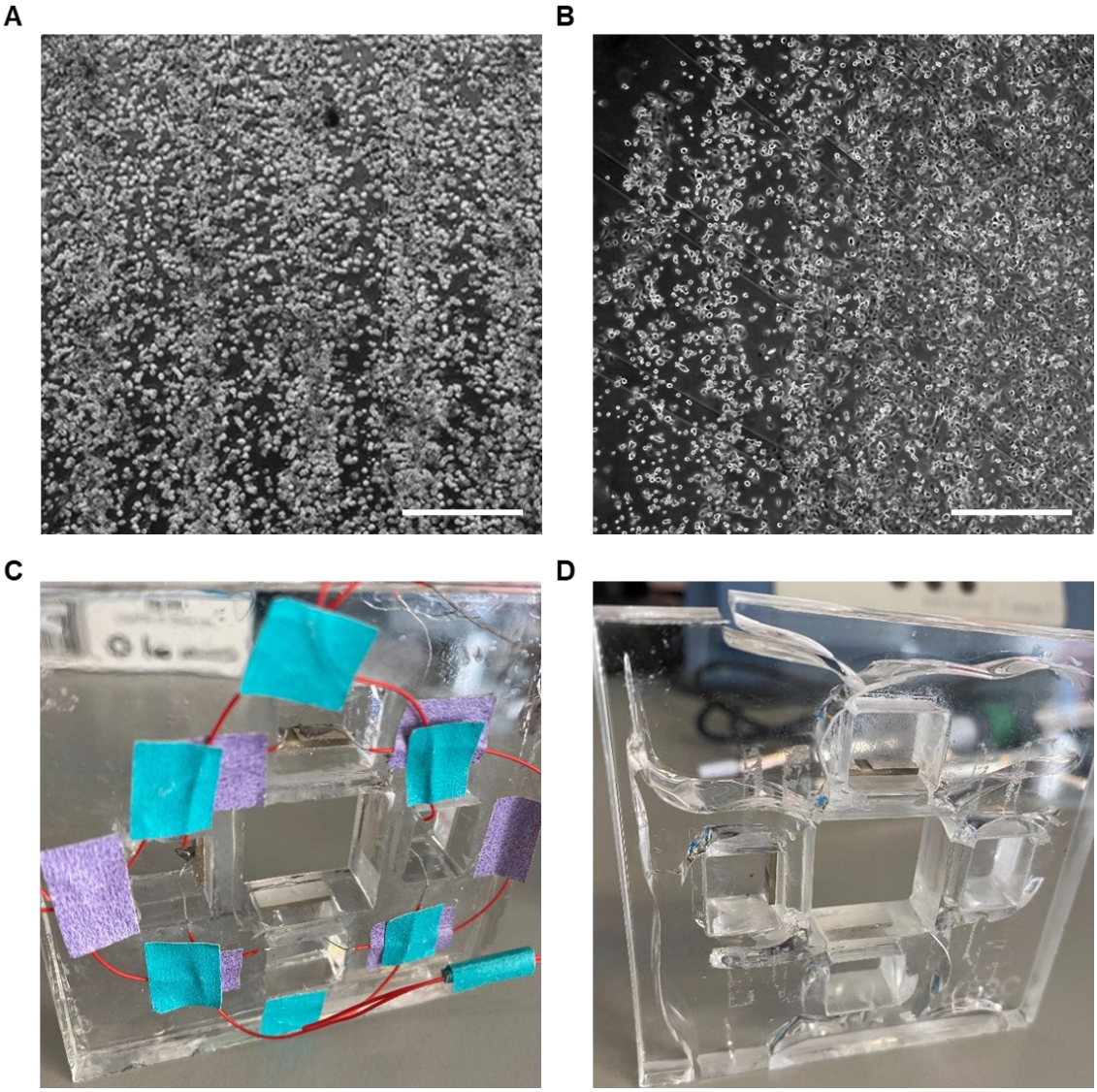


Figure 2-15 ***Live cell patterning in sterilised KP3 device.*** *(A). Live acoustically patterned hiPSC-CMs on MEA 1 hour after patterning with ultrasound. (B). Live acoustically patterned hiPSC-CMs on MEA 24 hours after patterning with ultrasound. (C). KP3 acoustic component before submergence in ethanol. (D). Acoustic component of KP3 device after submergence in ethanol. Scale bars = 500 µm.*

2.5 Conclusions and future work

Overall, the work described in this chapter has successfully engineered a novel acoustic patterning setup, compatible with commercial MEA chips. Device design was adapted to match the dimensions of the MEA chips and the effect of culture cavity geometry on cell alignment was identified, with flat MEA chips producing high quality tight cell arrays on the edges of the device. Computational predictions using Huygens pressure modelling were used to determine the ideal combinations of central cavity and transducer dimensions and inform the design of three different acoustic patterning devices, which further improve the patterning quality in the centre of the MEA at the recording area. A novel modular approach to acoustic patterning device fabrication was used, which compartmentalised the MEA chip away from the acoustic patterning compartment, thereby containing major improvements to the patterning process. First, using a 3D printed base for sequential component assembly provided full flexibility to central cavity and transducer dimensions irrespective of the MEA chip geometry. Second, the high precision of 3D printing led to a fixed positioning of the MEA within the device, increasing the predictability of the cell array distribution on the MEA. Third, unnecessary cell loss was significantly reduced with the updated central cavity dimensions. Additionally, the use of a silicone gasket allowed the recording area of the MEA to be isolated from the contact pads, thereby facilitating future interface of the acoustically-patterned cellular arrays on the MEA surface with the recording headstage for electrophysiological measurements. The modular acoustic patterning device was then used to achieve rapid cell patterning, with cellular arrays established in the bulk cell medium within the first 30 s of ultrasound exposure and maintaining their alignment when sedimented down onto the MEA surface after 7 min of patterning. By lowering the patterning frequency, the inter-line spacing was refined to achieve alignment with every other MEA electrode array for efficient cell-electrode contact and future recordings of electrical signal propagation. An appropriate sterilisation protocol was established to adapt the device for aseptic cell culture experiments and to minimise the ethanol-induced acrylic device microfracturing. Importantly, the fully optimised device, patterning and sterilisation protocol

were successfully applied to live hiPSC-CMs, producing good quality hiPSC-CM arrays aligned with every other electrode array, adhered to the patterning surface and maintaining visible patterning quality after 24 hours in culture as well as exhibiting spontaneous beating, characteristic of hiPSC-CM physiology.

Taken together, the developed novel modular platform showed the potential of acoustic patterning for drug screening applications, aligning hiPSC-CMs in physiologically-relevant geometry of uniform arrays on the MEA surface capable of informative and quantifiable readout. The future steps for the project would include: i) cell density optimisation to achieve distinct line separation, ii) long-term culture of the patterned hiPSC-CMs on the MEA to yield synchronous function of the cells within each line, iii) recording the propagation of electrical activity across each acoustically-patterned array using the MEA headstage and, iv) a proof-of-concept drug screening study, subjecting the patterned hiPSC-CMs to drugs with known inotropic effects, such as isoproterenol or metoprolol.

There were several considerations regarding setup reliability that delayed the progression of the study. Firstly, the sealing of the device was not always stable, occasionally resulting in cell suspension leakage. Addition of the silicone gasket significantly reduced, but did not fully eliminate additional solution flow, which could disrupt the pattern generated by the acoustic field. To further improve the sealing precision of the device, computational fluid dynamics can be used in the future to identify the necessary pressure points for clamping. Secondly, some variability in resonant frequencies was observed between the devices, leading to inconsistent patterning results at lower frequencies required for cell and electrode array alignment. To mitigate that, each device was characterised through frequency sweeps prior to experiments, and only those with resonance in 1.85 – 1.95 MHz region were used for experiments. Importantly, devices were reused over several dozens of patterning experiments, improving the overall throughput of the platform. To improve the predictability of resonant frequencies from device to device in the future, thereby ensuring the consistent inter-line spacing and electrode alignment and further upscaling the experiments, the

fully finalised device design can be machined and assembled in a mechanical workshop to increase the fabrication precision.

The preparation for each experiment was extensive (3-5 days), with the thorough sterilisation protocol implemented to ensure aseptic hiPSC-CM cell culture. While reducing ethanol sterilisation step minimised the alcohol-induced acrylic fracturing, some reduction in the quality of live cell patterning was observed. Alcohol-free sterilisation protocols, such as cold plasma treatment previously shown to be compatible with acrylic-based dentures for medical purposes, could be used in the future (Asnaashari et al., 2019). As a result, the overall preparation time would be decreased and patterning quality would be enhanced, ultimately streamlining the acoustic patterning platform towards translation into a good manufacturing practice, large-scale experiments in an industrial-scale drug screening setting.

Solution-based acoustic patterning allowed a degree of structural complexity to be introduced to an otherwise unpatterned monolayer hiPSC-CM culture systems, advancing them towards a more physiologically-relevant structure of the native cardiac tissue. While this approach of approximating the cardiac tissue to 2D anisotropic cellular arrays is valuable, it is not fully representative of the inherent complexity of the 3D native cardiac tissue. Also, while the pre-differentiation of hiPSC-CMs in monolayer cultures and subsequent cell dissociation for the patterning experiments ensured reproducible purity of hiPSC-CM population, it disrupted cell-cell contacts developed during the differentiation process required for sustained synchronous electrical activity. Additionally, hiPSC-CMs cultured on a hard glass surface in 2D could differ in their electrophysiological profiles in comparison to 3D cardiac fibres surrounded by a soft extracellular matrix. Finally, in solution-based acoustic trapping, pattern stabilisation relies solely on cell adhesion. That made the pattern susceptible to small perturbations, with vibrations from the cell culture hood or any other benchtop lab equipment able to disturb the cells that initially patterned well. Although after 45 minutes the cells formed initial attachments with the MEA surface, the post-patterning handling of device

disassembly and MEA chip transfer to a Petri dish with media for culture disrupted the pattern further since the cells were not fully adherent yet. As a result, hiPSC-CM distribution throughout the MEA chip showed only a small difference in cell density between regions of low and high pressure of the acoustic field, with the inter-line space exhibiting a gradient in cell density rather than a clear boundary. It would be interesting to see if hiPSC-CMs would remain contained in linear arrays if the patterning boundary was clear, which can be achieved in the future through cell density optimisation to determine the optimal width of the cellular array and aforementioned improvements in device fabrication.

Transitioning from solution-based to hydrogel-based patterning could build upon the optimised 2D solution-based patterning and address some of the above considerations. Hydrogel-based acoustic patterning was previously applied to engineer a variety of tissues, from aligning endothelial cells to produce vascular networks, to levitating neuronal progenitors to replicate multi-layered cortical tissue (Garvin et al., 2013; Bouyer et al., 2016). The next chapter will explore how hydrogel-based acoustic patterning can be applied to engineer cardiac muscle for drug screening applications.

CHAPTER 3. *IN SITU* CARDIAC DIFFERENTIATION OF ACOUSTICALLY-PATTERNED STEM CELL CONSTRUCTS.

3.1 Introduction

3.1.1 Hydrogel properties, applications and fabrication methods

2D monolayer cell models are known for their well-established, high-throughput protocols for culture and characterisation, easier readout modalities and a vast amount of literature with comparable results. However, 2D modelling of the native tissue is an extremely reductionist approach, lacking the structural and biological intricacy integral to cell behaviour and function (Kapałczyńska et al., 2018). *In vivo,* the microenvironment of cells is very complex: they are often in either direct or indirect communication with multiple other cell phenotypes and are dispersed through the 3D volume of extracellular matrix (ECM), interacting across all surfaces of the extracellular membrane with the matrix and other adjacent cells (Zuppinger, 2019). Their behaviour is also regulated by a variety of stimuli, including, but not limited to biochemical, electrical and mechanical signals (Branco et al., 2019). Since these sophisticated interactions and processes occur in 3D, *in vitro* biological models need to mimic the same spatial arrangements in order to replicate natural functions of tissue, which can be achieved by using either self-assembly or material-based techniques (Primo et al., 2021).

Hydrogels are a class of materials broadly described as networks of cross-linked polymer chains or colloidal particles capable of absorbing and retaining water (Helgeson, Chapin & Doyle, 2011; Bertsch et al., 2022; Maitra, Shukla & Kumar Shukla, 2014). Their high-water content, tuneable material properties and nanoscale topography make them an attractive matrix for 3D cell culture platforms, acting as an ECM mimic (Tibbitt & Anseth, 2009). The source and chemical composition of a hydrogel determine its physical and chemical properties. Physical properties include material stiffness, swelling ratio and porosity, while chemical properties include pH responsiveness, photosensitivity, thermal dependency and conductivity (Chyzy & Plonska-Brzezinska, 2020).

Hydrogels are formed by a hydrogelation process, whereby a liquid precursor solution (sol) is triggered to assemble in interconnected insoluble networks of either monolithic polymeric chains or colloidal particle aggregates (gel), held together by physical or chemical interactions, or both (Nele et al., 2020). Physical crosslinking is usually achieved through weak molecular entanglement and non-covalent bonding of the polymer chains, such as electrostatic interactions and hydrogen bonding, requiring little input energy to reverse the gelation process (Maitra, Shukla & Kumar Shukla, 2014; Parhi, 2017). Non-covalent linkage can be stimulated, for example, by a change in temperature through ionic interactions, through pH modulation or in the presence of an ionic crosslinker (e.g. calcium ions in alginate-based gels) (Ghavaminejad et al., 2020). On the contrary, strong covalent bonds formed in chemically-crosslinked hydrogels are harder to break, leading to improved stability and mechanical integrity of such hydrogels. The covalent crosslinking usually occurs through a chemical reaction between reactive functional groups of the hydrogel precursor. Some of the common chemical reactions include free radical polymerisation, Schiff base coupling, azide-alkyne cycloaddition, Diels-Alder linkage, or Michael-addition reaction, which can be triggered by heat or irradiation with light (Ghavaminejad et al., 2020). Importantly, the crosslinking density of chemically-crosslinked hydrogels can be controlled by varying either the density of functional groups or the exposure parameters of the trigger. The triggers of hydrogelation in turn can be characterised as either direct or indirect (Nele et al., 2020). Direct triggers change the polymer state itself, leading to the intrinsic assembly of polymer networks upon exposure to a certain condition (e.g. changes in temperature, pH, enzyme addition). On the contrary, indirect triggers act upon an intermediary non-polymeric initiator, changing its state and subsequently leading to its interaction with the polymer, leading to crosslinking (Nele et al., 2020)

Photopolymerisation is a widely used indirect gelation mechanism, whereby covalent crosslinking occurs upon irradiation with ultraviolet (UV), visible or near-infrared (NIR) light (Ghavaminejad et al., 2020). Relying on electromagnetic radiation, photopolymerisation provides external control over crosslinking properties and dynamics, and can be performed at room or physiological temperatures.

Generally, photopolymerisation occurs when light irradiation is absorbed by a suitable photoinitiator (e.g. Irgacure 2959, eosin Y, lithium-acyl phosphinate (LAP)), leading to its activation and initiation of either chain-growth or step-growth reactions (Lim et al., 2020). Chain-growth mechanisms include free-radical polymerisation, whereby upon irradiation a photoinitiator decomposes into free radicals that react with the functional groups of the polymer precursor, initiating covalent bond formation (Choi et al., 2019). By varying photoitiniator concentration, light exposure time and intensity, the mechanical properties, swelling ratio and degradation rates of photo-crosslinkable hydrogels can be precisely controlled, making them a valuable tool for biomedical applications (Sun et al., 2021).

Indeed, in recent years hydrogels have been widely used in the field of cardiac tissue engineering to enable *in vivo* repair strategies and *in vitro* modelling. Table 3-1 shows a summary of some previously described hydrogel-based cardiac systems used in animal myocardial infarction (MI) models. In cardiac repair, hydrogels provide mechanical support and biochemical guidance, and show considerable potential both as acellular constructs and cellularised scaffolds. Injection of fibrin on its own, for example, enhanced the recruitment of endothelial cells, improving vascularisation and cardiac function in a rat MI model (Christman et al., 2004a, 2004b; Yagi et al., 2015). Using fibrin gels to encapsulate hiPSC-CMs also showed improvements in vascularisation, scar reduction, and systolic/diastolic function in both small and intermediate-size animal models (Zimmermann et al., 2006; Weinberger et al., 2016; Jabbour et al., 2021). Hybrid hydrogel systems can also be used for drug development modelling, with electrically-stimulated hiPSC-CM-fibroblast cocultures in a collagen/Matrigel/fibrin gel validated as effective platforms for screening 12 cardiotoxic compounds (Nunes et al., 2013; Feric et al., 2019). Doping hydrogels with conductive elements (e.g. gold nanoparticles, graphene, carbon nanotubes) can also be used to mimic the intrinsic electrical conductivity of the heart for *in vitro* engineering purposes, demonstrating improved functionality of the encapsulated cells (Baei et al., 2020).

Table 3-1 ***Overview of hydrogel systems commonly used for myocardial infarction repair in animal models.*** *Adapted from (Sun & Nunes, 2015). PEG – poly(ethylene glycol), pNIPAAMm - poly(N-isopropylacrylamide).*

Type of hydrogel	Material	Gelation mechanism	Pros	Cons	References
Natural	Collagen	Thermal	Biocompatible, Biodegradable	Slow gelation	(Shafy et al., 2013; Huang et al., 2005)
	Fibrin	Peptide self-assembly	Biocompatible, Biodegradable, Availability	Slow gelation, low mechanical strength, fast degradation *in vivo*	(Christman et al., 2004a, 2004b; Zimmermann et al., 2006; Weinberger et al., 2016; Jabbour et al., 2021)
	Matrigel	Thermal	Biocompatible, resemble to native ECM, faster vascularization	Potentially tumorigenic	(Chong et al., 2014; Fernandes et al., 2010; Ou et al., 2011)
	Hyaluronic acid	Redox inhibitor	Biocompatible biodegradable	Modifications needed for crosslinking	(Macarthur et al., 2013; Li et al., 2021a)
	Alginate	Ionic	Non-thrombogenic, relatively bio-inert	Modifications needed for cell binding	(Dvir et al., 2009; Leor et al., 2009; Landa et al., 2008; Yu et al., 2009)
Synthetic	PEG	Peptide self-assembly	Bio-inert, biocompatible	Low cell adhesion, non-degradable	(Speidel et al., 2017; Chow et al., 2017)
	pNIPAAMm	Thermal	High extensibility	Slower degradation	(Miki et al., 2012; Dvir et al., 2009)

3.1.2 GelMA-based hydrogels in tissue engineering

As shown in Table 3-1, hydrogels of both natural and synthetic origins can be used to engineer the 3D cardiac microenvironment. Naturally-occurring materials include proteins (collagen, gelatin, fibrin) or polysaccharides (chitosan, alginate, hyaluronic acid) which are extracted from biological tissues. They often contain bioactive ECM molecules that allow the cells to adhere, proliferate and interact with the material. Naturally-derived hydrogels are commonly characterised by bioactivity, biocompatibility and biodegradability, making them suitable matrices for tissue engineering, however, they suffer from batch-to-batch variability and poor mechanical integrity. Alternatively, synthetic polymers (e.g. poly(ethylene glycol) PEG, poly(N-isopropylacrylamide) pNIPAAM,

poly(acrylic acid) PAA) offer the reproducible fine-tuning of the chemical composition and mechanical properties of the gel. The available chemistries allow predictable control over the dynamics and triggers of hydrogelation, as well as providing designer characteristics, such as conductivity or degradability. However, synthetic polymers are often bioinert, requiring additional functionalisation to enable effective cell adhesion and dynamic matrix remodelling (e.g. integrin-binding or enzyme-degradable peptides), necessary for effective cell culture.

Semi-synthetic hydrogels therefore offer a compromise, combining the bioactivity of natural hydrogels and the tunability of synthetic polymers. Gelatin methacryloyl (GelMA) is a widely used example, synthesised by covalently attaching photopolymerisable methacryloyl groups to gelatin, a natural polymer. Gelatin is a protein extracted from bones or connective tissues by partial hydrolysis of the collagen triple helix. At temperatures above 40°C, gelatin molecules behave as random coils and exist in a liquid state, but upon cooling they undergo physical cross-linking through non-covalent interactions and partially restore the helix-like structure (Wang et al., 2018; Gornall & Terentjev, 2008). Gelatin can be harvested from a variety of animal sources (e.g. porcine, bovine or fish), which affects its chemical and physical properties, such as molecular weight, isoelectric point, solubility and Bloom strength (Said & Sarbon, 2022). As a major component of native ECM, gelatin is rich in bioactive peptide sequences, such as RGD peptides and matrix metalloproteinase (MMP)-cleavable motifs, permitting cell adhesion and matrix remodelling, making it an extremely attractive biomaterial. However, the thermal instability and poor control over mechanical properties make this biomaterial poorly suited for biological applications.

The amino acid structure of gelatin includes lysine and hydroxylysine residues, which contain reactive primary amines and hydroxyl groups, that can be utilised for chemical functionalisation (Yue et al., 2017). In 2000, Van Den Bulcke et al. first achieved modification of those groups with methacrylic anhydride (MAA) to stabilise gelatin crosslinks (van den Bulcke et al., 2000). The original synthesis was carried out in a phosphate buffer at 50°C, and produced methacrylic acid as a by-

product, thus lowering the pH. Since then, several synthesis optimisations have been described, with carbonate buffer and sequential pH adjustment throughout the reaction yielding more consistent modification of gelatin with methacryloyl groups (Hoon Lee et al., 2015). Importantly, the methacryloyl groups undergo radical photopolymerisation upon exposure to UV or visible light in the presence of a photoinitiator, forming covalent crosslinks. By varying the amount of reacted MAA, the degree of functionalisation of GelMA can also be controlled, and consequently, the material properties of GelMA, such as stiffness, swelling ratio and porosity (Hoon Lee et al., 2015). GelMA pre-gels also maintain the thermal sensitivity of gelatin, therefore making it possible to crosslink GelMA both physically and chemically.

GelMA has been shown to support the survival, contractility, and ultrastructure of isolated rat cardiomyocytes, thus demonstrating its compatibility with cardiac cell cultures (Noshadi et al., 2017). Its tunable properties and bioactivity also make GelMA a versatile material, suitable for many fabrication techniques. For example, photopatterned GelMA microgrooves were used to align isolated rat cardiomyocytes in a heart-on-a-chip device (Li et al., 2020b). In extrusion-based additive manufacturing, GelMA was also used to 3D-print isolated rat cardiomyocytes and cardiac fibroblasts (Koti et al., 2019). Indeed, the solubility and low viscosity of GelMA pre-gel at 37°C make it an excellent candidate for acoustic cell patterning applications, which has previously been described in a number of systems (Deshmukh et al., 2022; Hu et al., 2022; Armstrong et al., 2018; Naseer et al., 2017). Overall, GelMA hydrogels are a useful biomaterial for creating patterned biomimetic structures.

3.1.3 Hydrogel bioprinting

The viscoelastic properties of hydrogels also allow them to be used as acellular or cellular bioinks. For example, seeding hiPSC-CM, endothelial and smooth muscle cells onto biomimetic 3D-printed ECM scaffolds has been shown to produce aligned functional tissue with improved degree of maturity shown by increased calcium handling (Gao et al., 2017). hiPSC-CMs have also been printed

directly as part of a collagen-based bioink, producing a multi-layered ring construct, responsive to pharmacological agents (Esser & Engel, 2021). The flexibility of 3D printing design makes it possible to build complex large-scale cardiac constructs. In a recent work by Kupfer *et al*. an organoid with two perfusable chambers was 3D printed using a composite GelMA-collagen methacryloyl (ColMA) hydrogel (Kupfer et al., 2020). The chambers were perfusable and exhibited spontaneous contractions, allowing it to replicate *in vitro* the fundamental pressure-volume relationship of the heart chambers. Although 3D printing is an exciting biofabrication method for cardiac tissue engineering, it has several disadvantages limiting its use for micropatterning. The resolution of the print is generally limited either by the technical specifications, for example the droplet size ranging from 20 to 300 µm for jet-ink printing, or by the nozzle diameter (commonly ≥ 200 µm) in extrusion printing (Derby, 2008; Roth et al., 2004; Graham et al., 2017; Miri et al., 2019). While reducing droplet size and nozzle diameter is theoretically possible, it is associated with an increase in shear forces, which can severely reduce cell viability in cellular bioinks, with only a few studies successfully reporting ≈100 µm resolution in practice (Graham et al., 2017, Bishop et al., 2017; Miri et al., 2019). Digital light processing-based bioprinting of hiPSC-derived hepatic progenitor cells has been used to print liver lobule-mimics with 50 µm feature resolution, however light-assisted printing methods generally suffer from UV-mediated phototoxicity (Ma et al., 2016; Miri et al., 2019). More advanced 3D printing inks and technologies are being developed to address this limitation. For example, using lower intensity and longer wavelength near-infrared (NIR) light sources can improve the cytocompatibility of light-assisted 3D printing technologies, however, its resolution is currently limited at ≈ 300 µm features (Méndez-Ramos et al., 2016; Stevens et al., 2022). Alternatively, 3D-printers using two-photon polymerisation technologies (e.g. Nanoscribe GT+) were shown to achieve sub-micron feature resolution while remaining cytocompatible (Bunea et al., 2021). The high cost of such equipment and low throughput of the print remain the main disadvantages of the two-photon polymerisation-based fabrication technologies.

Overall, while the large-scale structure of the organs and tissues can be successfully replicated, the intricate micro- and nano-scale structures of the tissue are inaccessible to 3D printing technologies due to low resolution. Additionally, all 3D printing technologies are also limited by bioink viscosity and compatibility.

3.1.4 Acoustic patterning in hydrogel systems

Controlled transition between liquid and gel states of hydrogels can be exploited by remote field engineering. The hydrogelation is used to immobilise cell or particle patterns generated by remote fields in the pre-gel solution. These approaches manipulate the cells into complex, pre-defined geometries within unpatterned bulk hydrogel material, generating 3D structures encapsulated in a matrix, contrasting with 3D printing where the organisation of the cells is limited by the patterning of the material. To that effect, magnetic, optical and acoustic patterning have previously been implemented with hydrogel systems. For example, a ring magnet was used to pattern hiPSC-CMs in collagen, producing beating cardiac constructs with cells aligned with magnetic field lines, while optical tweezers were used to assemble individual ESCs in PEG hydrogels to model early development (Zwi-Dantsis et al., 2020; Kirkham et al., 2015)

Acoustic cell manipulation is a versatile technique, compatible with any cell type and across a range of biomaterial systems, with low viscosity of the pregel solution as the main prerequisites. Its flexibility led to development of a vast range of systems in different hydrogels, cell types and applications. While it is possible to produce a range of acoustic field geometries, discussed in section 2.1.1.2, biomimetic engineering applications are often inspired by the natural cytoarchitecture of the tissue. Ordered arrays of cells are present in a number of tissues, including skeletal and heart muscle, vasculature, cochlear hair cells, and corneal photoreceptors. Ultrasound standing waves are capable of recreating some of these architectures by accumulating cells in the low acoustic potential energy, produced by alternating zero (nodes) and high (anti-nodes) pressure regions. In this section,

the diversity of existing acoustic patterning systems in hydrogels and their application for tissue engineering will described.

Early studies confirmed that using bulk acoustic waves (BAWs) to acoustically assemble fibroblasts in collagen leads to linear organisation of the cells as well as collagen fibres and fibronectin distribution (Garvin, Hocking & Dalecki, 2010). Building upon this system and inspired by the tubular geometry of the vessels *in vivo*, BAWs have been used to engineer 3D branching microvessel networks of endothelial cells in collagen (Comeau et al., 2017; Garvin et al., 2013). In another approach, surface standing acoustic wave (SSAW)-based devices have been used to produce collateral cylindroids of endothelial and smooth muscle cells, that showed increased secretion of anti-inflammatory cytokines (Kang et al., 2018). The aligned constructs, immobilised in catechol-conjugated hyaluronic acid hydrogel have increased perfusion of the ischemic muscle and reduced fibrosis upon implantation, demonstrating the therapeutic potential of using acoustically patterned tissue grafts. More recently, Faraday waves have been used to replicate ring-like vessels surrounding a tumour spheroid in fibrin, modelling the vascularised cancer niche for drug screening applications (di Marzio et al., 2022). Employing modulation of SAW devices has allowed the creation of more advanced vascular architectures, such as lumens, lattice, and honeycomb structures of endothelial and smooth muscle cells (Hu et al., 2022, 2020). The patterning has also been performed in GelMA sheets that can be stacked to produce intricate biomimetic 3D cocultures (Hu et al., 2020). It is evident that acoustic patterning methods have an array of applications across vascular tissue engineering.

Neuronal tissue is also known for its ordered structure, making it an attractive target tissue for patterning technologies. Indeed, bioacoustic levitation (BAL) in gelatin-hydroxyphenylpropionic acid (Gtn-HPA) has aligned PC-12 cells and led to somewhat directional neurite growth upon differentiation, consistent with other solution-based patterning studies (Cheng et al., 2019; Gesellchen et al., 2014). Similarly, a fibrin gel with sheets of embryonic stem cell-derived

neuroprogenitors has been produced using BAL and differentiated into 3D neural constructs, mimicking the multi-layered structure of the cortex (Bouyer et al., 2016).

Tissues comprising the musculoskeletal system also have been successfully engineered using sound waves. A recent study demonstrated how sequential gelation of GelMA can be used to align cells (adipose stem cells or chondrocytes) and functional particles (collagen or polycaprolactone (PCL) microaggregates) in a single construct (Chansoria et al., 2022). The particles promoted cell adhesion in linear arrays, and the pattern was retained after a 4-week long culture. When assessing the osteogenic potential of adipose stem cell (ASC) arrays encapsulated in PhotoCol hydrogel, the patterned cells have been found to exhibit significantly higher alkaline phosphatase (ALP) activity and osteocalcin expression (Martinez Villegas, Rasouli & Tabrizian, 2022). Acoustically organising primary calf chondrocytes into single-cell arrays suspended in agarose has shown to be compatible with a hyaline cartilage differentiation protocol. The resultant engineered tissue showed characteristic deep zone cartilage cytoarchitecture, with strong alignment of collagen fibres (Armstrong et al., 2022). Improved tissue functionality was observed in aligned C2C12 myoblasts in GelMA, which demonstrated increased *MRF4* expression, indicative of increased myotube maturation, and anisotropic mechanical properties (Armstrong et al., 2018).

Heart muscle is another tissue that is well-known for its hierarchical micropatterned organisation. The alignment of individual cardiomyocytes is paramount for the directional propagation of action potentials and coordinated contraction of the muscle. The ultimate goal of cardiac tissue engineering is in replicating this microenvironment *in vitro*, which has been achieved by applying acoustic patterning to isolated primary cardiomyocytes and hiPSC-derived cardiomyocytes. To that effect, beating aligned cardiac tissue was formed 7 days after neonatal rat cardiomyocytes were patterned in GelMA using a SSAW-based device in GelMA (Naseer et al., 2017; Li et al., 2022). Alternatively, Faraday waves could also micropattern differentiated hiPSC-CMs into both linear and ring-like structures in fibrin, which exhibited improved contractile function (Serpooshan et al., 2017).

While these studies laid the groundwork of the proof-of-principle of cardiomyocyte acoustic patterning, their characterisation of the final tissue construct was limited.

3.1.5 hiPSC *in situ* differentiation

As previously discussed in Chapter 1, hiPSC-derived cardiomyocytes are the current gold standard cell source for cardiac tissue engineering, commonly produced using small molecule differentiation protocols on monolayer hiPSC cultures. Matrigel and its analogues are commonly used as coatings for hiPSC attachment, but other hydrogels have also previously been used as substrates for hiPSC differentiation (e.g. directed differentiation of hiPSCs cultured on fibrin gels towards retinal pigment epithelial cells) (Gandhi et al., 2018). The classic bottom-up workflow of cardiac tissue engineering includes expansion and differentiation of hiPSCs in a monolayer, cardiomyocyte purification, dissociation of hiPSC-CMs, and finally incorporation of hiPSC-CMs into a biomaterial. Although this approach was taken by Serpooshan *et al.* used to successfully produce acoustically-patterned beating heart tissues *in vitro*, it involved disruption of cell-cell junctions formed during the hiPSC expansion stage (Serpooshan et al., 2017). Those intercellular connections are critical for the recapitulation of early cardiac development, making their preservation an important goal for biomimetic engineering approaches.

Differentiating hiPSCs within hydrogels is known as *in situ* differentiation and allows the maintenance of both the cell-cell interactions and the 3D microenvironment. Indeed, it was shown to be possible to directly differentiate hiPSCs, encapsulated in heparinised gelatin hydrogels, into cells of all three germ layers (Arkenberg, Koehler & Lin, 2022). Several natural and synthetic hydrogel systems have been developed for *in situ* differentiation of hiPSCs into a variety of cell phenotypes, including: i) mammary gland differentiation in collagen I hydrogels (Qu et al., 2017), ii) hepatocytes in peptide nanofiber hydrogels (Luo et al., 2018), iii) pancreatic islets in composite methacrylated polyvinyl alcohol (PVAMA)/alginate/gelatin hydrogels (Kuo, Lee & Rajesh, 2019), iv) vascular smooth muscle cells in alginate hydrogels (Wang et al., 2006), and others (Poorna et al., 2021). In the cardiac

field, however, the starting cell type has commonly been already somewhat committed to the mesodermal or cardiac lineage. These cell sources have included cardiosphere-derived cells or cardiac 'stem' cells isolated by their c-kit^{+} expression (Mayfield et al., 2014; Xu et al., 2014; Li et al., 2016b). Although these examples provide evidence of partial cardiac differentiation in hydrogels, the latter cell type in particular should be treated with caution due to the controversy surrounding the validity of c-kit^{+} cell discovery, since these cells were recently found to possess and endothelial, rather than cardiac, phenotype (Sultana et al., 2015, Kretzschmar et al., 2018; Sultana et al., 2015).

In recent years, there has been a growing interest in achieving full cardiac *in situ* differentiation. In 2016, Kerscher et al. pioneered cardiac differentiation of hiPSCs in hybrid PEG-fibrinogen hydrogels, achieving beating 3D engineered heart tissue with advanced ultrastructure (Kerscher et al., 2016). The authors also demonstrated the same principle in a GelMA system, highlighting the compatibility of cardiac differentiation protocols with different biomaterials (Kerscher et al., 2017). hiPSCs suspended in pre-gel could also be integrated with a microfluidic device to generate uniform PEG-fibrinogen microspheres. Their differentiation successfully produced spheroids that expressed cardiac markers and demonstrated physiological response to electrical and pharmacological stimulation (Finklea et al., 2021). These results show how hiPSC-hydrogel formulations can be also utilised in fabrication technologies, paving the way to generating complex 3D macrostructures.

A critical innovation by Kupfer et al. demonstrated how to incorporate hiPSCs into GelMA/ColMA bioinks supplemented with ECM proteins in order to 3D print biomimetic chambered organoids (Kupfer et al., 2020). The walls of the organoid were laden with cardiac cells forming contiguous muscle. The chambers were perfusable and capable of pumping function, mimicking the pressure-volume relationship observed in the native heart. This study significantly advanced the field, for the first time combining 3D printing technology with *in situ* cardiac differentiation and recreating the organotypic structure of the heart. The 3D printing allowed the replication of the physiological geometry of the heart, with the presence of the chambers making it possible to investigate the

effects of disease or drug of interest on the pumping function. The use of hiPSCs allowed the incorporation of disease-specific and patient-specific cells as well as the study of developmental processes. Undoubtedly, this technology forms the future of *in vitro* whole-heart models for a vast number of applications.

Ongoing efforts aim to integrate acoustic with microfluidic and 3D printing set-ups, allowing the intrinsic patterning of cells within bulk printed materials. For example, two acoustic traps were added sequentially to a perfusable microfluidic device to allow *in situ* patterning of alginate-encapsulated fibroblasts (Koo et al., 2020). This set up produced bifurcating networks of cells within the bulk hydrogel, resembling vasculature. In another BAW-based acoustofluidic device, arrays of myoblasts were generated during extrustion of individual GelMA fibres (Deshmukh et al., 2022). While the success of this integration revolutionises the cell patterning field, promising to achieve macro-scale patterning of complex biomimetic 3D printed structures, the patterning quality, uniformity and scalability of the system still need to be improved.

3.2 Aims and objectives

Overall, acoustic manipulation is an attractive engineering technology for cell patterning, capable of macro-scale organisation of cells within the hydrogel construct. Indeed, acoustic patterning has been applied before to both isolated and hiPSC-derived cardiomyocytes, however there is no work to date demonstrating its use with stem cells prior to differentiation. Combining an acoustic cell manipulation system with cardiac hiPSC differentiation protocols would demonstrate the capability of this technique to produce cardiac tissue with organised cytoarchitecture *in situ*.

In this chapter, the main aim is to engineer functional cardiac tissue consisting of uniform 3D arrays of hiPSC-CMs using a non-invasive cytocompatible acoustic patterning technique. To achieve that, the existing concepts of *in situ* cardiac differentiation will be combined with previously established acoustic patterning protocols in GelMA hydrogels. It is envisaged that this work will i) demonstrate for the first time the compatibility of acoustic cell manipulation with hiPSC culture and

differentiation protocols, and ii) develop a useful anisotropic platform for the functional assessment of engineered cardiac tissue. To achieve these goals, the objectives have been identified to broadly consist of optimisation, characterisation and functional assessment.

Optimisation includes:

i) Development and validation of an appropriate acoustic patterning set-up;

ii) Screening a library of suitable material systems for their mechanical properties, compatibility with acoustic setup and compatibility with cell culture;

iii) Optimisation of appropriate cell culture conditions to ensure pattern preservation, cell survival and differentiation.

Characterisation is performed on the fully optimised patterning and material system and includes:

i) Assessment of changes in the cell behaviour from the undifferentiated to fully differentiated patterned construct;

ii) Observation of how cell patterning affects the distribution of different cell phenotypes within the patterned construct;

iii) Characterisation of the dynamic changes in gene expression throughout the process of differentiation.

Functional assessment is based on the calcium activity in fully differentiated constructs and it includes:

i) Assessment of the spontaneous calcium activity in engineered cardiac tissues,

ii) Evaluation of calcium signal directionality in patterned and unpatterned cardiac tissues.

iii) Comparison of the response eficiency to electrical stimulation between patterned and unpatterned cardiac tissues.

3.3 Materials and methods

3.3.1 GelMA synthesis

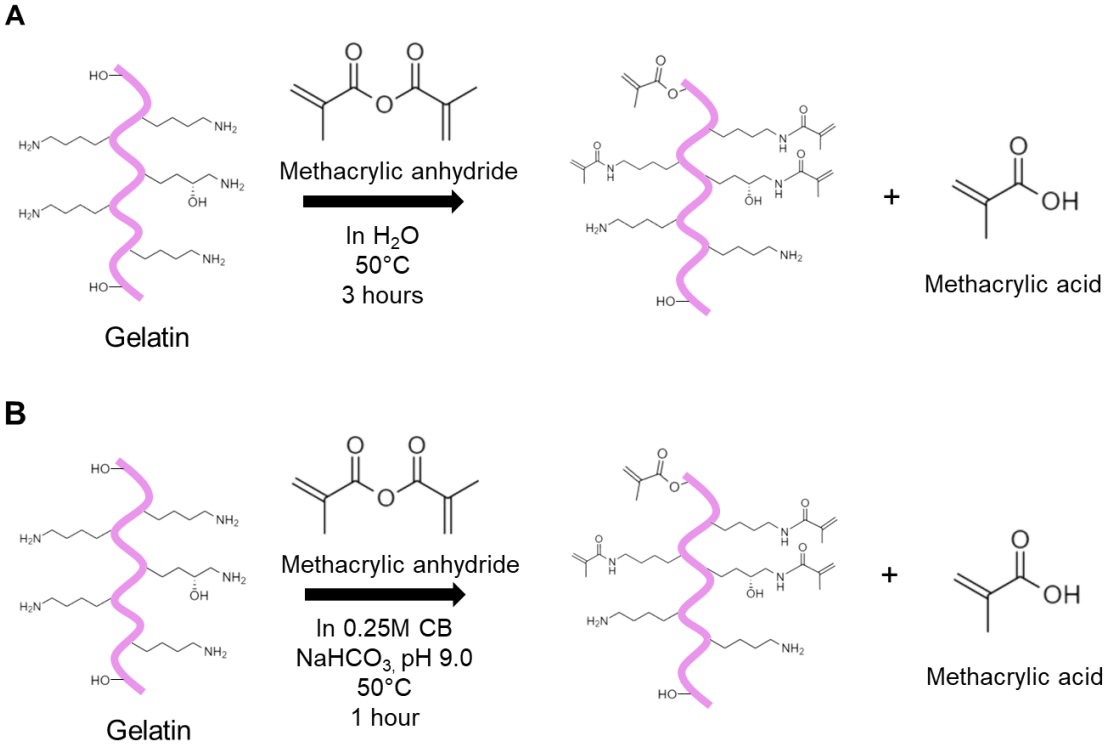


Figure 3-1 ***Schematic of the reaction schemes for gelatin methacryloyl (GelMA) synthesis using (A) the protocol by Meinert et al., 2016, (B) the protocol by Hoon Lee et al., 2015.*** *CB – carbonate buffer. $NaHCO_3$ used for pH adjustment.*

GelMA synthesis was performed following the methods previously published in literature. To achieve a high degree of methacryloyl functionalisation (80% and above), the protocol by Meinert et al., 2016 was used (Figure 3-1A). 5 g of porcine skin type A gelatin (Sigma-Aldrich, UK) was soaked in 50 mL UltraPure water in a round-bottom flask. The resulting solution was heated to 50°C in an oil bath, and gently stirred for 1 hour until the gelatin was fully dissolved at 10% (w/v) final concentration. Under vigorous stirring, 3 mL (0.6 mL per 1 g of gelatin) of methacrylic anhydride (Sigma-Aldrich, UK) was slowly added to the solution dropwise, and allowed to react with gelatin for 3 hours. The solution was then transferred to 50 mL Falcon tubes and centrifuged at 3,500 g for 3 minutes at room temperature to remove unreacted anhydride. The supernatant with the final product was transferred into a beaker with 100 mL of UltraPure water heated to 40°C, while the pellet with

unreacted anhydride was discarded. 12-14 kDa MWCO Spectra/Por dialysis membranes (VWR, UK) were cut to 20 cm length and soaked in UltraPure water to dilute sodium azide used for storage. The reaction mixture was then dialysed in fresh UltraPure water at 40°C for 5-7 days, stirring continuously, with water changed twice daily. After dialysis, GelMA solution was pH-adjusted to 7.4 through dropwise addition of 1 M $NaHCO_3$ solution, aliquoted into 50 mL Falcon tubes and sterilised by passing through 0.2 μm syringe filter. The aliquots were then frozen overnight at -80°C and freeze-dried for 4-7 days until the GelMA was fully dry. The synthesised material was stored at -20°C.

To fine-tune the degree of methacryloyl functionalisation, the protocol by (Hoon Lee et al., 2015) was used. 10 g of porcine skin type A gelatin were dissolved in 100 mL of 0.25 M carbonate buffer while stirring in a 50°C oil bath (Figure 3-1B). Once all gelatin is dissolved, the pH was adjusted to 9.0 using $NaHCO_3$. To produce 20% and 40% functionalised GelMA, 125 μL and 250 μL of methacrylic anhydride were added respectively to a vigorously stirring gelatin solution and allowed to react for 1 h. The final product was then dialysed, sterilised, pH-adjusted to 7.4 and freeze-dried as described above.

3.3.2 Fluoraldehyde assay

Fluoraldehyde reagent solution contains o-Phthaldialdehyde, which is able to bind to unreacted amine groups on the gelatin, thereby allowing us to quantify the degree of methacryloyl substitution in homemade and commercial GelMAs. Porcine skin type A gelatin (Sigma-Aldrich, UK) was dissolved at 37°C in PBS at 1 mg/mL concentration and used to prepare the solutions for the standard curve (0, 0.02, 0.5, 1 mg/mL). The GelMA of interest was dissolved at 37°C in PBS at 0.5 mg/mL concentration. All the solutions were allowed to cool down to room temperature. Fluoraldehyde™ o-Phthaldialdehyde Reagent Solution (ThermoFisher Scientific, UK) was warmed up to room temperature and mixed at a 2:1 volume ratio with the GelMA and gelatin solutions. The samples

were thoroughly mixed to allow for a complete reaction to occur and plated in triplicates in a 96-well opaque plate. The fluorescence intensity of the samples was then measured with 340 nm excitation and 455 nm emission wavelengths using the SpectraMax® M5 Microplate Reader (Molecular Devices, US).

The concentration of unfunctionalized gelatin was determined through the linear fit of the standard curve, where:

$$[Unfunctionalised] = \frac{(Sample - Intercept)}{Slope},$$

Therefore, the degree of functionalisation could be calculated as:

$$DoF = \frac{(0.5\ mg/mL - [Unfunctionalised])}{0.5\ mg/mL} \times 100\%$$

3.3.3 Rheology measurements

Rheology measurements were performed using Anton Paar Modular Compact Rheometer (MCR 302) to characterise and compare the viscoelastic properties of the commercial and homemade GelMA hydrogels. Fish and porcine GelMA purchased from Gelomics (Australia) were used, with porcine GelMA available from two different synthesis batches.

For the studies comparing the rheological properties of different animal sources, GelMA and a photoinitiator lithium phenyl(2,4,6-trimethylbenzoyl)phosphinate (LAP, Tokyo Chemical Industry, UK) were dissolved in Gibco Essential 8 medium (ThermoFisher Scientific, UK) at a stock concentration of 100 mg/mL and 20 mM respectively. To prepare the pre-gel solutions, 440 µL of GelMA stock and 110 µL of LAP stock were diluted with 550 µL of Essential 8 to produce 40 mg/mL GelMA, 2 mM LAP final solution. 1 mL of the pre-gel solution was then cast in a well of a µ-Slide 2-Well ibidi plate (Ibidi, UK) coated with 1 mL of 2% (w/v) ultra-low gelling temperature agarose

(Merck, UK), dissolved in PBS. LAD-1 Array Driver (Bioresearch Centre, Japan) was used at a maximum intensity of 13.6 V to drive the LEDA-405 LED Array (Bioresearch Centre, Japan) positioned on top of the ibidi plate for 1 minute to cure the gels. The gels were then demoulded from the plate by trituration with PBS and washed three times with PBS to remove excess photoinitiator. To perform the rheology measurements, sandblasted bottom (PP50/SS/S) and top (PP25/S 62966) plates were fitted on the Anton Paar Modular Compact Rheometer (MCR 302, Anton Paar, UK). The gels were loaded onto the bottom plate and trimmed using a scalpel to a 25 mm diameter circle. The frequency and strain sweeps were performed at 37°C with a humidifying chamber to keep the gels hydrated. The frequency sweep ranging from 0.1 to 100 Hz was performed with strain fixed at 0.1%, while the strain sweep ranging from 0.1 to 100% was performed with frequency fixed at 1 Hz. All conditions were run in triplicates.

For the experiments comparing bottles of the same synthesis batch, GelMAs from 9 different bottles of porcine type A GelMA (Gelomics, Australia) were used. The stock concentrations and pre-gel solutions were prepared as described above. Double-layered gels were prepared by casting 500 µL of pre-gel solution onto a well of a µ-Slide 2-Well ibidi plate coated with 500 µL of 2% (w/v) ultra-low gelling temperature agarose (Merck, UK). The first layer of the gel was cured for 1 minute using the LEDA-405 LED Array positioned on top of the ibidi plate. The second layer was cast on top of the first layer by adding 1 mL of pre-gel solution. The second layer was cured for 1 minute using the LEDA-405 LED Array, allowing the second layer to crosslink and bind to the first layer. The gels were then demoulded, washed with PBS and measured on the rheometer as described above.

3.3.4 Acoustic cell patterning in hydrogels

3.3.4.1 Device fabrication

10 mm-thick acrylic frames were laser cut by Mr Steven Nelson at Imperial Mechanical Instrumentation Workshop. Four outer cavities were cut to 15.93 mm × 9.85 mm dimensions, flanked by 2.5 mm long and 1.5 mm deep edges to allow for transducer fitting. The spacing between the adjacent transducers was 9.5 mm. The central cavity was cut to 76.5 mm × 26.5 mm dimensions, fitting an ibidi plate. NCE51 (Noliac, Denmark), customised piezoelectric transducers with wrap-around silver electrodes (20 mm × 4 mm × 1 mm), were mounted onto the transducer cavity edges using GP medium-viscocity superglue (Everbuild, UK) and soldered using 0.5 mm diameter low temperature $Sn_{62}Pb_{36}Ag_2$ solder alloy (RS Components, UK) with Kylar insulated 0.05 mm^2 electrical wire (RS components, UK). The device was sealed with 110 mm × 67 mm acetate sheet using Fixo Gum Rubber Cement (Marabu, UK).

3.3.4.2 Cell culture

Cultrex Reduced Growth Factor Basement Membrane Extract (R&D Systems, USA) solution was diluted 1:1 with RPMI 1640 medium (Gibco, UK) and aliquoted for storage. The aliquots were further diluted at 1:80 ratio with DMEM/F12 medium for coating (Gibco, UK). 6-well tissue culture plates were treated (Corning, UK) with 1 mL of basement membrane solution and incubated for 1 hour at 37°C. WTC-11-GCaMP cell line of human induced pluripotent stem cells (hiPSCs, courtesy of Prof Bruce Conklin, Gladstone Institute, USA) were then seeded at 25,000 cells/cm^2 and cultured for 4 days, with daily Essential 8 (E8, Gibco, UK) media changes, until they reached 80-90% confluency. To collect the cells for patterning, 4 wells of hiPSCs were washed with PBS and incubated for 7 minutes at room temperature with 1 mL of 0.5 mM UltraPure EDTA solution. The solution was aspirated and the cells were first dissociated through trituration with 1 mL E8 media, and then diluted to make up 8.8×10^6 cells/mL cell suspension.

3.3.4.3 Patterning setup and preparation

An acoustic patterning device was positioned on the Polarbear Plus Heating/Cooling Block (Cambridge Reactor Design, UK) set to 37°C, and opposing transducer pairs were connected to a TG120 20 MHz Function Generator (Aim TTi, UK), supplying 20 V_{p-p}. A Digital Storage Oscilloscope RS PRO IDS6052U (RS Components, UK) was used monitor the waveform throughout the experiment. Ultra-low gelling temperature agarose (2%, w/v) was dissolved in PBS prior to coating sterile 2-well ibidi dishes (0.5 mL for double layer gels, 1 mL for single layer gels). The agarose-coated plate was positioned in the central cavity of the acoustic patterning device filled with 8 mL of sterile deionized water and weighed down using four 10 mm diameter 2.2g weights.

Acoustic patterning with live cells in hydrogels was performed in sterile conditions under the cell culture safety hood. All the components were sterilised prior to the experiment. The acoustic patterning device and LEDA-405 LED Array were wiped with 70% (v/v) ethanol and subsequently irradiated with UV light for 1 hour. The agarose used for coating was autoclaved prior to the experiment. LAP photoinitiator solution was filter sterilised through 0.2 µm syringe filter, while GelMA solutions were prepared from homemade and commercial materials that were sterilised during synthesis. All other tools (tweezers, spatulas, weights, blades) were sterilised by autoclaving.

Stock solutions of LAP and GelMA were prepared fresh for each experiment at 20 mM and 10% (w/v) respectively and allowed to dissolve fully at 37°C in the waterbath. GelMA was supplemented with 12.5 µM small-molecule ROCK-inhibitor thiazovivin (Stratech Scientific, UK) to support the cell survival during dissociation and patterning. The LAP solution and aliquots of 440 µL GelMA solutions were kept in sterile 1.5 mL Eppendorf tubes (Eppendorf, UK) at 37°C on the heating block, protected from light.

To prepare the supporting layer pre-gel solution, 440 µL of GelMA stock and 110 µL of LAP stock were diluted with 550 µL of E8 to produce 40 mg/mL GelMA, 2 mM LAP final solution. 500 µL of pre-

gel solution was cast per well of the 2-well ibidi plate and cured for 1 minute with blue light using the LEDA-405 LED Array positioned on top of the ibidi plate. The patterning layer pre-gel solution was prepared by mixing 440 µL of GelMA stock, 110 µL of LAP stock and 550 µL of the iPSC cell suspension. 1 mL of pre-gel solution was added on top of the supporting layer in the acoustic patterning device, exposed to 2.0 MHz sinusoidal ultrasound standing wave at 11.8 – 12.2 V_{p-p} for 15 minutes and crosslinked for 1 minute with blue light using the LEDA-405 LED Array. The resulting double-layer hydrogel construct was demoulded by pipetting 1 mL E8 media, washed 3 times with E8 to remove the remaining photoinitiator and transferred into E8 solution supplemented with 5 µM thiazovivin. The single-layer hydrogels were generated using the same protocol but omitting the supporting layer step. For fish GelMA experiments, irradiation time with blue light was increased to 7 minutes

The gels that were used for reverse transcription quantitative polymerase chain reaction (RT-qPCR) experiments were dissected into four equivalent parts for different timepoint data collection. Tissue culture 6-well or 12-well plates were coated with 1 mL of Anti-Adherence Rinsing solution (STEMCELL Technologies, UK) for 1 minute, washed 3 times with PBS and used for culturing whole gels and quartered gels respectively.

3.3.4.4 Tissue engineering

The protocol for tissue engineering the patterned gels was based on the work by (Kupfer et al., 2020). The gels were kept in E8 medium with 5 µM thiazovivin for 1 day post patterning and then the media was replaced either with fresh E8 medium to allow for proliferation or with RB- media, made of RPMI 1640 (Gibco, UK) supplemented with B27 without insulin (Gibco, UK), and 12 µM small-molecule Wnt activator CHIR99021 (CHIR, tebu-bio, France) to induce the differentiation process. The cells were exposed to CHIR-containing media for 24 hours, after which the media was

replaced with fresh RB- media for 2 days. On day 4, the media was changed to RB- media supplemented with 5 µM small-molecule Wnt inhibitor IWP-2 (Sigma-Aldrich, UK) for 48 hours. On day 6, the media was removed and replaced with RPMI 1640 media supplemented with B27 (Gibco, UK) supplement (RB+ media). The gels were fed fresh media every 2 days until day 20 or later.

Brightfield imaging at different stages of differentiation was carried out using an Axio Observer Z1 widefield microscope (Zeiss, UK) with a 2.5x or 10x objective, using a tiling mode for imaging whole-gel overviews.

3.3.5 Gel immunostaining

3.3.5.1 Single-layer gels

To preserve the gels for staining and imaging, they were fixed using a 4% (v/v) paraformaldehyde (PFA) aqueous solution (ThermoFisher Scientific, UK) for 15 minutes at room temperature. The single-layered gels were permeabilised with 0.2% (v/v) Triton-X (Sigma-Aldrich, UK) solution for 1 hour and blocked with 0.1% (v/v) Triton-X prepared in a strong blocking solution (made of 5% (w/v) Bovine Serum Albumin (BSA, Sigma-Aldrich, UK), 1% (w/v) Glycine (Sigma-Aldrich, UK), and 2% (v/v) donkey serum and filtered through 0.2 µm membrane to remove clumps) for 2 hours at room temperature on an orbital shaker at 110 rpm. The samples were washed three times with PBS and stained with primary antibodies prepared in 10% (v/v) blocking solution overnight at 4°C on a rocker. The primary antibodies used were rabbit anti-cTnT (1:500, ab45932, Abcam, UK), mouse anti-CD31 (1:200, MA3100, ThermoFischer Scientific, UK), mouse anti-OCT4 (1:400, ab184665, Abcam, UK), chicken anti-Vimentin (1:2000, PA1-10003, ThermoFisher Scientific, UK). The samples were washed three times with PBS for 1 hour on the orbital shaker at 110 rpm and stained with corresponding AlexaFluor (ThermoFisher Scientific, UK) donkey anti-rabbit 647, donkey anti-mouse 555 and goat anti-chicken 488 secondary antibodies diluted 1:500 in 10% (v/v) blocking solution for 2 hours on an orbital shaker at 110 rpm. The samples were washed for 30 minutes three times with PBS and

counterstained with diamidino-2-phenylindole (DAPI, ThermoFisher, UK) diluted 1:1000 in PBS for 30 minutes, with three subsequent 10-minute PBS washes.

3.3.5.2 Double-layer gels

The protocol for double-layered gels had longer incubation timings and higher antibody concentrations to allow deeper gel penetration. The fixed samples were treated with 0.5% (v/v) Triton X-100 detergent prepared in strong blocking solution for 3 hours at room temperature on an orbital shaker at 110 rpm. After permeabilization and blocking the gels were washed three times with PBS and stained with primary antibodies, made up in 10% (v/v) strong blocking solution with 0.2% (v/v) Tween-20 (Sigma-Aldrich, UK). The primary antibodies used were rabbit anti-cTnT (1:250, ab45932, Abcam, UK), rabbit anti-actinin (1:200, ab68167, Abcam, UK), rabbit anti-SOX2 (1:300, ab97959, Abcam, UK), mouse anti-αSMA (1:250, ab7817, Abcam, UK), mouse anti-CD31 (1:100, MA3100, ThermoFisher Scientific, UK), mouse anti-SSEA4 (1:100, ab16287, Abcam, UK), chicken anti-Vimentin (1:1000, PA1-10003, ThermoFisher Scientific, UK). The samples were incubated overnight at 4°C on a rocker and subjected to three 1-hour PBS washes on an orbital shaker at 110 rpm. Secondary antibody solutions were prepared in 10% Strong Blocking Solution with 0.2% (v/v) Tween-20 at 1:250 dilution, using corresponding donkey anti-rabbit 647 (ThermoFisher, UK), donkey anti-mouse 555 (ThermoFisher, UK), goat anti-chicken 488 (ThermoFisher, UK). The samples were stained overnight at 4°C on a rocker and subjected to three 1-hour PBS washes on an orbital shaker at 110 rpm. The samples were counterstained with DAPI diluted in PBS at 1:500 factor for 30 minutes, with three 10-minute washes.

3.3.5.3 Imaging

Immunofluorescently-labelled samples were imaged on Leica TCS SP8 inverted confocal microscope (Leica, UK), with a 405 nm diode laser used for DAPI, while 561 nm DPSS and 633 nm HeNe lasers were used to excite secondary antibodies. The HyD detectors were used for the 405 nm and 633 nm lasers and PMT detector was used for the 561 laser. The images were acquired at 16-bit, 1024 × 1024 resolution. Gels stained for α-actinin and α-SMA were imaged using a 5x magnification objective (add details) to demonstrate the distribution of lines within the gel, and a 10x objective for closer inspection of the cell distribution in each line. cTnT and CD31-labelled gels were imaged using a 10x objective only. SOX2-labelled gels were imaged using a 40x magnification water-immersed 40x objective to visualise nuclear localisation of SOX2 and DAPI. All images were acquired as Z-stacks through the whole volume of visible signal, with the step sizes of 5, 3.5 and 0.6 µm for 5x, 10x and 40x objectives respectively.

3.3.6 RNA extraction, cDNA synthesis and RT-qPCR

Reverse Transcription – quantitative Polymerase Chain Reaction (RT-qPCR) was performed to investigate the changes in gene expression of patterned and unpatterned gels over time. hiPSCs were patterned and cultured as described above and the samples were dissected to isolate the patterned and unpatterned regions at days 1, 4, 6 and 20. The gels were then collected into 2 mL DNA LoBind Eppendorf tubes (Eppendorf, UK) with a 5-mm stainless steel bead (Qiagen, UK), digested using 600 µL Trizol (ThermoFisher Scientific, UK) and immediately stored at -80°C. To mechanically lyse the gels, the samples were thawed on ice, sealed with parafilm M (Sigma-Aldrich, UK) and homogenised by vigorous shaking at 30 Hz for 1 hour on the TissueLyser II bead mill (Qiagen, UK). The RNA was extracted by adding 120 µL (20% v/v) molecular biology grade chloroform (ThermoFisher Scientific, UK) to the tubes, mixing gently and incubating for 2 minutes at room temperature. The aqueous and organic phases were separated by centrifugation at 12,000 g, 4°C for 15 minutes, and the aqueous phase was collected into a new DNA LoBind Eppendorf tube. The

samples were mixed with equal volumes of 100% molecular biology grade Absolute Ethanol (ThermoFisher Scientific) and their RNA was isolated using Direct-zol RNA MiniPrep Zymo Kit (Zymo Research, US) following the manufacturer's instructions. Briefly, 700 µL of the sample solution was loaded onto the Zymo-Spin IIC column and centrifuged at 12,000 g, 4°C for 30 seconds. The flow-through was discarded and the step was repeated until all the sample had passed through the column. The column was then transferred into a new collection tube and treated twice with 400 µL of Direct-zol RNA PreWash solution, centrifuged at 12,000 g, 4°C for 30 seconds. 700 µL of Direct-zol RNA Wash buffer was added to each tube and passed through the column at 12,000 g, 4°C for 2 minutes. Finally, the column was transferred into a 2 mL DNA LoBind Eppendorf tube and the sample was eluted with 50 µL of RNAse/DNAse-free water (Zymo Research, US) by centrifuging at 12,000 g, 4°C for 1 minute. The RNA concentration and purity were measured using the Nanodrop (ThermoFisher Scientific, UK), and the samples were stored at -80°C. cDNA synthesis was performed using QuantiTect Reverse Transcription Kit (Qiagen, UK) following the manufacturer's instructions. Each RNA sample was diluted with RNAse/DNAse-free water (Qiagen, UK) to the final template RNA amount lying within the 10-1000 ng range in the total volume of 12 µL. To remove any genomic DNA contaminants, 2 µL of DNA wipeout buffer was added to each sample, the tubes were briefly centrifuged and incubated for 2 minutes at 42°C using LifePro Thermal Cycler (BIOER Technology, China). After briefly centrifuging the samples, 6 µL of reverse transcription master mix consisting of 4 µL Quantiscript RT buffer, 1 µL Quantiscript reverse transcriptase and 1 µL RT primer mix was added to each tube. The samples were briefly vortexed, centrifuged and placed on a thermocycler, where the polymerisation reaction occurred for 15 minutes at 42°C, followed by enzyme deactivation for 3 minutes at 95°C. The resulting cDNA samples were centrifuged and diluted with RNAse/DNAse-free water to 5 ng/mL loading concentration and stored at -20°C or used immediately for RT-qPCR. All samples were plated in triplicates using VIAFLO electronic multichannel pipette (Integra Biosciences, UK) at 2 µL of target cDNA per well of Applied Biosystems MicroAmp™ Optical 384-Well Reaction Plate (ThermoFisher Scientific, UK). FAM-MGB conjugated TaqMan Gene Expression Probes

(ThermoFisher Scientific, UK) were used for all genes of interest (*POU5F1, NANOG, MESP, ISL-1, TNNT2, MYH6*) and housekeeping genes (*RPL13, GAPDH, HRPT1*). 0.5 µL of the TaqMan probe was mixed with 4.5 µL of TaqMan Fast Advanced Master Mix (ThermoFisher Scientific, UK) and 2.5 µL RNAse/DNAse-free water, briefly centrifuged and plated at 8 µL of the final gene mix per well. The plate was sealed with MicroAmp™ Optical Adhesive Film (ThermoFisher Scientific, UK) and briefly centrifuged to collect all the samples at the bottom of the wells. The RT-qPCR reaction was then carried out using QuantStudio™ 6 Flex Real-Time qPCR System (ThermoFisher Scientific, UK), with 1 cycle of a two-step hold stage (50°C for 2 minutes, then 95°C for 20 seconds) and 50 cycles of a two-step PCR stage (95°C for 1 second, then 60°C for 20 seconds). The temperature ramp-up rate was 1.9 °C/s for the hold stage and 1.6 °C/s for the PCR stage. The detected Ct values were first normalised against the housekeeping genes to determine ΔCt values and then compared with day 1 timepoint as a control sample for all samples apart from *MYH6*, where the control was set at day 4 due to the absence of *MYH6* expression on day 1. The changes in gene expression levels were assessed as the relative fold change using the $2^{-\Delta\Delta Ct}$ method. Mixed-effects model with Sidak's multiple comparison test was performed on all datasets, pairing the patterned and unpatterned samples obtained from the same gel, with one d20 unpatterned condition excluded due to housekeeping gene failure. For analysis of gene expression at day 20 endpoint, a relative fold change using the $2^{-\Delta\Delta Ct}$ method was calculated against the average ΔCt values of unpatterned controls. Statistical significance for day 20 sample comparison was determined using a paired two-tailed Wilcoxon test.

3.3.7 Ultrasound exposure studies

3.3.7.1 AlamarBlue™ metabolic activity assay

An alamarBlue™ Cell Viability Assay (ThermoFisher Scientific, UK) was used to determine the effects of ultrasound and light exposure on the metabolic activity of the hiPSCs. The cells were dissociated

with EDTA as described above and diluted with E8 media supplemented with 2 µM ROCK inhibitor to a final concentration of 4×10^6 cells/mL. A 2-well ibidi plate was coated with 2% (w/v) ultra-low gelling temperature agarose, positioned inside the acoustic patterning device and set up on the PolarBear Heating/Cooling Block set at 37°C. A TG120 20 MHz Function Generator was connected to a single transducer pair, driving it at 20 V_{p-p} input voltage, while the second pair remained disconnected and at 0 V_{p-p} input voltage, acting as a control. 1 mL of hiPSC cell suspension was added to each well of the ibidi plate and the cells were exposed to ultrasound for 15 minutes, with gentle shaking every 5 minutes to prevent the clumping of the cells. After 15 minutes, 500 µL of cells were removed from both wells, forming the ultrasound-treated and untreated (control) samples. The remaining cells were exposed to 1 minute of blue light using LEDA-405 LED Array, and collected as ultrasound and light-treated and light-treated only samples. All the conditions were plated in triplicates at 10,000 cells/well on a basement membrane-coated 96-well tissue culture plate (Corning, UK). To produce a standard curve, untreated cells were seeded at 0, 1×10^3, 5×10^3, 1×10^4, 2.5×10^4, 5×10^4, 1×10^5, 1×10^6 cells/well. The exposure experiment was repeated three times. The plate was incubated at 37°C for 24 hours, after which the media was changed to fresh E8 media to allow the cells to recover from splitting and to form clusters. 48 hours after seeding, alamarBlue™ Reagent (ThermoFisher Scientific, UK) was diluted at 10% (v/v) in E8 and used to replace the media in the wells, as well as added to the empty wells to produce a blank measurement. The plate was incubated at 37°C for 6 hours in the dark and 100 µL of the coloured supernatant were transferred into a white 96-well opaque plate (Corning, UK). The fluorescent signal was measured using a SpectraMax® M5 Microplate Reader (Molecular Devices, US) at 570 nm excitation, 590 nm cut-off and 610 nm emission wavelengths and 6 flashes per read. Blank readings were subtracted to obtain the final fluorescence values for each sample. The second order polynomial function was fitted through the standard curve samples, allowing the number of metabolically active cells to be determined for each well. The triplicate measurements were averaged, and all the conditions were

normalised to the average untreated value set as 1. Finally, a one-way repeat measures ANOVA was performed to determine the significance between the conditions.

3.3.7.2 PicoGreen DNA quantification assay

The effect of ultrasound and light exposure on cell proliferation was investigated through DNA quantification using Quant-iT™ PicoGreen™ dsDNA Assay Kit (ThermoFisher Scientific, UK). The hiPSCs were dissociated and the exposure to ultrasound and/or light was performed as described above (see alamarBlue™ section), resulting in the following four treatment conditions: untreated (control), ultrasound-exposed, light-exposed and ultrasound and light exposed. The cell suspensions were prepared in E8 media supplemented with 2 µM ROCK inhibitor and seeded at 30,000 cells/well in 48-well basement membrane-coated tissue culture plates (Corning, UK). The cells were plated in triplicate for each condition, across two separate plates, and the full exposure experiment was repeated four times. The samples were incubated at 37°C for 24 hours, after which one of the plates was processed for DNA collection (day 1). The second plate was fed fresh E8 media daily for another 48 hours, after which its DNA was also collected (day 3). To extract the DNA from samples, the wells were washed once with 400 µL of PBS, which was then removed and replaced with 100 µL of sterile RNAse/DNAse-free UltraPure water (Gibco, UK). The plates were then sealed using parafilm and immediately transferred to -80°C. To lyse the cells, the plates were warmed up to room temperature until all the ice in the wells was melted, and then frozen down at -80°C again for 30 minutes, with 3 subsequent freeze-thaw cycles. 100 µL of the cell lysate from each well was then transferred into 0.5 mL LoBind DNA Eppendorf tubes (Eppendorf, UK) and stored at -80°C until all the samples and all the timepoints were processed. PicoGreen DNA quantification assay was then carried out on these lysates, following the manufacturer's instructions. Briefly, 20X concentrated TE buffer was diluted using sterile RNAse/DNAse-free UltraPure water to prepare a 1X TE working solution, which was

used to prepare the standards and the samples. All the samples were diluted in TE buffer at a 1:20 ratio and plated in duplicate in white opaque 96-well plates. A standard λ dsDNA solution was first diluted at a 1:50 ratio to prepare a 2 mg/mL stock solution for a high-range standard curve, and then was further diluted at a 1:40 ratio to achieve 50 ng/mL for a low-range standard curve. The standards were plated at 500, 100, 25, 10, 2.5 and 0 ng/mL concentrations. The PicoGreen dsDNA reagent was diluted 200-fold in TE buffer and 100 µL volume was added to each well of the 96-well plate and mixed well. The samples were incubated for 7 minutes at room temperature, protected from light, and the fluorescence intensity was measured using SpectraMax M5 plate reader with 6 flashes per well set at 480 nm excitation, 520 nm emission wavelengths. A linear function was fit through the standard curve and used to determine the DNA concentration of each sample. The duplicate readings were averaged per well, and triplicate technical repeats were averaged per sample. The fold change in DNA content was then calculated in respect to each sample's day 1 value, and the level of significance was determined using one-way ANOVA with Tukey and Geisser-Greenhouse corrections.

3.3.7.3 Viability staining

To visualise the changes in the distribution of viable and non-viable cells throughout the tissue engineering process, the gels were stained using 4 mM Ebioscience Calcein Blue AM Viability Dye (ThermoFisher Scientific, UK), which identified viable cells, and 2 mM LIVE/DEAD® ethidium homodimer-1 (ThermoFisher Scientific, UK) which identified nonviable cells. The blue calcein was used to avoid interference with the endogenous fluorescent GFP signal, which could occur when applying green calcein from more commonly used LIVE/DEAD® kits. Both double-layer and single-layer gels were stained on days 1, 4, 6 and 20 of culture. For timepoints 1, 4 and 6, the staining solution was prepared fresh, with calcein diluted at 1:250 ratio and ethidium homodimer-1 diluted

at 1:500 ratio in PBS. The gels were washed once in 2 mL of PBS and then briefly incubated in 2 mL of staining solution at room temperature and immediately imaged without any subsequent washes to retain the staining. For day 20 timepoint, the concentration of the staining solution was increased to 1:62.5 for calcein, and the gels were fixed with 4% (v/v) paraformaldehyde solution immediately after staining to stop the spontaneous contractility of the cells during imaging. All gels were imaged using Leica SCS SP8 microscope.

3.3.8 Calcium imaging and electrical stimulation

The electrophysiology of the gels was assessed through imaging their calcium transients after 20 days of culture. Spontaneous calcium activity was recorded using live cell widefield microscopy, with the imaging chamber kept at 37°C, 5% CO_2 conditions throughout the recording. The gels were kept in 6-well plates in RB+ cell culture media.

For electrical field stimulation experiments, the gels were washed once in 3 mL of warm PBS, which was then replaced with 3 mL 37°C-warm filter-sterilised HEPES-buffered Tyrode Solution (Alfa Aesar, UK). The gels were allowed to acclimatise for 15 minutes, after which they were transferred to the imaging chamber. Two 5.3 cm long platinum electrodes were inserted into the well, with the tips of the electrodes touching the bottom, and connected to the MyoPacer Cell Stimulator (IonOptix, Ireland). The spontaneous activity was recorded for 15 seconds, after which the gels were paced at 1, 2 and 3 Hz frequencies for 15 seconds each, with 15-second intervals in between the stimulation to allow for the cells to recover. The pulse width was kept at 20 ms for all samples; double-layered gels were stimulated at 15 V to account for the increased thickness of the material. The full recording lasted 120 seconds, with the final 30 seconds the gels remaining unstimulated. Each gel was recorded at 3 separate fields of view (FoV) at 2.5x magnification, 3 FoV at 10x magnification of patterned regions, and 1 FoV of unpatterned regions. The gels were allowed to recover between

each recording until the spontaneous calcium activity resumed. Upon completion of the experiment, the gels were washed once in 3 mL of PBS, fixed with 4% (v/v) PFA for 15 minutes, washed three times with 3 mL of PBS and stored in 1% (v/v) AA-PBS solution at 4°C until further use for immunofluorescent staining.

Calcium videos and brightfield imaging were carried out using an Axio Observer Z1 widefield microscope (Zeiss, UK). The videos were acquired either at 2.5x or 10x magnification using a 4 × 4 binning mode with exposure set at 10 ms, at 100 frames per second (fps) acquisition rate. The brightfield images were acquired with a 2.5x or 10x objective, using a tiling mode for imaging whole-gel overviews.

3.3.9 Analysis

3.3.9.1 Frequency analysis

Calcium videos were processed in Fiji image analysis software (v. 1.53f51). A 30 × 30 pixel region of interest (ROI) was placed on each independent region that exhibited calcium activity, and the traces of changes in signal intensity were acquired using Intensity macro provided by the Imperial College Facility for Imaging by Light Microscopy (FILM). The resulting .csv file was segmented into four to isolate the regions of spontaneous, 1 Hz, 2 Hz and 3 Hz stimulated calcium activity. The traces were then analysed using a MATLAB code, kindly provided by Dr Richard Wang and Dr Hyemin Kim, to detect the peaks of calcium signal and their respective timestamps. A peak was defined as the signal elevated above a certain threshold of the whole signal range, and the output peak number was checked manually for each ROI to ensure all the peaks in a given trace were detected. If some peaks were missing, the threshold values were adjusted until timestamps for all peaks were detected. Baseline and 1 Hz segments were generally analysed with 0.65 threshold, defining the peak as the trace elevated above 65% of total signal range, while 2 Hz and 3 Hz traces showed higher signal intensity and were analysed with threshold values ranging from 0.35 – 0.95 (ROI-specific). Peak frequency was then calculated as the inverse of the adjacent peak difference, and the total output

frequency for each stimulation mode of each ROI was calculated as the average of all peak frequencies of a given region.

3.3.9.2 Activation maps and directionality analysis

Two MATLAB codes for the analysis of calcium signal directionality were written and kindly provided by Dr Richard Wang. The acquired 10x videos of calcium propagation through the gel were segmented into individual ROIs to isolate individual lines (length of ROI is dependent on the line, width set at 366 µm). The resulting videos were pre-processed using FIJI software. First, the background and autofluorescence of the region were removed by subtracting a single inactive frame from the whole video, and a median filter (2.0 px diameter) was applied. The threshold was then adjusted to detect the active calcium wavefront and remove the noise. The image was made binary, and the binary functions 'Close-' and 'Fill holes' were applied. The video was then trimmed to only contain a single activation pulse. The remaining outliers were removed (3.0-pixel diameter, 50 threshold), and the final pre-processed image was saved in .tiff format.

For frame-by-frame visualisation of signal progression, the panel of frames with 20 ms intervals was created using Fiji. For signal propagation through sequential ROIs, 218 × 613 µm ROIs were positioned at 760 µm intervals along a single active calcium line, captured at 2.5x magnification. The intensity profiles were measured using Intensity macro in Fiji provided by Dr Stephen Rothery, generating a .csv file. The intensity was normalised to [0,1], set at minima and maxima of individual traces respectively, and a second order polynomial with 10 neighbours was applied to smooth the signal using GraphPad Prism software (GraphPad Software, USA v 8.4.2).

The activation maps were generated by running .tiff images through a MATLAB code that applied a colour gradient to the timeseries. The radial histograms were generated by running the .tiff files on

another MATLAB code, which determined propagation distance and angle of direction from each active pixel in one frame to the nearest active pixel in consecutive frames. The distribution of those angles was represented in a radial histogram with the binning set at 5°.

3.3.9.3 Statistical analysis

All statistical analysis was performed using GraphPad Prism v8.4.2 (GraphPad Software, USA). The RT-qPCR data of gene expression over time was analysed using a pairwise mixed-effects model, with Sidak multiple comparison test correction applied, pairing the patterned and unpatterned samples from the same gel. The housekeeping genes across different timepoints were analysed using a mixed effects model with Tukey multiple comparison correction, while the differences between patterned and unpatterned housekeeping gene expression at d20 were analysed using a paired two-tailed Wilcoxon test. The statistical difference between $2^{-\Delta\Delta C}$t values of each gene at d20 were analysed using a paired two-tailed Wilcoxon signed-rank test. AlamarBlue™ metabolic activity and PicoGreen proliferation data were analysed using a one-way repeated measures ANOVA, pairing the same biological samples between the exposure conditions, with Tukey correction for multiple comparisons and Geisser-Greenhouse correction for variability of differences applied. For PicoGreen DNA quantity distribution analysis, a one-way ANOVA with Tukey and Geisser-Greenhouse corrections was performed without any matching. Change in output frequency dependent on electrical stimulation was analysed using a paired mixed effects analysis model with Tukey and Geisser-Greenhouse corrections applied, matching across corresponding ROIs. The difference between patterned and unpatterned groups for each stimulation mode was analysed using a two-tailed Mann-Whitney test. All significance values were reported as * - $p < 0.05$, ** - $p < 0.01$, *** - $p < 0.001$ and **** - $p < 0.0001$.

3.4 Results and discussion

3.4.1 Optimisation of hiPSC patterning in hydrogels

3.4.1.1 Device design and patterning conditions optimisation

Theoretically, during the patterning process, acoustic radiation force is the primary force experienced by the cells and is responsible for guiding them towards the zero-pressure nodes. The magnitude of this force depends on the properties of both the cell itself (volume, density and compressibility) and the surrounding medium (density and compressibility) within which the patterning occurs. In practice, however, this force is diminished by other forces acting on the cells, for example, gravity (in the case of acoustic levitation), acoustic streaming and viscous drag. The latter, in particular, is a challenge for hydrogel-based acoustic patterning, as the viscosity of the medium can severely disrupt the patterning process. A controlled, triggered transition from a solution to a gel is therefore required for successful patterning in hydrogels, with minimal viscosity of the pre-gel solution being a key factor in patterning quality.

Photocrosslinkable GelMA hydrogels were previously shown to be compatible with acoustic patterning at 40 mg/mL concentration, forming the foundation for the protocol used in this study (Armstrong et al., 2018). The acoustic-patterning device that fits a 35-mm diameter Petri dish (Figure 3-2A) and the passivation of the patterning surface with 2% (v/v) agarose were reproduced in order to minimise the surface friction between the cells and the culture plate as well as reduces acoustic streaming (Bernassau et al., 2014; Armstrong et al., 2018). While the protocol worked well in these devices, the curvature of the dishes disrupted the pattern formation at the edges of the pattern region. Furthermore, the transducer length was limited to 12.5 mm. Together, those factors resulted in linear cellular arrays occupying ≈44.2% of the whole hydrogel when patterning using both pairs of transducers, and limited to a maximum length of 12 mm per line (Figure 3-2B). Additionally, the throughput per device was set at one gel per experiment, which was not efficient. To improve on those factors, a new patterning device capable of housing a 2-well ibidi plate was designed (Figure

3-2C). The major advantage of using those plates is that the wells are rectangular, thus minimising the wave interference at the edges. Making use of the ibidi plate dimensions, the device was fitted with customised 20 mm long transducers, allowing to increase the length of individual lines. As a result, it was possible to pattern two gels at the time, with ≈50.2% of the gel occupied by the pattern and individual lines reaching 20 mm in length (Figure 3-2D). Another improvement of the new device design was that the transducers were mounted onto the outer surface of the acrylic frame, allowing the sound waves to pass directly into the wall of the ibidi plate. In the original design, the transducers were placed inside an acrylic cavity, thus the sound had to travel through the acrylic first before entering the patterning cavity, dampening the amplitude of the standing wave field. Taken together, the new device allowed us to generate tightly patterned uniform lines of fixed hiPSCs with higher fidelity, as well as increasing the throughput and length of individual lines of cells (Figure 3-2). It should be noted that 2-D patterning would not be possible in the new setup with a single

transducer pair, however 1-D patterning was sufficient for the target linear cardiac fibre arrangement.

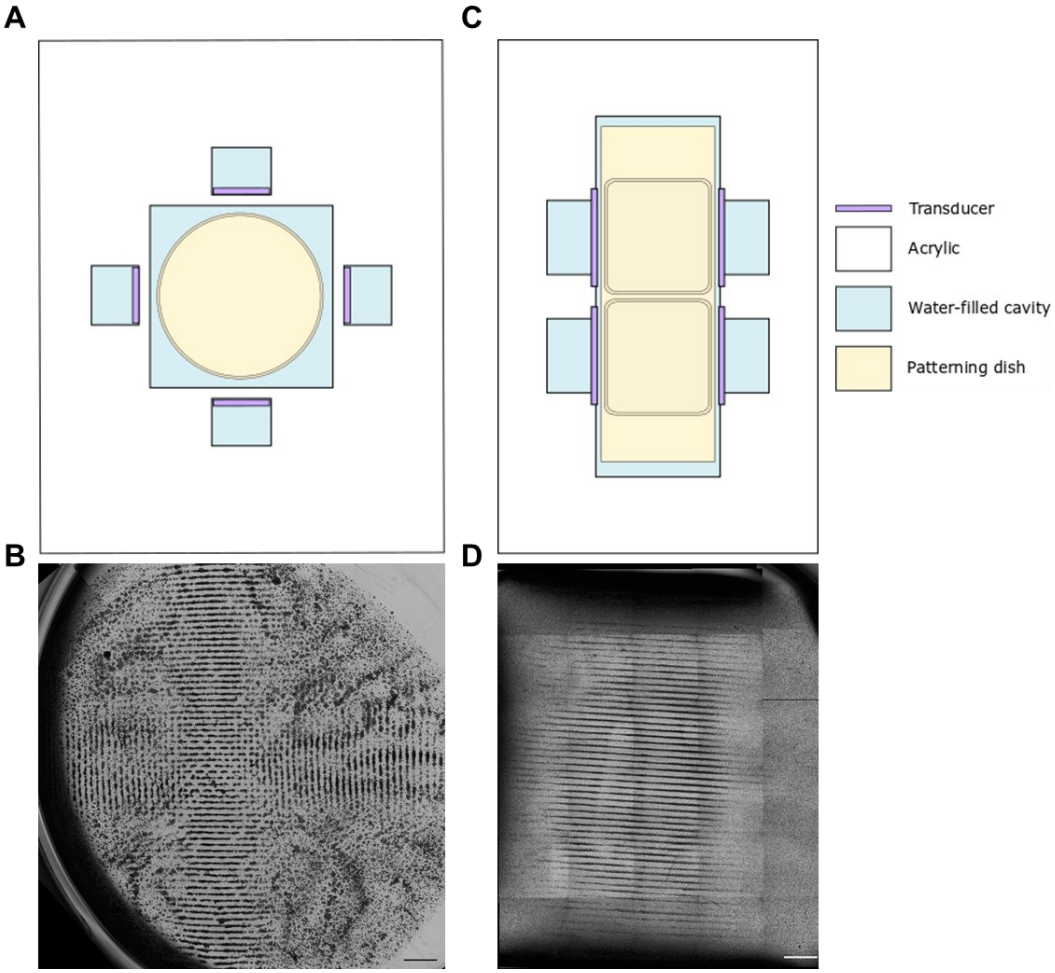


Figure 3-2 ***Acoustic patterning device design optimisation*** *(A). Schematic of a typical acoustic patterning device fit with a 35-mm Petri dish for cell culture. Adapted from (Armstrong et al., 2018). (B). Representative brightfield overview image of hiPSCs patterned at 2.0 MHz in 4% (w/v) GelMA using a 35-mm acoustic patterning device. (C). Schematic of a new acoustic patterning device capable of fitting a 2-well ibidi plate. (D). Representative brightfield overview image of hiPSCs patterned at 2.0 MHz in 4% (w/v) GelMA using an ibidi-compatible acoustic patterning device. Scale bars = 2000 µm.*

The above optimisations were performed with fixed cells in PBS solution. When patterning those in 4% (w/v) GelMA at room temperature, a considerable decline in patterning quality was observed, with some clusters of cells appearing in between the lines (Figure 3-3B). This was attributed to an increased viscosity of the pre-gel medium in comparison to the cell media solution. The viscosity of thermosetting polymers, such as GelMA, is temperature dependent, which allowed us to decrease

GelMA viscosity by increasing the temperature (Pepelanova et al., 2018). Using a PolarBear during the patterning and crosslinking processes, the temperature was maintained stable at 37°C, to keep it compatible with the cell culture conditions and to avoid heat-induced degradation of GelMA. After 15 minutes, the cells were arranged in a uniform linear array (Figure 3-3C). Although there was some compromise regarding patterning quality, overall the hydrogel contained distinct areas of high and low cell density, thus confirming that successful acoustic patterning of cells is possible in porcine GelMA at 37°C.

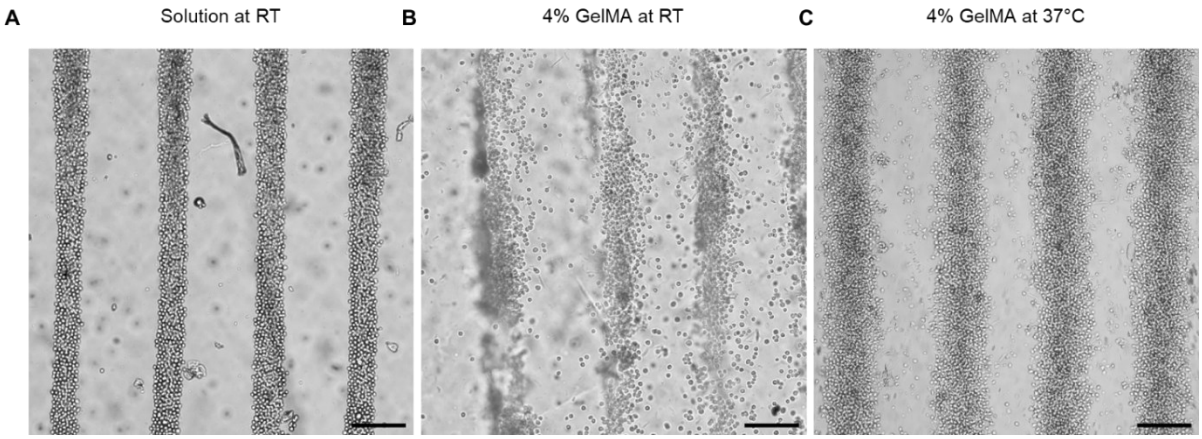


Figure 3-3 ***Effect of temperature on acoustic patterning in thermosetting GelMA hydrogels.*** *(A). Fixed MDA-MB-231 cells acoustically patterned in PBS solution at room temperature. (B). Fixed MDA-MB-231 cells acoustically patterned at 2.0 MHz in 4% (w/v) GelMA at room temperature. (C). Fixed MDA-MB-231 cells acoustically patterned at 2.0 MHz in 4% (w/v) GelMA 37°C. Scale bars = 200 µm.*

3.4.1.2 GelMA degree of functionalisation quantification

GelMA is a semi-synthetic polymer synthesised from gelatin, which can induce biological signalling and allow cell adhesion, and methacryloyl, which can undergo rapid covalent photopolymerisation with light, allowing for tunable mechanical properties of the bulk hydrogel. Taken together those properties make GelMA an extremely attractive material for tissue engineering applications. During synthesis, the lysine groups of the gelatin are substituted with methacrylate side groups. The extent of such substitution is known as the degree of functionalisation (DoF), and it is measured as the percentage of substituted lysines in comparison to the fully unmodified gelatin. The methacryloyl

groups form covalent bonds upon polymerisation, with a higher number of bonds corresponding to stiffer gel, and as the DoF determines the maximum available binding sites on the GelMA, it directly affects the mechanical properties of the bulk material. The DoF can be determined using a fluoraldehyde assay, where the fluorescent fluoraldehyde reagent binds unreacted lysine groups, allowing the quantification of differences between unfunctionalized gelatin and functionalised GelMA formulations.

Previously published protocols for GelMA synthesis were used to synthesise a library of porcine GelMA formulations of varying stiffnesses, confirmed with a fluoraldehyde assay to range from 20% to 95% (Figure 3-4, Table 3-2) (Hoon Lee et al., 2015; Meinert et al., 2016). After hiPSCs were seeded in those GelMAs and cultured for 4 days, the lower DoF gels showed no organised cell growth, with the majority of the cells scattered throughout the gel in single-cell fashion (Figure 3-5). On the contrary, at higher DoF (80%, 95%) the cells compacted into dense opaque clusters. Going forward, all experiments were performed with GelMA functionalised at least at 80%.

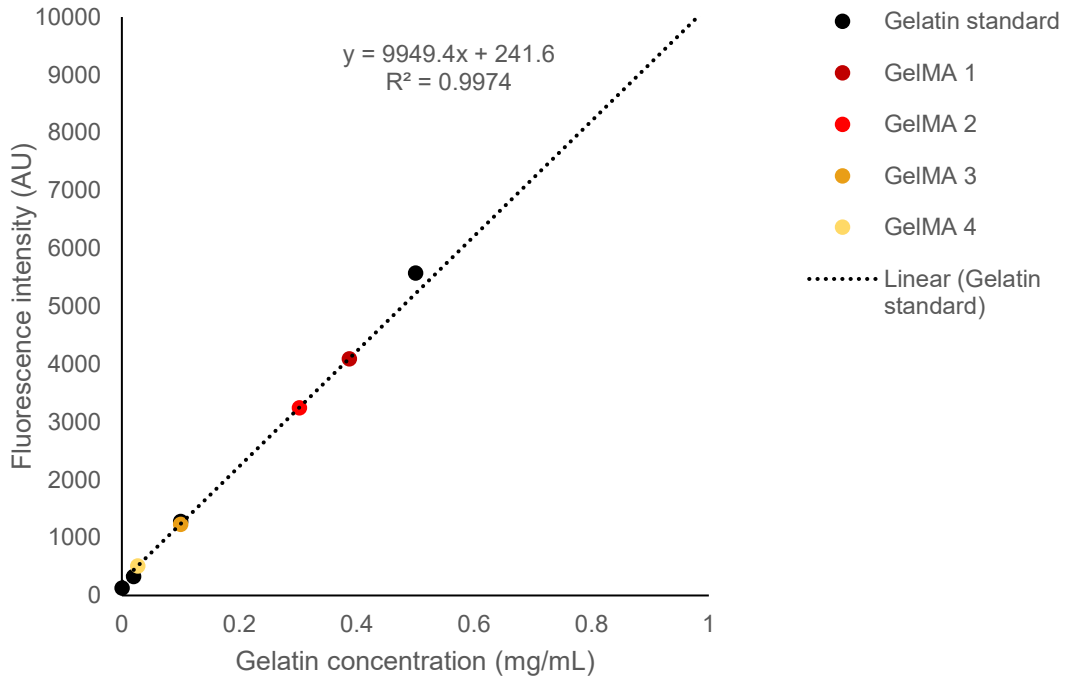


Figure 3-4 ***Fluoraldehyde assay results of home-made GelMA characterisation.*** *Fluorescence intensity of the fluoraldehyde reagent reacted with the gelatin standards (0, 0.02, 0.1, 0.5 and 1 mg/mL) and four different batches of GelMA prepared at 0.5mg/mL. Black dots indicate the fluorescence intensity measurements from the gelatin standard curve, coloured dots indicate the unfunctionalized gelatin concentrations of four different batches of GelMA synthesis, calculated from the fluorescence intensity measurements of the sample and the fitted linear equation (dashed line) from the standard curve. n = 3, N = 1, where n is the number of measurements per sample, and N is the number of fluoraldehyde assays performed.*

Synthesis batch	Protocol used	[MAA] (ml/g)	Fluorescence (AU)	DoF (%)
1	Hoon Lee et al., 2015	0.0125	4094	22.5
2	Hoon Lee et al., 2015	0.025	3247	39.6
3	Meinert et al, 2016	0.6	1235	80.0
4	Meinert et al., 2016	0.6	512	94.6

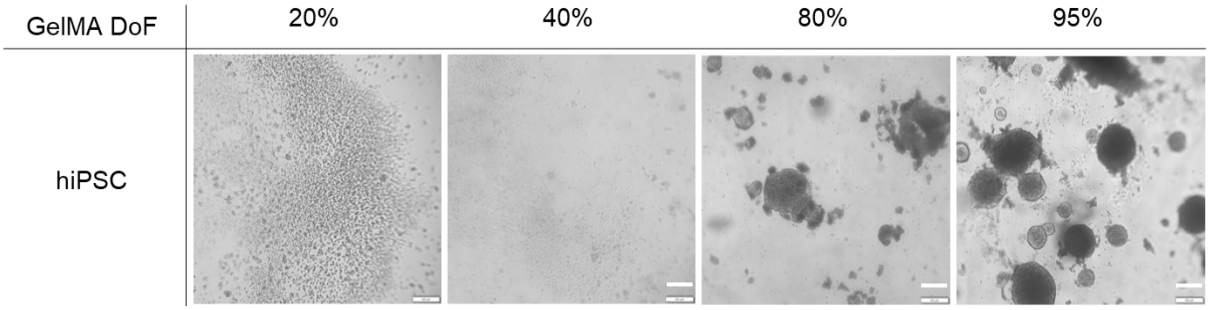


Figure 3-5 ***Survival of hiPSCs in home-made GelMA hydrogels.*** *Brightfield images of hiPSCs seeded in four GelMA hydrogel formulations and cultured for 4 days. Scale bars = 200 µm.*

However, while synthesising GelMA in-house, several inconsistencies were observed. Firstly, although the protocol did generate a range of DoFs, the details of the process were not as predictable as described in literature: while batches 1 and 2 were theoretically aiming to synthesise 40% and 60% DoF respectively, after quantifying the product it was determined to be 2-fold lower than expected, making the synthesis route unreliable (Hoon Lee et al., 2015). Also, despite the pH adjustment step prior to freeze drying the material, upon reconstitution, the homemade GelMA showed a variation in pH. This batch-to-batch variability caused inconsistency in experiments since the pH affects gelation timing as well as cell viability and behaviour. Overall, with the whole process of synthesis taking approximately 7-10 days, synthesising GelMA in-house was unreliable and time-consuming. As an alternative, filter-sterilised, pH-adjusted 80% DoF porcine GelMA was purchased from Gelomics in bulk, allowing to keep the pH and DoF consistent for all future experiments.

3.4.1.3 Light source optimisation

Photo-curable hydrogels require a photoinitiator and a light source, most commonly ultraviolet light, in order to initiate radical polymerisation and form covalent bonds. GelMA systems are traditionally cured using Irgacure 2959 or LAP photoinitiators activated by 365 nm light. However, UV irradiation and free-radical-induced damage of photo-crosslinkable hydrogels can induce cytotoxicity, with several studies reporting a decrease in viability with prolonged UV exposure and increasing initiator concentrations (Lim et al., 2019; Monteiro et al., 2018; Fedorovich et al., 2009). Additionally, when using stem cells, UV wavelengths pose an additional risk of introducing UV-mediated mutations, leading to genetic instability disrupting the differentiation process as a whole (Dahle, Kvam & Stokke, 2005; Dahle & Kvam, 2003). Indeed, when hiPSCs encapsulated in GelMA were cured with 5 or 10 minutes of 365 nm light, after 4 days in culture the shorter UV exposure showed a lot more cell growth than that with longer UV exposure (Figure 3-6).

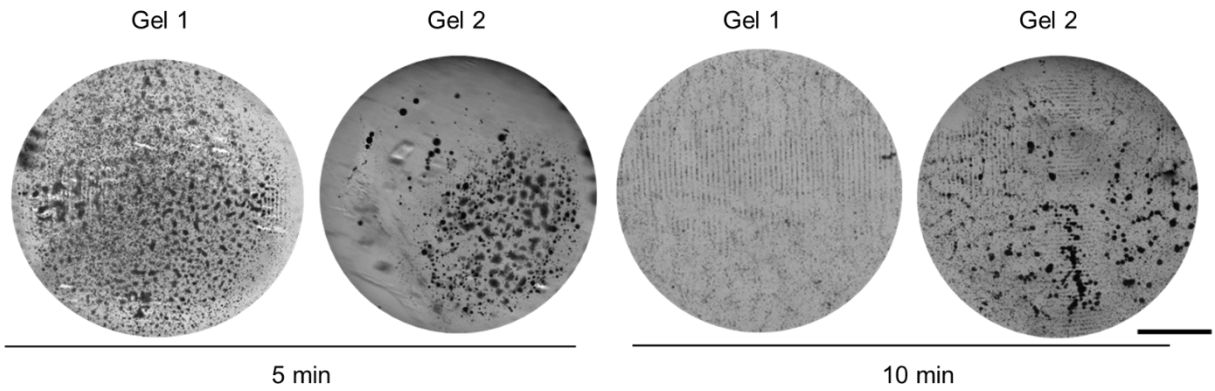


Figure 3-6 ***Effect of 365 nm UV light exposure on hiPSC cell growth.*** *Brightfield overview images of hiPSC cluster formation at day 4 in hydrogels cross-linked using 5 or 10 minutes of 365 nm UV exposure. Scale bar = 2000 µm.*

Other light sources with longer wavelengths would therefore be preferred for curing gels with sensitive biological systems. Since LAP photoinitiator is also capable of absorbing light in the 400 nm region, polymerisation of GelMA with visible, cytocompatible light is possible (Khoshakhlagh et al., 2019; Fairbanks et al., 2009). A LEDA-405 LED array, a device containing 96 individual LEDs emitting light at 405 nm wavelength, was therefore used as a visible light source for hydrogel crosslinking. First, GelMA gelation timing with a blue light source was optimised by irradiating the pre-gel solution for 0, 0.5, 1, 2, 3 and 5 minutes with 405 nm light (Figure 3-7A). The solution at 0 minutes demonstrated the spreading of the liquid over the syringe surface, which was also evident at 0.5 minute irradiation. From as little as 1 minute of light exposure, the hydrogel was visibly cured, maintaining the puck-like shape. Therefore, 1 minute exposure was chosen for all blue light source porcine GelMA experiments, as it used the minimum exposure time for hydrogel curing.

GelMA can also be produced with gelatin derived from fish skin, which has a shorter polymer chain length, making this material easily soluble and liquid at room temperature (Yoon et al., 2016). Porcine GelMA, on the other hand, is soluble and liquid only at temperatures above 35°C, and has a higher viscosity than fish, requiring consistent and accurate temperature control with little permissible error for successful high-quality acoustic patterning (Derkach et al., 2020). Therefore, fish GelMA's lower viscosity and higher solubility make it an ideal candidate for acoustic patterning. In the sections 3.4.1.3-3.4.1.7, the properties of porcine and fish GelMAs and behaviour of

acoustically-patterned hiPSCs in these materials are compared to select the best system compatible with both the patterning process and long-term hiPSC culture.

Indeed, patterning cells in fish GelMA generated clear uniform lines, comparable in quality to porcine (Figure 3-14). The gelation timing for fish GelMA was optimised, similarly to porcine, by varying the irradiation time of the LEDA-405 array, exposing the pre-gel solutions to 0, 1, 3, 5, 7 and 9 minutes of 405 nm light (Figure 3-7B). Gelation was first observed after 7 minutes of curing, and this irradiation time was used for all future fish GelMA experiments. At this stage of the project, both fish and porcine GelMAs were used for characterisation and cell culture optimisations to determine the most suitable material for successful *in situ* differentiation.

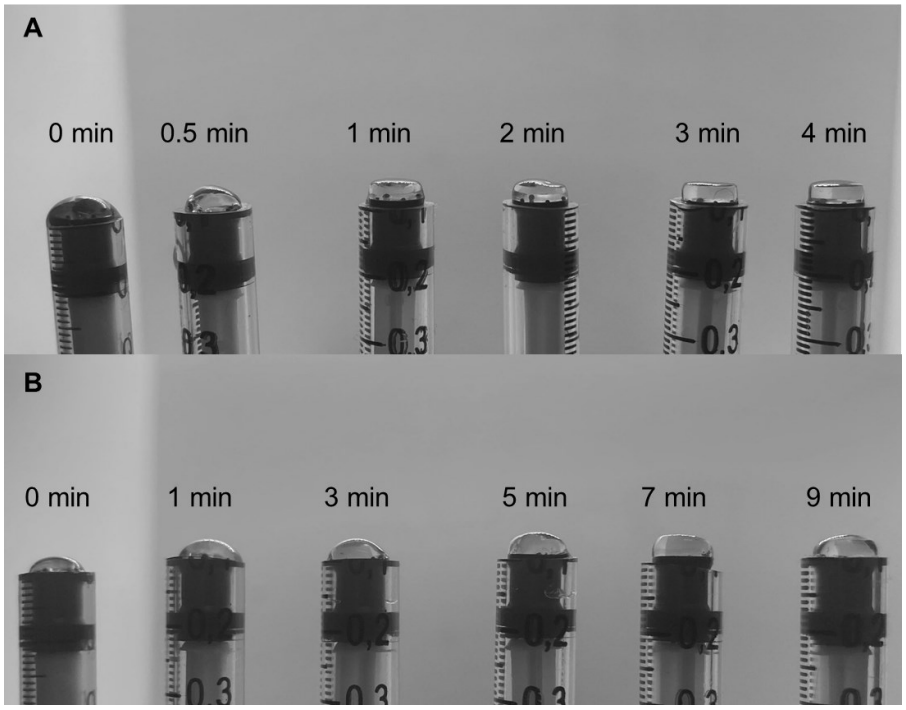


Figure 3-7 ***Optimisation of gelation timing for porcine (A) and fish (B) GelMA hydrogels cross-linked by LAP photoinitiator with 405 nm blue light source.*** *(A). Porcine hydrogel formation after 0, 0.5, 1, 2, 3 or 4 minutes of light exposure. (B). Fish hydrogel formation after 0, 1, 3, 5, 7 or 9 minutes of light exposure.*

For the direct comparison of light sources, hiPSCs were then encapsulated in Porcine GelMA cured with either 365 nm UV lamp or 405 nm LED array, cultured for 4 days and differentiated, using CHIR99021 Wnt-activator to initiate mesoderm induction on day 4 and C59 Wnt-inhibitor to direct the cells towards cardiac lineage on day 7. Brightfield imaging was performed after each differentiation step, with pre-differentiated hiPSCs imaged at day 4, mesoderm-specified cells upon completion of CHIR99021 treatment imaged at day 6 and cardiac lineage-specified progenitors upon completion of C59 treatment imaged at day 9 (Figure 3-8). The differences between UV and visible light irradiation were observed from the hiPSC stage, where the cell clusters in 365 nm-cured gel appeared more translucent, with some non-compacted cells visible in the middle (Figure 3-8A). The 405 nm-cured gel showed opaque, continuous, elongated cell clusters from day 4. Both gels exhibited cell death after differentiation initiation, however, the clusters of 405 nm-cured gel remained longer and more opaque (Figure 3-8B). At cardiac progenitor stage, 365 nm-cured gels lost all cell cluster formation, characteristic of cell death, while the clusters in 405 nm cured-gels were growing and invading the gel, characteristic of cell migration (Figure 3-8). Importantly, despite the ongoing growth of the cell clusters, the patterned structures within the 405 nm cured gels were preserved throughout differentiation. 405 nm light source was therefore chosen as a safer, more cytocompatible light source, and used for all future experiments.

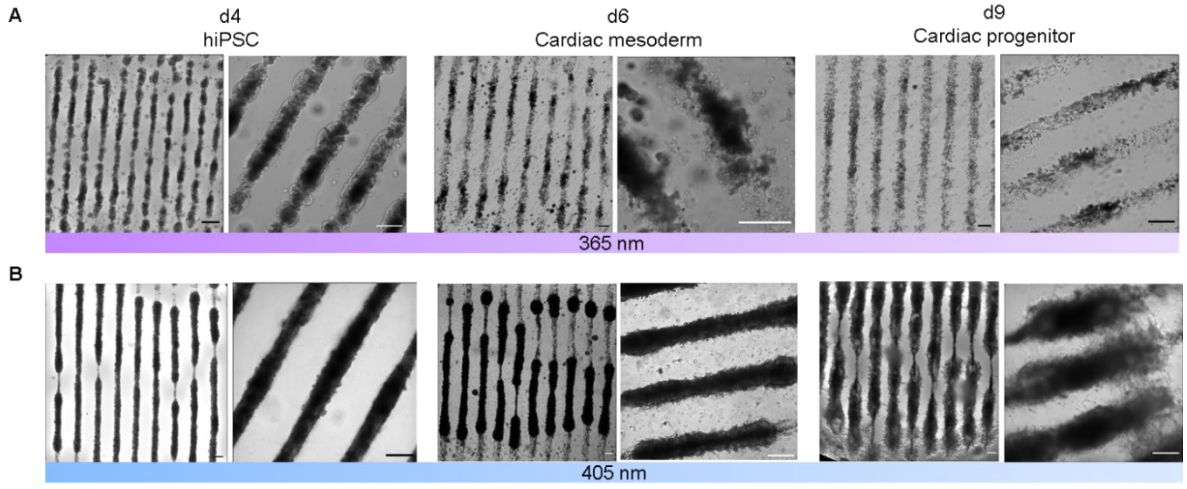


Figure 3-8 ***Effect of light source on hiPSC survival and differentiation.*** *Acoustically-patterned (2.0 MHz) hiPSCs in porcine GelMA (4% w/v) crosslinked with LAP photoinitiator using (A) a 365 nm UV light source, or (B) a 405 nm blue light LED array. The samples were imaged with a brightfield microscope immediately prior to differentiation initiation (d4, hiPSCs), after mesoderm specification (d6, mesoderm) and after cardiac lineage specification (d9, cardiac progenitor). All stages are shown as overviews (scale bar = 500 µm) and close-ups (scale bar = 200 µm).*

3.4.1.4 Hydrogel rheology for assessment of viscoelastic properties

After optimising the time to gelation of the hydrogels, the viscoelastic properties of commercial GelMA materials were characterised using rheometry. The hydrogels were prepared by adding 1 mL of 4% (w/v) GelMA mixed with 2 mM LAP precursor solution to an ibidi 2-well plate and cured using a 405 nm LED array to replicate the experimental conditions used for hiPSC patterning. The changes in the storage (G') and loss (G'') moduli of both porcine and fish GelMA were assessed through the frequency and strain sweeps. G' is a measure of elastic energy stored within the material during the deformation, while G'' refers to the energy lost during the deformation. Initially a strain sweep from 0.1 to 100% strain was measured to determine the linear viscoelastic region (LVR) of the two materials. Both fish and porcine GelMA exhibited a fully linear viscoelastic region across this range, with G' higher than G'' throughout the measurement, with no deviation in their tan δ, demonstrating the ability of these materials to withstand deformation to shear (Figure 3-9A). The plateau storage modulus of fish GelMA was 15.21 ± 4.10 Pa, while porcine GelMA was determined to be 32.2 ± 5.83 Pa. As the magnitude of G' of porcine GelMA was two-fold higher, this material was considered to be more stiff compared with fish GelMA. This behaviour was expected given the longer molecular chain length of porcine gelatin versus that of fish gelatin, amounting to higher theoretical crosslinking density, ultimately increasing the mechanical stiffness of the material (Yoon et al., 2016). For comparison with other biomaterials, the storage modulus of decellularized cardiac ECM was recorded as ≈ 100 Pa, while G' of hydrogel inks used for hiPSC-CM 3D-bioprinting is commonly within kPa range (Singelyn & Christman, 2011; Hall & Ogle, 2018; Kupfer et al., 2020). Therefore, fish GelMA was an order of magnitude softer than cardiac ECM, porcine GelMA was stiffer, reaching a third of the storage modulus of cardiac ECM, but both of those systems would be considered as soft gels in comparison to other existing biomaterials.

A frequency sweep was performed with strain fixed at 0.1% (within the LVR) to demonstrate the viscoelastic properties of the hydrogels over a range of frequencies (Figure 3-9B). The G' and G'' of both materials remained stable up to 3.5 Hz. After this yield point, a gradual increase was observed in both moduli, indicating the materials to be frequency-dependent at high frequencies. The G'' increased at a higher rate, until the crossover, or flow point, was reached at ≈ 49 Hz and 56 Hz for fish and porcine GelMA respectively. With higher frequency, the rate of deformation of the gel increased, causing the viscous behaviour to dominate over elastic, leading to the crossover point between two moduli. At the crossover point, consistently above 40 Hz, the hydrogels ultimately transitioned from gel to liquid. In the context of human physiology, while 3.5 Hz is out of range for the resting heart rate, in extremely rare cases of tachycardia this value could be superseded (Chhabra et al., 2012).

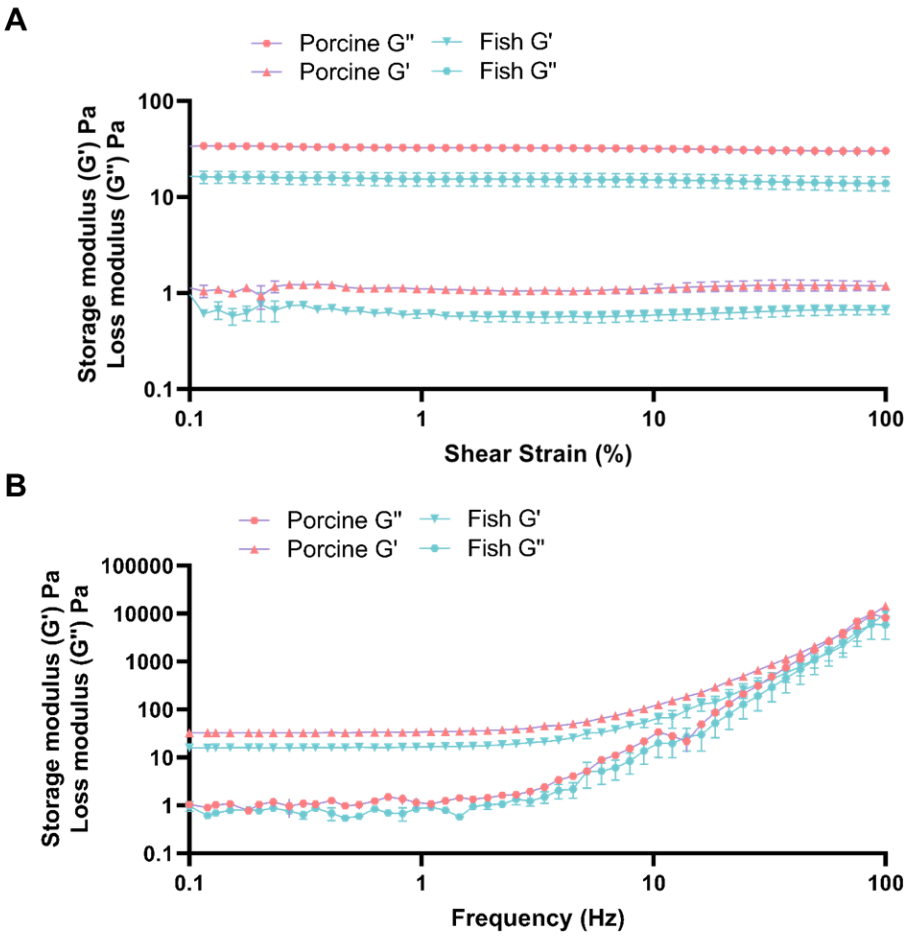


Figure 3-9 ***Viscoelastic properties of commercial porcine and fish GelMA, purchased from Gelomics.*** *(A). Strain sweep performed at 1 Hz frequency. (B). Frequency sweep performed at 0.1% strain. All measurements done at 37°C, n = 3, N = 1, where n is the number of replicate gels and N is the number of GelMA bottles used for each animal source.*

3.4.1.5 GelMA batch variation assessment

The move towards commercial GelMA was initiated in order to address the synthesis variability concerns, discussed previously. Porcine GelMA of batch #LU20L03 (batch 1) was purchased in bulk (10 bottles of 1 g material) from Gelomics and used for the majority of experiments in this project, yielding on average 8-10 hydrogels per bottle. The same batch number indicated that all bottles were products of the same synthesis reaction, limiting the batch-to-batch variability. However, while performing patterning experiments, variability in hydrogel stiffness between bottles was noted.

To investigate this further, a different batch #LU22C12 (batch 2) of 10 bottles of porcine GelMA was purchased from Gelomics and extensive characterisation of each bottle was performed. Based on the results from rheometry of porcine and fish GelMA, for the discussion below the gels of ≈ 30 Pa are considered as 'stiff' while those approaching ≈ 15 Pa are deemed 'soft'. Each bottle was given an ID number, ranging from GM2_4 to GM2_10. Some differences were already visible in the lyophilised material, with GM2_5, GM2_7 and GM2_10 appearing more compacted and sponge-like, maintaining their shape during the weighting process (Figure 3-10A). All other bottles were crystalline and closer in texture to powder, with the crystals separating from each other during weighing. These materials were then dissolved in media to make a 4% (w/v) GelMA/2mM LAP precursor solution. The hydrogels were prepared by first crosslinking 0.5 mL precursor solution in an ibidi 2-well plate using a 405 nm LED array, followed by crosslinking another layer on top, containing 1 mL of precursor solution to replicate the final optimised experimental conditions used for hiPSC patterning in a double layer formation (discussed in detail in section 3.4.3). The resultant hydrogels were demoulded from the plates and imaged (Figure 3-10B). The area of hydrogels from GM2_5, GM2_7 and GM2_10 was the smallest visually, suggesting the least amount of spreading/swelling and thus the highest crosslinking density, followed by GM2_8. Hydrogels from GM2_6 and GM2_9 were slightly more swollen, with GM2_4 occupying the largest area of the petri dish of all other conditions.

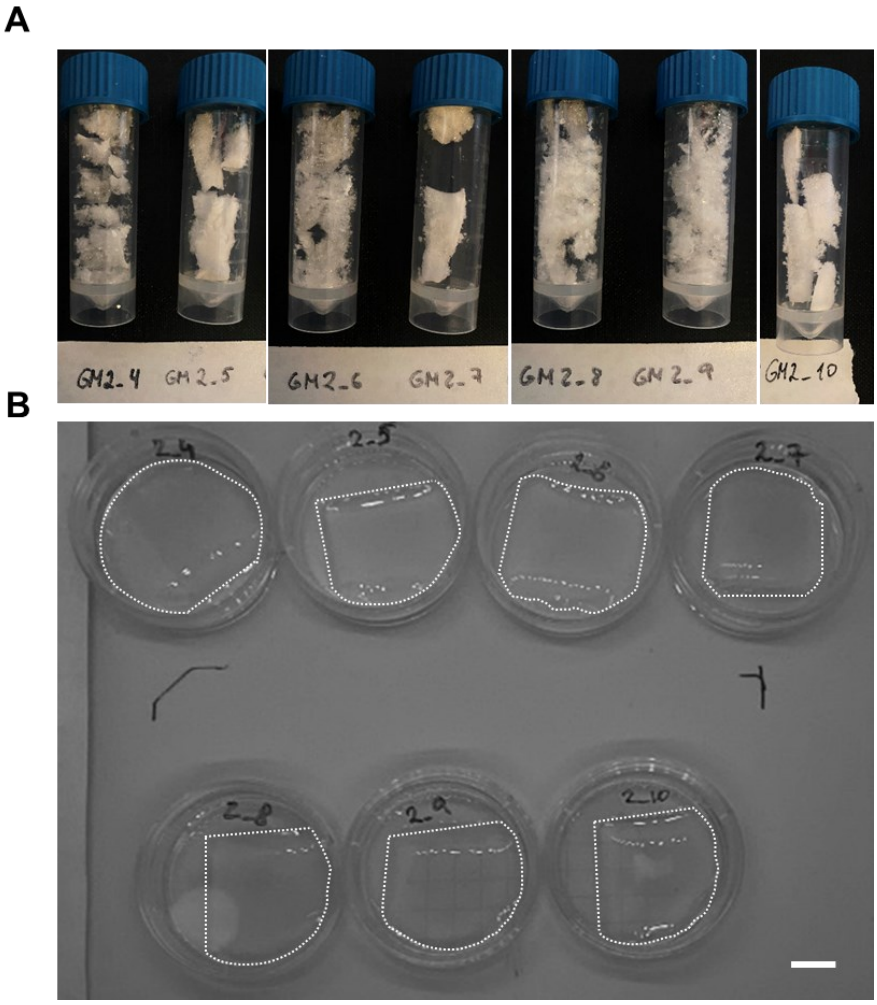


Figure 3-10 ***Visual comparison between 7 samples of porcine GelMA from batch 2.*** *(A). Visual assessment of lyophilised GelMA material obtained from each sample. (B). Hydrogels prepared from each sample in an ibidi 2-well dish using 2 mM LAP and 1 minute of 405 nm exposure. Dashed lines indicate the hydrogel boundaries. Scale bar = 10 mm.*

Rheology of those gels was then performed to quantify the differences in their viscoelastic properties. It should be noted that the absolute rheology measurements were specific to the double-layer configuration of these hydrogels, and therefore the magnitude could not be directly compared to the single-layer gel measurements described in Figure 3-9. The hydrogels displayed similar viscoelastic behaviour to that previously described, with a with a linear viscoelastic region from 0.01% - 100% strain (bar GM2_10) (Figure 3-11A). Additionally, all batch 2 gels exhibited the same characteristic frequency dependency dynamics at high frequency values (Figure 3-11B). GM2_4 and GM2_9 storage moduli were the lowest at 11.6 Pa and 10.86 Pa respectively, while GM2_10 had the highest storage modulus at 29.2 Pa, as suspected from the visual observations of both the hydrogels and the raw lyophilised materials The overall coefficient of variation of G' in combined samples from batch 2 was calculated to be 36.42%.

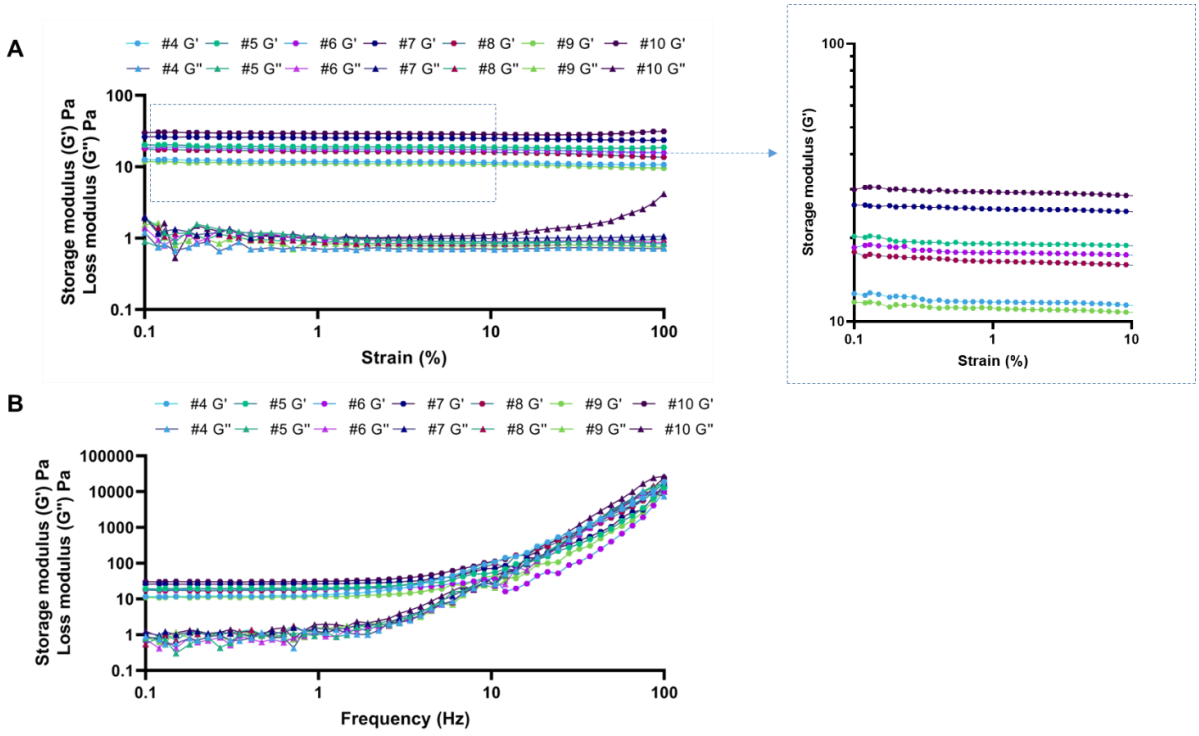


Figure 3-11 ***Variability in mechanical properties of 7 different bottles of commercial GelMA samples of batch 2.*** *(A). Strain sweep performed at 1 Hz frequency, with a zoomed in region showing G' variability between 0.1% and 10% strain. (B). Frequency sweep performed at 0.1% strain. All measurements done at 37°C, n = 1, N = 1, where n is the number of replicate gels for each GelMA bottle and N is the number of independent experiments.*

The viscoelastic properties of GelMA from batch 1 and batch 2 were then directly compared using rheometry, with GM2_10 chosen from batch 2 as the stiffest material (Figure 3-12). Surprisingly, the storage modulus of GM2_10 at 15.88 ± 1.40 Pa was 2-fold lower than that of batch 1 (32.2 ± 5.83 Pa) and was closer in magnitude to fish GelMA material (15.21 ± 4.10 Pa). Overall, these results showed that the storage modulus of the material from batch 2 was 2-fold lower than that of batch 1. The inter-replicate coefficient of variation of each condition was measured as 26.95% for Fish GelMA, 18.08% for Porcine GelMA batch 1 and 8.79% for Porcine GelMA batch 2.

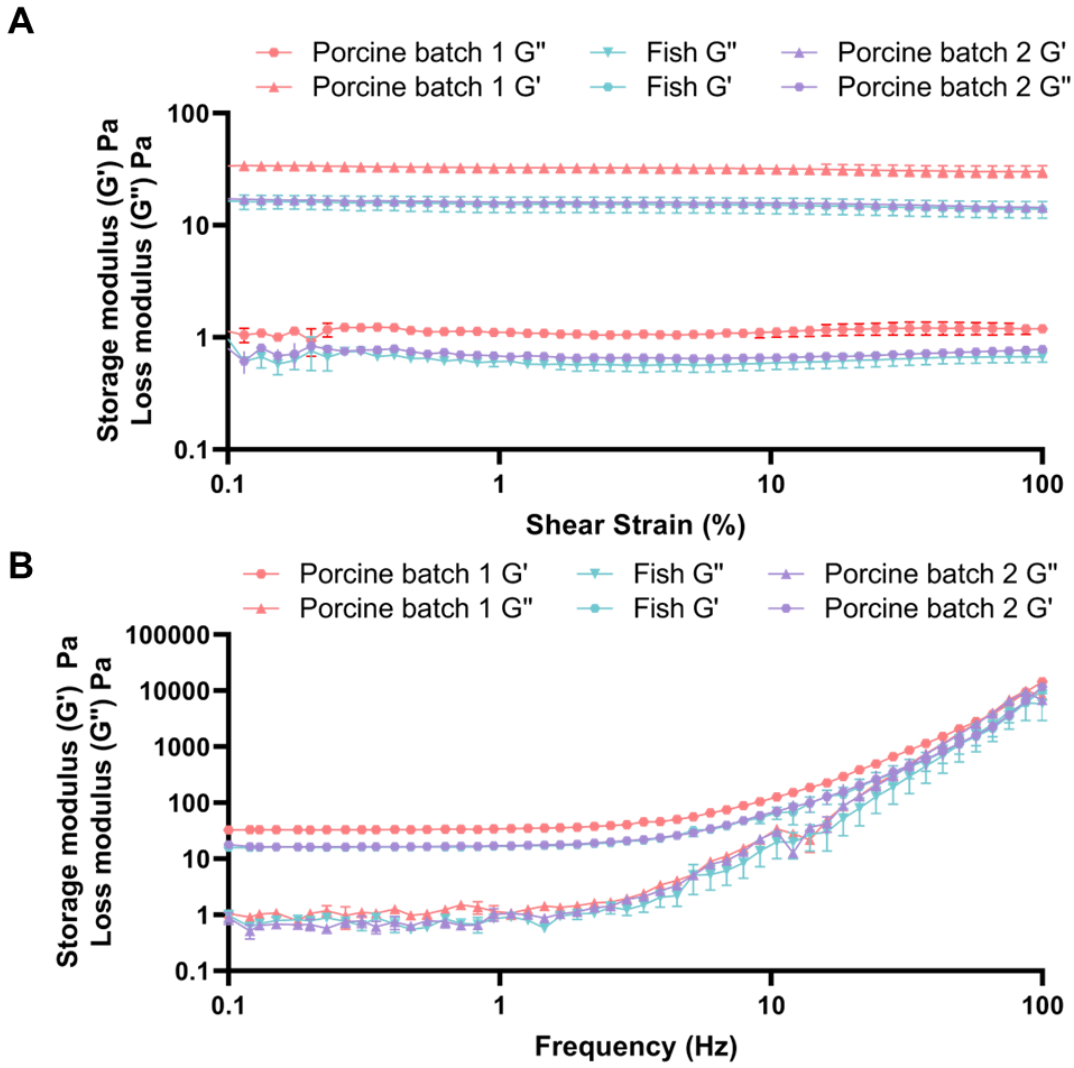


Figure 3-12 ***Comparison of storage and loss moduli between the two batches of porcine GelMA and one batch of fish GelMA.*** *(A). Strain sweep performed at 1 Hz frequency. (B). Frequency sweep performed at 0.1% strain. All measurements done at 37°C, n = 3, N = 1, where n is the number of replicate gels and N is the number of GelMA bottles used for each condition. Note that the data for Porcine batch 1 and Fish GelMA is the same as in Figure 3-9, experimentally the measurements were performed within the same experiment but were used to produce two separate figures for the clarity of thesis narrative.*

A fluoraldehyde assay was then used to compare one bottle of stiffer GelMA from batch 1 with two bottles of softer material from batch 2 (GM2_4 and GM2_10 samples). This experiment was expected to determine any inconsistencies in lyophilisation, that could potentially cause some bottles to be wetter than others, with the remaining water weight lowering the effective concentration of GelMA. However, all bottles showed high DoF, with values ranging between 87-91%, suggesting that was not the issue (Table 3-3).

Table 3-3 ***Fluoraldehyde assay results of three porcine GelMA samples from two different batches.*** *DoF – degree of functionalisation, GM2 – batch 2, GM1 – batch 1. n = 1, N = 1*

GelMA sample	DoF (%)
GM2-10	88.8
GM2-4	87.4
GM1	90.8

To conclude, the rheological behaviour of batch 2 was found to be more variable between bottles within the same batch (36.42% variation coefficient) than between replicate hydrogels made from the same bottle (8.79% variation coefficient), while the DoF confirmed through fluoraldehyde assay was consistent. Fluoraldehyde reagent determines DoF of GelMA indirectly, reacting with available primary amines, with degree of methacrylate functionalisation calculated as the percentage of occupied amine groups relative to fully unreacted gelatin (Benson & Hare, 1975; Claaßen et al., 2018). In practice, however, methacrylation can also occur with the hydroxyl groups of hydroxylysine residues of gelatin, which would not be detected by fluoraldehyde assay (Yue et al., 2017). To precisely quantify degree of methacrylation directly and accurately, the samples should be analysed using nuclear magnetic resonance (NMR) (Claaßen et al., 2018).

The bottle-to-bottle gel stiffness variability was a major limitation of the project since the different material properties were found to affect hiPSC cluster growth as well as pattern preservation

(discussed below). To maximise consistency, all optimisations and experiments were carried out using the GelMA bottles from batch 1 with ≈32 Pa storage modulus.

3.4.1.6 Cell density optimisation

To determine the optimal cell density for hiPSC cluster formation, hiPSCs were acoustically patterned at 0.75, 1, 2 and 4 × 10^6 cells/mL concentration in fish GelMA formulations, with brightfield images taken 24 hours after patterning. It was evident that the 4 × 10^6 cells/mL was the only condition generating continuous clusters (Figure 3-13). Using the optimised cell density, hiPSCs were then patterned in porcine GelMA and left in culture for 24 hours A small reduction in patterning quality was observed in porcine GelMA, however, the patterned cells still formed continuous opaque clusters. Morphologically, hiPSC clusters in fish GelMA appeared smoother than

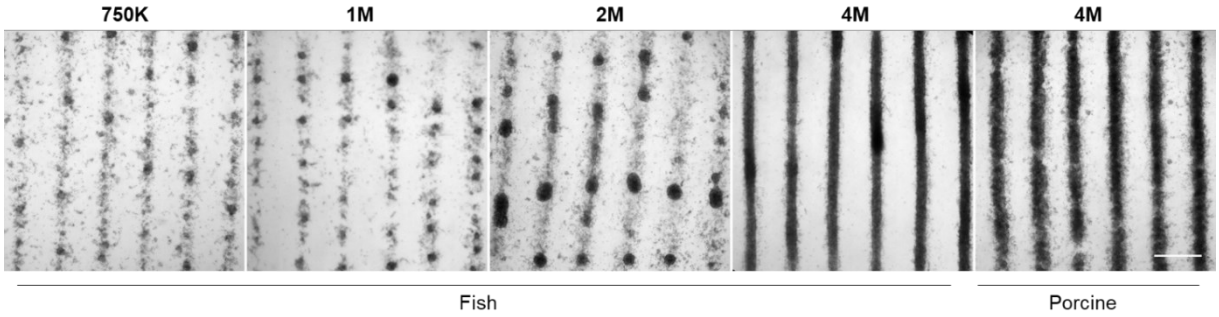


Figure 3-13 ***Cell density optimisation of hiPSC acoustic patterning in GelMA.*** *Brightfield images of hiPSCs 24 hours after acoustic patterning at 0.75, 1, 2 or 4 × 10^6 cells/mL concentration in 4% (w/v) fish or porcine GelMA using 2.0 MHz ultrasound wave. Scale bar = 500 µm.*

in porcine GelMA.

3.4.1.7 CHIR induction timing optimisation

To investigate the differences between the fish and porcine GelMA materials, hiPSCs patterned at 4 × 10^6 cells/mL in both porcine and fish GelMA formulations were subjected to the full differentiation process and observed throughout. The protocol was based on previously published literature for hiPSC differentiation in GelMA (Kupfer et al., 2020). First, the cells were imaged 1 day after

patterning, showing clear formation of continuous cell clusters in both fish and porcine GelMA hydrogels (D1, hiPSC, Figure 3-14). The gels were maintained in E8 stem cell culture medium for 3 days, during which the clusters in fish GelMA reduced in length, while the cellular arrays in porcine GelMA remained the same (D3, hiPSC). CHIR99021 was then added for 48 hours, activating the Wnt signalling pathway, thus initiating mesoderm induction of the cells, and the hydrogels were imaged after another 24 hours of recovery in basal media (D6, mesoderm). Although the ultrasound-exposed region was still visible in both conditions, the lines within the fish GelMA drastically reduced in length, leaving only a few elongated cell clusters, while the porcine GelMA maintained the lines throughout the patterned region (Figure 3-14). The gels were then directed towards cardiac lineage through the addition of IWP-2 molecule as an alternative Wnt inhibitor to the previously used C59-Wnt molecule for 48 hours and imaged again on day 9 (D9, cardiac progenitor). The cells encapsulated in fish GelMA were clumped up within the gel, losing the linear geometry and forming connections between adjacent patterned regions. The lines within the porcine GelMA remained at their original length, with the patterning still clearly visible; however, the lines appeared thinner than at mesoderm stage. Overall, hiPSC cells appeared to be visually healthier in fish material, while the material properties of porcine GelMA better preserved the pattern through the timecourse of differentiation. The shortening of the lines in fish GelMA could be explained by the likely lower cross-linking density of the softer fish material than that of porcine facilitating cell spreading and migration (Yoon et al., 2016). The whole cell clusters of hiPSCs therefore could easily pass through the gel, reducing the aspect ratio of the patterned lines.

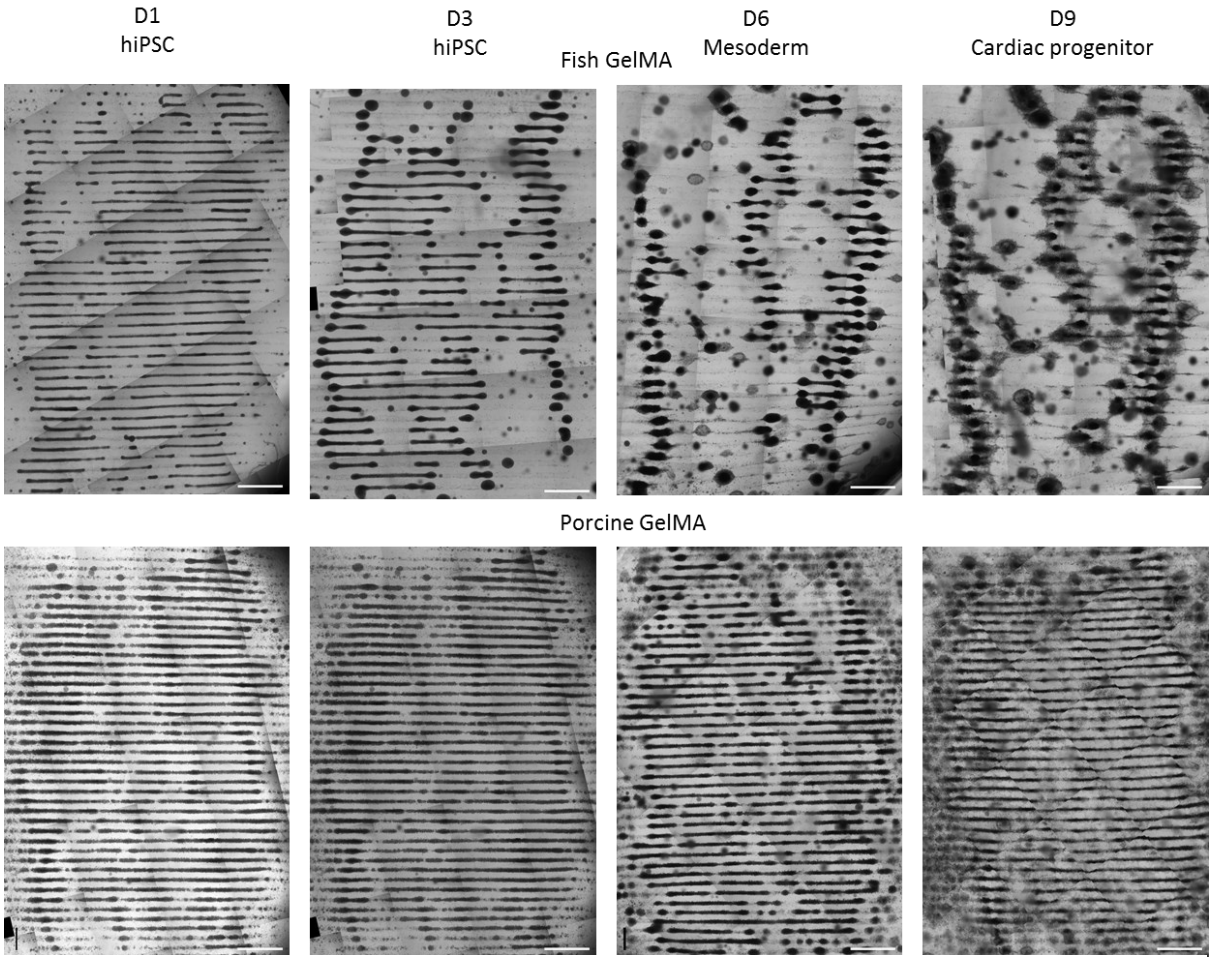


Figure 3-14 ***Pattern preservation in acoustically-assembled hiPSC arrays over the course of cardiac differentiation.*** *Brightfield overview images of hiPSC acoustically patterned (2.0 MHz, 4 × 10^6 cells/mL) in fish (top panels) and porcine (bottom panels) GelMA taken 1 day after the patterning (D1, hiPSC), 3 days after the patterning (D3, hiPSC), after completion of mesoderm induction step (D6, mesoderm) and after completion of cardiac specification (D9, cardiac progenitor). Scale bars = 2000 µm.*

Notably, some of the line shortening was first visible during hiPSC growth from day 1 to day 3, followed by the most extreme reduction in length occurring after mesoderm induction, making days 1-6 the focus area for further optimisations. It was hypothesised that minimising the timing of the growth phase (day 1-3) might limit this initial reduction, helping to preserve the patterned structures through differentiation. Therefore, six gels were cast with acoustically patterned hiPSCs using previously optimised parameters, with half of the gels made from fish GelMA and the other half from porcine GelMA. Mesoderm induction was then initiated by adding CHIR 1, 2 or 3 days after patterning, keeping the rest of the protocol steps the same for all gels and imaging them upon the completion of IWP-2 treatment (Figure 3-15). The exact days of specific differentiation stages for each condition would differ depending on the timing of initiation, therefore labels of the brightfield

images were corresponding to the differentiation stage, rather than elapsed time after acoustic patterning. Namely, 'hiPSC' were taken as immediately prior to differentiation induction, 'After CHIR' as upon completion of CHIR99021 treatment for mesoderm induction and 'After IWP' as upon completion of cardiac specification with IWP-2 (Figure 3-16, Figure 3-17). Overview images were taken at cardiac progenitor stage to show the line length of the cell clusters after full differentiation completion.

In fish GelMA, after differentiation induction on day 3, no elongated clusters at all were visible (Figure 3-16). After induction on day 2, although the patterning region was visible, the cells appeared dull and transparent, indicating no clusters-like growth and, likely, substantial cell death. The highest pattern fidelity and cell survival were observed when differentiation was initiated on day 1. This trend was less drastic in porcine GelMA, where the patterning was seen at all timepoints of CHIR inductions, however, the lines in the gel differentiated on day 3 were thinner and more interrupted than those of day 2 and day 1, indicative of a large amount of cell death at later CHIR induction time (Figure 3-17). Therefore, consistent with the hypothesis, earlier CHIR induction led to higher pattern fidelity in both fish and porcine GelMA materials. In literature, it is common to see hiPSCs expanded within a hydrogel for 3-14 days prior to differentiation to allow the cells to recover from dissociation and reach sufficient confluency (Finklea et al., 2021; Kerscher et al., 2016, 2017; Kupfer et al., 2020). In this case, earlier differentiation induction was beneficial to maintain the patterned structure since acoustic patterning generated high local cell density within each line, removing the need for hiPSC growth prior to differentiation.

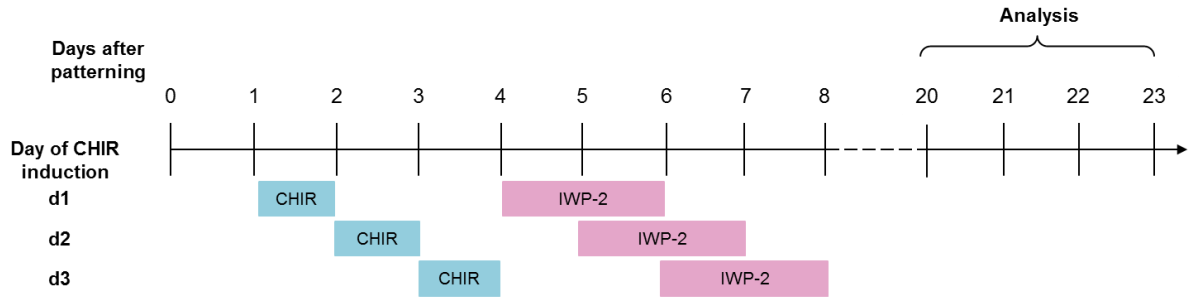


Figure 3-15 ***Optimisation of differentiation induction timing.*** *CHIR99021 small molecule (CHIR) was added for 24 h to the gels on day 1, 2 or 3 after patterning (d1, d2 or d3 of CHIR induction respectively). IWP-2 molecule was added 2 days after CHIR for 48 hours total. All small molecules were added in RB- media. The samples were then maintained in RB+ media until functional analysis at days 20-23.*

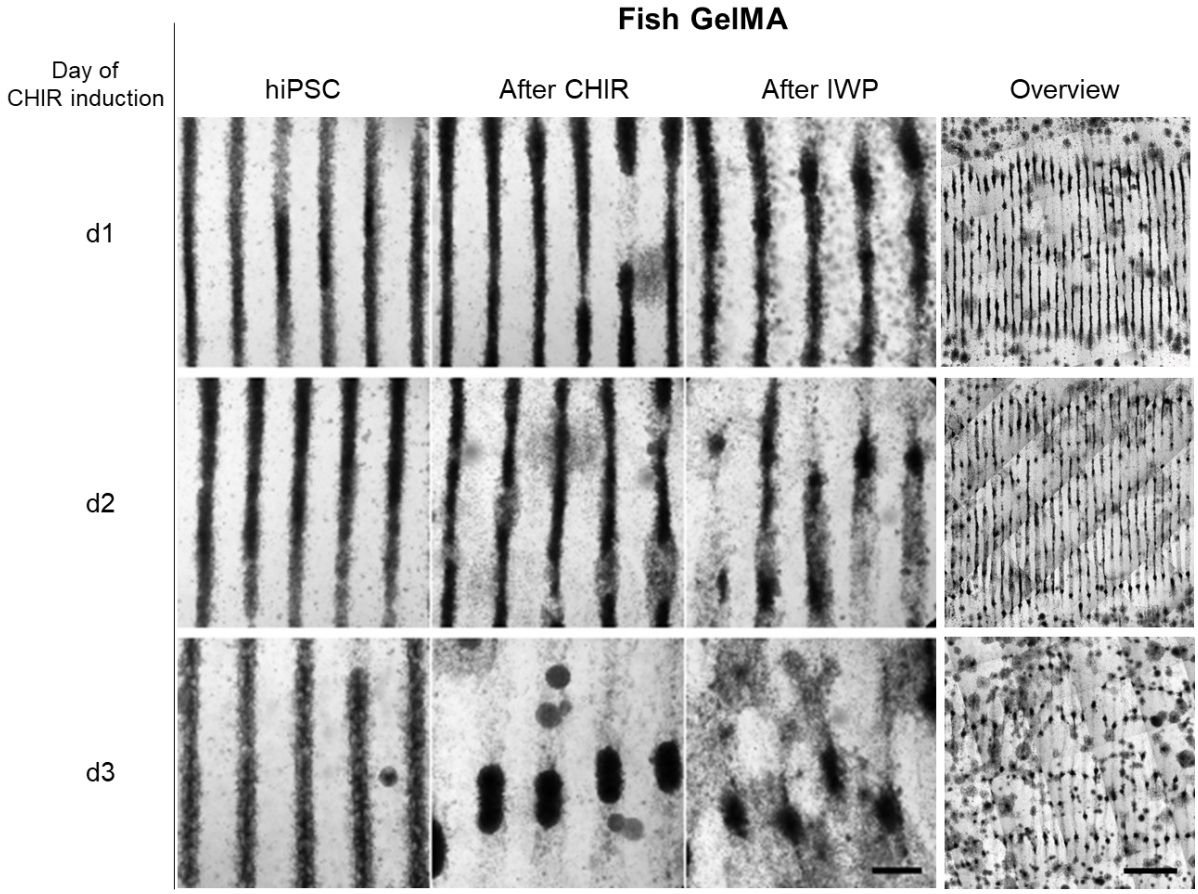


Figure 3-16 ***Effect of differentiation induction timing on pattern preservation in acoustically-patterned fish GelMA hydrogels.*** *Brightfield images of changes in hiPSC cluster morphology over the course of differentiation (hiPSC stage, after CHIR mesoderm stage, after IWP cardiac progenitor stage) when subjected to CHIR induction 1 day (top panels), 2 days (middle panels) or 3 days (bottom panels) after acoustic patterning (2.0 MHz, 4 × 10^6 cells/mL). Overview images show a tiled image encompassing the full length of the patterned region of the hydrogel. Scale bars = 500 µm close up, 2000 µm overview.*

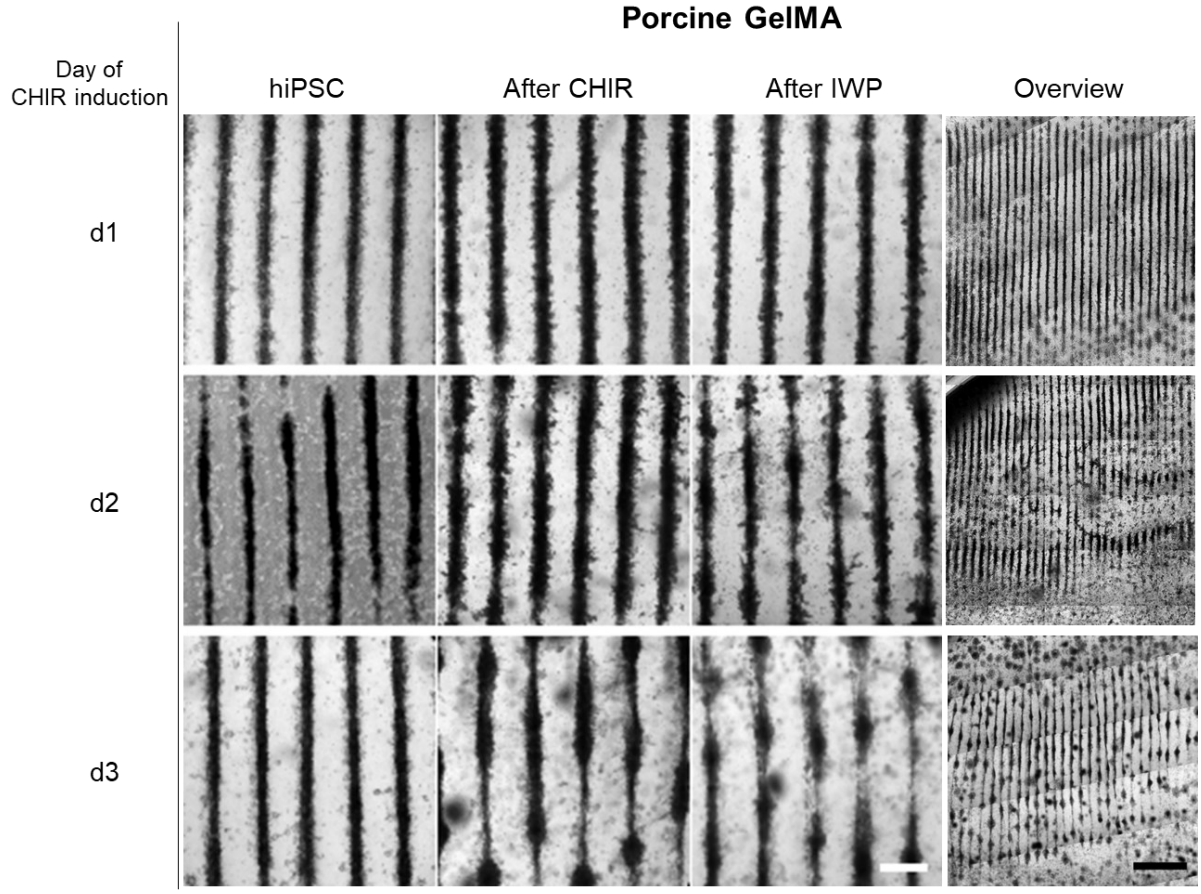


Figure 3-17 ***Effect of differentiation induction timing on pattern preservation in acoustically-patterned porcine GelMA hydrogels.*** *Brightfield images of changes in hiPSC cluster morphology over the course of differentiation (hiPSC stage, after CHIR mesoderm stage, after IWP cardiac progenitor stage) when subjected to CHIR induction 1 day (top panels), 2 days (middle panels) or 3 days (bottom panels) after acoustic patterning (2.0 MHz, 4 × 10^6 cells/mL). Overview images show a tiled image encompassing the full length of the patterned region of the hydrogel. Scale bars = 500 µm close up, 2000 µm overview.*

While the brightfield images of elongated cell clusters provided evidence for high-quality cell patterning and success of pattern preservation, it was not possible to conclude from those results whether the system generated patterned cardiac fibres, with the cell phenotype of differentiated constructs not confirmed at this stage. Although immunofluorescent imaging would identify the cell types present in the constructs (discussed in detail in section 3.4.4.2), the success of differentiation was also partially estimated from the presence of spontaneous contractions, characteristic of hiPSC-CMs, indicating the functionality of the engineered tissue.

Excitation-contraction coupling is the property of cardiac (and skeletal) muscle, whereby tissue contraction is achieved through myofilament activation *via* depolarisation-induced cytoplasmic calcium influx (Bers, 2002). Given their regulatory role in cardiac function, intracellular calcium

dynamics are key measurements of tissue electrophysiology, often used to characterise functional advances in maturation of engineered cardiac tissues (Ronaldson-Bouchard et al., 2018; Nunes et al., 2013; Han et al., 2016). The presence of spontaneously-contracting hiPSC-CMs can therefore be non-invasively recorded experimentally using fluorescence microscopy via calcium imaging. Calcium transients can be visualised by loading the cells with calcium-sensitive dyes (Fluo-4, Fluo-8) or by using hiPSC lines transfected with genetically-encoded calcium indicators (GECIs) (Jaimes et al., 2016a). The latter include GCaMP sensor, generated by the fusion of GFP with calmodulin and M13 peptide, derived from myosin light chain kinase (Jiang et al., 2018). In the presence of calcium, calmodulin undergoes a conformational change, causing deprotonation of GFP, leading to fluorescent signal emission, making calcium-dependent interactions detectable by fluorescence microscopy. In this work, while all cell types derived from hiPSC-GCaMP cell line would contain the GCaMP modification, only electroactive cells such as cardiomyocytes would exhibit calcium handling. In all experiments, hiPSC cell line modified with a fast variant of GCaMP, GCaMP6f, has been used (courtesy of Professor Bruce Conklin)

Timelapse widefield imaging was conducted on day 20 of hydrogel culture to visualise calcium transients in differentiated cardiac tissue engineered constructs, identifying active calcium-handling cells and determining the distribution of functional cardiomyocytes within the gels (Figure 3-18). Isochronal activation maps were then generated using MATLAB code provided by Dr Richard Wang to show the distribution of all active pixels within each imaged video. For each condition, a projection of an acquired calcium video was shown for reference with the corresponding activation map demonstrating calcium handling regions only. Unfortunately, porcine day 2 induction hydrogel was infected during cell culture and could not be included in the following analysis. The calcium signal was detected across the linear cell clusters in both fish and porcine hydrogels initiated with CHIR on day 1, confirming the functionality of those cardiac lines. In fish GelMA gels induced on days 2 or 3, and a porcine GelMA gel induced on day 3 only, the regions with active calcium signal were circular and sparse within the gels, suggesting poor cardiac differentiation efficiency. Overall, taken

together with the brightfield imaging, the earlier differentiation induction with CHIR on day 1 produced well-patterned, uniform, functional cardiac lines in GelMA from both porcine and fish animal sources. With that in mind, all further differentiation protocols were performed with CHIR induction starting on day 1.

Overall, the comparative studies of porcine and fish GelMA showed that porcine GelMA had superior mechanical properties. The amino acid structure of porcine GelMA has a higher imino acid content (proline and hydroxyproline, amino acids that contain a carbon atom that is bound to a carboxyl and imine groups) than that of fish GelMA, improving its structural stability, and these differences in material stiffness were confirmed through rheology measurements described in section 3.4.1.4 (Araghi et al., 2015; Yoon et al., 2016). On the contrary, fish GelMA provided better support to hiPSCs, however, upon CHIR timing optimisation and differentiation there was no difference detected between the ability of porcine and fish GelMA to produce functional patterned cardiomyocytes. As a result, either of those systems could be used for *in situ* differentiation of hiPSCs going forward, and the choice between materials would depend on the ease of handling. The higher mechanical strength of porcine GelMA made the gels easier to manipulate in preparation for further analysis and characterisation, and, therefore, was chosen for all future experiments.

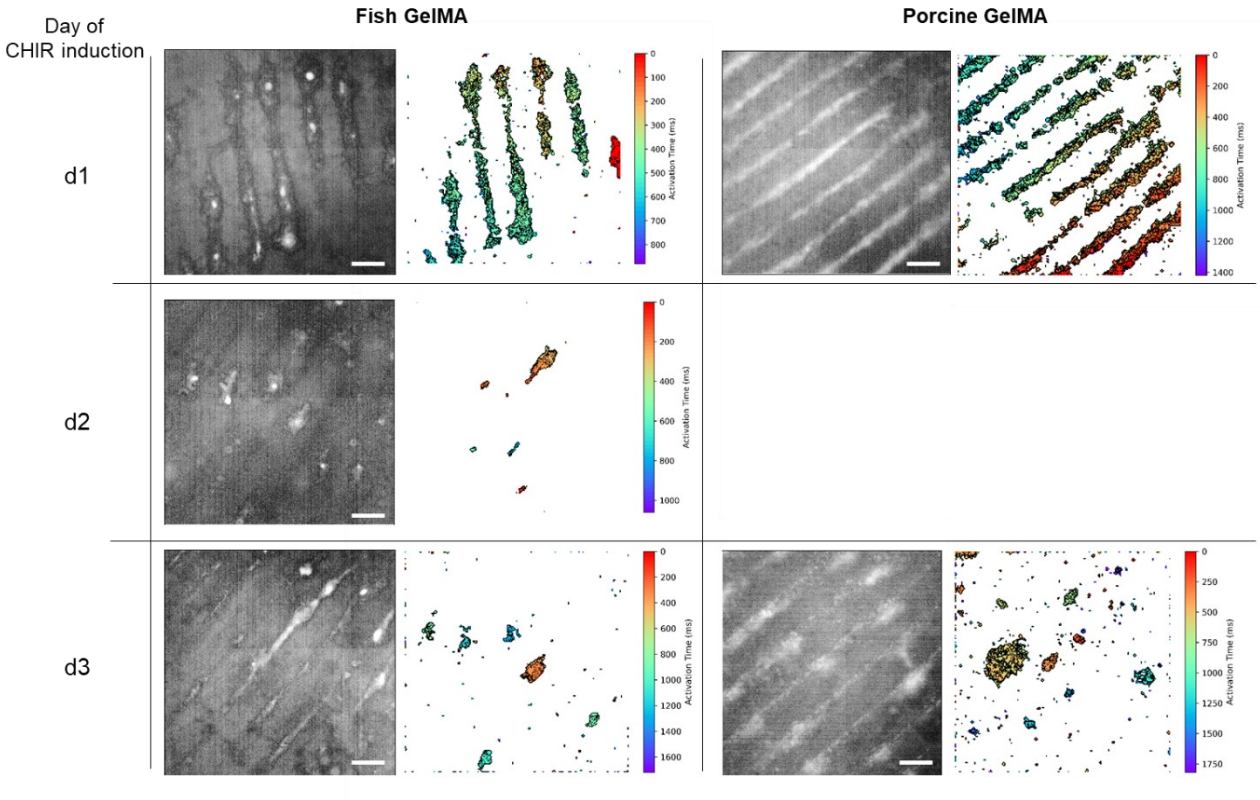


Figure 3-18 ***Calcium activation maps of functional cardiomyocytes in differentiated acoustically-assembled fish and porcine GelMA hydrogels, with differentiation initiated 1 day, 2 days or 3 days after patterning.*** *For each condition: left - average projection of the endogenous fluorescent signal acquired during calcium imaging, right – corresponding MATLAB activation map isolating calcium-handling pixels. Scale bar = 500 µm.*

3.4.2 Effects of ultrasound and light exposure on hiPSC physiology

Uncompromised cell physiology at the start of the culture is essential for the success of tissue engineering protocols. Acoustic patterning has been previously applied to cell cultures, with several studies reporting conflicting results on effects on cell biology. The differences in cellular response could be dependent on the acoustic parameters (voltage, frequencies, exposure duration, temperature) as well as on the cell type, with different cell membranes reacting differently to the generated acoustic forces. For example, while HeLa cells showed poor viability after exposure to 8 $V_{p\text{-}p}$ standing wave for 5 and 10 minutes, human dermal fibroblast (HDF) cell lines were found to be unaffected by the same conditions (Levario-Diaz et al., 2020). The exposure of an immortalized mouse myoblast cell line (C2C12) to acoustic waves for 15 minutes showed no significant effect on cell metabolism, proliferation or differentiation (Armstrong et al., 2018). Likewise, no difference was

observed when the same patterning conditions were applied to isolated chondrocytes (Armstrong et al., 2022).

Stem cell-derived neuronal progenitors and cardiomyocytes have been previously used in acoustic experiments and demonstrated unaffected metabolic activity after exposure to acoustic levitation and SSAW patterning respectively (Serpooshan et al., 2017; Bouyer et al., 2016). However, no studies to date applied acoustic standing waves to hiPSCs directly, which are extremely plastic cells and can often be sensitive to external stimuli (Liu, Lerou & Lahav, 2014), leading to cell death or spontaneous differentiation. Here, it was investigated how exposure to BAW in the optimised setup affected cell viability, pluripotency, metabolism, and differentiation.

3.4.2.1 Viability assessment in acoustically-patterned cardiac constructs

To assess the effect of ultrasound on hiPSC viability, the cells were patterned in 4% (w/v) porcine GelMA using a 2.00 MHz standing acoustic wave for 15 minutes and crosslinked with a 405 nm visible light source. The live cells were stained with calcein, and the dead cells were identified by their ethidium homodimer inclusion. Immediately after patterning, a continuous linear array of hiPSCs was clearly observed within the hydrogel (Figure 3-19A,B). The cells were viable and clustered in uniform regular linear arrays. In the unpatterned control, there were no linear structures observed (Figure 3-19C). After 24 hours in culture, the viability staining was repeated. The dead cells remained rounded, while the viable cells spread and joined together to form continuous linear clusters (Figure 3-19D,E). The unpatterned control demonstrated cluster formation that lacked directionality (Figure 3-19F). Overall, these results demonstrated that acoustically-patterned hiPSCs were able to successfully form viable uniform linear structures observed immediately after exposure and after 24 hours in culture.

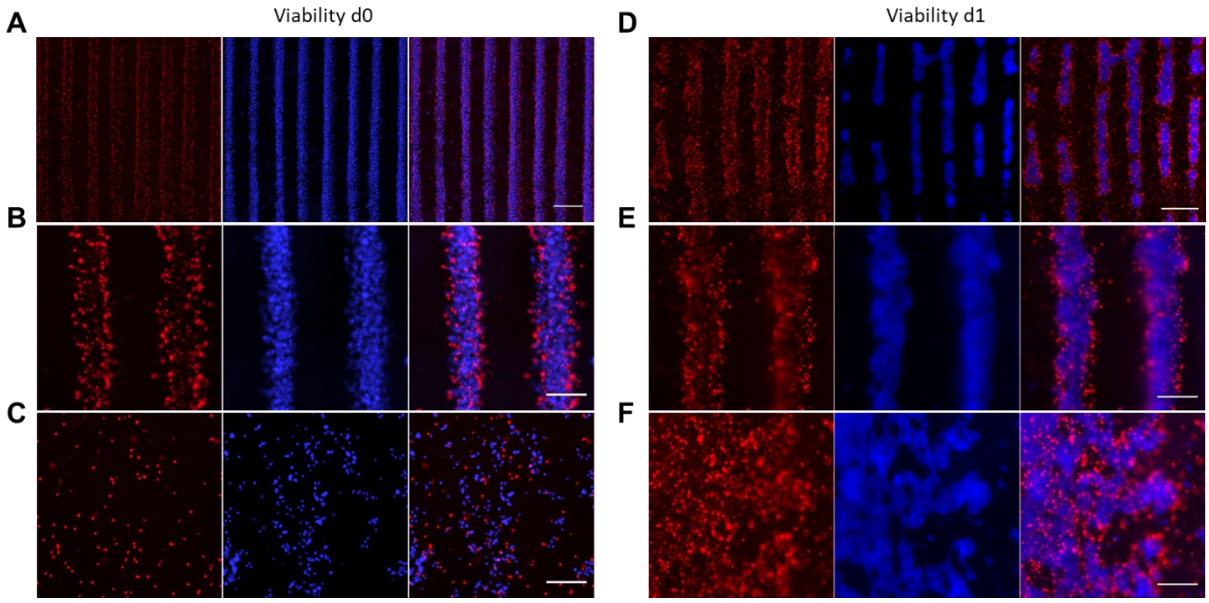


Figure 3-19 ***Widefield fluorescent microscopy of a LIVE/DEAD® viability assay of acoustically-patterned and unpatterned porcine GelMA hydrogel constructs on day 0 (A-C) and day 1 (D-F) after exposure to ultrasound.*** *All panels show the distribution of non-viable (red, left) and viable (green, centre) cells across the hydrogel. (A). Overview of the patterned region at 2.5x magnification on day 0. (B). 10x image of the patterned region on day 0. (C). 10x image of the unpatterned region on day 0. (D). Overview of the patterned region at 2.5x magnification on day 1. (E). 10x image of the patterned region on day 1. (F). 10x image of the patterned region on day 1. Scale bars = 500 µm overview, 200 µm close-up.*

3.4.2.2 Pluripotency assessment in acoustically-patterned cardiac constructs

Spontaneous differentiation of hiPSCs, characterised in part by the downregulation of pluripotency markers, can severely impact the success of their differentiation. To confirm the stem cell maintenance in the patterned hiPSCs, the cells were cultured for 24 hours after exposure to ultrasound, fixed in 4% (v/v) PFA and immunostained for three pluripotency markers: OCT3/4, SOX2 and SSEA4. OCT3/4 and SOX2 were used since they are nuclear transcription factors used for hiPSC reprogramming (Radzisheuskaya et al., 2013; Wang et al., 2012), while SSEA4 is a surface membrane glycolipid antigen, commonly used for stem cell characterisation (Sivasubramaniyan et al., 2015; Fong et al., 2009). On low-magnification (10X) scale, a uniform and continuous distribution of SOX2-positive nuclei was apparent throughout the length of the construct (Figure 3-20A). On high-magnification scale (40X), all individual nuclei were visibly expressing both SOX2 and OCT3/4 (Figure 3-20B,C). SSEA4 was also stably expressed through the patterned line (Figure 3-20D). Taken

together, these results showed that despite the patterning and crosslinking processes, the highly uniform linear clusters of hiPSCs remained pluripotent, showing promise for subsequent differentiation of patterned constructs.

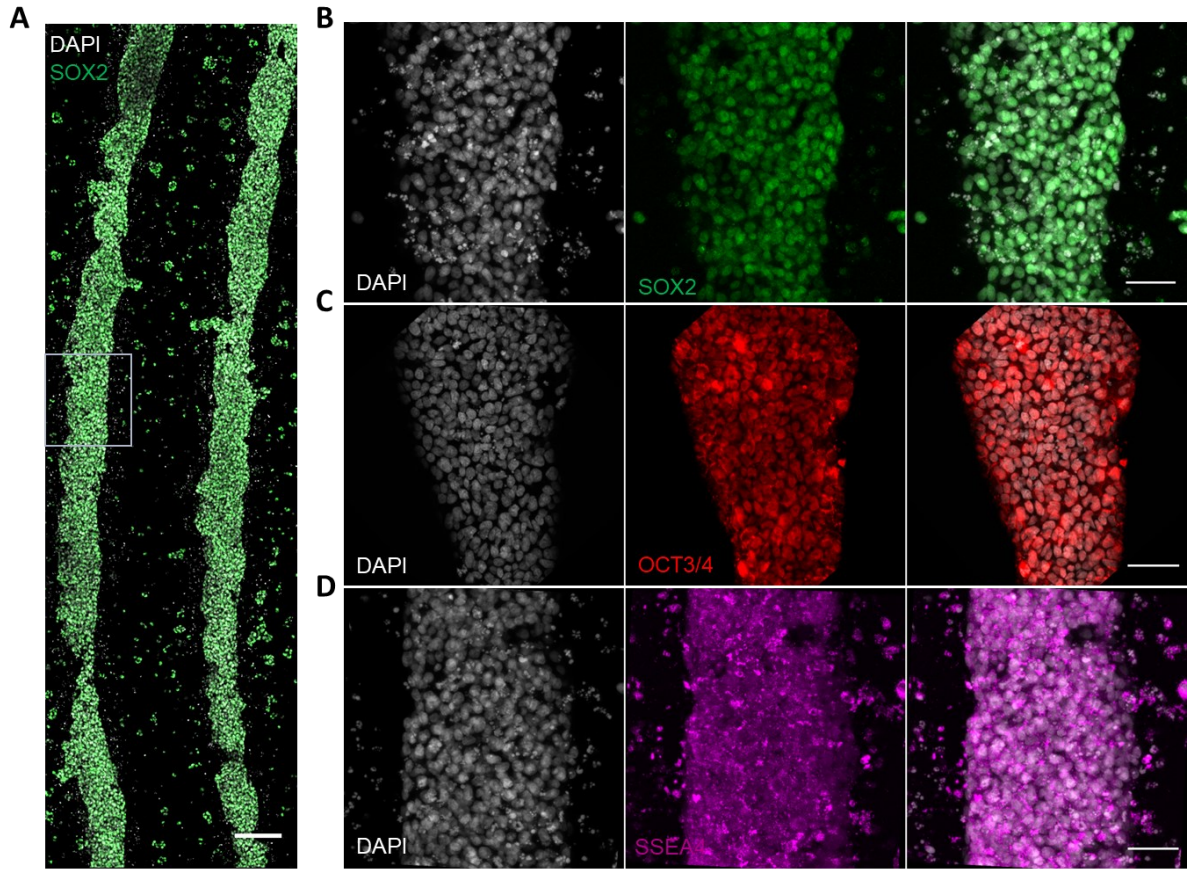


Figure 3-20 ***Pluripotency marker fluorescence immunostaining of acoustically-patterned hiPSC clusters in porcine GelMA hydrogels 1 day after ultrasound exposure.*** *(A). Low magnification (10x) tiled confocal image of SOX2 (green) expression in linear hiPSC clusters. White box indicates the relative size of high magnification images (40x). Scale bar = 200 µm. (B). High magnification confocal image of SOX2 expression. (C). High magnification confocal image of OCT3/4 expression (D). High magnification confocal image of SSEA4 expression. (B-D) images shown as DAPI counterstain (left), marker immunostaining (centre) and overlay (right). (B) corresponds to the higher magnification of the area outlined in a dashed square in (A). Scale bars = 50 µm.*

3.4.2.3 Metabolic activity and proliferation assessment upon ultrasound and light exposure

While the LIVE/DEAD® staining demonstrated that the hiPSCs formed viable linear structures upon exposure to ultrasound, this only allowed a qualitative comparison of the membrane integrity of the cells rather than quantifiable viable functionality. AlamarBlue™ assay is a common method used to

assess the metabolic activity of the cells. The alamarBlue™ Reagent contains resazurin, a non-fluorescent dye that is able to permeate through the cell membrane and react with reductive by-products of metabolism (NADPH, FADH, FMNH, NADH and the cytochromes), generating a brightly fluorescent resorufin, that can be detected and quantified (Rampersad, 2012). AlamarBlue™ assay was therefore performed to investigate the effects of ultrasound and light exposure on the hiPSC metabolic activity.

hiPSCs were resuspended in media and added to an acoustic patterning device that either remained turned off (Unexposed) or was supplied with 20 V_{p-p} of 2.00 MHz ultrasound standing wave for 15 minutes (Ultrasound), after which half of the cells from each treatment were collected, counted, and seeded. The remaining cells were then exposed to 1 minute of 405 nm light, and collected, counted and seeded as "Light" only and "Ultrasound and Light" conditions. After 24 hours in culture, the media was changed once to remove the ROCK inhibitor and the cells were allowed to grow for another 24 hours until the alamarBlue™ assay was carried out (Figure 3-21). There was no difference observed in metabolic activity of cells after exposure to ultrasound alone. Illuminating cells with 405 nm visible light also was not statistically different to the control, despite a clear visible downward trend in all samples. It is possible the difference could be significant if the N number was increased to reduce the standard deviation. Exposing the cells to both ultrasound and light showed a significant decline to 83% of metabolic activity ($p = 0.035$).

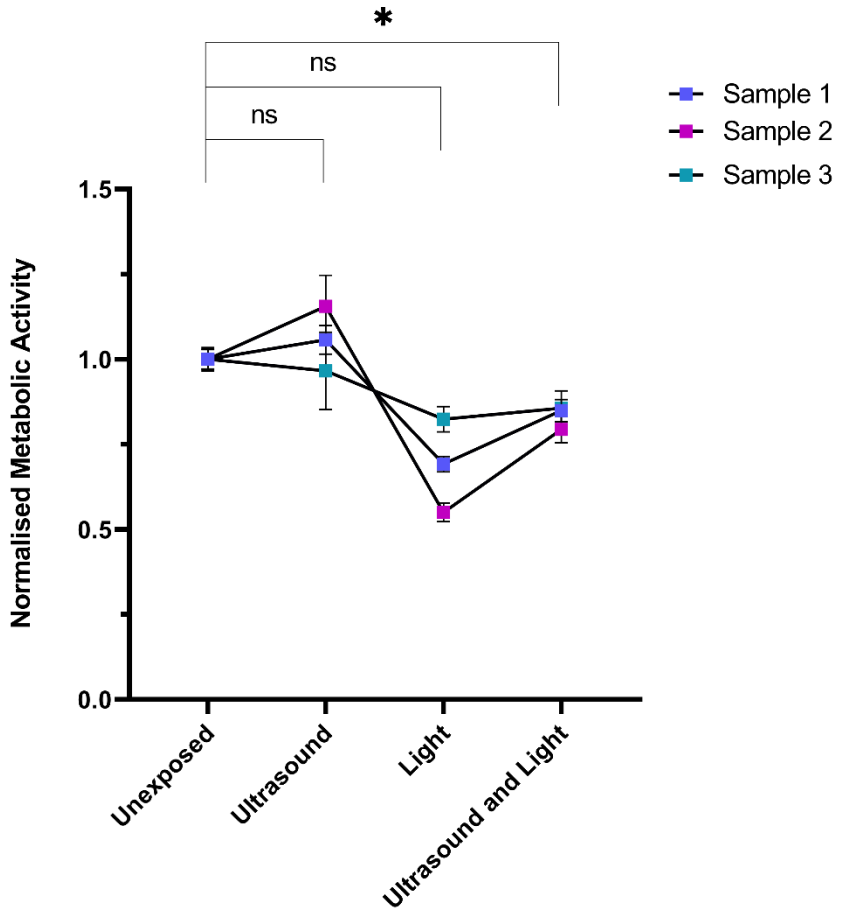


Figure 3-21 ***AlamarBlue™ assay 48 hours after hiPSC ultrasound (2.0 MHz) and blue light (405 nm, 1 minute) exposure on hiPSC metabolic activity.*** *Each point represents a mean metabolic activity with error bars showing standard deviation, normalised to average unexposed control. Connecting lines represent paired biological samples. One-way repeated measures ANOVA with Tukey correction for multiple comparisons and Geisser-Greenhouse sphericity correction. * - $p < 0.05$, ns – $p > 0.05$. n = 3, N = 3, where n is the number of replicate wells seeded for the measurements per each condition, and N is the number of independent cell exposure experiments.*

Although cell proliferation is also often reported using alamarBlue™ assay, the relationship between the metabolic activity and cell number is non-linear, making it an inaccurate assay for cell growth characterisation (Quent et al., 2010; Rampersad, 2012). To account for cell growth, DNA content was quantified using PicoGreen reagent - a fluorescent dye capable of binding double stranded DNA. The PicoGreen Assay was thus performed on day 1 and day 3 after exposure of the cells to the patterning conditions. Similarly to the alamarBlue™ experiment, the cells were subjected to conditions equivalent to those used in patterning experiments (20 $V_{p\text{-}p}$, 2.00 MHz frequency, 15 minutes

ultrasound exposure, and/or 1 minute 405 nm light exposure), and collected, counted and seeded as “Unexposed”, “Ultrasound” only, “Light” only and “Ultrasound and Light” conditions. After 24 hours in culture, DNA was extracted from one plate (day 1) via three consecutive freeze-thaw cycles in water, while the media of the other plate was changed daily, and DNA was collected on day 3. The samples for both timepoints were then quantified using PicoGreen assay (Figure 3-22A,B). There was no difference between the concentration of DNA of Unexposed and Ultrasound conditions, with average 29.11 ng/mL and 25.51 ng/mL respectively on day 1, and 293.9 ng/mL and 276.5 ng/mL on day 3. Interestingly, the DNA concentration of Light Only condition was 14.72 ng/mL on day 1, which was significantly lower than the Unexposed control on day 1 ($p = 0.0104$). At day 3, the DNA content of Light Only was at 99.27 ng/mL, significantly lower than that of all other conditions ($p < 0.0001$ for Unexposed and Ultrasound, $p = 0.0027$ for Light and Ultrasound). Interestingly, the DNA content of Ultrasound and Light was at 217.4 ng/mL, significantly higher in respect to Light Only, while also not significantly different from Unexposed or Ultrasound, suggesting that Ultrasound exposure might rescue the light-induced DNA degradation. However, when looking at proliferation as the fold change in DNA concentration, there were no significant differences between the four treatment groups (Figure 3-22C). These results demonstrate that exposure to ultrasound and/or light does not affect hiPSC proliferation, despite the detrimental effect of light exposure on the overall DNA content.

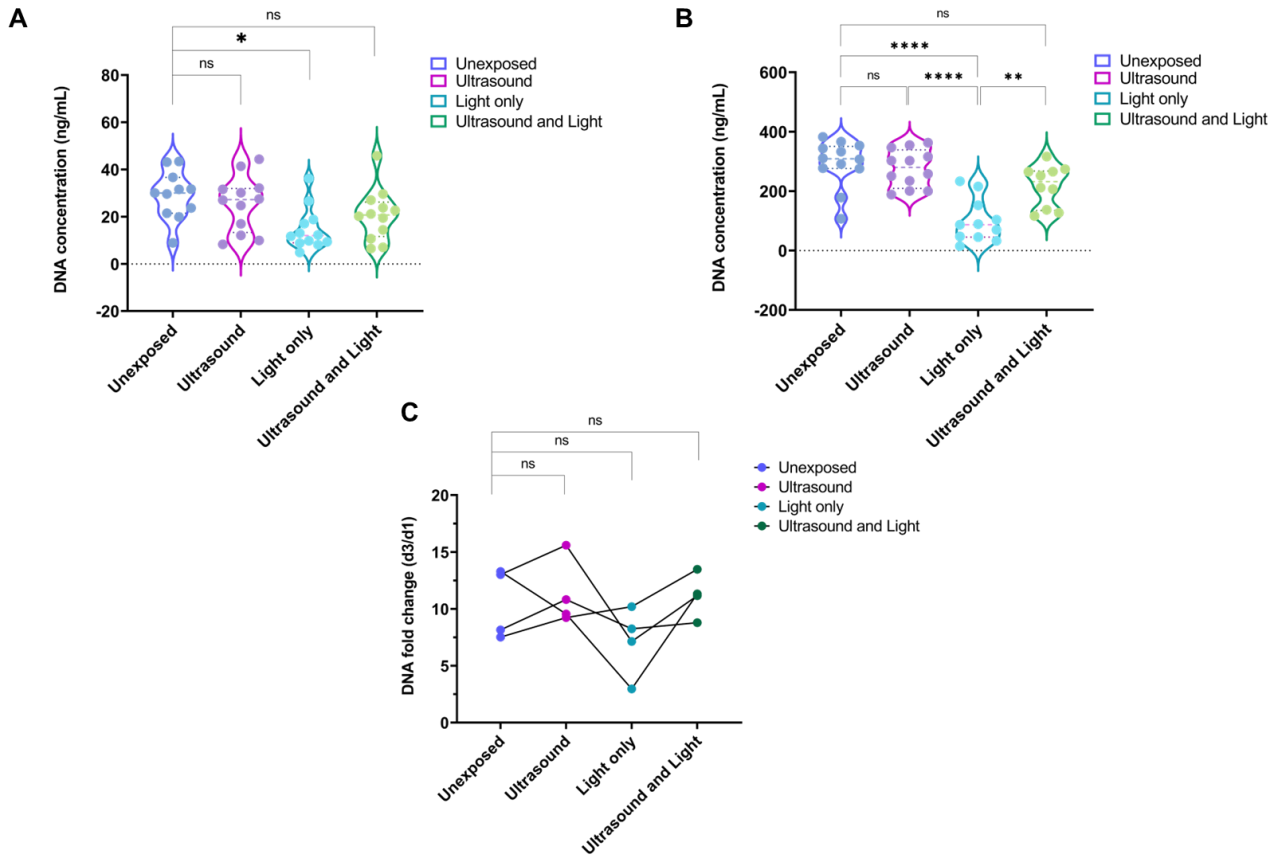


Figure 3-22 ***PicoGreen quantification of DNA content 1 day (A), 3 days (B) and fold change (C) indicating proliferation rate after hiPSC ultrasound (2.0 MHz) and blue light (405 nm, 1 minute) exposure.*** *(A). Violin plot of DNA concentration distribution of all replicates within each group 1 day after exposure, showing the median and interquartile range. (B). Violin plot of DNA concentration distribution of all replicates within each group 3 days after exposure, showing the median and interquartile range. (C). Average fold change in DNA content from day 1 to day 3. Connecting lines represent paired biological samples. (A-B) One-way ANOVA with Tukey correction for multiple comparisons and Geisser-Greenhouse sphericity correction, (C) One-way repeated measures ANOVA with Tukey correction for multiple comparisons and Geisser-Greenhouse sphericity correction. * - p < 0.05, ** - p < 0.01, *** - p < 0.001, **** - p < 0.0001, ns – p > 0.05. N = 4, n = 3, where n is the number of replicate wells seeded for the measurements per each condition, and N is the number of independent cell exposure experiments..*

Metabolic activity and proliferation are essential measures of cell behaviour, required for the validation of any tissue engineering protocols. While the application of ultrasound did not impact cell physiology, expectedly, some detrimental effects were observed in the exposure conditions that contained a light source. In particular, the metabolic activity of the cells significantly declined to 83% upon application of both ultrasound and light. LEDA light source has a peak emission at 405 nm, which is considered visible; however, the width of the peak can contain a small component in the UV region known to be cytotoxic, potentially explaining the decline in metabolic activity. Reduction in DNA content was observed at both timepoints for Light Only and Ultrasound and Light application,

which could also follow the light-induced cell death, since the non-viable cells would detach and be washed away, with their DNA not collected for analysis. However, since the actual rate of proliferation for those conditions was not statistically different, it is concluded that the process of proliferation remained unaffected.

Additionally, one of the limitations of the exposure experiments themselves was that they were carried out in cell suspension in media lacking the LAP photoinitiator, which absorbs the light. Therefore, it is possible that the cytotoxic effects of light observed are overestimated compared to the full patterning setup.

Interestingly, while the Light Only condition showed reduction in metabolic activity and proliferation, a slight recovery was observed upon the application of ultrasound in both assays. It is possible to speculate that the aggregation of cells with ultrasound could protect some cells from immediate light exposure, thus reducing its phototoxicity, however, there is no direct evidence supporting this theory. Furthermore, the differences between Light only and Ultrasound and Light conditions were ultimately not statistically significant for either metabolic activity or proliferation. Introducing further biological repeats would reveal whether ultrasound truly can shield the cells from detrimental effects of light exposure.

Importantly, these experiments demonstrated that the ultrasound exposure does not affect the viability, metabolic activity, proliferation and pluripotency of the cells, making this platform and setup compatible with stem cell applications. The only significant effect observed was that of light exposure, however, even then the metabolic activity remained at 83%, indicating a high number of viable and active hiPSCs.

3.4.3 Differentiation of patterned cardiac constructs *in situ*

Interestingly, while the patterned constructs with differentiation induction on day 1 definitively contained linear arrays of cardiomyocytes as demonstrated by activation mapping in Figure 3-18, the

connectivity of these cells was not contained within individual lines. The contraction and calcium handling were synchronised across the whole engineered tissue, as evidenced by the activation maps, where a clear gradient from bottom right to top left shows the directionality of the calcium signal orthogonal to the patterning orientation (Figure 3-18). This suggested that some electrical coupling occurred between the cell lines, making the whole construct functionally interconnected.

An alternative fabrication approach was developed in order to isolate the cardiac fibres individually. Prior to acoustic patterning, a 500 µL solution of GelMA and LAP was added to the patterning cavity and cured with 405 nm LED array for 1 minute, creating a supporting layer of GelMA. The rest of the patterning process remained the same, with the acoustically-patterned GelMA layer crosslinked on top of the supporting GelMA layer, yielding a double layer GelMA construct (Figure 3-23B). The supporting GelMA of a double layer gel was visible in cross-section as a clear hydrogel, enclosing the cell layer containing growing clusters (Figure 3-23D). In parallel, the original single layer patterning experiment was performed, where the cells were patterned on top of an agarose layer and subsequently exposed directly to the media after demoulding (Figure 3-23A,C). Both gel types were cultured according to the optimised differentiation protocol.

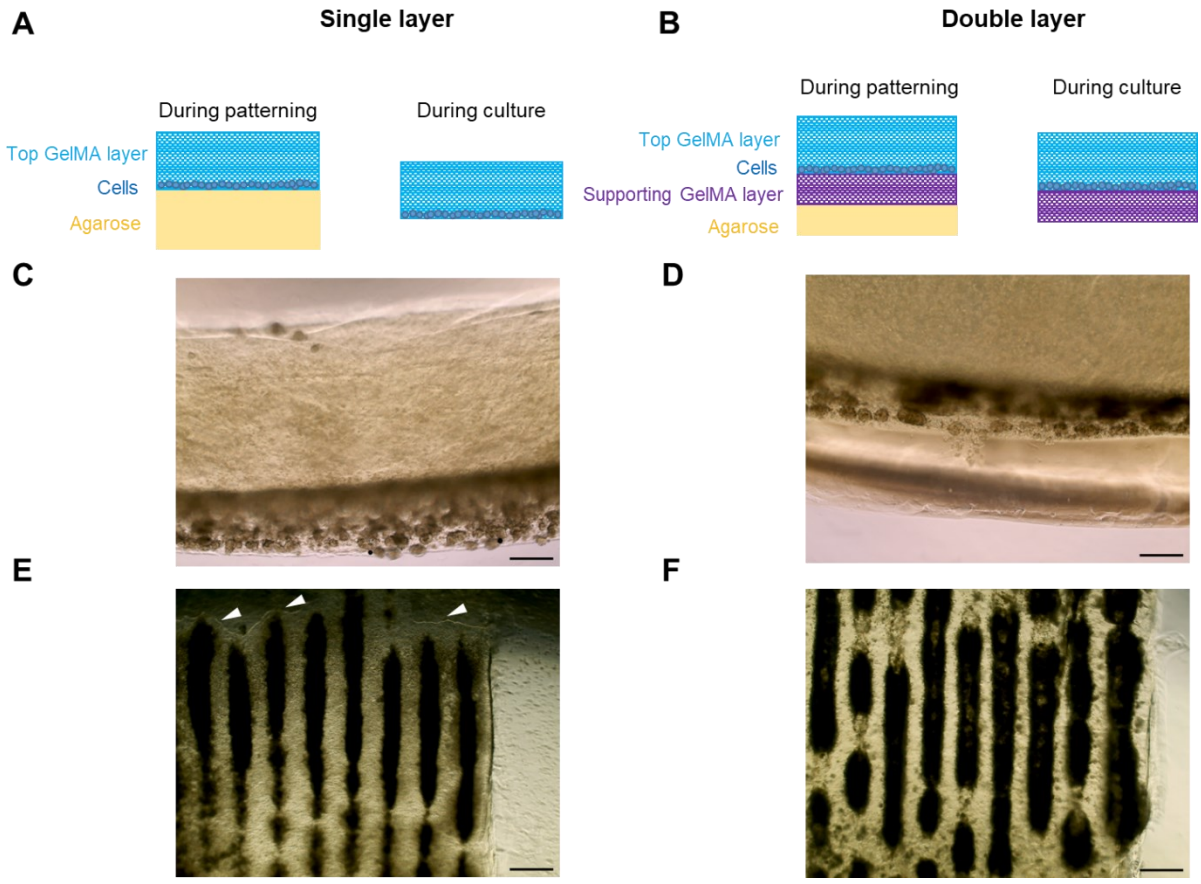


Figure 3-23 ***Fabrication of supporting GelMA layer for prevention of interconnectivity between adjacent patterned cellular arrays.*** *(A). Schematic representation of the original single layer fabrication protocol, with hiPSC cells encapsulated in the top GelMA layer were patterned on top of 2% (w/v) agarose. After demoulding from agarose for culture (right), the cells were presented at the bottom surface of the top GelMA layer. (B). Schematic representation of the updated double layer fabrication protocol, with hiPSC cells encapsulated in the top GelMA layer were patterned on top of a supporting layer of GelMA, which in turn was cured prior to patterning on top of 2% (w/v) agarose. After demoulding from agarose for culture (right), the cells were trapped between the top and supporting layers of GelMA. (C). Brightfield image of a cross-section of a single layer gel after 3 days in culture. (D). Brightfield image of a cross-section of a double layer gel after 3 days in culture. (E). hiPSC acoustically-patterned arrays in a single layer GelMA gel, imaged on day 4 after patterning following the completion of CHIR induction. White arrows indicate the presence of cell monolayer on the surface of the gel. (F). hiPSC acoustically-patterned arrays in a double layer GelMA gel, imaged on day 4 after patterning following the completion of CHIR induction. Scale bars = 500 µm.*

Some differences between the two methods were observed after CHIR induction. A thin film was visible at the edges of the lines patterned in single layer gels, indicative of cells breaking out of the gel and forming a monolayer on the surface (Figure 3-23E). This feature was not visible in double layer gels (Figure 3-23F). Furthermore, the hydrogel in between the adjacent lines of single layer gel remained optically clear, while the corresponding regions in the single layer gel were opaque, suggesting some cell infiltration of the inter-line space. Free-radical polymerisation of GelMA during

photocrosslinking is known to be inhibited by the presence of oxygen, thus the polymer chains on the outermost surface of the gel remain unreacted, and therefore available (Lim et al., 2016; Simič et al., 2021). In double layer gels, this property allowed to successfully crosslink the supporting GelMA layer to the patterned layer, thus encapsulating the cells and restricting their growth on the surface, ultimately generating independent live arrays of cells within the gel.

To confirm this observation, LIVE/DEAD® staining was performed on single layer and double layer gels through the differentiation process, with images taken at day 1 (hiPSC stage), day 4 (CHIR stage, mesoderm), day 6 (IWP stage, cardiac progenitor) and day 23 (final cardiac construct) (Figure 3-24). At hiPSC stage, the two gel types behaved the same, showing distinctly patterned clusters of live cells surrounded by the dead cells on the periphery (Figure 3-24A). At CHIR stage, the patterning remained visible in both gel types, however it was more apparent in the double layer gels, where the clusters of live cells were still restricted to the lines (Figure 3-24B). In single layer gels some live cells were visible in the inter-line space, and the live cells remained single-cell and did not form clusters. By the IWP stage, the differences between two methodologies were the most pronounced (Figure 3-24C). A clear monolayer of cells was visible in the single layer hydrogel, similar to the film seen on brightfield images, with indistinguishable patterning. On the contrary, the double layer gels still showed clear arrays of live cells, with unoccupied inter-line space. On day 23, the live cells of the double layer gels remained distinctly localised to the patterned region, while the single layer gel lines merged into one large construct (Figure 3-24D).

The cells within single layer gels were in GelMA suspension during the patterning process, and sedimented at the bottom of the hydrogel by gravity. The subsequent crosslinking of the gel generated bonds between the GelMA chains, and those bonds were responsible for maintaining the patterning and preventing the cells from interconnecting. However, since the cells were localised near the surface of the gel, their proliferation during differentiation caused them to eventually break out onto the surface, where the cells grew and differentiated as a monolayer, causing the lines to

interconnect. Therefore, increasing the distance between the cells and the hydrogel surface could prevent their breakout.

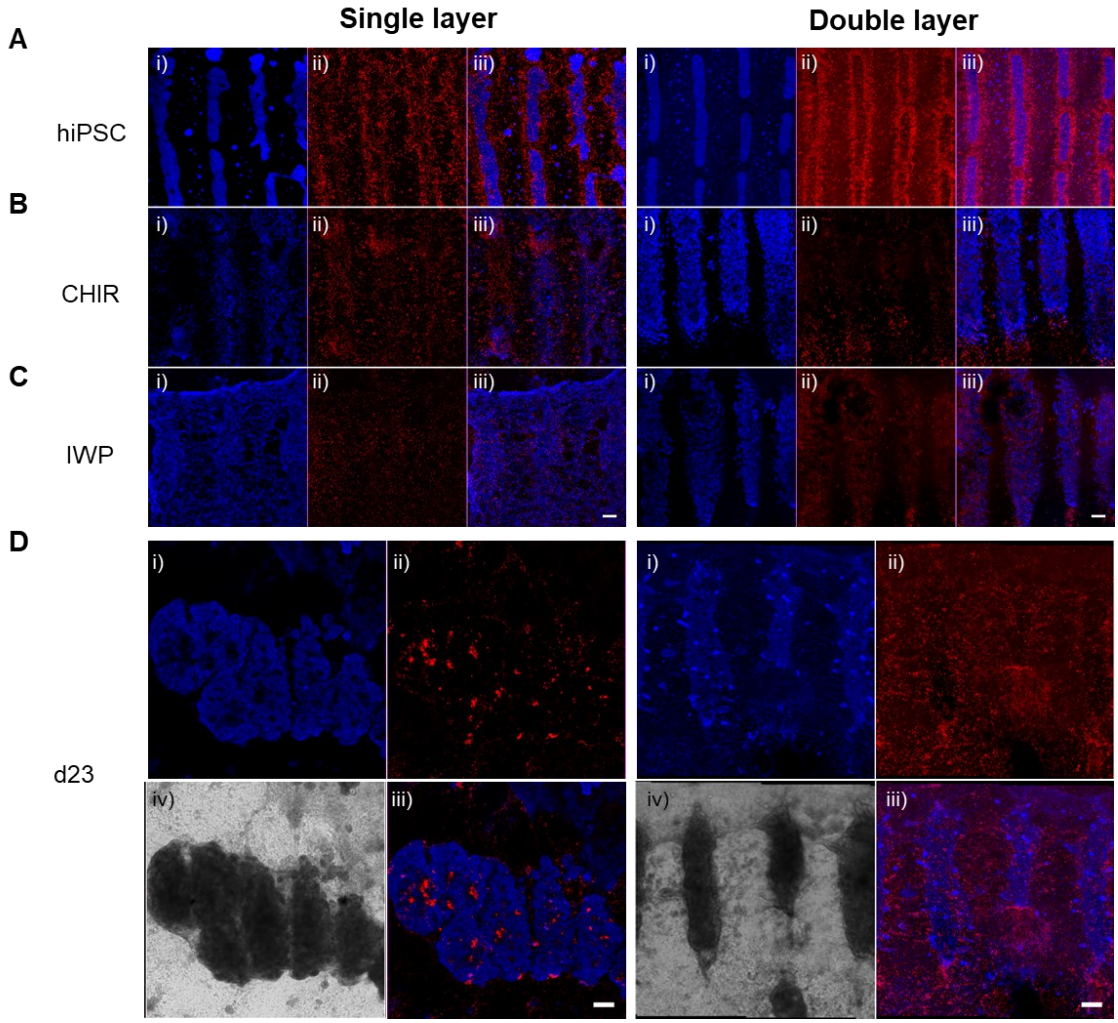


Figure 3-24 ***Changes in the morphology of acoustically-patterned hiPSCs during differentiation in single layer and double layer GelMA hydrogels.*** *LIVE/DEAD® viability staining of single (left) and double (right) GelMA hydrogels at (A) hiPSC stage, 1 day after patterning, (B) CHIR stage, 4 days after patterning, (C) IWP stage, 6 days after patterning, and (D) upon differentiation completion, 23 days after patterning. For each stage, distribution of (i) viable cells, blue; (ii) non-viable cells, red and iii) overlay of viable and non-viable cells is shown. In (D), (iv) shows a brightfield image of the imaged construct. Scale bars = 200 µm.*

To investigate the distribution of functional cardiomyocytes in those hydrogels, the calcium signal within the single layer and double layer gels was recorded and analysed using MATLAB code to generate activation maps (Figure 3-25). The colour gradient in the activation map showed the order in which the pixels become active: red corresponded to the earliest activation site, followed by

yellow and green, and finally with blue and purple indicating the last activated region. In single layer gels, the adjacent lines followed exactly the order of activation map gradient from red to purple, suggesting the signal propagation orthogonal to the direction of patterning across the whole gel (Figure 3-25A). Such activity is consistent with the LIVE/DEAD® imaging, suggesting interconnection and coordinated activity of the electrically active cells within the bulk hydrogel.

In the double layer gels, each line corresponded to a distinct colour, suggesting activation through the length of each line. However, the order of activation of adjacent lines did not follow the order of the colourmap gradient (Figure 3-25B). This demonstrated that the lines were activated independently of each other, suggesting no or little interconnectivity of electroactive cells within adjacent lines of the hydrogel. The clear differences in activation patterns between single layer and double layer gels are best visualised through videos, which can be viewed in the supporting videos provided along with this thesis.

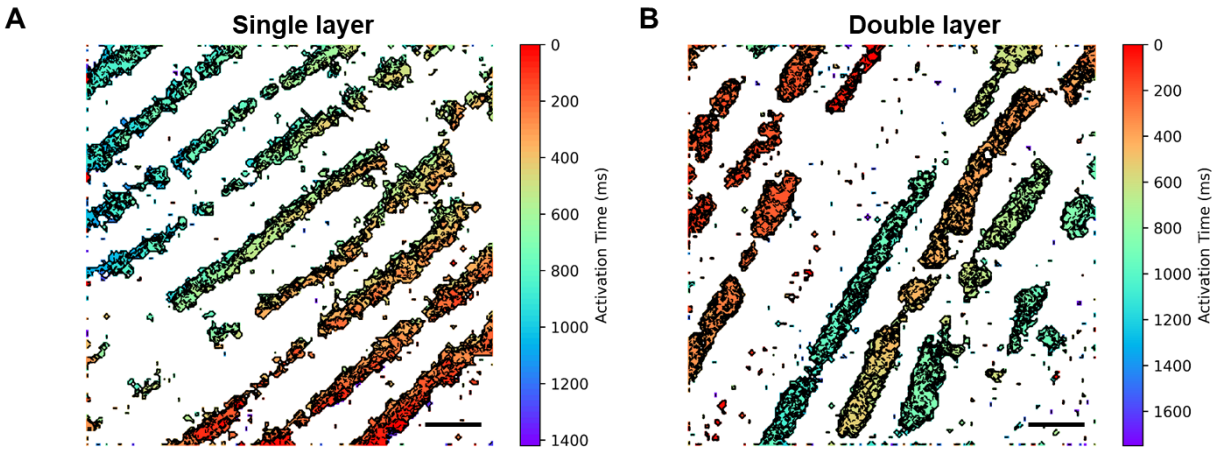


Figure 3-25 ***Distribution and activation sequence of functional cardiomyocytes within acoustically-patterned single layer (A) and double layer (B) GelMA hydrogels.*** *Maps showing the order of pixel activation from the early frames (red-orange) to intermediate activation time (yellow-green) to late frames (blue-purple). Activation map of single layer (A) is reproduced from Figure 3-18 (Porcine GelMA d1 of CHIR induction). Scale bars = 500 µm.*

To confirm these differences further, single layer and double layer hydrogels were fixed, immunostained and imaged in triplicate using confocal microscopy. The differences in staining protocols between single layer and double layer gels will be discussed in section 3.4.4.2. Cardiac troponin T (cTnT) staining was used to identify the distribution of cardiomyocytes within the gels. All

stained gels contained cTnT-positive areas (Figure 3-26). In single layer gels, the distribution of cTnT varied. Replicate 1 contained distinctly localised cardiac fibres, without any interconnected regions (Figure 3-26A). Replicate 2 retained the patterning, however, the cardiac fibres were interconnected at the edges. Replicate 3 contained some patterned fibres within the gel, interspersed with regions of large monolayers interconnecting adjacent lines. All double layer gels contained distinctly defined, continuous cTnT-positive lines, although the signal intensity and the patterning quality were lower in replicate 3 (Figure 3-26B). These results were consistent with LIVE/DEAD® staining (Figure 3-24) and activation mapping (Figure 3-25), demonstrating the presence of adjacent line interconnectivity of single layer gels and independent cardiac fibre production in double layer gels. Overall, while both single layer and double layer gels contained patterned cardiomyocyte fibres, the consistency of pattern preservation was higher in the double layer gels.

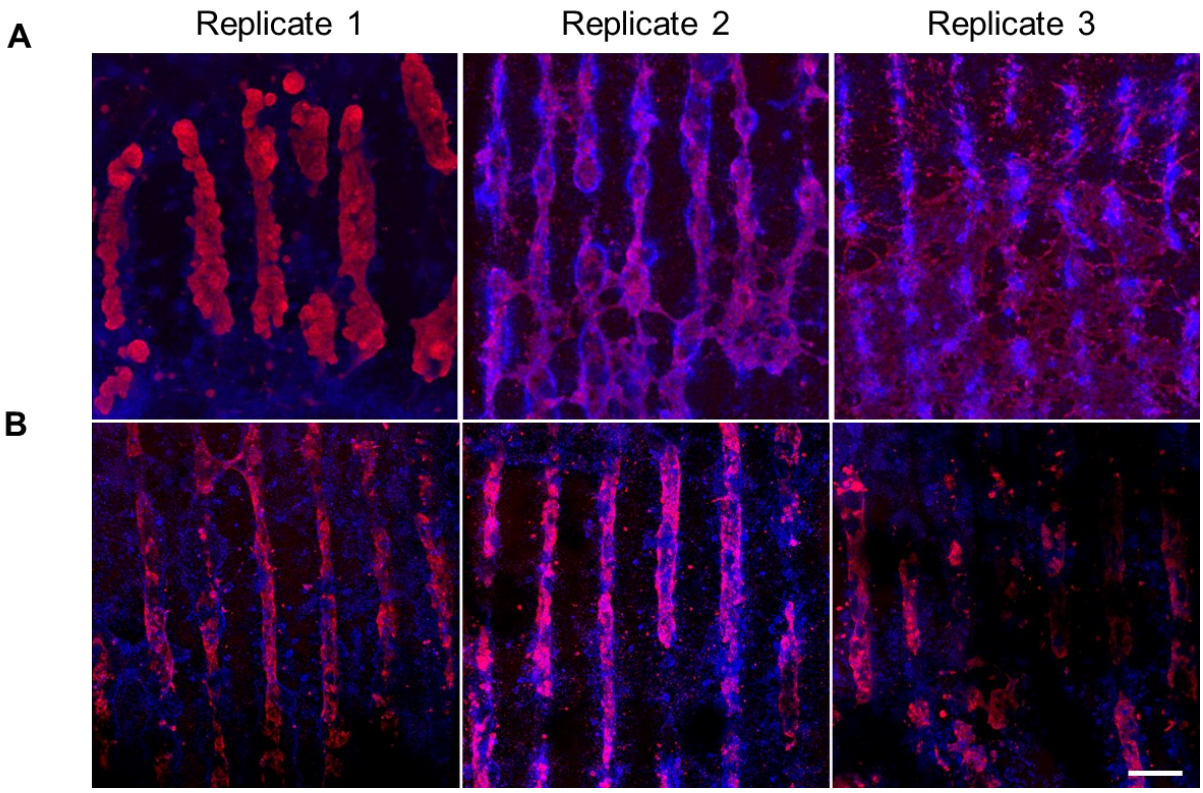


Figure 3-26 ***Immunofluorescent staining of cTnT showing the distribution of cardiomyocytes in single layer (A) and double layer (B) acoustically-patterned GelMA hydrogels.*** *All samples were counterstained with DAPI (blue). Scale bar = 500 µm.*

Physiologically, the heart muscle possesses structural directionality, with cardiomyocytes arranged in parallel bundles (Saffitz et al., 1994). The use of acoustic patterning in this project aimed to

replicate such architecture, generating uniformly distributed, functional cardiac fibres, which was successfully achieved in both single layer and double layer gels. The main difference between the two approaches was the interconnectivity of the adjacent fibres, amounting to the cell breakout onto the surface of the gel, while the fibres within the double layer gels were independent of each other.

Some interconnectivity is also evident in the native cardiac tissue, with the lateral branching of the parallel bundles forming a cardiomyocyte network (Kanzaki et al., 2010). Such branching decreases the efficiency of the one-dimensional signal propagation on the cardiomyocyte level; however, it has been previously suggested that it aids synchronisation and improves the performance of cardiac muscle on the whole-organ level (Wilson, Sands & Ennis, 2021). Therefore, based on physiology, interconnected gels would be a preferred model of engineered cardiac tissue.

However, while interconnectivity increases tissue complexity, when considering the end application of drug screening a more reductionist approach might be preferred. The aim of the project is to introduce directionality to cardiac cultures, thereby allowing the investigation of drug-induced perturbations to signal propagation within the tissue. The interconnectivity of single layer gels is stochastic, with some gels showing larger extent of branching than others, while a few gels even developed as a full cardiomyocyte monolayer, losing the patterning entirely. Such heterogeneity would not be appropriate for drug screening studies, which rely on reproducible and uniform models.

In adult cardiac muscle, the cardiomyocytes possess strong structural and electrical anisotropy. Electrical anisotropy is defined by the faster (≈3 and 10 times for ventricular and atrial tissue respectively) conduction velocity of a primary activation wavefront longitudinally to the myofiber alignment than the transverse signal propagation occurring through adjacent cardiomyocyte branching (Saffitz et al., 1994; Glukhov et al., 2012; Napiwocki et al., 2021). The structure of adult cardiomyocytes allows synchronisation of adjacent cardiomyocytes without completely redirecting

the overall signal direction. hiPSC-CMs, on the other hand, do not possess intrinsic structural orientation, leading to isotropic radial calcium wave propagation in monolayer cultures (Napiwocki et al., 2021; Lee et al., 2012). Therefore, when patterned hiPSC-CMs interconnect, they can redirected signal propagation, as was seen in a single layer gel, where calcium wavefront was propagating orthogonally to the cell patterning direction (Figure 3-25A). Individual isolated cardiac fibres with restricted and consistently predictable signal direction would therefore be a preferred model to investigate the effects of drugs of interest on signal propagation. Additionally, the presence of several independently functional lines in each gel produces internal technical repeats, highly beneficial for drug screening purposes. Overall, both single layer and double layer gels have value in cardiac tissue engineering, with the former better suited for cardiac tissue grafts and the latter for cardiac drug screening. While keeping this in mind, the remainder of this chapter will focus on the characterisation of double layer gels.

The final platform for the generation of uniform cardiac fibres was therefore optimised to be a double layer Porcine GelMA hydrogel, with 4 million cells/mL seeding density, patterned for 15 minutes and crosslinked for 1 minute using a 405 nm LED array, starting differentiation on day 1 and kept in culture for at least 20 days. The following sections of the chapter will focus on the characterisation of those final gels.

3.4.4 Characterisation of acoustically-patterned cardiac constructs

3.4.4.1 Gene expression during in situ *differentiation*

The differentiation process occurs through progressive manipulation of gene regulatory pathways, ultimately resulting in downregulation of pluripotency genes and upregulation of cardiac genes. To evaluate the dynamics of gene expression of *in situ* differentiated hydrogels, markers of key developmental stages were profiled at the relevant timepoints: d1 (pluripotent state, 1 day after ultrasound exposure), d4 (mesoderm stage, after CHIR99021 primitive streak induction), d6 (cardiac

progenitor stage, following IWP-2 specification initiation) and d20+ (committed cardiomyocytes, samples collected within day 20-23 range) (Figure 3-27). Six genes of interest were identified and analysed: two markers of pluripotency *POU5F1* and *NANOG,* a marker of early mesoderm formation *MESP1,* a marker of cardiac mesoderm specification *ISL1* and two markers of fully differentiated cardiomyocytes *TNNT2* and *MYH6*. The detailed discussion on the role of the proteins encoded by each marker is provided below, in the context of the RT-qPCR results. All RT-qPCR results were normalised to *RPL13* housekeeping gene, previously used for gene expression analysis for mesoderm and cardiac differentiation and found to be amplified in the early RT-qPCR cycles of acoustically-patterned samples (Figure 3-28) (Altomare et al., 2016; Kreuser et al., 2020).

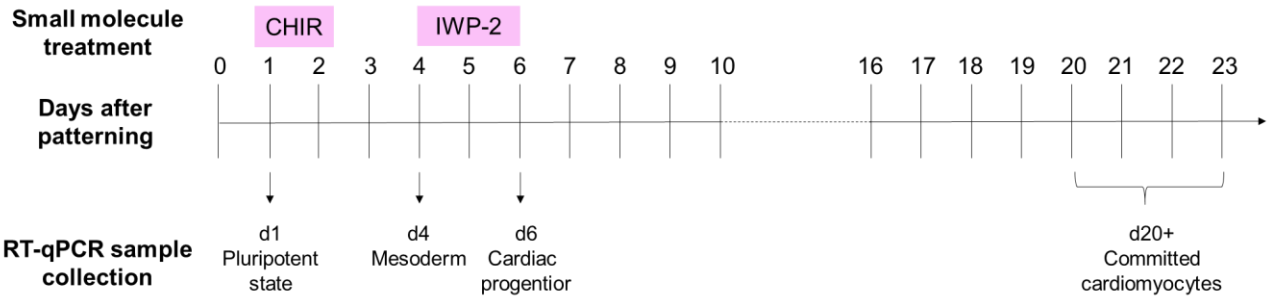


Figure 3-27 ***Schematic of the timeline for RT-qPCR sample collection.*** *Both patterned and unpatterned samples were collected throughout the differentiation progression: at day 1 after patterning (pluripotent state), day 4 (mesoderm following CHIR99021 induction), day 6 (cardiac progenitor following IWP-2 treatment) and day 20+ (committed cardiomyocytes, collected upon completion of the differentiation protocol between day 20 and day 23 after patterning).*

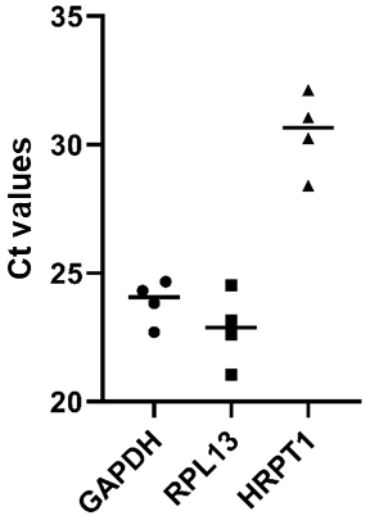


Figure 3-28 ***Ct values of three candidate housekeeping genes:*** **GAPDH, RPL13** ***and*** **HRPT1** ***measured in four acoustically-patterned samples collected from two different timepoints. n = 3, N = 4, where n is the number of replicate wells and N is the number of independent samples used for the measurements.***

The samples were patterned using the optimised patterning protocol, and each gel was dissected parallel to the patterning direction using a sterile blade to yield 4 equivalent sections, one for each timepoint. Prior to RNA collection, each gel was dissected into patterned and unpatterned regions, thus producing biologically paired samples. The samples were then mechanically homogenised using a TissueLyser, followed by RNA extraction and cDNA synthesis. Finally, amplification was performed for the genes of interest: *POU5F1*, *NANOG, MESP1, ISL1, TNNT2* and *MYH6* TaqMan probes, using QuantStudio 6. The fold change was calculated relative to the respective d1 values of patterned and unpatterned samples, apart from *MYH6*, where the samples were normalised to d4 due to undetected amplification of d1 samples.

The patterned and unpatterned samples followed the same general trend in gene expression over the course of differentiation (Figure 3-29). Upon CHIR induction of differentiation at day 4, *POUF51* expression decreased (12.5-fold patterned, 33.3-fold unpatterned), and continued to decline at each subsequent stage of differentiation, reaching an overall 250-fold decrease in patterned and 100-fold decrease in unpatterned d20+ samples relative to d1. *NANOG* expression decreased faster than *POUF51* at d4 (66.6-fold decrease patterned, 250-fold decrease unpatterned), with patterned samples reaching 143-fold reduction in d20+ samples, while equivalent unpatterned samples slightly recovered in the final timepoint to 71-fold overall reduction. The highest expression of *MESP1* was seen at d4, with 37 and 24-fold increase for patterned and unpatterned samples respectively, after which the expression declined, with d20 expression showing no difference in fold change in comparison to d1 (1.1-fold change patterned, 0.713 unpatterned). *ISL1* gene expression rose at d4 also, with unpatterned samples reaching a maximum 247-fold increase and subsequently declining to 117-fold and 40-fold difference in d6 and d20+ samples respectively. *ISL1* in patterned samples increased to 195-fold on day 4 and continued to climb up to 269-fold increase on day 6, with a subsequent decline to 67-fold difference in d20+ endpoint samples. *TNNT2* and *MYH6* expression increased gradually in both samples, reaching the highest fold increase (2747-fold patterned, 6238-

fold unpatterned for *TNNT2* and 17220-fold patterned, 15078-fold unpatterned for *MYH6*) in expression by d20.

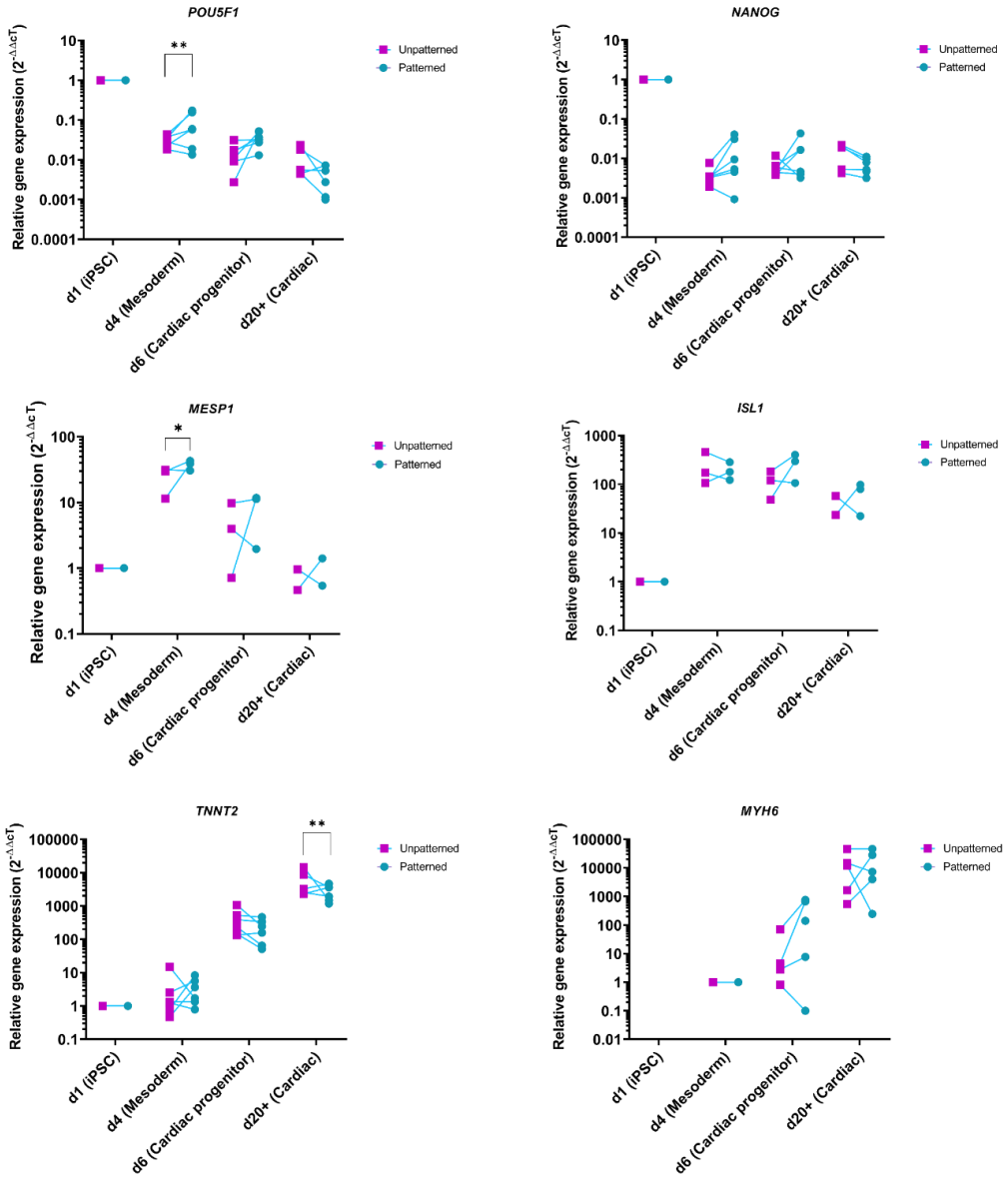


Figure 3-29 ***Changes in relative expression of pluripotency (*POU5F1, NANOG*), intermediate differentiation (*MESP1, ISL1*) and cardiac (*TNNT2 *and* MYH6*) genes in acoustically-patterned and unpatterned samples over time.*** *Connecting lines indicate biological patterned and unpatterned pairs. All samples are normalised to* RPL13 *housekeeping gene and calibrated against their respective d1 (hiPSC) timepoint. Repeated measures mixed effects model with Sidak multiple comparison correction and Geisser-Greenhouse sphericity correction. N = 6 for patterned and N = 5 for unpattered for each timepoint in* POU5F1, NANOG *and* TNNT2*; N = 3 for patterned in* MESP1 *and* ISL1 *all timepoints, N=3 for unpatterned* MESP1 *and* ISL1 *d1, d4 and d6 timepoints and N = 2 for d20+ unpatterned timepoint; N = 5 for each timepoint and both conditions of* MYH6*. n = 3 for all samples. n is the number of replicate wells, and N is the number of independent samples used for the measurements. * - p < 0.05, ** - p < 0.01, *** - p < 0.001 and **** - p < 0.0001.*

NANOG is one of the six core transcription factors, used for somatic cell reprogramming to iPSCs (Bayart & Cohen-Haguenauer, 2013, Wang et al., 2012; Silva et al., 2009). It was found to be essential for the completion of pluripotency establishment, however, its expression does not influence pluripotency maintenance or self-renewal capacity. The rapid decline in *NANOG* expression over differentiation therefore demonstrated the immediate loss of the ground state of pluripotency upon CHIR induction (Silva et al., 2009; Saunders, Faiola & Wang, 2013). *POU5F1* is another transcription factor used in somatic cell reprogramming. This gene encodes for OCT3/4, a transcription factor known to be an essential regulator of the pluripotent state and self-renewal (Wang et al., 2012). It also was found to be important for directing cell fate during differentiation (Radzisheuskaya et al., 2013). Such dual modality of OCT4 could explain its more gradual decline through the differentiation process in comparison to the other pluripotent cell marker, *NANOG.*

MESP1 is a marker of early mesoderm formation and encodes a transcription factor responsible for regulation of cardiac transcription factors, thus directing the mesoderm towards cardiovascular fate (Chan et al., 2013a). The peak expression of *MESP1* at CHIR induction stage is consistent with its role in cardiogenesis. *ISL1* upregulation after CHIR induction demonstrated the cardiac mesoderm progenitor specification. While this transcription factor is a marker of cardiac progenitors, it is also known to play a crucial role in conduction system development, and specifically, pacemaker cell specification, thus explaining its sustained upregulation beyond mesoderm and cardiac progenitor stages (van Eif et al., 2020; Liang et al., 2015).

TNNT2 and *MYH6* genes encode the structural proteins involved in the contractile machinery of the cardiomyocytes, and therefore are paramount to generating functional cardiac cells. Specifically, *TNNT2* gives rise to cTnT, a protein that enables calcium-regulated binding of actin and myosin. Translation of *MYH6* produces α-myosin heavy chain, a component of the myosin motor proteins, responsible for generation of force and motion of the contraction. Both those markers are specific to committed cardiomyocytes, with *TNNT2* known to be expressed slightly earlier than *MYH6* during

heart development. Expectedly, both *TNNT2* and *MYH6* levels increased throughout the differentiation process, confirming the progressive commitment and specification to functional cardiomyocytes, with *MYH6* expression only detectable after the CHIR induction on day 4, consistent with its later upregulation.

The gene expression data was analysed using a mixed effects model with repeated measures pairing the respective patterned and unpatterned samples. All genes showed significant change in expression over time (Table 3-4). At mesoderm stage, *POU5F1* and *MESP1* expression was significantly higher in patterned than in unpatterned samples ($p = 0.008$, $p = 0.0322$), while at day 20 *TNNT2* was significantly lower in patterned than unpatterned samples ($p = 0.009$) (Figure 3-29,Table 3-5). For all other timepoints and genes, there was no significant difference between the patterned and unpatterned samples (Table 3-5). These findings were surprising, as functionally there was a clear improvement in the patterned samples (discussed in sections 3.4.4.2 and 3.4.5.2 and 3.4.5.3), so the opposite difference in cardiac gene expression was expected. One of the possible reasons could be that the calibrators for ΔΔCt value calculation for patterned and unpatterned were their respective d1 samples. Therefore, while it can be concluded that the magnitude of change in *TNNT2* gene expression in unpatterned samples relative to unpatterned day 1 was larger than that in patterned samples relative to patterned day 1, the direct comparison of its expression between patterned and unpatterned samples remained unknown.

Table 3-4 ***A summary of p-values and significance levels of the effect of time on a given gene expression.*** *Repeated measures mixed effects model with Sidak multiple comparison correction and Geisser-Greenhouse sphericity correction. N = 6 for patterned and N = 5 for unpattered for each timepoint in* POU5F1, NANOG *and* TNNT2*; N = 3 for patterned in* MESP1 *and* ISL1 *all timepoints, N=3 for unpatterned* MESP1 *and* ISL1 *d1, d4 and d6 timepoints and N = 2 for d20+ unpatterned timepoint; N = 5 for each timepoint and both conditions of MYH6. n = 3 for all samples. n is the number of replicate wells, and N is the number of independent samples used for the measurements * - p < 0.05, ** - p < 0.01, *** - p < 0.001 and **** - p < 0.0001.*

Gene name	Time p-value	Significance
POU5F1	<0.0001	****
NANOG	<0.0001	****
MESP1	<0.0001	****
ISL1	0.0305	*
TNNT2	<0.0001	****
MYH6	0.0243	*

Table 3-5 ***A summary of adjusted p-values of Sidak multiple comparisons test between patterned and unpatterned samples at each differentiation stage for 6 genes of interest performed on repeated measures mixed model of RT-qPCR results.*** *For each timepoint, N = 6 for patterned and N = 5 for unpattered in* POU5F1, NANOG *and* TNNT2*; N = 3 for patterned in* MESP1 *and* ISL1 *all timepoints, N=3 for unpatterned* MESP1 *and* ISL1 *d1, d4 and d6 timepoints and N = 2 for d20+ unpatterned timepoint; N = 5 for each timepoint and both conditions of* MYH6*. n = 3 for all samples. n is the number of replicate wells, and N is the number of independent samples used for the measurements * - p < 0.05, ** - p < 0.01, *** - p < 0.001 and **** - p < 0.0001.*

Timepoint	*POU5F1* p-value	*NANOG* p-value	*MESP1* p-value	*ISL1* p-value	*TNNT2* p-value	*MYH6* p-value
d1 (hiPSC)	>0.9999	>0.9999	>0.9999	>0.9999	>0.9999	N/A
d4 (Mesoderm)	0.008(*)	0.0980	0.0322(*)	0.8840	>0.9999	>0.9999
d6 (Cardiac progenitor)	0.4614	0.3137	0.8973	0.1508	>0.9995	0.9998
d20+ (Committed cardiac)	0.9815	0.5172	>0.9999	0.9961	0.0091 (**)	0.9347

Since RT-qPCR results heavily rely on the normalisation methods, the stability of the housekeeping gene throughout differentiation process was analysed post-hoc on both patterned and unpatterned samples. Surprisingly, while *RPL13* Ct values of patterned samples remained stable (Figure 3-30A), there was a significant difference between d4 and d6 timepoints of unpatterned samples (p = 0.012, Figure 3-30B). The same difference was observed in another housekeeping gene, *GAPDH*, (p = 0.024,

Figure 3-30D), also commonly used for cardiac gene expression analysis (Balafkan et al., 2020; Zwi et al., 2009). *GAPDH* expression in patterned samples remained stable, like *RPL13* (Figure 3-30A,C). Since housekeeping genes were unstable throughout differentiation of unpatterned samples, the comparisons between patterned and unpatterned conditions, as well as the analysis of unpatterned gene expression over time would be inaccurate. However, the Ct values of both housekeeping genes were not significantly different between patterned and unpatterned samples at d20 timepoint (p = 0.4375 for both, Figure 3-30E,F), allowing us to investigate further how the gene expression was affected by patterning at differentiation endpoint.

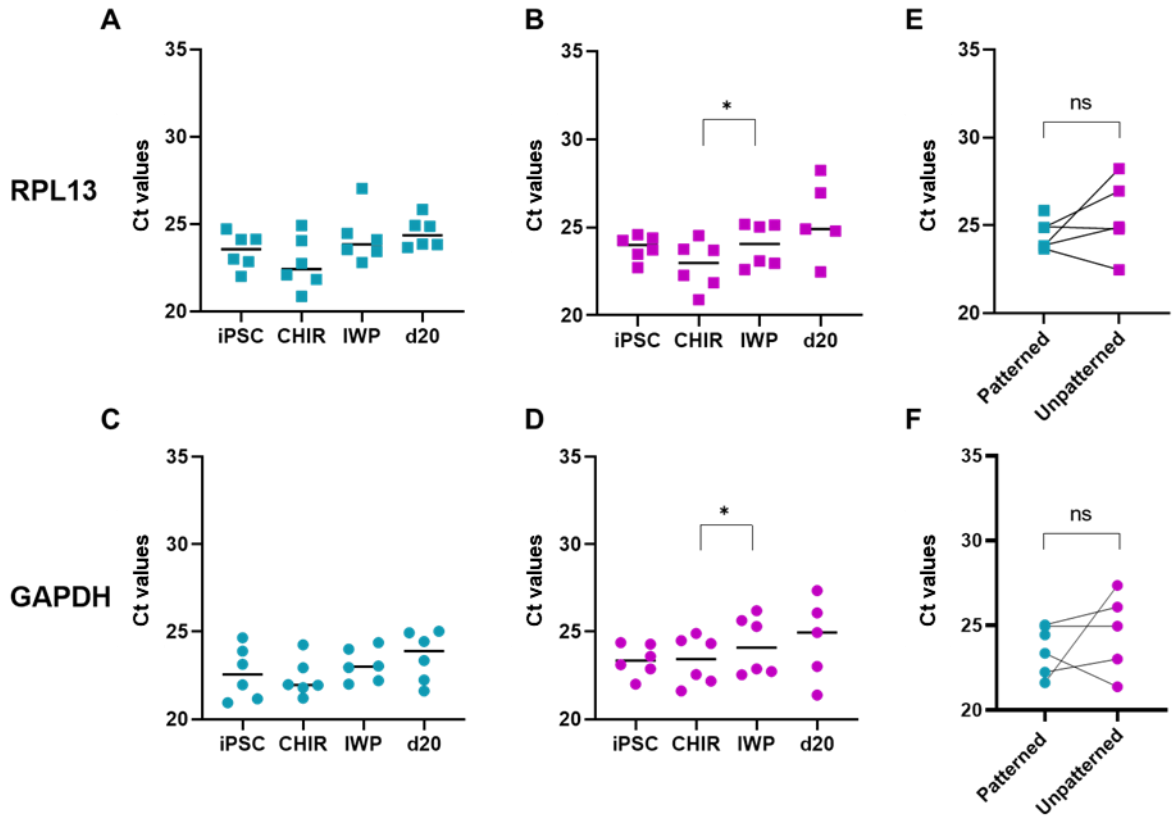


Figure 3-30 ***Post-hoc analysis of Ct values of two housekeeping genes (*GAPDH and RPL13*) in patterned (A,C) and unpatterned (B,D) samples separated by time of sample collection.*** *(A).* RPL13 *Ct values at hiPSC, CHIR, IWP and d20 timepoints of patterned samples. (B).* RPL13 *Ct values at hiPSC, CHIR, IWP and d20 timepoints of unpatterned samples. (C).* GAPDH *cT values at hiPSC, CHIR, IWP and d20 timepoints of patterned samples.(D).* GAPDH *Ct values at hiPSC, CHIR, IWP and d20 timepoints of unpatterned samples. (E). Comparison of* RPL13 *Ct values in patterned and unpatterned samples collected on day 20 (F). Comparison of* GAPDH *Ct values in patterned and unpatterned samples collected on day 20. Interconnecting lines show biological pairs of patterned and unpatterned samples. n = 3 for all samples, N = 6 for all patterned conditions and hiPSC, CHIR and IWP of unpatterned conditions. N = 5 for d20 of unpatterned conditions. n is the number of replicate wells, and N is the number of independent samples used for the measurements. Statistical significance determined by repeated measures mixed effects model with Sidak multiple comparison correction and Geisser-Greenhouse sphericity correction. ns – non-significant, *- p < 0.05, ** - p < 0.01, *** - p < 0.001 and **** - p < 0.0001.*

To investigate that, gene expression analysis for *POU5F1*, *NANOG, TNNT2* and *MYH6* was performed on samples collected from endpoint d20 gels only (Figure 3-31). To calculate the fold change in gene expression ($2^{-\Delta\Delta Ct}$), ΔCt, the difference in cycle thresholds between the target and housekeeping genes, was calculated for patterned and unpatterned samples relative to *RPL13,* and all samples were then calibrated relative to the average ΔCt of all unpatterned controls. There was no significant difference in the relative gene expression of *POU5F1, NANOG, TNNT2* and *MYH6* between patterned and unpatterned samples (p = 0.2661, p = 0.6772, p = 0.2036 and p = 0.1099 respectively). Overall, these results suggested that the pluripotency markers and early cardiac markers gene expression remained unaffected by the patterning.

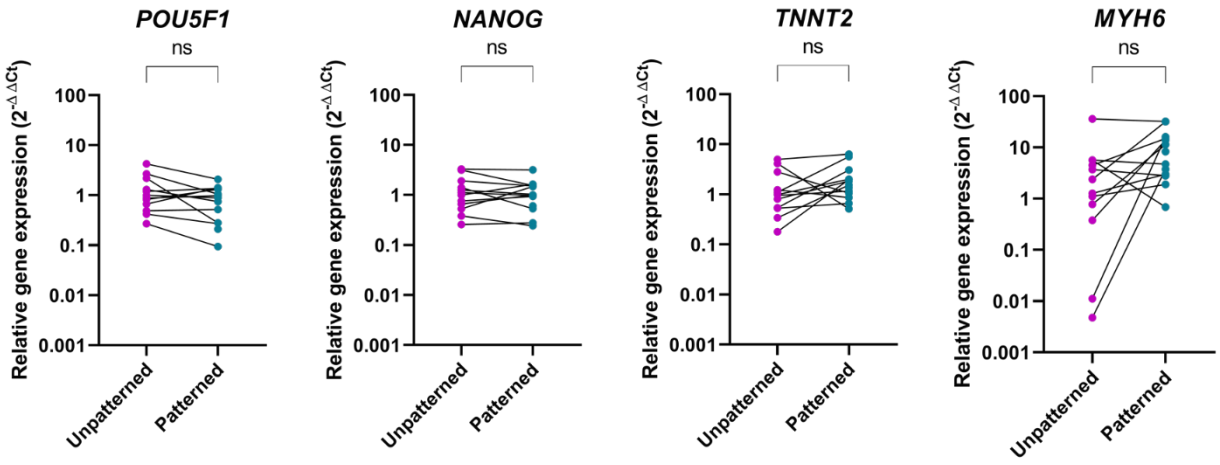


Figure 3-31 ***Comparison of relative gene expression of pluripotent (*POU5F1 and NANOG*) and cardiac (*TNNT2 and MYH6*) target genes between patterned and unpatterned samples collected at day 20+.*** *The ΔΔCt values were calculated using the average unpatterned ΔCt for a given gene of interest. Interconnecting lines show biological pairs of patterned and unpatterned samples. Statistical significance is calculated using a paired two-tailed Wilcoxon test. N = 13 patterned, N = 12 unpatterned. n = 3 for all samples. n is the number of replicate wells, and N is the number of independent samples used for the measurements. ns – non-significant.*

3.4.4.2 Immunofluorescent staining

3.4.4.2.1 Immunofluorescent staining optimisation

The protocol for single layer immunofluorescent staining was based on the previously published methods for wholemount GelMA staining (Kupfer et al., 2020). Briefly, the protocol included a 0.2%

(v/v) Triton-X permeabilization step for 1 hour, followed by 2 hour blocking in 0.1% (v/v) Triton-X-containing blocking solution. The samples were then incubated with primary antibodies overnight, washed, and incubated with secondary antibodies for 2 hours. However, when the same approach was applied to double layer hydrogels, the signal intensity was significantly reduced in the centre of the gel, while the cells located on the edges were overexposed (Figure 3-32A). Increasing the concentration of permeabilization step from 0.25% to 0.5% (v/v) Triton-X did not improve the staining quality (Figure 3-32B). Doubling the primary and secondary antibody concentrations increased the signal, however also increased the background significantly (Figure 3-32C). Finally, increasing the incubation time for secondary antibodies to overnight allowed penetration through the gel, and improved the signal-to-noise ratio in the centre of the gel (Figure 3-32D). The edges of the gel remained overexposed, so for all future double layer gels the areas on the edge were not imaged to ensure consistency.

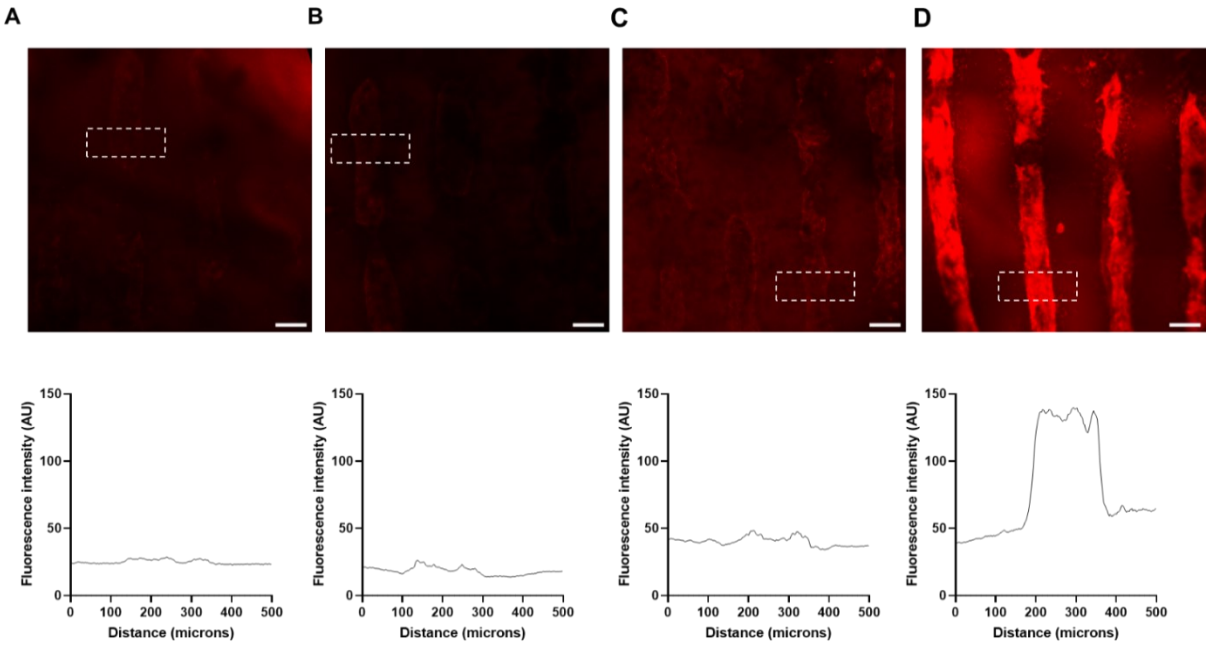


Figure 3-32 ***Fluorescence immunostaining protocol optimisation of double layer acoustically-patterned cardiac gels.*** *For each protocol, a representative image is shown with a white box placed over the width of a single patterned line. The average intensity profile of the outlined region is shown in the bottom panel. (A). Staining protocol previously published in literature (Kupfer et al. 2020) with 0.25% (v/v) Triton-X. (B). Updated protocol with 0.5% (v/v) Triton-X permeabilization step. (C). Staining protocol with 2-fold increase in primary and secondary antibody concentrations. (D). Optimised staining protocol with overnight primary and secondary antibody incubation steps. Scale bars = 200 µm.*

Indeed, the cells within the single layer gels were located close to the surface, while the supporting layer of the double layer gels encapsulated the cells, increasing the construct thickness and decreasing the imaging quality. However, since the quality of the imaging remained the same for double layer and single layer gels when recording calcium signal using the endogenous GFP, the material thickness does not reduce the fluorescent signal emitted from the sample (data not shown). Therefore, the solution to improving the staining of thicker double layer gels was to increase the incubation time to allow for more antibodies to diffuse into the depth of the gel, staining all the available binding sites.

3.4.4.2.2 Characterisation of cell phenotype composition of cardiac double layer gels

Differentiation from hiPSC to cardiomyocytes is a non-linear process that involves multiple stages of development, progressing from pluripotent cells to mesoderm and cardiac progenitors before yielding cardiac cell phenotypes. While the modern protocols have been optimised to achieve

maximum differentiation efficiency, some non-cardiac cell types still spontaneously arise over the course of cell culture. Using immunofluorescent staining, cell types produced during the *in situ* differentiation could be identified, and the effect of patterning on the localisation of these cells was investigated.

The gels, fixed after 20 days of differentiation, were stained for 5 markers: SOX2 for undifferentiated hiPSCs, cTnT and sarcomeric α-actinin for cardiomyocytes, CD31 for endothelial cells and smooth muscle actin (α-SMA) for myofibroblasts and smooth muscle cells. Pluripotent marker SOX2 was not expressed in the differentiated gels, confirming that most of the cells were committed to their lineage (Figure 3-33).

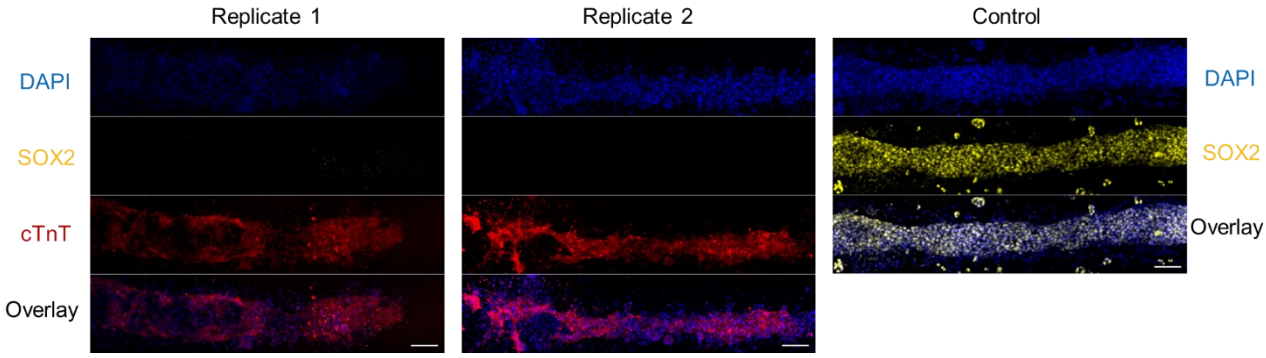


Figure 3-33 ***Immunofluorescent staining for pluripotency marker (SOX2) of two differentiated acoustically-patterned hydrogels (replicate 1 and replicate 2) 20 days after ultrasound exposure and one control undifferentiated patterned gel 1 day after ultrasound exposure.*** *Representative images shown for each replicate, each replicate represents a different biological repeat. All samples counterstained with DAPI. Differentiated samples counterstained with cTnT as positive control. Scale bar = 100 µm.*

cTnT and sarcomeric α-actinin are structural proteins forming the filaments of the sarcomere responsible for cardiac contractility, often used as cardiomyocyte markers in immunofluorescent staining (Fan et al., 2015; Sehnert et al., 2002). Both cardiac markers were expressed preferentially in the patterned region, forming continuous cardiac fibres, uniformly distributed through the gel (Figure 3-34). The width of the engineered fibres was within 130-190 µm range, comparable with the 200 µm spacing of perimysium – connective tissue encapsulating individual cardiac fibres in the myocardium (Kanzaki et al., 2010). Aligned geometry of cardiac markers was seen consistently across

the triplicates. The signal intensity varied from sample to sample, which likely would correlate with the number of cardiomyocytes per line.

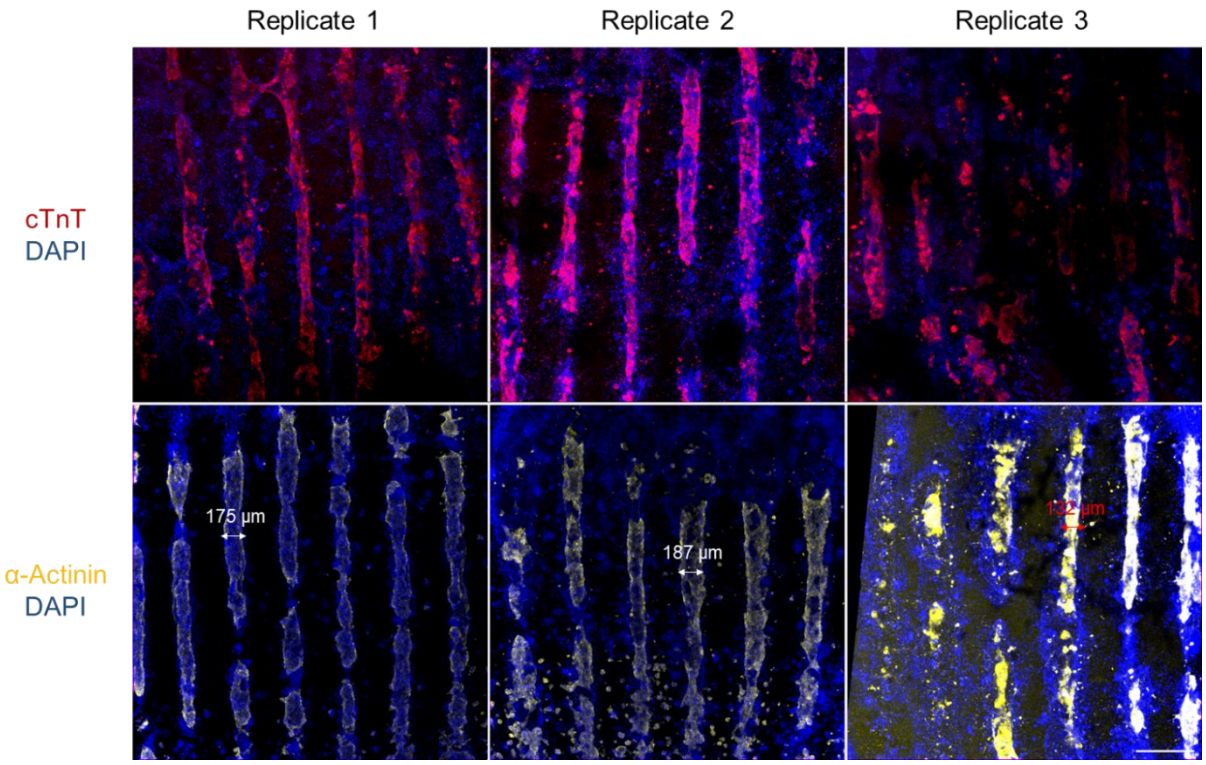


Figure 3-34 ***Overview confocal images of immunostaining of cardiomyocyte markers' cTnT (red) and α-Actinin (yellow) distribution in three double layer acoustically-patterned hydrogels differentiated up to day 20.*** *Replicates 1, 2 and 3 refer to three different biological repeats. All samples counterstained for DAPI (blue). The cTnT and α-Actinin samples are not paired. The measurements of line width indicate 175 µm, 187 µm and 132 µm for replicates 1, 2 and 3 respectively. Scale bar = 500 µm.*

The unpatterned controls of two gels contained disorganised cells weakly expressing cTnT and α-actinin that were dispersed as single cells and did not form continuous structures (Figure 3-35, Figure 3-36). However, clusters with high expression of cTnT and α-actinin were present in a single replicate of each immunostaining panel. The replicates of cTnT and α-actinin were not biologically paired and therefore this result was representative of a general variability in cardiac marker expression in the unpatterned gel. Endothelial cells, expressing CD31, were present in all samples. In patterned gels, CD31-positive cells were in proximity to the cardiac fibres, while in the unpatterned controls they were distributed randomly (Figure 3-35). This was likely due to the ultrasound-assisted cell aggregation prior to differentiation causing a higher probability of all hiPSC-derived cell types to

localise within patterned regions than in the vacant space between the adjacent lines. However, spindle-like cells, positive for α-SMA, were present throughout the whole patterned gel, with some SMA-positive cells surrounding the α-actinin-positive cardiomyocytes, and others invading the inter-line space of the patterned gels (Figure 3-36). In unpatterned controls, those non-cardiomyocytes were uniformly spread throughout the gel with no obvious structure formation, due to random distribution of hiPSCs in the starting hydrogels leading to spontaneous and disorganised differentiation.

Endothelial cells and fibroblasts were previously shown to regulate cardiomyocyte activity in direct co-culture, consistent with the physiological complexity of heart (King et al., 2022). Differentiating the hiPSCs *in situ* allowed to replicate this cellular heterogeneity, with at least 3 cell phenotypes found to be present in the *in situ* differentiated cardiac hydrogels. Aggregation of hiPSCs using acoustic patterning prior to differentiation consistently produced anisotropic cardiomyocyte-rich fibres with physiologically-relevant dimensions. The patterning was also observed to affect the distribution of non-myocytes, though to a lesser extent than cardiomyocytes. The difference in cell type localisation in patterned gels is likely due to high proliferation rates of myofibroblasts and endothelial cells in comparison to nearly non-proliferative cardiomyocytes (Kawamoto & Asahara, 2007; Helary et al., 2006; Minter-Dykhouse, Nelson & Folmes, 2022; Zhao et al., 2020). Taken together with the RT-qPCR data, these results showed that while the patterning only had a small effect on the cardiac gene expression, it introduced a higher degree of structural organisation of cardiomyocytes in comparison to unpatterned controls.

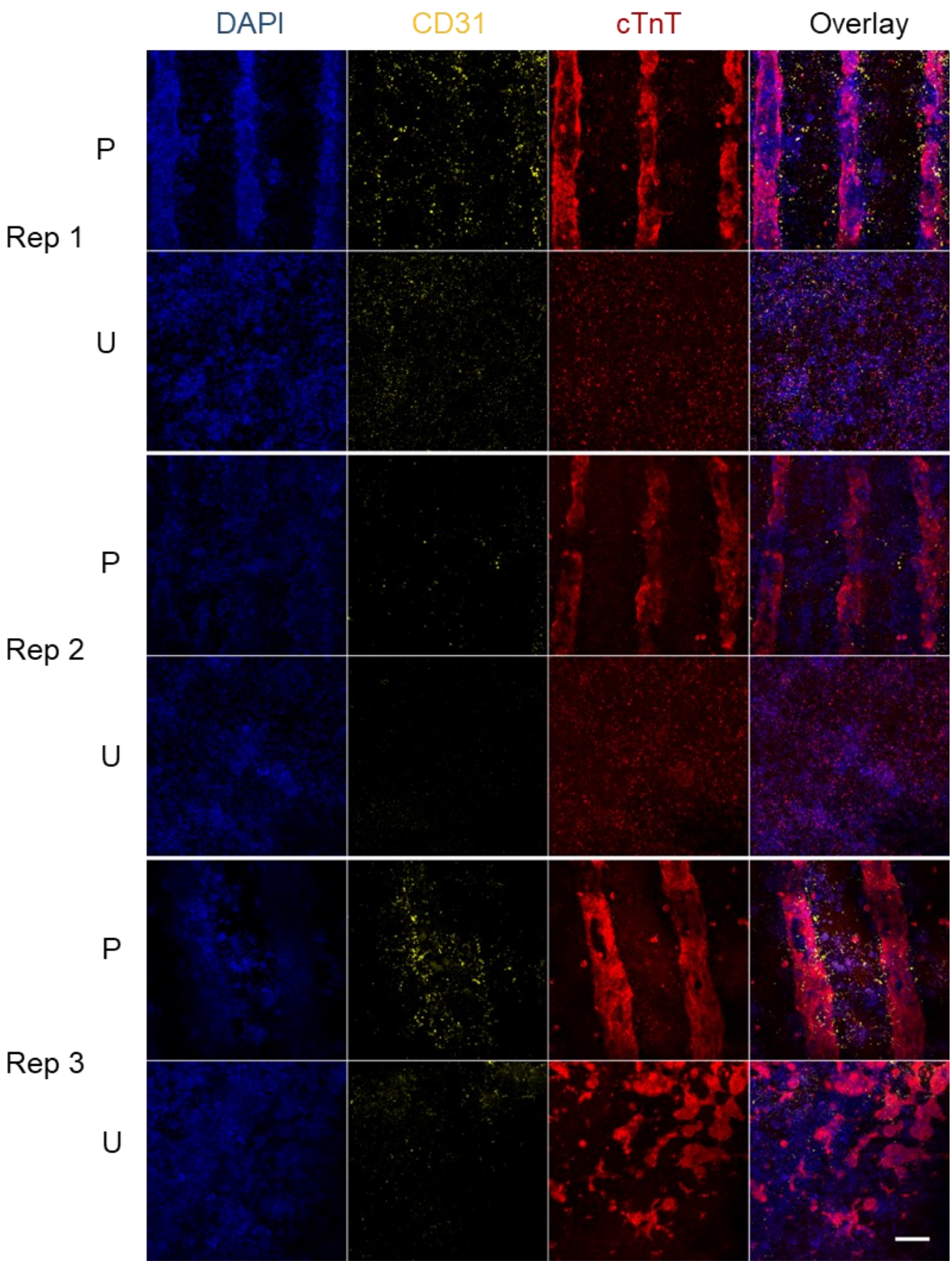


Figure 3-35 ***10x magnification confocal imaging of immunostaining for cardiomyocyte marker cTnT (red) and endothelial cell marker-CD31 (yellow) distribution in three double layer hydrogels differentiated up to day 20.*** *Replicates (Rep) 1, 2 and 3 refer to three different biological repeats. P – patterned region of the gel, U – unpatterned region of the gel. Patterned and unpatterned samples were paired. All samples counterstained for DAPI (blue). Scale bar = 200 µm.*

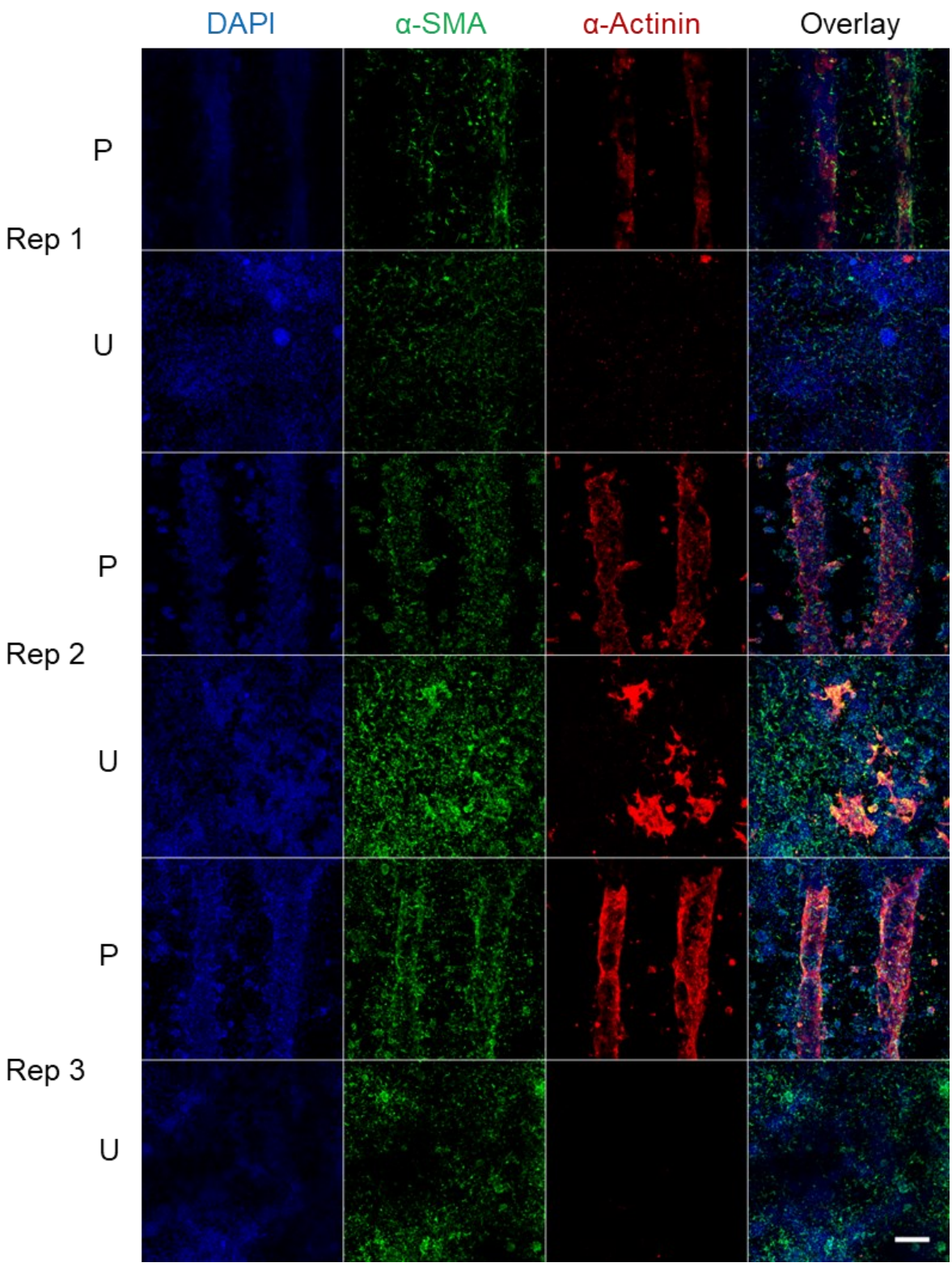


Figure 3-36 ***Medium magnification confocal imaging (10x) of immunostaining for cardiomyocyte marker α-actinin (red) and smooth muscle/myofibroblast cell marker α-SMA (green) distribution in three double layer hydrogels differentiated up to day 20.*** *Replicates (Rep) 1, 2 and 3 refer to three different biological repeats. P – patterned region of the gel, UP – unpatterned region of the gel. Patterned and unpatterned samples were paired. All samples counterstained for DAPI (blue). Scale bar = 200 µm.*

3.4.5 Functional electrophysiological assessment of differentiated cardiac hydrogels

3.4.5.1 Spontaneous calcium activity

The results obtained from the RT-qPCR and confocal imaging confirmed that applying cardiac differentiation protocols to acoustically-patterned hiPSCs *in situ* produced arrays of cells expressing cardiac markers (Figure 3-29, Figure 3-31, Figure 3-34). The imaging also demonstrated that the cardiac markers localised to each array exclusively, with no protrusions into adjacent lines, thus confirming their independence from each other (Figure 3-34). Since cardiac tissue is electroactive, the next characterisation step was to evaluate the electrophysiological properties of the acoustically patterned hydrogels. Analysis of spontaneous calcium signals is a common tool of engineered cardiac tissue characterisation, which allows to assess the behaviour of the functional cardiomyocytes within the tissue and provides a quantifiable output for drug screening studies.

Day 20 timepoint was chosen as the earliest consistent onset of spontaneous calcium activity, consistent with literature, and used for all future studies (Huang et al., 2020; Tsao et al., 2018; Pioner et al., 2019). However, it should be noted that these results would only be comparable to other day 20 samples, as the electrophysiological parameters would likely change over time. Culture time is one of the major factors responsible for the cardiomyocyte behaviour and maturation status, with longer culture times generally known to improve cell ultrastructure and conduction of hiPSC-CMs (Yang, Pabon & Murry, 2014). For example, the sarcomeric M-band was found in cardiomyocytes after 1 year in culture, while conduction velocity was significantly upregulated after 2 months (Kadota et al., 2013; Kamakura et al., 2013). Therefore, while the below discussion characterises the electrophysiology of acoustically-patterned cardiac fibres 20 days after exposure to ultrasound and 19 days after differentiation initiation, future work on the changes in electrophysiology of cardiac fibres over time in culture would be valuable.

Spontaneous contractions and calcium activity were observed in individual cardiac fibres of acoustically-patterned hydrogels on day 20. The majority of the lines within the gel exhibited calcium oscillations, as shown by the representative traces of recorded calcium activity in individual cardiac fibres within the gel, confirming the presence of functional cardiomyocytes after *in situ* differentiation of acoustically patterned hydrogels (Figure 3-37). If the tissue was an electrically-coupled interconnected syncytium, the same signal would propagate through all regions of the gel, leading to synchronous calcium traces. The variation in calcium transient profiles across the gels therefore suggested asynchronous behaviour and independency of adjacent cardiac fibres. This phenomenon can be clearly observed in the supporting videos provided. A future analysis of phase and frequency differences between individual fibres could further strengthen this observation.

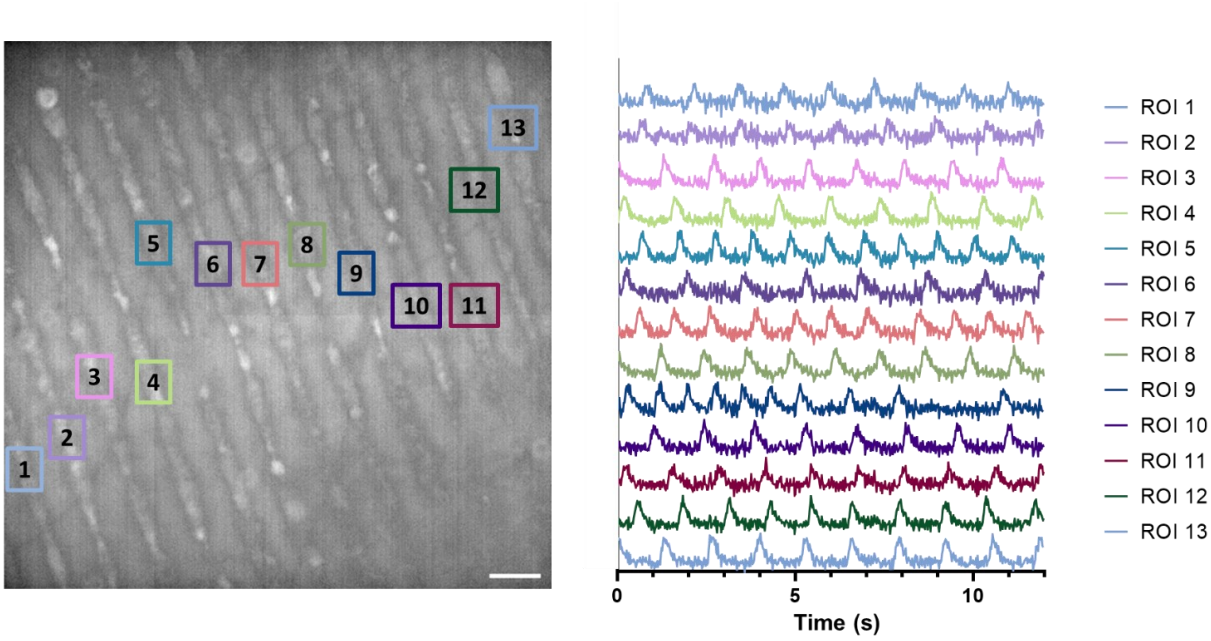


Figure 3-37 ***Spontaneous calcium activity in acoustically-patterned double layer cardiac hydrogels on day 20 after ultrasound exposure.*** *A representative frame acquired during widefield calcium imaging, demonstrating the spatial distribution of 13 calcium-handling cardiac fibres across the hydrogel with outlined regions of interest (ROIs) (left) and extracted spontaneous calcium traces for a single ROI of each cardiac fibre (right). Scale bar = 500 µm.*

3.4.5.2 Directional propagation of calcium signal in patterned hydrogels

While the linear organisation of cardiomyocytes within the hydrogel was evident from confocal microscopy, it was important to investigate how this geometry would affect the direction of signal

propagation. Fluorescence microscopy was therefore used to record spontaneous calcium signal within the samples, as above, and the signal propagation was inspected.

The timeseries of calcium activation of three different gels was assessed frame-by-frame, with 20 ms interval between each image. Unpatterned replicates 1 and 2 were mostly comprised of individual cell clusters, that depolarised independently (Figure 3-38A,B). This was observed by random order of activation from one frame to another, with no single apparent propagation front. Replicate 3, however, had several interconnected islands of cells, that activated in syncytium, demonstrating a propagating calcium wavefront, with the whole width of FoV activated by 120 ms, corresponding to ≈ 1.1 cm/s conduction velocity (Figure 3-38C). However, it also contained disconnected clusters of cells that depolarised independently, appearing at 220, 320 and 340 ms timepoints (indicated by black arrows). The structures in unpatterned replicate 3 were also branching, thereby splitting the signal, leading to an unpredictable propagation path.

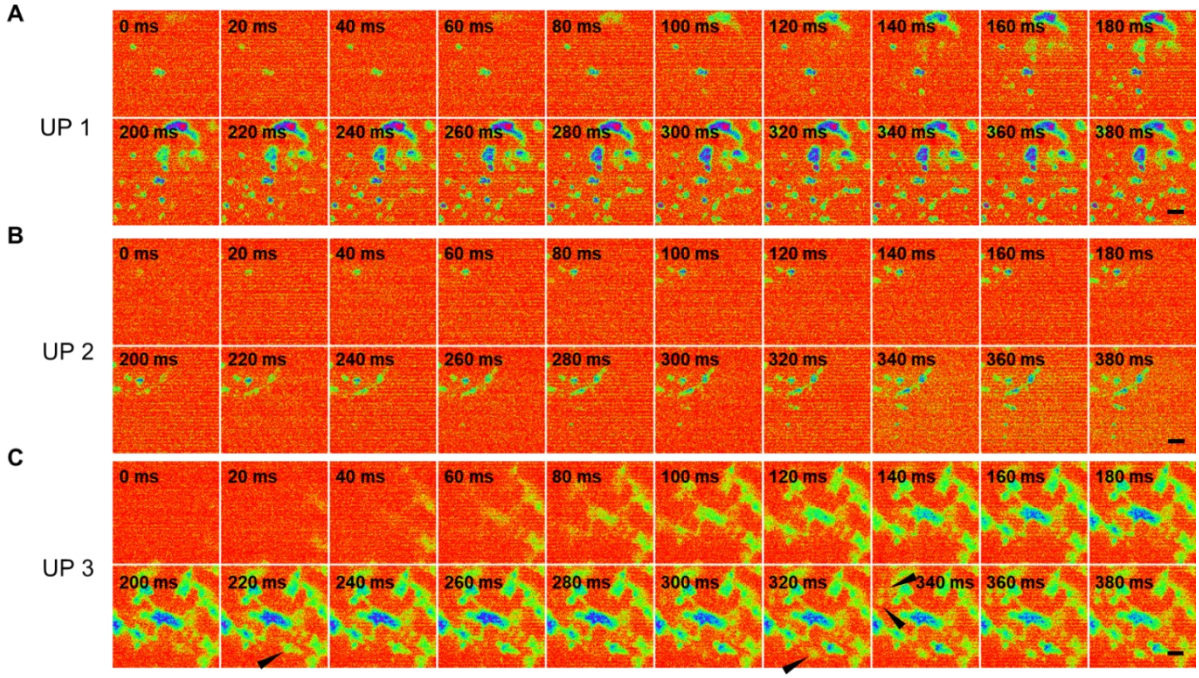


Figure 3-38 ***Frame-by-frame analysis of calcium signal propagation in three independent unpatterned samples.*** *Heatmaps of signal intensity from raw calcium videos of three biological replicates of unpatterned cardiac gels taken at 10x magnification.UP – unpatterned. (A). Replicate 1. (B). Replicate 2. (C). Replicate 3. Acquisition rate – 10 ms, every other frame is shown in the figure (20 ms interval). For each sample, top row (left to right) shows progression from 0 ms to 180 ms, bottom row (left to right) shows progression from 200 ms to 380 ms. Black arrows indicate independent clusters in unpatterned replicate 3. Scale bars = 200 µm.*

In the patterned dataset, the path of calcium activation was more consistently directional, with the depolarisation originating either on the right (replicates 1 and 3) or on the left (replicate 2), and gradually progressing until the full length of the line was activated (Figure 3-38). The width of the FoV was fully activated at 80 ms for replicates 1 and 2 (≈ 1.57 cm/s and 1.62 cm/s conduction velocity respectively), and 100 ms for replicate 1 (≈ 1.31 cm/s). This was on average 0.4 cm/s faster than the propagation of unpatterned replicate 3, however, since only one of the control gels showed propagation, the conclusive statistical comparison between conduction velocities of patterned and unpatterned samples could not be drawn. Conduction velocity measurements were also roughly estimated from the width of FoV and time taken for its full activation, and would need to be measured more precisely with calcium imaging at higher temporal resolution. Nevertheless, these results clearly showed that acoustic patterning of hiPSCs prior to differentiation led to a well-defined linear activation path in comparison to unpatterned controls.

To further substantiate the observation of directional propagation, the intensity of the calcium signal was measured along the length of a single line across 5 ROIs at regular 790 µm intervals (Figure 3-40A). The shift in peak intensity was observed from ROI 1 to ROI 5, demonstrating the sequential propagation of the signal. Another line from the same gel was also analysed and showed the shift in peak intensity in reverse order, with the signal starting from ROI 6 and progressing to ROI 1 (Figure 3-40B). It was not possible to determine the position of ROI 3 within the sequence due to a low signal-to-noise ratio at the region, however the order of peaks for all other ROIs indicated directional propagation.

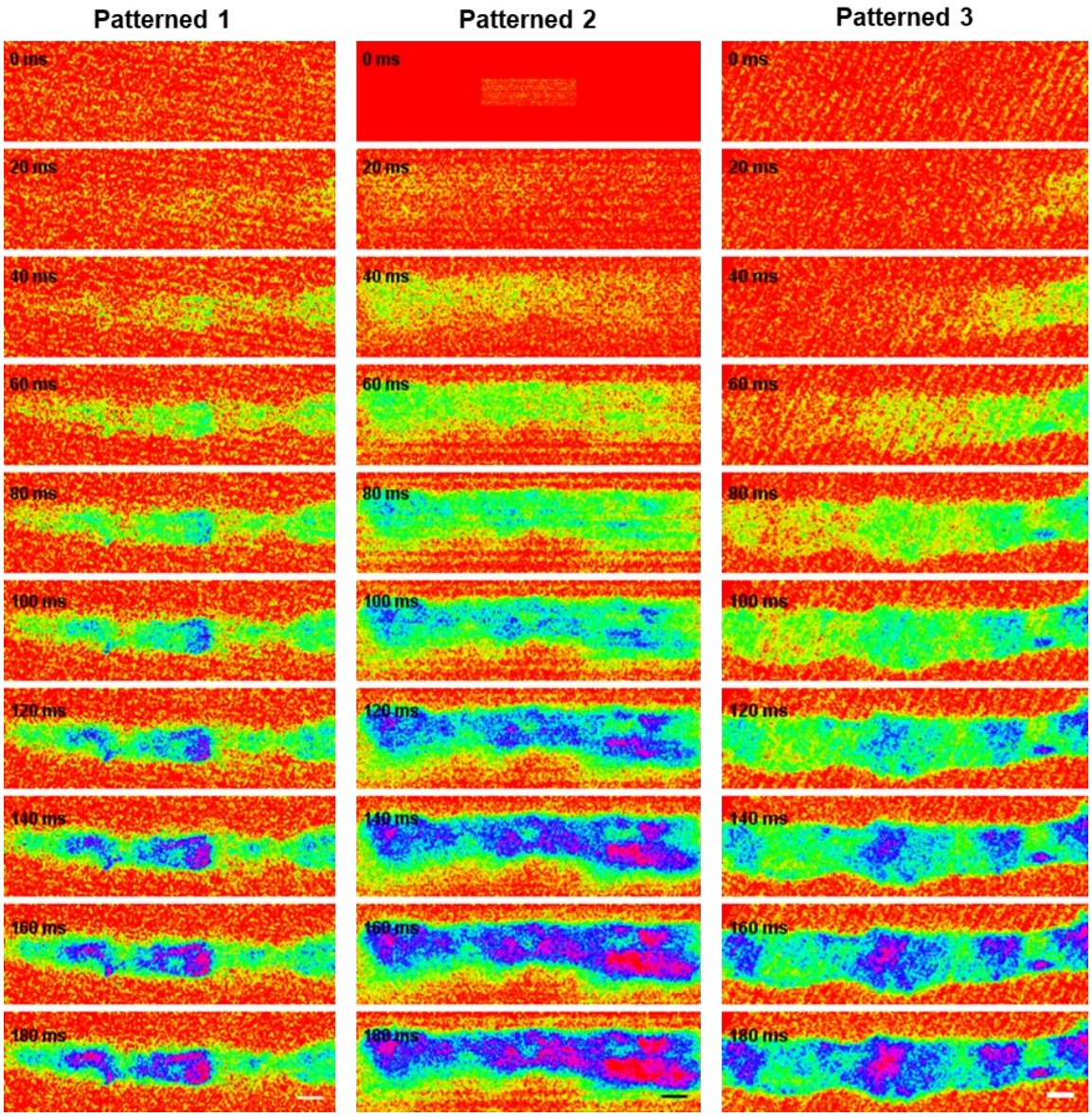


Figure 3-39 ***Frame-by-frame analysis of calcium signal propagation in three independent patterned samples.*** *Heatmaps of signal intensity from raw calcium videos of three biological replicates of patterned cardiac gels taken at 10x magnification. Acquisition rate – 10 ms, every other frame is shown in the figure (20 ms interval). Each sample shows progression from 0 ms to 180 ms (top to bottom). Note that the repeated streaking is due to the camera noise. Scale bars = 100 µm.*

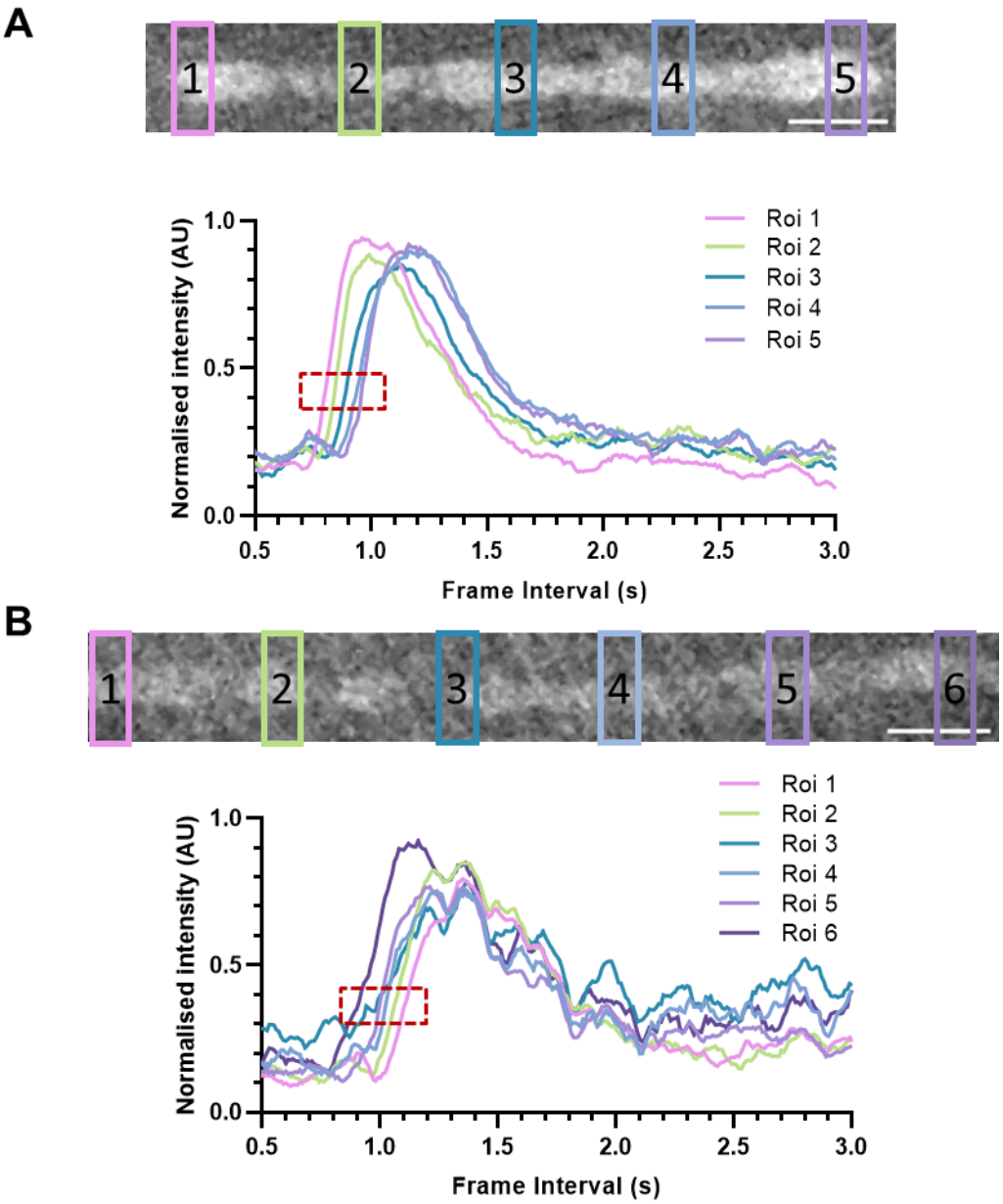


Figure 3-40 ***Sequential calcium activation along the longitudinal axis of acoustically-patterned cardiac fibres.*** *(A) and (B) show two technical replicates obtained from the same gel. Each panel shows ROIS distribution across a single frame from fluorescent calcium imaging, showing the engineered fibre when fully activated (top). Interval between ROIs is 790 µm. Bottom panel shows normalised fluorescence intensity of each ROI during a single calcium transient. All calcium traces were smoothed using a second order polynomial with 10 neighbours averaging. Red box indicates the depolarisation region with the order of ROI activation. Scale bars = 500 µm.*

Overall, these results suggested that using acoustic patterning to arrange hiPSC-CMs into linear geometry also regulated consistent spontaneous calcium signals with predictable path of conduction. This feature could be exploited for the calcium dynamics assessment in future drug screening studies, allowing to measure electrophysiological response to the drug of interest through measurements of conduction velocity and parameters of calcium dynamics (e.g. time-to-peak, time to 80% decay, time to 20% decay, decay constant).

Biologically, in a healthy native myocardium, the functional anisotropy of signal conduction is achieved through the structural anisotropy of the tissue (Clerc, 1976). Longitudinal conduction within the cytoplasm of an elongated cardiomyocyte occurs at a faster rate than the gap junction-regulated lateral conduction to the neighbouring cells of the syncytium (Kotadia et al., 2020; Clerc, 1976). In the data shown above, longitudinal conduction was observed parallel with the alignment of acoustically-patterned cardiac fibres. In unpatterned samples either no conduction was observed at all, or extensive transverse conduction was present. Overall, acoustic patterning allowed to produce consistently directional functional cardiac fibres in comparison to unpatterned control. However, these results remained qualitative due to the low spatial and temporal resolution of the acquired signal. In contrast with adult cardiomyocytes, hiPSC-CM are structurally and functionally immature, showing no inherent directional preference in conduction, therefore it is likely that the observed directional conduction occurred due to a physical restriction of the cells to a linear pattern. Similar findings were recently demonstrated when extrusion-printed anisotropic macrofilaments comprised of hiPSC-CMs exhibited a clear calcium transient front, consistently propagating parallel to the length of the engineered tissue (Ahrens et al., 2022). The effect of acoustic patterning on individual hiPSC-CM morphology would need to be investigated further, and direct comparison of longitudinal and transverse conduction velocities in acoustically-patterned fibres would inform the underlying mechanism of observed directionality of the signal.

Quantifying the directionality of the signal would allow to better define the consistency of direction propagation. To better quantify the propagation consistency, the angle of directionality of the propagation was next calculated using a custom MATLAB code, written by Dr Richard Wang applied to the videos of spontaneous calcium signal. Briefly, the video recordings of calcium transients were converted into a binary stack of images before applying a nearest distance transformation. To that effect, the frames were analysed in pairs, as frame (n) and frame (n+1). For each pixel in (n+1), the location of a nearest pixel was identified in the previous frame (n), thereby identifying its origin pixel. Distance and angle vector travelled by this pixel from (n) to (n+1) therefore can be calculated.

This process is repeated for each pixel, and a frequency histogram of all angle vectors is formed. The frequency of the angle vectors is then weighted by distance travelled. The frequency histograms for each video then combine frequency histogram of the pairs of frames. The output file showed all angles of propagation for the whole stack, which were plotted as a radial histogram.

To produce the binary images, the original video was pre-processed as follows. First, as the activity of adjacent lines was independent of each other, the individual cardiac fibres were cropped. Next, the background was subtracted, and the image was filtered using a median filter with 2.0 px diameter. A threshold was then applied to produce a binary image, and the outliers generated by noise were removed. Binary functions 'Close gaps' and/or 'Fill holes' in Fiji software were applied to cluster together the adjacent pixels (Figure 3-41).

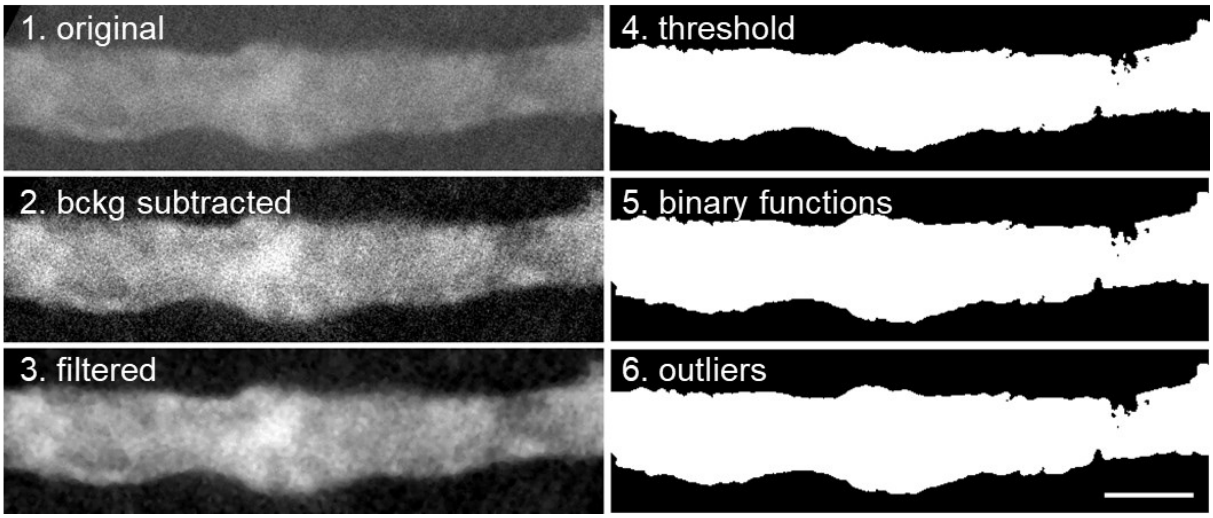


Figure 3-41 ***Progression of a frame obtained from calcium imaging through pre-processing steps.*** *The raw data file used from Figure 3-39 Patterned 3. Binary functions step includes 'Close gaps' and 'Fill holes' functions in Fiji. Scale bar = 200 µm.*

The success of pre-processing varied greatly. While some final binary images corresponded well with the observed original signal (Figure 3-42A), a lot of data was lost in others after applying the 'Fill holes' function. For example, in Figure 3-42B the activation was progressing gradually through the first 8 frames until a large increase in distance travelled was observed in frame 9. Indeed, this would skew the results and make them appear strongly directional when quantified using the nearest distance transformation method. In Figure 3-42C, while the progression of the signal was visible in

'Threshold' or 'Closed gaps' images, after 'Fill holes' function was applied all the signal was removed until frame 8, at which the line appeared in full, showing no propagation. The same effect was observed in unpatterned samples (Figure 3-42D), where the whole clusters of active pixels were removed by 'Fill holes' function, making it impossible to analyse the control data.

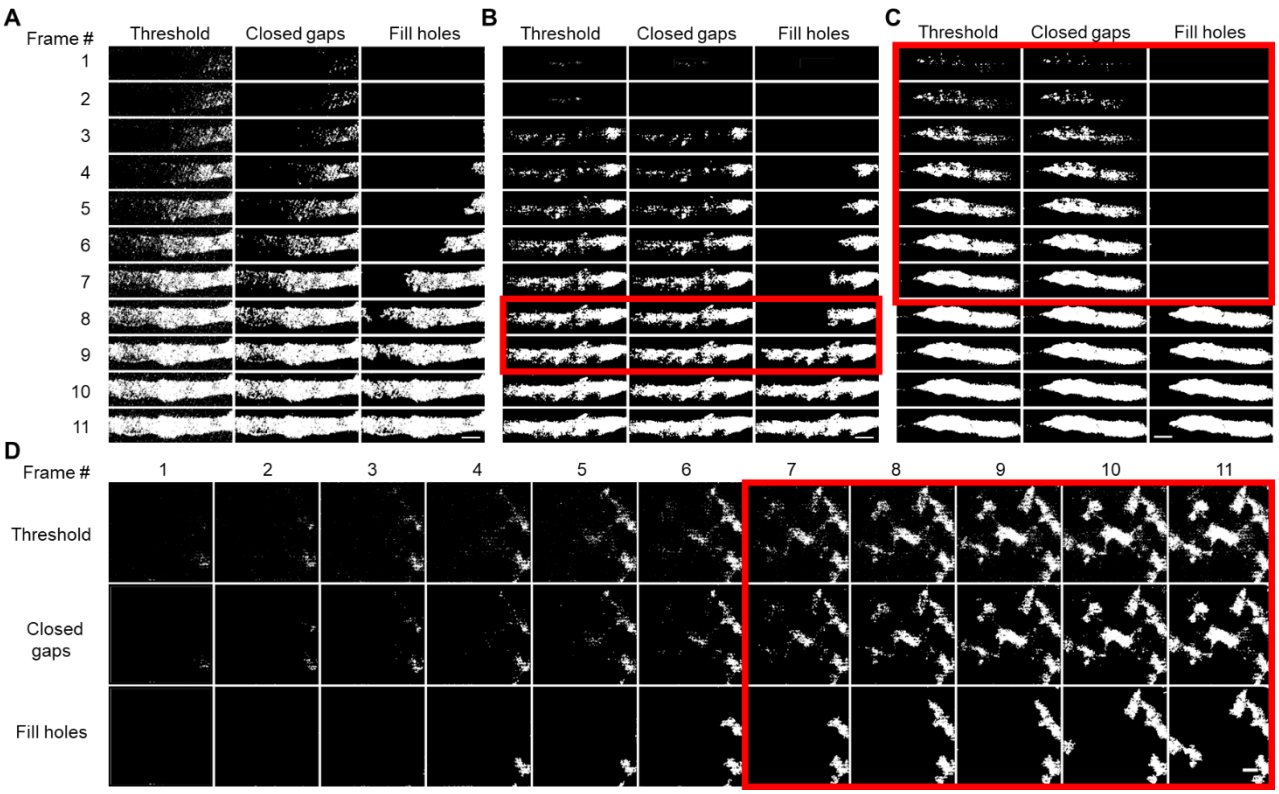


Figure 3-42 ***Image pre-processing artefacts after applying binary functions 'Close gaps' and 'Fill holes'.*** *Each subfigure shows the first 11 frames of a calcium transient video after thresholding, closing the gaps and fill holes functions have been applied. Red boxes indicate the frames in which the 'Fill holes' function significantly reduces the original signal. (A). Replicate 1 of a patterned cardiac fibre calcium signal with consistent pre-processing results. Note that the raw data is equivalent to Figure 3-39, Figure 3-41. (B). Replicate 2 of a patterned cardiac fibre calcium signal, with pre-processing artefact occurring in frames 8 and 9 after 'Fill holes' function is applied. (C). Replicate 3 of a patterned cardiac fibre calcium signal, with pre-processing artefacts removing all active pixels in frames 1-7. (D). Calcium signal in the unpatterned sample, with pre-processing artefacts removing large areas of active pixels in frames 7-11. Note that the raw data is equivalent to Figure 3-38C. Scale bars = 200 µm.*

To further improve upon the MATLAB analysis code and reduce the effects of noise from adjacent activated areas, a rolling projection macro was applied to show frame (n+1) as the sum of all frames preceding it, thereby only considering new activated pixels. The rolling projection was applied to two samples after thresholding, after which 'Close gaps' and 'Fill holes' functions were applied (Figure 3-43). In replicate 1 the rolling projection improved the signal, showing a more step-wise progression in frames 6-8 in comparison with the original processing protocol (Figure 3-43A). However, in replicate 2 the projection data was identical to the original protocol (Figure 3-43B). It was evident that the 'Fill holes' function was unreliable and depended largely on the quality of the input file.

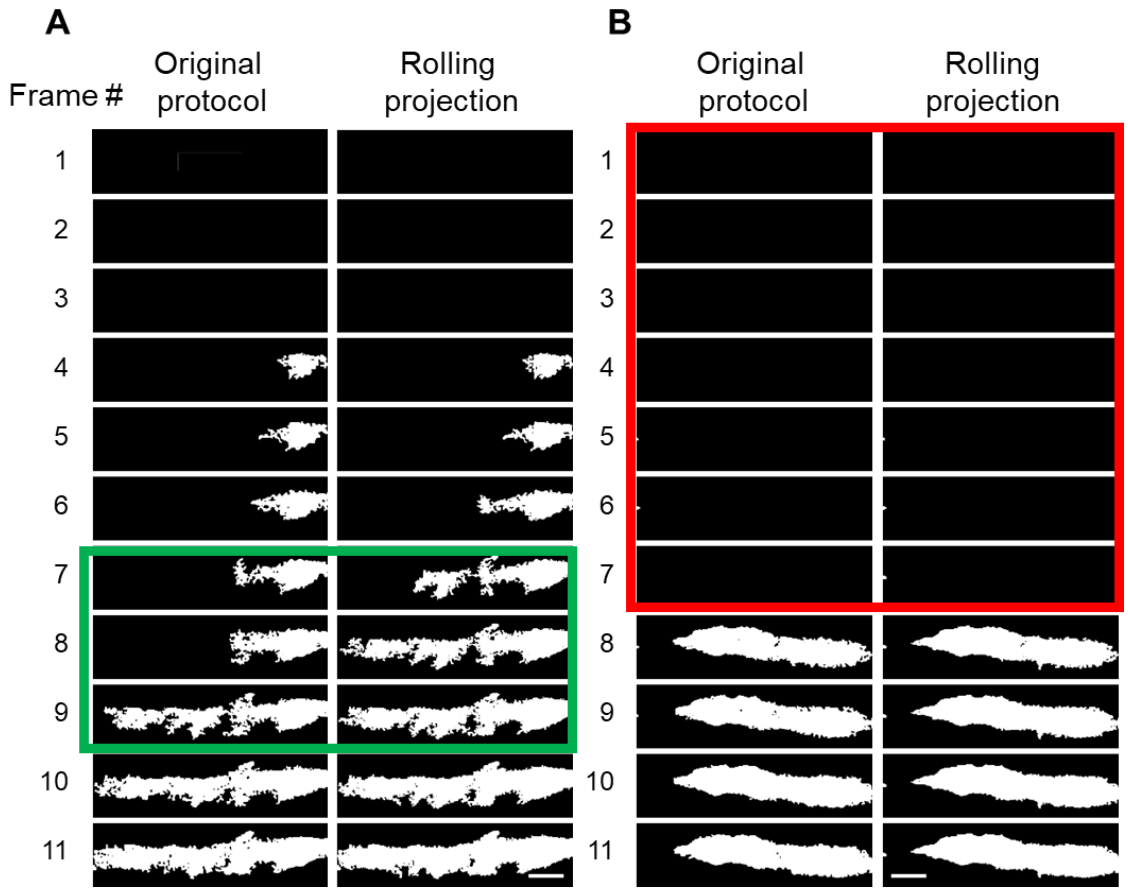


Figure 3-43 ***Processed frames of the calcium videos using the original pre-processing protocol (left) or the updated protocol with a rolling projection preceding the binary function step.*** *Original protocol refers to the pre-processing algorithm outlined in Figure 3-41. (A). Replicate 1. Introducing the rolling projection improved signal progression in frames 8-9 of the sample from Figure 3-42B. (B). Replicate 2. Introducing the rolling projection did not improve the signal progression in frames 8-9 of the sample from Figure 3-42C. Green box indicates frames with reduced pre-processing artefact, red box indicates the frames with sustained artefact. Scale bars = 200 µm.*

To investigate the need for 'Fill holes' binary function step, the sample that was successfully pre-processed without artefacts (Figure 3-42A) was thus processed up to 'Close gaps' in conjunction with the MATLAB code for angular quantification. The histogram appeared isotropic, with the angle distribution showing strong components at 0°, 90°, 180° and 270° (Figure 3-44A). This artefact likely was caused by the square shape of the pixels limiting the vector direction to 90° increments. Next, the same sample was fully pre-processed, including the 'Fill holes' function and also analysed with MATLAB. The angle distribution increased the frequency of angles around 0° approximately 20-fold Figure 3-44B). The same 0°, 90°, 180° and 270 components were still visible, but at a much lower magnitude. It is possible that the 'Fill holes' function applies smoothing to the binary image, thereby reducing the effect of pixel geometry on calculated vector angles. As a result, the data would be averaged and produce combined 'colonies' of pixels, which would also increase individual distanced travelled for each pixel, and, consequently, increase the weighting of the dominant angular vectors. Therefore, the pre-processing algorithm would introduce an inherent directionality bias to the data, making it an inappropriate directionality quantification method.

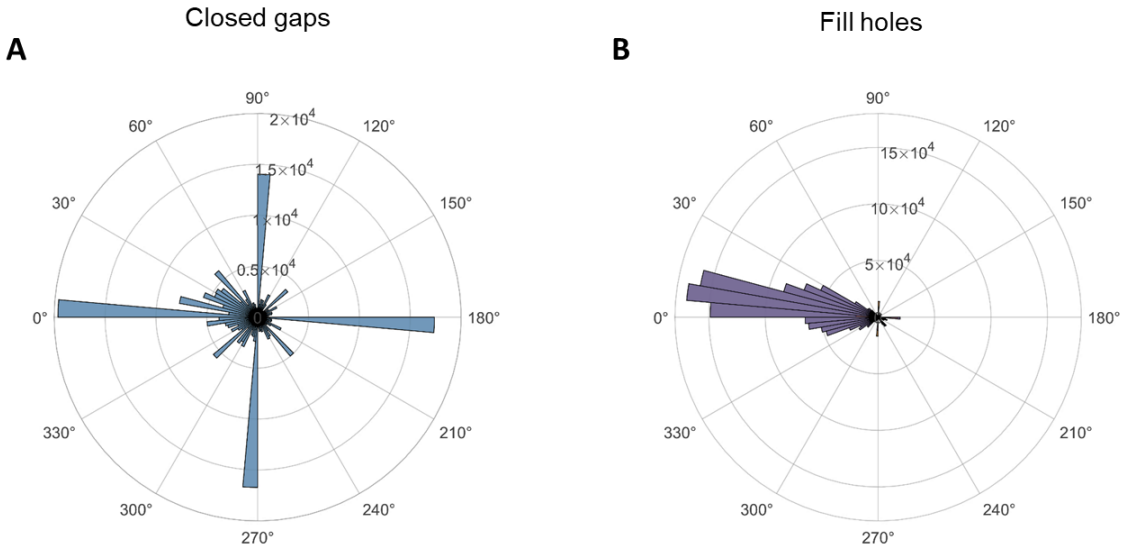


Figure 3-44 ***The effect of 'Close gaps' and 'Fill holes' binary functions on the vector angle distribution of calcium propagation signal in the sample from Figure 3-42A.*** *Closed gaps refers to the pre-processing protocol applied only up to 'Closed gaps' function. Fill holes refers to the pre-processing protocol that includes both 'Closed gaps' and 'Fill holes' functions.*

Overall, while some efforts were made to quantify the direction of calcium signal propagation, there was a significant bias introduced by signal pre-processing and this method was not pursued further. Future improvements in signal propagation data acquisition at a higher acquisition rate and improved signal-to-noise ratio would likely improve compatibility of the data with this analysis protocol.

The trade-off between the temporal and spatial resolution of the camera was a major limitation of the data used for directionality studies. The sampling rate for calcium transient recordings varies depending on the type of analysis and desired magnification, with higher magnification and calcium transient kinetics analysis usually requiring higher sampling rates. 100 fps is an acceptable frame rate for calcium recordings at low magnification, which was the highest possible to achieve within the hardware of Axio Observer Z1 microscope, making the temporal resolution of the results sufficient and comparable to others in literature (Dempsey et al., 2016; Lauterbach et al., 2015; Ronaldson-Bouchard et al., 2018). However, to achieve this rate, 4 × 4 binning was applied during the image acquisition, significantly reducing the quality of the acquired signal. Higher magnification could be used to improve the signal-to-noise ratio; however the field of view would be reduced and the structural anisotropy of the cardiac fibres would not be visible. 100 fps acquisition rate at 10x magnification was therefore considered a reasonable compromise.

The low spatial resolution also led to limitations within the analysis of functional anisotropy. While it was possible to assess how the signal propagates parallel to the cardiomyocyte alignment with acoustics, the lateral signal propagation could not be measured due to low signal-to-noise ratio on the scale of cardiac fibre width (≈150-200 μm), therefore the functional anisotropy of the cardiac fibres was not fully evaluated. Overall, while it was possible to conclude some directionality of calcium signal within the cardiac fibres, more advanced calcium imaging setup is required for its high throughput quantification. Finally, it should be noted that the imaging was performed on a single plane, therefore the propagation in 3D was unaccounted for.

3.4.5.3 Electrical field stimulation of acoustically-patterned hydrogels

Calcium traces were also recorded during electrical stimulation to investigate the responsiveness of the constructs during pacing. The typical stimulation profile started with 15 seconds of spontaneous signal recording, followed by 15 seconds stimulation at 1 Hz, 2 Hz and 3 Hz, separated by 15 second resting intervals in between subsequent frequency increases (Figure 3-45). The data was collected from 14 patterned gels, each containing between 7 and 30 active cardiac fibres acting as individual region of interest (ROI). 6 unpatterned gels were analysed as controls, with ROI numbers ranging from 1 to 13, where each ROI contained an isolated calcium-active region. The peaks of calcium activity were detected from the intensity traces, and the interval between them was used to calculate the output frequency of each active region during pacing (Figure 3-46).

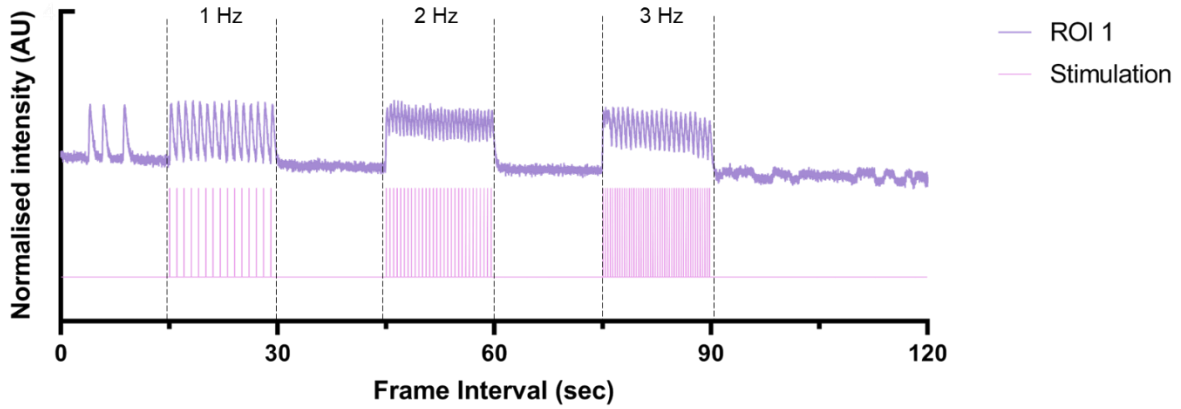


Figure 3-45 ***A typical stimulation profile and a representative output trace from a single regin of interest (ROI) during the electrical field stimulation experiments.*** *The stimulation profile is shown in pink, and the response recorded from a cardiac fibre is shown in purple. 15 seconds of spontaneous activity recorded prior to 15 second-long 1 Hz stimulation, followed by 15 seconds rest, 15 seconds of 2 Hz stimulation, another 15 seconds of rest and the final 15 second 3 Hz stimulation. The recording continued for another 30 seconds in the absence of field stimulation. All stimulation performed at 15 V, 20 ms.*

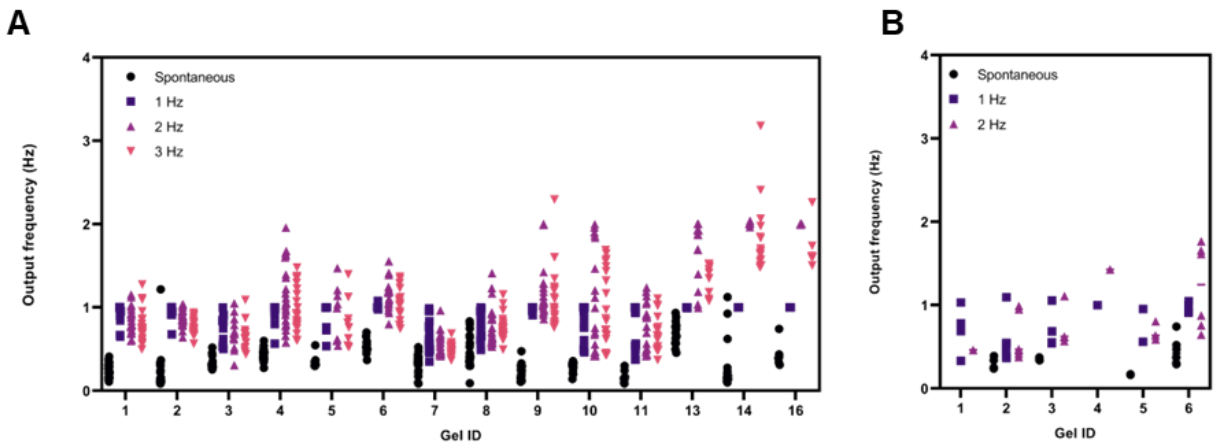


Figure 3-46 ***Calculated output frequency distribution in patterned (A) and unpatterned (B) samples during spontaneous calcium activity and during 1 Hz, 2 Hz and 3 Hz pacing.*** *Each data point represents a single ROI. The gel ID refers indicates different biological replicates. Gel ID of patterned and unpatterned samples were assigned independently. Patterned N = 14, n = 7 – 30, unpatterned N = 6, n = 1-13. N is the number of analysed independent gels, n is the number of calcium-handling lines (or independent active regions for the unpatterned controls).*

The output frequency for both conditions increased significantly when electrical stimulation was applied at 1 Hz, 2 Hz and 3 Hz ($p \leq 0.0001$ for all comparisons, Table 3-6). The mean spontaneous frequency of patterned cardiac fibres and unpatterned controls was comparable, with 0.35 ± 0.19 Hz and 0.32 ± 0.11 Hz respectively and no significant statistical difference detected ($p = 0.60$, Figure 3-47, Table 3-7). The majority of the cardiac fibres were able to closely match the input frequency at 1 Hz, with mean output frequency of 0.88 ± 0.18 Hz. This was significantly higher than the unpatterned samples, with 0.67 ± 0.23 Hz average frequency ($p < 0.0001$, Table 3-7). The unpatterned data was bimodally distributed, suggesting there were two populations of calcium-handling regions: those that were nearly following the pacing, and those that were not (Figure 3-47). The same type of distribution was observed for the patterned dataset paced at 2 Hz: while the average output frequency of 1.02 ± 0.47 Hz showed that most cardiac fibres were generally unable to follow this stimulation, a small cluster of ROIs successfully produced an output of 2 Hz (Figure 3-47). The mean output frequency for unpatterned control at 2 Hz was at 0.74 ± 0.36 Hz, significantly smaller than the patterned ($p < 0.0001$, Table 3-7). Patterned samples were also subjected to a 3 Hz stimulation, generating a large range of output frequencies spanning between 0.36 and 3.18 Hz with 0.91 ± 0.41 Hz mean, and demonstrating the lack of consistent electrophysiological response. Taken together, these results showed that acoustically patterned cardiac fibres respond better to the

external electrical stimulation that the disorganised unpatterned controls but the majority are not able to follow the stimulation beyond 1 Hz.

Table 3-6 ***Significance testing of effects of electrical stimulation on output frequency using repeated measures mixed effects model with Tukey's multiple comparisons correction and Geisser-Greenhouse correction.*** *Adjusted p-values reported. Sp – spontaneous. Patterned N = 14, n = 7-30, unpatterned N = 6, n = 1-13. N is the number of analysed independent gels, n is the number of calcium-handling lines (or independent active regions for the unpatterned controls).*

Comparison	Patterned p-value	Unpatterned p-value
Sp vs 1 Hz	<0.0001	<0.0001
Sp vs 2 Hz	<0.0001	<0.0001
Sp vs 3 Hz	<0.0001	N/A

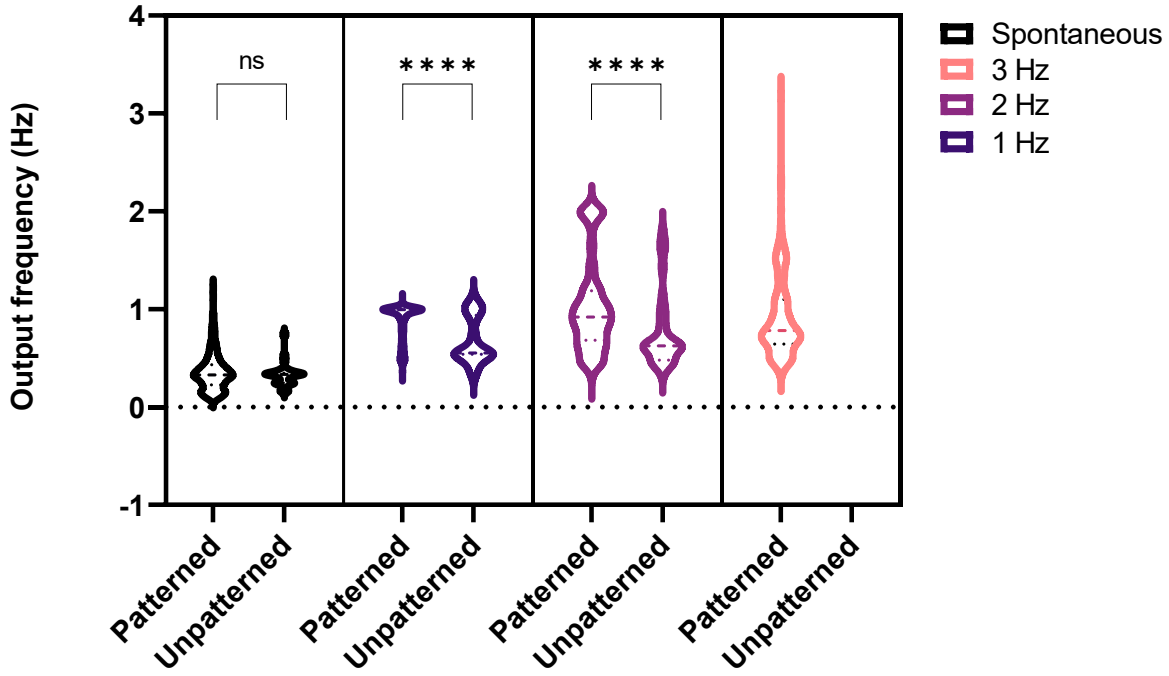


Figure 3-47 ***Recorded output frequency of calcium signal in acoustically-patterned cardiac fibres and unpatterned controls under 1 Hz, 2 Hz, 3 Hz electrical field stimulation.*** *Violin plots showing the median and the interquartile range (dashed lines) of the patterned and unpatterned samples at each stimulation frequency. Statistical significance calculated using a two-tailed Mann Whitney test. ns – p > 0.05, **** p < 0.0001. Patterned N = 14, n = 7-30, unpatterned N = 6, n = 1-13. N is the number of analysed independent gels, n is the number of calcium-handling lines (or independent active regions for the unpatterned controls).*

Table 3-7 ***Significance testing of differences in output frequency response to electrical field stimulation between patterned and unpatterned in situ differentiated cardiac hydrogels. T****wo-tailed unpaired Mann-Whitney test. Patterned N = 14, n = 7-30, unpatterned N = 6, n = 1-13. N is the number of analysed independent gels, n is the number of calcium-handling lines (or independent active regions for the unpatterned controls).*

Comparison (Patterned vs Unpatterned)	p-value	Significance
Spontaneous	0.5987	ns
1 Hz	<0.0001	****
2 Hz	<0.0001	****

The natural frequency of adult human cardiomyocytes is at ≈1 Hz, therefore the functionality of the engineered cardiac tissue should be assessed at this physiological frequency. The spontaneous activity of *in situ* differentiated cardiac hydrogels was significantly lower than that, consistent with electrophysiological parameters of other immature hiPSC-CM systems (Davis et al., 2021; Feyen et al., 2020). The cardiac fibres precisely and consistently followed the pacing when an external electrical field was supplied with 1 Hz input frequency, producing a physiologically relevant response upon stimulation. Such modality can be exploited in a drug screening context, evaluating whether the pacing ability is maintained upon the application of a drug of interest and identifying any incidents of arrythmia.

The patterned cardiac fibres showed a more advanced electrophysiological response to field stimulation than the unpatterned controls. This is consistent with other studies, demonstrating improved calcium dynamics in micropatterned hiPSC-CMs (Rao et al., 2013; Feinberg et al., 2013; Pong et al., 2011). However, the role of anisotropy on calcium handling parameters in cardiomyocytes has previously showed inconsistent results, with some studies reporting no observable effects (Xu et al., 2017; Rodriguez et al., 2019). An in-depth analysis of calcium transient kinetics, along with a detailed investigation on the hiPSC-CM ultrastructure, would be required to understand how the organisation of acoustically-patterned cardiac fibres relates to their more advanced electrophysiological response in comparison to randomly arranged unpatterned controls. Additionally, other factors arising from *in situ* differentiation such as differences in local cell densities

and ratios of cardiomyocytes to non-cardiomyocyte cell types between patterned and unpatterned samples could also have an effect on their electrophysiology (King et al., 2022).

The lack of pacing at higher frequencies was likely due to relatively short culture times, as the acoustically-patterned cardiac hydrogels were grown only up to 20 days. In literature, hiPSC-CMs were previously shown to capture frequencies up to 6 Hz (Ronaldson-Bouchard et al., 2018). However, the culture lasted over 33 days and included intensity-training, with cardiomyocytes exposed to field stimulation with frequency increasing daily throughout the culture, making it incomparable with the results described above. While the ability of the cells to follow high frequency pacing would demonstrate further functional flexibility and advanced electrophysiological machinery of the system, the ability of most cardiac fibres to follow 1 Hz stimulation is a sufficient modality for a human drug screening platform.

3.5 Conclusions and future work

In this chapter, a new device for acoustic cell manipulation was successfully designed, fabricated and applied to pattern hiPSCs in GelMA hydrogels. The optimal degree of functionalisation of GelMA hydrogels was determined, with formulations above 80% best supporting the survival and growth of hiPSCs. To mediate UV-mediated toxicity observed in the early studies of crosslinked hydrogels, an alternative light source with peak emission in the visible 405 nm wavelength was implemented to optimise the gelation timing of two potential biomaterials, enhance hiPSC viability and reduce the risk of mutations. A range of assessments then evaluated the effects of ultrasound and light exposure on hiPSC survival and behaviour. Viability, proliferation, metabolic activity and pluripotency of hiPSCs were shown to be unperturbed by exposure to ultrasound and light, highlighting the compatibility of the protocol with stem cell cultures.

During cell culture, the softer fish GelMA provided a more favourable environment for hiPSC growth, however, its material properties caused a reduction in hiPSC clusters' length, leading to the loss of patterning. Reducing the timing of differentiation initiation (CHIR-triggered mesoderm induction) to

1 day successfully preserved high quality hiPSC arrays throughout differentiation, leading to formation of linear functional cardiac constructs in both fish and porcine GelMA. Since porcine hydrogels demonstrated higher stiffness than fish hydrogels, as shown by rheology data, they were chosen as the final hydrogel composition, closer resembling the stiffness of cardiac ECM. By using two strategies for hiPSC array encapsulation prior to differentiation, two distinctly different cardiac tissues were successfully produced, having the potential to tune the presence or absence of interconnectivity in adjacent cardiac fibres depending on the target application of these *in vitro* models.

The patterning was found to have little effect on the dynamics of gene expression of key markers over the course of differentiation, however the patterned samples demonstrated a much more prominent formation of continuous structures with highly expressed cardiac markers than the controls, visualised by immunofluorescent labelling. *In situ* differentiation also allowed to generate non-cardiac cell types usually represented in the native myocardium, with endothelial and myofibroblast/smooth muscle phenotypes detected in both patterned and unpatterned constructs. Interestingly, the patterned hydrogels exhibited an improved electrophysiological functionality of the tissue, demonstrated by better frequency capture during electrical stimulation than the unpatterned controls. Restricting the cells to a linear geometry using ultrasound also led to spontaneous calcium signal consistently parallel to the long axis of the cardiac constructs. The predictability of propagation path in the acoustically-patterned cardiac fibres makes them useful tools to investigate the effects of different treatments on calcium signal transmission.

Overall, this study demonstrated that applying an acoustic field to hiPSCs prior to differentiation can be used to engineer complex heterocellular cardiac tissues containing macrostructured fibres with physiologically relevant dimensions. However, there were several considerations in this work. Firstly, while hydrogel encapsulation allows to produce tissues in 3D, the force of gravity accumulates the cells at the bottom of the hydrogel, making the tissue thickness limited to approximately 100 µm,

making it a 2.5D rather than a 3D model. To address this, more advanced 3D acoustic patterning strategies could be implemented in the future, for example by using pre-gel material density modulation or through 3D acoustic hologram-based patterning (Armstrong et al., 2022; Melde et al., 2022).

Secondly, rheology demonstrated large variance in material stiffness of commercial GelMA which could have led to a larger gel-to-gel variability in characterisation results. Future studies should include a systematic GelMA optimisation (e.g. synthesis optimisation to reduce variance, photoinitiator concentration optimisation) for hiPSC culture and differentiation, as well as full characterisation of the properties of the final material (dynamics of finalised GelMA formulation crosslinking under blue light, NMR to measure degree of methacrylation).

Thirdly, gene expression analysis showed conflicting results, with significantly larger *TNNT2* fold change from day 1 to day 20 in unpatterned samples than in patterned. This was inconsistent with the immunofluorescent imaging of its corresponding protein cTnT which was significantly more pronounced in the patterned samples, as well as the RT-qPCR analysis at endpoint day 20, where *TNNT2* showed no difference between patterned and unpatterned samples. A direct comparison of *TNNT2* expression between patterned and unpatterned samples at d1 with a common calibrator, for example a monolayer of hiPSCs, would help to elucidate the cause of this discrepancy. Furthermore, flow cytometry could be performed to quantify and compare the ratios of the different cell types in patterned and unpatterned samples.

Fourthly, although the heterogeneity of cell phenotypes within the *in situ* cardiac fibres is more representative of the native myocardium, the differences in proliferation rates of those cell types could lead to complications in long-term cell culture, with non-myocytes outcompeting the cardiomyocyte population. If such challenges arise, metabolic selection on patterned hydrogels could be implemented to allow for significantly longer-term experiments.

Additionally, while the directional propagation in acoustically-patterned cardiac fibres was observed consistently, the platform would benefit from an in-depth characterisation of the structural and functional anisotropy. It would be interesting to investigate whether the patterning caused the microscopic alignment of individual cardiomyocytes within the cardiac fibre as well as the bulk tissue alignment. High-resolution optical mapping would also provide quantitative information on longitudinal and transverse conduction velocities during signal propagation. Notably, a comparison between bottom-up and top-down engineering approaches could be included, determining the possible structural and functional benefits of *in situ* differentiated cardiac fibres over pre-differentiated acoustically-aligned hiPSC-CMs.

Furthermore, although the independence of adjacent cardiac fibres was apparent from viability staining, immunofluorescent staining, and calcium transient imaging, quantifying these results through phase-frequency comparison of independent and interconnected constructs could strengthen the observation. Some groundwork on the image pre-processing protocol has been laid out through the nearest distance transformations, and areas for further improvement of image pre-processing have been identified to allow for more precise and unbiased propagation angle quantification.

Importantly, the work described in this chapter has successfully shown for the first time the application of acoustic cell patterning with hiPSCs and *in situ* differentiation protocols, yielding a novel biomimetic *in vitro* cardiac tissue engineered platform with distinctly micropatterned functional cardiac fibres. The optimisation of functional independence between adjacent cardiac fibres ensured that each acoustically-patterned hydrogel contained several internal technical replicates, while the genetically-encoded calcium indicator allowed for successful imaging of calcium transients as a potential quantifiable output. These features would be particularly useful for drug screening applications. The extensive characterisation of the patterned constructs sets them up well for the initial proof-of-concept drug screening studies with known inotropic compounds, such as

metoprolol and isoproterenol. Finally, *in situ* differentiation of acoustically-patterned disease-specific hiPSC cell lines would be an key advancement towards disease modelling and personallised medicine.

To conclude, the work in this chapter demonstrates how *in situ* differentiation can be combined with patterning approaches such as acoustic cell manipulation to produce a functional aligned engineered cardiac tissue for drug screening and, possibly disease modelling applications. The next chapter will explore an alternative application of *in situ* differentiation in a material-guided cell patterning approach with an outlook for cardiac tissue remuscularisation.

CHAPTER 4. INTERCONNECTED FIBRE-REINFORCED CARDIAC SCAFFOLDS FOR TISSUE REMUSCULARISATION

4.1 Introduction and motivation

Ischemic heart disease is caused by a disruption in oxygen supply to the myocardium, and, if left untreated, leads to myocardial infarction followed by severe cardiomyocyte death and fibrosis (Li et al., 2007). The proliferation rate of the cells residing in the myocardium (≈1% turnover per year in adult humans) is not sufficient for regeneration, deeming the loss of adult cardiomyocytes essentially irreversible (Eschenhagen et al., 2017; Bahit, Kochar & Granger, 2018; Bergmann et al., 2009). Available surgical and pharmacological treatments are only palliative and do not address the issue of severe cell death (Saludas et al., 2017). With whole-heart transplantation as the main treatment option heavily relying on donor compatibility and availability, cell therapies with exogenous cardiomyocytes administered at different stages of disease progression have been extensively explored as a strategy for cardiac regeneration (Alrefai et al., 2015; Jain et al., 2001; Park et al., 2019; Zhang et al., 2005; Ban et al., 2014). While there is a vast amount of literature on delivery of other, non-cardiomyocyte cell types (e.g. ESC and hiPSC stem cells, mesenchymal stem cells, skeletal myoblasts, fibroblasts, and others), only cardiac lineage-committed cells would be capable of functional remuscularisation of the cardiac muscle without the risk of teratoma formation or off-target cell differentiation (He & Chen, 2020; Laflamme & Murry, 2011; Nussbaum et al., 2007). Therefore, in the below discussion cardiomyocyte-based delivery strategies were prioritised where possible, and all c-kit$^+$ 'cardiac stem cell' studies were omitted due to the recent discovery of their endothelial, rather than cardiac stem cell, identity (Kretzschmar et al., 2018; Sultana et al., 2015).

4.1.1 Approaches and challenges of cardiomyocyte cell therapies

4.1.1.1 Intramyocardial injection for cardiomyocyte delivery

Recent advances in hiPSC/hESC cardiac differentiation protocols offer an excellent alternative source of functional exogenous cardiomyocytes for myocardial repair, with the promise of autologous transplants generated from patient-specific samples with reduced immunogenicity compared to allogeneic cardiomyocytes (Sharma, Wu & Wu, 2013; Guha et al., 2013). To deliver exogenous cells to an infarcted area, intramyocardial injection of hiPSC-CMs in solution has been used in several studies with inconsistent outcomes (Caspi et al., 2007; Citro et al., 2014; Zhao et al., 2018). Survival and homing of hESC-CMs injected into infarcted rat hearts were associated with functional restoration up to 30 days post-transplantation (Caspi et al., 2007). Injecting hiPSC-CMs into rat myocardium also improved cardiac function and reduced fibrosis (Citro et al., 2014). However, while some exogenous cells were detected 4 weeks post-injection, the extent of delivery or the functional coupling with the native tissue were not assessed. Similarly, although a restoration of myocardial function was observed 4 weeks after injection during the subacute stage of myocardial infarction in primates, the low number of exogenous cells failed to fully remuscularise the damaged muscle (Zhao et al., 2018). Importantly, the grafting success in all the above studies was not quantified, providing only a qualitative evaluation of cell retention. The observed functional improvements are attributed to paracrine effects of the secretome, neoangiogenesis and inflammation, consistent with the results of other non-cardiomyocyte-based cell therapies (Santoso et al., 2020; Menasché, 2020; Alrefai et al., 2019; Sanganalmath & Bolli, 2013). Increasing cell retention and encouraging the remuscularisation of the damaged myocardium therefore remains a goal of cardiac regenerative medicine.

Monitoring the cells immediately post-injection demonstrated that the majority of the cell loss occurs in the early hours of transplantation, with the data from two independent studies ranging from 6.9±5.9% to 13.4±3.4% explanted cells detected 3-4 hours post-administration (Li et al., 2021b; Collantes et al., 2017; Zlabinger et al., 2018). The mechanical washout, the hostile environment of the infarction zone, the absence of supporting ECM, and the shear forces generated during injection are likely among the effects that reduce the survival and retention of the transplanted

cardiomyocytes (Abdelwahid et al., 2015; Feyen et al., 2017). Several strategies have been implemented to improve retention up to clinically relevant levels, for example by using immunosuppressants, cell aggregation into spheroids prior to injection, or injecting a huge excess (4-7.5 × 10^8 cardiomyocytes) into the host tissue (Mattapally et al., 2018; Liu et al., 2018b; Guan et al., 2020; Shiba et al., 2016). However, despite these attempts, the delivery efficiency remains relatively low, and the functional integration of the graft with the host is not certain. Moreover, the non-specific delivery of freely injected cells to other organs continues to be a source of concern (Hou et al., 2005).

4.1.1.2 Injectable hydrogel-based systems for increased cardiomyocyte retention

Biomaterials can be used as vehicles for cell therapy to improve the targeting and retention of exogenous cardiomyocytes during transplantation. Hydrogels can provide a matrix for exogenous cell delivery and hinder them from the harsh microenvironment of the infarct while keeping the cells localised and minimising mechanical washout (Wu & Liu, 2022). The versatility of available hydrogel formulations and modifications allows the material physical and chemical properties to be tailored to the application, for example by matching the stiffness of the heart, improving cell adhesion to the matrix, reducing oxidative stress or inducing angiogenesis (Peña et al., 2018; Wang et al., 2019; Yao et al., 2015). Co-injecting thermo-responsive hydrogels, such as chitosan, with exogenous cardiomyocytes has permitted cell encapsulation *in situ,* leading to a 2-fold retention increase and moderate improvement in cardiac function (Lu et al., 2009).

Pre-formed cell-laden hydrogels have also been used, with PEG hydrogel-encapsulated cardiac progenitor cells injection into mouse heart showing 6.5- and 2.6-fold increase in retention in comparison to solution control 3 and 7 days after administration respectively (Speidel et al., 2017). However, in this study no signal was detected 14 days after injection. In a follow-up study, no engraftment of hiPSC-CMs was observed 10 weeks post PEG hydrogel administration, however, myocardial remodelling was reduced, and ejection fraction (a proportion of ejected blood over total

volume of the heart) was improved significantly in comparison to the control (Chow et al., 2017). In contrast, when mouse ESC-CMs were delivered to the myocardium within self-assembling peptide amphiphilic hydrogels, the cells were still detected in the host tissue after 14 weeks (Ban et al., 2014). Similarly, injection of hiPSC-CMs within a nanocolloidal gelatin-based hydrogel showed a two-fold increase in retention in comparison to solution-injected cells; however, this number was negligible relative to the cell density of the target tissue (Wu et al., 2023). Furthermore, it was not confirmed whether the cells in the above studies exited the material matrix and infiltrated the host tissue. Controlling the rate of hydrogel degradation can be used to gradually reduce the biomaterial thickness and encourage host-graft interactions. For example, using MMP-2-sensitive hyaluronic acid-based hydrogel for hiPSC-CM delivery has been shown to significantly decrease the infarct and scarring areas, as well as improve the ejection fraction of the heart in comparison to saline cell injection (Li et al., 2021a). Despite a clear increase in cell retention in comparison to MMP-2-insensitive control, after hydrogel degradation at 4 weeks the cell numbers rapidly declined, suggesting a limited timescale of cell homing.

While this is a non-exhaustive account of the injectable hydrogel systems, taken together the above studies are characterised by three main outcomes. i) Injectable hydrogels can further improve the functional benefits of intramyocardial injection cell delivery; ii) encapsulating cardiomyocytes in hydrogels can moderately improve cell retention in comparison to saline injection; iii) the extent of the cardiomyocyte retention is not sufficient to explain the functional benefits of the therapy. The decrease in infarct site, thickening of the ventricular wall, improved ejection fraction and fractional shortening are likely caused by the synergy of the structural support of the biomaterial and early paracrine effects of the encapsulated cells, rather than remuscularisation of the damaged myocardium (Zheng et al., 2021; Li et al., 2020a). There are also practical limitations to intramyocardial injection of hydrogels, such as needle-induced tissue damage and a lack of stable interface between the material and the infarction area. As the heart is constantly contracting, the

hydrogel can be displaced away from the infarction zone, minimising its benefits, and leading to off-target delivery.

4.1.1.3 Cardiac patches as an alternative mode of cell therapy

Targeted delivery of exogenous cells using cardiac patches secured directly on the heart by ligation, suturing or adhesives can be used to address the above concerns (Mei & Cheng, 2020). 3D hydrogel-based hiPSC-CM systems, sometimes known as engineered heart tissues (EHTs), have been fabricated and affixed to the heart in a number of studies (Gao et al., 2018; Wendel et al., 2015; Riegler et al., 2015; Schaaf et al., 2011; Zimmermann et al., 2006; Weinberger et al., 2016). For example, a fibrin patch, loaded with hiPSC-CMs and other cell types, was still detected at the surgery site after 4 weeks, along with improved cardiac function and neovasculature formation (Gao et al., 2018). However, only 11% retention was reported, and host-graft electrical coupling was not investigated. When examining the ligation site 4 weeks post-surgery, a layer of collagenous tissue separating the graft from the host was observed (Wendel et al., 2015). Despite the absence of direct contact, improved cardiac function and *de novo* microvasculature formation were reported, confirming the predominant role of paracrine effects and structural support of hydrogel-based cell therapies. Likewise, despite 25% cell retention 4 weeks post-surgery, a thin layer of fibrotic tissue was present at the interface between a collagen-based graft and the host (Riegler et al., 2015). In the same study, acellular patches improved cardiac function to the same extent as cellularised constructs, questioning the role of cardiomyocyte delivery entirely.

Eschenhagen and colleagues have been optimising culture conditions of complex fibrin-based EHTs, designed to advance the maturation state of encapsulated hiPSC-CMs through sustained mechanical and electrical stimulation (Schaaf et al., 2011; Zimmermann et al., 2006; Hirt et al., 2014; Jabbour et al., 2021; Weinberger et al., 2016). A promising 12% of the infarct area was remuscularised 4 weeks after implanting their EHTs on infarcted guinea pig hearts, with a small number of animals showing

electrical coupling with the host (Weinberger et al., 2016). However, a large electrophysiologically-advanced hiPSC-CM-fibrin patch affixed to a rabbit heart showed a decline down to 20% cell retention after 4 weeks, fibrotic tissue at the host-graft border zone and no functional coupling (Jabbour et al., 2021). Despite the lack of integration, host vasculature was invading the graft, infarct size was reduced, and partial restoration of cardiac function was still observed. Similarly, despite an improvement in graft vascularisation and wall thickness, penetrating further into the infarcted tissue with poly(vinyl alcohol) microneedles did not lead to remuscularisation 3 weeks post-surgery (Tang et al., 2018).

Due to heterogeneity in methodology (e.g. retention quantification, surgery types, patch delivery sites and disease stages, animal models, and functional coupling assessments), it is challenging to draw conclusive comparisons between all the systems described above. There do appear to be functional benefits to cardiac patch implantation to the infarcted heart, although the exact mechanisms remain unknown and insufficient graft-host integration and lack of remuscularisation are consistently reported. Several speculations surround the poor engraftment of existing cardiac patches. One of them could be that the implantation of biomaterials provokes a strong foreign body response, leading to inflammation and the formation of a scar layer between the graft and the host. Alternatively, the hydrogel network encapsulating cardiomyocytes itself could be acting as a barrier, constraining effective cell-cell contact formation. With some hydrogels incorporating cell adhesion proteins, the exogenous cells might preferentially reside within the graft as it contains more favourable conditions than the hypoxic inflammatory infarct site (Chen et al., 2010). In this chapter, it is hypothesised that those challenges can be addressed by a reverse approach to cardiac patch engineering: using the biomaterial as a substrate for *in situ* expansion and differentiation, thereby enclosing the material within a cell mass. It is speculated that a direct interface between microstructurally-organised exogenous cells and the native myocardium would promote cell transfer and integration.

4.1.2 Electrospinning methods for cardiac tissue engineering

4.1.2.1 Principles of electrospinning

Solid polymeric fibrous scaffolds are a class of structured material substrates often used for cardiac tissue engineering. Comprised of nano- to micro-scale diameter fibres, these scaffolds are characterised by their high surface-to-volume ratio and high mechanical strength, making them useful ECM mimics that provide structural support for cell adhesion. There are numerous methods to generate fibre-like structures, for example self-assembly, fibre deposition modelling and 3D-printing, however they suffer from a limited range of available material chemistries and low fibre resolution (Bhardwaj & Kundu, 2010; Bi & Huang, 2022).

Electrospinning is one of the most popular methods for manufacturing fibrous substrates. Compatible with a wide range of synthetic and natural polymers, it is used to produce uniform fibres with tightly-controlled diameters, ranging from 3 to 5000 nm (Subbiah et al., 2005; Meireles et al., 2018). Typically, an electrospinning device consists of a polymer-loaded syringe with a needle, a high voltage source and a conductive collector (Unnithan, Arathyram & Kim, 2015; Muthukrishnan, 2022; Kitsara et al., 2017). A pressure pump continuously drives the polymer solution or melt into the needle supplied with voltage. The resultant electrostatic forces acting on a liquid droplet exceed the surface tension, forming a conical shape at the needle tip, known as a Taylor cone. When the applied voltage surpasses a critical threshold, a thin strand of polymer is ejected across the high potential electric field, landing onto a collector acting as a grounded counter electrode, leading to fibre deposition. The properties of the resultant fibrous scaffolds can be controlled by varying the parameters of the polymer (e.g. molecular weight, concentration, viscosity, conductivity), the setup (flow rate, voltage, distance to the collector, collector configuration) or spinning environment (temperature and humidity) (Kitsara et al., 2017). There are numerous modifications to the electrospinning technique, including but not limited to multi-axial, needle-free, ultrasound-

enhanced, gas-assisted, temperature-assisted electrospinning methods, allowing to produce an array of polymeric fibrous scaffold types (Muthukrishnan, 2022).

Based on the polymer state prior to fabrication, electrospinning methods can be divided into two categories: solution and melt electrospinning. Solution methods rely on the solubilisation of the polymer in a suitable solvent, that subsequently evaporates during jetting. Charge density accumulation during solvent evaporation, combined with low viscosity and high conductivity, results in electrostatic repulsion forces that overcome surface tension, resulting in buckling and whipping of the jet. However, unidirectional alignment of the fibres on the deposited scaffold can be achieved using a rotating collector, which has been used extensively to replicate the structure of the cardiac ECM and used to guide cardiomyocyte orientation (Han et al., 2016; Hsiao et al., 2013; Kai et al., 2011; Khan et al., 2015; J. Li et al., 2016; Y. Liu et al., 2016; Wanjare et al., 2017). To that effect, both isolated neonatal rat cardiomyocytes and hiPSC-CMs have been shown to align with the electrospun fibres, showing contractile and electrical improvements in maturation relative to unpatterned controls (Khan et al., 2015; Wanjare et al., 2017; Liu et al., 2016; Kai et al., 2011; Li et al., 2016a).

4.1.2.2 Melt electrospinning writing

Although solution electrospinning is used across a wide variety of biomedical applications, it can be limited by solvent-polymer compatibility and reliance on halogenated and toxic solvents (chloroform, trifluoroethanol, dimethylformamide) (Avossa et al., 2022). Furthermore, the global architecture of the scaffold is poorly controlled due to the electrostatic repulsion of adjacent deposited fibres and an inherent lack of multidirectional control during deposition. Melt electrospinning writing (MEW) is an emerging technique whereby the polymer in the absence of solvent is melted inside a syringe and extruded under high voltage onto a motion-controlled stage (Figure 4-1). Higher viscosity and lower conductivity of the melt produce a more stable continuous jet than solution-based methods (Aytac & Wang, 2022). Computer-encoded stage movement allows

the overall geometry of the print to be predictably defined, yielding highly-ordered scaffolds deposited layer-by-layer (Jin et al., 2021; Liashenko et al., 2020). Such precision printing is achieved at the expense of thermoplastic polymer availability and larger filament diameter. Nevertheless, micron-scale fibres have been shown to be compatible with cell adhesion, leaving material compatibility as the main limitation of MEW (Pham, Sharma & Mikos, 2006). Low melting temperature and rapid solidification of polycaprolactone (PCL) makes it the most common polymer used for MEW, which can be further tailored by blending or co-polymerisation with other polymers (e.g. poly(hydroxymethylglycolide), poly(L-lactide-*co*-acryloyl carbonate), oligo-3,4-ethylenedioxythiophene), or doping with functional molecules (e.g. hydroxyapatite particles, poly-pyrrole) (Spicer et al., 2020; Chen et al., 2016; Castilho et al., 2017). The biocompatibility, biodegradability, and mechanical strength of PCL have made it a versatile and attractive material for tissue engineering (Malikmammadov et al., 2018; Shahverdi et al., 2022).

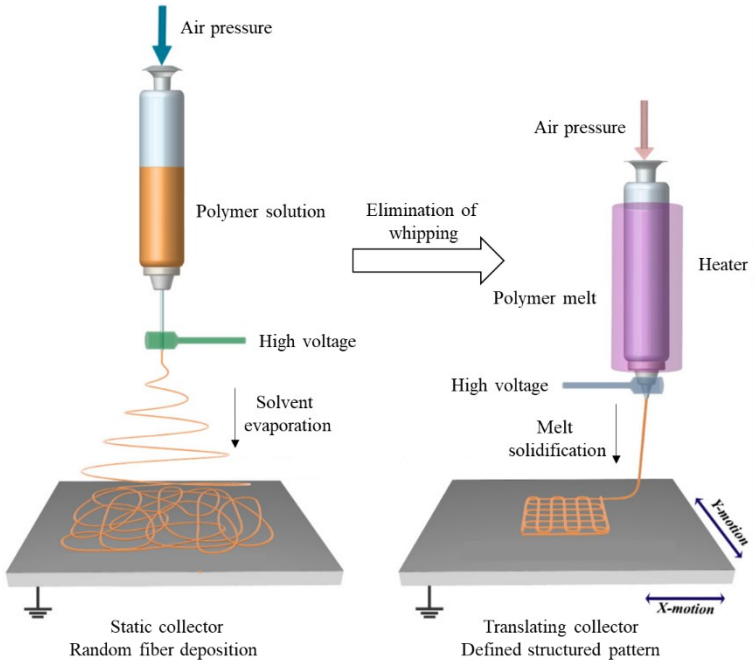


Figure 4-1 ***Electrospinning methods.*** *Solution electrospinning (left) containing a polymer solution in a syringe, which is jetted across onto a static collector leading to a random fibre deposition upon solvent evaporation. Melt electrospinning (right) implements a heater to melt the thermoplastic polymer, leading to extrusion of the melt onto a translating collector, eading to formation of a defined scaffold pattern. Figure adapted from* (Afghah et al., 2019; Hochleitner et al., 2015) *with permission under Creative Commons Licence.*

4.1.2.3 Melt electrospun fibrous scaffolds in tissue engineering

Ordered fibrous polymeric scaffolds have found a wide range of applications in bioengineering, used to produce mimics of bone, cartilage, corneal, cardiac and neural tissues (Abbasi, Ivanovski, et al., 2020; Bosworth et al., 2021; Castilho et al., 2018; Korpershoek et al., 2021; Loewner et al., 2022; Spicer et al., 2020). Broadly, there are three main modes of application for MEW scaffolds. Firstly, the printed structures can be used as acellular structures, able to withstand physiologically-relevant forces of mobile load-bearing organs. For example, implantation of calcium phosphate-coated MEW scaffolds into rodent long bone defects showed a significant increase in *de novo* bone formation after 8 weeks, while growth factor-doped PCL constructs improved the compressive modulus of injured rabbit cartilage 12 weeks post-surgery (Abbasi, Lee, et al., 2020; Y. Han et al., 2020). Auxetic electroconductive PCL-polypyrrole scaffolds were also shown to endure stress and strain similar to those of human myocardium, making them an interesting platform for future animal studies (Olvera et al., 2020).

Another approach is to use fibrous scaffolds as reinforcement of cell-laden hydrogels to provide structural support. To that effect, anisotropic scaffold geometries have been explored to replicate the structure of the myocardium. Cardiac progenitor cells encapsulated in collagen hydrogels were shown to align along the direction of rectangular poly(hydroxymethylglycolide-co-ε-caprolactone) (pHMGCL) scaffolds (Castilho et al., 2017). When a similar system was applied to hiPSC-CM, cell alignment along the direction of 200 µm-spaced rectangular PCL-reinforced collagen hydrogels was associated with an increase in conduction velocity (Montero-Calle et al., 2022). In another study, however, scaffolds with hexagonal geometry showed a significant increase in hiPSC-CM sarcomere length and ion channel expression, indicative of a more advanced maturation state than the rectangular features (Castilho et al., 2018). Patches with hexagonal geometries were also able to better withstand deformation during injection through a 26G needle, demonstrating their potential for *in vivo* applications (Castilho et al., 2018). The ongoing investigation on the inclusion of non-

cardiomyocyte cell types might further advance the hexagonal scaffold-reinforced collagen-GelMA constructs towards replicating the complexity of native myocardium (van Mil et al., 2022). Additionally, 3D tubes with serpentine microstructures embedded in elastin-like recombinamer hydrogel have allowed to mimic the architecture and mechanics of the heart valve, demonstrating the clinical relevance of MEW-reinforced hydrogels (Saidy et al., 2019., 2022).

MEW-fabricated scaffolds can also be used directly as solid 3D substrates for cell attachment and growth. This method is heavily explored in connective tissue engineering, such as bone and cartillage. For example, hMSCs successfully calcified and deposited ECM proteins on hydroxyapatite-coated PCL scaffolds (Eichholz et al., 2021, 2022). In another study, meniscus cells and hMSCs were cultured on MEW-printed PCL scaffolds for 28 days, showing a gradual increase in yield stress, ultimate strength and proteoglycan deposition of the cell-laden constructs (Korpershoek et al., 2021). Varying the spacing between the units of the MEW-fabricated scaffolds also has provided mechanistic insights into the effects of scaffold dimensions on differentiation potentials of hMSCs, chondrocytes, osteoblasts and tendon stem cells (Abbasi, Ivanovski, et al., 2020; Buenzli et al., 2020; Y. Han et al., 2021). Surprisingly, however, there is little evidence of a direct seeding approach applied to cardiomyocyte systems. Only one study, currently in pre-print, has used MEW scaffolds alone as substrates for direct hiPSC-CM attachment on conductive gold-coated PCL fibres, however, the cells were also partially adhered to the underlying tissue culture plastic, questioning the integrity of its interface with the material (Zhang et al., 2022).

Overall, there is a growing interest in utilising MEW scaffolds for cardiac tissue engineering strategies, with the prospect of cardiac patch applications. However, aside from the acellular work, most systems use scaffolds as supporting structures for cell-laden hydrogels, making them susceptible to poor engraftment and fibrotic boundary formation, discussed above.

4.1.3 Living myocardial slices for *ex vivo* cardiac tissue modelling

The therapeutic potential of cardiomyocyte-based cardiac patches is commonly assessed using *in vivo* infarcted animals, allowing to investigate systemic effects of exogenous cell delivery, comprised of at least inflammation, fibrosis, lymphatic drainage, cardiac function, non-specific homing and many others (Mayfield et al., 2014; Jabbour et al., 2021; Peng et al., 2021). Although it is the most accurate model of the target application, the complexity of *in vivo* system combined with the inconsistencies in experimental parameters (animal type, disease model, administration time post infarction, total engraftment duration) do not allow to study the contribution of each component in isolation. Given the inadequate engraftment success of cardiac patches, more simplified models would be useful to pinpoint the key constraints to myocardium remuscularisation. *Ex vivo* Langendorff isolated heart model allows to exclusively focus on the cardiac response to transplantation, however, it is only suitable for acute experiments (5-6 hours long) and are more often used for cardiac function assessment for end-point *in vivo* studies (Jain et al., 2001; Zhang et al., 2005). Furthermore, the ethical consideration for both *in vivo* and Langendorff models do not allow for medium- or high-throughput studies, limiting the design space of experiments.

Myocardial slices are ultra-thin organotypic sections of the heart that preserve the complex multicellularity, architecture, and physiology of the native tissue (Pitoulis et al., 2020b). The slices remain viable and contractile in culture for several days (dependent on the culture conditions and animal source), and their thickness (100-400 µm) remains within the boundaries of oxygen diffusion (≈200 µm from either side) (Watson, Terracciano & Perbellini, 2019). They have previously been generated from a variety of model animal sources (rodents, dogs, pigs) as well as from donor human tissues (Watson et al., 2017). Multiple slices can be produced from each heart, increasing the throughput of experiments, and minimising the number of sacrificed animals.

The potential of myocardial slices as targets for exogenous cell delivery has previously been explored in several culture systems. For example, when hESCs were injected into a rat myocardial slice, the exogenous cells were still detected in the tissue after 60 days in culture and showed some

upregulation of the cardiomyocyte-specific markers (Habeler et al., 2009). Murine and human ESC-CM clusters were also co-cultured with murine slices, on an MEA surface and on top of the slice respectively (Hannes et al., 2008; Pillekamp et al., 2007). The latter study showed promise in hESC-CM delivery, with exogenous cells detected on the surface of the injured slice after 10 days of co-culture (Pillekamp et al., 2007). Importantly, the effects of cardiomyocyte interaction with the slice tissue can be assessed functionally, through contractility measurements or MEA electrical signal recordings (Pillekamp et al., 2007; Hannes et al., 2008). Taken together, myocardial slices serve as an excellent functional *ex vivo* platform for cardiomyocyte delivery, acting as an intermediate between the simplistic monolayer cardiomyocyte cultures and complex whole-heart models.

4.2 Aims and objectives

It is hypothesised that the efficiency of cardiomyocyte delivery to the heart can be greatly enhanced by providing a direct interface between microstructurally organised exogenous cells and the native myocardium. To this end, the aim is to develop an ordered fibrous polymeric scaffold that will support the 3D *in situ* expansion and cardiac differentiation of hiPSCs. To achieve that, the inspiration was taken from other studies that successfully seeded highly proliferative cell lines (hMSCs, osteoblasts) on MEW-fabricated scaffold, providing uniform volumetric coverage and, in parts, a full closure of scaffold features (Buenzli et al., 2020; Abbasi et al., 2020). It is predicted that *in situ* differentiation will allow to produce highly-cellularised cardiac constructs with cells presented outside of the material, capable of direct cell-cell interface with the myocardium.

The following objectives have been outlined for this project:

i) To determine the optimal parameters for uniform hiPSC seeding and cardiac differentiation, including process optimisation, scaffold geometry and cell seeding density;

ii) To characterise the electrophysiology and cellular composition of the resultant *in situ* differentiated cardiac meshes;

iii) To optimise the interface between the cardiac meshes and living myocardial slices as models of functional cardiac tissue;

iv) To evaluate exogenous cell delivery efficiency and functional effects on the host tissue as a result of the interface.

Notably, the purpose of the patterned scaffold in this chapter is to address the challenges in exogenous cell transfer to the native cardiac tissue, rather than to replicate the physiological arrangement of cardiomyocytes in the heart. To that effect, the geometry of the scaffold was chosen to be a uniform isotropic mesh to achieve an even coverage of the tissue upon interface and to avoid any possible variability in cell transfer depending on the scaffold dimension and orientation relative

to the direction of the cardiac fibres in the native tissue. The fabrication and differentiation protocols described in Chapter 4 can be adapted to anisotropic scaffolds with dimensions inspired by the native myocardium in the future work, however, they remain outside of the scope for the proof-of-principle cell transfer studies described below.

4.3 Methods

4.3.1 Melt electrospinning writing

The scaffold MEW protocol for scaffold fabrication was established previously by Dr Christopher Grigsby and Dr Kaja Ritzau-Reid. For this project, scaffold fabrication was performed by Dr Christopher Grigsby, Dr Kaja Ritzau-Reid or Ekaterina Pchelintseva. Two grades of polycaprolactone (PCL, Sigma-Aldrich, UK), 45 kDa and 80 kDa were dissolved in anhydrous chloroform (Sigma-Aldrich, UK) and mixed at a 50:50 (v/v) ratio. The blend was precipitated at a 1:5 (v/v) ratio into cold diethyl ether (Saveen Werner, Sweden), collected in a glass Petri dish and air-dried overnight. The resulting blend was then packed into a 3cc polypropylene syringe (G.A. Lindberg ChemTech AB, Sweden), melted and degassed in the vacuum oven at 85°C, 5 mbar. The syringe was then fitted with a 23G blunt needle (G.A. Lindberg ChemTech AB, USA) and positioned in the heating chamber of a custom-made Direct Writing Melt Electrospinner (Hutmacher lab, QUT, Australia). The syringe temperature was lowered to 55-65°C during the printing. The printing parameters were set at 10 kV accelerating voltage, 1500 mm/min axis velocity and 1.0 feeding N_2 pressure. The printed material was collected onto a stage positioned 10 mm away from the syringe nozzle. Custom G-codes were written to specify the geometry of the prints, loaded into the MACH 3 CNC software (ARTSOFT, USA) and used to control the motion of the two stepper motors of the electrospinner. Each pattern was repeated 10 times, creating scaffolds with 10 stacked layers of filament. Upon fabrication completion, the scaffolds were moved to a Petri dish and air-dried overnight.

4.3.2 Scanning electron microscopy (SEM)

Sample preparation and SEM imaging were performed together with Dr Kaja Ritzau-Reid. Uncoated and basement membrane-coated PCL scaffolds (coating conditions specified below) were cut into smaller sections using microscissors (Agar Scientific, UK) and secured on SEM specimen pin stubs (Agar Scientific, UK) using adhesive carbon tape (Agar Scientific, UK). A thin gold layer was then deposited on the samples for 30 seconds using the Q150T Sample Preparation System (Quorum

Technologies, UK). A JSM 6010LA Scanning Electron Microscope (JEOL, Japan) was used to image the samples at 20 kV acceleration voltage and x30 x40, x500, x550 and x1000 magnifications.

4.3.3 Cell culture

4.3.3.1 Scaffold preparation for cell culture experiments

The scaffolds were mounted onto autoclaved 6-well CellCrown inserts (Scaffdex, Finland) and washed in 1% (v/v) antibiotic-antimycotic (AA) solution (Gibco, UK) overnight. Prior to use, the scaffolds were washed three times with PBS and UV sterilised for 30 minutes under the cell culture hood. The scaffolds were then incubated with 3 mL of Cultrex Reduced Growth Factor Basement Membrane Extract Basement membrane (R&D Systems, USA) diluted 1:160 (v/v) in DMEM/F12 (Gibco, UK) for 1 hour, followed by one PBS wash. Costar® Ultra-low attachment 6-well plates (Corning, UK) were treated with 1 mL Anti-Adherence Rinsing Solution (Stem Cell Technologies, Canada) for 1 minute and washed three times with PBS. The assembled scaffolds were placed in the 6-well plate and pushed down until the scaffolds made full contact with the bottom of the well.

4.3.3.2 In situ *hiPSC differentiation on the scaffold*

WTC-11-GCaMP6f hiPSC cells, cultured to 80-90% confluency as described in section 2.3.4. were harvested by applying 1 mL of 0.5 mM EDTA (Gibco, UK) solution and incubating the plate for 7 minutes at room temperature. The EDTA solution was then removed, and the cell monolayer was detached by trituration with 1mL of E8 media (Gibco, UK) supplemented with 2 µM thiazovivin (Stratech Scientific, UK), using the P1000 Gibson pipette. The cells were counted and diluted to either 0.25×10^6 or 1×10^6 cells per scaffold. The plate was shaken orthogonally three times and incubated for 15 minutes at 37°C before repeated orthogonal shaking. The scaffolds were then incubated for 24 hours to allow the cells to adhere to the fibres, after which the cell crowns were lifted halfway up the wells, allowing the cells to be cultured in suspension. The scaffolds were fed fresh E8 media daily until cardiac differentiation protocol was initiated on day 4.

6 µM of the small-molecule Wnt activator CHIR99021 (tebu-bio, France) solution was prepared in RB- media, consisting of RPMI 1640 (Gibco, UK) supplemented with B27 without insulin (Gibco, UK), and added to each well for 48 hours. On day 6, the media was changed for RB- media for 24 hours, after which RB- media with 2.5 µM small-molecule Wnt inhibitor Wnt-C59 (Stratech Scientific, UK) was added for 24 hours. The solution was then replaced with RB- media daily until spontaneous beating was observed, after which RPMI 1640 (Gibco, UK) supplemented with B27 (Gibco, UK) was added (RB+ media) and exchanged for fresh media every 2 days. On day 11-13, the scaffolds were transferred to a new 6-well plate and cultured in RB+ media until reaching day 20, 30 or 40, when they were used for functional experiments.

4.3.3.3 hiPSC-CM seeding on the scaffold for slice interface optimisation

To optimise the protocol for scaffold and cardiac slice integration, the scaffolds were seeded with hiPSC-CMs cultured according to a monolayer cardiac differentiation protocol, as outlined in section 2.3.4. Briefly, the scaffolds were assembled, sterilised, coated in basement membrane solution and positioned at the bottom of the ultra-low adherence 6-well plate as described above. hiPSC-CMs were washed twice with 2 mL of PBS and incubated for 3 hours at 37°C with filter-sterilised collagenase type II (Gibco, UK) prepared at 200 U/mL in PBS with 1 mM HEPES (Gibco, UK) buffer and 2 µM of thiazovivin (Stratech Scientific, UK). The reaction was quenched with an equal volume of 24 µg/mL of DNAse I (Roche, Switzerland) diluted in RPMI 1640. The cells were gently triturated with a 10 mL stripette, collected into a Falcon tube (Corning, UK) and centrifuged at 100 g for 15 minutes at room temperature. The supernatant was discarded, and the pellet was resuspended with RB+ media containing 20% (v/v) FBS and 2 µM thiazovivin. The hiPSC-CMs were seeded on the scaffolds at 2.5-3 × 10^6 cells per well, gently shaken orthogonally and incubated for 15 minutes at 37°C. The orthogonal shaking was then repeated, and the cells were incubated at 37°C for 24 hours before lifting the scaffolds halfway up the well. The cells were then cultured in fresh RB+ media for at least 1 day prior to cardiac slice integration experiments.

4.3.4 Optical mapping

4.3.4.1 Calcium imaging

The electrophysiology of the cardiac meshes was assessed through imaging their calcium transients after 15, 20, 30 or 40 days of culture. Spontaneous calcium activity was recorded using an Axio Observer Z1 widefield microscope (Zeiss, UK) with the imaging chamber kept at 37°C throughout the recording. The spontaneous videos were acquired either at 2.5x magnification using a 4 × 4 binning mode with exposure set at 20 ms, with 50 fps acquisition rate. The meshes were kept in 6-well plates in RB+ cell culture media.

For electrical field stimulation experiments, the meshes were washed once in 3 mL of warm PBS, which was then replaced with 3 mL 37°C filter-sterilised HEPES-buffered Tyrode Solution (Alfa Aesar, UK or home-made recording solution outlined in Table 4-1). The scaffolds were allowed to acclimatise for 15 minutes. Two 5.3 cm long platinum electrodes were inserted into the well, with the tips of the electrodes touching the bottom, and connected to the MyoPacer Cell Stimulator (IonOptix, Ireland). The spontaneous activity was recorded for 15 seconds, after which the meshes were paced using 5V and 20 ms width pulses at 1, 2 and 3 Hz frequencies for 15 seconds each, with 15-second intervals in between the stimulation to allow for the cells to recover. The full recording lasted 120 seconds, with the final 30 seconds recording without stimulation. Each mesh was recorded at 3 separate FoV at 2.5x magnification. The meshes were allowed to recover between each recording until the spontaneous calcium activity resumed. Upon completion of the experiment, the meshes were washed once in 3 mL of PBS, fixed with 4% (v/v) PFA for 15 minutes, washed three times with 3 mL of PBS and stored in 1% (v/v) AA solution at 4°C until further use for immunofluorescent staining.

4.3.4.2 Generation of activation maps

Open-source Fiji image analysis software (v. 1.53f51) was used for all image and video processing and analysis. Briefly, the acquired .czi videos of spontaneous calcium signal were imported into Fiji

and a single activation cycle was isolated manually. The inactive frames were used to generate an average background signal, which was subsequently subtracted from every frame of the video. 2 × 2 binning was applied, followed by a median filter with 1 px diameter. The threshold was then adjusted to convert the activation signal into a binary image, and outliers were removed (2.0-pixel diameter, 50 threshold). The final pre-processed image was saved in .tiff format. A colour gradient was then applied to the timeseries using a custom MATLAB code, kindly developed by Dr Richard Wang, generating activation maps of spontaneous calcium signal propagation. For geometry comparison, the colour bars were produced for each video independently, while for the change in signal over time the colour bars were fixed ranging from 0 to 1600 ms to allow for conduction velocity comparison.

4.3.4.3 Calcium image analysis

6 ROIs were randomly positioned on each video of the spontaneous calcium signal and the Intensity macro provided by Dr Stephen Rothery from the Imperial FILM Facility was used to generate intensity traces of calcium flashes over time. The resulting .csv files were then imported into Clampfit 10.7 software (Molecular Devices, Open-Source) and used to analyse three calcium peaks of each ROI. Cursors 1,2 and 3 were positioned at the start of a peak, while cursor 4 was positioned at the end of peak repolarisation. Using the "Statistics" package of the software, the baseline and the peak amplitude of the signal were determined. The change in fluorescence (F/F0) values were calculated for each peak as:

$$\frac{(Peak\ amplitude + Baseline)}{(Baseline)},$$

and the value for each ROI was calculated as the average of three peaks, while the value for each mesh was calculated as the average of 6 ROIs. Four meshes were analysed for each timepoint.

For frequency analysis, the traces of changes in signal intensity for the whole of the scaffold were acquired using the Intensity macro. The resulting .csv files were then analysed using a MATLAB code,

kindly provided by Dr Richard Wang and Dr Hyemin Kim, to detect the peaks of calcium signal and their respective timestamps. A peak was defined as the signal elevated above a certain threshold of the whole signal range. Peak frequency was calculated as the inverse of adjacent peak difference, and the total output frequency for each stimulation mode of each ROI was calculated as the average of all peak frequencies of a given region.

4.3.5 Cardiac slice preparation and co-culture with cardiac meshes

All animal procedures were performed in collaboration with Professor Cesare Terracciano and according to the UK Home Office Animals (Scientific Procedures) Act 1986 and Directive 2010/63/EU of the European Parliament on the protection of animals used for scientific purposes. Adult rat myocardial slices were prepared by Dr Raquel Nunez-Toldra, Laura Nicastro or Dr Worrapong Kit-Anan, with some assistance from Ekaterina Pchelintseva. The myocardial slice preparation protocol has established previously by Watson et al., and the summary of the general protocol is outlined here (Watson et al., 2019). Male Sprague-Dawley rats with body mass ≈ 300- g were sedated with 4% (v/v) isoflurane and 4 L/min O_2 and sacrificed. The heart and surrounding tissue were excised and submerged in cold Tyrode's solution (Table 4-1, pH 7.4) containing 3 g/L 2,3-butanedione 2-monoxime (BDM, Sigma-Aldrich, UK) and 1000 U/mL heparin (Sigma-Aldrich, UK). The left ventricle was isolated from the rest of the heart and incised to produce an open flat cardiac tissue. The sample was then affixed endocardial side up using surgical glue Histoacryl Blue Tissue Adhesive (B. Braun Medical Ltd, Germany) to a 4% (v/v) agarose block cured on a 2.5 cm^2 sample holder. The holder was mounted onto a 7000 smz-2 high-precision vibratome (Campden Instruments, UK) and lowered into a bath filled with cold oxygenated Tyrode's solution. The tissue was sectioned with a ceramic blade (Campden Instruments, UK) into four to six 300 µm-thick myocardial slices. Each slice was trimmed into a rectangle and measured using callipers, after which two 3D-printed polylactic acid (PLA) handles (13 mm × 5 mm, 2 mm ridge thickness) were affixed on the two edges of the slice, perpendicular to the direction of cardiac fibres (Watson et al., 2019). The handles were used to

position the slice onto the movable posts of an autoclaved custom-made stainless-steel stretcher. The slice was stretched to 17.5%, representative of a physiological load with a 2.2 µm sarcomere length. Four stretchers were inserted into the grooves of a custom-made slice culture chamber (Watson et al., 2019).

Table 4-1 ***Chemical composition of the Tyrode's solution for slice preparation (slicing) and electrophysiological measurements (recording).***

Chemical	Concentration for slicing (mM)	Concentration for recording (mM)
NaCl	140	140
KCl	9.0	4.5
Glucose	10.32	10.32
$MgCl_2$	1.0	1.0
$CaCl_2$	1.0	1.8

Slice culture media was prepared by adding 2% (v/v) FBS, 3% (v/v) penicillin-streptomycin (P/S), 0.1% (v/v) insulin-transferrin-selenium, 4 nM adrenaline, 4 nM noradrenaline, 100 nM dexamethasone, 1 nM triiodothyronine and 0.02 g/L ascorbic acid to Medium 199 (Gibco, UK), and warmed in a waterbath. For mesh-slice interfacing experiments, the cardiac mesh was either: i) placed directly on top of the stretched slice inside the culture chamber with the cell crown still attached; ii) glued to the slice on the opposite side to the handle attachment using Histoacryl adhesive, or iii) sandwiched between the slice and the adhesive-covered handles. For all cases, 60 mL of slice culture media was added to the culture chamber for 1 hour during the scaffold integration at 37°C with 5% CO_2, after which the chamber was filled up to 175 mL media in total and connected to the pump for perfusion. The slices were cultured for 72 hours under electrical stimulation (1 Hz, 10 ms pulse width and 15 V) supplied by a Myopacer Cell Stimulator (IonOptix, Ireland). 40 mL of media was refreshed daily during culture.

4.3.6 Viability assessment of Histoacryl tissue adhesive

To visualise the acute toxicity effects of Histoacryl tissue adhesive, a myocardial slice was fixed with 4% (v/v) PFA for 15 minutes and used as a model for practicing a glue-based interface. The 3D-printed handles were affixed to the slice, after which the slice was inverted and a thin trace of Histoacryl was applied using a 21G BD Microlance needle (BD, USA). The slice was then lowered into a scaffold seeded with 1×10^6 hiPSCs and expanded in culture for 2 days prior to the experiment. After 1 minute, the cell crown was excised away from the scaffold using microscissors (Agar Scientific, UK) and the construct was stained using Ebioscience Calcein Blue AM Viability Dye (ThermoFisher Scientific, UK), and LIVE/DEAD® ethidium homodimer-1 (ThermoFisher Scientific, UK) according to the manufacturer's instructions.

For longer term toxicity assessment, a live myocardial slice was interfaced with the hiPSC-CM-seeded cardiac mesh using the same protocol and cultured for 72 hours prior to viability staining with the LIVE/DEAD® kit (ThermoFisher Scientific, UK).

4.3.7 Force transducer measurements and analysis

After 3 days in culture, the contractility of the slices was measured using an F30 Isometric Force Transducer (Harvard Apparatus, USA). Briefly, the stretcher was decompressed and the slice was gently released into a force transducer bath filled with the recording Tyrode's solution (Table 4-1) warmed to 37°C and bubbled with 100% O_2. The handles were used to immobilise the slice between the reference and the sensor hooks of the force transducer. The slices were stimulated using a Myopacer Cell Stimulator (1 Hz, 10 ms pulse width and 15 V) and carefully stretched to the physiological load of 17.5% using the microcontroller. The contractility was recorded for 15-20 minutes, after which the slice was removed from the force transducer setup and returned to physiological stretch on the stretcher. The slice was then fixed with 4% (v/v) PFA for 15 minutes, washed three times with PBS and stored in 1% (v/v) AA solution in PBS until staining.

Clampfit 10.7 software (Molecular Devices, Open-Source) was used to analyse force transducer data. Briefly, four consecutive transients were randomly selected from the recording after the full physiological stretch was reached. Each transient was selected using two cursor pairs, with one pair positioned at the baseline preceding the transient peak, and the other pair encompassing the peak from activation start to finish. The 'Statistics' function was used to measure baseline and peak amplitude. The passive and active contractile forces were then normalised to the cross-sectional area of the slice (300 µm thickness × width of the slice parallel to the contraction direction).

4.3.8 Fluorescence immunostaining

Prior to staining, a biopsy punch (6 mm diameter, Kai Medical, Japan) or a steel blade (RS PRO, UK) were used to cut each fixed mesh into 6 or 4 samples respectively. The processing was performed on top of an autoclaved 10-mm thick sheet of PDMS (VWR, UK), prepared according to the manufacturer's instructions by mixing the elastomer and the crosslinker components at 10:1 (w/w) ratio followed by overnight curing in a 60°C oven.

4.3.8.1 Wholemount immunostaining of cardiac meshes

Cardiac meshes fixed either on day 30 or 40 of culture were permeabilised for 15 minutes in 0.5% (v/v) triton X-100 (Sigma-Aldrich, UK) solution prepared in PBS and washed three times. The samples were then blocked for 2.5 hours in the blocking solution, containing 10% (v/v) donkey serum (Merck Millipore, Germany), 1% (w/v) BSA (Sigma-Aldrich, UK) and 0.3 M glycine (Sigma-Aldrich, UK) in PBS. Prior to use, the blocking solution was filter-sterilised to remove aggregates. The primary antibody solution was prepared by diluting the blocking solution with PBS at 10% (v/v) and adding the following antibodies: mouse anti-CD31 (1:200, MA3100, ThemoFischer Scientific, UK), rabbit anti-cTnT (1:500, ab45932, Abcam, UK) and chicken anti-vimentin (1:4000, PA-1-10003, ThermoFisher Scientific, UK). The samples were stained with primary antibodies overnight at 4°C on a rocker and subjected to three 20-minute washes in PBS on a shaker. A secondary antibody solution was prepared in 10% (v/v) blocking solution and contained the following AlexaFluor (ThermoFisher

Scientific, UK) antibodies at 1:1000 dilution: 488 goat anti-chicken, 555 donkey anti-mouse, 647 donkey anti-rabbit. The samples were incubated at room temperature on a rocker for 2 hours in the dark and subjected to three immediate PBS washes. Prior to imaging, DAPI (ThermoFisher, UK) counterstain was prepared at 1:1000 dilution in PBS and added to the samples for 10 minutes at room temperature.

4.3.8.2 Optical tissue clearing protocol

An optical clearing protocol, adapted from previously published methods, was used to increase the imaging volume of cardiac meshes. First, the samples were washed once with PBS. PBS-TxDBN staining solution was prepared by mixing 2% (v/v) triton X-100 (Sigma-Aldrich, UK) and 5% (w/v) BSA (Sigma-Aldrich, UK) and 20% (v/v) dimethyl sulfoxide (DMSO, Sigma-Aldrich, UK) in PBS, followed by filter-sterilisation. The meshes were permeabilised and blocked with PBS-TxDBN solution under gentle shaking for 24 hours at room temperature. Primary antibody solutions were prepared in PBS-TxDBN and added to the samples for a 24-hour incubation at room temperature on a shaker. The following antibodies were used: rabbit anti-cTnT (1:100 ab45932, Abcam, UK) and chicken anti-vimentin (1:800, PA1-10003, ThermoFisher Scientific, UK). The samples were then washed in PBS-TxDBN solution three times over 24 hours. AlexaFluor secondary antibodies (488 goat anti-chicken, 555 donkey anti-mouse, 647 donkey anti-rabbit) were prepared at 1:200 dilution in PBS-TxDBN and added to the samples for a 24-hour incubation at room temperature on a shaker. The post-fixation was then performed using 4% (v/v) PFA solution overnight at 4°C. The meshes were then dehydrated through sequential addition of 30%, 50%, 70% and 100% (v/v) 1-propanol (Sigma-Aldrich, UK). The 100% (v/v) 1-propanol (Sigma-Aldrich, UK) dehydration step was repeated twice. Each step was carried out for at least 4 hours at 4°C. The meshes were then transferred to an 8-well Ibidi chambered µ-slide (Ibidi, Germany) and submerged in ethyl cinnamate (Sigma-Aldrich) for 1 hour at room temperature prior to imaging.

4.3.8.3 Wholemount immunostaining of cardiac mesh – cardiac slice co-cultures

The protocol for staining myocardial slices interfaced with cardiac meshes was adapted from the previously published protocol on slice immunostaining (Nunez-Toldra et al., 2022). First, the blocking solution, containing 10% (v/v) donkey serum (Merck Millipore, Germany), 1% (w/v) BSA (Sigma-Aldrich, UK) and 0.3 M glycine (Sigma-Aldrich, UK) in PBS, was prepared and filter-sterilised to remove aggregates. To permeabilise and block the samples, 1.5% (v/v) triton X-100 (Sigma-Aldrich, UK) was then prepared in blocking solution and added for 3 hours at room temperature on an orbital shaker set at 70 rpm. Primary antibodies (rabbit anti-GFP, 1:1500, ab290 (Abcam, UK) and AlexaFluor-647 mouse anti-cTnT [13-11], 1:200, cat. #565744 (BD Biosciences, USA)) were prepared in 10% (v/v) blocking solution with 0.2% (v/v) Tween-20 (Sigma-Aldrich, UK). Following a single PBS wash, the samples were incubated with the primary antibody solution at 4°C on a rocker overnight. The samples were subjected to three 1-hour washes with PBS on the orbital shaker set at 70 rpm. Donkey anti-rabbit AlexaFluor-488 secondary antibody (1:1000, ThermoFisher Scientific, UK) was prepared in 10% (v/v) blocking solution with 0.2% (v/v) Tween-20 (Sigma-Aldrich, UK) and added to the samples for 2 hours in the dark. The samples were then washed in PBS for 30 minutes three times on the orbital shaker set at 70 rpm. The slices were then counterstained with DAPI (ThermoFisher, UK) 1 µg/mL solution prepared in PBS for 15 minutes and washed three times in PBS for 10 minutes prior to imaging.

4.3.9 Image acquisition

Brightfield images of the cellularised scaffolds were acquired using either an Axio Observer Z1 widefield microscope (Zeiss, UK) using a 2.5x magnification lens, either with or without tiling. An EVOS XL Core imaging system (Invitrogen, UK) was used to image scaffolds prior and immediately after cell seeding.

Fluorescent imaging of the cardiac mesh-slice interface *in situ* on the cardiac stretcher was performed using Leica SP5 upright confocal microscope (Leica, UK) with 25x objective and 633 nm

laser. All other fluorescent images were acquired using Leica TCS SP8 inverted confocal microscope (Leica, UK) with a 405 nm diode laser used for DAPI, while 561 nm DPSS and 633 nm HeNe lasers were used to excite secondary antibodies. The images were acquired at 8-bit, 512 × 512 resolution. Overview images of the cardiac meshes stained for α-cTnT were acquired using a 5x magnification objective, while a 10x objective was used for closer inspection of α-cTnT, α-Vimentin and α-CD31. 40x objective was used to image optically cleared meshes.

4.4 Results and discussion

4.4.1 Optimisation of PCL scaffolds for stem cell culture and cardiac differentiation

40 mm × 40 mm large fibrous PCL scaffolds were fabricated using a melt electrowriting protocol previously established by Dr Kaja Ritzau-Reid and Dr Christopher Grigsby and described extensively in Dr Ritzau-Reid's PhD thesis (Ritzau-Reid., 2022). Briefly, linear fibres were deposited orthogonally to create a net-like scaffold that maintained a highly ordered geometric structure (Figure 4-2A). The scaffolds therefore consisted of intersectional junctions, where two fibres crossed over (Figure 4-2C) and straight linear regions of individual fibres (Figure 4-2E). All scaffolds were produced by repeated stacking of ten PCL filaments, with each layer distinctly visible under SEM (Figure 4-2E).

While PCL is a biocompatible and biodegradable polymer, its highly hydrophobic structure can limit cell adhesion and proliferation (Edlund, Sauter & Albertsson, 2011). Post-fabrication surface functionalisations with adhesion peptides, growth factors or ECM proteins have been extensively implemented to promote cell attachment on PCL materials (Qin et al., 2022; Xu, Wang & Yang, 2010; Chung et al., 2005). Stem cells and their derivatives are commonly cultured on Matrigel-coated surfaces, and such coatings have been previously applied to PCL to enable hiPSC-CM adhesion (Han et al., 2016). Therefore, prior to seeding the fibrous scaffolds with hiPSCs, the material was incubated for 1 hour in basement membrane solution used for monolayer hiPSC expansion. The protein coating was evenly distributed between PCL layers (Figure 4-2D,F).

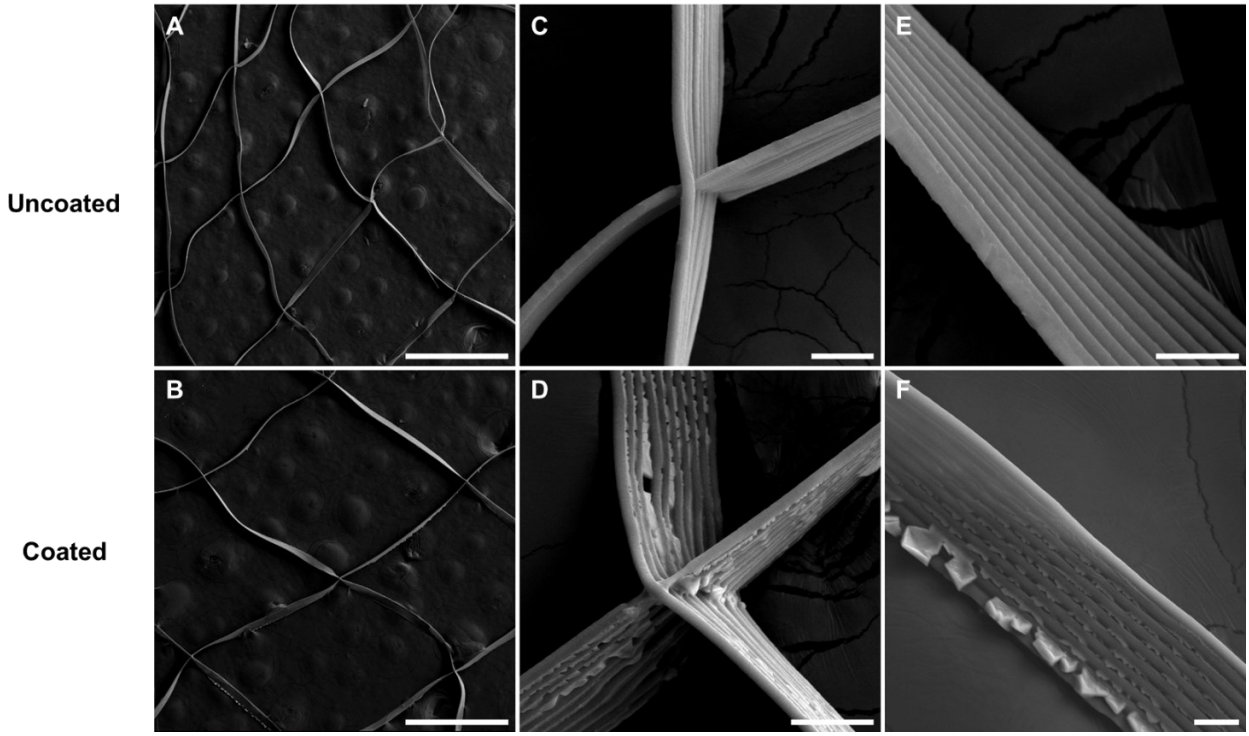


Figure 4-2 ***SEM imaging of structural organisation of uncoated (A,C,E) and coated (B,D,F) 1000 µm melt electrospun PCL scaffolds. (****A). Overview image of uncoated PCL scaffold at x30 magnification. (B). Overview image of basement membrane-coated PCL scaffold at 40x magnification. (C) 500x magnification image of the junction zone of the uncoated scaffold. (D) 500x magnification image of the junction zone of the coated scaffold. (E). 1000x magnification image of a linear region of an uncoated PCL fibre. (F). 550x magnification image of a linear region of a basement membrane-coated PCL fibre. Imaging and sample preparation was performed together with Dr Kaja Ritzau-Reid. Scale bars: A,B = 500 µm, C,D = 50 µm, E,F = 20 µm.*

For cell culture, a scaffold was immobilised inside a cell crown which ensured the material was stretched at the bottom of the crown (Figure 4-3A). hiPSCs were then seeded onto the scaffold and allowed to adhere, with cell attachment on the fibres visible after 24 hours (Figure 4-3B). The seeded scaffolds were then lifted halfway up the culture well and the cells were cultured in suspension in stem cell maintenance media for 3-4 days to allow them to proliferate and grow around the fibrous substrate (Figure 4-3C). After expansion, most cells accumulated at the junctions of the scaffold, forming interconnected rhomboid-shape constructs with circular lumens in the middle of the square structure (Figure 4-3C). Originally, the seeding was inconsistent throughout the scaffold, with most cell growth occurring on the edges of the scaffold, while the central junctions remained vacant, leading to 77.2% occupancy (Figure 4-3D). To improve scaffold coverage, the culture plate was gently agitated 15 minutes after cell seeding, leading to a more uniform cell distribution with 100% junction occupancy (Figure 4-3E).

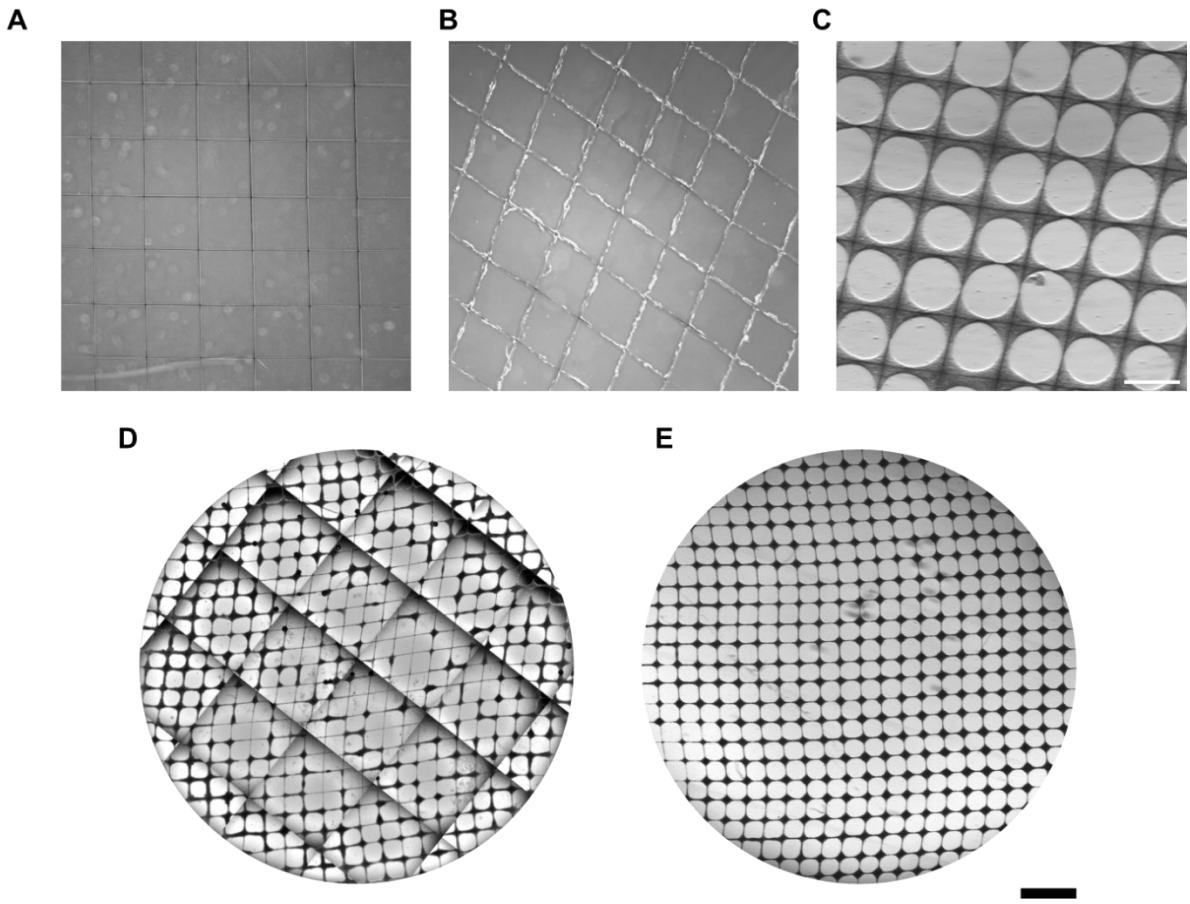


Figure 4-3 ***Optimisation of hiPSC seeding on the fibrous PCL scaffolds. (****A). Brightfield image of an unoccupied 500 µm PCL scaffold immobilised and stretched with the cell crown. (B). Brightfield image of hiPSCs attached to the fibres of the scaffold 24 hours after seeding. (C). Formation of hiPSC constructs on the scaffold 72 hours after culture in suspension. (D). Distribution of cells on the scaffold 8 days after seeding. (E). Distribution of cells on the scaffold 8 days after seeding with an additional agitation step. Scale bars: top panel 500 µm, bottom panel = 2000 µm.*

MEW printing is a tunable fabrication method, which can be used to generate a vast variety of highly-ordered structures, extruding filaments ranging from 0.82 to 180 µm diameter (Hochleitner et al., 2014, 2015a). The G-code programmable motorised collector stage offers precise control over the scaffold geometry, producing triangular, rectangular, hexagonal, sinusoidal and complex auxetic patterns with variable unit spacing (Jin et al., 2021; Liashenko et al., 2020).

To explore the limits of the cell seeding protocol on PCL fibres, hiPSCs were seeded on three scaffolds with varying geometries and unit spacings: large rectangular scaffolds with 1500 µm × 1000 µm dimensions (Figure 4-4A), medium square scaffolds with 800 µm × 800 µm dimensions (Figure 4-4B) or small square scaffolds with 500 µm × 500 µm dimensions (Figure 4-4C) and allowed to proliferate for two days. These geometries were chosen as they were previously validated for hESC

culture and differentiation to neural organoids (Ritzau-Reid., 2022). All three conditions generated uniform interconnected hiPSC constructs. The optimised scaffold fabrication, functionalisation and cell seeding protocol was therefore highly reproducible and independent of scaffold geometry and dimensions, highlighting the versatility of PCL scaffolds as hiPSC culture systems. With the focus of the project aiming to generate uniform interconnected cardiac tissue for myocardium remuscularisation, isotropic geometries were chosen as a starting point for future experiments on cardiac differentiation. However, other scaffold dimensions could also be of interest, for example with rectangular scaffolds providing a platform to study the effects of anisotropic substrates on 3D hiPSC differentiation.

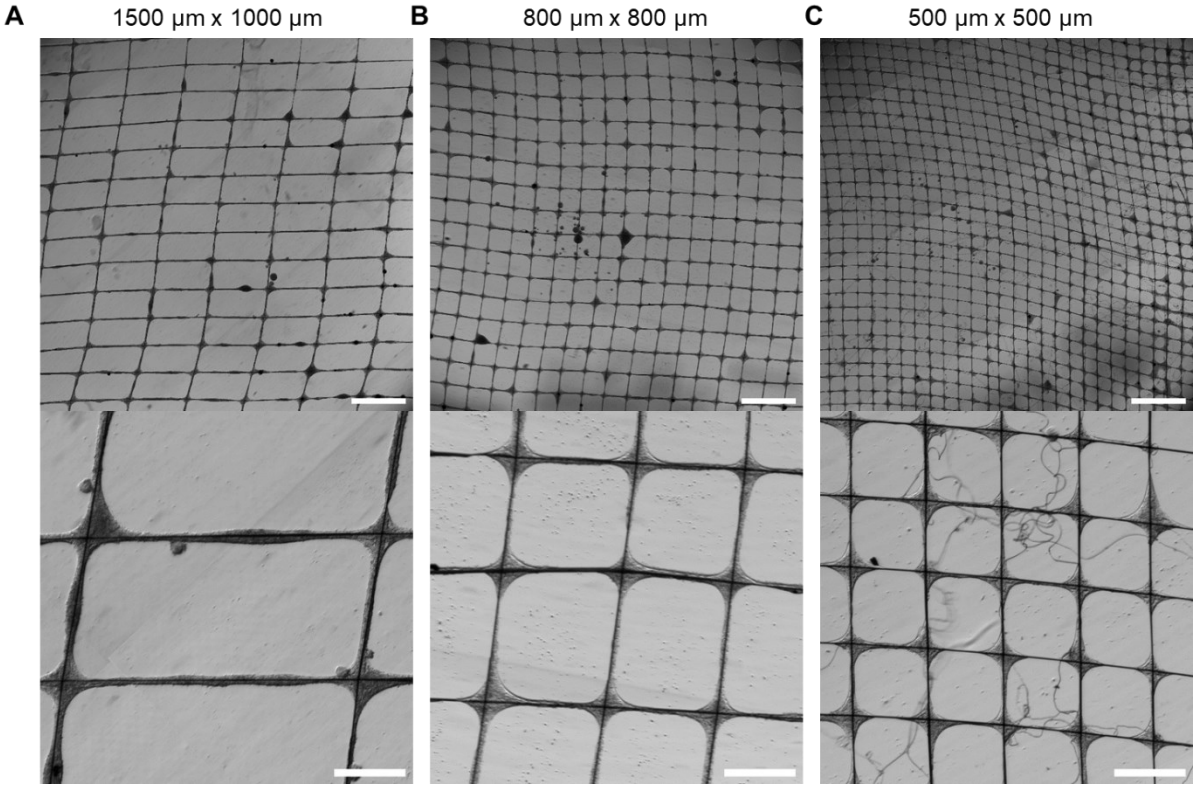


Figure 4-4 ***Brightfield images of the uniform distribution of hiPSC constructs on PCL scaffolds with varying geometries.*** *(A). Rectangular scaffold with 1500 µm × 1000 µm dimensions. (B). Square scaffold with 800 µm × 800 µm dimensions. (C). Square scaffold with 500 µm × 500 µm dimensions. Scale bars: top panels (overview) = 2000 µm, bottom panels (close-up) = 500 µm.*

4.4.2 Cell seeding density optimisation for cardiac differentiation

Using 500 µm scaffolds, the cells were then seeded at low (250,000 cells per scaffold, equivalent to ≈ 50 cells/junction) or high (1,000,000 cells per scaffold, equivalent to ≈ 200 cells/junction)

concentrations to investigate the effect of starting cell seeding density on cardiac differentiation efficiency. The two conditions were run in duplicates (scaffolds #1 and 2 with low cell density and scaffolds #3 and 4 with high cell density), and the seeded cells were cultured in E8 stem cell maintenance media for 4 days, allowing them to proliferate and form translucent interconnected hiPSC constructs (Figure 4-5A). Notably, despite the variable cell concentration, there was no apparent difference in cell distribution between all four scaffolds (Figure 4-5A). Mesoderm induction was then initiated by the addition of Wnt-pathway activator CHIR99021 for 48 hours (Figure 4-5B). All scaffolds increased in cell mass, demonstrated by the increased opacity of the constructs. Cell growth on scaffold #3 appeared uneven, with every other row demonstrating large cell growth and decreased lumen diameter. However, this morphology disappeared after Wnt inhibitor Wnt-C59 (referred to as C59 from now on) was supplemented into the media to induce cardiac specification. The cells on scaffolds #2, #3 and #4 appeared largely the same, forming smooth cell constructs, while the cellular structures on scaffold #1 exhibited were slightly coarse (Figure 4-5C). This difference in morphology became more pronounced by day 15, after the removal of C59 and scaffold maintenance in cardiomyocyte media (Figure 4-5D). Overall, all replicates maintained the original uniform pattern of cell distribution on the material scaffold. The coarse cells on scaffold #1 were highly compacted, with rough morphology of the cell mass. Scaffolds #2 and #3 appeared smooth and translucent, lined with spindle-like cells. The area of cell growth on scaffold #2 was larger than on the other scaffolds, with some cells fully filling the inter-fibre space. Scaffold #4 consisted of a mixture of the two morphologies, with some junctions occupied by spindle-like smooth cells and others by rough densely packed cells.

Importantly, functionally the spindle-like scaffolds did not exhibit any spontaneous contractility, therefore the differentiation on scaffolds #3 and #4 was unsuccessful in generating cardiac structures. On the other hand, the cells with coarse morphology were beating (data not shown). Since scaffolds #1 and #4 belonged to two different cell density groups, it is likely the variability in differentiation efficiency was not affected by the cell density and was rather caused by the

stochasticity of the differentiation process. Furthermore, there lack of clear differences in cell distribution on the scaffolds suggested that either increasing the seeding density beyond 250,000 per well does not increase the number of cells attaching to the scaffold, or that there is a threshold of cell growth on the scaffold that cannot be exceeded. Taken together with one scaffold per condition generating spontaneously beating cardiomyocytes, it can be concluded that either cell seeding density can be used for cardiac differentiation on scaffolds. 250,000 cells per well density was therefore chosen for all future experiments as it reduced the hiPSC waste during seeding and scaffold #1 had a more uniform distribution of the beating cells than scaffold #4. It should be noted that all future studies were performed on scaffolds that exhibited spontaneous contractions, while fully spindle-like scaffolds were omitted.

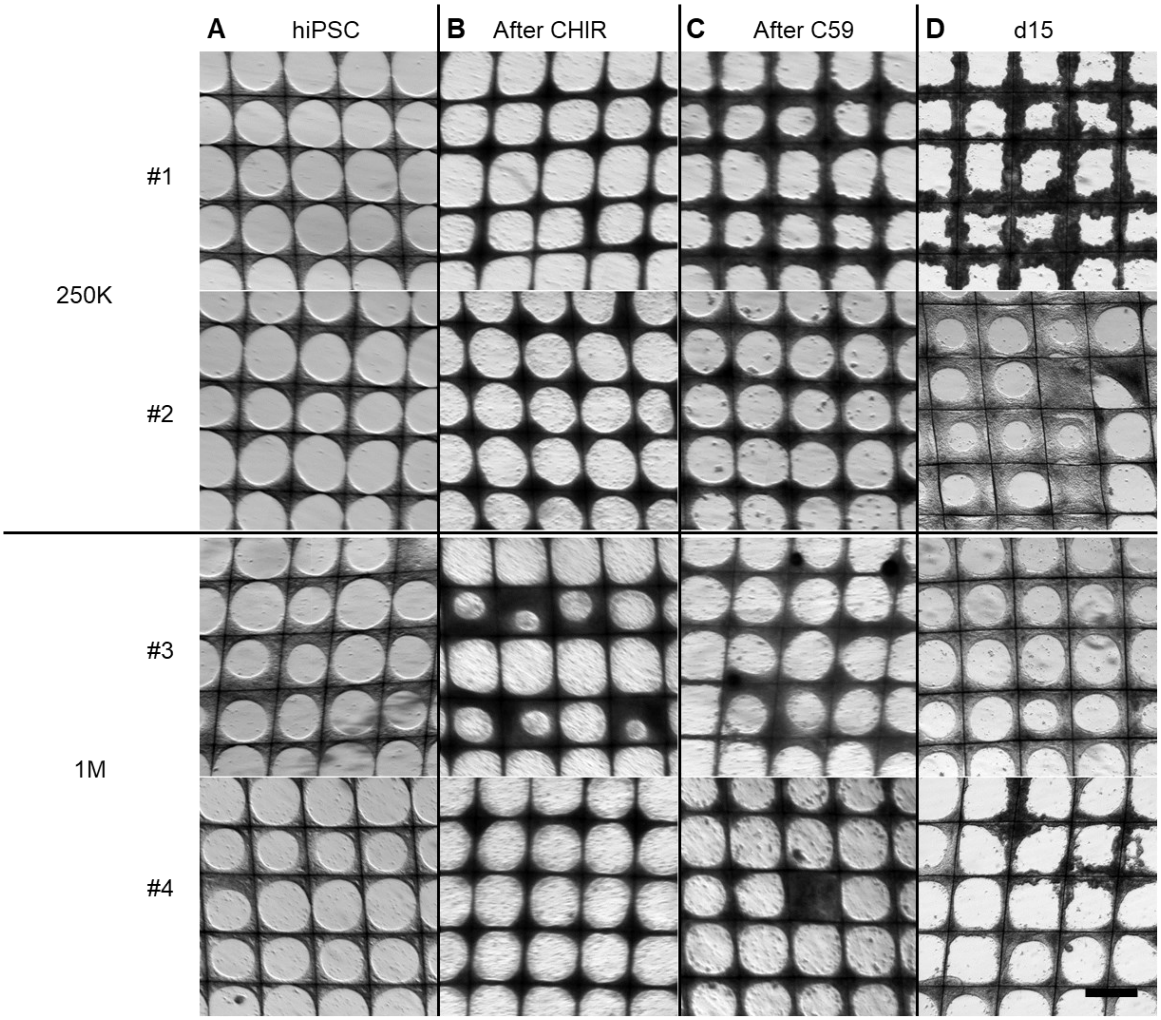


Figure 4-5 ***Effect of cell density on construct morphology over the course of cardiac differentiation.*** *Brightfield images of four 500 µm PCL scaffolds seeded with 0.25 × 10^6(top panels) or 1 × 10^6 hiPSCs (bottom panels) during differentiation. The cells were imaged on (A) day 4, prior to differentiation initiation, (B) day 7, after CHIR-mediated mesoderm specification, (C) day 11, after Wnt-C59- induced cardiac progenitor specification and (D) day 15, after first spontaneous contractions were observed. Scale bar = 500 µm.*

4.4.3 Generation of two distinct cardiac construct types through geometry modulation

The hiPSC seeding and differentiation protocol was then applied to square scaffolds with 800 µm and 500 µm inter-fibre spacing, and the cells were cultured up to day 30 (Figure 4-6). Interestingly, varying the scaffold spacing led to two distinct types of structures: the larger spacing contained dense spherical nodes on the scaffold junctions, interconnected with thinner cellularised segments (Figure 4-6A). The cells differentiated on a 500 µm spacing scaffold were more evenly distributed, forming interconnected meshes of cells (Figure 4-6B). Both types of structures were then immunostained for cTnT to investigate the localisation of cardiac phenotypes on the scaffolds. For both 800 µm and 500 µm scaffolds, most cells expressed cTnT both at the junctions and the connections between them, confirming the predominantly cardiac identity of the differentiated cells differentiated, thus producing interconnected cardiac nodes and cardiac meshes respectively (Figure 4-6C,D).

Timelapse calcium imaging was then performed on the structures with two different geometries to visualise the differences in conduction propagation. Since hiPSCs used for differentiation contained the GCaMP6f fluorescent reporter, discussed previously in section 3.4.1.7, the calcium signal generated by electroactive cells on the scaffold was recorded and used to generate activation maps with colour-coded timing of active regions (Figure 4-6E,F). The earliest activated region was shown in red-orange, intermediate activation times were shown in yellow-green, and the latest active areas were shown in blue-purple.

The earliest activated cardiac nodes were not connected and firing independently, shown in red (Figure 4-6E). Three cardiac nodes in the centre of the FoV were functionally interconnected, shown by the calcium active connections in between the nodes and the gradual progression of the activation map through the orange, yellow and green. The other two nodes were active in the later frames of the recording but lacked the electroactive connections to the rest of the structures,

therefore likely firing independently. In contrast, the cardiac meshes formed a functional electroactive syncytium, with fully interconnected FoV, and the signal gradually progressing from the top-right corner in the downward direction (Figure 4-6F). The FoV of the 500 µm mesh achieved full activation faster than that of the 800 µm, with 600 ms and 1600 ms signal duration respectively shown by the differences in the magnitude of colour bar. However, since the cardiac nodes were not interconnected, signal quantification along the clear propagation path would need to be performed to conduction velocity in the two structure types.

Overall, the two different scaffold spacings allowed the production of two distinct cardiac tissues. While the cardiac nodes could be an interesting high-throughput platform for cardiac spheroid or organoid production, it suffered from the inconsistency in interconnectivity and variability in tissue thickness between the junction and connecting areas. It was hypothesised that the uniform distribution of the cardiomyocytes on 500 µm cardiac mesh would make it a more promising configuration for cardiac patch applications. Therefore, 500 µm geometry was chosen for future characterisation and cardiomyocyte delivery experiments.

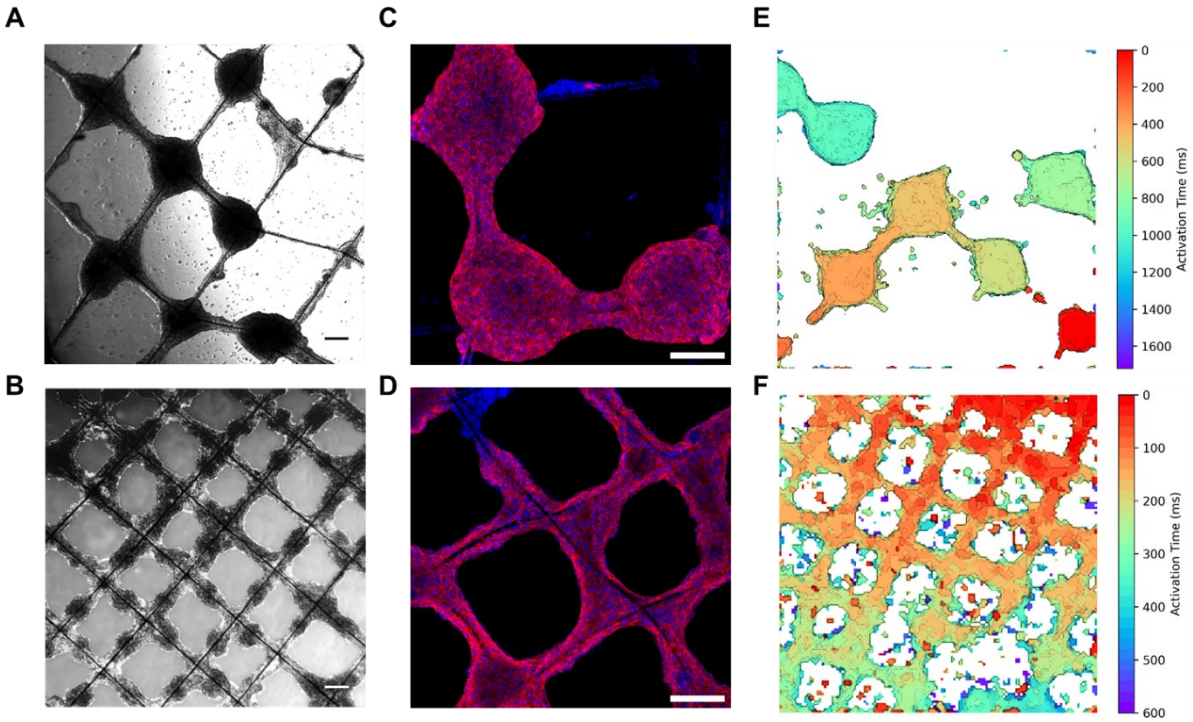


Figure 4-6 ***Geometry-dependent differences in characteristics between the cardiac nodes grown on 800 µm (A,C,E) and cardiac meshes grown on 500 µm (B,D,F) scaffolds at day 30. (****A,B). Brightfield images of the cardiac constructs. (C,D). Immunofluorescent staining for cTnT (red) and DAPI (blue). (E,F). Activation maps of spontaneous calcium signal. Scale bars = 200 µm.*

4.4.4 Morphological and electrophysiological changes in cardiac meshes

The first spontaneous contractions of hiPSC-CM cardiac meshes were commonly observed around day 10-15 of the cardiac differentiation protocol, consistent with the timeframes previously described in the literature (Huang et al., 2020; Tsao et al., 2018; Pioner et al., 2019). Increasing the time of culture of hiPSC-CMs is known to lead to improved electrophysiological and structural maturation of the cardiomyocytes (Ahmed et al., 2020; Lundy et al., 2013; Lewandowski et al., 2018). The differentiated cardiac meshes were therefore monitored upon completion of the differentiation protocol for up to 40 days and the changes in their various features were compared over time (Figure 4-7). First, changes in morphology were assessed through brightfield microscopy, shown by representative images of a single scaffold repeatedly observed over the course of the culture (Figure 4-7A). At day 20, hiPSC-CMs appeared to be spread over a larger area, likely at a lower cell density demonstrated by the translucence of the engineered tissue (Figure 4-7A). Locally, the cells organised into oval structures with hollow cavities, that in turn formed rosette-like shapes at the scaffold junctions. As the culture time increased, the hollow cavities disappeared, and the cells closely compacted around the PCL fibre by day 30. There was no difference in the overall morphology of the cells between the meshes at day 40.

Calcium transients were then recorded via fluorescent widefield microscopy recording the fluctuations in calcium activity from the top layer of the engineered constructs and converted into activation maps to investigate how signal propagation within the cardiac mesh changed with culture time (Figure 4-7B). At day 20, the calcium signal was originating simultaneously in several locations across the mesh, shown by two distinct red regions on the opposite sides of the activation map (Figure 4-7B). Two calcium transients originating from these sources interacted in the centre, leading to lateral deviation of the propagation paths in an orthogonal direction to the original wavefronts. Conversely, in constructs imaged on day 30 and 40 the signal originated from a single source, with a distinct linear propagation path. Furthermore, the activation maps suggested an increase in

conduction velocity over time, with full FoV activation time at day 20 reaching 1400-1600 ms, while at day 30 and day 40 the calcium signal crossed the path of the whole FoV within 800 and 600 ms respectively. Indeed, these preliminary results are only qualitative and would benefit from detailed quantification of change in conduction velocity over time.

In addition to propagation directionality and velocity, the frequency of spontaneous calcium transients also increased over time (Figure 4-7C). A representative trace at day 20 contained only 6 peaks across the 12 seconds of the recording, in comparison to 10 peaks for day 30 and 12 peaks for day 40 construct respectively. The interval between the peaks also stabilised over time: while at days 20 and 40 the separation between the adjacent transients was variable, at day 40 the peaks were consistently produced approximately every second. However, the magnitude of the calcium transients was not affected by the culture time: there was no significant difference between day 20, day 30 or day 40 timepoints (Figure 4-7D, $p = 0.4719$, $p > 0.9999$ and $p = 0.2313$).

Overall, the prolonged culture of the cardiac meshes led to structural remodelling of the cells on the scaffold and was associated with improved propagation of calcium transients. The electrophysiological characteristics were consistent with those described in the literature for monolayer cultures, with several independently contracting areas observed at the early stages of differentiation that later synchronised into a single functional syncytium as the cells matured (Ye et al., 2013). This phenomenon can be explained by the cardiac differentiation process yielding a heterogenous population with multiple cardiomyocyte subtypes (ventricular, atrial and pacemaker) arranged randomly. In early cultures, clusters of pacemaker cells would spontaneously fire and initiate the signal at several locations, but as the cells mature the signal stabilises and synchronises across the whole construct. The increase in the frequency of the calcium transients was likely related to the gradual advancement of ion channel expression and modulation, which in turn could regulate the contractile force (Rees et al., 2018; Eisner et al., 2017). Taken together, these results demonstrated that the day 20 cardiac meshes were morphologically and functionally less advanced

than day 30 and day 40 constructs, and therefore the two later timepoints were used for future investigations.

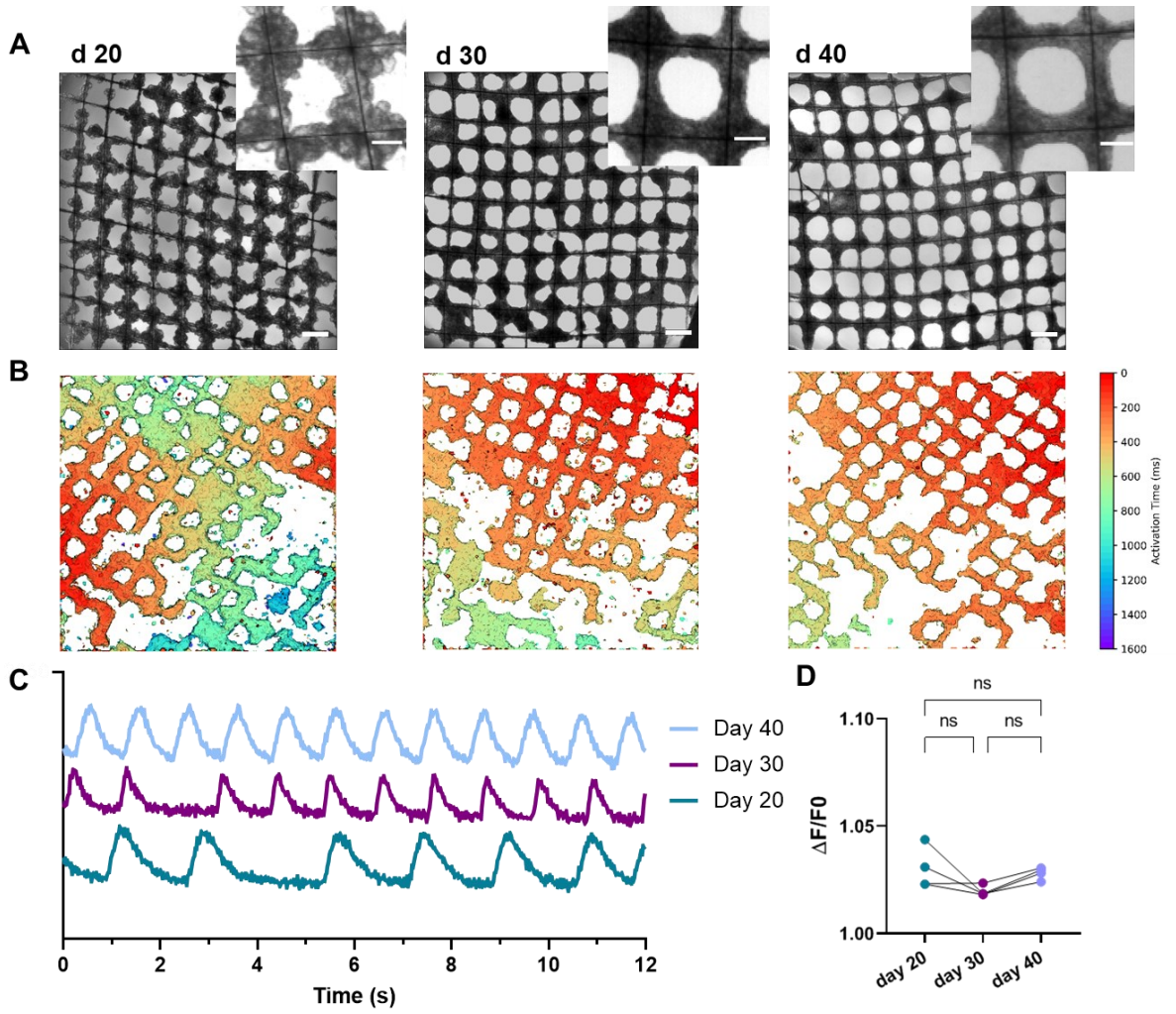


Figure 4-7 ***Morphological and electrophysiological transformation of cardiac meshes over time.*** *(A). Brightfield images of a representative cardiac mesh taken at day 20, day 30 and day 40. Scale bars = 500 µm overview, 200 µm close-up. (B). Activation maps of spontaneous calcium signal generated by a representative cardiac mesh on day 20, day 30 and day 40. (C). Representative traces of calcium transients recorded at day 20, day 30 and day 40. (D). Average calcium transient amplitude of cardiac meshes at day 20, day 30 and day 40. Repeated measures Friedman test with Dunn's multiple comparison correction, ns – non-significant. N = 4, n = 15-21, where N is the number of independent scaffolds used for analysis and n is the number of analysed peaks per scaffold.*

To determine the efficiency of field stimulation capture by the differentiated cardiac meshes, the calcium signal was recorded while the constructs were subjected to a series of pulses of gradually increasing frequency. Briefly, calcium transients of each cardiac mesh were recorded for 15 seconds under 1 Hz, 2 Hz, and 3 Hz pacing, with 15-second recovery intervals in between the stimulations

(Figure 4-8A). The peaks of calcium activity were detected from the intensity traces, and the average interval between them was used to calculate the output frequency of each video during pacing (Figure 4-8B). The final output frequency for each mesh was calculated as the average of two videos for each scaffold, and three scaffolds were analysed per condition.

There was no significant difference between the spontaneous frequency of day 30 (0.70 ± 0.17 Hz) and day 40 (0.92 ± 0.08 Hz) meshes ($p > 0.9999$). At 1 Hz applied field stimulation, both timepoints followed the pacing, with 0.98 ± 0.003 Hz output frequency for day 30 and 0.98 ± 0.02 Hz for day 40. When the stimulation frequency was further increased to 2 Hz, day 30 meshes were able to capture the frequency better (1.93 ± 0.12 Hz) than the day 40 meshes (1.58 ± 0.47 Hz), however, the differences were not significant ($p > 0.9999$). At 3 Hz, the limit of frequency capture was surpassed for both timepoints, with output frequency only at 1.48 ± 0.02 Hz and 1.37 ± 0.09 Hz for day 30 and day 40 respectively. Again, there was no significant difference between the two timepoints ($p > 0.9999$).

When compared to the results of electrical field stimulation of acoustically-patterned hydrogels from Chapter 3, the cardiac meshes had a wider range of frequency capture. 5 out of 6 stimulated meshes (83%) were able to pace around 2 Hz, while only 6 out of 16 analysed gels (37.5%) contained at least one ROI capable of following 2 Hz stimulation supplied at three times the voltage (Figure 4-8, Figure 3-46). There are several possible explanations for such differences. Firstly, as discussed above, since the culture length plays a major role in advancing cardiac electrophysiology, day 20 hydrogel constructs could lack some key ion channels and currents in comparison to day 30 and 40 cardiac meshes. Secondly, in hydrogels the cardiomyocytes were embedded inside a material, which was not the case for the cells grown on the outside of the scaffold. Finally, aggregating the cardiomyocytes with ultrasound could result in a higher local cell density, requiring an even higher amount of supplied power for frequency capture.

Overall, increasing the culture duration of cardiac meshes did not cause a difference in their response to electrical stimulation. Importantly, however, both constructs were able to follow physiological stimulation at 1 Hz, suggesting their compatibility with tissues co-cultured in simulated healthy human heart conditions.

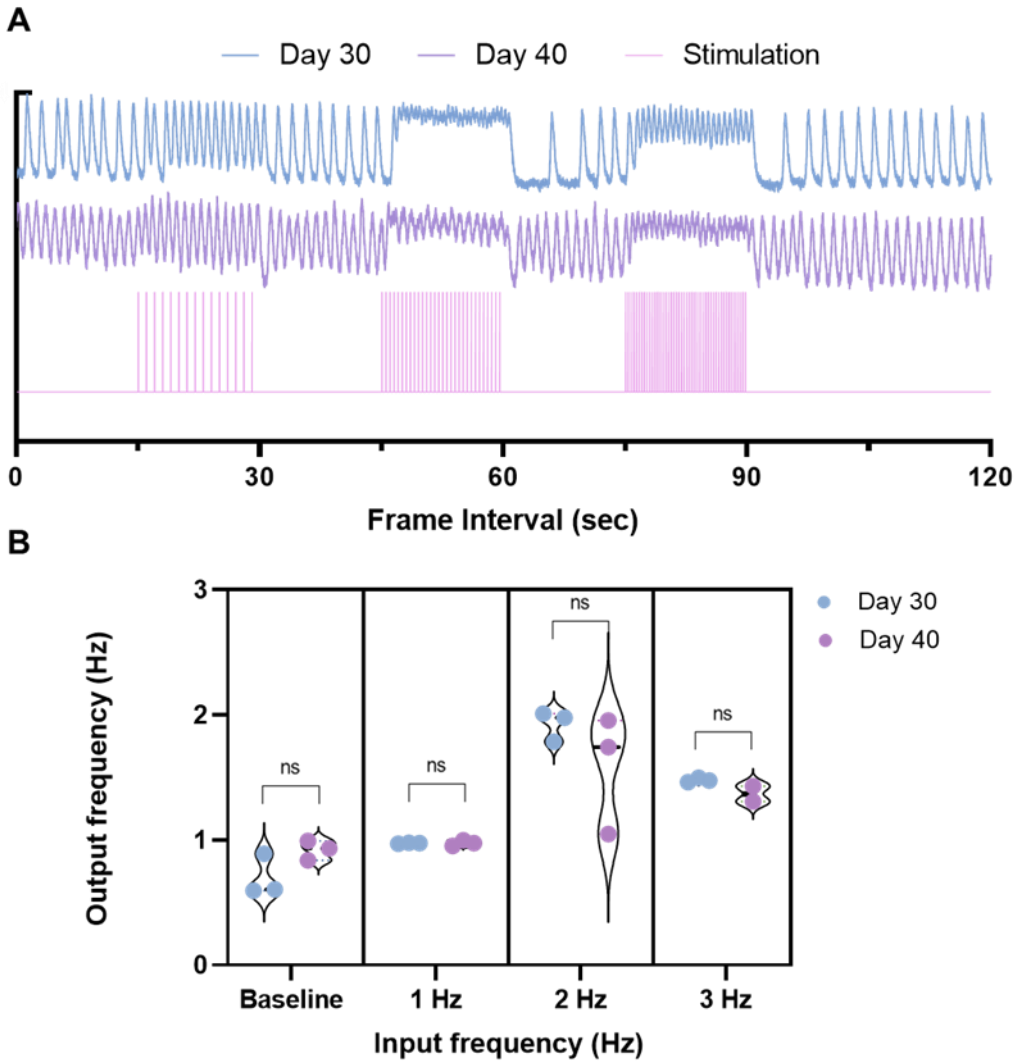


Figure 4-8 ***Electrical field stimulation of cardiac meshes at day 30 and day 40.*** *(A). A typical stimulation profile (pink) and representative traces of cardiac mesh response to the stimulation at day 30 (blue) and day 40 (purple). (B). Violin plots of the average output frequency of calcium signal measured during spontaneous generation of transients (Baseline) and upon exposure to 1 Hz, 2 Hz and 3 Hz field stimulation. Repeated measures Friedman's test with Dunn multiple comparison correction. ns – p > 0.05. N = 3, n = 2, where N is the number of independent scaffolds used for analysis and n is the number of videos acquired per scaffold.*

4.4.5 Immunofluorescent cell phenotype profiling of cardiac meshes

As previously described in Chapter 3, differentiation of hiPSCs *in situ* generates multiple cardiomyocyte and non-cardiomyocyte subtypes. Immunofluorescent staining of cardiac meshes at day 30 and day 40 was used to confirm the identity and compare the distribution of cell phenotypes present on the material scaffold. First, the meshes were stained in duplicates for cardiomyocyte marker cTnT - a structural protein involved in the cardiomyocyte contractile machinery. Four scaffolds were imaged using confocal microscopy with tiling to demonstrate the large-scale distribution of cardiomyocytes on the scaffold (Figure 4-9). Three scaffolds (Rep 1 of day 30, Rep 1 and 2 of day 40) were rich in cTnT-positive cells, that were evenly distributed across the mesh, consistent with the functional syncytium previously observed using calcium imaging. Although Rep 2 of day 30 mesh contained some cTnT-positive regions, it demonstrated a considerably lower cTnT signal, with many connecting regions only stained for DAPI. Since this trend was not seen in the other replicate of the same timepoint, this result was likely a representation of the stochasticity of the cardiac differentiation process with variable success rates. Although immature hiPSC-CMs have a higher proliferation capacity than the native adult cardiomyocytes, they have been shown to contain <5% of EdU-incorporating cells in monolayer cultures 25 days after differentiation induction (Minter-Dykhouse, Nelson & Folmes, 2022; Zhao et al., 2020). Therefore, the number of cTnT-positive proportion of cells would remain relatively stable over time due to low proliferation rates.

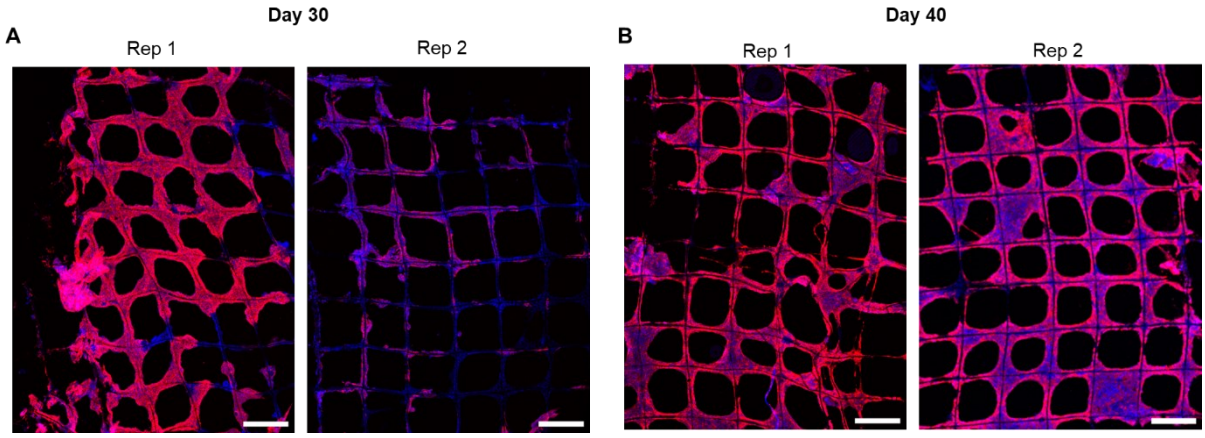


Figure 4-9 ***Immunofluorescent staining of cardiomyocyte distribution in cardiac meshes at day 30 (A) and day 40 (B).*** *Four cardiac meshes stained for cTnT (red) and DAPI (blue). Scale bar = 500 µm.*

The presence of other cell types in the cardiac meshes was then investigated through immunofluorescent staining for endothelial marker CD31 and mesenchymal cell type marker Vimentin (Figure 4-10). Vimentin is a cytoskeletal intermediate filament protein often used as a fibroblast marker in literature, however, its expression in other cells of mesenchymal origin, including endothelial, has been noted (Boraas & Ahsan, 2016). While fibroblasts are a prevalent non-cardiac cell type generated as a by-product of cardiac differentiation, they are challenging to stain due to the large heterogeneity of fibroblast cell populations and the lack of a universal marker (Kempf & Zweigerdt, 2018; Janmaat et al., 2015). Their identification therefore often requires complex staining panels, either consisting of antibodies against multiple fibroblast-related proteins (anti-discoidin domain receptor 2 (DDR2), anti-fibroblast-specific protein 1 (FSP1)) or combining positive vimentin staining with negative staining for other non-fibroblast markers in an elimination-based strategy (Goodpaster et al., 2008; Kong et al., 2013; Choi et al., 2008). Using the latter approach, in cardiac meshes the fibroblast populations were approximated to $Vim^{+}CD31^{-}$ cells.

When imaged using a 10x magnification lens on a confocal microscope, vimentin-positive cells were identified in all four cardiac meshes (Figure 4-10). Notably, in both day 30 samples the expression of vimentin was considerably weaker than that in day 40 samples, owing to the highly proliferative nature of this cell type. $Vim^{+}CD31^{-}$ cells appeared to be evenly present throughout the cardiac meshes.

CD31-positive cells were also identified in all four samples across the two timepoints (Figure 4-10). Replicate 2 of the day 30 timepoint showed a noticeably smaller number of CD31-positive cells than the other three samples, with endothelial cells scattered individually through the cardiac mesh area. In replicate 1 of the day 30 timepoint, some of the CD31-positive cells appeared to fuse and form long continuous structures. Some of those structures were linear and localised close to the PCL fibres of the scaffold. The same arrangement was a lot more pronounced in both day 40 samples, with the highest CD31 expression observed in replicate 2 of the day 40 cardiac mesh. While the

fused CD31-positive formations were present throughout the cardiac mesh, it appeared that the tubes were preferentially localising at areas of high tension (either proximally to the PCL fibre or on the periphery of the tissue stretched in between two fibres).

The observed CD31-positive structures were likely formed through the spontaneous self-organisation of endothelial cells into vascular networks, a characteristic property of this cell type. Notably, late-stage endothelial progenitor cells were previously found to be more prone to tubular fusion, consistent with the observation in cardiac meshes (Mukai et al., 2008). However, to determine whether these structures formed functional tubular vasculature, higher magnification and resolution imaging would be required to identify the presence of vessel lumens in 3D structures.

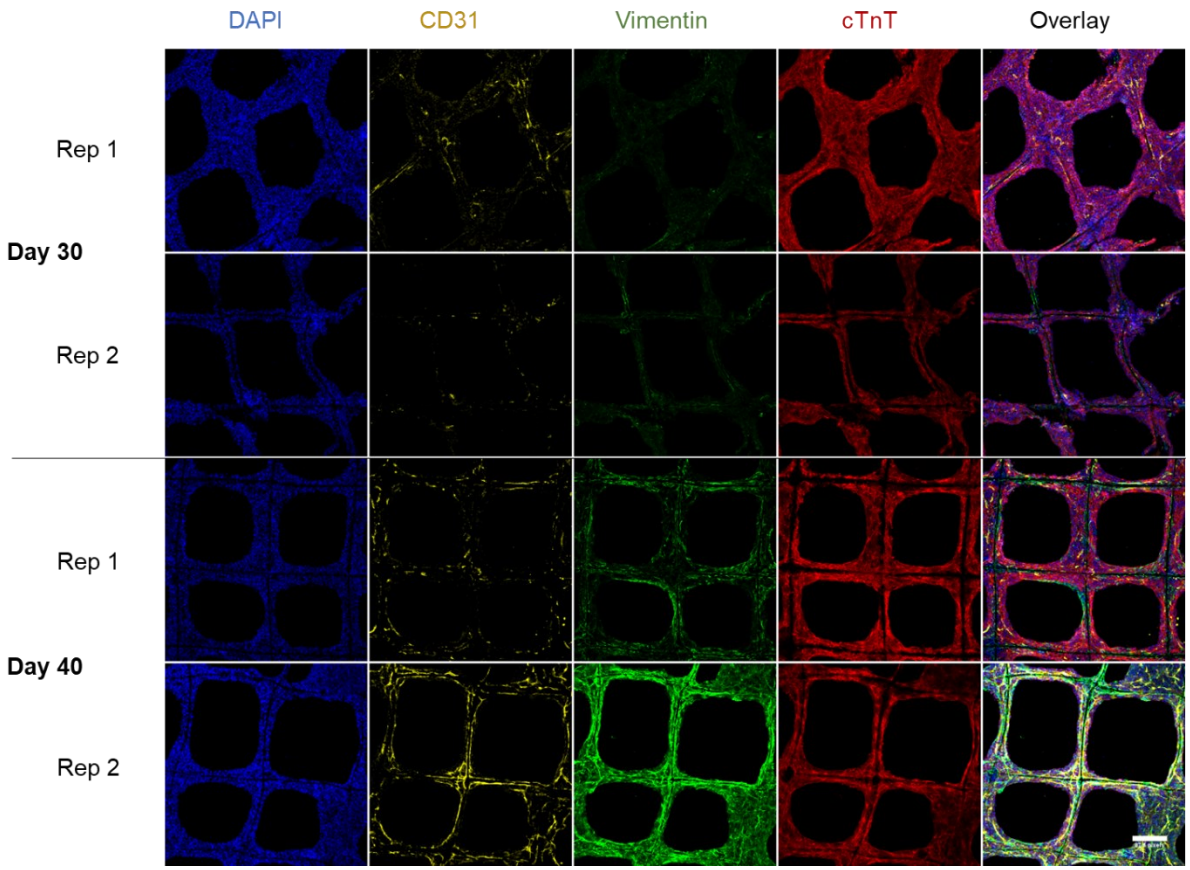


Figure 4-10 ***Immunofluorescent staining of cardiac, endothelial and mesenchymal marker expression on cardiac meshes at day 30 and day 40.*** *Average projections of z-stack confocal images. CD31 (yellow) – endothelial cell marker, Vimentin (green) – mesenchymal/fibroblast marker, cTnT – cardiac marker. Scale bar = 200 µm.*

Although wholemount immunofluorescent staining is sufficient for the relative characterisation of cell phenotypes in the differentiated constructs, the thickness of the tissue limits the penetration of

the light beam into the sample. To reconstruct the full volume of the cardiac meshes at high magnification, an adapted optical clearing protocol was applied to the samples (Zukor, Kent & Odelberg, 2010). The samples were originally stained for cTnT, CD31 and vimentin, however, CD31 staining was unsuccessful, likely due to the harsh conditions of the staining solution containing 2% (v/v) triton-X surfactant potentially disintegrating the proteins within the cell membranes.

Z-stacks containing the full volume of the cells located on the junctions of cardiac meshes were acquired in day 30 and day 40 samples (Figure 4-11A,C). At day 30, acellular cavities were visible proximally to the PCL fibre both at the linear and cross-over regions (Figure 4-11A), while at day 40 the cells appeared to be in contact with the PCL fibre (Figure 4-11C). It is possible these cavities were remnant of the oval cavities seen through brightfield at earlier stages of construct growth. Vimentin-positive cells were clearly localising along the direction of the fibre, appearing to fully coat the surface of the fibre by day 40. Although the cause for the preferential differentiation into vimentin-positive cells at the material interface was not in the scope of this project, further investigation uncovering the reason for this phenomenon would be interesting. For example, differentiating hiPSCs on a 2D PCL surface would uncover the role of material source on stem cell fate, while systematically varying the tension applied to the melt electrospun scaffolds during culture would determine how a change in local mechanical forces affects the localisation of cells of mesenchymal origin.

cTnT-positive cells were present through the volume of the structure, with decreasing cell density towards the middle of the construct. Cardiomyocyte-rich microtissues at the scaffold junctions were 97 µm- and 75 µm- thick at day 30 and day 40 respectively, shown by the full volume of the z-stack was reconstructed in 3D (Figure 4-11B,D). On the extremities of the construct the cardiomyocytes from either side of the PCL fibres were in full contact, forming a continuous layer of cells on top of the scaffold, thereby fully enclosing the material inside the cell mass.

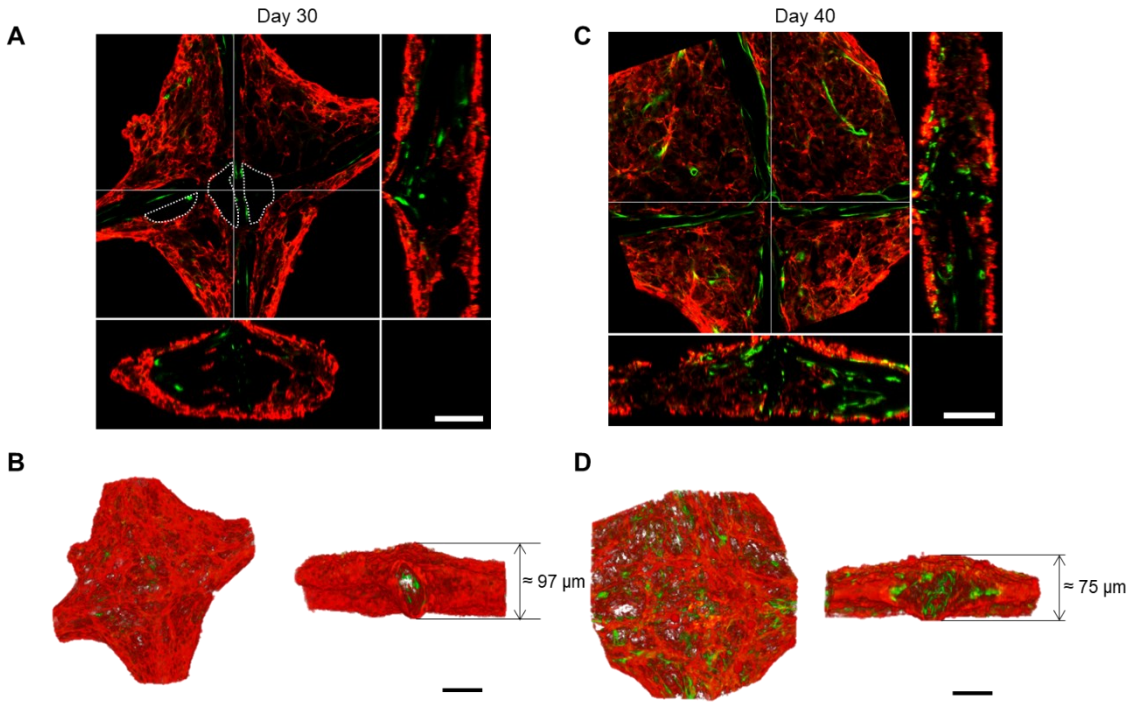


Figure 4-11 ***Full-volume immunofluorescent staining at the junction areas of optically-cleared cardiac meshes.*** *(A). An average projection of a z-stack image of cTnT (red) and vimentin (green) marker distribution with orthogonal x-z and y-z views of day 30 cardiac mesh. Dashed line demonstrates cell-free cavity formation. (B). Top and side views of a 3D-reconstruction of the cell distribution on the scaffold junction at day 30. (C). An average projection of a z-stack image of cTnT (red) and vimentin (green) marker distribution with orthogonal x-z and y-z views of day 40 cardiac mesh. (D). Top and side views of a 3D-reconstruction of the cell distribution on the scaffold junction at day 40. Scale bars = 50 µm.*

4.4.6 *Ex vivo* myocardiac slice as a model for cardiomyocyte delivery

Combining the observations from immunofluorescent staining with the ability of cardiac meshes to follow electrical stimulation under physiological conditions suggested that from day 30, cardiac mesh systems could be a potential platform for cardiomyocyte delivery to native cardiac tissue. In this scenario, the PCL fibres in the core of the mesh would provide structural support for cardiomyocyte microtissues, allowing to affix them to the native tissue. The cardiomyocytes encapsulating the PCL would directly interface with the native myocardium, facilitating early contact between the exogenous and endogenous cells. For proof-of-concept testing of cardiomyocyte delivery via the cardiac mesh, rat myocardial slices were chosen as a model of the functional healthy target tissue.

The details of optimisations of the interface between cardiac meshes and myocardial slices are extensively described below. However, all the experiments followed the same general procedure

consisting of four main steps: mesh setup, myocardial slice preparation, mesh-slice integration, and culture (Figure 4-12). Although a detailed account of the procedure can be found in the section 4.3.5, a brief outline of the process is described below to facilitate the explanations of interface optimisation.

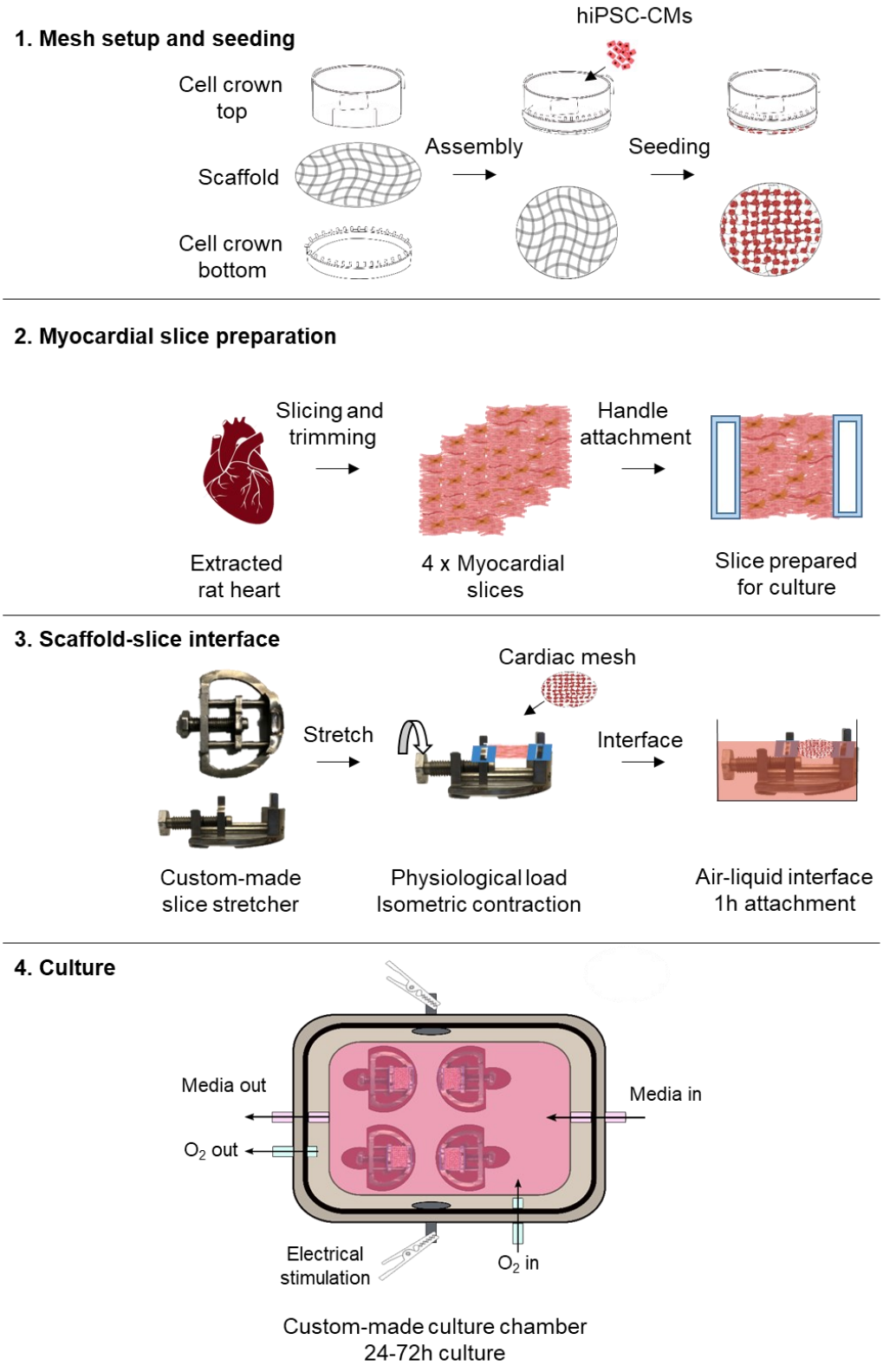


Figure 4-12 ***Schematic of the preparation and setup of cardiac mesh interface experiments with myocardial slices.*** *Schematic prepared using Biorender.com, Inkscape and Microsoft PowerPoint.*

Mesh setup. I*n situ* differentiation of hiPSCs on PCL fibres required a minimum of 30 days culture and had a variable success rate, making fully differentiated cardiac meshes a precious resource. Seeding monolayer differentiated hiPSC-CMs directly onto a PCL scaffold allowed to quickly and reproducibly generate cell-laden scaffolds for slice interface process optimisation. Furthermore, *in situ* differentiated cardiac meshes resulted in a heterogenous population containing non-myocyte phenotypes. Although the diversity of cell types is an overall advantage of the *in situ* differentiated system, such heterogeneity would complicate the interpretation of which cell types are transferred onto the slice during initial cardiomyocyte delivery results. Monolayer cultures were purified through metabolic selection, ensuring only cardiomyocyte population delivery was assessed.

Melt electrospun PCL scaffolds were immobilised by the two components of the cell crown, allowing to isotropically stretch the material at the very bottom of the assembled culture system (Figure 4-12). Purified monolayer hiPSC-CMs were then seeded onto the scaffold and allowed to attach for 24 hours, forming a model of a cardiac mesh with cardiomyocytes attached to PCL fibres at the bottom of the cell crown. The cell crown allowed to easily handle the mesh and ensure the material was kept taut. These cardiac meshes with pre-differentiated hiPSC-CMs were used unless otherwise stated.

Slice preparation (Watson et al., 2017, 2019)**.** A heart was extracted from a rat and processed to isolate and open the right ventricle. The opened ventricle was affixed to an agarose block using Histoacryl tissue glue and cut into 300 µm-thick slices using a high-precision vibratome. After discarding the slices obtained from the epicardial and endocardial layers, four myocardial slices per animal were produced. Each slice was then trimmed to produce a rectangular piece of tissue, with myocardial fibre alignment parallel to the length of the slice. Two 3D-printed handles were then immersed in Histoacryl surgical glue, excess glue was blotted off and the handles were affixed to the slice, perpendicular to the fibre alignment.

Scaffold-slice interface. The attached handles were used to immobilise the slice between two posts of a custom-made stretcher device. The screw of the stretcher was used to apply a physiological (17.5%) stretch to the cardiac slice, allowing it to contract isometrically during culture. The slice was then positioned into a culture chamber partially filled with media, with the liquid reaching the slice surface but not submerging it fully. While the exact stages at which the mesh was introduced onto the slice varied across experiments, for all samples the cardiac mesh and the slice were left to interact for 1 hour in the air-liquid interface without electrical stimulation or perfusion, theoretically allowing for initial cell-cell attachments to form (Hachim et al., 2022).

Culture. Post-interface, a custom-made culture chamber was gently filled with the remaining media, fully submerging the slice and the mesh. Each chamber allowed to culture four slices simultaneously. The culture conditions required for slice survival and maintenance involved continuous media perfusion, daily supplementation with fresh media, 1 Hz stimulation at 15 V, and media oxygenation. After culture, the slices were either analysed functionally using force transducer measurements, stained live and imaged immediately, or fixed in 4% (v/v) PFA for subsequent immunofluorescent staining.

4.4.7 Optimisation of cardiac mesh and slice interface

4.4.7.1 Pilot interface study

During the pilot cardiomyocyte delivery study, a cell crown with cardiac nodes differentiated *in situ* on the 800 µm spacing scaffold was placed directly on top of the slice immobilised on the stretcher inside the culture chamber (Figure 4-13A). The cellularised scaffold was incised at the site of contact with metal posts of the stretcher and incubated in the air-liquid interface for 1 hour prior to 24-hour culture. The slice and the cell crown were then removed from the stretcher, and the cellularised scaffold was excised from the cell crown using microscissors prior to fixation. Unfortunately, during

the cell crown excision, the mesh was visibly separated from the slice, likely due to relatively larger pulling forces on the material in comparison to gentle cell-cell contacts produced in culture.

Nevertheless, two interfaced slices and one control slice were immunostained with anti-GFP antibody to detect any delivered hiPSC-derived cells (Figure 4-13B,C). Since the hiPSC-CMs were produced from GCaMP6f-modified hiPSC cell line, all derived cells would contain GFP protein fused with calmodulin and M13 peptide (Jiang et al., 2018), while no GFP would be expressed by the endogenous cells of the myocardial slice. The cellularised scaffold was gently removed from the slice surface prior to imaging to allow visualisation of only truly delivered cardiomyocytes. The autofluorescence of the slice was used to visualise the boundaries of the tissue.

Both slices interfaced with cellularised scaffolds contained several GFP-positive cells on their surface (Figure 4-13B). In replicate 1, exogenous cells were visibly localised in between each myocardial fibre, with the largest delivered cell mass observed in the large vacant space at the bottom of the image. A larger FoV of replicate 1 can be seen in Figure 4-13C, showing the distribution of hiPSC-derived cells across ≈ 5 mm-long distance. In replicate 2, all exogenous cells were clustered around a circular feature of the slice, which most likely was a cross-section of a microvessel. The control slice did not contain any GFP-positive cells.

The successful cell transfer appeared to occur either in between the advacent cardiac fibres, or in the vicinity of a microvessel. The former site could be attractive to exogenous cells because of the lower local cell density in inter-fibre space in comparison to the tightly packed endogenous cardiac fibres with little room availability for delivery. It is possible that attraction of exogenous cells towards the microvessel is due to the paracrine signalling of the endothelial cells, which is known to promote survival of engrafted cardiomyocytes (Sun et al., 2020). While this was a promising result of successful exogenous cell delivery to a healthy myocardial slice after only 24 hours in culture, the experiment contained several limitations. Firstly, the *in situ* differentiated scaffold with cardiac nodes was used, which did not undergo metabolic selection for hiPSC-CM purification. Therefore,

the delivered cells could be non-cardiac in nature, in theory decreasing the delivery efficiency of functional cardiomyocytes. Pre-differentiated hiPSC-CMs were therefore seeded directly onto the PCL scaffolds for all future experiments. Secondly, while several exogenous cells were delivered, they were not present in large numbers throughout the whole slice surface. To address this, maximum culture time for rat myocardial slices (72 hours) was employed for all future experiments in an attempt to increase delivery efficiency. Thirdly, as mentioned above, the excision of the cell crown from the interfaced slice caused a separation of the scaffold and the slice, compromising the validity of any further functional assessments of the co-culture. Furthermore, although the presence of the cell crown during interface and culture allowed to weigh the cellularised scaffold down and keep the construct in place, such an interfacing strategy had no translational potential.

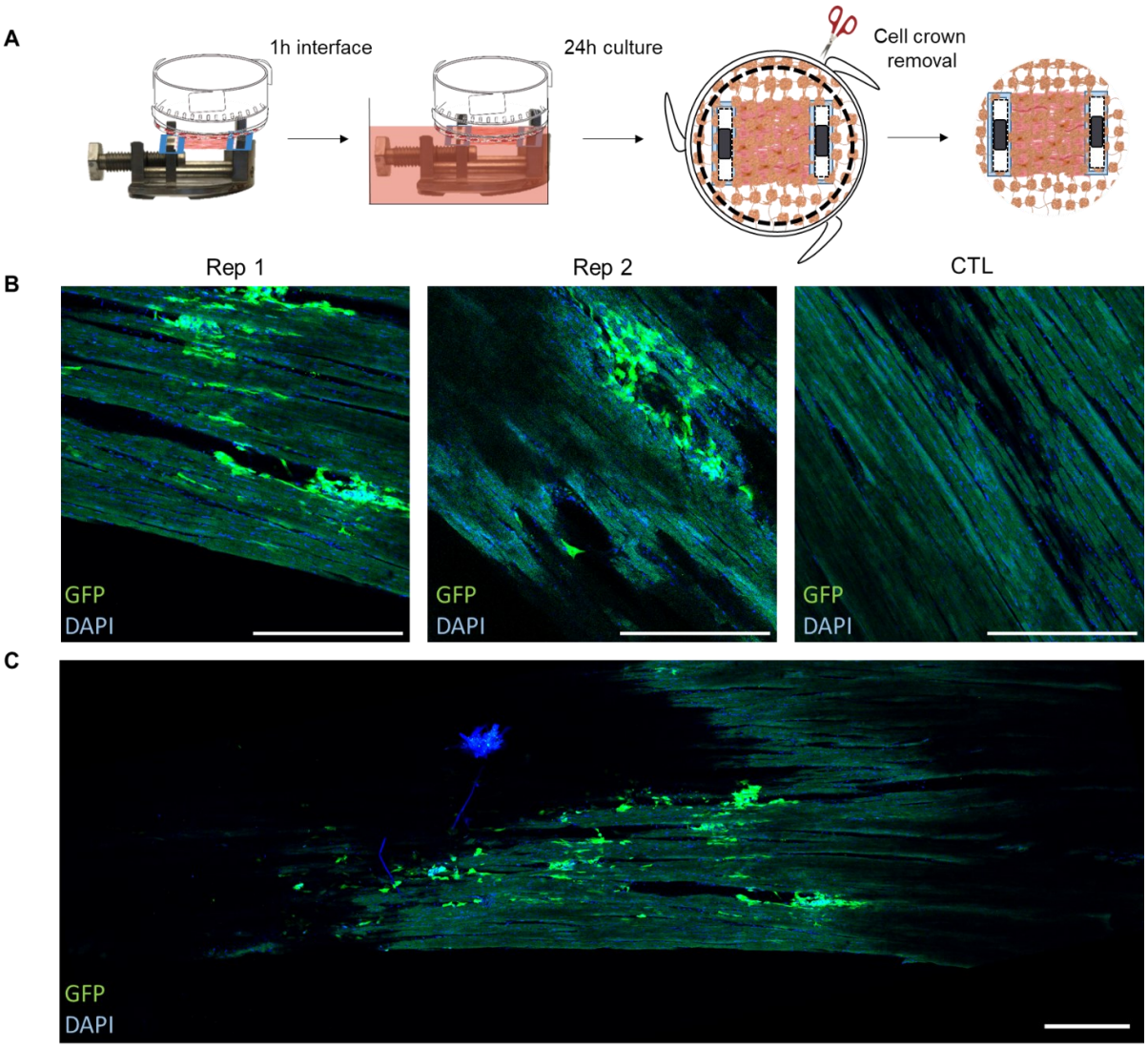


Figure 4-13 ***Exogenous cardiomyocyte delivery to a myocardial slice during the pilot study.*** *(A). Schematic of the cardiac mesh interface with cardiac slice using cell crown. Figure created using Biorender.com and Microsoft PowerPoint. (B). Confocal images of GFP-positive (green) exogenous transferred onto the myocardial slices. Replicates 1, 2 – slices interfaced with a mesh, CTL – control. All samples were counterstained with DAPI (blue). (C). Overview image of replicate 1 GFP-positive cell distribution. Scale bar = 500 µm, interface n = 2, control n = 1.*

4.4.7.2 Histoacryl tissue adhesive-based interface strategy

An alternative, more robust and clinically-relevant method for slice interface needed to be developed to address the aforementioned challenges. Preferably, the cardiac mesh would need to be attached to the slice and removed from the cell crown prior to both interface and culture, to ensure cell crown removal does not compromise cell-cell connections.

Histoacryl tissue adhesive is a synthetic n-butyl-2-cyanoacrylate-based glue that undergoes anionic polymerisation in weak bases, therefore rapidly crosslinking when exposed to hydroxide ions in water-rich environments (Sastri, 2022). It is clinically approved for use in skin wounds and is characterised by high adhesive strength, compatible with high stress-bearing conditions (Schneider & Otto, 2012). In myocardial slice preparation, Histoacryl glue is used to form a strong bond between the edges of the slice and the handles required for its immobilisation on the stretcher (Watson et al., 2017). It was hypothesised that, since it was already used on cardiac slices, the same adhesive could be used to attach the cardiac mesh to the slice.

In the updated interface protocol, the cardiac slice with handles was inverted, exposing the surface of the myocardial side of the slice on the top (Figure 4-14A). Thin traces of Histoacryl glue were applied using a needle to the edges of the slice at the handle attachment region. The slice was then inverted back to its original orientation and gently lowered into the cell crown on top of the cardiac mesh. After the adhesive bond was formed within 1 minute of slice-mesh interaction, the mesh was excised away from the cell crown using microscissors. The slice-mesh construct was then stretched, placed in the culture chamber, exposed to an air-liquid interface for 1 hour and cultured for 72 hours.

Histoacryl glue is a synthetic compound associated with a degree of cytotoxicity, which could spread over the cardiac mesh and lead to the death of exogenous cells. To investigate the extent of glue toxicity in a trial study, a scaffold seeded with live hiPSCs was attached to a fixed cardiac slice using Histoacryl. The mesh was then labelled with LIVE/DEAD® viability stain and the centre of the slice

was imaged immediately (Figure 4-14B). Calcein-positive diamond-shaped hiPSC clusters on the PCL scaffold confirmed the absence of instant detrimental effects from Histoacryl application. Longer-term cytotoxicity was also investigated by LIVE/DEAD® staining of a cardiac mesh affixed to a living myocardial slice using the protocol outlined above. No major cell death was observed after 72 hours of co-culture, with viable hiPSC-CMs present on the PCL scaffold on top of a viable slice (Figure 4-14C). Overall, it was concluded that the use of Histoacryl glue for cardiac mesh attachment to the slice did not interfere with the viability of exogenous cells throughout the duration of the slice experiment.

Next, the effects of scaffold and glue application on slice contractility were investigated through force transducer measurements performed after 72 hours of co-culture (Figure 4-14D). The analysed data included the recordings of the slices from all experiments that used Histoacryl glue for mesh attachment to the slice. Importantly, all slices interfaced with cardiac meshes were contracting after culture, demonstrating their viability and preserved functionality. The average passive force ("Baseline) of the slices interfaced with the mesh was 14.26 ± 9.09 mN/mm^2 (n = 6, N = 3), which was significantly higher than that of 3.82 ± 2.68 mN/mm^2 of the control slices (n = 3, N = 3, p = 0.04). The active force ("Amplitude"), however, was unaffected by the presence of the glue and the mesh, with mean control and mesh condition contractility measured as 2.49 ± 2.02 mN/mm^2 and 1.72 ± 1.91 mN/mm^2 respectively (p = 0.60).

The differences in passive forces could be explained by increased tissue stiffness caused by the presence of the cardiac mesh and increased amount of glue (Pitoulis et al., 2020a). However, the individual contributions of the mesh and the glue to tissue stiffness would need to be investigated further, by introducing a second control condition with extra applied glue. Additionally, the amount of applied glue was not consistent between experiments and would need to be tightly controlled for in the future.

Physiologically, the increased stiffness of a healthy myocardium is associated with a reduction in diastolic relaxation speed and a limit in cardiomyocyte contraction velocity (Emig et al., 2021; Jang et al., 2017). However, in some disease cases (e.g. early stage of post-myocardial infarction, dilated cardiomyopathy) the tissue can substantially soften (Emig et al., 2021). Therefore, there could be a potential application for a cardiac mesh-induced increase in passive force providing mechanical support and restoring healthy mechanics in otherwise diseased myocardium.

The lack of significant difference in the active force of interfaced and control slices suggests that the contractile function of the tissue remained unaffected. However, the recorded amplitudes were considerably lower than the forces of healthy rat myocardial slices previously reported in the literature, generally ranging between 5 and 15 mN/mm^2 (Pitoulis et al., 2022; Nunez-Toldra et al., 2022; Watson et al., 2019). The culture protocol included 1 hour of an air-liquid interface that both control and interfaced slices were exposed to, which could be the reason for some reduction in the active force. Indeed, when the myocardial slices were interfaced with silicone nanoneedle chips in the same air-liquid approach and cultured for 24 hours, the amplitude of the active force ranged from 1 to 6 mN/mm^2 (Hachim et al., 2022). Combined with longer overall culture time, known to reduce the contractility of the slice, the low amplitude of contractility in mesh interface experiments could be justified (Perbellini et al., 2018; Brandenburger et al., 2012). Finally, significantly increasing the N number would be key to determine the validity of this speculation.

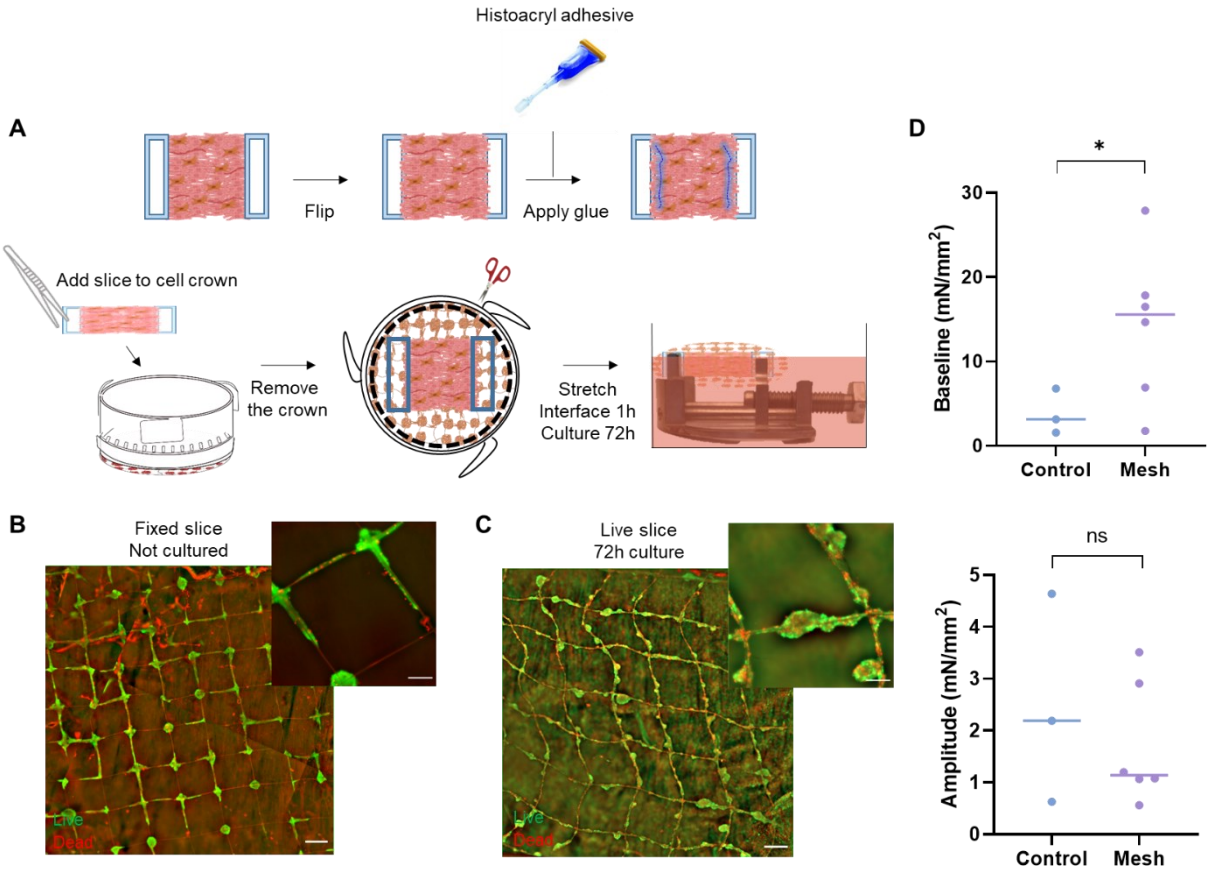


Figure 4-14 ***Alternative mesh-slice interface protocol using Histoacryl tissue adhesive.*** *(A). Schematic of the cardiac mesh interface with a fully assembled slice using Histoacryl tissue adhesive. Figure created using Biorender.com and Microsoft PowerPoint. (B). Viability staining of live (green) and dead (red) hiPSCs seeded on a 500 µm scaffold and interfaced with a fixed myocardial slice using the Histoacryl method. (C). Viability staining of live and dead hiPSC-CMs seeded on a 500 µm scaffold, interfaced using the Histoacryl method and cultured for 72 hours on a live myocardial slice. Scale bars = 200 µm overview, 100 µm close-up. (D). Force transducer measurements of average passive (Baseline) and active (Amplitude) forces generated by the slices after 72 hours in culture with meshes interfaced using Histoacryl. Control n = 3, Mesh n = 6, both N = 3, where n is the number of slices and N is the number of animals used. Welch;s unpaired t-test, ns – p > 0.05, * - p < 0.05.*

As the compatibility of both the exogenous cells and myocardial slices with the Histoacryl-based attachment method was confirmed, the slices were next immunostained for GFP and cTnT to determine the delivery efficiency of the new approach. The distribution of delivered cells onto the slices was assessed by whole-slice widefield fluorescent imaging (Figure 4-15A). The delivery efficiency remained limited, with only a few GFP-positive locations detected in both interfaced slices. Furthermore, some GFP-positive cells were present on the control slice. The locations with delivered cells were then imaged at higher magnification (Figure 4-15B). Replicate 1 contained clusters of GFP-positive cells on top of the myocardial fibres. Replicate 2 showed GFP-labelled cells individually interspersed across the myocardial tissue. The control contained a marginally smaller number of delivered cells.

The low delivery efficiency of the Histoacryl-based attachment of cardiac mesh to the slice was not surprising, as during the experiment the bonding of the two components was inconsistent. In an attempt to minimise the volume of applied glue, some meshes were poorly adhered to the slice, with multiple corners lifting off the slice either during or after culture. However, the overall interface process was more stable in comparison to the cell crown-based interface method, minimising post-interface mesh handling and facilitating functional measurements upon culture completion. Thus, while Histoacryl adhesive was deemed a cytocompatible strategy for the mesh-slice interface, the mode of application of the glue needed to be further improved.

The presence of GFP-positive cells on the control slice was surprising and likely caused by the simultaneous culture of the control and interfaced slices in the same culture chamber. It is therefore possible that if some hiPSC-CMs were detached from the fibre during the interface process, they could be introduced onto the control slice surface *via* the flow of media perfusion. Ideally, the control and interfaced slices would be fully separated during culture. However, optimisation of the interface protocol was a priority at the time, and it was hypothesised that once the slice-mesh co-culture is consistent, there would be a clear difference between the control and mesh conditions. Therefore, for all future experiments the mesh and control slices were still cultured in the same chamber, while separate chambers were planned to be used for the optimised large-scale study. It should be noted, however, that the non-specific transfer of exogenous cells was not observed in any follow-up experiments.

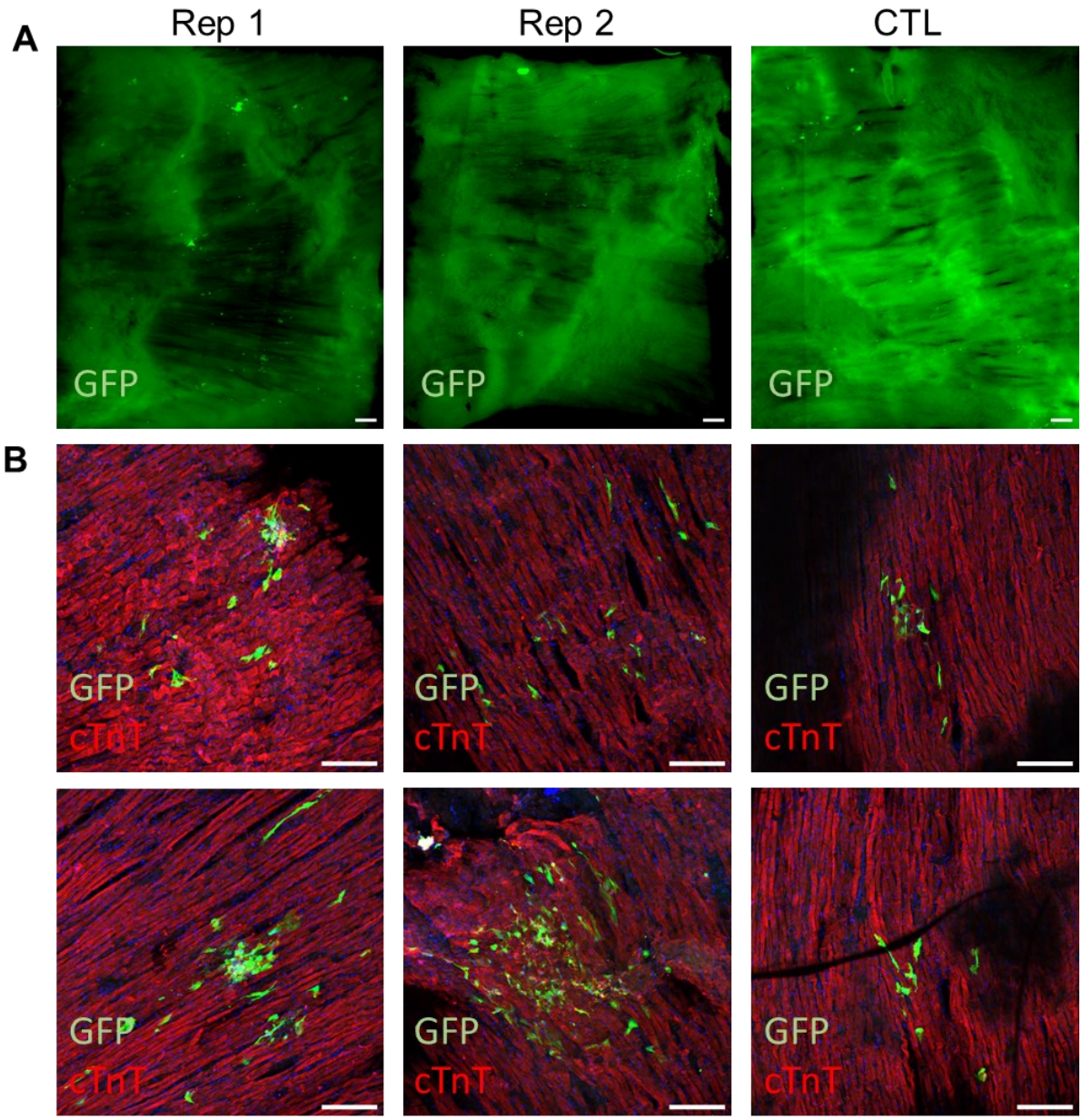


Figure 4-15 ***Immunofluorescent staining of hiPSC-CMs delivered to the myocardial slice using the Histoacryl interface method.*** *(A). Widefield fluorescent imaging of exogenous hiPSC-CMs labelled with GFP antibody (green) on the whole slice surface. Replicates 1,2 – slices interfaced with cardiac meshes, CTL – control. Scale bar = 500 µm. (B). Confocal imaging of GFP (green) and cTnT (red) at 10x magnification of exogenous hiPSC-CMs on cardiac slices. Replicates 1,2 – slices interfaced with cardiac meshes All samples were counterstained with DAPI. Interface n = 2, control n = 1. Scale bars = 200 µm.*

4.4.7.3 Refining the Histoacryl tissue adhesive-based strategy for mesh-slice interface

To improve the consistency of bonding, the attachment between the mesh and the slice was performed during an earlier stage of myocardial slice preparation. Once the fresh sliced tissue was trimmed into a rectangular shape, the slice was covered with the cardiac mesh stretched at the bottom of the cell crown (Figure 4-16A). The 3D-printed handles were then dipped in Histoacryl glue, blotted off and affixed to the slice on top of the cardiac mesh. Once the bond was formed between the slice, mesh and handles, the cell crown was excised away using the microscissors. The slice stretching and culture was then performed as previously described. This method robustly produced bound slice-mesh constructs, which were then stained for GFP and cTnT to determine whether the more stable interface improved the efficiency of exogenous cell delivery.

Tiled confocal imaging was used to visualise the distribution of delivered cells across three interfaced slices and one control (Figure 4-16B). All interfaced slices contained a small amount of GFP-labelled cells, while no exogenous hiPSC-CMs were observed on the control slice. The mode of delivery remained punctate, with only a small number of GFP-positive cells present on each interfaced slice. However, when compared to the distribution observed in Figure 4-15A, the overall area of delivery appeared larger, with GFP-positive cells scattered across the whole area of replicates 1 and 2. A closer inspection of the four quadrants of replicate 2 confirmed the specificity of the observed signal, with visible GFP-positive cell bodies present in each quadrant (Figure 4-16C). While the widespread locations of delivered cells suggested a more even contact between the meshes and the slices, the low number of delivered cells remained an issue.

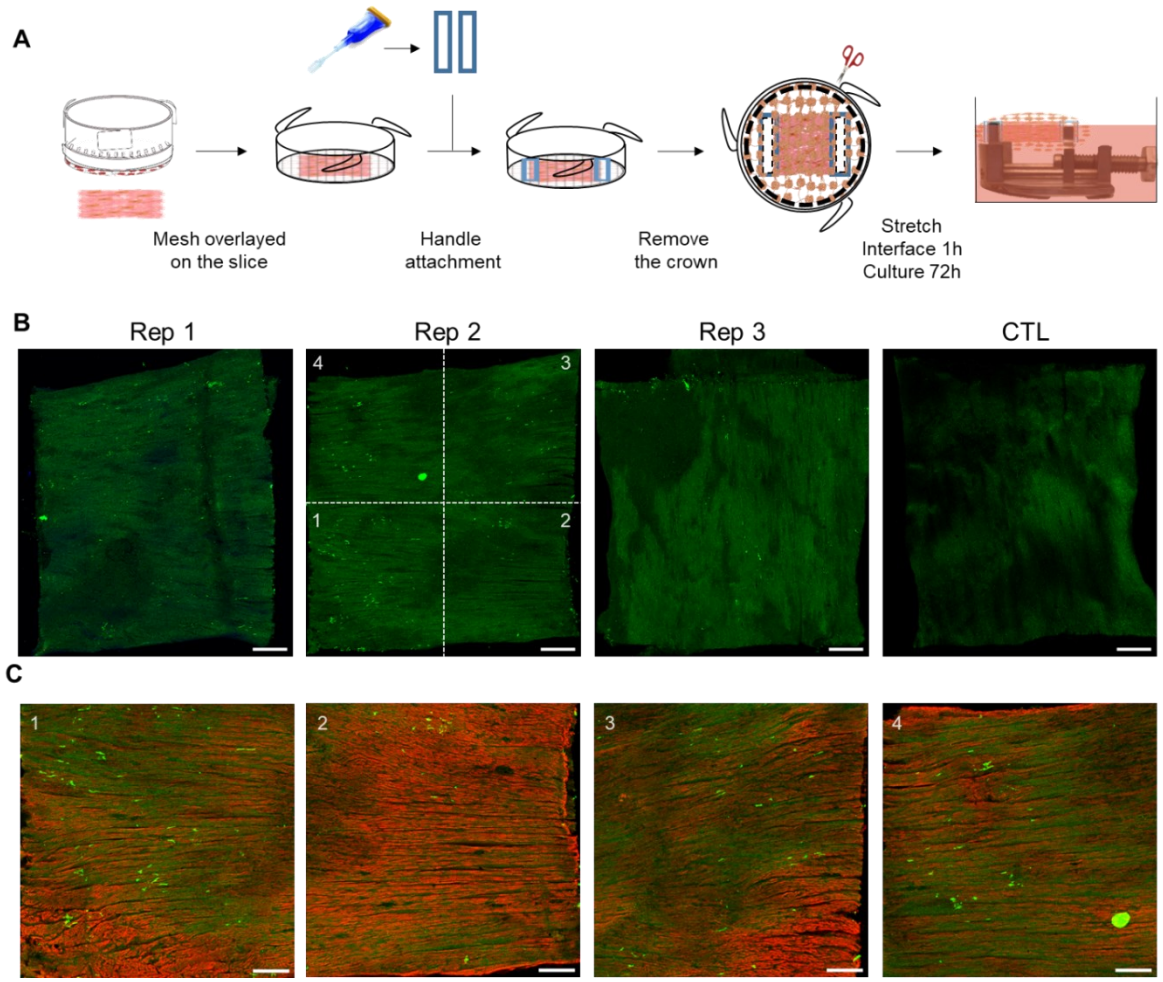


Figure 4-16 ***Adapted protocol for interfacing cardiac meshes with myocardial slices and its delivery efficiency.*** *(A). Schematic of the updated interface process with cardiac mesh applied to the slice prior to handle attachment. Figure created using Biorender.com and Microsoft PowerPoint. (B). Confocal imaging of GFP-positive (green) exogenous hiPSC-CM delivery to myocardial slices using the adapted Histoacryl adhesive interface protocol. Each image demonstrates the whole surface of a cardiac slice. Replicates 1,2,3 – slices interfaced with cardiac meshes, CTL – control. Scale bars = 1000 µm. (C). GFP (green) signal distribution across four quadrants of replicate 2 slice, counterstained with cTnT (red). Interface n = 3, control n = 1. Scale bars = 500 µm.*

The effect of mesh orientation on delivery efficiency to the slice was then investigated to determine whether the seeded hiPSC-CMs are predominantly localised at the bottom or on the top of the PCL fibres. The slices were either covered with the mesh cell crown up, as previously described, or lifted on top of a 4% (w/v) agarose block, allowing to invert the cell crown before the interface (Figure 4-17A). For both configurations, the 3D-printed handles were glued to the slice edges using Histoacryl adhesive, followed by the standard slice culture protocol.

Exogenous cardiomyocyte delivery to one slice with regular mesh orientation and two slices with inverted mesh orientation was visualised using GFP immunostaining and tiled confocal microscopy of whole slices (Figure 4-17B-D). All three slices contained punctate GFP-positive cells on their surface. The number of delivered hiPSC-CMs was lowest on the slice with regular mesh orientation, with GFP-positive signal mostly localising to the edges of the slice (Figure 4-17B). hiPSC-CMs delivered *via* inverted cardiac meshes were spread across the whole surface of the slice in both replicates 1 and 2, and showed similar distribution of GFP-positive cells (Figure 4-17C,D). Replicate 2 contained two large clusters positively stained for GFP, likely detached from the PCL fibre but not fully integrated into the slice (Figure 4-17D). Although these results showed slightly higher delivery efficiency and coverage area of inverted cardiac meshes in comparison to regular orientation, the overall numbers remained very low. Furthermore, the inverted results showed no improvement in comparison with the regularly orientated meshes from Figure 4-16. Overall, it was concluded that the mesh orientation did not cause a pronounced improvement on exogenous hiPSC-CM delivery to the myocardial slice.

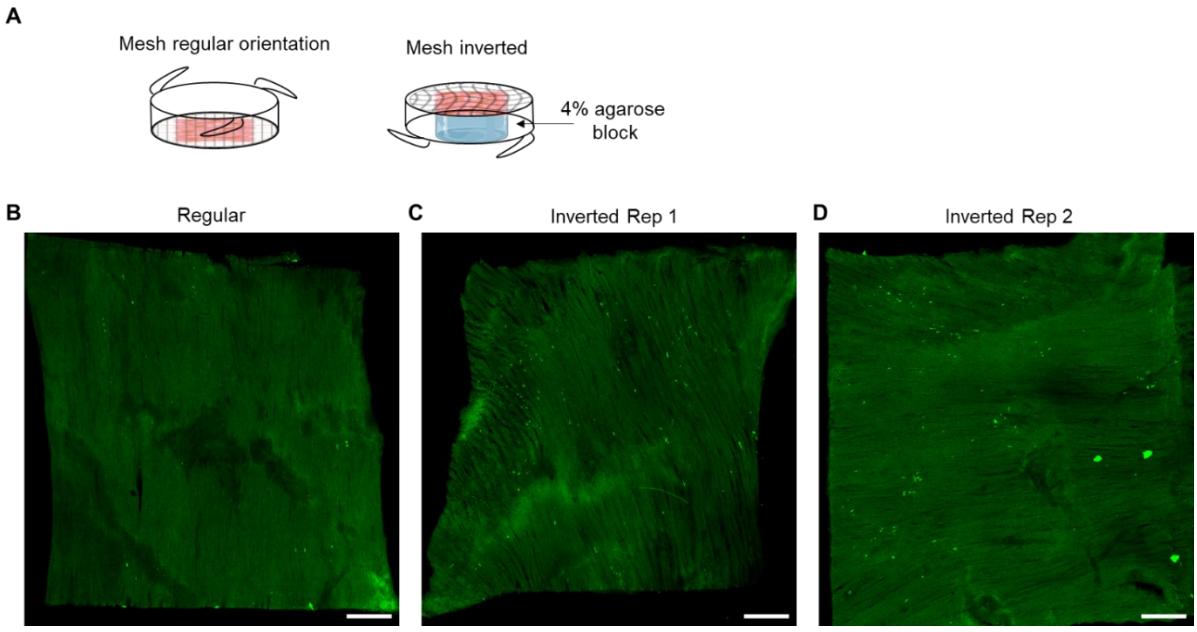


Figure 4-17 ***The effect of cardiac mesh orientation on hiPSC-CM delivery to the slice.*** *(A). Schematic of the bottom-down cardiac mesh orientation (regular) and inverted cardiac mesh orientation, achieved using a 4% (w/v) agarose block. Figure created using Biorender.com and Microsoft PowerPoint. (B). Confocal imaging of GFP signal (green) from exogenous hiPSC-CMs delivered to a myocardial slice using regular orientation.(C,D). Confocal imaging of GFP signal (green) from exogenous hiPSC-CMs delivered to myocardial slices using inverted orientation. Scale bars = 1000 µm.*

4.4.7.4 Troubleshooting the slice-mesh interface

One of the possible causes of low delivery efficiency could be an unstable contact between the mesh and the slice. Although the initial physical contact between the two was ensured by the air-liquid interface, confirmed visually, the consistency of the cell-slice contact during culture remained unknown. *In situ* volumetric imaging of the cardiac meshes on the slice could allow to visualise whether the two components of the culture remain in proximity. To achieve that, stretched slices interfaced with meshes would be removed from the culture chamber, fixed and immediately imaged directly on the stretcher using an upright confocal microscope (Figure 4-18A). This approach should minimise any post-culture disruptions of the cell-cell contacts.

Exogenous hiPSC-CMs on a PCL scaffold were labelled with SiR-Actin fluorescent dye prior to attachment to the slice to enable quick tracking of exogenous cells without the need for extensive immunostaining protocols post fixation. However, when the samples were imaged a strong SiR-Actin

signal was detected from both hiPSC-CMs of the mesh and the cells of the slice, possibly as a result of plasma membrane efflux pumps releasing SiR-Actin molecules into the media during culture (Gerasimaite et al., 2020). Regardless, the samples were imaged despite the lack of a specific signal as the difference in morphology between the slice and the scaffold allowed to visualise the differences of the interface.

Z-stacks of three junction areas of a cardiac mesh were acquired and presented either as a 2D projection of all acquired images for the top-down view or a reconstructed 3D structure rotated orthogonally to the imaging plane for the side view (Figure 4-18B-D). Each image demonstrated a different modality of mesh and slice interface. Full contact between the two was clearly visible in Figure 4-18B, with the cell mass at the scaffold junction completely aligning with the surface of the slice. Partial contact in Figure 4-18C was visible, with half of the exogenous hiPSC-CM mass lifting off the slice surface. Finally, the cell mass at the junction of Figure 4-18D was completely detached from the slice, with a visible SiR-Actin-negative gap in between the cardiac mesh and the slice surface. Indeed, these results confirmed that although process of handling of the cardiac mesh and the slice was optimised, on the microscopic scale the interface remained variable. There are multiple reasons for such variable contact: some liquid could be trapped in the setup, slightly lifting the mesh off the slice surface; after adhesion of the mesh to the slice and handles the material could be unevenly stretched over the surface of the slice, partially coming off; the variability in the thickness of seeded hiPSC-CM clusters could lead to only partial coverage of the PCL fibre, with some material layers separating the cells from the slice. Finally, the physiological stretch of the slice does not reach the limit of tissue elasticity, therefore the slice surface is not perfectly flat, with some areas potentially dipping below the plane of a taut cardiac mesh. Although the exact reasons for the unstable mesh-slice interface are unknown, extensive optimisation of the culture setup would be required to improve this co-culture system.

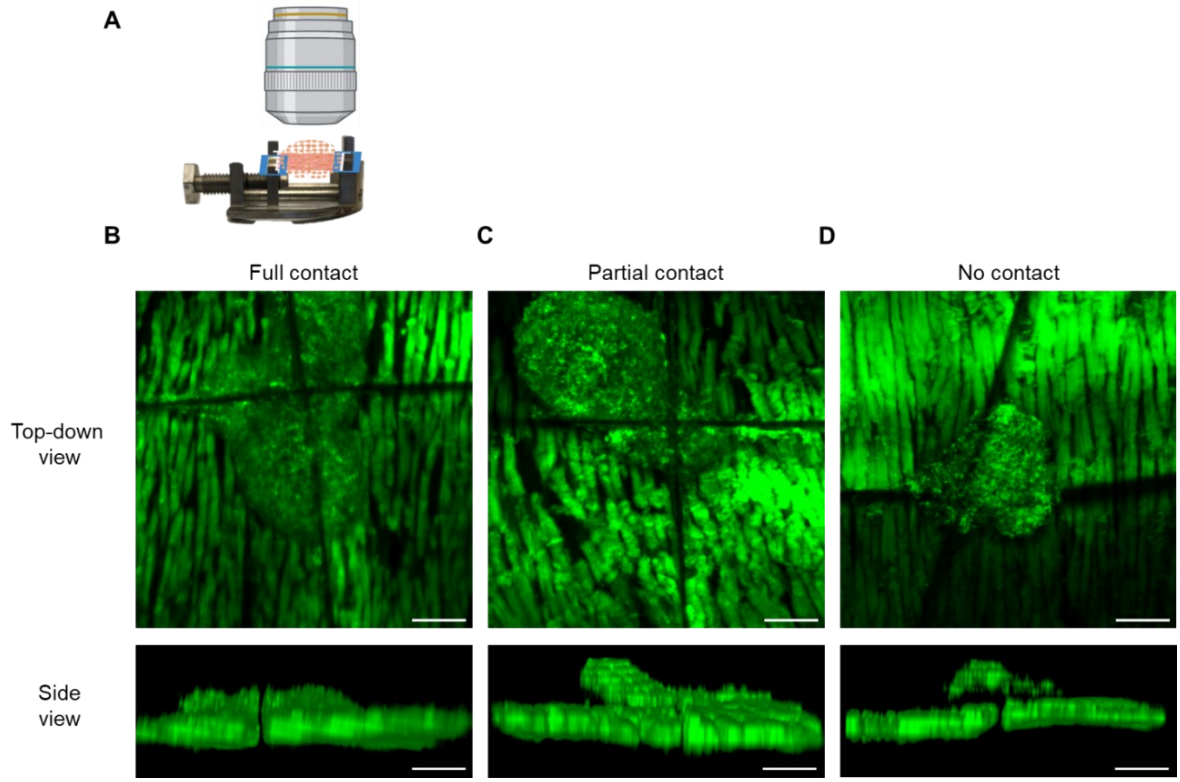


Figure 4-18 ***Confocal imaging of the cardiac mesh-slice interface in situ using an upright microscope.*** *(A) Schematic of the configuration for imaging a cardiac slice interfaced with the mesh on a stretcher. Figure created using Biorender.com and Microsoft PowerPoint. (B). A z-stack of SiR-Actin-labelled hiPSC-CM cardiac mesh in full contact with the slice. (C). A z-stack of SiR-Actin-labelled hiPSC-CM cardiac mesh in partial contact with the slice. (D). A z-stack of SiR-Actin-labelled hiPSC-CM cardiac mesh showing no contact with the slice. All configurations show as an average projection of the signal (top-down) and as a 3D-reconstruction of orthogonal orientation (side view). Scale bars = 100 µm.*

4.4.7.5 Investigation of the required timescale for hiPSC-CM transfer from the cardiac mesh

Another possible reason for the low efficiency of hiPSC-CM delivery to the myocardial slices could be the short timescale of the co-culture. As rat myocardial slices with static preload could be kept viable for up to 72 hours (unpublished), therefore the mesh could only be allowed to interact with the slice for a maximum of 3 days.

A simple *in vitro* study was therefore performed to investigate the dynamics of hiPSC-CM transfer from the cardiac mesh. A 24-well culture plate was coated with a basement membrane solution, usually applied to tissue culture plastic to enable hiPSC-CM adhesion during monolayer replating. A cardiac mesh was lowered into the plate and pushed to the bottom until the mesh made contact

with the surface of the well. The mesh was then cultured up to 33 days, with brightfield images of 3 ROIs taken on day 3 (slice culture equivalent) and day 7, as well as fluorescent imaging of the LIVE/DEAD® staining at the experimental endpoint (Figure 4-19). Indeed, after 3 days in contact with the functionalised surface, some cells were visibly attached to the bottom of the well, with ROI1 containing the largest adhered area (Figure 4-19A). However, the transferred cell number remained low and comparable with the extent of transfer observed on 72-hour cocultures of meshes and myocardial slices. As the culture progressed up to day 7, the area of hiPSC-CM attachment to the flat surface has increased in all three ROIs (Figure 4-19B). On day 33, live hiPSC-CMs were visibly spread over 28% of the FoV of the well bottom, with the transfer occurring at most PCL fibre junctions (Figure 4-19C). The left half of the FoV remained unoccupied by the cells, however, the mesh in that region appeared out-of-focus, suggesting a lack of physical contact between the mesh and the surface. Importantly, while the coverage of the well bottom has continuously increased up to 33 days of monitoring, many hiPSC-CM clusters were not transferred to the surface, still clearly residing on the PCL scaffold (Figure 4-19C).

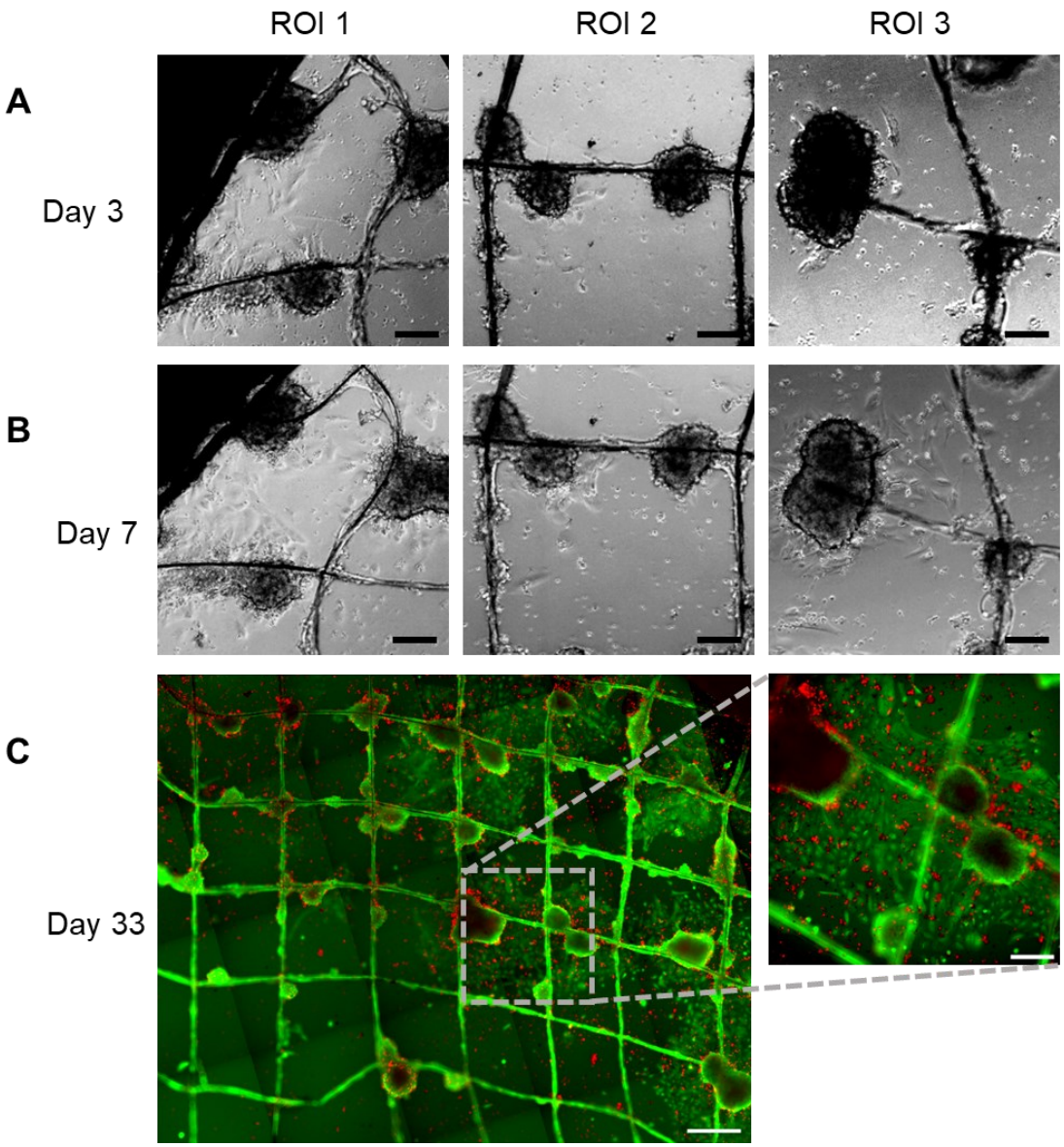


Figure 4-19 ***hiPSC-CM transfer onto a basement membrane-functionalised tissue culture surface.*** *(A,B.) Brightfield imaging of three ROIs of hiPSC-CM clusters on the PCL scaffold interfaced with a flat basement membrane-functionalised surface for 3 days (A) and 7 days (B). Magnification = 10x, Scale bar = 200 µm. (C). Widefield fluorescent imaging of LIVE/DEAD® viability staining on the 1000 µm hiPSC-CM cardiac mesh after 33 days in contact with functionalised tissue culture plastic. Live cells shown in green, dead cells shown in red. Scale bars = 500 µm overview, 200 µm close-up.*

Experimentally, hiPSC-CM transfer onto a basement membrane-coated surface had several limitations. Firstly, the migration onto a static acellular 2D surface poorly represents myocardial tissue containing closely packed contracting adult cardiomyocytes. An improvement of this study would be to investigate the migration dynamics of hiPSC-CMs when cultured on top of a monolayer of isolated cardiomyocytes. Indeed, isolated neonatal rat cardiomyocytes have been used elsewhere to validate the therapeutic effects of microneedle-based cardiomyocyte delivery *in vitro* (Tang et al.,

2018). Secondly, the experiment would need to be repeated with a significant increase in N number and quantification of the cell delivery. Nevertheless, these preliminary results suggested that prolonging culture time could increase the delivery efficiency, thereby requiring a different cardiac tissue model compatible with long-term culture. The length of cardiac slice culture can be extended by compromising the physiological culture conditions or using a different animal source. Mechanically-loaded (preload and afterload) human cardiac slices were kept in culture up to 4 months, remaining stable for the first 8 days after which a decline in cardiac gene expression was observed (Fischer et al., 2019). Rabbit slices could be cultured for up to 5 days with no change in slice contractility under mechanical preload conditions (Watson et al., 2019). Alternatively, dog myocardial slices were cultured in both loaded and unloaded conditions for 8 days but reduced in contractility approximately 7-fold in comparison to day 0 (Perbellini et al., 2018).

Finally, transwell-based unloaded myocardial human slice culture yielded viable tissue for up to 28 days, albeit showing a nearly 60-fold reduction in contractility in comparison to day 0 (Brandenburger et al., 2012). On the same timescale, exogenous cardiomyocytes did not show infiltrate the host tissue *v* when delivered as a scaffold-free patch, suggesting even longer timescales could be required for functional improvement (Yeung et al., 2019). Therefore, for future experiments the compromise between sufficient duration and physiological relevance of culture conditions for myocardial slices would need to be considered. Alternatively, *in vivo* studies with the *in situ* differentiated cardiac mesh would provide information on a longer timescale and allow to investigate the role of the nascent microvasculature in the cardiac mesh for graft-host integration. However, extensive proof-of-concept in vitro experiments of successful hiPSC-CM delivery to monolayers of isolated adult cardiomyocytes would be required to justify the transition to *in vivo.*

4.5 Conclusions and future work

In this chapter, a new platform for cell patterning was developed using highly geometric fibrous PCL scaffolds as substrates for hiPSC attachment, expansion and *in situ* differentiation. hiPSC adhesion on the material was achieved by functionalising the PCL surface with basement membrane proteins and the uniformity of cell seeding was optimised through a repeated cycle of agitation. The optimal starting cell density for successful cardiac differentiation was determined to be at 0.25×10^6 cells/scaffold, with a higher concentration of the cell suspension showing no further improvement in scaffold coverage or differentiation success. The consistency of the seeding protocol was demonstrated across three different scaffold geometries. When subjected to cardiac differentiation protocol, the larger spacing of the fibres on the scaffold led to the generation of partially inter-connected cardiac nodes, while the smaller spacing produced more uniform fully connected cardiac meshes. Both types of constructs were highly expressing the cardiac-specific marker cTnT.

The cardiac meshes were then investigated further, with their morphology, electrophysiology and multicellularity compared at two timepoints. No significant difference was detected in response to spontaneous activity or electrical stimulation of the meshes between day 30 and day 40 groups, with meshes consistently following 1 Hz stimulation, representative of the physiological human frequency. The cellular makeup of the meshes showed stable content and distribution of cardiomyocytes around the PCL fibres over time, while the amount of non-cardiomyocytes, detected by vimentin and CD31 staining, increased with longer culture duration, indicative of proliferation. Endothelial cells assembled into continuous structures, suggesting possible tubulogenesis occurring with tissue maturation. Overall, the first half of this chapter outlined the optimisation process for hiPSC culture and differentiation on PCL fibres and characterised the change in the resultant engineered tissue over time in culture.

The second half of the chapter laid the groundwork for the proof-of-concept study on cardiac mesh-mediated hiPSC-CM delivery to a functional cardiac tissue, modelled with rat myocardial slices. The protocol for mesh-slice interaction experiments was refined and used cyanoacrylate Histoacryl tissue

adhesive to secure the mesh on the slice edges. As a result, both hiPSC-CMs and myocardial slices were shown to be viable at the endpoint of culture. The slices interfaced with the mesh showed an increase in passive force indicative of higher tissue stiffness, while no effect was observed on the magnitude of the active force.

Although undeniably some exogenous cardiomyocytes were delivered to the tissue in all co-culture experiments, the results demonstrated that the delivery efficiency remained low despite the changes in the interface strategy, increase in co-culture time or mesh orientation. Two likely causes for the low efficiency were investigated and discussed: inconsistent physical contact between the mesh and the slice throughout the mesh and insufficient time of co-culture for effective hiPSC-CM transfer. Overall, the second half of this chapter optimised the protocol for cardiac mesh and myocardial slice co-culture and demonstrated a proof-of-principle exogenous hiPSC-CM delivery onto the slice surface.

There were several considerations and limitations to the experiments of this chapter. Firstly, the cardiac mesh production was limited by the inherent variability in the efficiency of existing differentiation protocols, sometimes producing constructs fully occupied by non-contractile spindle-like cells. This phenomenon is likely linked with the variable cell cycle stage at differentiation initiation, and in the future could be mitigated, for example, by chemically synchronising the cycle of the culture with nocodazole or by transfecting the starting hiPSC cell line with cell-cycle activators (Yiangou et al., 2019; Zhu et al., 2018; Pauklin & Vallier, 2013).

In the cardiac mesh-mediated delivery study, most experiments used PCL scaffolds seeded with pre-differentiated hiPSC-CMs, rather than *in situ* differentiated interconnected cardiac meshes. When seeding hiPSC-CMs directly onto the fibres, the cell density and scaffold coverage were substantially lower than those differentiated *in situ*, thereby containing less cells available for delivery. Furthermore, there was no information on whether the directly seeded hiPSC-CM clusters were seeded through the full volume of the PCL fibres, making it plausible that some could be attached in

the middle of the material, contributing to the poor contact between the mesh and the slice. Therefore, the fully optimised *in situ* differentiated meshes should be used for any future studies to avoid inconsistencies in fibre coating. The pilot delivery study was the only one that used *in situ* differentiated cardiac nodes on 800 µm-spacing scaffolds and showed a relatively high number of cells delivered locally after only 24 hours. It would be interesting to investigate the differences in the delivery potential between 800 µm cardiac nodes and 500 µm cardiac meshes, and if those could be attributed to the thickness and the weight of the engineered tissue.

Injured myocardial slices could be explored as an alternative model for exogenous cell delivery. It can be speculated that as healthy cardiac tissue is densely packed with adult cardiomyocytes, the space and niche for exogenous cell delivery could be limited. An infarcted myocardium with large areas of native myocardial death could be a more clinically relevant model, and pose as an attractive site for exogenous cell engraftment experiments, which could be modelled *ex vivo* by myocardial slices subjected to cryoinjury (Dries et al., 2021). However, it should be noted that *in vivo* the infarcted myocardium is characterised by a high inflammatory response, low oxygen supply and low pH, which are often attributed to poor delivery efficiency (Mancuso et al., 2020; Li et al., 2007; Zhang et al., 2014; Lee et al., 2020). Finally, it is possible that the species mismatch between the rat myocardial slices and human iPSC-CMs contributes to the low engraftment efficiency. Taken together, to investigate the full potential of cardiac meshes in myocardial remuscularisation, the interface experiments need to be redesigned with the final optimised cardiac meshes applied to an injured human myocardial tissue for medium- to long-term culture.

To conclude, in this chapter hiPSCs were successfully seeded and expanded on ordered melt electrospun PCL scaffolds, generating interconnected 3D clusters evenly distributed over the material. Upon exposure to an established *in situ* cardiac differentiation protocol, the cellularised scaffolds produced structures with a high cardiomyocyte content. Furthermore, the tunability of the system was demonstrated by varying the dimensions of the PCL scaffold units, producing either

globular cardiac nodes with larger 800 µm spacing or interconnected cardiac meshes with 500 µm spacing. The cardiac meshes also formed a synchronous functional syncytium, capable of capturing electrical stimulation at physiological frequency, making them promising candidates for exogenous cell delivery to the native myocardium. A significant foundation of the future *ex vivo* experiments was also laid out through optimisation of the interface between hiPSC-CM seeded cardiac meshes. Refinement of the interface and *ex vivo* slice culture time would open the opportunities for long-term evaluation of the possible functional effects following the graft and host integration, in particular, if performed on human donor injured cardiac tissue.

CONCLUSIONS AND FUTURE WORK

The geometry and arrangement of cardiomyocytes within the myocardial wall is highly organised, which significantly contributes to the anisotropic synchronous function of the heart tissue. Recapitulating this intricate cytoarchitecture therefore is critical for successful engineering of cardiac tissue *in vitro,* however, the existing models often lack cellular organisation. The work of this thesis aimed to demonstrate how two different patterning technologies, namely acoustic cell manipulation or material-guided cell assembly, can be used to develop three novel *in vitro* cardiac tissue models with improved structural complexity.

Chapter 2 focussed on developing a model containing 2D cardiomyocyte arrays on top of an MEA chip by using solution-based acoustic patterning. The system would have an advantage over the traditional hiPSC-CM monolayer systems as its defined geometry would allow the propagation of the electrical signal to be monitored in real time, having impact in the context of drug screening studies. To achieve this objective, a previous acoustic patterning device design was reconfigured into a novel modular platform, that provided central cavity design flexibility, minimised hiPSC-CM cell loss and ensured isolation of MEA contact pads. The patterning parameters, such as time and frequency, as well as the sterilisation protocol of the device were optimised to achieve successful acoustic patterning of live hiPSC-CMs on an MEA chip. In comparison to topographically-patterned MEAs described previously elsewhere, this approach could have a moderate improvement in throughput as it did not require extensive surface treatment and each device could be reused repeatedly (Wang et al., 2013; Liu et al., 2016). Frequency modulation of acoustically-patterned MEA systems also achieved similar alignment efficiency as the previous work by Natarajan et al., aligning the cells with every other electrode array using photolithography to pattern a PEG self-assembled monolayer (Natarajan et al., 2011). The main limitation of this work relied on the technical variability in device assembly leading to some inconsistency in performance, however, these issues can be addressed through more precise fabrication and assembly in a good manufacturing practice setting.

In the future, as the platform was only demonstrated for short-term (24 hour) cell culture, longer term experiments would need to be performed to determine the ability of the patterned cells to form an electrically-coupled functional syncytium and to assess whether any cell migration would occur, changing pattern fidelity over time. In these experiments, cell density would need to be optimised, time in culture required for synchronous behaviour would need to be determined, and the difference in the rate of cell migration with varying the inter-line spacing would need to be assessed. A significant improvement in these studies can be achieved by implementing methods of quantifying patterning quality, which would allow for more robust and systemic decision-making at the optimisation stage. Although the majority of the acoustic patterning studies available in literature rely on the visual qualitative assessment of patterning quality, sophisticated image analysis tools, such as Voronoi tessellation previously validated for acoustically-patterned myoblasts, provide a range of quantitative metrics (e.g. number of cell clusters, their density and area) (Armstrong et al., 2019). Such analysis would also be useful as a quality control measure for acoustically-patterned hiPSC-CM arrays on MEAs as the platform progresses towards validation as a drug screening platform. Furthermore, after optimising the long-term culture of electrically-coupled patterned fibres, electrical stimulation and recording on the MEA would need to be performed on patterned and unpatterned cultures, comparing signal propagation and action potential dynamics between the conditions. Finally, the response of acoustically-patterned hiPSC-CMs when subjected to a panel of candidate inotropic agents (e.g. metoprolol, isoproterenol, verapamil) would be investigated to demonstrate the performance of- our platform in a proof-of-concept drug screening study.

Building upon the expertise in acoustic patterning and device fabrication of Chapter 2, Chapter 3 aimed to increase the biological complexity of a cardiac *in vitro* model by using hydrogel-based acoustic patterning and *in situ* differentiation. It was inspired by the work previously done in the Stevens group, whereby acoustic patterning in hydrogels was combined with skeletal muscle or cartilage tissue engineering protocols, producing anisotropic constructs (Armstrong et al., 2022, 2018). However, in the past, the patterned cells were already fully or partially committed to their

target lineage. The results in Chapter 3 show for the first time how acoustic patterning was successfully applied to non-committed hiPSCs, producing uniform linear hiPSC clusters embedded in a porcine GelMA hydrogel. Notably, the optimised patterning and gelation protocols have not affected the viability, pluripotency, metabolic activity or proliferation of hiPSCs, confirming their cytocompatibility with such delicate cell systems.

Subsequent optimisation of the cardiac differentiation protocol timing successfully directed the linear hiPSC clusters towards cardiac fate and preserved the high-quality patterning throughout the differentiation process. Two distinct modalities could be produced through varying the number of hydrogel layers: interconnected and independent cardiac fibres embedded in GelMA hydrogels. The higher consistency of independent cardiac fibre generation made them more preferable for drug screening platforms, and so they were chosen for further in-depth characterisation studies. The fully differentiated cardiac fibres were ≈130-190 µm in width, resembling the dimensions of the native perimysium (Kanzaki et al., 2010). In theory, these dimensions could be achieved with the main alternative of acoustic patterning 3D bioprinting, whose usual resolution approaches 200 µm (Graham et al., 2017, Miri et al., 2019). However, the previously published work of 3D printing hiPSCs to date was on a larger scale, with the reported print resolution at 400 - 630 µm (Li et al., 2018b; Kupfer et al., 2020). Those studies also observed that hiPSCs were randomly distributed through the bulk material, therefore the cells tended to form spherical aggregates rather than continuous linear clusters. Overall, the acoustically patterned cardiac fibres developed in Chapter 3 supersede the resolution and linear feature fidelity of existing 3D printing hiPSC patterning systems.

When comparing the properties of patterned and unpatterned cardiac hydrogels, conflicting results were observed in gene expression: though the magnitude of a cardiac marker *TNNT2* expression increased more in unpatterned than in patterned samples, when directly compared at differentiation end-point, its expression was not significantly different in patterned samples. While the comparison in gene expression remains inconclusive and would require a different calibrator,

stark differences in cardiac-specific protein markers clearly demonstrated a higher level of organisation in patterned samples over unpatterned controls. The linear architecture also led to an improved electrophysiological response to electric field stimulation, with more patterned cardiac fibres following physiological stimulation at 1 Hz than the randomly organised hydrogels. These results are in accordance with other patterning studies that demonstrated that topography-based and fibre-guided alignment of stem cell-derived cardiomyocytes led to more efficient calcium handling (Allen et al., 2019; Rao et al., 2013). Interestingly, in these studies the cardiac marker gene expression also remained unaffected by the degree of alignment. Finally, restricting hiPSCs to linear arrays prior to cardiac differentiation resulted in consistently linear calcium wavefront propagation, a feature beneficial for future conduction velocity quantifications.

Overall, the work of Chapter 3 successfully produced a novel *in vitro* cardiac platform with micropatterned cardiac fibres immobilised within a bulk hydrogel. Nevertheless, there are several recommendations for future experiments to further characterise and validate this platform. Firstly, the curing time and LAP concentration should be varied systematically to produce a range of GelMAs with different mechanical properties to investigate in detail the effects of material stiffness on hiPSC survival and differentiation efficiency. In the present study, only two GelMA formulations were assessed, providing limited insights into the stiffness effects on differentiation. The changes of stiffness of the engineered construct throughout culture and at experimental end-point should also be assessed, to better characterise the construct and to provide a direct comparison with the mechanical properties of the native tissue.

Secondly, while the distribution of cardiac and non-cardiac protein markers was assessed on the macroscale via immunofluorescence imaging at low magnification, performing high-resolution confocal imaging of the cells within a single cardiac fibres would provide information on whether acoustic patterning also leads to any ultrastructural changes within the hiPSC-CMs, for example a subcellular alignment of the key contractile proteins (e.g. cTnT, α-actinin).

Thirdly, although the presence of non-cardiac cell types, such as endothelial cells and smooth muscle cells, was demonstrated, the ratios of cell phenotypes present in the construct should be quantified using flow cytometry. This metric would also allow the comparison of differentiation efficiency between patterned and unpatterned samples.

Fourthly, since the results of the electrical stimulation experiments demonstrated a more advanced electrophysiological response in patterned gels over the unpatterned controls, a higher resolution calcium transient analysis combined with an RT-qPCR investigation of the changes in key ion channel gene expression would be welcome to underpin the mechanisms of the observed functional improvement.

A more in-depth analysis of signal propagation in cardiac fibres would further advance this study. While the signal was observed to propagate across a single fibre, whether the electrical coupling was anisotropic was not determined. To investigate that, higher magnification optical mapping would need to be performed to quantify and compare the lateral and longitudinal propagation velocities.

It would also be interesting to determine what functional benefits are caused by the *in situ* differentiation approach. To achieve this, electrophysiological parameters in response to electrical stimulation should be compared between patterned hydrogels differentiated *in situ* and acoustically-patterned arrays of hiPSC-CMs immobilised in hydrogels. This comparison would suggest whether the maintenance of cell-cell contacts from hiPSC stage through to committed cardiac fibres, as well as the presence of non-myocyte cell phenotypes in *in situ* differentiated constructs plays a role in improving the cardiac maturation of the patterned constructs. Furthermore, a comparison of anisotropic signal propagation described above would serve as a useful readout in these experiments to determine the differences in electrical coupling that could arise from patterning at hiPSC stage.

The work described in Chapter 4 is the first known demonstration of the *in situ* differentiation of acoustically-patterned fully non-committed hiPSCs into cardiac tissue. As the new methods of

combining acoustic patterning and 3D printing evolve, our approach could be used to add cellular microstructure to the bulk of the 3D printed material (Koo et al., 2020; Deshmukh et al., 2022), further increasing the physiological relevance of the engineered tissues. The acoustically-patterned cardiac fibres have several possible applications that can be explored in the future. The inclusion of GCaMP6f calcium indicator equips the acoustically patterned cardiac platform with an endogenous quantifiable readout for drug screening, allowing to assess effects of compounds of interest on calcium handling kinetics and conduction velocities. Also, although the main purpose of this work was to advance available patterned cardiac tissue engineered models for drug screening, the system developed in this thesis serves as a platform technology that can be adapted to engineering other tissues. For example, it would be interesting to apply hiPSC differentiation protocols to retinal pigment or optic epithelial cells to replicate the ordered architectures retina and cochlea respectively (Chen et al., 2018; Ye et al., 2020).

In Chapter 4, an *in situ* differentiation approach was investigated as a method of encapsulating a support fibrous scaffold within a 3D cell mass, producing a novel cardiac patch for tissue remuscularisation of injured myocardium. The scaffold was fabricated using melt electrospinning writing of a PCL blend, allowing highly ordered geometries to be produced. The work described in Chapter 4 was inspired by the previous findings in the Stevens group, whereby melt electrospun scaffolds have been used to guide stem cell differentiation to neural organoids (Ritzau-Reid., 2022). Building on these previous studies, the results showed the first application of such scaffolds combined with *in situ* differentiation within the field of cardiac tissue engineering. Interestingly, varying scaffold dimensions affected the configuration of the differentiated cardiac constructs: the larger spacing led to the formation of globular structures at the scaffold junctions and thin linear connecting regions, while uniform interconnected cardiac meshes were produced with smaller scaffold dimensions. Immunostaining of the cardiac meshes demonstrated high hiPSC-CM content, with cardiomyocytes surrounding the material in 3D. Such constructs have superior material coverage and encapsulation than the previously reported melt electrospun scaffolds seeded directly

with pre-differentiated hiPSC-CMs, as well as improved global geometry in comparison to traditional solution electrospinning methods that are often used to align hiPSC-CMs (Allen et al., 2019; Zhang et al., 2022). Combined with their consistent frequency capture of physiological electrical stimulation at 1 Hz, the cardiac meshes were an exciting candidate for translation to proof-of-principle tissue remuscularisation *ex vivo* experiments. Using rat myocardial slices as the model of native tissue and simplified scaffolds with directly seeded hiPSC-CMs, extensive interface optimisation determined the optimal protocol for future large-scale slice-mesh co-cultures and showed a promising proof-of-principle scaffold-mediated exogenous hiPSC-CM delivery to the slice. While the direct comparison with existing injection-based or hydrogel patch-based methods could not be drawn from these results, the exogenous cells from the cellularised scaffold were transferred to the myocardial slice after as little as 24 hours. To investigate how the extent of cell delivery can be improved, two possible explanations for the low scale transfer were evaluated. Firstly, volumetric imaging of the mesh-slice co-culture revealed a variable consistency of the interface across the myocardial slice surface. It would be interesting to see if this variability still occurs when *in situ* differentiated mesh with larger 3D thickness is used. Secondly, extending culture time would likely significantly increase the efficiency of the cell transfer, as suggested by a 33-day long culture of the mesh on a functionalised tissue culture plastic. Interestingly, also, when assessing the contractility of the slice after the interface, significantly higher tissue stiffness was observed. The meshes could therefore have an added benefit in providing mechanical support to the damaged myocardium, known to restore ventricular wall stiffness and, consequently, improve cardiac function (Domenech et al., 2016; Yang et al., 2019; Christman et al., 2004a).

Taken together, the work described in Chapter 4 laid the foundation for a novel design of engineering cardiac patches for tissue remuscularisation and paved the way for future *ex vivo* interface studies. There are several follow-up experiments that would improve the existing work described in this chapter. For example, majority of the cell transfer optimisation experiments were performed with hiPSC-CMs seeded directly onto the scaffold, rather than differentiated *in situ*.

Interfacing cardiac slices with *in situ* differentiated cardiac meshes would provide a higher local cell density of exogenous cells, which could increase their engraftment. Also, while little cell transfer to the native tissue was observed, cell delivery was only assessed qualitatively. Dissociating cardiac slices after exogenous cell delivery and performing flow cytometry would allow quantification of GFP^+ exogenous cells, thus enabling direct comparison between different cell transfer methods and improving the interpretation of the future *ex vivo* studies.

Preliminary results on the rate of cell transfer from the cardiac mesh were observed when the mesh was cultured on a Matrigel-functionalised tissue culture plate. While these results confirmed that the length of cardiac slice culture (3 days) was insufficient for hiPSC-CM engraftment, the experimental design was too simplistic to make exact predictions of the required timeline. Observing cell transfer from a seeded mesh onto a monolayer of isolated adult cardiomyocytes would offer a better mimic of the cardiac mesh-slice interface.

There were also questions regarding whether a healthy rat myocardial slice is an appropriate model for cell transfer. It was hypothesised that the healthy cardiac slices lack the niche for exogenous cells, having the most optimal performance and cell density already. To that effect, the meshes should be interfaced with diseased models of cardiac slices (e.g. cryoinjury model) to determine whether exogenous cells would transfer more readily to a tissue with a significant cell loss. Additionally, to investigate whether the graft-host species mismatch affects cell transfer, human donor cardiac slices should be used in the future studies.

Importantly, the functional performance and coupling of the exogenous cells with the host should be assessed for all future transfer experiments. This can be done indirectly, via immunofluorescent staining of cell junction proteins between the graft and the host. Alternatively, for direct measurements of the coupling, electrical point stimulation of the host tissue should be used while monitoring changes in calcium activity via the fluorescent GCaMP reporter of exogenous cells.

Finally, if a successful cell transfer is achieved in the proposed experiments, *in vivo* validation of cardiac mesh-mediated hiPSC-CM delivert would be of interest. Notably, previously observed nascent *de novo* microvasculature formation in *in situ* differentiated cardiac meshes could facilitate graft-host integration in an *in vivo* setting.

Overall, the work of this thesis highlights how advanced patterning technologies can be applied to engineer more physiologically relevant cardiac *in vitro* models, useful for drug screening and regenerative medicine applications. Implementing these approaches in the future would allow to better replicate the complex architecture of the native tissue, improving the predictability of physiological response and graft-host integration respectively.

REFERENCES

Abbasi, N., Ivanovski, S., Gulati, K., Love, R.M. & Hamlet, S. (2020) Role of offset and gradient architectures of 3-D melt electrowritten scaffold on differentiation and mineralization of osteoblasts. *Biomaterials Research*. 24 (1), 1–16. doi:10.1186/S40824-019-0180-Z/FIGURES/10.

Abbate, R., Sticchi, E. & Fatini, C. (2008) Genetics of cardiovascular disease. *Clinical Cases in Mineral and Bone Metabolism*. 5 (1), 63. Retrieved from : https://pubmed.ncbi.nlm.nih.gov/22460848/.

Abdelwahid, E., Kalvelyte, A., Stulpinas, A., de Carvalho, K.A.T., Guarita-Souza, L.C. & Foldes, G. (2015) Stem cell death and survival in heart regeneration and repair. (2015) *Apoptosis*. 21 (3), 252–268. doi:10.1007/S10495-015-1203-4.

Abdullah Said, M., Verweij, N. & van der Harst, P. (2018) Associations of combined genetic and lifestyle risks with incident cardiovascular disease and diabetes in the UK biobank study. *JAMA Cardiology*. 3 (8), 693. doi:10.1001/JAMACARDIO.2018.1717.

Afghah, F., Dikyol, C., Altunbek, M. & Koc, B. (2019) Biomimicry in bio-manufacturing: developments in melt electrospinning writing technology towards hybrid biomanufacturing. (2019) *Applied Sciences*. 9 (17), 3540. doi:10.3390/APP9173540.

Ahmed, R.E., Anzai, T., Chanthra, N. & Uosaki, H. (2020) A brief review of current maturation methods for human induced pluripotent stem cells-derived cardiomyocytes. *Frontiers in Cell and Developmental Biology*. 8. doi:10.3389/FCELL.2020.00178.

Ahrens, J.H., Uzel, S.G.M., Skylar-Scott, M., Mata, M.M., Lu, A., Kroll, K.T., Lewis, J.A., Ahrens, J.H., Uzel, S.G.M., Skylar-Scott, M., Mata, M.M., Lu, A., Kroll, K.T., Lewis, J.A. & Paulson, J.A. (2022) Programming cellular alignment in engineered cardiac tissue via bioprinting anisotropic organ building blocks. *Advanced Materials*. 34 (26), 2200217. doi:10.1002/ADMA.202200217.

Alford, P.W., Feinberg, A.W., Sheehy, S.P. & Parker, K.K. (2010) Biohybrid thin films for measuring contractility in engineered cardiovascular muscle. *Biomaterials*. 31 (13), 3613. doi:10.1016/J.BIOMATERIALS.2010.01.079.

Allen, A.C.B., Barone, E., Momtahan, N., Crosby, C.O., Tu, C., Deng, W., Polansky, K. & Zoldan, J. (2019) Temporal impact of substrate anisotropy on differentiating cardiomyocyte alignment and functionality. *Tissue Engineering. Part A*. 25 (19–20), 1426. doi:10.1089/TEN.TEA.2018.0258.

Alrefai, M.T., Murali, D., Paul, A., Ridwan, K.M., Connell, J.M. & Shum-Tim, D. (2015) Cardiac tissue engineering and regeneration using cell-based therapy. *Stem cells and cloning : advances and applications*. 8, 81–101. doi:10.2147/SCCAA.S54204.

Alrefai, M.T., Tarola, C.L., Raagas, R., Ridwan, K., Shalal, M., Lomis, N., Paul, A., Alrefai, M.D., Prakash, S., Schwertani, A. & Shum-Tim, D. (2019) Functional assessment of pluripotent and mesenchymal stem cell derived secretome in heart disease. *Annals of stem cell research*. 2 (1), 29. Retrieved from: https://www.ncbi.nlm.nih.gov/pmc/articles/PMC7020557/

Altomare, C., Pianezzi, E., Cervio, E., Bolis, S., Biemmi, V., Benzoni, P., Camici, G.G., Moccetti, T., Barile, L. & Vassalli, G. (2016) Human-induced pluripotent stem cell-derived cardiomyocytes from cardiac progenitor cells: effects of selective ion channel blockade. *EP Europace*. 18 (4), 67–76. doi:10.1093/EUROPACE/EUW352.

Ambhore, A., Teo, S.G., Omar, A.R. bin & Poh, K.K. (2014) ECG series. Importance of QT interval in clinical practice. *Singapore Medical Journal*. 55 (12), 607. doi:10.11622/SMEDJ.2014172.

Amit, M. & Itskovitz-Eldor, J. (2006) Sources, derivation, and culture of human embryonic stem cells. *Seminars in reproductive medicine*. 24 (5), 298–303. doi:10.1055/S-2006-954939.

APC International, Ltd. (2002) *Piezoelectric ceramics : principles and applications.* APC International. Retrieved from: https://www.americanpiezo.com/piezo-theory/determining-resonance-frequency.html

Araghi, M., Moslehi, Z., Nafchi, A.M., Mostahsan, A., Salamat, N. & Garmakhany, A.D. (2015) Cold water fish gelatin modification by a natural phenolic cross-linker (ferulic acid and caffeic acid). *Food Science & Nutrition*. 3 (5), 370–375. doi:10.1002/FSN3.230.

Archer, C.R., Sargeant, R., Basak, J., Pilling, J., Barnes, J.R. & Pointon, A. (2018) Characterization and validation of a human 3D cardiac microtissue for the assessment of changes in cardiac pathology. *Scientific Reports*. 8 (1), 1–15. doi:10.1038/s41598-018-28393-y.

Arkenberg, M.R., Koehler, K. & Lin, C.C. (2022) Heparinized gelatin-based hydrogels for differentiation of induced pluripotent stem cells. *Biomacromolecules*. 23, 4141–4152. https://doi.org/10.1021/acs.biomac.2c00585.

Armstrong, J.P.K., Maynard, S.A., Pence, I.J., Franklin, A.C., Drinkwater, B.W. & Stevens, M.M. (2019) Spatiotemporal quantification of acoustic cell patterning using Voronoï tessellation. *Lab on a Chip*. 19 (4), 562–573. doi:10.1039/C8LC01108G.

Armstrong, J.P.K., Pchelintseva, E., Treumuth, S., Campanella, C., Meinert, C., Klein, T.J., Hutmacher, D.W., Drinkwater, B.W. & Stevens, M.M. (2022) Tissue engineering cartilage with deep zone cytoarchitecture by high-resolution acoustic cell patterning. *Advanced Healthcare Materials*. 2200481. doi:10.1002/ADHM.202200481.

Armstrong, J.P.K., Puetzer, J.L., Serio, A., Guex, A.G., Kapnisi, M., et al. (2018) Engineering anisotropic muscle tissue using acoustic cell patterning. *Advanced Materials*. 30 (43), 1802649. doi:10.1002/adma.201802649.

Armstrong, J.P.K. & Stevens, M.M. (2020) Using remote fields for complex tissue engineering. *Trends in Biotechnology*. 38 (3), 254–263. doi:10.1016/j.tibtech.2019.07.005.

Asakura, K., Hayashi, S., Ojima, A., Taniguchi, T., Miyamoto, N., Nakamori, C., Nagasawa, C., Kitamura, T., Osada, T., Honda, Y., Kasai, C., Ando, H., Kanda, Y., Sekino, Y. & Sawada, K. (2015) Improvement of acquisition and analysis methods in multi-electrode array experiments with iPS cell-derived cardiomyocytes. *Journal of pharmacological and toxicological methods*. 75, 17–26. doi:10.1016/J.VASCN.2015.04.002.

Asnaashari, M., Motamedi, S., Asnaashari, N. & Azari-Marhabi, S. (2019) Antimicrobial activity of cold plasma treatment on acrylic denture bases: an in vitro evaluation. *Journal of Lasers in Medical Sciences*. 10 (1), 13. doi:10.15171/JLMS.2019.S3.

Augustsson, P. & Laurell, T. (2012) Acoustofluidics 11: Affinity specific extraction and sample decomplexing using continuous flow acoustophoresis. *Lab on a Chip*. 12 (10), 1742–1752. doi:10.1039/C2LC40200A.

Avossa, J., Herwig, G., Toncelli, C., Itel, F. & Rossi, R.M. (2022) Electrospinning based on benign solvents: current definitions, implications and strategies. *Green Chemistry*. 24 (6), 2347–2375. doi:10.1039/D1GC04252A.

Aytac, Z. & Wang, X. (2022) Melt electrospinning writing. *Electrospun Nanofibers*. 93–119. doi:10.1007/978-3-030-99958-2_4.

Babiarz, J.E., Ravon, M., Sridhar, S., Ravindran, P., Swanson, B., Bitter, H., Weiser, T., Chiao, E., Certa, U. & Kolaja, K.L. (2012) Determination of the human cardiomyocyte mRNA and miRNA differentiation network by fine-scale profiling. *Stem cells and development*. 21 (11), 1956–1965. doi:10.1089/SCD.2011.0357.

Badie, N. & Bursac, N. (2009) Novel micropatterned cardiac cell cultures with realistic ventricular microstructure. *Biophysical Journal*. 96 (9), 3873. doi:10.1016/J.BPJ.2009.02.019.

Baei, P., Hosseini, M., Baharvand, H. & Pahlavan, S. (2020) Electrically conductive materials for in vitro cardiac microtissue engineering. *Journal of Biomedical Materials Research Part A*. 108 (5), 1203–1213. doi:10.1002/JBM.A.36894.

Bahit, M.C., Kochar, A. & Granger, C.B. (2018) Post-myocardial infarction heart failure. *JACC: Heart Failure*. 6 (3), 179–186. doi:10.1016/J.JCHF.2017.09.015.

Balafkan, N., Mostafavi, S., Schubert, M., Siller, R., Liang, K.X., Sullivan, G. & Bindoff, L.A. (2020) A method for differentiating human induced pluripotent stem cells toward functional cardiomyocytes in 96-well microplates. *Scientific Reports*. 10 (1), 1–14. doi:10.1038/s41598-020-73656-2.

Ban, K., Park, H.J., Kim, S., Andukuri, A., Cho, K.W., Hwang, J.W., Cha, H.J., Kim, S.Y., Kim, W.S., Jun, H.W. & Yoon, Y.S. (2014) Cell therapy with embryonic stem cell-derived cardiomyocytes encapsulated in injectable nanomatrix gel enhances cell engraftment and promotes cardiac repair. *ACS Nano*. 8 (10), 10815–10825. https://doi.org/10.1021/nn504617g.

Barnes, R.M. & Black, B.L. (2016) *Nodal signaling and congenital heart defects. Etiology and morphogenesis of congenital heart disease: from gene function and cellular interaction to morphology.* Tokyo: Springer. 183–192. doi:10.1007/978-4-431-54628-3_24.

Bartolucci, C., Forouzandehmehr, M., Severi, S. & Paci, M. (2022) A novel in silico electromechanical model of human ventricular cardiomyocyte. *Frontiers in Physiology*. 13, 1056. doi:10.3389/FPHYS.2022.906146/BIBTEX.

Benson, J.R. & Hare, P.E. (1975) O-phthalaldehyde: fluorogenic detection of primary amines in the picomole range. Comparison with fluorescamine and ninhydrin. *Proceedings of the National Academy of Sciences of the United States of America*. 72 (2), 619. doi:10.1073/PNAS.72.2.619.

Bergmann, O., Bhardwaj, R.D., Bernard, S., Zdunek, S., Barnabé-Heide, F., Walsh, S., Zupicich, J., Alkass, K., Buchholz, B.A., Druid, H., Jovinge, S. & Frisén, J. (2009) Evidence for cardiomyocyte renewal in humans. *Science* .324 (5923), 98–102. doi:10.1126/SCIENCE.1164680.

Bernassau, A.L., Gesellchen, F., MacPherson, P.G.A., Riehle, M. & Cumming, D.R.S. (2012) Direct patterning of mammalian cells in an ultrasonic heptagon stencil. *Biomedical Microdevices*. 14 (3), 559–564. https://doi.org/10.1007/s10544-012-9633-z.

Bernassau, A.L., Glynne-Jones, P., Gesellchen, F., Riehle, M., Hill, M. & Cumming, D.R.S. (2014) Controlling acoustic streaming in an ultrasonic heptagonal tweezers with application to cell manipulation. *Ultrasonics*. 54 (1), 268–274. doi:10.1016/J.ULTRAS.2013.04.019.

Bers, D.M. (2002) Cardiac excitation–contraction coupling. *Nature*. 415 (6868), 198–205. doi:10.1038/415198a.

Bertsch, P., Andrée, L., Besheli, N.H. & Leeuwenburgh, S.C.G. (2022) Colloidal hydrogels made of gelatin nanoparticles exhibit fast stress relaxation at strains relevant for cell activity. *Acta Biomaterialia*. 138, 124–132. doi:10.1016/J.ACTBIO.2021.10.053.

Bhardwaj, N. & Kundu, S.C. (2010) Electrospinning: A fascinating fiber fabrication technique. *Biotechnology Advances*. 28 (3), 325–347. doi:10.1016/J.BIOTECHADV.2010.01.004.

BHF, H.I.T. (2022) Global heart & circulatory diseases factsheet. *British Heart Foundation*.

Bi, X. & Huang, R. (2022) 3D printing of natural fiber and composites: A state-of-the-art review. *Materials & Design*. 222, 111065. doi:10.1016/J.MATDES.2022.111065.

Biechele, S., Cox, B.J. & Rossant, J. (2011) Porcupine homolog is required for canonical Wnt signaling and gastrulation in mouse embryos. *Developmental biology*. 355 (2), 275–285. doi:10.1016/J.YDBIO.2011.04.029.

Bishop, E.S., Mostafa, S., Pakvasa, M., Luu, H.H., Lee, M.J., Wolf, J.M., Ameer, G.A., He, T.-C. & Reid, R.R. (2017) 3-D bioprinting technologies in tissue engineering and regenerative medicine: Current and future trends. *Genes & Diseases*. 4 (4), 185–195. doi:10.1016/J.GENDIS.2017.10.002.

Blazeski, A., Zhu, R., Hunter, D.W., Weinberg, S.H., Zambidis, E.T. & Tung, L. (2012) Cardiomyocytes derived from human induced pluripotent stem cells as models for normal and diseased cardiac electrophysiology and contractility. *Progress in biophysics and molecular biology*. 110 (2–3), 166–177. doi:10.1016/J.PBIOMOLBIO.2012.07.013.

Boraas, L.C. & Ahsan, T. (2016) Lack of vimentin impairs endothelial differentiation of embryonic stem cells. *Scientific Reports*. 6. doi:10.1038/srep30814.

Borger, D.K., McMahon, B., Lal, T.R., Serra-Vinardell, J., Aflaki, E. & Sidransky, E. (2017) Induced pluripotent stem cell models of lysosomal storage disorders. *Disease Models & Mechanisms*. 10 (6), 691–704. doi:10.1242/DMM.029009.

Bouyer, C., Chen, P., Güven, S., Demirtaş, T.T., Nieland, T.J.F., Padilla, F. & Demirci, U. (2016) A Bio-acoustic levitational (BAL) assembly method for engineering of multilayered, 3D brain-like constructs, using human embryonic stem cell derived neuro-progenitors. *Advanced Materials*. 28 (1), 161–167. doi:10.1002/adma.201503916.

Branco, M.A., Cotovio, J.P., Rodrigues, C.A.V., Vaz, S.H., Fernandes, T.G., Moreira, L.M., Cabral, J.M.S. & Diogo, M.M. (2019) Transcriptomic analysis of 3D cardiac differentiation of human induced pluripotent stem cells reveals faster cardiomyocyte maturation compared to 2D culture. *Scientific Reports*. 9 (1), 1–13. doi:10.1038/s41598-019-45047-9.

Brand, T. (2003) Heart development: molecular insights into cardiac specification and early morphogenesis. *Developmental Biology*. 258 (1), 1–19. doi:10.1016/S0012-1606(03)00112-X.

Brandão, K.O., Tabel, V.A., Atsma, D.E., Mummery, C.L. & Davis, R.P. (2017) Human pluripotent stem cell models of cardiac disease: from mechanisms to therapies. *Disease models & mechanisms*. 10 (9), 1039–1059. doi:10.1242/dmm.030320.

Brandenburger, M., Wenzel, J., Bogdan, R., Richardt, D., Nguemo, F., Reppel, M., Hescheler, J., Terlau, H. & Dendorfer, A. (2012) Organotypic slice culture from human adult ventricular myocardium. *Cardiovascular Research*. 93 (1), 50–59. doi:10.1093/CVR/CVR259.

Breckenridge, R.A., Mohun, T.J. & Amaya, E. (2001) A role for BMP signalling in heart looping morphogenesis in *Xenopus*. *Developmental Biology*. 232 (1), 191–203. doi:10.1006/DBIO.2001.0164.

Bremner, S.B., Gaffney, K.S., Sniadecki, N.J. & Mack, D.L. (2022) A change of heart: human cardiac tissue engineering as a platform for drug development. *Current Cardiology Reports*. 24 (5), 473–486. doi: 10.1007/s11886-022-01668-7.

Brugger, M.S., Grundeen, S., Doyle, A., Theogarajan, L., Wixforth, A. & Westerhausen, C. (2018) Orchestrating cells on a chip: Employing surface acoustic waves towards the formation of neural networks. *Physical Review E*. 98, 12411. doi:10.1103/PhysRevE.98.012411.

Buckingham, M., Meilhac, S. & Zaffran, S. (2005) Building the mammalian heart from two sources of myocardial cells. *Nature Reviews Genetics*. 6 (11), 826–835. doi:10.1038/nrg1710.

Buenzli, P.R., Lanaro, M., Wong, C.S., McLaughlin, M.P., Allenby, M.C., Woodruff, M.A. & Simpson, M.J. (2020) Cell proliferation and migration explain pore bridging dynamics in 3D printed scaffolds of different pore size. *Acta biomaterialia*. 114, 285–295. doi:10.1016/J.ACTBIO.2020.07.010.

van den Bulcke, A.I., Bogdanov, B., de Rooze, N., Schacht, E.H., Cornelissen, M. & Berghmans, H. (2000) Structural and rheological properties of methacrylamide modified gelatin hydrogels. *Biomacromolecules*. 1 (1), 31–38. https://doi.org/10.1021/bm990017d.

Bunea, A.-I., Iniesta, N. del C., Droumpali, A., Wetzel, A.E., Engay, E. & Taboryski, R. (2021) Micro 3D printing by two-photon polymerization: configurations and parameters for the nanoscribe system. *Micro*. 1 (2), 164–180. doi:10.3390/MICRO1020013.

Burridge, P.W., Matsa, E., Shukla, P., Lin, Z.C., Churko, J.M., Ebert, A.D., Lan, F., Diecke, S., Huber, B., Mordwinkin, N.M., Plews, J.R., Abilez, O.J., Cui, B., Gold, J.D. & Wu, J.C. (2014) Chemically defined generation of human cardiomyocytes. *Nature Methods.* 11 (8), 855–860. doi:10.1038/nmeth.2999.

Cai, H., Ao, Z., Hu, L., Moon, Y., Wu, Z., Lu, H.C., Kim, J. & Guo, F. (2020) Acoustofluidic assembly of 3D neurospheroids to model Alzheimer's disease. *Analyst*. 145 (19), 6243–6253. doi:10.1039/D0AN01373K.

Campbell, C. & Burgess, J.C. (1999) Surface acoustic wave devices and their signal processing applications. *The Journal of the Acoustical Society of America*. 89 (3), 1479. doi:10.1121/1.400569.

Carlos-Oliveira, M., Lozano-Juan, F., Occhetta, P., Visone, R. & Rasponi, M. (2021) Current strategies of mechanical stimulation for maturation of cardiac microtissues. *Biophysical Reviews*. 13 (5), 717–727. doi:10.1007/S12551-021-00841-6/FIGURES/4.

Carson, D., Hnilova, M., Yang, X., Nemeth, C.L., Tsui, J.H., Smith, A.S.T., Jiao, A., Regnier, M., Murry, C.E., Tamerler, C. & Kim, D.H. (2016) Nanotopography-induced structural anisotropy and sarcomere development in human cardiomyocytes derived from induced pluripotent stem cells. *ACS Applied Materials and Interfaces*. 8 (34), 21923–21932. doi:10.1021/ACSAMI.5B11671/.

Caspi, O., Huber, I., Kehat, I., Habib, M., Arbel, G., Gepstein, A., Yankelson, L., Aronson, D., Beyar, R. & Gepstein, L. (2007) Transplantation of human embryonic stem cell-derived cardiomyocytes improves myocardial performance in infarcted rat hearts. *Journal of the American College of Cardiology*. 50 (19), 1884–1893. doi:10.1016/J.JACC.2007.07.054.

Castilho, M., Feyen, D., Flandes-Iparraguirre, M., Hochleitner, G., Groll, J., Doevendans, P.A.F., Vermonden, T., Ito, K., Sluijter, J.P.G. & Malda, J. (2017) Melt electrospinning writing of poly-hydroxymethylglycolide-co-ε-caprolactone-based scaffolds for cardiac tissue engineering *Advanced healthcare materials,* 6(18). doi:10.1002/adhm.201700311.

Castro, J.O., Ramesan, S., Rezk, A.R. & Yeo, L.Y. (2018) Continuous tuneable droplet ejection via pulsed surface acoustic wave jetting. *Soft Matter*. 14 (28), 5721–5727. doi:10.1039/C7SM02534C.

Chan, S.S.K., Shi, X., Toyama, A., Arpke, R.W., Dandapat, A., Iacovino, M., Kang, J., Le, G., Hagen, H.R., Garry, D.J. & Kyba, M. (2013a) Mesp1 patterns mesoderm into cardiac, hematopoietic, or skeletal myogenic progenitors in a context-dependent manner. *Cell Stem Cell*. 12 (5), 587–601. doi:10.1016/J.STEM.2013.03.004.

Chan, Y.C., Ting, S., Lee, Y.K., Ng, K.M., Zhang, J., Chen, Z., Siu, C.W., Oh, S.K.W. & Tse, H.F. (2013b) Electrical stimulation promotes maturation of cardiomyocytes derived from human embryonic stem cells. *Journal of Cardiovascular Translational Research*. 6 (6), 989–999. doi:10.1007/S12265-013-9510-Z.

Chansoria, P., Asif, S., Gupta, N., Piedrahita, J. & Shirwaiker, R.A. (2022) Multiscale anisotropic tissue biofabrication via bulk acoustic patterning of cells and functional additives in hybrid bioinks. *Advanced Healthcare Materials*. 11 (10), 2102351. doi:10.1002/ADHM.202102351.

Chen, F., Hochleitner, G., Woodfield, T., Groll, J., Dalton, P.D. & Amsden, B.G. (2016) Additive manufacturing of a photo-cross-linkable polymer via direct melt electrospinning writing for producing high strength structures. *Biomacromolecules*. 17 (1), 208–214. doi:10.1021/ACS.BIOMAC.5B01316.

Chen, J., Hong, F., Zhang, C., Li, L., Wang, C., Shi, H., Fu, Y. & Wang, J. (2018) Differentiation and transplantation of human induced pluripotent stem cell-derived otic epithelial progenitors in mouse cochlea. *Stem Cell Research & Therapy*. 9 (1). doi:10.1186/S13287-018-0967-1.

Chen, L., Chen, C., Wang, P. & Song, T. (2017) Mechanisms of cellular effects directly induced by magnetic nanoparticles under magnetic fields. *Journal of Nanomaterials*. 15 (6), 463-4. doi:10.1155/2017/1564634.

Chen, Q.Z., Ishii, H., Thouas, G.A., Lyon, A.R., Wright, J.S., Blaker, J.J., Chrzanowski, W., Boccaccini, A.R., Ali, N.N., Knowles, J.C. & Harding, S.E. (2010) An elastomeric patch derived from poly(glycerol

sebacate) for delivery of embryonic stem cells to the heart. *Biomaterials*. 31 (14), 3885–3893. doi:10.1016/J.BIOMATERIALS.2010.01.108.

Chen, T. & Vunjak-Novakovic, G. (2019) Human tissue-engineered model of myocardial ischemia-reperfusion injury. *Tissue engineering. Part A*. 25 (9–10), 711–724. doi:10.1089/TEN.TEA.2018.0212.

Chen, Y., Nawaz, A.A., Zhao, Y., Huang, P.H., McCoy, J.P., Levine, S.J., Wang, L. & Huang, T.J. (2014) Standing surface acoustic wave (SSAW)-based microfluidic cytometer. *Lab on a Chip*. 14 (5), 916–923. doi:10.1039/C3LC51139A.

Cheng, K.W., Alhasan, L., Rezk, A.R., Al-Abboodi, A., Doran, P.M., Yeo, L.Y. & Chan, P.P.Y. (2019) Fast three-dimensional micropatterning of PC12 cells in rapidly crosslinked hydrogel scaffolds using ultrasonic standing waves. *Biofabrication*. 12 (1), 015013. doi:10.1088/1758-5090/AB4CCA.

Chhabra, L., Goel, N., Prajapat, L., Spodick, D.H. & Goyal, S. (2012) Mouse heart rate in a human: diagnostic mystery of an extreme tachyarrhythmia. *Indian Pacing and Electrophysiology Journal*. 12 (1), 32. doi:10.1016/S0972-6292(16)30463-6.

Choi, J.R., Yong, K.W., Choi, J.Y. & Cowie, A.C. (2019) Recent advances in photo-crosslinkable hydrogels for biomedical applications. *BioTechniques*. 66 (1), 40–53. doi:10.2144/BTN-2018-0083.

Choi, S., Lee, W., Yun, J., Seo, J. & Lim, I. (2008) Expression of Ca-activated K channels and their role in proliferation of rat cardiac fibroblasts. *The Korean Journal of Physiology & Pharmacology.* 12 (2), 51–58. doi:10.4196/KJPP.2008.12.2.51.

Chong, J.J.H., Yang, X., Don, C.W., Minami, E., Liu, Y.W., et al. (2014) Human embryonic-stem-cell-derived cardiomyocytes regenerate non-human primate hearts. *Nature*. 510 (7504), 273–277. doi:10.1038/NATURE13233.

Chow, A., Stuckey, D.J., Kidher, E., Rocco, M., Jabbour, R.J., Mansfield, C.A., Darzi, A., Harding, S.E., Stevens, M.M. & Athanasiou, T. (2017) Human induced pluripotent stem cell-derived cardiomyocyte encapsulating bioactive hydrogels improve rat heart function post myocardial infarction. *Stem Cell Reports*. 9 (5), 1415–1422. doi:10.1016/J.STEMCR.2017.09.003.

Christman, K.L., Fok, H.H., Sievers, R.E., Fang, Q. & Lee, R.J. (2004a) Fibrin glue alone and skeletal myoblasts in a fibrin scaffold preserve cardiac function after myocardial infarction. *Tissue engineering*. 10 (3–4), 403–409. doi:10.1089/107632704323061762.

Christman, K.L., Vardanian, A.J., Fang, Q., Sievers, R.E., Fok, H.H. & Lee, R.J. (2004b) Injectable fibrin scaffold improves cell transplant survival, reduces infarct expansion, and induces neovasculature formation in ischemic myocardium. *Journal of the American College of Cardiology*. 44 (3), 654–660. doi:10.1016/J.JACC.2004.04.040.

Chung, T.W., Yang, M.G., Liu, D.Z., Chen, W.P., Pan, C.I. & Wang, S.S. (2005) Enhancing growth human endothelial cells on Arg-Gly-Asp (RGD) embedded poly (ε-caprolactone) (PCL) surface with nanometer scale of surface disturbance. *Journal of Biomedical Materials Research Part A*. 72A (2), 213–219. doi:10.1002/JBM.A.30225.

Citro, L., Naidu, S., Hassan, F., Kuppusamy, M.L., Kuppusamy, P., Angelos, M.G. & Khan, M. (2014) Comparison of human induced pluripotent stem-cell derived cardiomyocytes with human mesenchymal stem cells following acute myocardial infarction. *PLOS ONE*. 9 (12), e116281. doi:10.1371/JOURNAL.PONE.0116281.

Claaßen, C., Claaßen, M.H., Truffault, V., Sewald, L., Tovar, G.E.M., Borchers, K. & Southan, A. (2018) Quantification of substitution of gelatin methacryloyl: best practice and current pitfalls. *Biomacromolecules*. 19 (1), 42–52. doi:10.1021/ACS.BIOMAC.7B01221.

Clerc, L. (1976) Directional differences of impulse spread in trabecular muscle from mammalian heart. *The Journal of Physiology*. 255 (2), 335. doi:10.1113/JPHYSIOL.1976.SP011283.

Cohen, S., Sazan, H., Kenigsberg, A., Schori, H., Piperno, S., Shpaisman, H. & Shefi, O. (2020) Large-scale acoustic-driven neuronal patterning and directed outgrowth. *Scientific Reports.* 10 (1), 1–11. doi:10.1038/s41598-020-60748-2.

Colin-York, H. & Fritzsche, M. (2018) The future of traction force microscopy. *Current Opinion in Biomedical Engineering*. 5, 1–5. doi:10.1016/J.COBME.2017.10.002.

Collantes, M., Pelacho, B., García-Velloso, M.J., Gavira, J.J., Abizanda, G., Palacios, I., Rodriguez-Borlado, L., Álvarez, V., Prieto, E., Ecay, M., Larequi, E., Peñuelas, I. & Prósper, F. (2017) Non-invasive in vivo imaging of cardiac stem/progenitor cell biodistribution and retention after intracoronary and intramyocardial delivery in a swine model of chronic ischemia reperfusion injury. *Journal of Translational Medicine*. 15 (1). doi:10.1186/S12967-017-1157-0.

Collins, B., Bandosz, P., Guzman-Castillo, M., Pearson-Stuttard, J., Stoye, G., McCauley, J., Ahmadi-Abhari, S., Araghi, M., Shipley, M.J., Capewell, S., French, E., Brunner, E.J. & O'Flaherty, M. (2022) What will the cardiovascular disease slowdown cost? Modelling the impact of CVD trends on dementia, disability, and economic costs in England and Wales from 2020–2029. *PLOS ONE*. 17 (6), e0268766. doi:10.1371/JOURNAL.PONE.0268766.

Collins, D.J., Morahan, B., Garcia-Bustos, J., Doerig, C., Plebanski, M. & Neild, A. (2015) Two-dimensional single-cell patterning with one cell per well driven by surface acoustic waves. *Nature Communications 2015 6:1*. 6 (1), 1–11. doi:10.1038/ncomms9686.

Comeau, E.S., Hocking, D.C. & Dalecki, D. (2017) Ultrasound patterning technologies for studying vascular morphogenesis in 3D. *Journal of Cell Science*. 130 (1), 232–242. doi:10.1242/jcs.188151.

Conlon, F.L., Lyons, K.M., Takaesu, N., Barth, K.S., Kispert, A., Herrmann, B. & Robertson, E.J. (1994) A primary requirement for nodal in the formation and maintenance of the primitive streak in the mouse. *Development*. 120 (7), 1919–1928. doi:10.1242/DEV.120.7.1919.

Correia, M., Santos, F., da Silva Ferreira, R., Ferreira, R., Bernardes de Jesus, B. & Nóbrega-Pereira, S. (2022) Metabolic determinants in cardiomyocyte function and heart regenerative strategies. *Metabolites*. 12 (6). doi:10.3390/METABO12060500.

Cox, L., Croxford, A. & Drinkwater, B.W. (2022) Dynamic patterning of microparticles with acoustic impulse control. *Scientific Reports*. 12 (1), 1–14. doi:10.1038/s41598-022-18554-5.

Cox, L., Melde, K., Croxford, A., Fischer, P. & Drinkwater, B.W. (2019) Acoustic hologram enhanced phased arrays for ultrasonic particle manipulation. *Physical Review Applied*. 12 (6), 064055. doi:10.1103/PHYSREVAPPLIED.12.064055/FIGURES/10/MEDIUM.

Cui, H., Liu, C., Esworthy, T., Huang, Y., Yu, Z.X., Zhou, X., San, H., Lee, S.J., Hann, S.Y., Boehm, M., Mohiuddin, M., Fisher, J.P. & Zhang, L.G. (2020) 4D physiologically adaptable cardiac patch: A 4-month in vivo study for the treatment of myocardial infarction. *Science Advances*. 6 (26). doi:10.1126/SCIADV.ABB5067.

Czirok, A., Isai, D.G., Kosa, E., Rajasingh, S., Kinsey, W., Neufeld, Z. & Rajasingh, J. (2017) Optical-flow based non-invasive analysis of cardiomyocyte contractility. *Scientific Reports*. 7 (1), 1–11. doi:10.1038/s41598-017-10094-7.

Dahle, J. & Kvam, E. (2003) Induction of delayed mutations and chromosomal instability in fibroblasts after UVA-, UVB-, and X-radiation 1. *Cancer Research*. 63, 1464–1469. Retrieved from: https://pubmed.ncbi.nlm.nih.gov/12670891/

Dahle, J., Kvam, E. & Stokke, T. (2005) Bystander effects in UV-induced genomic instability: Antioxidants inhibit delayed mutagenesis induced by ultraviolet A and B radiation. *Journal of Carcinogenesis*. 4, 11. doi:10.1186/1477-3163-4-11.

Dai, D.F., Danoviz, M.E., Wiczer, B., Laflamme, M.A. & Tian, R. (2017) Mitochondrial maturation in human pluripotent stem cell derived cardiomyocytes. *Stem cells international*. 5153625. doi:10.1155/2017/5153625.

Davis, J., Chouman, A., Creech, J., da Rocha, A.M., Ponce-Balbuena, D., Jimenez Vazquez, E.N., Nichols, R., Lozhkin, A., Madamanchi, N.R., Campbell, K.F. & Herron, T.J. (2021) *In vitro* model of ischemic heart failure using human induced pluripotent stem cell–derived cardiomyocytes. *JCI Insight*. 6 (10). doi:10.1172/JCI.INSIGHT.134368.

Dempsey, G.T., Chaudhary, K.W., Atwater, N., Nguyen, C., Brown, B.S., McNeish, J.D., Cohen, A.E. & Kralj, J.M. (2016) Cardiotoxicity screening with simultaneous optogenetic pacing, voltage imaging and calcium imaging. *Journal of Pharmacological and Toxicological Methods*. 81, 240–250. doi:10.1016/J.VASCN.2016.05.003.

Denning, C., Borgdorff, V., Crutchley, J., Firth, K.S.A., George, V., Kalra, S., Kondrashov, A., Hoang, M.D., Mosqueira, D., Patel, A., Prodanov, L., Rajamohan, D., Skarnes, W.C., Smith, J.G.W. & Young, L.E. (2016) Cardiomyocytes from human pluripotent stem cells: From laboratory curiosity to industrial biomedical platform. *Biochimica et biophysica acta*. 1863 (7B), 1728–1748. doi:10.1016/J.BBAMCR.2015.10.014.

Derby, B. (2008) Bioprinting: inkjet printing proteins and hybrid cell-containing materials and structures. *Journal of Materials Chemistry*. 18 (47), 5717–5721. doi:10.1039/B807560C.

Derkach, S.R., Voron'ko, N.G., Kuchina, Y.A. & Kolotova, D.S. (2020) Modified fish gelatin as an alternative to mammalian gelatin in modern food technologies. *Polymers.* 12 (12), 3051. doi:10.3390/POLYM12123051.

Desbiolles, B.X.E., de Coulon, E., Bertsch, A., Rohr, S. & Renaud, P. (2019) Intracellular recording of cardiomyocyte action potentials with nanopatterned volcano-shaped microelectrode arrays. *Nano Letters*. 19 (9), 6173–6181. doi:10.1021/ACS.NANOLETT.9B02209.

Deshmukh, D. v, Reichert, P., Zvick, J., Labouesse, C., Künzli, V., Dudaryeva, O., Bar-Nur, O., Tibbitt, M.W., Dual, J., Deshmukh, D. v, Reichert, P., Künzli, V., Dual, J., Labouesse, C., Dudaryeva, O., Tibbitt, M.W., Zvick, J. & Bar-Nur, O. (2022) Continuous production of acoustically patterned cells within hydrogel fibers for musculoskeletal tissue engineering. *Advanced Functional Materials*. 32 (30), 2113038. doi:10.1002/ADFM.202113038.

Ding, X., Shi, J., Lin, S.C.S., Yazdi, S., Kiraly, B. & Huang, T.J. (2012) Tunable patterning of microparticles and cells using standing surface acoustic waves. *Lab on a chip*. 12 (14), 2491. doi:10.1039/C2LC21021E.

Domenech, M., Polo-Corrales, L., Ramirez-Vick, J.E. & Freytes, D.O. (2016) Tissue engineering strategies for myocardial regeneration: Acellular versus cellular scaffolds? *Tissue Engineering - Part B: Reviews*. 22 (6), 438–458. doi:10.1089/TEN.TEB.2015.0523.

Drakhlis, L., Biswanath, S., Farr, C.M., Lupanow, V., Teske, J., et al. (2021) Human heart-forming organoids recapitulate early heart and foregut development. *Nature Biotechnology*. 39 (6), 737–746. doi:10.1038/S41587-021-00815-9.

Dries, E., Bardi, I., Nunez-Toldra, R., Meijlink, B. & Terracciano, C.M. (2021) CaMKII inhibition reduces arrhythmogenic Ca^{2+} events in subendocardial cryoinjured rat living myocardial slices. *Journal of General Physiology*. 153 (6). doi:10.1085/JGP.202012737/212078.

Duelen, R. & Sampaolesi, M. (2017) Stem cell technology in cardiac regeneration: a pluripotent stem cell promise. *EBioMedicine*. 16, 30–40. doi:10.1016/J.EBIOM.2017.01.029.

Dung Luong, T. & Trung Nguyen, N. (2012) surface acoustic wave driven microfluidics – a review. *Micro and Nanosystemse*. 2 (3), 217–225. doi:10.2174/1876402911002030217.

Dvir, T., Kedem, A., Ruvinov, E., Levy, O., Freeman, I., Landa, N., Holbova, R., Feinberg, M.S., Dror, S., Etzion, Y., Leor, J. & Cohen, S. (2009) Prevascularization of cardiac patch on the omentum improves its therapeutic outcome. *Proceedings of the National Academy of Sciences of the United States of America*. 106 (35), 14990–14995. doi:10.1073/PNAS.0812242106.

Eichholz, K. F., Federici, A., Riffault, M., Woods, I., Mahon, O. R., O'Driscoll, L., & Hoey, D. A. (2021). Extracellular vesicle functionalized melt electrowritten scaffolds for bone tissue engineering. *Advanced NanoBiomed Research*, *1*(10), 2100037. https://doi.org/10.1002/ANBR.202100037

Eichholz, K. F., Freeman, F. E., Pitacco, P., Nulty, J., Ahern, D., Burdis, R., Browe, D. C., Garcia, O., Hoey, D. A., & Kelly, D. J. (2022). Scaffold microarchitecture regulates angiogenesis and the regeneration of large bone defects. *Biofabrication*, *14*(4), 045013. https://doi.org/10.1088/1758-5090/AC88A1

Edlund, U., Sauter, T. & Albertsson, A.C. (2011) Covalent VEGF protein immobilization on resorbable polymeric surfaces. *Polymers for Advanced Technologies*. 22 (12), 2368–2373. doi:10.1002/PAT.1772.

van Eif, V.W.W., Stefanovic, S., Mohan, R.A. & Christoffels, V.M. (2020) Gradual differentiation and confinement of the cardiac conduction system as indicated by marker gene expression. *Biochimica et Biophysica Acta - Molecular Cell Research*. 1867 (3), 118509. doi:10.1016/J.BBAMCR.2019.07.004.

Eisner, D.A., Caldwell, J.L., Kistamás, K. & Trafford, A.W. (2017) Calcium and excitation-contraction coupling in the heart. *Circulation Research*. 121 (2), 181. doi:10.1161/CIRCRESAHA.117.310230.

Emig, R., Zgierski-Johnston, C.M., Timmermann, V., Taberner, A.J., Nash, M.P., Kohl, P. & Peyronnet, R. (2021) Passive myocardial mechanical properties: meaning, measurement, models. *Biophysical Reviews 2021 13:5*. 13 (5), 587–610. doi:10.1007/S12551-021-00838-1.

England, J. & Loughna, S. (2013) Heavy and light roles: myosin in the morphogenesis of the heart. *Cellular and Molecular Life Sciences*. 70 (7), 1221. doi:10.1007/S00018-012-1131-1.

Ermis, M., Antmen, E. & Hasirci, V. (2018) Micro and nanofabrication methods to control cell-substrate interactions and cell behavior: A review from the tissue engineering perspective. *Bioactive Materials*. 3 (3), 355–369. doi:10.1016/J.BIOACTMAT.2018.05.005.

Eschenhagen, T., Bolli, R., Braun, T., Field, L.J., Fleischmann, B.K., et al. (2017) Cardiomyocyte regeneration. *Circulation*. 136 (7), 680–686. doi:10.1161/CIRCULATIONAHA.117.029343.

Esser, T.U. & Engel, F.B. (2021) Direct 3D printing of hiPSC-cardiomyocytes in collagen-based bioinks. *European Heart Journal*. 42 (1). doi:10.1093/EURHEARTJ/EHAB724.3236.

Fairbanks, B.D., Schwartz, M.P., Bowman, C.N. & Anseth, K.S. (2009) Photoinitiated polymerization of PEG-diacrylate with lithium phenyl-2,4,6-trimethylbenzoylphosphinate: polymerization rate and cytocompatibility. *Biomaterials*. 30 (35), 6702–6707. doi:10.1016/J.BIOMATERIALS.2009.08.055.

Fan, X., Hughes, B.G., Ali, M.A.M., Cho, W.J., Lopez, W. & Schulz, R. (2015) Dynamic alterations to α-actinin accompanying sarcomere disassembly and reassembly during cardiomyocyte mitosis. *PLOS ONE*. 10 (6), e0129176. doi:10.1371/JOURNAL.PONE.0129176.

Fedorovich, N.E., Oudshoorn, M.H., van Geemen, D., Hennink, W.E., Alblas, J. & Dhert, W.J.A. (2009) The effect of photopolymerization on stem cells embedded in hydrogels. *Biomaterials*. 30 (3), 344–353. doi:10.1016/J.BIOMATERIALS.2008.09.037.

Feinberg, A.W., Ripplinger, C.M., van der Meer, P., Sheehy, S.P., Domian, I., Chien, K.R. & Parker, K.K. (2013) Functional differences in engineered myocardium from embryonic stem cell-derived versus neonatal cardiomyocytes. *Stem Cell Reports*. 1 (5), 387. doi:10.1016/J.STEMCR.2013.10.004.

Feng, W., Schriever, H., Jiang, S., Bais, A., Wu, H., Kostka, D. & Li, G. (2022) Computational profiling of hiPSC-derived heart organoids reveals chamber defects associated with NKX2-5 deficiency. *Communications Biology*. 5 (1), 1–18. doi:10.1038/s42003-022-03346-4.

Feric, N.T., Pallotta, I., Singh, R., Bogdanowicz, D.R., Gustilo, M.M., Chaudhary, K.W., Willette, R.N., Chendrimada, T.P., Xu, X., Graziano, M.P. & Aschar-Sobbi, R. (2019) Engineered cardiac tissues generated in the biowire ii: a platform for human-based drug discovery. *Toxicological Sciences*. 172 (1), 89–97. doi:10.1093/TOXSCI/KFZ168.

Fernandes, S., Naumova, A. v., Zhu, W.Z., Laflamme, M.A., Gold, J. & Murry, C.E. (2010) Human embryonic stem cell-derived cardiomyocytes engraft but do not alter cardiac remodeling after chronic infarction in rats. *Journal of Molecular and Cellular Cardiology*. 49 (6), 941–949. doi:10.1016/J.YJMCC.2010.09.008.

Feyen, D.A.M., van den Hoogen, P., van Laake, L.W., van Eeuwijk, E.C.M., Hoefer, I., Pasterkamp, G., Chamuleau, S.A.J., Grundeman, P.F., Doevendans, P.A. & Sluijter, J.P.G. (2017) Intramyocardial stem cell injection: go(ne) with the flow. *European Heart Journal*. 38 (3), 184–186. doi:10.1093/EURHEARTJ/EHW056.

Feyen, D.A.M., Mckeithan, W.L., Bruyneel, A.A.N., Eschenhagen, T., Metallo, C.M., et al. (2020) Metabolic maturation media improve physiological function of human iPSC-derived cardiomyocytes. *CellReports*. 32, 107925. doi:10.1016/j.celrep.2020.107925.

Finklea, F.B., Tian, Y., Kerscher, P., Seeto, W.J., Ellis, M.E. & Lipke, E.A. (2021) Engineered cardiac tissue microsphere production through direct differentiation of hydrogel-encapsulated human pluripotent stem cells. *Biomaterials*. 274, 120818. doi:10.1016/J.BIOMATERIALS.2021.120818.

Fischer, C., Milting, H., Fein, E., Reiser, E., Lu, K., Seidel, T., Schinner, C., Schwarzmayr, T., Schramm, R., Tomasi, R., Husse, B., Cao-Ehlker, X., Pohl, U. & Dendorfer, A. (2019) Long-term functional and structural preservation of precision-cut human myocardium under continuous electromechanical stimulation in vitro. *Nature Communications*. 10 (1), 1–12. doi:10.1038/s41467-018-08003-1.

Flanigan, M. & Gaskell, S.M. (2004) A review of cardiac anatomy and physiology. *Home healthcare nurse*.22 (1). doi:10.1097/00004045-200401000-00011.

Fong, C.Y., Peh, G.S.L., Gauthaman, K. & Bongso, A. (2009) Separation of SSEA-4 and TRA-1-60 labelled undifferentiated human embryonic stem cells from a heterogeneous cell population using magnetic-activated cell sorting (MACS) and fluorescence-activated cell sorting (FACS). *Stem Cell Reviews and Reports*. 5 (1). doi:10.1007/s12015-009-9054-4.

Frampton, K.D., Martin, S.E. & Minor, K. (2003) The scaling of acoustic streaming for application in micro-fluidic devices. *Applied Acoustics*. 64 (7), 681–692. doi:10.1016/S0003-682X(03)00005-7.

Freire, A.G., Resende, T.P. & Pinto-Do-Ó, P. (2014) Building and repairing the heart: What can we learn from embryonic development? *BioMed Research International*. 2014. doi:10.1155/2014/679168.

Fu, J., Jiang, M., Mirando, A.J., Yu, H.M.I. & Hsu, W. (2009) Reciprocal regulation of Wnt and Gpr177/mouse Wntless is required for embryonic axis formation. *Proceedings of the National Academy of Sciences of the United States of America*. 106 (44), 18598. doi:10.1073/PNAS.0904894106.

Fu, W. bin, Wang, W.E. & Zeng, C. yu (2018) Wnt signaling pathways in myocardial infarction and the therapeutic effects of Wnt pathway inhibitors. *Acta Pharmacologica Sinica*. 40 (1), 9–12. doi:10.1038/s41401-018-0060-4.

Gandhi, J.K., Manzar, Z., Bachman, L.A., Andrews-Pfannkoch, C., Knudsen, T., Hill, M., Schmidt, H., Iezzi, R., Pulido, J.S. & Marmorstein, A.D. (2018) Fibrin hydrogels as a xenofree and rapidly degradable support for transplantation of retinal pigment epithelium monolayers. *Acta Biomaterialia*. 67, 134–146. doi:10.1016/J.ACTBIO.2017.11.058.

Gao, L., Gregorich, Z.R., Zhu, W., Mattapally, S., Oduk, Y., Lou, X., Kannappan, R., Borovjagin, A. v., Walcott, G.P., Pollard, A.E., Fast, V.G., Hu, X., Lloyd, S.G., Ge, Y. & Zhang, J. (2018) Large cardiac muscle patches engineered from human induced-pluripotent stem cell-derived cardiac cells improve recovery from myocardial infarction in swine. *Circulation*. 137 (16), 1712–1730. doi:10.1161/CIRCULATIONAHA.117.030785/-/DC1.

Gao, L., Kupfer, M.E., Jung, J.P., Yang, L., Zhang, P., da Sie, Y., Tran, Q., Ajeti, V., Freeman, B.T., Fast, V.G., Campagnola, P.J., Ogle, B.M. & Zhang, J. (2017a) Myocardial tissue engineering with cells derived from human-induced pluripotent stem cells and a native-like, high-resolution, 3-dimensionally printed scaffold. *Circulation Research*. 120 (8), 1318–1325. doi:10.1161/CIRCRESAHA.116.310277.

Garitaonandia, I., Amir, H., Boscolo, F.S., Wambua, G.K., Schultheisz, H.L., et al. (2015) Increased risk of genetic and epigenetic instability in human embryonic stem cells associated with specific culture conditions. *PLOS ONE*. 10 (2), e0118307. doi:10.1371/journal.pone.0118307.

Garvin, K.A., Dalecki, D., Yousefhussien, M., Helguera, M. & Hocking, D.C. (2013) Spatial patterning of endothelial cells and vascular network formation using ultrasound standing wave fields. *Journal of Acoustical Society of America*. 134, 1483–1490. doi:10.1121/1.4812867.

Gerasimaite, R., Seikowski, J., Schimpfhauser, J., Kostiuk, G., Gilat, T., D'Este, E., Schnorrenberg, S. & Lukinavičius, G. (2020) Efflux pump insensitive rhodamine–jasplakinolide conjugates for G- and F-actin imaging in living cells. *Organic & Biomolecular Chemistry*. 18 (15), 2929–2937. doi:10.1039/D0OB00369G.

Gesellchen, F., Bernassau, A.L., Déjardin, T., Cumming, D.R.S. & Riehle, M.O. (2014) Cell patterning with a heptagon acoustic tweezer – application in neurite guidance. *Lab Chip*. 14 (13), 2266–2275. doi:10.1039/C4LC00436A.

Ghavaminejad, A., Ashammakhi, N., Wu, X.Y., Khademhosseini, A., Ghavaminejad, A., Wu, X.Y., Ashammakhi, N. & Khademhosseini, A. (2020) Crosslinking strategies for 3D bioprinting of polymeric hydrogels. *Small*. 16 (35), 2002931. doi:10.1002/SMLL.202002931.

Gherghiceanu, M., Barad, L., Novak, A., Reiter, I., Itskovitz-Eldor, J., Binah, O. & Popescu, L.M. (2011) Cardiomyocytes derived from human embryonic and induced pluripotent stem cells: comparative ultrastructure. *Journal of cellular and molecular medicine*. 15 (11), 2539–2551. doi:10.1111/J.1582-4934.2011.01417.X.

Giacomelli, E., Meraviglia, V., Campostrini, G., Cochrane, A., Cao, X., et al. (2020) Human-iPSC-derived cardiac stromal cells enhance maturation in 3d cardiac microtissues and reveal non-cardiomyocyte contributions to heart disease. *Cell Stem Cell*. 26 (6), 862-879.e11. doi:10.1016/J.STEM.2020.05.004.

Gilsbach, R., Preissl, S., Grüning, B.A., Schnick, T., Burger, L., Benes, V., Würch, A., Bönisch, U., Günther, S., Backofen, R., Fleischmann, B.K., Schübeler, D. & Hein, L. (2014) Dynamic DNA methylation orchestrates cardiomyocyte development, maturation and disease. *Nature Communications.* 5 (1), 1–13. doi:10.1038/ncomms6288.

Gilsbach, R., Schwaderer, M., Preissl, S., Grüning, B.A., Kranzhöfer, D., Schneider, P., Nührenberg, T.G., Mulero-Navarro, S., Weichenhan, D., Braun, C., Dreßen, M., Jacobs, A.R., Lahm, H., Doenst, T., Backofen, R., Krane, M., Gelb, B.D. & Hein, L. (2018) Distinct epigenetic programs regulate cardiac myocyte development and disease in the human heart in vivo. *Nature Communications*. 9 (1), 1–14. doi:10.1038/s41467-017-02762-z.

Glukhov, A. v., Fedorov, V. v., Kalish, P.W., Ravikumar, V.K., Lou, Q., Janks, D., Schuessler, R.B., Moazami, N. & Efimov, I.R. (2012) Conduction remodeling in human end-stage nonischemic left ventricular cardiomyopathy. *Circulation*. 125 (15), 1835–1847. doi:10.1161/CIRCULATIONAHA.111.047274/-/DC1.

Goldfracht, I., Protze, S., Shiti, A., Setter, N., Gruber, A., Shaheen, N., Nartiss, Y., Keller, G. & Gepstein, L. (2020a) Generating ring-shaped engineered heart tissues from ventricular and atrial human pluripotent stem cell-derived cardiomyocytes. *Nature Communications 2020 11:1*. 11 (1), 1–15. doi:10.1038/s41467-019-13868-x.

Goodpaster, T., Legesse-Miller, A., Hameed, M.R., Aisner, S.C., Randolph-Habecker, J. & Coller, H.A. (2008) An immunohistochemical method for identifying fibroblasts in formalin-fixed, paraffin-embedded tissue. *Journal of Histochemistry and Cytochemistry*. 56 (4), 347. doi:10.1369/JHC.7A7287.2007.

Gornall, J.L. & Terentjev, E.M. (2008) Helix–coil transition of gelatin: helical morphology and stability. *Soft Matter*. 4 (3), 544–549. doi:10.1039/B713075A.

Graham, A.D., Olof, S.N., Burke, M.J., Armstrong, J.P.K., Mikhailova, E.A., Nicholson, J.G., Box, S.J., Szele, F.G., Perriman, A.W. & Bayley, H. (2017) High-resolution patterned cellular constructs by droplet-based 3D printing. *Scientific Reports*. 7 (1), 1–11. doi:10.1038/s41598-017-06358-x.

Guan, X., Xu, W., Zhang, H., Wang, Q., Yu, J., Zhang, R., Chen, Y., Xia, Y., Wang, J. & Wang, D. (2020) Transplantation of human induced pluripotent stem cell-derived cardiomyocytes improves

myocardial function and reverses ventricular remodeling in infarcted rat hearts. *Stem Cell Research and Therapy*. 11 (1), 1–11. doi:10.1186/S13287-020-01602-0/.

Guex, A.G., di Marzio, N., Eglin, D., Alini, M. & Serra, T. (2021) The waves that make the pattern: a review on acoustic manipulation in biomedical research. *Materials Today Bio*. 10, 100110. doi:10.1016/J.MTBIO.2021.100110.

Guha, P., Morgan, J.W., Mostoslavsky, G., Rodrigues, N.P. & Boyd, A.S. (2013) Lack of immune response to differentiated cells derived from syngeneic induced pluripotent stem cells. *Cell stem cell*. 12 (4), 407–412. doi:10.1016/J.STEM.2013.01.006.

Guo, H.L. & Li, Z.Y. (2013) Optical tweezers technique and its applications. *Science China Physics, Mechanics and Astronomy 2013 56:12*. 56 (12), 2351–2360. doi:10.1007/S11433-013-5355-3.

Gupta, M.K., Illich, D.J., Gaarz, A., Matzkies, M., Nguemo, F., Pfannkuche, K., Liang, H., Classen, S., Reppel, M., Schultze, J.L., Hescheler, J. & Ari, T. (2010) Global transcriptional profiles of beating clusters derived from human induced pluripotent stem cells and embryonic stem cells are highly similar. *BMC developmental biology*. 10. doi:10.1186/1471-213X-10-98.

Habeler, W., Pouillot, S., Plancheron, A., Pucéat, M., Peschanski, M. & Monville, C. (2009) An *in vitro* beating heart model for long-term assessment of experimental therapeutics. *Cardiovascular Research*. 81 (2), 253–259. doi:10.1093/CVR/CVN299.

Hachim, D., Zhao, J., Bhankharia, J., Nuñez-Toldra, R., Brito, L., Seong, H., Becce, M., Ouyang, L., Grigsby, C.L., Higgins, S.G., Terracciano, C.M. & Stevens, M.M. (2022) Polysaccharide-polyplex nanofilm coatings enhance nanoneedle-based gene delivery and transfection efficiency. *Small*. 18 (36), 2202303. doi:10.1002/SMLL.202202303.

Hackett, C.H. & Fortier, L.A. (2011) Embryonic stem cells and iPS cells: sources and characteristics. *The Veterinary clinics of North America. Equine practice*. 27 (2), 233–242. doi:10.1016/j.cveq.2011.04.003.

Halbach, M.D., Egert, U., Hescheler, J. & Banach, K. (2003) Estimation of action potential changes from field potential recordings in multicellular mouse cardiac myocyte cultures. *Cellular Physiology and Biochemistry*. 13 (5), 271–284. doi:10.1159/000074542.

Hall, M.L. & Ogle, B.M. (2018) Cardiac extracellular matrix modification as a therapeutic approach. *Advances in Experimental Medicine and Biology*. 1098, 131. doi:10.1007/978-3-319-97421-7_7.

Han, J., Wu, Q., Xia, Y., Wagner, M.B. & Xu, C. (2016) Cell alignment induced by anisotropic electrospun fibrous scaffolds alone has limited effect on cardiomyocyte maturation. *Stem Cell Research*. 16 (3), 740–750. doi:10.1016/J.SCR.2016.04.014.

Han, L., Li, Y., Tchao, J., Kaplan, A.D., Lin, B., Li, Y., Mich-Basso, J., Lis, A., Hassan, N., London, B., Bett, G.C.L., Tobita, K., Rasmusson, R.L. & Yang, L. (2014) Study familial hypertrophic cardiomyopathy using patient-specific induced pluripotent stem cells. *Cardiovascular Research*. 104 (2), 258–269. doi:10.1093/CVR/CVU205.

Hanft, L.M. & McDonald, K.S. (2010) Length dependence of force generation exhibit similarities between rat cardiac myocytes and skeletal muscle fibres. *The Journal of Physiology*. 588 (15), 2891. doi:10.1113/JPHYSIOL.2010.190504.

Hang, C.T., Yang, J., Han, P., Cheng, H.L., Shang, C., Ashley, E., Zhou, B. & Chang, C.P. (2010) Chromatin regulation by Brg1 underlies heart muscle development and disease. *Nature*. 466 (7302), 62–67. doi:10.1038/NATURE09130.

Hannes, T., Halbach, M., Nazzal, R., Frenzel, L., Saric, T., Khalil, M., Hescheler, J., Brockmeier, K. & Pillekamp, F. (2008) Biological pacemakers: characterization in an in vitro coculture model. *Journal of electrocardiology*. 41 (6), 562–566. doi:10.1016/J.JELECTROCARD.2008.06.017.

Hayakawa, T., Kunihiro, T., Dowaki, S., Uno, H., Matsui, E., Uchida, M., Kobayashi, S., Yasuda, A., Shimizu, T. & Okano, T. (2012) Noninvasive evaluation of contractile behavior of cardiomyocyte monolayers based on motion vector analysis. *Tissue Engineering - Part C: Methods*. 18 (1), 21–32. doi:10.1089/TEN.TEC.2011.0273.

He, L. & Chen, X. (2020) Cardiomyocyte induction and regeneration for myocardial infarction treatment: cell sources and administration strategies. *Advanced Healthcare Materials*. 9 (22), 2001175. doi:10.1002/ADHM.202001175.

Helary, C., Ovtracht, L., Coulomb, B., Godeau, G. & Giraud-Guille, M.M. (2006) Dense fibrillar collagen matrices: A model to study myofibroblast behaviour during wound healing. *Biomaterials*. 27 (25), 4443–4452. doi:10.1016/J.BIOMATERIALS.2006.04.005.

Helgeson, M.E., Chapin, S.C. & Doyle, P.S. (2011) Hydrogel microparticles from lithographic processes: Novel materials for fundamental and applied colloid science. *Current Opinion in Colloid & Interface Science*. 16 (2), 106–117. doi:10.1016/J.COCIS.2011.01.005.

Hirt, M.N., Boeddinghaus, J., Mitchell, A., Schaaf, S., Börnchen, C., Müller, C., Schulz, H., Hubner, N., Stenzig, J., Stoehr, A., Neuber, C., Eder, A., Luther, P.K., Hansen, A. & Eschenhagen, T. (2014) Functional improvement and maturation of rat and human engineered heart tissue by chronic electrical stimulation. *Journal of Molecular and Cellular Cardiology*. 74, 151–161. doi:10.1016/j.yjmcc.2014.05.009.

Ho, B.X., Pang, J.K.S., Phua, Q.H., Liew, L.C., Poh, B.M., Chen, Y., Loh, Y.-H., An, O., Yang, H.H., Seshachalam, V.P., Koh, J.L., Chan, W.-K., Ng, S.Y. & Soh, B.-S. (2021) Generation of human chambered cardiac organoids from pluripotent stem cells for improved modelling of cardiovascular diseases. *bioRxiv*. 2021.05.21.445153. doi:10.1101/2021.05.21.445153.

Hoang, P., Wang, J., Conklin, B.R., Healy, K.E. & Ma, Z. (2018) Generation of spatial-patterned early-developing cardiac organoids using human pluripotent stem cells. *Nature Protocols*. 13 (4), 723–737. doi:10.1038/nprot.2018.006.

Hochleitner, G., Hümmer, J.F., Luxenhofer, R. & Groll, J. (2014) High definition fibrous poly(2-ethyl-2-oxazoline) scaffolds through melt electrospinning writing. *Polymer*. 55 (20), 5017–5023. doi:10.1016/J.POLYMER.2014.08.024.

Hochleitner, G., Jüngst, T., Brown, T.D., Hahn, K., Moseke, C., Jakob, F., Dalton, P.D. & Groll, J. (2015) Additive manufacturing of scaffolds with sub-micron filaments via melt electrospinning writing. *Biofabrication*. 7 (3). doi:10.1088/1758-5090/7/3/035002.

Honek, J. (2017) Preclinical research in drug development. *Medical Writing: Preclinical Studies.* 26 (4), 5–8. Retrieved from: https://journal.emwa.org/preclinical-studies/preclinical-research-in-drug-development

Hong, S.H., Gorce, J.B., Punzmann, H., Francois, N., Shats, M. & Xia, H. (2020) Surface waves control bacterial attachment and formation of biofilms in thin layers. *Science Advances*. 6 (22), 9386–9413. doi:10.1126/SCIADV.AAZ9386.

Hoon Lee, B., Shirahama, H., Cho, N.-J. & Poh Tan, L. (2015) Efficient and controllable synthesis of highly substituted gelatin methacrylamide for mechanically stiff hydrogels. *RSC advances,* 5(128), 106094-106097. doi:10.1039/c5ra22028a.

Horikoshi, Y., Yan, Y., Terashvili, M., Wells, C., Horikoshi, H., Fujita, S., Bosnjak, Z.J. & Bai, X. (2019) Fatty acid-treated induced pluripotent stem cell-derived human cardiomyocytes exhibit adult cardiomyocyte-like energy metabolism phenotypes. *Cells*. 8 (9). doi:10.3390/CELLS8091095.

Horvath, P., Aulner, N., Bickle, M., Davies, A.M., del Nery, E., Ebner, D., Montoya, M.C., Östling, P., Pietiäinen, V., Price, L.S., Shorte, S.L., Turcatti, G., von Schantz, C. & Carragher, N.O. (2016) Screening out irrelevant cell-based models of disease. *Nature Reviews. Drug Discovery*. 15(11), 751–769. https://doi.org/10.1038/nrd.2016.175.

Hou, D., Youssef, E.A.S., Brinton, T.J., Zhang, P., Rogers, P., Price, E.T., Yeung, A.C., Johnstone, B.H., Yock, P.G. & March, K.L. (2005) Radiolabeled cell distribution after intramyocardial, intracoronary, and interstitial retrograde coronary venous delivery: implications for current clinical trials. *Circulation*. 112 (9 Suppl). doi:10.1161/CIRCULATIONAHA.104.526749.

Hsiao, C.W., Bai, M.Y., Chang, Y., Chung, M.F., Lee, T.Y., Wu, C.T., Maiti, B., Liao, Z.X., Li, R.K. & Sung, H.W. (2013) Electrical coupling of isolated cardiomyocyte clusters grown on aligned conductive nanofibrous meshes for their synchronized beating. *Biomaterials*. 34 (4), 1063–1072. doi:10.1016/J.BIOMATERIALS.2012.10.065.

Hu, X., Zheng, J., Hu, Q., Liang, L., Yang, D., Cheng, Y., Li, S. sen, Chen, L.J. & Yang, Y. (2022) Smart acoustic 3D cell construct assembly with high-resolution. *Biofabrication*. 14 (4), 045003. doi:10.1088/1758-5090/AC7C90.

Hu, X., Zhu, J., Zuo, Y., Yang, D., Zhang, J., Cheng, Y. & Yang, Y. (2020) Versatile biomimetic array assembly by phase modulation of coherent acoustic waves. *Lab on a Chip*. 20 (19), 3515–3523. doi:10.1039/D0LC00779J.

Huang, C.Y., Peres Moreno Maia-Joca, R., Ong, C.S., Wilson, I., DiSilvestre, D., Tomaselli, G.F. & Reich, D.H. (2020) Enhancement of human iPSC-derived cardiomyocyte maturation by chemical conditioning in a 3D environment. *Journal of Molecular and Cellular Cardiology*. 138, 1–11. doi:10.1016/J.YJMCC.2019.10.001.

Huang, N.F., Yu, J., Sievers, R., Li, S. & Lee, R.J. (2005) Injectable biopolymers enhance angiogenesis after myocardial infarction. *Tissue engineering*. 11 (11–12), 1860–1866. doi:10.1089/TEN.2005.11.1860.

Huebsch, N., Charrez, B., Neiman, G., Siemons, B., Boggess, S.C., et al. (2022) Metabolically driven maturation of human-induced-pluripotent-stem-cell-derived cardiac microtissues on microfluidic chips. *Nature Biomedical Engineering*. 6 (4), 372–388. doi:10.1038/s41551-022-00884-4.

Hwang, H.S., Kryshtal, D.O., Feaster, T.K., Sánchez-Freire, V., Zhang, J., Kamp, T.J., Hong, C.C., Wu, J.C. & Knollmann, B.C. (2015) Comparable calcium handling of human iPSC-derived cardiomyocytes generated by multiple laboratories. *Journal of Molecular and Cellular Cardiology*. 85, 79–88. doi:10.1016/J.YJMCC.2015.05.003.

Iseoka, H., Miyagawa, S., Fukushima, S., Saito, A., Masuda, S., Yajima, S., Ito, E., Sougawa, N., Takeda, M., Harada, A., Lee, J.K. & Sawa, Y. (2018) pivotal role of non-cardiomyocytes in electromechanical and therapeutic potential of induced pluripotent stem cell-derived engineered cardiac tissue. *Tissue engineering. Part A*. 24 (3–4), 287–300. doi:10.1089/TEN.TEA.2016.0535.

Itzhaki, I., Rapoport, S., Huber, I., Mizrahi, I., Zwi-Dantsis, L., Arbel, G., Schiller, J. & Gepstein, L. (2011) Calcium handling in human induced pluripotent stem cell derived cardiomyocytes. *PLoS ONE*. 6 (4). doi:10.1371/JOURNAL.PONE.0018037.

Ivashchenko, C.Y., Pipes, G.C., Lozinskaya, I.M., Lin, Z., Xiaoping, X., Needle, S., Grygielko, E.T., Hu, E., Toomey, J.R., Lepore, J.J. & Willette, R.N. (2013) Human-induced pluripotent stem cell-derived cardiomyocytes exhibit temporal changes in phenotype. *American Journal of Physiology - Heart and Circulatory Physiology*. 305 (6). doi:10.1152/AJPHEART.00819.2012.

Jabbour, R.J., Owen, T.J., Pandey, P., Reinsch, M., Wang, B., et al. (2021) In vivo grafting of large engineered heart tissue patches for cardiac repair. *JCI Insight*. 6 (15). doi:10.1172/JCI.INSIGHT.144068.

Jaimes, R., Walton, R.D., Pasdois, P., Bernus, O., Efimov, I.R. & Kay, M.W. (2016a) A technical review of optical mapping of intracellular calcium within myocardial tissue. *American journal of physiology. Heart and circulatory physiology*. 310 (11), 1388–1401. doi:10.1152/AJPHEART.00665.2015.

Jaimes, R., Walton, R.D., Pasdois, P., Bernus, O., Efimov, I.R. & Kay, M.W. (2016b) Arrhythmias, electrophysiology, and optical mapping: A technical review of optical mapping of intracellular calcium within myocardial tissue. *American Journal of Physiology - Heart and Circulatory Physiology*. 310 (11), 1388. doi:10.1152/AJPHEART.00665.2015.

Jain, M., DerSimonian, H., Brenner, D.A., Ngoy, S., Teller, P., Edge, A.S.B., Zawadzka, A., Wetzel, K., Sawyer, D.B., Colucci, W.S., Apstein, C.S. & Liao, R. (2001) Cell therapy attenuates deleterious ventricular remodeling and improves cardiac performance after myocardial infarction. *Circulation*. 103 (14), 1920–1927. doi:10.1161/01.CIR.103.14.1920.

Jang, J., Yi, H.G. & Cho, D.W. (2016) 3D Printed Tissue Models: Present and Future. *ACS Biomaterials Science and Engineering*. 2 (10), 1722–1731. doi:10.1021/ACSBIOMATERIALS.6B00129.

Jang, S., Vanderpool, R.R., Avazmohammadi, R., Lapshin, E., Bachman, T.N., Sacks, M. & Simon, M.A. (2017) Biomechanical and hemodynamic measures of right ventricular diastolic function: translating tissue biomechanics to clinical relevance. *Journal of the American Heart Association*. 6 (9). doi:10.1161/JAHA.117.006084.

Janmaat, C.J., de Rooij, K.E., Locher, H., de Groot, S.C., de Groot, J.C.M.J., Frijns, J.H.M. & Huisman, M.A. (2015) Human dermal fibroblasts demonstrate positive immunostaining for neuron- and glia-specific proteins. *PLOS ONE*. 10 (12), e0145235. doi:10.1371/JOURNAL.PONE.0145235.

Jans, D., Callewaert, G., Krylychkina, O., Hoffman, L., Gullo, F., Prodanov, D. & Braeken, D. (2017) Action potential-based MEA platform for *in vitro* screening of drug-induced cardiotoxicity using human iPSCs and rat neonatal myocytes. *Journal of Pharmacological and Toxicological Methods*. 87, 48–52. doi:10.1016/J.VASCN.2017.05.003.

Janssen, P.M.L. (2010) Kinetics of cardiac muscle contraction and relaxation are linked and determined by properties of the cardiac sarcomere. *American Journal of Physiology - Heart and Circulatory Physiology*. 299 (4), 1092. doi:10.1152/AJPHEART.00417.2010.

Jiang, F., Yin, K., Wu, K., Zhang, M., Wang, S., Cheng, H., Zhou, Z. & Xiao, B. (2021) The mechanosensitive Piezo1 channel mediates heart mechano-chemo transduction. *Nature Communications*. 12 (1), 1–14. doi:10.1038/s41467-021-21178-4.

Jiang, Y., Zhou, Y., Bao, X., Chen, C., Randolph, L.N., Du, J. & Lian, X.L. (2018) An ultrasensitive calcium reporter system via CRISPR-Cas9-mediated genome editing in human pluripotent stem cells. *iScience*. 9, 27–35. doi:10.1016/j.isci.2018.10.007.

Jin, Y., Xie, C., Gao, Q., Zhou, X., Li, G., Du, J. & He, Y. (2021) Fabrication of multi-scale and tunable auxetic scaffolds for tissue engineering. *Materials & Design*. 197, 109277. doi:10.1016/J.MATDES.2020.109277.

Joyce, B.T., Gao, T., Zheng, Y., Ma, J., Hwang, S.J., et al. (2021) Epigenetic age acceleration reflects long-term cardiovascular health. *Circulation Research*. 129, 770–781. doi:10.1161/CIRCRESAHA.121.318965.

Kadota, S., Minami, I., Morone, N., Heuser, J.E., Agladze, K. & Nakatsuji, N. (2013) Development of a reentrant arrhythmia model in human pluripotent stem cell-derived cardiac cell sheets. *European Heart Journal*. 34 (15), 1147–1156. doi:10.1093/EURHEARTJ/EHS418.

Kai, D., Prabhakaran, M.P., Jin, G. & Ramakrishna, S. (2011) Guided orientation of cardiomyocytes on electrospun aligned nanofibers for cardiac tissue engineering. *Journal of Biomedical Materials Research Part B: Applied Biomaterials*. 98B (2), 379–386. doi:10.1002/JBM.B.31862.

Kałużna, E., Nadel, A., Zimna, A., Rozwadowska, N. & Kolanowski, T. (2022) Modeling the human heart ex vivo—current possibilities and strive for future applications. *Journal of Tissue Engineering and Regenerative Medicine*. 16 (10), 853–874. doi:10.1002/TERM.3335.

Kamakura, T., Makiyama, T., Sasaki, K., Yoshida, Y., Wuriyanghai, Y., Chen, J., Hattori, T., Ohno, S., Kita, T., Horie, M., Yamanaka, S. & Kimura, T. (2013) Ultrastructural maturation of human-induced pluripotent stem cell-derived cardiomyocytes in a long-term culture. *Circulation Journal*. 77 (5), 1307–1314. doi:10.1253/CIRCJ.CJ-12-0987.

Kang, B., Shin, J., Park, H.J., Rhyou, C., Kang, D., Lee, S.J., Yoon, Y. sup, Cho, S.W. & Lee, H. (2018) High-resolution acoustophoretic 3D cell patterning to construct functional collateral cylindroids for ischemia therapy. *Nature communications*. 9 (1). doi:10.1038/S41467-018-07823-5.

Kanzaki, Y., Terasaki, F., Okabe, M., Fujita, S., Katashima, T., Otsuka, K. & Ishizaka, N. (2010) Three-dimensional architecture of cardiomyocytes and connective tissue in human heart revealed by scanning electron microscopy. *Circulation*. 122 (19), 1973–1974. doi:10.1161/CIRCULATIONAHA.110.979815.

Kapałczyńska, M., Kolenda, T., Przybyła, W., Zajączkowska, M., Teresiak, A., Filas, V., Ibbs, M., Bliźniak, R., Łuczewski, Ł. & Lamperska, K. (2018) 2D and 3D cell cultures – a comparison of different types of cancer cell cultures. *Archives of Medical Science : AMS*. 14 (4), 910. doi:10.5114/AOMS.2016.63743.

Kawamoto, A. & Asahara, T. (2007) Role of progenitor endothelial cells in cardiovascular disease and upcoming therapies. *Catheterization and Cardiovascular Interventions*. 70 (4), 477–484. doi:10.1002/CCD.21292.

Kawamura, M., Miyagawa, S., Fukushima, S., Saito, A., Miki, K., Ito, E., Sougawa, N., Kawamura, T., Daimon, T., Shimizu, T., Okano, T., Toda, K. & Sawa, Y. (2013) Enhanced survival of transplanted human induced pluripotent stem cell-derived cardiomyocytes by the combination of cell sheets with the pedicled omental flap technique in a porcine heart. *Circulation*. 128 (11). doi:10.1161/CIRCULATIONAHA.112.000366.

Kawamura, M., Miyagawa, S., Miki, K., Saito, A., Fukushima, S., Higuchi, T., Kawamura, T., Kuratani, T., Daimon, T., Shimizu, T., Okano, T. & Sawa, Y. (2012) Feasibility, safety, and therapeutic efficacy of human induced pluripotent stem cell-derived cardiomyocyte sheets in a porcine ischemic cardiomyopathy model. *Circulation*. 126 (11). doi:10.1161/CIRCULATIONAHA.111.084343.

Kehat, I., Kenyagin-Karsenti, D., Snir, M., Segev, H., Amit, M., Gepstein, A., Livne, E., Binah, O., Itskovitz-Eldor, J. & Gepstein, L. (2001) Human embryonic stem cells can differentiate into myocytes with structural and functional properties of cardiomyocytes. *The Journal of Clinical Investigation*. 108 (3), 407–414. doi:10.1172/JCI12131.

Kempf, H. & Zweigerdt, R. (2018) Scalable cardiac differentiation of pluripotent stem cells using specific growth factors and small molecules. *Advances in Biochemical Engineering/Biotechnology*. 163, 39–69. doi:10.1007/10_2017_30.

Kerscher, P., Kaczmarek, J.A., Head, S.E., Ellis, M.E., Seeto, W.J., Kim, J., Bhattacharya, S., Suppiramaniam, V. & Lipke, E.A. (2017) Direct production of human cardiac tissues by pluripotent stem cell encapsulation in gelatin methacryloyl. *ACS Biomaterials Science and Engineering*. 3 (8), 1499–1509. doi:10.1021/ACSBIOMATERIALS.6B00226.

Kerscher, P., Turnbull, I.C., Hodge, A.J., Kim, J., Seliktar, D., Easley, C.J., Costa, K.D. & Lipke, E.A. (2016) Direct hydrogel encapsulation of pluripotent stem cells enables ontomimetic differentiation and growth of engineered human heart tissues. *Biomaterials*. 83, 383–395. doi:10.1016/J.BIOMATERIALS.2015.12.011.

Keung, W., Chan, P.K.W., Backeris, P.C., Lee, E.K., Wong, N., Wong, A.O.T., Wong, G.K.Y., Chan, C.W.Y., Fermini, B., Costa, K.D. & Li, R.A. (2019) Human cardiac ventricular-like organoid chambers and tissue strips from pluripotent stem cells as a two-tiered assay for inotropic responses. *Clinical Pharmacology & Therapeutics*. 106 (2), 402–414. doi:10.1002/CPT.1385.

Khan, M., Xu, Y., Hua, S., Johnson, J., Belevych, A., Janssen, P.M.L., Gyorke, S., Guan, J. & Angelos, M.G. (2015) Evaluation of changes in morphology and function of human induced pluripotent stem cell derived cardiomyocytes (hiPSC-CMs) cultured on an aligned-nanofiber cardiac patch. *PLOS ONE*. 10 (5), e0126338. doi:10.1371/JOURNAL.PONE.0126338.

Khoshakhlagh, P., Bowser, D.A., Brown, J.Q. & Moore, M.J. (2019) Comparison of visible and UVA phototoxicity in neural culture systems micropatterned with digital projection photolithography. *Journal of Biomedical Materials Research Part A*. 107 (1), 134–144. doi:10.1002/JBM.A.36540.

Kim, D.H., Kshitiz, Smith, R.R., Kim, P., Ahn, E.H., Kim, H.N., Marbán, E., Suh, K.Y. & Levchenko, A. (2012) Nanopatterned cardiac cell patches promote stem cell niche formation and myocardial regeneration. *Integrative Biology : Quantitative Biosciences From Nano to Macro*. 4 (9), 1019–1033. doi:10.1039/C2IB20067H.

Kim, K., Doi, A., Wen, B., Ng, K., Zhao, R., et al. (2010) Epigenetic memory in induced pluripotent stem cells. *Nature*. 467 (7313), 285–290. doi:10.1038/nature09342.

King, O., Cruz-Moreira, D., Sayed, A., Kermani, F., Kit-Anan, W., Sunyovszki, I., Wang, B.X., Downing, B., Fourre, J., Hachim, D., Randi, A.M., Stevens, M.M., Rasponi, M. & Terracciano, C.M. (2022) Functional microvascularization of human myocardium in vitro. *Cell Reports Methods*. 2 (9), 100280. doi:10.1016/J.CRMETH.2022.100280.

Kirkham, G.R., Britchford, E., Upton, T., Ware, J., Gibson, G.M., Devaud, Y., Ehrbar, M., Padgett, M., Allen, S., Buttery, L.D. & Shakesheff, K. (2015) Precision assembly of complex cellular

microenvironments using holographic optical tweezers. *Scientific Reports 2015.* 5 (1), 1–7. doi:10.1038/srep08577.

Kitsara, M., Agbulut, O., Kontziampasis, D., Chen, Y. & Menasché, P. (2017) Fibers for hearts: A critical review on electrospinning for cardiac tissue engineering. *Acta Biomaterialia*. 48, 20–40. doi:10.1016/J.ACTBIO.2016.11.014.

Knight, W.E., Ali, H.R., Nakano, S.J., Wilson, C.E., Walker, L.A. & Woulfe, K.C. (2020) *Ex vivo* methods for measuring cardiac muscle mechanical properties. *Frontiers in Physiology*. 11, 616996. doi:10.3389/FPHYS.2020.616996.

Kofron, C.M., Kim, T.Y., Munarin, F., Soepriatna, A.H., Kant, R.J., Mende, U., Choi, B.R. & Coulombe, K.L.K. (2021) A predictive in vitro risk assessment platform for pro-arrhythmic toxicity using human 3D cardiac microtissues. *Scientific Reports*. 11 (1), 1–16. doi:10.1038/s41598-021-89478-9.

Kong, P., Christia, P., Saxena, A., Su, Y. & Frangogiannis, N.G. (2013) Lack of specificity of fibroblast-specific protein 1 in cardiac remodeling and fibrosis. *American Journal of Physiology - Heart and Circulatory Physiology*. 305 (9), 1363. doi:10.1152/AJPHEART.00395.2013.

Koo, K.I., Lenshof, A., Huong, L.T. & Laurell, T. (2020) acoustic cell patterning in hydrogel for three-dimensional cell network formation. *Micromachines*. 12 (1), 3. doi:10.3390/MI12010003.

Korpershoek, J. V., de Ruijter, M., Terhaard, B. F., Hagmeijer, M. H., Saris, D. B. F., Castilho, M., Malda, J., & Vonk, L. A. (2021). Potential of melt electrowritten scaffolds seeded with meniscus cells and mesenchymal stromal cells. *International Journal of Molecular Sciences* 22(20), 11200. https://doi.org/10.3390/IJMS222011200

Kotadia, I., Whitaker, J., Roney, C., Niederer, S., O'Neill, M., Bishop, M. & Wright, M. (2020) Anisotropic cardiac conduction. *Arrhythmia & Electrophysiology Review*. 9 (4), 202. doi:10.15420/AER.2020.04.

Koti, P., Muselimyan, N., Mirdamadi, E., Asfour, H. & Sarvazyan, N.A. (2019) Use of GelMA for 3D printing of cardiac myocytes and fibroblasts. *Journal of 3D Printing in Medicine, 3(1), 11–22.* https://doi.org/10.2217/3dp-2018-0017

Kretzschmar, K., Post, Y., Bannier-Hélaouët, M., Mattiotti, A., Drost, J., Basak, O., Li, V.S.W., van den Born, M., Gunst, Q.D., Versteeg, D., Kooijman, L., van der Elst, S., van Es, J.H., van Rooij, E., van den Hoff, M.J.B. & Clevers, H. (2018) Profiling proliferative cells and their progeny in damaged murine hearts. *Proceedings of the National Academy of Sciences of the United States of America*. 115 (52), 12245–12254. doi:10.1073/PNAS.1805829115.

Kreuser, U., Buchert, J., Haase, A., Richter, W. & Diederichs, S. (2020) Initial WNT/β-Catenin activation enhanced mesoderm commitment, extracellular matrix expression, cell aggregation and cartilage tissue yield from induced pluripotent stem cells. *Frontiers in Cell and Developmental Biology*. 8, 1219. doi:10.3389/FCELL.2020.581331/BIBTEX.

Kuo, Y.C., Lee, I.H. & Rajesh, R. (2019) Self-assembled ternary poly(vinyl alcohol)-alginate-gelatin hydrogel with controlled-release nanoparticles for pancreatic differentiation of iPS cells. *Journal of the Taiwan Institute of Chemical Engineers*. 104, 27–39. doi:10.1016/J.JTICE.2019.09.010.

Kupfer, M.E., Lin, W.-H., Ravikumar, V., Qiu, K., Wang, L., Gao, L., Bhuiyan, D., Lenz, M., Ai, J., Mahutga, R.R., Townsend, D., Zhang, J., McAlpine, M.C., Tolkacheva, E.G. & Ogle, B.M. (2020) *In situ* expansion, differentiation and electromechanical coupling of human cardiac muscle in a 3D

bioprinted, chambered organoid. *Circulation Research*. 127(2), 207-224. doi:10.1161/circresaha.119.316155.

Kussauer, S., David, R. & Lemcke, H. (2019) hiPSCs derived cardiac cells for drug and toxicity screening and disease modeling: what micro- electrode-array analyses can tell us. *Cells*. 8 (11). doi:10.3390/CELLS8111331.

Laflamme, M.A., Chen, K.Y., Naumova, A. v., Muskheli, V., Fugate, J.A., et al. (2007) Cardiomyocytes derived from human embryonic stem cells in pro-survival factors enhance function of infarcted rat hearts. *Nature Biotechnology*. 25 (9), 1015–1024. doi:10.1038/nbt1327.

Laflamme, M.A. & Murry, C.E. (2011) Heart regeneration. *Nature*. 473 (7347), 326–335. doi:10.1038/NATURE10147.

Landa, N., Miller, L., Feinberg, M.S., Holbova, R., Shachar, M., Freeman, I., Cohen, S. & Leor, J. (2008) Effect of injectable alginate implant on cardiac remodeling and function after recent and old infarcts in rat. *Circulation*. 117 (11), 1388–1396. doi:10.1161/CIRCULATIONAHA.107.727420.

Laurell, T., Petersson, F. & Nilsson, A. (2007) Chip integrated strategies for acoustic separation and manipulation of cells and particles. *Chemical Society Reviews*. 36 (3), 492–506. doi:10.1039/B601326K.

Lauterbach, M.A., Ronzitti, E., Sternberg, J.R., Wyart, C. & Emiliani, V. (2015) Fast calcium imaging with optical sectioning via hilo microscopy. *PLOS ONE*. 10 (12), e0143681. doi:10.1371/JOURNAL.PONE.0143681.

Lee, E.A., Yim, H., Heo, J., Kim, H., Jung, G. & Hwang, N.S. (2014) Application of magnetic nanoparticle for controlled tissue assembly and tissue engineering. *Archives of Pharmacal Research*. 37 (1), 120–128. doi:10.1007/S12272-013-0303-3/FIGURES/5.

Lee, P., Klos, M., Bollensdorff, C., Hou, L., Ewart, P., Kamp, T.J., Zhang, J., Bizy, A., Guerrero-Serna, G., Kohl, P., Jalife, J. & Herron, T.J. (2012) Simultaneous voltage and calcium mapping of genetically purified human induced pluripotent stem cell-derived cardiac myocyte monolayers. *Circulation research*. 110 (12), 1556–1563. doi:10.1161/CIRCRESAHA.111.262535.

Lee, T.M., Harn, H.J., Chiou, T.W., Chuang, M.H., Chen, C.H., Chuang, C.H., Lin, P.C. & Lin, S.Z. (2020) Host pre-conditioning improves human adipose–derived stem cell transplantation in ageing rats after myocardial infarction: Role of NLRP3 inflammasome. *Journal of Cellular and Molecular Medicine*. 24 (21), 12272–12284. doi:10.1111/JCMM.15403.

Leibacher, I., Schatzer, S. & Dual, J. (2013) Impedance matched channel walls in acoustofluidic systems. *Lab on a Chip*. 14 (3), 463–470. doi:10.1039/C3LC51109J.

Lekka, M., Gnanachandran, K., Kubiak, A., Zieliński, T. & Zemła, J. (2021) Traction force microscopy – Measuring the forces exerted by cells. *Micron*. 150, 103138. doi:10.1016/J.MICRON.2021.103138.

Lemoine, M.D., Mannhardt, I., Breckwoldt, K., Prondzynski, M., Flenner, F., Ulmer, B., Hirt, M.N., Neuber, C., Horváth, A., Kloth, B., Reichenspurner, H., Willems, S., Hansen, A., Eschenhagen, T. & Christ, T. (2017) Human iPSC-derived cardiomyocytes cultured in 3D engineered heart tissue show physiological upstroke velocity and sodium current density. *Scientific Reports*. 7 (1), 1–11. doi:10.1038/s41598-017-05600-w.

Leonard, A., Bertero, A., Powers, J.D., Beussman, K.M., Bhandari, S., Regnier, M., Murry, C.E. & Sniadecki, N.J. (2018) Afterload promotes maturation of human induced pluripotent stem cell

derived cardiomyocytes in engineered heart tissues. *Journal of Molecular and Cellular Cardiology*. 118, 147–158. doi:10.1016/J.YJMCC.2018.03.016.

Leor, J., Tuvia, S., Guetta, V., Manczur, F., Castel, D., Willenz, U., Petneházy, Ö., Landa, N., Feinberg, M.S., Konen, E., Goitein, O., Tsur-Gang, O., Shaul, M., Klapper, L. & Cohen, S. (2009) Intracoronary injection of in situ forming alginate hydrogel reverses left ventricular remodeling after myocardial infarction in Swine. *Journal of the American College of Cardiology*. 54 (11), 1014–1023. doi:10.1016/J.JACC.2009.06.010.

Levario-Diaz, V., Bhaskar, P., Carmen Galan, M. & Barnes, A.C. (2020) Effect of acoustic standing waves on cellular viability and metabolic activity. *Scientific Reports*. 10 (1), 1–11. doi:10.1038/s41598-020-65241-4.

Lewandowski, J., Rozwadowska, N., Kolanowski, T.J., Malcher, A., Zimna, A., Rugowska, A., Fiedorowicz, K., Łabędź, W., Kubaszewski, Ł., Chojnacka, K., Bednarek-Rajewska, K., Majewski, P. & Kurpisz, M. (2018) The impact of in vitro cell culture duration on the maturation of human cardiomyocytes derived from induced pluripotent stem cells of myogenic origin. *Cell Transplantation*. 27 (7), 1047–1067. doi:10.1177/0963689718779346.

Lewis-Israeli, Y.R., Wasserman, A.H., Gabalski, M.A., Volmert, B.D., Ming, Y., Ball, K.A., Yang, W., Zou, J., Ni, G., Pajares, N., Chatzistavrou, X., Li, W., Zhou, C. & Aguirre, A. (2021) Self-assembling human heart organoids for the modeling of cardiac development and congenital heart disease. *Nature Communications*. 12 (1), 1–16. doi:10.1038/s41467-021-25329-5.

Li, A., Koch, Z. & Ideker, T. (2022) Epigenetic aging: Biological age prediction and informing a mechanistic theory of aging. *Journal of Internal Medicine*. 292 (5), 733–744. doi:10.1111/JOIM.13533.

Li, D.S., Avazmohammadi, R., Rodell, C.B., Hsu, E.W., Burdick, J.A., Gorman, J.H., Gorman, R.C. & Sacks, M.S. (2020a) How hydrogel inclusions modulate the local mechanical response in early and fully formed post-infarcted myocardium. *Acta Biomaterialia*. 114, 296–306. doi:10.1016/J.ACTBIO.2020.07.046.

Li, H., Yu, B., Yang, P., Zhan, J., Fan, X., Chen, P., Liao, X., Ou, C., Cai, Y. & Chen, M. (2021a) Injectable AuNP-HA matrix with localized stiffness enhances the formation of gap junction in engrafted human induced pluripotent stem cell-derived cardiomyocytes and promotes cardiac repair. *Biomaterials*. 279, 121231. doi:10.1016/J.BIOMATERIALS.2021.121231.

Li, J., Hu, S., Zhu, D., Huang, K., Mei, X., Abad, B.L. de J. & Cheng, K. (2021b) All roads lead to rome (the heart): cell retention and outcomes from various delivery routes of cell therapy products to the heart. *Journal of the American Heart Association*. 10 (8), 20402. doi:10.1161/JAHA.120.020402.

Li, J., Minami, I., Yu, L., Tsuji, K., Nakajima, M., Qiao, J., Suzuki, M., Shimono, K., Nakatsuji, N., Kotera, H., Liu, L. & Chen, Y. (2016a) Extracellular recordings of patterned human pluripotent stem cell-derived cardiomyocytes on aligned fibers. *Stem Cells International*. 2016. doi:10.1155/2016/2634013.

Li, L., Chen, Z., Shao, C., Sun, L., Sun, L., Zhao, Y., Li, L.J., Sun, L.Y., Zhao, Y.J., Chen, Z.Y. & Shao, C.M. (2020b) Graphene Hybrid Anisotropic Structural Color Film for Cardiomyocytes' Monitoring. *Advanced Functional Materials*. 30 (3), 1906353. doi:10.1002/ADFM.201906353.

Li, R.A., Keung, W., Cashman, T.J., Backeris, P.C., Johnson, B. v., Bardot, E.S., Wong, A.O.T., Chan, P.K.W., Chan, C.W.Y. & Costa, K.D. (2018a) Bioengineering an electro-mechanically functional

miniature ventricular heart chamber from human pluripotent stem cells. *Biomaterials*. 163, 116–127. doi:10.1016/J.BIOMATERIALS.2018.02.024.

Li, S., Guo, F., Chen, Y., Ding, X., Li, P., Wang, L., Cameron, C.E. & Huang, T.J. (2014) Standing surface acoustic wave based cell coculture. *Analytical chemistry*. 86 (19), 9853–9859. doi:10.1021/ac502453z.

Li, Y., Jiang, X., Li, L., Chen, Z.N., Gao, G., Yao, R. & Sun, W. (2018b) 3D printing human induced pluripotent stem cells with novel hydroxypropyl chitin bioink: scalable expansion and uniform aggregation. *Biofabrication*. 10 (4), 044101. doi:10.1088/1758-5090/AACFC3.

Li, Y., Zheng, T., Jia, C., Wang, X., Li, A. & Fu, Y. (2022) A LiNbO3 substrate surface acoustic wave microfluidic chip for patterning of cardiomyocytes. *2nd International Conference on Bioinformatics and Intelligent Computing.* 2(1), 489-494. doi:10.1145/3523286.3524686.

Li, Z., Fan, Z., Xu, Y., Niu, H., Xie, X., Liu, Z. & Guan, J. (2016b) Thermosensitive and highly flexible hydrogels capable of stimulating cardiac differentiation of cardiosphere-derived cells under static and dynamic mechanical training conditions. *ACS Applied Materials and Interfaces*. 8 (25), 15948–15957. doi:10.1021/ACSAMI.6B04932.

Li, Z., Wu, J.C., Sheikh, A.Y., Kraft, D., Cao, F., Xie, X., Patel, M., Gambhir, S.S., Robbins, R.C., Cooke, J.P. & Wu, J.C. (2007) Differentiation, survival, and function of embryonic stem cell derived endothelial cells for ischemic heart disease. *Circulation*. 116 (11). doi:10.1161/CIRCULATIONAHA.106.680561.

Lian, X., Zhang, J., Azarin, S.M., Zhu, K., Hazeltine, L.B., Bao, X., Hsiao, C., Kamp, T.J. & Palecek, S.P. (2012) Directed cardiomyocyte differentiation from human pluripotent stem cells by modulating Wnt/β-catenin signaling under fully defined conditions. *Nature Protocols*. 8 (1), 162–175. doi:10.1038/nprot.2012.150.

Lian, X., Zhang, J., Zhu, K., Kamp, T.J. & Palecek, S.P. (2013) *Insulin inhibits cardiac mesoderm, not mesendoderm, formation during cardiac differentiation of human pluripotent stem cells and modulation of canonical Wnt signaling can rescue this inhibition*. Stem cells (Dayton, Ohio). 31 (3), 447. doi:10.1002/STEM.1289.

Liang, P., Lan, F., Lee, A.S., Gong, T., Sanchez-Freire, V., Wang, Y., Diecke, S., Sallam, K., Knowles, J.W., Wang, P.J., Nguyen, P.K., Bers, D.M., Robbins, R.C. & Wu, J.C. (2013) Drug screening using a library of human induced pluripotent stem cell-derived cardiomyocytes reveals disease-specific patterns of cardiotoxicity. *Circulation*. 127 (16), 1677–1691. doi:10.1161/CIRCULATIONAHA.113.001883.

Liang, P., Sallam, K., Wu, H., Li, Y., Itzhaki, I., et al. (2016) Patient-specific and genome-edited induced pluripotent stem cell–derived cardiomyocytes elucidate single-cell phenotype of Brugada syndrome. *Journal of the American College of Cardiology*. 68 (19), 2086–2096. doi:10.1016/J.JACC.2016.07.779.

Liang, X., Zhang, Q., Cattaneo, P., Zhuang, S., Gong, X., et al. (2015) Transcription factor ISL1 is essential for pacemaker development and function. *The Journal of Clinical Investigation*. 125 (8), 3256–3268. doi:10.1172/JCI68257.

Liashenko, I., Hrynevich, A., Dalton, P.D., Liashenko, I., Hrynevich, A. & Dalton, P.D. (2020) Designing outside the box: unlocking the geometric freedom of melt electrowriting using microscale layer shifting. *Advanced Materials*. 32 (28), 2001874. doi:10.1002/ADMA.202001874.

Liau, B., Zhang, D. & Bursac, N. (2012) Functional cardiac tissue engineering. *Regenerative Medicine*. 7 (2), 187–206. doi:10.2217/RME.11.122.

Lieu, D.K., Liu, J., Siu, C.W., McNerney, G.P., Tse, H.F., Abu-Khalil, A., Huser, T. & Li, R.A. (2009) Absence of transverse tubules contributes to non-uniform Ca^{2+} wavefronts in mouse and human embryonic stem cell-derived cardiomyocytes. *Stem Cells and Development*. 18 (10), 1493–1500. doi:10.1089/SCD.2009.0052.

Lim, K.S., Galarraga, J.H., Cui, X., Lindberg, G.C.J., Burdick, J.A. & Woodfield, T.B.F. (2020) Fundamentals and Applications of Photo-Cross-Linking in Bioprinting. *Chemical Reviews*. 120 (19), 10662–10694. doi:10.1021/ACS.CHEMREV.9B00812.

Lim, K.S., Klotz, B.J., J Lindberg, G.C., W Melchels, F.P., Hooper, G.J., Malda, J., Gawlitta, D., F Woodfield, T.B., Lim, K.S., J Lindberg, G.C., Hooper, G.J., F Woodfield, T.B., Klotz, B.J., Gawlitta, D., Malda, J. & W Melchels, F.P. (2019) Visible light cross-linking of gelatin hydrogels offers an enhanced cell microenvironment with improved light penetration depth. *Macromolecular Bioscience*. 19 (6), 1900098. doi:10.1002/MABI.201900098.

Lim, K.S., Schon, B.S., Mekhileri, N. v., Brown, G.C.J., Chia, C.M., Prabakar, S., Hooper, G.J. & Woodfield, T.B.F. (2016) New Visible-light photoinitiating system for improved print fidelity in gelatin-based bioinks. *ACS Biomaterials Science and Engineering*. 2 (10), 1752–1762. doi:10.1021/ACSBIOMATERIALS.6B00149.

Lim, S.Y., Sivakumaran, P., Crombie, D.E., Dusting, G.J., Pébay, A. & Dilley, R.J. (2013) Trichostatin A enhances differentiation of human induced pluripotent stem cells to cardiogenic cells for cardiac tissue engineering. *Stem Cells Translational Medicine*. 2 (9), 715. doi:10.5966/SCTM.2012-0161.

Lin, M.Z. & Schnitzer, M.J. (2016) Genetically encoded indicators of neuronal activity. *Nature Neuroscience 2016 19:9*. 19 (9), 1142–1153. doi:10.1038/nn.4359.

Lin, Y.D., Ko, M.C., Wu, S.T., Li, S.F., Hu, J.F., et al. (2014) A nanopatterned cell-seeded cardiac patch prevents electro-uncoupling and improves the therapeutic efficacy of cardiac repair. *Biomaterials science*. 2 (4), 567–580. doi:10.1039/C3BM60289C.

Linnenberger, A., Fiedler, C., Roberts, J., Skaalure, S., Bryant, S., Anna Linnenberger, al, Roberts, J.J., Skaalure, S.C., Bryant, S.J., Cole, M.C. & McLeod, R.R. (2013). Optical trapping for tissue scaffold fabrication. *Optical Trapping and Optical Micromanipulation X.* 8810, 308-317. doi:10.1117/12.2027869.

Liße, D., Monzel, C., Vicario, C., Manzi, J., Maurin, I., Coppey, M., Piehler, J., Dahan, M., Liße, D., Monzel, C., Vicario, C., Manzi, J., Coppey, M., Dahan, M., Piehler, J. & Maurin, I. (2017) Engineered ferritin for magnetogenetic manipulation of proteins and organelles inside living cells. *Advanced Materials*. 29 (42), 1700189. doi:10.1002/ADMA.201700189.

Liu, J., Volkers, L., Jangsangthong, W., Bart, C.I., Engels, M.C., Zhou, G., Schalij, M.J., Ypey, D.L., Pijnappels, D.A. & de Vries, A.A.F. (2018a) Generation and primary characterization of iAM-1, a versatile new line of conditionally immortalized atrial myocytes with preserved cardiomyogenic differentiation capacity. *Cardiovascular Research*. 114 (14), 1848. doi:10.1093/CVR/CVY134.

Liu, J.C., Lerou, P.H. & Lahav, G. (2014) Stem cells: balancing resistance and sensitivity to DNA damage. *Trends in Cell Biology*.24 (5). doi:10.1016/j.tcb.2014.03.002.

Liu, P., Wakamiya, M., Shea, M.J., Albrecht, U., Behringer, R.R. & Bradley, A. (1999) Requirement for Wnt3 in vertebrate axis formation. *Nature Genetics 1999 22:4*. 22 (4), 361–365. doi:10.1038/11932.

Liu, Y., Lu, J., Xu, G., Wei, J., Zhang, Z. & Li, X. (2016) Tuning the conductivity and inner structure of electrospun fibers to promote cardiomyocyte elongation and synchronous beating. *Materials Science and Engineering: C*. 69, 865–874. doi:10.1016/J.MSEC.2016.07.069.

Liu, Y.W., Chen, B., Yang, X., Fugate, J.A., Kalucki, F.A., et al. (2018b) Human ESC-Derived cardiomyocytes restore function in infarcted hearts of non-human primates. *Nature biotechnology*. 36 (7), 597. doi:10.1038/NBT.4162.

Long, C., Li, H., Tiburcy, M., Rodriguez-Caycedo, C., Kyrychenko, V., Zhou, H., Zhang, Y., Min, Y.L., Shelton, J.M., Mammen, P.P.A., Liaw, N.Y., Zimmermann, W.H., Bassel-Duby, R., Schneider, J.W. & Olson, E.N. (2018) Correction of diverse muscular dystrophy mutations in human engineered heart muscle by single-site genome editing. *Science Advances*. 4 (1). doi:10.1126/SCIADV.AAP9004.

Lopez, C.M., Chun, H.S., Berti, L., Wang, S., Putzeys, J., van den Bulcke, C., Weijers, J.W., Firrincieli, A., Reumers, V., Braeken, D. & van Helleputte, N. (2018) A 16384-electrode 1024-channel multimodal CMOS MEA for high-throughput intracellular action potential measurements and impedance spectroscopy in drug-screening applications. *Digest of Technical Papers - IEEE International Solid-State Circuits Conference*. 61, 464–466. doi:10.1109/ISSCC.2018.8310385.

Louch, W.E., Bito, V., Heinzel, F.R., Macianskiene, R., Vanhaecke, J., Flameng, W., Mubagwa, K. & Sipido, K.R. (2004) Reduced synchrony of Ca2+ release with loss of T-tubules-a comparison to Ca^{2+} release in human failing cardiomyocytes. *Cardiovascular Research*. 62 (1), 63–73. doi:10.1016/J.CARDIORES.2003.12.031.

Louch, W.E., Sheehan, K.A. & Wolska, B.M. (2011) Methods in cardiomyocyte isolation, culture, and gene transfer. *Journal of Molecular and Cellular Cardiology*. 51 (3), 288. doi:10.1016/J.YJMCC.2011.06.012.

Lu, H.F., Leong, M.F., Lim, T.C., Chua, Y.P., Lim, J.K., Du, C. & Wan, A.C.A. (2017) Engineering a functional three-dimensional human cardiac tissue model for drug toxicity screening. *Biofabrication*. 9 (2), 025011. doi:10.1088/1758-5090/AA6C3A.

Lu, W.N., Lü, S.H., Wang, H. bin, Li, D.X., Duan, C.M., Liu, Z.Q., Hao, T., He, W.J., Xu, B., Fu, Q., Song, Y.C., Xie, X.H. & Wang, C.Y. (2009) Functional improvement of infarcted heart by co-injection of embryonic stem cells with temperature-responsive chitosan hydrogel. *Tissue Engineering - Part A*. 15 (6), 1437–1447. doi:10.1089/TEN.TEA.2008.0143.

Lundy, S.D., Zhu, W.Z., Regnier, M. & Laflamme, M.A. (2013) Structural and functional maturation of cardiomyocytes derived from human pluripotent stem cells. *Stem Cells and Development*. 22 (14), 1991–2002. doi:10.1089/SCD.2012.0490.

Luo, Y., Lou, C., Zhang, S., Zhu, Z., Xing, Q., Wang, P., Liu, T., Liu, H., Li, C., Shi, W., Du, Z. & Gao, Y. (2018) Three-dimensional hydrogel culture conditions promote the differentiation of human induced pluripotent stem cells into hepatocytes. *Cytotherapy*. 20 (1), 95–107. doi:10.1016/J.JCYT.2017.08.008.

Lyra-Leite, D.M., Gutiérrez-Gutiérrez, Ó., Wang, M., Zhou, Y., Cyganek, L. & Burridge, P.W. (2022) A review of protocols for human iPSC culture, cardiac differentiation, subtype-specification, maturation, and direct reprogramming. *STAR Protocols*. 3 (3). doi:10.1016/J.XPRO.2022.101560.

Ma, X., Qu, X., Zhu, W., Li, Y.S., Yuan, S., Zhang, H., Liu, J., Wang, P., Lai, C.S.E., Zanella, F., Feng, G.S., Sheikh, F., Chien, S. & Chen, S. (2016) Deterministically patterned biomimetic human iPSC-derived hepatic model via rapid 3D bioprinting. *Proceedings of the National Academy of Sciences of the United States of America*. 113 (8), 2206–2211. doi:10.1073/PNAS.1524510113/.

Ma, Z., Holle, A.W., Melde, K., Qiu, T., Poeppel, K., Mauricio Kadiri, V., Fischer, P., Ma, Z., Melde, K., Qiu, T., Poeppel, K., Kadiri, V.M., Fischer, P. & Holle, A.W. (2020a) Acoustic holographic cell patterning in a biocompatible hydrogel. *Advanced Materials*. 32 (4), 1904181. doi:10.1002/ADMA.201904181.

Ma, Z., Koo, S., Finnegan, M.A., Loskill, P., Huebsch, N., Marks, N.C., Conklin, B.R., Grigoropoulos, C.P. & Healy, K.E. (2014) Three-dimensional filamentous human diseased cardiac tissue model. *Biomaterials*. 35 (5), 1367–1377. doi:10.1016/J.BIOMATERIALS.2013.10.052.

Ma, Z., Melde, K., Athanassiadis, A.G., Schau, M., Richter, H., Qiu, T. & Fischer, P. (2020b) Spatial ultrasound modulation by digitally controlling microbubble arrays. *Nature Communications.* 11 (1), 1–7. doi:10.1038/s41467-020-18347-2.

Macarthur, J.W., Purcell, B.P., Shudo, Y., Cohen, J.E., Fairman, A., Trubelja, A., Patel, J., Hsiao, P., Yang, E., Lloyd, K., Hiesinger, W., Atluri, P., Burdick, J.A. & Woo, Y.J. (2013) Sustained release of engineered stromal cell-derived factor 1-α from injectable hydrogels effectively recruits endothelial progenitor cells and preserves ventricular function after myocardial infarction. *Circulation*. 128 (11 Suppl 1). doi:10.1161/CIRCULATIONAHA.112.000343.

Maitra, J., Shukla, V.K. & Kumar Shukla, V. (2014) Cross-linking in hydrogels-a review. *American Journal of Polymer Science*. (2), 25–31. doi:10.5923/j.ajps.20140402.01.

Maiullari, F., Costantini, M., Milan, M., Pace, V., Chirivì, M., Maiullari, S., Rainer, A., Baci, D., Marei, H.E.-S., Seliktar, D., Gargioli, C., Bearzi, C. & Rizzi, R. (2018) A multi-cellular 3D bioprinting approach for vascularized heart tissue engineering based on HUVECs and iPSC-derived cardiomyocytes. *Scientific reports*. 8 (1), 13532. doi:10.1038/s41598-018-31848-x.

Malikmammadov, E., Tanir, T.E., Kiziltay, A., Hasirci, V. & Hasirci, N. (2018) PCL and PCL-based materials in biomedical applications. *Journal of Biomaterials Science, Polymer Edition*. 29 (7–9), 863–893. doi:10.1080/09205063.2017.1394711.

Mancuso, A., Barone, A., Cristiano, M.C., Cianflone, E., Fresta, M. & Paolino, D. (2020) Cardiac stem cell-loaded delivery systems: a new challenge for myocardial tissue regeneration. *International Journal of Molecular Sciences*. 21 (20), 1–21. doi:10.3390/IJMS21207701.

Mannhardt, I., Eder, A., Dumotier, B., Prondzynski, M., Kr-amer, E., Traebert, M., Flenner, F., Stathopoulou, K., Lemoine, M.D., Carrier, L., Christ, T., Eschenhagen, T. & Hansen, A. (2017) Blinded contractility analysis in hiPSC-cardiomyocytes in engineered heart tissue format: comparison with human atrial trabeculae. *Toxicological Sciences*. 158 (1), 164–175. doi:10.1093/TOXSCI/KFX081.

Marks, A.R. (2003) Calcium and the heart: a question of life and death. *The Journal of Clinical Investigation*. 111 (5), 597–600. doi:10.1172/JCI18067.

Martinez Villegas, K., Rasouli, R. & Tabrizian, M. (2022) Enhancing metabolic activity and differentiation potential in adipose mesenchymal stem cells via high-resolution surface-acoustic-wave contactless patterning. *Microsystems & Nanoengineering*. 8 (1), 1–14. doi:10.1038/s41378-022-00415-w.

di Marzio, N., Ananthanarayanan, P., Guex, A.G., Alini, M., Riganti, C. & Serra, T. (2022) Sound-based assembly of a microcapillary network in a saturn-like tumor model for drug testing. *Materials Today Bio*. 16. doi:10.1016/J.MTBIO.2022.100357.

Mattapally, S., Zhu, W., Fast, V.G., Gao, L., Worley, C., Kannappan, R., Borovjagin, A. v. & Zhang, J. (2018) Cardiac regeneration and repair: spheroids of cardiomyocytes derived from human-induced

pluripotent stem cells improve recovery from myocardial injury in mice. *American Journal of Physiology - Heart and Circulatory Physiology*. 315 (2), 327. doi:10.1152/AJPHEART.00688.2017.

Mayfield, A.E., Tilokee, E.L., Latham, N., McNeill, B., Lam, B.K., Ruel, M., Suuronen, E.J., Courtman, D.W., Stewart, D.J. & Davis, D.R. (2014) The effect of encapsulation of cardiac stem cells within matrix-enriched hydrogel capsules on cell survival, post-ischemic cell retention and cardiac function. *Biomaterials*. 35 (1), 133–142. doi:10.1016/J.BIOMATERIALS.2013.09.085.

McNally, L.A., Altamimi, T.R., Fulghum, K. & Hill, B.G. (2021) Considerations for using isolated cell systems to understand cardiac metabolism and biology. *Journal of Molecular and Cellular Cardiology*. 153, 26. doi:10.1016/J.YJMCC.2020.12.007.

Mei, X. & Cheng, K. (2020) Recent Development in Therapeutic Cardiac Patches. *Frontiers in Cardiovascular Medicine*. 7, 610364. doi:10.3389/FCVM.2020.610364.

Meinert, C., Kaemmerer, E., Martine, L.C., Yue, K., Levett, P.A., Klein, T.J., W Melchels, F.P., Loessner, D., Khademhosseini, A. & Hutmacher, D.W. (2016) Functionalization, preparation and use of cell-laden gelatin methacryloyl-based hydrogels as modular tissue culture platforms. *Nature protocols*, 11(4),727-746. doi:10.1038/nprot.2016.037.

Meireles, A.B., Corrêa, D.K., da Silveira, J.V.W., Millás, A.L.G., Bittencourt, E., de Brito-Melo, G.E.A. & González-Torres, L.A. (2018) Trends in polymeric electrospun fibers and their use as oral biomaterials. *Experimental Biology and Medicine*. 243 (8), 665. doi:10.1177/1535370218770404.

Melde, K., Mark, A.G., Qiu, T. & Fischer, P. (2016) Holograms for acoustics. *Nature*. 537 (7621), 518–522. doi:10.1038/nature19755.

Melde, K., Shi, M., Kremer, H., Seneca, S., Frey, C., Platzman, I., Degel, C., Schmitt, D., Schölkopf, B. & Fischer, P. (2022) Directed acoustic assembly in 3D. *arXiv preprint*. doi:10.48550/arxiv.2210.07153.

Menasché, P. (2020) Cell therapy with human esc-derived cardiac cells: clinical perspectives. *Frontiers in Bioengineering and Biotechnology*. 8, 1241. doi:10.3389/FBIOE.2020.601560/BIBTEX.

Miki, K., Uenaka, H., Saito, A., Miyagawa, S., Sakaguchi, T., Higuchi, T., Shimizu, T., Okano, T., Yamanaka, S. & Sawa, Y. (2012) Bioengineered myocardium derived from induced pluripotent stem cells improves cardiac function and attenuates cardiac remodeling following chronic myocardial infarction in rats. *Stem Cells Translational Medicine*. 1 (5), 430. doi:10.5966/SCTM.2011-0038.

Millard, D., Dang, Q., Shi, H., Zhang, X., Strock, C., et al. (2018) Cross-site reliability of human induced pluripotent stem cell-derived cardiomyocyte based safety assays using microelectrode arrays: results from a blinded CiPA pilot study. *Toxicological Sciences*. 164 (2), 550–562. doi:10.1093/TOXSCI/KFY110.

Mills, R.J., Parker, B.L., Quaife-Ryan, G.A., Voges, H.K., Needham, E.J., Bornot, A., Ding, M., Andersson, H., Polla, M., Elliott, D.A., Drowley, L., Clausen, M., Plowright, A.T., Barrett, I.P., Wang, Q.D., James, D.E., Porrello, E.R. & Hudson, J.E. (2019) Drug screening in human PSC-cardiac organoids identifies pro-proliferative compounds acting via the mevalonate pathway. *Cell Stem Cell*. 24 (6), 895-907.e6. doi:10.1016/J.STEM.2019.03.009.

Minami, I., Yamada, K., Otsuji, T.G., Yamamoto, T., Shen, Y., Otsuka, S., Kadota, S., Morone, N., Barve, M., Asai, Y., Tenkova-Heuser, T., Heuser, J.E., Uesugi, M., Aiba, K. & Nakatsuji, N. (2012) A small molecule that promotes cardiac differentiation of human pluripotent stem cells under defined, cytokine- and xeno-free conditions. *Cell reports*. 2 (5), 1448–1460. doi:10.1016/J.CELREP.2012.09.015.

Minter-Dykhouse, K., Nelson, T.J. & Folmes, C.D.L. (2022) Uncoupling of proliferative capacity from developmental stage during directed cardiac differentiation of pluripotent stem cells. *Stem Cells and Development*. 31 (17–18), 521–528. doi:10.1089/SCD.2022.0041.

Miri, A.K., Mirzaee, I., Hassan, S., Mesbah Oskui, S., Nieto, D., Khademhosseini, A. & Zhang, Y.S. (2019) Effective bioprinting resolution in tissue model fabrication. *Lab on a Chip*. 19 (11), 2019–2037. doi:10.1039/C8LC01037D.

Mishina, Y., Suzuki, A., Gilbert, D.J., Copeland, N.G., Jenkins, N.A., Ueno, N. & Behringer, R.R. (1995) Genomic organization and chromosomal location of the mouse type I BMP-2/4 receptor. *Biochemical and biophysical research communications*. 206 (1), 310–317. doi:10.1006/BBRC.1995.1043.

Mitcheson, J.S., Hancox, J.C. & Levi, A.J. (1996) Action potentials, ion channel currents and transverse tubule density in adult rabbit ventricular myocytes maintained for 6 days in cell culture. *Pflugers Archiv : European Journal of Physiology*. 431 (6), 814–827. doi:10.1007/S004240050073.

Mohamed, T.M.A., Ang, Y.S., Radzinsky, E., Zhou, P., Huang, Y., Elfenbein, A., Foley, A., Magnitsky, S. & Srivastava, D. (2018) Regulation of cell cycle to stimulate adult cardiomyocyte proliferation and cardiac regeneration. *Cell*. 173 (1), 104-116.e12. doi:10.1016/J.CELL.2018.02.014.

Monteiro, N., Thrivikraman, G., Athirasala, A., Tahayeri, A., França, C.M., Ferracane, J.L. & Bertassoni, L.E. (2018) Photopolymerization of cell-laden gelatin methacryloyl hydrogels using a dental curing light for regenerative dentistry. *Dental Materials*. 34 (3), 389–399. doi:10.1016/J.DENTAL.2017.11.020.

Montero-Calle, P., Flandes-Iparraguirre, M., Mountris, K., S de la Nava, A., Laita, N., Rosales, R.M., Iglesias-García, O., de-Juan-Pardo, E.M., Atienza, F., Fernández-Santos, M.E., Peña, E., Doblaré, M., Gavira, J.J., Fernández-Avilés, F., Prósper, F., Pueyo, E. & Mazo, M.M. (2022) Fabrication of human myocardium using multidimensional modelling of engineered tissues. *Biofabrication*. 14 (4), 045017. doi:10.1088/1758-5090/AC8CB3.

Moretti, A., Bellin, M., Welling, A., Jung, C.B., Lam, J.T., Bott-Flügel, L., Dorn, T., Goedel, A., Höhnke, C., Hofmann, F., Seyfarth, M., Sinnecker, D., Schömig, A. & Laugwitz, K.-L. (2010) Patient-specific induced pluripotent stem-cell models for long-QT syndrome. *New England Journal of Medicine*. 363 (15), 1397–1409. doi:10.1056/NEJMOA0908679.

Mukai, N., Akahori, T., Komaki, M., Li, Q., Kanayasu-Toyoda, T., Ishii-Watabe, A., Kobayashi, A., Yamaguchi, T., Abe, M., Amagasa, T. & Morita, I. (2008) A comparison of the tube forming potentials of early and late endothelial progenitor cells. *Experimental Cell Research*. 314 (3), 430–440. doi:10.1016/J.YEXCR.2007.11.016.

Mummery, C., Ward-van Oostwaard, D., Doevendans, P., Spijker, R., van den Brink, S., Hassink, R., van der Heyden, M., Opthof, T., Pera, M., Brutel de la Riviere, A., Passier, R. & Tertoolen, L. (2003) Differentiation of human embryonic stem cells to cardiomyocytes: role of coculture with visceral endoderm-like cells. *Circulation*. 107 (21), 2733–2740. doi:10.1161/01.CIR.0000068356.38592.68.

Mummery, C.L., Campostrini, G., Windt, L.M., van Meer, B.J. & Bellin, M. (2021) Cardiac tissues from stem cells new routes to maturation and cardiac regeneration. *Circulation Research*. 128, 775–801. doi:10.1161/CIRCRESAHA.121.318183.

Muthukrishnan, L. (2022) An overview on electrospinning and its advancement toward hard and soft tissue engineering applications. *Colloid and Polymer Science*. 300 (8), 875–901. doi:10.1007/S00396-022-04997-9.

Naito, A.T., Shiojima, I., Akazawa, H., Hidaka, K., Morisaki, T., Kikuchi, A. & Komuro, I. (2006) Developmental stage-specific biphasic roles of Wnt/β-catenin signaling in cardiomyogenesis and hematopoiesis. *Proceedings of the National Academy of Sciences of the United States of America*. 103 (52), 19812–19817. doi:10.1073/PNAS.0605768103.

Nakane, T., Masumoto, H., Tinney, J.P., Yuan, F., Kowalski, W.J., Ye, F., LeBlanc, A.J., Sakata, R., Yamashita, J.K. & Keller, B.B. (2017) Impact of cell composition and geometry on human induced pluripotent stem cells-derived engineered cardiac tissue. *Scientific Reports*. 7 (1), 45641. doi:10.1038/srep45641.

Nakazato, T., Kawamura, T., Uemura, T., Liu, L., Li, J., Sasai, M., Harada, A., Ito, E., Iseoka, H., Toda, K., Sawa, Y. & Miyagawa, S. (2022) Engineered three-dimensional cardiac tissues maturing in a rotating wall vessel bioreactor remodel diseased hearts in rats with myocardial infarction. *Stem Cell Reports*. 17, 1170–1182. doi:10.1016/j.stemcr.2022.03.012.

Napiwocki, B.N., Lang, D., Stempien, A., Zhang, J., Vaidyanathan, R., Makielski, J.C., Eckhardt, L.L., Glukhov, A. v., Kamp, T.J. & Crone, W.C. (2021) Aligned human cardiac syncytium for *in vitro* analysis of electrical, structural, and mechanical readouts. *Biotechnology and Bioengineering*. 118 (1), 442–452. doi:10.1002/BIT.27582.

Naseer, S.M., Manbachi, A., Samandari, M., Walch, P., Gao, Y., Zhang, Y.S., Davoudi, F., Wang, W., Abrinia, K., Cooper, J.M., Khademhosseini, A. & Shin, S.R. (2017) Surface acoustic waves induced micropatterning of cells in gelatin methacryloyl (GelMA) hydrogels. *Biofabrication*. 9 (1), 015020. doi:10.1088/1758-5090/aa585e.

Natarajan, A., Stancescu, M., Dhir, V., Armstrong, C., Sommerhage, F., Hickman, J.J. & Molnar, P. (2011) Patterned cardiomyocytes on microelectrode arrays as a functional, high information content drug screening platform. *Biomaterials*. 32 (18), 4267–4274. doi:10.1016/j.biomaterials.2010.12.022.

Nele, V., Wojciechowski, J.P., Armstrong, J.P.K., Stevens, M.M., Nele, V., Wojciechowski, J.P., Armstrong, J.P.K. & Stevens, M.M. (2020) Tailoring gelation mechanisms for advanced hydrogel applications. *Advanced Functional Materials*. 30 (42), 2002759. doi:10.1002/ADFM.202002759.

Nestor, C.E., Ottaviano, R., Reinhardt, D., Cruickshanks, H.A., Mjoseng, H.K., McPherson, R.C., Lentini, A., Thomson, J.P., Dunican, D.S., Pennings, S., Anderton, S.M., Benson, M. & Meehan, R.R. (2015) Rapid reprogramming of epigenetic and transcriptional profiles in mammalian culture systems. *Genome biology*. 16 (1), 11. doi:10.1186/s13059-014-0576-y.

Nichols, M.K., Krishna Kumar, R., Bassindale, P.G., Tian, L., Barnes, A.C., Drinkwater, B.W., Patil, A.J., Mann, S., Nichols, M.K., Krishna Kumar, R., Tian, L., Patil, A.J., Mann, S., Bassindale, P.G., Barnes, A.C. & Drinkwater, B.W. (2018) Fabrication of micropatterned dipeptide hydrogels by acoustic trapping of stimulus-responsive coacervate droplets. *Small*. 14 (26), 1800739. doi:10.1002/SMLL.201800739.

Nielles-Vallespin, S., Khalique, Z., Ferreira, P.F., de Silva, R., Scott, A.D., Kilner, P., McGill, L.A., Giannakidis, A., Gatehouse, P.D., Ennis, D., Aliotta, E., Al-Khalil, M., Kellman, P., Mazilu, D., Balaban, R.S., Firmin, D.N., Arai, A.E. & Pennell, D.J. (2017) Assessment of myocardial microstructural dynamics by in vivo diffusion tensor cardiac magnetic resonance. *Journal of the American College of Cardiology*. 69 (6), 661–676. doi:10.1016/J.JACC.2016.11.051.

Noshadi, I., Hong, S., Sullivan, K.E., Shirzaei Sani, E., Portillo-Lara, R., Tamayol, A., Shin, S.R., Gao, A.E., Stoppel, W.L., Black, L.D., Khademhosseini, A. & Annabi, N. (2017) *In vitro* and *in vivo* analysis of visible light crosslinkable gelatin methacryloyl (GelMA) hydrogels. *Biomaterials Science*. 5 (10), 2093–2105. doi:10.1039/C7BM00110J.

Nunes, S.S., Miklas, J.W., Liu, J., Aschar-Sobbi, R., Xiao, Y., Zhang, B., Jiang, J., Massé, S., Gagliardi, M., Hsieh, A., Thavandiran, N., Laflamme, M.A., Nanthakumar, K., Gross, G.J., Backx, P.H., Keller, G. & Radisic, M. (2013) Biowire: a new platform for maturation of human pluripotent stem cell derived cardiomyocytes. *Nature methods*. 10 (8), 781. doi:10.1038/NMETH.2524.

Nunez-Toldra, R., Kirwin, T., Ferraro, E., Pitoulis, F.G., Nicastro, L., Bardi, I., Kit-Anan, W., Gorelik, J., Simon, A.R. & Terracciano, C.M. (2022) Mechanosensitive molecular mechanisms of myocardial fibrosis in living myocardial slices. *ESC Heart Failure*. 9 (2), 1400–1412. doi:10.1002/EHF2.13832.

Nussbaum, J., Minami, E., Laflamme, M.A., Virag, J.A.I., Ware, C.B., Masino, A., Muskheli, V., Pabon, L., Reinecke, H. & Murry, C.E. (2007) Transplantation of undifferentiated murine embryonic stem cells in the heart: teratoma formation and immune response. *The FASEB Journal*. 21 (7), 1345–1357. doi:10.1096/FJ.06-6769COM.

Obergrussberger, A., Goetze, T.A., Brinkwirth, N., Becker, N., Friis, S., Rapedius, M., Haarmann, C., Rinke-Weiß, I., Stölzle-Feix, S., Brüggemann, A., George, M. & Fertig, N. (2018) An update on the advancing high-throughput screening techniques for patch clamp-based ion channel screens: implications for drug discovery. *Expert Opinion On Drug Discovery*. 13 (3), 269–277. doi:10.1080/17460441.2018.1428555.

Olofsson, K., Carannante, V., Ohlin, M., Frisk, T., Kushiro, K., Takai, M., Lundqvist, A., Önfelt, B., & Wiklund, M. (2018). Acoustic formation of multicellular tumor spheroids enabling on-chip functional and structural imaging. *Lab on a Chip*, *18*(16), 2466–2476. https://doi.org/10.1039/C8LC00537K

Onódi, Z., Visnovitz, T., Kiss, B., Hambalkó, S., Koncz, A., et al. (2022) Systematic transcriptomic and phenotypic characterization of human and murine cardiac myocyte cell lines and primary cardiomyocytes reveals serious limitations and low resemblances to adult cardiac phenotype. *Journal of Molecular and Cellular Cardiology*. 165, 19–30. doi:10.1016/J.YJMCC.2021.12.007.

O'Shea, C., Kabir, S.N., Holmes, A.P., Lei, M., Fabritz, L., Rajpoot, K. & Pavlovic, D. (2020) Cardiac optical mapping – state-of-the-art and future challenges. *The International Journal of Biochemistry & Cell Biology*. 126, 105804. doi:10.1016/J.BIOCEL.2020.105804.

Otsuji, T.G., Kurose, Y., Suemori, H., Tada, M. & Nakatsuji, N. (2012) Dynamic link between histone H3 acetylation and an increase in the functional characteristics of human ESC/iPSC-derived cardiomyocytes. *PloS one*. 7 (9). doi:10.1371/JOURNAL.PONE.0045010.

Ou, L., Li, W., Zhang, Y., Wang, W., Liu, J., et al. (2011) Intracardiac injection of matrigel induces stem cell recruitment and improves cardiac functions in a rat myocardial infarction model. *Journal of Cellular and Molecular Medicine*. 15 (6), 1310–1318. doi:10.1111/J.1582-4934.2010.01086.X.

Ovsianikov, A., Mühleder, S., Torgersen, J., Li, Z., Qin, X.H., van Vlierberghe, S., Dubruel, P., Holnthoner, W., Redl, H., Liska, R. & Stampfl, J. (2014) Laser photofabrication of cell-containing hydrogel constructs. *Langmuir : the ACS journal of surfaces and colloids*. 30 (13), 3787–3794. doi:10.1021/LA402346Z.

Paige, S.L., Osugi, T., Afanasiev, O.K., Pabon, L., Reinecke, H. & Murry, C.E. (2010) Endogenous Wnt/beta-catenin signaling is required for cardiac differentiation in human embryonic stem cells. *PloS one*. 5 (6). doi:10.1371/JOURNAL.PONE.0011134.

Parhi, R. (2017) Cross-linked hydrogel for pharmaceutical applications: a review. *Advanced Pharmaceutical Bulletin*. 7 (4), 515. doi:10.15171/APB.2017.064.

Parikh, S.S., Blackwell, D.J., Gomez-Hurtado, N., Frisk, M., Wang, L., Kim, K., Dahl, C.P., Fiane, A., Tønnessen, T., Kryshtal, D.O., Louch, W.E. & Knollmann, B.C. (2017) Thyroid and glucocorticoid hormones promote functional t-tubule development in human-induced pluripotent stem cell-derived cardiomyocytes. *Circulation Research*. 121 (12), 1323–1330. doi:10.1161/CIRCRESAHA.117.311920/-/DC1.

Park, S.J., Kim, R.Y., Park, B.W., Lee, S., Choi, S.W., Park, J.H., Choi, J.J., Kim, S.W., Jang, J., Cho, D.W., Chung, H.M., Moon, S.H., Ban, K. & Park, H.J. (2019) Dual stem cell therapy synergistically improves cardiac function and vascular regeneration following myocardial infarction. *Nature Communications*. 10 (1). doi:10.1038/s41467-019-11091-2.

Passier, R., van Laake, L.W. & Mummery, C.L. (2008) Stem-cell-based therapy and lessons from the heart. *Nature.* 453 (7193), 322–329. doi:10.1038/nature07040.

Pauklin, S. & Vallier, L. (2013) The cell-cycle state of stem cells determines cell fate propensity. *Cell*. 155 (1), 135. doi:10.1016/J.CELL.2013.08.031.

Peña, B., Laughter, M., Jett, S., Rowland, T.J., Taylor, M.R.G., Mestroni, L. & Park, D. (2018) Injectable hydrogels for cardiac tissue engineering. *Macromolecular bioscience*. 18 (6), e1800079. doi:10.1002/MABI.201800079.

Peng, H., Shindo, K., Donahue, R.R. & Abdel-Latif, A. (2021) Cardiac cell therapy: insights into the mechanisms of tissue repair. *International Journal of Molecular Sciences*. 22 (3), 1–15. doi:10.3390/IJMS22031201.

Peng, Y., Gregorich, Z.R., Valeja, S.G., Zhang, H., Cai, W., Chen, Y.C., Guner, H., Chen, A.J., Schwahn, D.J., Hacker, T.A., Liu, X. & Ge, Y. (2014) Top-down proteomics reveals concerted reductions in myofilament and Z-disc protein phosphorylation after acute myocardial infarction. *Molecular & Cellular Proteomics*. 13 (10), 2752. doi:10.1074/MCP.M114.040675.

Pepelanova, I., Kruppa, K., Scheper, T. & Lavrentieva, A. (2018) Gelatin-methacryloyl (GelMA) hydrogels with defined degree of functionalization as a versatile toolkit for 3D cell culture and extrusion bioprinting. *Bioengineering*. 5 (3). doi:10.3390/BIOENGINEERING5030055.

Perbellini, F., Watson, S.A., Scigliano, M., Alayoubi, S., Tkach, S., Bardi, I., Quaife, N., Kane, C., Dufton, N.P., Simon, A., Sikkel, M.B., Faggian, G., Randi, A.M., Gorelik, J., Harding, S.E. & Terracciano, C.M. (2018) Investigation of cardiac fibroblasts using myocardial slices. *Cardiovascular Research*. 114 (1), 77–89. doi:10.1093/CVR/CVX152.

Pham, Q.P., Sharma, U. & Mikos, A.G. (2006) Electrospun poly (ε-caprolactone) microfiber and multilayer nanofiber/microfiber scaffolds: Characterization of scaffolds and measurement of cellular infiltration. *Biomacromolecules*. 7 (10), 2796–2805. doi:10.1021/BM060680J.

Pianezzi, E., Altomare, C., Bolis, S., Balbi, C., Torre, T., Rinaldi, A., Camici, G.G., Barile, L. & Vassalli, G. (2020) Role of somatic cell sources in the maturation degree of human induced pluripotent stem cell-derived cardiomyocytes. *Biochimica et Biophysica Acta- Molecular Cell Research*. 1867 (3), 118538. doi:10.1016/J.BBAMCR.2019.118538.

Pillekamp, F., Reppel, M., Rubenchyk, O., Pfannkuche, K., Matzkies, M., Bloch, W., Sreeram, N., Brockmeier, K., Hescheler, J., Ju¨, J. & Hescheler, J. (2007) Force measurements of human embryonic stem cell-derived cardiomyocytes in an *in vitro* transplantation model. *Stem Cells*. 25 (1), 174–180. doi:10.1634/STEMCELLS.2006-0094.

Pioner, J.M., Santini, L., Palandri, C., Martella, D., Lupi, F., et al. (2019) Optical investigation of action potential and calcium handling maturation of hipsc-cardiomyocytes on biomimetic substrates. *International Journal of Molecular Sciences*. 20 (15), 3799. doi:10.3390/IJMS20153799.

Pitoulis, F.G., Hasan, W., Papadaki, M., Clavere, N.G., Perbellini, F., Harding, S.E., Kirk, J.A., Boateng, S.Y., de Tombe, P.P. & Terracciano, C.M. (2020a) Intact myocardial preparations reveal intrinsic transmural heterogeneity in cardiac mechanics. *Journal of Molecular and Cellular Cardiology*. 141, 11–16. doi:10.1016/J.YJMCC.2020.03.007.

Pitoulis, F.G., Nunez-Toldra, R., Xiao, K., Kit-Anan, W., Mitzka, S., Jabbour, R.J., Harding, S.E., Perbellini, F., Thum, T., de Tombe, P.P. & Terracciano, C.M. (2022) Remodelling of adult cardiac tissue subjected to physiological and pathological mechanical load in vitro. *Cardiovascular Research*. 118 (3), 814–827. doi:10.1093/CVR/CVAB084.

Pitoulis, F.G., Watson, S.A., Perbellini, F. & Terracciano, C.M. (2020b) Myocardial slices come to age: an intermediate complexity in vitro cardiac model for translational research. *Cardiovascular Research*. 116 (7), 1275–1287. doi:10.1093/CVR/CVZ341.

Polonchuk, L., Chabria, M., Badi, L., Hoflack, J.C., Figtree, G., Davies, M.J. & Gentile, C. (2017) Cardiac spheroids as promising in vitro models to study the human heart microenvironment. *Scientific Reports*. 7 (1). doi:10.1038/s41598-017-06385-8.

Pong, T., Adams, W.J., Bray, M.A., Feinberg, A.W., Sheehy, S.P., Werdich, A.A. & Parker, K.K. (2011) Hierarchical architecture influences calcium dynamics in engineered cardiac muscle. *Experimental biology and medicine (Maywood, N.J.)*. 236 (3), 366–373. doi:10.1258/EBM.2010.010239.

Poorna, M.R., Jayakumar, R., Chen, J.P. & Mony, U. (2021) Hydrogels: A potential platform for induced pluripotent stem cell culture and differentiation. *Colloids and Surfaces B: Biointerfaces*. 207, 111991. doi:10.1016/J.COLSURFB.2021.111991.

Pothineni, N.V.K., Subramany, S., Kuriakose, K., Shirazi, L.F., Romeo, F., Shah, P.K. & Mehta, J.L. (2017) Infections, atherosclerosis, and coronary heart disease. *European Heart Journal*. 38 (43), 3195–3201. doi:10.1093/EURHEARTJ/EHX362.

Pozo, M.R., Meredith, G.W. & Entcheva, E. (2022) Human iPSC-cardiomyocytes as an experimental model to study epigenetic modifiers of electrophysiology. *Cells*. 11 (2). doi:10.3390/CELLS11020200.

Primo, G.A., Mata, A., Primo, G.A. & Mata, A. (2021) 3D patterning within hydrogels for the recreation of functional biological environments. *Advanced Functional Materials*. 31 (16), 2009574. doi:10.1002/ADFM.202009574.

Qin, X., Wu, Y., Liu, S., Yang, L., Yuan, H., Cai, S., Flesch, J., Li, Z., Tang, Y., Li, X., Zhuang, Y., You, C., Liu, C. & Yu, C. (2022) Surface modification of polycaprolactone scaffold with improved biocompatibility and controlled growth factor release for enhanced stem cell differentiation. *Frontiers in Bioengineering and Biotechnology*. 9, 1217. doi:10.3389/FBIOE.2021.802311/BIBTEX.

Qu, Y., Han, B., Gao, B., Bose, S., Gong, Y., Wawrowsky, K., Giuliano, A.E., Sareen, D. & Cui, X. (2017) Differentiation of human induced pluripotent stem cells to mammary-like organoids. *Stem Cell Reports*. 8 (2), 205–215. doi:10.1016/J.STEMCR.2016.12.023.

Quent, V.M.C., Loessner, D., Friis, T., Reichert, J.C. & Hutmacher, D.W. (2010) Discrepancies between metabolic activity and DNA content as tool to assess cell proliferation in cancer research. *Journal of cellular and molecular medicine*. 14 (4), 1003–1013. doi:10.1111/J.1582-4934.2010.01013.X.

Radzisheuskaya, A., le Bin Chia, G., dos Santos, R.L., Theunissen, T.W., Castro, L.F.C., Nichols, J. & Silva, J.C.R. (2013) A defined Oct4 level governs cell state transitions of pluripotency entry and differentiation into all embryonic lineages. *Nature Cell Biology*. 15 (6), 579–590. doi:10.1038/ncb2742.

Rajala, K., Pekkanen-Mattila, M. & Aalto-Setälä, K. (2011) Cardiac differentiation of pluripotent stem cells. *Stem Cells International*. 383709. doi:10.4061/2011/383709.

Rajamohan, D., Kalra, S., Duc Hoang, M., George, V., Staniforth, A., Russell, H., Yang, X. & Denning, C. (2016) Automated electrophysiological and pharmacological evaluation of human pluripotent stem cell-derived cardiomyocytes. *Stem Cells and Development*. 25 (6), 439–452. doi:10.1089/SCD.2015.0253.

Rampersad, S.N. (2012) Multiple applications of alamar blue as an indicator of metabolic function and cellular health in cell viability bioassays. *Sensors*. 12 (9), 12347–12360. doi:10.3390/S120912347.

Rao, C., Prodromakis, T., Kolker, L., Chaudhry, U.A.R., Trantidou, T., Sridhar, A., Weekes, C., Camelliti, P., Harding, S.E., Darzi, A., Yacoub, M.H., Athanasiou, T. & Terracciano, C.M. (2013) The effect of microgrooved culture substrates on calcium cycling of cardiac myocytes derived from human induced pluripotent stem cells. *Biomaterials*. 34 (10), 2399–2411. doi:10.1016/J.BIOMATERIALS.2012.11.055.

Reboud, J., Bourquin, Y., Wilson, R., Pall, G.S., Jiwaji, M., Pitt, A.R., Graham, A., Waters, A.P. & Cooper, J.M. (2012) Shaping acoustic fields as a toolset for microfluidic manipulations in diagnostic technologies. *Proceedings of the National Academy of Sciences of the United States of America*. 109 (38), 15162–15167. doi:10.1073/PNAS.1206055109.

Rees, C.M., Yang, J.H., Santolini, M., Lusis, A.J., Weiss, J.N. & Karma, A. (2018) The Ca^{2+} transient as a feedback sensor controlling cardiomyocyte ionic conductances in mouse populations. *eLife*. 7. doi:10.7554/ELIFE.36717.

Ren, T., Chen, P., Gu, L., Ogut, M.G. & Demirci, U. (2020) Soft ring-shaped cellu-robots with simultaneous locomotion in batches. *Advanced Materials*. 32 (8), 1905713. doi:10.1002/ADMA.201905713.

Reppel, M., Pillekamp, F., Brockmeier, K., Matzkies, M., Bekcioglu, A., Lipke, T., Nguemo, F., Bonnemeier, H. & Hescheler, J. (2005) The electrocardiogram of human embryonic stem cell-derived cardiomyocytes. *Journal of Electrocardiology*. 38 (4), 166–170. doi:10.1016/J.JELECTROCARD.2005.06.029.

Richards, D.J., Li, Y., Kerr, C.M., Yao, J., Beeson, G.C., Coyle, R.C., Chen, X., Jia, J., Damon, B., Wilson, R., Starr Hazard, E., Hardiman, G., Menick, D.R., Beeson, C.C., Yao, H., Ye, T. & Mei, Y. (2020) Human cardiac organoids for the modelling of myocardial infarction and drug cardiotoxicity. *Nature Biomedical Engineering*. 4 (4), 446–462. doi:10.1038/s41551-020-0539-4.

Riegler, J., Tiburcy, M., Ebert, A., Tzatzalos, E., Raaz, U., Abilez, O.J., Shen, Q., Kooreman, N.G., Neofytou, E., Chen, V.C., Wang, M., Meyer, T., Tsao, P.S., Connolly, A.J., Couture, L.A., Gold, J.D., Zimmermann, W.H. & Wu, J.C. (2015) human engineered heart muscles engraft and survive long-term in a rodent myocardial infarction model. *Circulation Research*. 117 (8), 720. doi:10.1161/CIRCRESAHA.115.306985.

Ritzau-Reid, K. (2022) Scaffold guided 3D brain organoid models. *PhD Thesis*. Imperial College London.

Robertson, C., Tran, D.D. & George, S.C. (2013) *Concise review: maturation phases of human pluripotent stem cell-derived cardiomyocytes.* Stem cells: Dayton, Ohio. 31 (5), 829–837. doi:10.1002/STEM.1331.

Rodriguez, M.L., Beussman, K.M., Chun, K.S., Walzer, M.S., Yang, X., Murry, C.E. & Sniadecki, N.J. (2019) Substrate stiffness, cell anisotropy, and cell-cell contact contribute to enhanced structural and calcium handling properties of human embryonic stem cell-derived cardiomyocytes. *ACS Biomaterials Science and Engineering*. 5 (8), 3876–3888. doi:10.1021/ACSBIOMATERIALS.8B01256/.

Ronaldson-Bouchard, K., Ma, S.P., Yeager, K., Chen, T., Song, L.J., Sirabella, D., Morikawa, K., Teles, D., Yazawa, M. & Vunjak-Novakovic, G. (2018) Advanced maturation of human cardiac tissue grown from pluripotent stem cells. *Nature*. 556 (7700), 239–243. doi:10.1038/s41586-018-0016-3.

Rossi, G., Broguiere, N., Miyamoto, M., Boni, A., Guiet, R., Girgin, M., Kelly, R.G., Kwon, C. & Lutolf, M.P. (2021) Capturing cardiogenesis in gastruloids. *Cell Stem Cell*. 28 (2), 230-240.e6. doi:10.1016/J.STEM.2020.10.013.

Roth, E.A., Xu, T., Das, M., Gregory, C., Hickman, J.J. & Boland, T. (2004) Inkjet printing for high-throughput cell patterning. *Biomaterials*. 25 (17), 3707–3715. doi:10.1016/J.BIOMATERIALS.2003.10.052.

Roth, G.M., Bader, D.M., Bader, D.M. & Pfaltzgraff, E.R. (2014) Isolation and physiological analysis of mouse cardiomyocytes. *Journal of Visualized Experiments : JoVE*. (91), 51109. doi:10.3791/51109.

Ruan, J.L., Tulloch, N.L., Razumova, M. v., Saiget, M., Muskheli, V., Pabon, L., Reinecke, H., Regnier, M. & Murry, C.E. (2016) Mechanical Stress conditioning and electrical stimulation promote contractility and force maturation of induced pluripotent stem cell-derived human cardiac tissue. *Circulation*. 134 (20), 1557–1567. doi:10.1161/CIRCULATIONAHA.114.014998.

Ryan, T.J., Kopanitsa, M. v, Indersmitten, T., Nithianantharajah, J., Afinowi, N.O., Pettit, C., Stanford, L.E., Sprengel, R., Saksida, L.M., Bussey, T.J., O'Dell, T.J., Grant, S.G.N. & Komiyama, N.H. (2013) Evolution of GluN2A/B cytoplasmic domains diversified vertebrate synaptic plasticity and behaviour. *Nature Neuroscience*. 16 (1), 25–32. doi:10.1038/nn.3277.

Saffitz, J.E., Kanter, H.L., Green, K.G., Tolley, T.K. & Beyer, E.C. (1994) Tissue-specific determinants of anisotropic conduction velocity in canine atrial and ventricular myocardium. *Circulation Research*. 74 (6), 1065–1070. doi:10.1161/01.RES.74.6.1065.

Said, N. S., & Sarbon, N. M. (2022). Physical and mechanical characteristics of gelatin-based films as a potential food packaging material: a review. *Membranes*, *12*(5), 442. https://doi.org/10.3390/MEMBRANES12050442

Saidy, N. T., Fernández-Colino, A., Heidari, B. S., Kent, R., Vernon, M., Bas, O., Mulderrig, S., Lubig, A., Carlos Rodríguez-Cabello, J., Doyle, B., Hutmacher, D. W., De-Juan-Pardo, E. M., Mela, P. (2022). Spatially heterogeneous tubular scaffolds for in situ heart valve tissue engineering using melt electrowriting. *Advanced Functional Materials*, *32*(21), 2110716. https://doi.org/10.1002/ADFM.202110716

Saidy, N. T., Wolf, F., Bas, O., Keijdener, H., Hutmacher, D. W., Mela, P., De-Juan-Pardo, E. M., Saidy, N. T., Bas, O., Hutmacher, D. W., De-Juan-Pardo, E. M., Wolf, F., Keijdener, H., & Mela, P. (2019). Biologically inspired scaffolds for heart valve tissue engineering via melt electrowriting. *Small*, *15*(24), 1900873. https://doi.org/10.1002/SMLL.201900873

Saito, Y., Nakamura, K., Yoshida, M., Sugiyama, H., Ohe, T., Kurokawa, J., Furukawa, T., Takano, M., Nagase, S., Morita, H., Kusano, K.F. & Ito, H. (2015) Enhancement of spontaneous activity by hcn4 overexpression in mouse embryonic stem cell-derived cardiomyocytes - a possible biological pacemaker. *PLoS ONE*. 10 (9). doi:10.1371/JOURNAL.PONE.0138193.

Sala, L., van Meer, B.J., Tertoolen, L.G.J., Bakkers, J., Bellin, M., et al. (2018) Musclemotion: A versatile open software tool to quantify cardiomyocyte and cardiac muscle contraction in vitro and in vivo. *Circulation Research*. 122 (3), e5–e16. doi:10.1161/CIRCRESAHA.117.312067/-/DC1.

Saleem, U., Meer, B.J.V., Katili, P.A., Yusof, N.A.N.M., Mannhardt, I., et al. (2020) Blinded, multicenter evaluation of drug-induced changes in contractility using human-induced pluripotent stem cell-derived cardiomyocytes. *Toxicological Sciences*. 176 (1), 103–123. doi:10.1093/TOXSCI/KFAA058.

Saludas, L., Pascual-Gil, S., Prósper, F., Garbayo, E. & Blanco-Prieto, M. (2017) Hydrogel based approaches for cardiac tissue engineering. *International Journal of Pharmaceutics*. 523 (2), 454–475. doi:10.1016/J.IJPHARM.2016.10.061.

Sanganalmath, S.K. & Bolli, R. (2013) Cell therapy for heart failure: a comprehensive overview of experimental and clinical studies, current challenges, and future directions. *Circulation research*. 113 (6), 810–834. doi:10.1161/CIRCRESAHA.113.300219.

Santoso, M.R., Ikeda, G., Tada, Y., Jung, J.H., Vaskova, E., Sierra, R.G., Gati, C., Goldstone, A.B., von Bornstaedt, D., Shukla, P., Wu, J.C., Wakatsuki, S., Joseph Woo, Y. & Yang, P.C. (2020) Exosomes from induced pluripotent stem cell–derived cardiomyocytes promote autophagy for myocardial repair. *Journal of the American Heart Association*. 9 (6). doi:10.1161/JAHA.119.014345.

Sastri, V.R. (2022) Three-dimensional printing, wearables, medical textiles, adhesives, and coatings. *Plastics in Medical Devices*. 381–421. doi:10.1016/B978-0-323-85126-8.00004-7.

Satin, J., Kehat, I., Caspi, O., Huber, I., Arbel, G., Itzhaki, I., Magyar, J., Schroder, E.A., Perlman, I. & Gepstein, L. (2004) Mechanism of spontaneous excitability in human embryonic stem cell derived cardiomyocytes. *The Journal of Physiology*. 559 (2), 479. doi:10.1113/JPHYSIOL.2004.068213.

Sato, K., Sinclair, J.E., Sadeghirad, H., Fraser, J.F., Short, K.R. & Kulasinghe, A. (2021) Cardiovascular disease in SARS-CoV-2 infection. *Clinical & Translational Immunology*. 10 (9), e1343. doi:10.1002/CTI2.1343.

Saunders, A., Faiola, F. & Wang, J. (2013) Concise review: pursuing self-renewal and pluripotency with the stem cell factor Nanog. *Stem Cells*. 31 (7), 1227–1236. doi:10.1002/STEM.1384.

Savarese, G. & Lund, L.H. (2017) Global public health burden of heart failure. *Cardiac Failure Review*. 3 (1), 7. doi:10.15420/CFR.2016:25:2.

Schaaf, S., Shibamiya, A., Mewe, M., Eder, A., Stöhr, A., Hirt, M.N., Rau, T., Zimmermann, W.H., Conradi, L., Eschenhagen, T. & Hansen, A. (2011) Human engineered heart tissue as a versatile tool in basic research and preclinical toxicology. *PLOS ONE*. 6 (10), e26397. doi:10.1371/JOURNAL.PONE.0026397.

Schlange, T., Andrée, B., Arnold, H.H. & Brand, T. (2000) BMP2 is required for early heart development during a distinct time period. *Mechanisms of development*. 91 (1–2), 259–270. doi:10.1016/S0925-4773(99)00311-1.

Schneider, G. & Otto, K. (2012) *In vitro* and *in vivo* studies on the use of Histoacryl® as a soft tissue glue. *European Archives of Oto-Rhino-Laryngology*. 269 (7), 1783–1789. doi:10.1007/S00405-011-1868-4.

Schultheiss, T.M., Burch, J.B.E. & Lassar, A.B. (1997) A role for bone morphogenetic proteins in the induction of cardiac myogenesis. *Genes & development*. 11 (4), 451–462. doi:10.1101/GAD.11.4.451.

Sehnert, A.J., Huq, A., Weinstein, B.M., Walker, C., Fishman, M. & Stainier, D.Y.R. (2002) Cardiac troponin T is essential in sarcomere assembly and cardiac contractility. *Nature Genetics*. 31 (1), 106–110. doi:10.1038/ng875.

Serpooshan, V., Chen, P., Wu, H., Lee, S., Sharma, A., Hu, D.A., Venkatraman, S., Ganesan, A.V., Usta, O.B., Yarmush, M., Yang, F., Wu, J.C., Demirci, U. & Wu, S.M. (2017) Bioacoustic-enabled patterning of human iPSC-derived cardiomyocytes into 3D cardiac tissue. *Biomaterials*. 131, 47–57. doi:10.1016/J.BIOMATERIALS.2017.03.037.

Shadrin, I.Y., Allen, B.W., Qian, Y., Jackman, C.P., Carlson, A.L., Juhas, M.E. & Bursac, N. (2017) Cardiopatch platform enables maturation and scale-up of human pluripotent stem cell-derived engineered heart tissues. *Nature Communications*. 8 (1). doi:10.1038/s41467-017-01946-x.

Shafy, A., Fink, T., Zachar, V., Lila, N., Carpentier, A. & Chachques, J.C. (2013) Development of cardiac support bioprostheses for ventricular restoration and myocardial regeneration. *European journal of cardio-thoracic surgery*. 43 (6), 1211–1219. doi:10.1093/EJCTS/EZS480.

Shah, V., Patel, S. & Shah, J. (2022) Emerging role of Piezo ion channels in cardiovascular development. *Developmental Dynamics*. 251 (2), 276–286. doi:10.1002/DVDY.401.

Shahverdi, M., Seifi, S., Akbari, A., Mohammadi, K., Shamloo, A. & Movahhedy, M.R. (2022) Melt electrowriting of PLA, PCL, and composite PLA/PCL scaffolds for tissue engineering application. *Scientific Reports*. 12 (1), 1–16. doi:10.1038/s41598-022-24275-6.

Sharma, A., Wu, J.C. & Wu, S.M. (2013) Induced pluripotent stem cell-derived cardiomyocytes for cardiovascular disease modeling and drug screening. *Stem Cell Research & Therapy*. 4 (6), 150. doi:10.1186/SCRT380.

Sheikh, F., Ross, R.S. & Chen, J. (2009) Cell-cell connection to cardiac disease. *Trends in cardiovascular medicine*. 19 (6), 182. doi:10.1016/J.TCM.2009.12.001.

Sheng, X., Reppel, M., Nguemo, F., Mohammad, F.I., Kuzmenkin, A., Hescheler, J. & Pfannkuche, K. (2012) Human pluripotent stem cell-derived cardiomyocytes: response to TTX and lidocain reveals strong cell to cell variability. *PLoS ONE*. 7 (9), 45963. doi:10.1371/JOURNAL.PONE.0045963.

Shiba, Y., Gomibuchi, T., Seto, T., Wada, Y., Ichimura, H., et al. (2016) Allogeneic transplantation of iPS cell-derived cardiomyocytes regenerates primate hearts. *Nature*. 538 (7625), 388–391. doi:10.1038/nature19815.

Silva, A.C., Matthys, O.B., Joy, D.A., Kauss, M.A., Natarajan, V., Lai, M.H., Turaga, D., Blair, A.P., Alexanian, M., Bruneau, B.G. & McDevitt, T.C. (2021) Co-emergence of cardiac and gut tissues promotes cardiomyocyte maturation within human iPSC-derived organoids. *Cell Stem Cell*. 28 (12), 2137-2152.e6. doi:10.1016/J.STEM.2021.11.007.

Silva, J., Nichols, J., Theunissen, T.W., Guo, G., van Oosten, A.L., Barrandon, O., Wray, J., Yamanaka, S., Chambers, I. & Smith, A. (2009) Nanog Is the Gateway to the Pluripotent Ground State. *Cell*. 138 (4), 722–737. doi:10.1016/J.CELL.2009.07.039.

Simič, R., Mandal, J., Zhang, K. & Spencer, N.D. (2021) Oxygen inhibition of free-radical polymerization is the dominant mechanism behind the “mold effect” on hydrogels. *Soft Matter*. 17 (26), 6394–6403. doi:10.1039/D1SM00395J.

Singelyn, J.M. & Christman, K.L. (2011) Modulation of Material Properties of a Decellularized Myocardial Matrix Scaffold. *Macromolecular Bioscience*. 11 (6), 731–738. doi:10.1002/MABI.201000423.

Sivasubramaniyan, K., Harichandan, A., Schilbach, K., Mack, A.F., Bedke, J., Stenzl, A., Kanz, L., Niederfellner, G. & Bühring, H.J. (2015) Expression of stage-specific embryonic antigen-4 (SSEA-4) defines spontaneous loss of epithelial phenotype in human solid tumor cells. *Glycobiology*. 25 (8). doi:10.1093/glycob/cwv032.

Speidel, A.T., Stuckey, D.J., Chow, L.W., Jackson, L.H., Noseda, M., Abreu Paiva, M., Schneider, M.D. & Stevens, M.M. (2017) Multimodal hydrogel-based platform to deliver and monitor cardiac progenitor/stem cell engraftment. *ACS Central Science*. 3 (4), 338–348. doi:10.1021/ACSCENTSCI.7B00039.

Spicer, C.D., Gelmi, A., Ponder Jr, J.F., Vilar, R., Serio, A., et al. (2020) An electroactive oligo-EDOT platform for neural tissue engineering. *Advanced Functional Materials*. 30 (42), 2003710. doi:10.1002/ADFM.202003710.

Stevens, K.R., Pabon, L., Muskheli, V. & Murry, C.E. (2009) Scaffold-free human cardiac tissue patch created from embryonic stem cells. *Tissue engineering. Part A*. 15 (6), 1211–1222. doi:10.1089/TEN.TEA.2008.0151.

Stevens, L.M., Tagnon, C. & Page, Z.A. (2022) ‘Invisible’ digital light processing 3D printing with near infrared light. *ACS Appl. Mater. Interfaces*. 14. doi:10.1021/acsami.1c22046.

Stillitano, F., Hansen, J., Kong, C.W., Karakikes, I., Funck-Brentano, C., Geng, L., Scott, S., Reynier, S., Wu, M., Valogne, Y., Desseaux, C., Salem, J.E., Jeziorowska, D., Zahr, N., Li, R., Iyengar, R., Hajjar, R.J. & Hulot, J.S. (2017) Modeling susceptibility to drug-induced long QT with a panel of subject-specific induced pluripotent stem cells. *eLife*. 6. doi:10.7554/ELIFE.19406.

Subbiah, T., Bhat, G.S., Tock, R.W., Parameswaran, S. & Ramkumar, S.S. (2005) Electrospinning of nanofibers. *Journal of Applied Polymer Science*. 96 (2), 557–569. doi:10.1002/APP.21481.

Sultana, N., Zhang, L., Yan, J., Chen, J., Cai, W., Razzaque, S., Jeong, D., Sheng, W., Bu, L., Xu, M., Huang, G.Y., Hajjar, R.J., Zhou, B., Moon, A. & Cai, C.L. (2015) Resident c-kit+ cells in the heart are not cardiac stem cells. *Nature Communications.* 6 (1), 1–10. doi:10.1038/ncomms9701.

Sun, A., He, X., Ji, X., Hu, D., Pan, M., Zhang, L. & Qian, Z. (2021) Current research progress of photopolymerized hydrogels in tissue engineering. *Chinese Chemical Letters*. 32 (7), 2117–2126. doi:10.1016/J.CCLET.2021.01.048.

Sun, N., Yazawa, M., Liu, J., Han, L., Sanchez-Freire, V., et al. (2012) Patient-specific induced pluripotent stem cells as a model for familial dilated cardiomyopathy. *Science Translational Medicine*. 4 (130). doi:10.1126/SCITRANSLMED.3003552/

Sun, X. & Nunes, S.S. (2015) Overview of hydrogel-based strategies for application in cardiac tissue regeneration. *Biomedical Materials*. 10 (3), 34005. doi:10.1088/1748-6041/10/3/034005.

Sun, X., Wu, J., Qiang, B., Romagnuolo, R., Gagliardi, M., Keller, G., Laflamme, M.A., Li, R.K. & Nunes, S.S. (2020) Transplanted microvessels improve pluripotent stem cell-derived cardiomyocyte

engraftment and cardiac function after infarction in rats. *Science Translational Medicine*. 12 (562), 2992. doi:10.1126/SCITRANSLMED.AAX2992.

Tachibana, M., Amato, P., Sparman, M., Gutierrez, N.M., Tippner-Hedges, R., et al. (2013) Human embryonic stem cells derived by somatic cell nuclear transfer. *Cell*. 153 (6), 1228. doi:10.1016/J.CELL.2013.05.006.

Takahashi, K. & Yamanaka, S. (2006) Induction of pluripotent stem cells from mouse embryonic and adult fibroblast cultures by defined factors. *Cell*. 126(4), 663-676. doi:10.1016/j.cell.2006.07.024.

Takebe, T., Zhang, B. & Radisic, M. (2017) synergistic engineering: organoids meet organs-on-a-chip. *Cell Stem Cell*. 21 (3), 297–300. doi:10.1016/J.STEM.2017.08.016.

Tan, Y., Kong, C. wing, Chen, S., Cheng, S.H., Li, R.A. & Sun, D. (2012) Probing the mechanobiological properties of human embryonic stem cells in cardiac differentiation by optical tweezers. *Journal of Biomechanics*. 45 (1), 123–128. doi:10.1016/J.JBIOMECH.2011.09.007.

Tan, Y., Sun, D., Cheng, S.H. & Li, R.A. (2011) Robotic cell manipulation with optical tweezers for biomechanical characterization. *Proceedings - IEEE International Conference on Robotics and Automation*. 4104–4109. doi:10.1109/ICRA.2011.5979577.

Tang, J., Wang, J., Huang, K., Ye, Y., Su, T., Qiao, L., Hensley, M.T., Caranasos, T.G., Zhang, J., Gu, Z. & Cheng, K. (2018) Cardiac cell–integrated microneedle patch for treating myocardial infarction. *Science Advances*. 4 (11). doi:10.1126/SCIADV.AAT9365.

Teo, B.K.K., Ankam, S., Chan, L.Y. & Yim, E.K.F. (2010) Nanotopography/mechanical induction of stem-cell differentiation. *Methods in Cell Biology*. 98, 241–294. doi:10.1016/S0091-679X(10)98011-4.

Terracciano, C. & Guymer, S. (2019) *Heart of the matter: key concepts in cardiovascular science*. London, United Kingdom: Springer. Retrieved from: https://link.springer.com/content/pdf/10.1007/978-3-030-24219-0.pdf

Tibbitt, M.W. & Anseth, K.S. (2009) Hydrogels as extracellular matrix mimics for 3D cell culture. *Biotechnology and Bioengineering*. 103 (4), 655–663. doi:10.1002/BIT.22361.

Tsao, C.J., Taraballi, F., Pandolfi, L., Velasquez-Mao, A.J., Ruano, R., Tasciotti, E. & Jacot, J.G. (2018) Controlled release of small molecules for cardiac differentiation of pluripotent stem cells. *Tissue Engineering - Part A*. 24 (23–24), 1798–1807. doi:10.1089/TEN.TEA.2018.0054.

Tulloch, N.L., Muskheli, V., Razumova, M. v., Korte, F.S., Regnier, M., Hauch, K.D., Pabon, L., Reinecke, H. & Murry, C.E. (2011) Growth of engineered human myocardium with mechanical loading and vascular coculture. *Circulation Research*. 109 (1), 47–59. doi:10.1161/CIRCRESAHA.110.237206.

Tzahor, E. & Lassar, A.B. (2001) Wnt signals from the neural tube block ectopic cardiogenesis. *Genes & Development*. 15 (3), 255. doi:10.1101/GAD.871501.

Uchino, K. (2012) Piezoelectric ceramics for transducers. *Ultrasonic Transducers: Materials and Design for Sensors, Actuators and Medical Applications*. 70–116. doi:10.1533/9780857096302.1.70.

Ueno, S., Weidinger, G., Osugi, T., Kohn, A.D., Golob, J.L., Pabon, L., Reinecke, H., Moon, R.T. & Murry, C.E. (2007) Biphasic role for Wnt/β-catenin signaling in cardiac specification in zebrafish and embryonic stem cells. *Proceedings of the National Academy of Sciences of the United States of America*. 104 (23), 9685–9690. doi:10.1073/PNAS.0702859104.

Unnithan, A.R., Arathyram, R.S. & Kim, C.S. (2015) Electrospinning of polymers for tissue engineering. *Nanotechnology Applications for Tissue Engineering*. 45–55. doi:10.1016/B978-0-323-32889-0.00003-0.

Velagaleti, R.S. & Vasan, R.S. (2007) Heart failure in the 21st century: is it a coronary artery disease problem or hypertension problem? *Cardiology Clinics*. 25 (4), 487. doi:10.1016/J.CCL.2007.08.010.

van der Velden, J., Klein, L.J., Zaremba, R., Boontje, N.M., Huybregts, M.A.J.M., Stooker, W., Eijsman, L., de Jong, J.W., Visser, C.A., Visser, F.C. & Stienen, G.J.M. (2001) Effects of calcium, inorganic phosphate, and pH on isometric force in single skinned cardiomyocytes from donor and failing human hearts. *Circulation*. 104 (10), 1140–1146. doi:10.1161/HC3501.095485.

van Mil, A., Castilho, M., Chirico, N., Ainsworth, M., Dokter, I., Maas, R. G. C. ;, Buikema, J. W., Malda, J., & Sluijter, J. P. G. (2022). Next generation bioengineered human myocardium. *Tissue Engineering Part A*. 28 (1), 654. https://doi.org/10.1089/TEN.TEA.2022.29025.ABSTRACTS

Verkerk, A.O. & Wilders, R. (2015) Pacemaker activity of the human sinoatrial node: an update on the effects of mutations in HCN4 on the hyperpolarization-activated current. *International Journal of Molecular Sciences*. 16 (2), 3071–3094. doi:10.3390/IJMS16023071.

Vliegen, H.W., van der Laarse, A., Cornelisse, C.J. & Eulderink, F. (1991) Myocardial changes in pressure overload-induced left ventricular hypertrophy. A study on tissue composition, polyploidization and multinucleation. *European Heart Journal*. 12 (4), 488–494. doi:10.1093/OXFORDJOURNALS.EURHEARTJ.A059928.

Vreeker, A., van Stuijvenberg, L., Hund, T.J., Mohler, P.J., Nikkels, P.G.J. & van Veen, T.A.B. (2014) Assembly of the cardiac intercalated disk during pre- and postnatal development of the human heart. *PLOS ONE*. 9 (4), e94722. doi:10.1371/JOURNAL.PONE.0094722.

Vunjak-Novakovic, G. (2017) Tissue engineering of the heart: an evolving paradigm. *The Journal of thoracic and cardiovascular surgery*. 153 (3), 593. doi:10.1016/J.JTCVS.2016.08.057.

Wang, B.X., Kit-Anan, W. & Terracciano, C.M.N. (2018) many cells make life work-multicellularity in stem cell-based cardiac disease modelling. *International journal of molecular sciences*. 19 (11). doi:10.3390/IJMS19113361.

Wang, C.S., Virgilio, N., Wood-Adams, P.M. & Heuzey, M.C. (2018) A gelation mechanism for gelatin/polysaccharide aqueous mixtures. *Food Hydrocolloids*. 79, 462–472. doi:10.1016/J.FOODHYD.2018.01.016.

Wang, G., McCain, M.L., Yang, L., He, A., Pasqualini, F.S., et al. (2014) Modeling the mitochondrial cardiomyopathy of Barth syndrome with induced pluripotent stem cell and heart-on-chip technologies. *Nature Medicine*. 20 (6), 616–623. doi:10.1038/nm.3545.

Wang, J., Greene, S.B. & Martin, J.F. (2011) Bmp Signaling in Congenital Heart Disease: New Developments and Future Directions. *Birth defects research. Part A, Clinical and molecular teratology*. 91 (6), 441. doi:10.1002/BDRA.20785.

Wang, L., Liu, L., Li, X., Magome, N., Agladze, K. & Chen, Y. (2013) Multi-electrode monitoring of guided excitation in patterned cardiomyocytes. *Microelectronic Engineering*. 111, 267–271. doi:10.1016/J.MEE.2012.11.018.

Wang, W., Chen, J., Li, M., Jia, H., Han, X., Zhang, J., Zou, Y., Tan, B., Liang, W., Shang, Y., Xu, Q., Sigen, A., Wang, W., Mao, J., Gao, X., Fan, G. & Liu, W. (2019) Rebuilding postinfarcted cardiac

functions by injecting TIIA@PDA nanoparticle-cross-linked ros-sensitive hydrogels. *ACS Applied Materials and Interfaces*. 11 (3), 2880–2890. doi:10.1021/ACSAMI.8B20158.

Wang, W., Liu, X., Xie, Y., Zhang, H., Yu, W., Xiong, Y., Xie, W. & Ma, X. (2006) Microencapsulation using natural polysaccharides for drug delivery and cell implantation. *Journal of Materials Chemistry*. 16 (32), 3252–3267. doi:10.1039/B603595G.

Wang, Z., Oron, E., Nelson, B., Razis, S. & Ivanova, N. (2012) Distinct lineage specification roles for NANOG, OCT4, and SOX2 in human embryonic stem cells. *Cell stem cell*. 10 (4), 440–454. doi:10.1016/J.STEM.2012.02.016.

Wang, Z. & Zhe, J. (2011) Recent advances in particle and droplet manipulation for lab-on-a-chip devices based on surface acoustic waves. *Lab on a Chip*. 11 (7), 1280–1285. doi:10.1039/C0LC00527D.

Wanjare, M., Hou, L., Nakayama, K.H., Kim, J.J., Mezak, N.P., Abilez, O.J., Tzatzalos, E., Wu, J.C. & Huang, N.F. (2017) Anisotropic microfibrous scaffolds enhance the organization and function of cardiomyocytes derived from induced pluripotent stem cells. *Biomaterials Science*. 5 (8), 1567–1578. doi:10.1039/C7BM00323D.

Watson, S.A., Duff, J., Bardi, I., Zabielska, M., Atanur, S.S., Jabbour, R.J., Simon, A., Tomas, A., Smolenski, R.T., Harding, S.E., Perbellini, F. & Terracciano, C.M. (2019) Biomimetic electromechanical stimulation to maintain adult myocardial slices in vitro. *Nature Communications.* 10 (1), 1–15. doi:10.1038/s41467-019-10175-3.

Watson, S.A., Scigliano, M., Bardi, I., Ascione, R., Terracciano, C.M. & Perbellini, F. (2017) Preparation of viable adult ventricular myocardial slices from large and small mammals. *Nature*. 12 (12), 2623–2639. doi:10.1038/nprot.2017.139.

Watson, S.A., Terracciano, C.M. & Perbellini, F. (2019) Myocardial slices: an intermediate complexity platform for translational cardiovascular research. *Cardiovascular Drugs and Therapy*. 33 (2), 239–244. doi:10.1007/S10557-019-06853-5.

Weinberger, F., Breckwoldt, K., Pecha, S., Kelly, A., Geertz, B., Starbatty, J., Yorgan, T., Cheng, K.H., Lessmann, K., Stolen, T., Marielle, S.C., Smith, G., Reichenspurner, H., Hansen, A. & Eschenhagen, T. (2016) Cardiac repair in guinea pigs with human engineered heart tissue from induced pluripotent stem cells. *Science Translational Medicine*. 8 (363). doi:10.1126/scitranslmed.aaf8781.

Wendel, J.S., Ye, L., Tao, R., Zhang, J., Zhang, J., Kamp, T.J. & Tranquillo, R.T. (2015) functional effects of a tissue-engineered cardiac patch from human induced pluripotent stem cell-derived cardiomyocytes in a rat infarct model. *Stem Cells Translational Medicine*. 4 (11), 1324–1332. doi:10.5966/SCTM.2015-0044.

White, S.M., Constantin, P.E. & Claycomb, W.C. (2004) Cardiac physiology at the cellular level: Use of cultured HL-1 cardiomyocytes for studies of cardiac muscle cell structure and function. *American Journal of Physiology - Heart and Circulatory Physiology*. 286 (3 55-3). doi:10.1152/AJPHEART.00986.2003/.

Wiechert, S., El-Armouche, A., Rau, T., Zimmermann, W.H. & Eschenhagen, T. (2003) 24-h Langendorff-perfused neonatal rat heart used to study the impact of adenoviral gene transfer. *American journal of physiology. Heart and circulatory physiology*. 285 (2). doi:10.1152/AJPHEART.00856.2002.

Wilson, A.J., Sands, G.B. & Ennis, D.B. (2021) Analysis of location-dependent cardiomyocyte branching. *Lecture Notes in Computer Science*. 12738, 189–199. doi:10.1007/978-3-030-78710-3_19.

Winslow, R. & Trayanova, N.A. (2011) Whole-heart modeling. *Circulation Research*. 108 (1), 113–128. doi:10.1161/CIRCRESAHA.110.223610.

World Health Organisation (WHO) (2021) *Cardiovascular diseases (CVDs)*. 11 June 2021. Cardiovascular diseases factsheet. https://www.who.int/news-room/fact-sheets/detail/cardiovascular-diseases-(cvds) [Accessed: 16 December 2022].

Wu, P., Deng, G., Sai, X., Guo, H., Huang, H. & Zhu, P. (2021) Maturation strategies and limitations of induced pluripotent stem cell-derived cardiomyocytes. *Bioscience Reports*. 41 (6), 20200833. doi:10.1042/BSR20200833/226678.

Wu, P., Sai, X., Li, Z., Ye, X., Jin, L., Liu, G., Li, G., Yang, P., Zhao, M., Zhu, S., Liu, N. & Zhu, P. (2023) Maturation of induced pluripotent stem cell-derived cardiomyocytes and its therapeutic effect on myocardial infarction in mouse. *Bioactive Materials*. 20, 286–305. doi:10.1016/J.BIOACTMAT.2022.05.024.

Wu, T. & Liu, W. (2022) Functional hydrogels for the treatment of myocardial infarction. *NPG Asia Materials*. 14 (1), 1–15. doi:10.1038/s41427-021-00330-y.

Xu, C., Wang, C., Zheng, T., Hu, Q. & Bai, C. (2018) Surface acoustic wave (SAW)-induced synthesis of HKUST-1 with different morphologies and sizes. *CrystEngComm*. 20 (45), 7275–7280. doi:10.1039/C8CE01144C.

Xu, C., Wang, L., Yu, Y., Yin, F., Zhang, X., Jiang, L. & Qin, J. (2017) Bioinspired onion epithelium-like structure promotes the maturation of cardiomyocytes derived from human pluripotent stem cells. *Biomaterials science*. 5 (9), 1810–1819. doi:10.1039/C7BM00132K.

Xu, F.J., Wang, Z.H. & Yang, W.T. (2010) Surface functionalization of polycaprolactone films via surface-initiated atom transfer radical polymerization for covalently coupling cell-adhesive biomolecules. *Biomaterials*. 31 (12), 3139–3147. doi:10.1016/J.BIOMATERIALS.2010.01.032.

Xu, H., Yi, B.A., Wu, H., Bock, C., Gu, H., Lui, K.O., Park, J.H.C., Shao, Y., Riley, A.K., Domian, I.J., Hu, E., Willette, R., Lepore, J., Meissner, A., Wang, Z. & Chien, K.R. (2011) Highly efficient derivation of ventricular cardiomyocytes from induced pluripotent stem cells with a distinct epigenetic signature. *Cell Research*. 22 (1), 142–154. doi:10.1038/cr.2011.171.

Xu, X.Q., Graichen, R., Soo, S.Y., Balakrishnan, T., Bte Rahmat, S.N., Sieh, S., Tham, S.C., Freund, C., Moore, J., Mummery, C., Colman, A., Zweigerdt, R. & Davidson, B.P. (2008) Chemically defined medium supporting cardiomyocyte differentiation of human embryonic stem cells. *Differentiation; research in biological diversity*. 76 (9), 958–970. doi:10.1111/J.1432-0436.2008.00284.X.

Xu, Y., Patnaik, S., Guo, X., Li, Z., Lo, W., Butler, R., Claude, A., Liu, Z., Zhang, G., Liao, J., Anderson, P.M. & Guan, J. (2014) Cardiac differentiation of cardiosphere-derived cells in scaffolds mimicking morphology of the cardiac extracellular matrix. *Acta Biomaterialia*. 10 (8), 3449–3462. doi:10.1016/J.ACTBIO.2014.04.018.

Yagi, K., Stein, L.C., Jin, Y., Pennec, Y. & Bonello, B. (2015) Overview of hydrogel-based strategies for application in cardiac tissue regeneration. *Biomedical Materials*. 10 (3), 034005. doi:10.1088/1748-6041/10/3/034005.

Yan, S., Zhang, J., Yuan, D. & Li, W. (2017) Hybrid microfluidics combined with active and passive approaches for continuous cell separation. *Electrophoresis*. 38 (2), 238–249. doi:10.1002/ELPS.201600386.

Yang, K.C., Breitbart, A., de Lange, W.J., Hofsteen, P., Futakuchi-Tsuchida, A., Xu, J., Schopf, C., Razumova, M. v., Jiao, A., Boucek, R., Pabon, L., Reinecke, H., Kim, D.H., Ralphe, J.C., Regnier, M. & Murry, C.E. (2018) Novel adult-onset systolic cardiomyopathy due to MYH7 E848G mutation in patient-derived induced pluripotent stem cells. *JACC: Basic to Translational Science*. 3 (6), 728–740. doi:10.1016/J.JACBTS.2018.08.008.

Yang, L., Soonpaa, M.H., Adler, E.D., Roepke, T.K., Kattman, S.J., Kennedy, M., Henckaerts, E., Bonham, K., Abbott, G.W., Linden, R.M., Field, L.J. & Keller, G.M. (2008) Human cardiovascular progenitor cells develop from a KDR+ embryonic-stem-cell-derived population. *Nature*. 453 (7194), 524–528. doi:10.1038/NATURE06894.

Yang, X., Pabon, L. & Murry, C.E. (2014) Engineering adolescence. *Circulation Research*. 114 (3), 511–523. doi:10.1161/CIRCRESAHA.114.300558.

Yang, X., Rodriguez, M., Pabon, L., Fischer, K.A., Reinecke, H., Regnier, M., Sniadecki, N.J., Ruohola-Baker, H. & Murry, C.E. (2014) Tri-iodo-l-thyronine promotes the maturation of human cardiomyocytes-derived from induced pluripotent stem cells. *Journal of Molecular and Cellular Cardiology*. 72, 296–304. doi:10.1016/j.yjmcc.2014.04.005.

Yang, Y., Lei, D., Huang, S., Yang, Q., Song, B., Guo, Y., Shen, A., Yuan, Z., Li, S., Qing, F.L., Ye, X., You, Z. & Zhao, Q. (2019) Elastic 3D-printed hybrid polymeric scaffold improves cardiac remodeling after myocardial infarction. *Advanced Healthcare Materials*. 8 (10), 1900065. doi:10.1002/ADHM.201900065.

Yang, Y., Ma, T., Li, S., Zhang, Q., Huang, J., Liu, Y., Zhuang, J., Li, Y., Du, X., Niu, L., Xiao, Y., Wang, C., Cai, F. & Zheng, H. (2021) Self-navigated 3d acoustic tweezers in complex media based on time reversal. *Research*. 2021, 1–13. doi:10.34133/2021/9781394.

Yao, X., Liu, Y., Gao, J., Yang, L., Mao, D., Stefanitsch, C., Li, Y., Zhang, J., Ou, L., Kong, D., Zhao, Q. & Li, Z. (2015) Nitric oxide releasing hydrogel enhances the therapeutic efficacy of mesenchymal stem cells for myocardial infarction. *Biomaterials*. 60, 130–140. doi:10.1016/J.BIOMATERIALS.2015.04.046.

Ye, K., Takemoto, Y., Ito, A., Onda, M., Morimoto, N., Mandai, M., Takahashi, M., Kato, R. & Osakada, F. (2020) Reproducible production and image-based quality evaluation of retinal pigment epithelium sheets from human induced pluripotent stem cells. *Scientific Reports.* 10 (1), 1–15. doi:10.1038/s41598-020-70979-y.

Ye, L., Zhang, S., Greder, L., Dutton, J., Keirstead, S.A., Lepley, M., Zhang, L., Kaufman, D. & Zhang, J. (2013) Effective cardiac myocyte differentiation of human induced pluripotent stem cells requires VEGF. *PLOS ONE*. 8 (1), e53764. doi:10.1371/JOURNAL.PONE.0053764.

Yiangou, L., Grandy, R.A., Morell, C.M., Tomaz, R.A., Osnato, A., Kadiwala, J., Muraro, D., Garcia-Bernardo, J., Nakanoh, S., Bernard, W.G., Ortmann, D., McCarthy, D.J., Simonic, I., Sinha, S. & Vallier, L. (2019) Method to synchronize cell cycle of human pluripotent stem cells without affecting their fundamental characteristics. *Stem Cell Reports*. 12 (1), 165. doi:10.1016/J.STEMCR.2018.11.020.

Yoon, H.J., Shin, S.R., Cha, J.M., Lee, S.H., Kim, J.H., Do, J.T., Song, H. & Bae, H. (2016) Cold water fish gelatin methacryloyl hydrogel for tissue engineering application. *PLoS ONE*. 11 (10). doi:10.1371/JOURNAL.PONE.0163902.

Yu, J., Christman, K.L., Chin, E., Sievers, R.E., Saeed, M. & Lee, R.J. (2009) Restoration of left ventricular geometry and improvement of left ventricular function in a rodent model of chronic ischemic cardiomyopathy. *The Journal of Thoracic and Cardiovascular Surgery*. 137 (1), 180–187. doi:10.1016/J.JTCVS.2008.08.036.

Yu, T.Y., Dehghani, H., Brain, K., Syeda, F., Holmes, A.P., Kirchhof, P. & Fabritz, L. (2017) Optical mapping design for murine atrial electrophysiology. *Computer Methods in Biomechanics and Biomedical Engineering: Imaging and Visualization*. 5 (5), 368–376. doi:10.1080/21681163.2015.1081079.

Yue, K., Li, X., Schrobback, K., Sheikhi, A., Annabi, N., Leijten, J., Zhang, W., Zhang, Y.S., Hutmacher, D.W., Klein, T.J. & Khademhosseini, A. (2017) Structural analysis of photocrosslinkable methacryloyl-modified protein derivatives. *Biomaterials*. 139, 163. doi:10.1016/J.BIOMATERIALS.2017.04.050.

Zhang, D., Shadrin, I.Y., Lam, J., Xian, H.Q., Snodgrass, H.R. & Bursac, N. (2013) Tissue-engineered cardiac patch for advanced functional maturation of human ESC-derived cardiomyocytes. *Biomaterials*. 34 (23), 5813–5820. doi:10.1016/j.biomaterials.2013.04.026.

Zhang, H., Fazel, S., Tian, H., Mickle, D.A.G., Weisel, R.D., Fujii, T. & Li, R.K. (2005) Increasing donor age adversely impacts beneficial effects of bone marrow but not smooth muscle myocardial cell therapy. *American Journal of Physiology - Heart and Circulatory Physiology*. 289 (5 58-5), 2089–2096. doi:10.1152/AJPHEART.00019.2005.

Zhang, J., Wilson, G.F., Soerens, A.G., Koonce, C.H., Yu, J., Palecek, S.P., Thomson, J.A. & Kamp, T.J. (2009) Functional cardiomyocytes derived from human induced pluripotent stem cells. *Circulation Research*. 104 (4). doi:10.1161/CIRCRESAHA.108.192237.

Zhang, M., Schulte, J.S., Heinick, A., Piccini, I., Rao, J., Quaranta, R., Zeuschner, D., Malan, D., Kim, K.P., Röpke, A., Sasse, P., Araúzo-Bravo, M., Seebohm, G., Schöler, H., Fabritz, L., Kirchhof, P., Müller, F.U. & Greber, B. (2015) Universal cardiac induction of human pluripotent stem cells in two and three-dimensional formats: implications for in vitro maturation. *Stem cells (Dayton, Ohio)*. 33 (5), 1456–1469. doi:10.1002/STEM.1964.

Zhang, P., Bachman, H., Ozcelik, A. & Huang, T.J. (2020) Acoustic microfluidics. *Annual review of analytical chemistry.* 13 (1), 17. doi:10.1146/ANNUREV-ANCHEM-090919-102205.

Zhang, Y., le Friec, A., Sun, D. & Chen, M. (2022) Sinusoidal stretchable fibrous electrodes regulate cardiac contraction. *Chemical Engineering Journal.* 455,140555. doi:10.2139/SSRN.4233073.

Zhang, Z., Liang, D., Gao, X., Zhao, C., Qin, X., Xu, Y., Su, T., Sun, D., Li, W., Wang, H., Liu, B. & Cao, F. (2014) Selective inhibition of inositol hexakisphosphate kinases (IP6Ks) enhances mesenchymal stem cell engraftment and improves therapeutic efficacy for myocardial infarction. *Basic Research in Cardiology*. 109 (4), 1–14. doi:10.1007/S00395-014-0417-X.

Zhao, M.T., Ye, S., Su, J. & Garg, V. (2020) Cardiomyocyte proliferation and maturation: two sides of the same coin for heart regeneration. *Frontiers in Cell and Developmental Biology*. 8. doi:10.3389/FCELL.2020.594226.

Zhao, X., Chen, H., Xiao, D., Yang, H., Itzhaki, I., et al. (2018) Comparison of non-human primate versus human induced pluripotent stem cell-derived cardiomyocytes for treatment of myocardial infarction. *Stem Cell Reports*. 10 (2), 422–435. doi:10.1016/J.STEMCR.2018.01.002.

Zhao, Y., Rafatian, N., Feric, N.T., Cox, B.J., Aschar-Sobbi, R., et al. (2019) A platform for generation of chamber-specific cardiac tissues and disease modelling. *Cell*. 176 (4), 913-927.e18. doi:10.1016/j.cell.2018.11.042.

Zheng, Z., Tan, Y., Li, Y., Liu, Y., Yi, G., Yu, C.Y. & Wei, H. (2021) Biotherapeutic-loaded injectable hydrogels as a synergistic strategy to support myocardial repair after myocardial infarction. *Journal of Controlled Release*. 335, 216–236. doi:10.1016/J.JCONREL.2021.05.023.

Zhou, P. & Pu, W.T. (2016) Recounting cardiac cellular composition. *Circulation Research*. 118 (3), 368. doi:10.1161/CIRCRESAHA.116.308139.

Zhu, W., Zhao, M., Mattapally, S., Chen, S. & Zhang, J. (2018) CCND2 overexpression enhances the regenerative potency of human induced pluripotent stem cell–derived cardiomyocytes: remuscularization of injured ventricle. *Circulation Research*. 122 (1), 88. doi:10.1161/CIRCRESAHA.117.311504.

Zimmermann, W.H., Melnychenko, I., Wasmeier, G., Didié, M., Naito, H., Nixdorff, U., Hess, A., Budinsky, L., Brune, K., Michaelis, B., Dhein, S., Schwoerer, A., Ehmke, H. & Eschenhagen, T. (2006) Engineered heart tissue grafts improve systolic and diastolic function in infarcted rat hearts. *Nature Medicine*. 12 (4), 452–458. doi:10.1038/NM1394.

Zlabinger, K., Lukovic, D., Hemetsberger, R., Gugerell, A., Winkler, J., et al. (2018) Matrix metalloproteinase-2 impairs homing of intracoronary delivered mesenchymal stem cells in a porcine reperfused myocardial infarction: Comparison with intramyocardial cell delivery. *Frontiers in Bioengineering and Biotechnology*. 6, 35. doi:10.3389/FBIOE.2018.00035.

Zukor, K.A., Kent, D.T. & Odelberg, S.J. (2010) Fluorescent whole-mount method for visualizing three-dimensional relationships in intact and regenerating adult newt spinal cords. *Developmental dynamics : an official publication of the American Association of Anatomists*. 239 (11), 3048–3057. doi:10.1002/DVDY.22441.

Zuppinger, C. (2019) 3D cardiac cell culture: a critical review of current technologies and applications. *Frontiers in Cardiovascular Medicine*. 6, 87. doi:10.3389/FCVM.2019.00087/BIBTEX.

Zwi, L., Caspi, O., Arbel, G., Huber, I., Gepstein, A., Park, I.H. & Gepstein, L. (2009) Cardiomyocyte differentiation of human induced pluripotent stem cells. *Circulation*. 120 (15), 1513–1523. doi:10.1161/CIRCULATIONAHA.109.868885.

Zwi-Dantsis, L., Wang, B., Marijon, C., Zonetti, S., Ferrini, A., Massi, L., Stuckey, D.J., Terracciano, C.M., Stevens, M.M., Zwi-Dantsis, L., Marijon, C., Massi, L., Stevens, M.M., Wang, B., Ferrini, A., Terracciano, C.M., Zonetti, S. & Stuckey, D.J. (2020) Remote magnetic nanoparticle manipulation enables the dynamic patterning of cardiac tissues. *Advanced Materials*. 32 (6), 1904598. doi:10.1002/ADMA.201904598.